Validation and Clinical Application of Novel Coronary Imaging Methods to Assess Metallic or Bioresorbable Coronary Stents

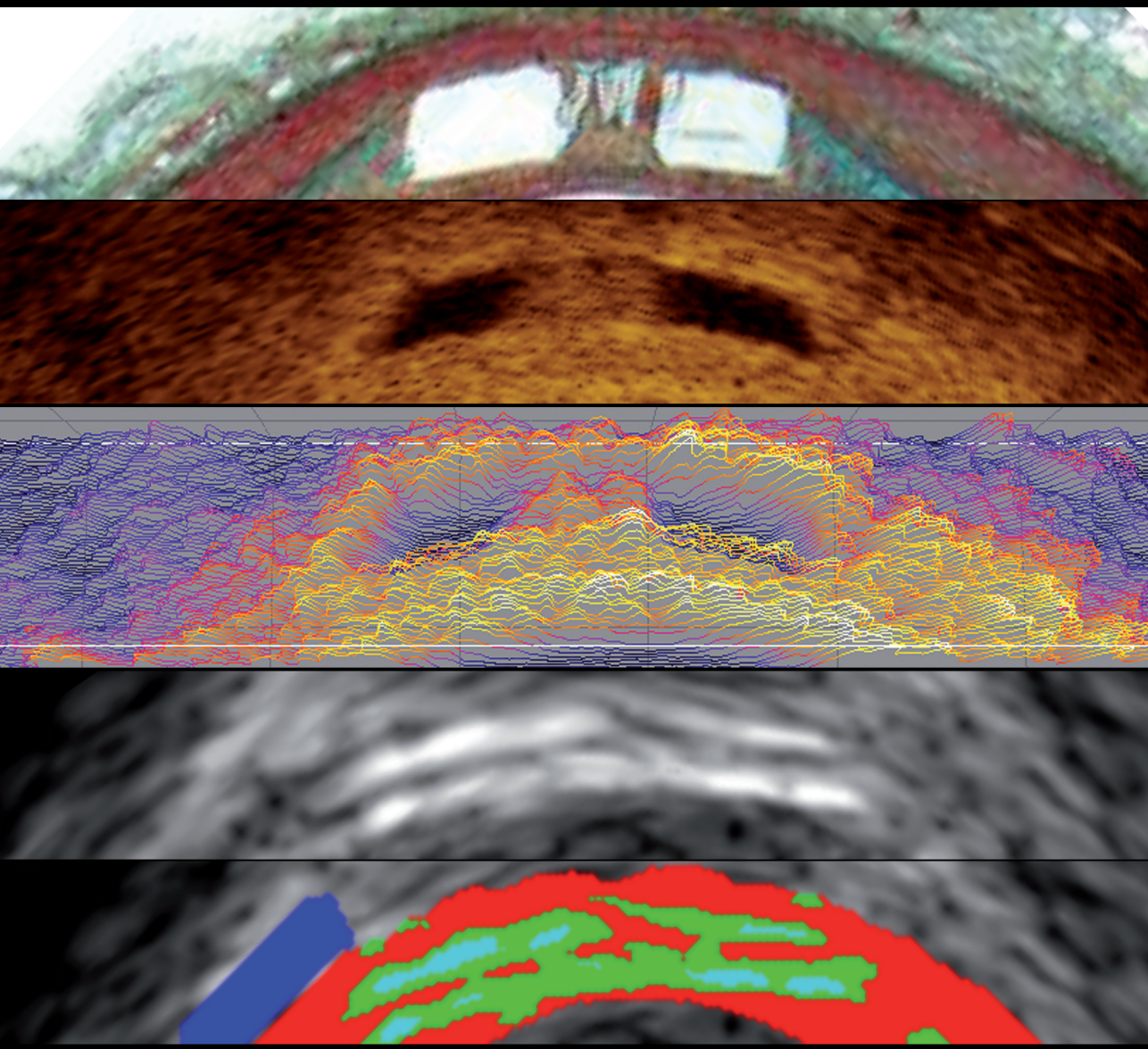

Shimpei Nakatani

Validation and Clinical Application of Novel Coronary Imaging Methods to Assess Metallic or Bioresorbable Coronary Stents

Shimpei Nakatani

Financial support by Abbott Vascular Japan for the publication of this thesis is gratefully acknowledged.

ISBN: 978-94-61-69-880-3

Validation and Clinical Application of Novel Coronary Imaging Methods to Assess Metallic or Bioresorbable Coronary Stents

Validatie en klinische toepasbaarheid van nieuwe intra-coronaire beeldvorming voor de evaluatie van metalen en oplosbare coronaire stents

Thesis

to obtain the degree of Doctor from the Erasmus University Rotterdam
by command of the rector magnificus

Prof.dr. H.A.P.Pols

and in accordance with the decision of the Doctorate Board

The public defense shall be held on
Monday the 23rd May 2016 at 13:30 o'clock

by

Shimpei Nakatani
born in Osaka, Japan

Erasmus University Rotterdam

DOCTORAL COMMITTEE

Promotor

Prof.dr. P.W.J.C. Serruys

The inner doctoral committee

Prof.dr. R.J. van Geuns

Dr. E.S. Regar

Prof.dr. J.H.C. Reiber (LUMC)

Co-promotor

Dr. Y. Onuma

To my father

TABLE OF CONTENTS

Chapter 1: Invention of methods to evaluate a bioresorbable scaffold

1.1 Automatic detection of bioresorbable scaffolds

Automatic detection of bioresorbable vascular scaffold struts in intravascular optical coherence tomography pullback runs.

Biomed Opt Express. 2014;5(10):3589-602.

Wang A, Nakatani S, Eggermont J, Onuma Y, Garcia-Garcia HM, Serruys PW, Reiber JH1, Dijkstra J.M.

[Original research paper, Impact Factor : 3.65]

1.2 Light intensity analysis of polymeric struts

Temporal evolution of strut light intensity after implantation of bioresorbable polymeric intracoronary scaffolds in the ABSORB cohort B trial-an application of a new quantitative method based on optical coherence tomography.

Circ J. 2014;78(8):1873-81.

Nakatani S, Onuma Y, Ishibashi Y, Eggermont J, Zhang YJ, Campos CM, Cho YK, Liu S, Dijkstra J, Reiber JH, Perkins L, Sheehy A, Veldhof S, Rapoza R, van Es GA, Garcia-Garcia HM, van Geuns RJ, Serruys PW; ABSORB Cohort B investigators.

[Original research paper, Impact Factor : 3.94]

1.3 Attenuation analysis of the light signal for calcified plaque

Impact of the orbital atherectomy system on a coronary calcified lesion: quantitative analysis by light attenuation in optical coherence tomography.

EuroIntervention. 2015;11(5):e1.

Sotomi Y, Shlofmitz RA, Nakatani S, Onuma Y, Serruys PW.

[Case report, Impact Factor : 3.77]

1.4 Discernment of metallic markers from calcification on MSCT

Fate of Bioresorbable Vascular Scaffold Metallic Radio-Opaque Markers at the Site of Implantation After Bioresorption.

JACC Cardiovasc Interv. 2015;8(8):1130-2.

Suwannasom P, Onuma Y, Campos CM, Nakatani S, Ishibashi Y, Tateishi H, Grundeken MJ, Stanetic B, Nieman K, Jonker H, Garcia-Garcia HM, Serruys PW; investigators of ABSORB Cohort A, B and EXTEND trials.

[Letter to the editor Impact Factor : 7.35]

Chapter 2: Comparative analysis method between a metallic and a bioresorbable device

2.1 "Apple and Apple" comparison on OCT

Comparative analysis method of permanent metallic stents (XIENCE) and bioresorbable poly-L-lactic (PLLA) scaffolds (Absorb) on optical coherence tomography at baseline and follow-up.

EuroIntervention. 2015;11(6). pii: 20150528-02.

Nakatani S, Sotomi Y, Ishibashi Y, Grundeken MJ, Tateishi H, Tenekecioglu E, Zeng Y, Suwannasom P, Regar E, Radu MD, Räber L, Bezerra H, Costa MA, Fitzgerald P, Prati F, Costa RA, Dijkstra J, Kimura T, Kozuma K, Tanabe K, Akasaka T, Di Mario C, Serruys PW, Onuma Y.

[Original research paper, Impact Factor : 3.77]

Chapter 3: Validation of the invented methods of coronary imaging

3.1 Validation of light intensity analysis of polymeric struts on OCT

Bioresorption and Vessel Wall Integration of a Fully Bioresorbable Polymeric Everolimus-Eluting Scaffold: Optical Coherence Tomography (OCT), Intravascular Ultrasound (IVUS) and Histological Study in Porcine Model with Four Years Follow-up

JACC Cardiovasc Interv. 2016:838-51.

Nakatani S, Ishibashi Y, Perkins L, Eggermont J, Sotomi Y, Grundeken M, Dijkstra J, Richard R, Virmani R, Serruys PW, Onuma Y

[Original research paper, Impact Factor : 7.35]

3.2 Validation of echogenicity analysis of polymeric struts on IVUS

Echogenicity as a surrogate for bioresorbable everolimus-eluting scaffold degradation: analysis at 1-, 3-, 6-, 12- 18, 24-, 30-, 36- and 42-month follow-up in a porcine model.

Int J Cardiovasc Imaging. 2015;31(3):471-82.

Campos CM, Ishibashi Y, Eggermont J, Nakatani S, Cho YK, Dijkstra J, Reiber JH, Sheehy A, Lane J, Kamberi M, Rapoza R, Perkins L, Garcia-Garcia HM, Onuma Y, Serruys PW.

[Original research paper, Impact Factor : 1.81]

3.3 Validation of shear flow disturbances around malapposed struts

Incomplete stent apposition causes high shear flow disturbances and delay in neointimal coverage as a function of strut to wall detachment distance: implications for the management of incomplete stent apposition.

Circ Cardiovasc Interv. 2014;7(2):180-9.

Foin N, Gutiérrez-Chico JL, Nakatani S, Torii R, Bourantas CV, Sen S, Nijjer S, Petraco R, Kousera C, Ghione M, Onuma Y, Garcia-Garcia HM, Francis DP, Wong P, Di Mario C, Davies JE, Serruys PW.

[Original research paper, Impact Factor: 6.32]

Chapter 4: Clinical Application of coronary imaging after a polymeric device implantation

4.1 Coronary artery aneurysm after a PLLA scaffold implantation

Development and receding of a coronary artery aneurysm after implantation of a fully bioresorbable scaffold.

Circulation. 2015;131(8):764-7.

Nakatani S, Ishibashi Y, Suwannasom P, Grundeken MJ, Høj Christiansen E, Onuma Y, Serruys PW; ABSORB Cohort B Investigators.

[Original research paper, Impact Factor: 15.07]

4.2 Disruption and late discontinuity after a PLLA scaffold implantation

Incidence and imaging outcomes of acute scaffold disruption and late structural discontinuity after implantation of the Absorb everolimus-eluting fully bioresorbable vascular scaffold: optical coherence tomography assessment in the ABSORB Cohort B trial.

JACC Cardiovasc Intv. 2014;7:1400-11.

Onuma Y, Serruys PW, Muramatsu T, Nakatani S, van Geuns RJ, de Bruyne B, Dudek D, Christiansen E, Smits PC, Chevalier B, McClean D, Koolen J, Windecker S, Whitbourn R, Meredith I, Garcia-Garcia HM, Veldhof S, Rapoza R, Ormiston JA.

[Original research paper, Impact Factor : 7.35]

4.3 In-Scaffold Restenosis (ISR)

Early (before 6 months), late (6-12 months) and very late (after 12 months) angiographic scaffold restenosis in the ABSORB Cohort B trial.

Eurointervention. 2015;10(11):1288-98.

Nakatani S, OnumaY, Ishibashi Y, Muramatsu T, Iqbal J, Zhang YJ, van Geuns RJ, Ormiston JA, Serruys PW; on behalf of the ABSORB Cohort B investigators.

[Original research paper, Impact Factor : 3.77]

4.4 Edge vascular response at mid-term follow-up

Scaffold and edge vascular response following implantation of everolimus-eluting bioresorbable vascular scaffold: a 3-year serial optical coherence tomography study.

JACC Cardiovasc Interv. 2014;7(12):1361-9.

Zhang YJ, Iqbal J, Nakatani S, Bourantas CV, Campos CM, Ishibashi Y, Cho YK, Veldhof S, Wang J, Onuma Y, Garcia-Garcia HM, Dudek D, van Geuns RJ, Serruys PW; ABSORB Cohort B Study Investigators.

[Original research paper, Impact Factor: 7.35]

4.5 Edge vascular response at long-term follow-up

Edge Vascular Response After Resorption of the Everolimus-Eluting Bioresorbable Vascular Scaffold: A 5-Year Serial Optical Coherence Tomography Study

Circ J. 2016 Mar 3. [Epub ahead of print]

Tateishi H, Suwannasom P, Sotomi Y, Nakatani S, Ishibashi Y, Tenekecioglu E, Abdelgani M, Cavalcante R, Zeng Y, Grundeken M, Albuquerque FN, Veldhof S, Onuma T, Serruys PW, On behalf of the investigators of the ABSORB Cohort B study Investigators.

[Original research paper, Impact Factor : 3.94]

4.6 Shielding the underlying plaque after a PLLA scaffold implantation

Bioresorbable vascular scaffold treatment induces the formation of neointimal cap that seals the underlying plaque without compromising the luminal dimensions: a concept based on serial optical coherence tomography data.

EuroIntervention. 2015;11(8):746-56.

Bourantas CV, Serruys PW, Nakatani S, Zhang YJ, Farooq V, Diletti R, Ligthart J, Sheehy A, van Geuns RJ, McClean D, Chevalier B, Windecker S, Koolen J, Ormiston J, Whitbourn R, Rapoza R, Veldhof S, Onuma Y, Garcia-Garcia HM.

[Original research paper, Impact Factor : 3.77]

4.7 Early performance of a PLLA scaffold in STEMI

Everolimus-eluting bioresorbable vascular scaffolds for treatment of patients presenting with ST-segment elevation myocardial infarction: BVS STEMI first study.

Eur Heart J. 2014;35:777-86.

Diletti R, Karanasos A, Muramatsu T, Nakatani S, Van Mieghem NM, Onuma Y, Nauta ST, Ishibashi Y, Lenzen MJ, Ligthart J, Schultz C, Regar E, de Jaegere PP, Serruys PW, Zijlstra F, van Geuns RJ.

[Original research paper, Impact Factor: 15.20]

Chapter 5: Clinical Application of coronary imaging after a metallic device implantation

5.1 Alteration of malapposed struts at 3-day follow-up in APPOSITON II Study

Incidence and potential mechanism of resolved, persistent and newly acquired malapposition three days after implantation of self-expanding or balloon-expandable stents in a STEMI population: insights from optical coherence tomography in the APPOSITION II study.

EuroIntervention. 2015;11(7). pii: 20150309-10.

Nakatani S, Onuma Y, Ishibashi Y, Karanasos A, Regar E, Garcia-Garcia HM, Tamburino C, Fajadet J, Vrolix M, Witzenbichler B, Eeckhout E, Spaulding C, Reczuch K, La Manna A, Spaargaren R, Capodanno D, Van Langenhove L, Verheye S, Serruys PW, van Geuns RJ.

[Original research paper, Impact Factor: 3.77]

5.2 Neointimal formation at mid-term follow-up in TROFI I study

Serial optical frequency domain imaging in STEMI patients: the follow-up report of TROFI study.

Eur Heart J Cardiovasc Imaging. 2014;15:987-95.

García-García HM, Muramatsu T, Nakatani S, Lee IS, Holm NR, Thuesen L, van Geuns RJ, van der Ent M, Borovicanin V, Paunovic D, Onuma Y, Serruys PW.

[Original research paper, Impact Factor : 4.11]

Introduction

Introduction

In the interventional cardiology field, intravascular imaging such as Intravascular Ultrasound (IVUS) and optical coherence tomography (OCT) has been developed to enable us detailed analysis of coronary arteries before and after intervention with a high-resolution image. Not only for the measurement of the luminal dimension and vessel device interaction, these technologies could be used for more specific analysis such as echogenicity on IVUS and light intensity on OCT, by taking the advantage of the physical properties of these imaging. As a non-invasive coronary imaging, multislice computed tomography coronary angiography (MSCT) could provide reliable assessment of the entire coronary arteries.

Implantation of a everolimus-eluting scaffold (Absorb scaffold, Abbott Vascular, Santa Clara, CA, USA) consists of a semi-crystalline poly-L-lactide (PLLA) backbone is a new approach that provides transient vessel support with drug delivery capability. Potential short- and long-term benefits of this technology have been repeatedly investigated with coronary imaging. In previous ABSORB studies of polymeric scaffolds, intravascular imaging has been used in vivo as a surrogate marker to understand the bioresorption process. However, the standardized methodology using these specific analyses (echogenicity on IVUS and light intensity on OCT) has not been established and was not validated with the histology.

In the studies of polymeric scaffolds without comparison with metallic stents, OCT methods have been developed to take advantage of the optical properties of PLLA; however, some of these were not applicable to metallic stents since images acquired by OCT after implantation of Absorb scaffold are different from those with metallic stents due to the translucency of polymeric materials. Taking into account the fact that many randomized trials comparing Absorb scaffolds and metallic stents with imaging endpoints are still ongoing, it was important to establish a standardized and comparative method for quantitative analysis on OCT.

Due to its high resolution of OCT, the assessment of stent performance assessed by OCT has become a standard in the systematic evaluation of coronary stents. However, the comparison of OCT data among different studies is still challenging by the statistical assessment. To allow a fully informed comparison of the groups, a graphical visualization where the clinically relevant units are plotted should ideally be reported.

The aims of this thesis is 1) to standardize the methodology of echogenicity on IVUS and light intensity on OCT and validate them by the comparison with histology, 2) to establish the comparative methods for assessing the metallic and polymeric device equally, 3) to develop the visualization of OCT analysis, 4) to apply these methods in clinical studies.

Chapter 1

Invention of methods to evaluate a bioresorbable scaffold

1.1 Automatic detection of bioresorbable scaffolds

Automatic detection of bioresorbable vascular scaffold struts in intravascular optical coherence tomography pullback runs.

Biomed Opt Express. 2014;5(10):3589-602.
[Original research paper, Impact Factor : 3.65]

Wang A, Nakatani S, Eggermont J, Onuma Y, Garcia-Garcia HM, Serruys PW, Reiber JH1, Dijkstra J.M.

Automatic detection of bioresorbable vascular scaffold struts in intravascular optical coherence tomography pullback runs

Ancong Wang,[1] Shimpei Nakatani,[2] Jeroen Eggermont,[1] Yoshi Onuma,[2] Hector M. Garcia-Garcia,[2] Patrick W. Serruys,[2] Johan H.C. Reiber,[1] and Jouke Dijkstra[1,*]

[1] *Division of Image Processing, Department of Radiology, Leiden University Medical Center, Leiden, Netherlands*
[2] *Cardialysis B.V. Rotterdam, Netherlands*
[*] *j.dijkstra@lumc.nl*

Abstract: Bioresorbable vascular scaffolds (BVS) have gained significant interest in both the technical and clinical communities as a possible alternative to metallic stents. For accurate BVS analysis, intravascular optical coherence tomography (IVOCT) is currently the most suitable imaging technique due to its high resolution and the translucency of polymeric BVS struts for near infrared light. However, given the large number of struts in an IVOCT pullback run, quantitative analysis is only feasible when struts are detected automatically. In this paper, we present an automated method to detect and measure BVS struts based on their black cores in IVOCT images. Validated using 3 baseline and 3 follow-up data sets, the method detected 93.7% of 4691 BVS struts correctly with 1.8% false positives. In total, the Dice's coefficient for BVS strut areas was 0.84. It concludes that this method can detect BVS struts accurately and robustly for tissue coverage measurement, malapposition detection, strut distribution analysis or 3D scaffold reconstruction.

OCIS codes: (100.6950) Tomographic image processing; (110.4500) Optical coherence tomography.

References and links

1. A. Grüntzig, "Transluminal dilatation of coronary-artery stenosis," Lancet **311**(8058), 263 (1978).
2. J. E. Sousa, P. W. Serruys, and M. A. Costa, "New frontiers in cardiology: drug-eluting stents: Part I," Circulation **107**(17), 2274–2279 (2003).
3. B. Kalesan, T. Pilgrim, K. Heinimann, L. Räber, G. G. Stefanini, M. Valgimigli, B. R. da Costa, F. Mach, T. F. Lüscher, B. Meier, S. Windecker, and P. Jüni, "Comparison of drug-eluting stents with bare metal stents in patients with ST-segment elevation myocardial infarction," Eur. Heart J. **33**(8), 977–987 (2012).
4. P. W. Serruys, A. T. Ong, J. J. Piek, F. J. Neumann, W. J. van der Giessen, M. Wiemer, A. Zeiher, E. Grube, J. Haase, L. Thuesen, C. Hamm, and P. C. Otto-Terlouw, "A randomized comparison of a durable polymer Everolimus-eluting stent with a bare metal coronary stent: The SPIRIT first trial," EuroIntervention **1**(1), 58–65 (2005).
5. S. Brugaletta, H. M. Garcia-Garcia, Y. Onuma, and P. W. Serruys, "Everolimus-eluting ABSORB bioresorbable vascular scaffold: present and future perspectives," Expert Rev. Med. Devices **9**(4), 327–338 (2012).
6. C. I. Stefanadis, "Stents for coronary artery disease: from covered to drug-eluting to bioabsorbable.," Hellenic J. Cardiol. **53**(1), 89–90 (2012).
7. D. Dudek, Y. Onuma, J. A. Ormiston, L. Thuesen, K. Miquel-Hebert, and P. W. Serruys, "Four-year clinical follow-up of the ABSORB everolimus-eluting bioresorbable vascular scaffold in patients with de novo coronary artery disease: the ABSORB trial," EuroIntervention **7**(9), 1060–1061 (2012).
8. J. Gomez-Lara, S. Brugaletta, R. Diletti, S. Garg, Y. Onuma, B. D. Gogas, R. J. van Geuns, C. Dorange, S. Veldhof, R. Rapoza, R. Whitbourn, S. Windecker, H. M. Garcia-Garcia, E. Regar, and P. W. Serruys, "A comparative assessment by optical coherence tomography of the performance of the first and second generation of the everolimus-eluting bioresorbable vascular scaffolds," Eur. Heart J. **32**(3), 294–304 (2011).

#205761 - $15.00 USD Received 31 Jan 2014; revised 5 Aug 2014; accepted 13 Aug 2014; published 12 Sep 2014

9. A. Karanasos, C. Simsek, P. Serruys, J. Ligthart, K. Witberg, R. J. van Geuns, G. Sianos, F. Zijlstra, and E. Regar, "Five-year optical coherence tomography follow-up of an everolimus-eluting bioresorbable vascular scaffold: changing the paradigm of coronary stenting?" Circulation **126**(7), e89–e91 (2012).
10. P. W. Serruys, J. A. Ormiston, Y. Onuma, E. Regar, N. Gonzalo, H. M. Garcia-Garcia, K. Nieman, N. Bruining, C. Dorange, K. Miquel-Hébert, S. Veldhof, M. Webster, L. Thuesen, and D. Dudek, "A bioabsorbable everolimus-eluting coronary stent system (ABSORB): 2-year outcomes and results from multiple imaging methods," Lancet **373**(9667), 897–910 (2009).
11. P. W. Serruys, Y. Onuma, J. A. Ormiston, B. de Bruyne, E. Regar, D. Dudek, L. Thuesen, P. C. Smits, B. Chevalier, D. McClean, J. Koolen, S. Windecker, R. Whitbourn, I. Meredith, C. Dorange, S. Veldhof, K. Miquel-Hebert, R. Rapoza, and H. M. García-García, "Evaluation of the second generation of a bioresorbable everolimus drug-eluting vascular scaffold for treatment of de novo coronary artery stenosis: six-month clinical and imaging outcomes," Circulation **122**(22), 2301–2312 (2010).
12. A. Sheehy, J. L. Gutiérrez-Chico, R. Diletti, J. P. Oberhauser, T. Glauser, J. Harrington, M. B. Kossuth, R. J. Rapoza, Y. Onuma, and P. W. Serruys, "In vivo characterisation of bioresorbable vascular scaffold strut interfaces using optical coherence tomography with Gaussian line spread function analysis," EuroIntervention **7**(10), 1227–1235 (2012).
13. N. Gonzalo, P. W. Serruys, N. Piazza, and E. Regar, "Optical coherence tomography (OCT) in secondary revascularisation: stent and graft assessment," EuroIntervention **5**(Suppl D), D93–D100 (2009).
14. J. L. Gutiérrez-Chico, M. D. Radu, R. Diletti, A. Sheehy, M. B. Kossuth, J. P. Oberhauser, T. Glauser, J. Harrington, R. J. Rapoza, Y. Onuma, and P. W. Serruys, "Spatial distribution and temporal evolution of scattering centers by optical coherence tomography in the poly(L-lactide) backbone of a bioresorbable vascular scaffold," Circ. J. **76**(2), 342–350 (2012).
15. B. D. Gogas, V. Farooq, Y. Onuma, and P. W. Serruys, "The ABSORB bioresorbable vascular scaffold: an evolution or revolution in interventional cardiology?" Hellenic J. Cardiol. **53**(4), 301–309 (2012).
16. S. Gurmeric, G. G. Isguder, S. Carlier, and G. Unal, "A new 3-D automated computational method to evaluate in-stent neointimal hyperplasia in in-vivo intravascular optical coherence tomography pullbacks," Med. Image Comput. Comput. Assist. Interv. **12**(Pt 2), 776–785 (2009).
17. G. Unal, S. Gurmeric, and S. G. Carlier, "Stent implant follow-up in intravascular optical coherence tomography images," Int. J. Cardiovasc. Imaging **26**(7), 809–816 (2010).
18. C. Xu, J. M. Schmitt, T. Akasaka, T. Kubo, and K. Huang, "Automatic detection of stent struts with thick neointimal growth in intravascular optical coherence tomography image sequences," Phys. Med. Biol. **56**(20), 6665–6675 (2011).
19. A. Wang, J. Eggermont, N. Dekker, H. M. Garcia-Garcia, R. Pawar, J. H. C. Reiber, and J. Dijkstra, "A robust automated method to detect stent struts in 3D intravascular optical coherence tomographic image sequences," Proc. SPIE **8315**, 83150L (2012).
20. G. Unal, S. Bucher, S. Carlier, G. Slabaugh, T. Fang, and K. Tanaka, "Shape-driven segmentation of the arterial wall in intravascular ultrasound images," IEEE Trans. Inf. Technol. Biomed. **12**(3), 335–347 (2008).
21. A. Wang, J. Eggermont, N. Dekker, H. M. Garcia-Garcia, R. Pawar, J. H. Reiber, and J. Dijkstra, "Automatic stent strut detection in intravascular optical coherence tomographic pullback runs," Int. J. Cardiovasc. Imaging **29**(1), 29–38 (2013).
22. J. M. S. Prewitt, "Object enhancement and extraction," in *Picture Processing and Psychopictorics*, B. S. Lipkin, ed. (Academic Press, New York, 1970), pp. 75–149.
23. E. W. Dijkstra, "A note on two problems in connexion with graphs," Numer. Math. **1**(1), 269–271 (1959).
24. W. K. Pratt, *Digital Image Processing* (John Wiley & Sons, Inc., 1978), p. 750.
25. A. Wang, J. Eggermont, N. Dekker, P. J. de Koning, J. H. Reiber, and J. Dijkstra, "3D assessment of stent cell size and side branch access in intravascular optical coherence tomographic pullback runs," Comput. Med. Imaging Graph. **38**(2), 113–122 (2014).

1. Introduction

In coronary artery disease (CAD), plaques build up in the vessels and obstruct the oxygen-rich blood supply to the heart muscle, which can cause angina or eventually a heart attack. Nowadays, stenting after angioplasty is one of the main treatment options for CAD. Stents are tiny tube-like devices that are usually made of metal meshes, designed to support the vessel wall to prevent the acute vessel recoil after the plain-old balloon angioplasty [1]. The first introduced stent was the bare metal stent (BMS), with a known risk of neointimal hyperplasia (NIH) which re-narrows of the vessel lumen [2]. The drug-eluting stent (DES) emerged as an alternative to the BMS. It can alleviate NIH significantly, but later, multiple risk factors became evident, such as late stent thrombosis and late acquired malapposition [3, 4]. As a result, a new concept of the temporary stent or scaffold was proposed. Such a device is designed to offer temporary radial strength to avoid the acute vessel closure as a consequence of the acute vessel recoil, and at a later stage, it will be fully absorbed, leading to restoration

#205761 - $15.00 USD Received 31 Jan 2014; revised 5 Aug 2014; accepted 13 Aug 2014; published 12 Sep 2014

of lumen patency and vascular flow [5, 6]. A series of temporary vascular stents, termed "Bioresorbable Vascular Scaffold (BVS)," have been developed and undergone extensive clinical evaluation in the past ten years [4, 7–10]. ABSORB BVS (Abbott Vascular, Santa Clara, California, US) is one of first developed temporary scaffolds which have been used for clinical treatment. It consists of a backbone of poly-L-lactide coated with poly-D,L-lactide which contains and controls the release of the antiproliferative drug everolimus (Novartis, Basel, Switzerland) [11]. The thickness of backbone with coated drug layer is 158 μm. ABSORB BVS will be fully absorbed approximately two years after implantation and has exhibited strong positive clinical and angiographic results [12].

Intravascular optical coherence tomography (IVOCT) is being increasingly used during BVS studies and clinical trials for accurate BVS analysis to assess the rate of bioresorption and to inspect the response of vessel walls [13]. As a relatively new optical signal acquisition technique, IVOCT imaging has a radial resolution of about 10 μm which is ten times higher than its comparable technique: intravascular ultrasound (IVUS). IVOCT has a limited penetration of 3 mm, but it provides a better signal-to-noise ratio than IVUS within the limitation. Furthermore, IVOCT imaging is particularly suitable for BVS struts as they are made of translucent polymers [12]. The transmitted light can readily pass through them and backscattering originates from the difference in refractive index between a strut and its environment (flush fluid or tissue), which results in bright boundaries. Besides, if a strut contains a big fracture which appears as a scattering center, it looks similar to confluent struts [14]. An IVOCT image with newly implanted BVS struts in two different coordinate systems is shown in Fig. 1. There are different BVS strut shapes; however, struts having bright boundaries and box-shape black cores account for 100% of the shapes at baseline, more than 82% at 28 days and 80% at 24 months of all the struts [15]. Therefore in this paper we will focus on the box-shape type of BVS struts. The strut area is measured based on its black core. The bright boundary is not included since when a strut is covered by tissue, its boundary cannot be precisely defined, while for a newly implanted strut, its thickness will be overestimated by measuring the distance between the leading-edges of its adluminal wall and abluminal wall [12].

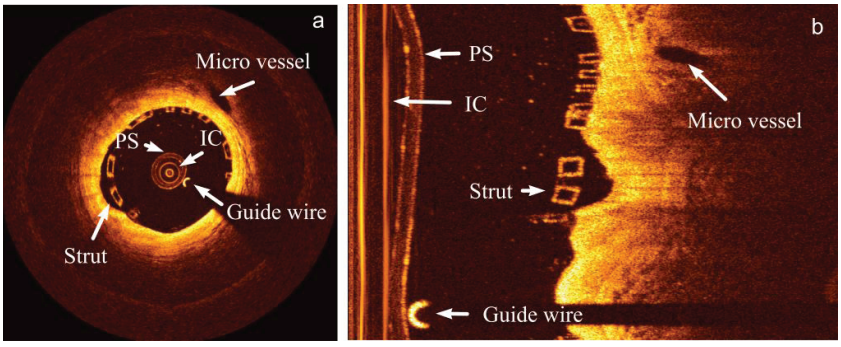

Fig. 1. A baseline IVOCT image in (a) the Cartesian coordinate system and (b) the polar coordinate system. In both images, the imaging catheter (IC), the protective sheath (PS), the guide wire, a micro vessel and a BVS strut are marked.

Many automated metallic stent strut detection methods [16–19] have been published. However, to the best of our knowledge, current BVS analyses in IVOCT images still rely on the labor intensive manual delineation of struts. Given the large number of struts in a pullback run, quantitative analysis is feasible only when struts can be detected automatically. In this paper, we present an automated method to detect BVS struts and to measure their black core areas in IVOCT pullback runs.

#205761 - $15.00 USD Received 31 Jan 2014; revised 5 Aug 2014; accepted 13 Aug 2014; published 12 Sep 2014

2. Method

To detect struts accurately, a-priori information of the input IVOCT data set type (baseline or follow-up) is requested, as the presented algorithm has two slightly different strategies for baseline and follow-up images with respect to some different parameters, false positive filters and the region of interest (ROI). However, in this section, the described procedures are implicitly used for both strategies, unless stated differently in context. As Fig. 2 shows, both strategies contain five main steps: **1**) Pre-processing. The bright components in the lumen including the imaging catheter, the guide wire and the protective sheath should be detected and masked; **2**) Image transformation. The lumen contour and center are detected so that we can transform Cartesian IVOCT images into new polar images based on the lumen center. In the new polar images, the shapes of BVS struts are usually more rectangular than these in the original polar images; **3**) Candidate strut detection. In the new polar images, short candidate segments describing black cores are detected and later clustered as candidate struts; **4**) False positive removal. These are removed using a series of false positive filters; **5**) Strut contour refining. The strut contours are refined to be smooth and accurate for area measurement and center calculation. In the following subsections, each step of the method is described in more detail.

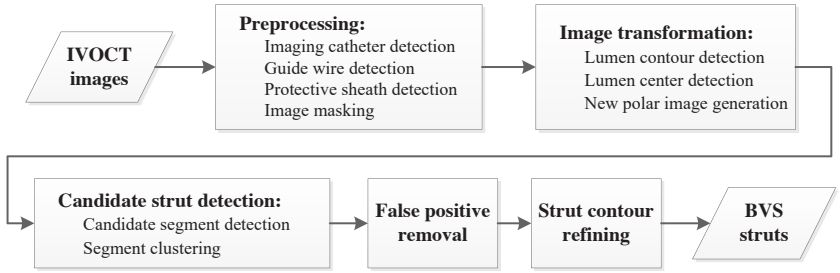

Fig. 2. The flow chart of the BVS strut detection method.

2.1 Preprocessing

Bright components inside the lumen, including the imaging catheter, the guide wire and the protective sheath, were masked to improve the further processing. The imaging catheter center is the center of Cartesian images, and as Fig. 1(a) shows, the imaging catheter produces a series of very bright concentric circles, which appear as vertical lines in the polar images as presented in Fig. 1(b). After a proper Z-offset correction, the imaging catheter is located in the same position in the whole pullback run and hence can be detected in the minimum image of the entire pullback run by checking the intensity sum of every column [20]. If a guide wire is used during the image acquisition, it blocks the light signal and consequently generates a black shadow behind it. According to its intensity profile, the guide wire and its shadow were detected using a previously developed method [21].

The imaging catheter is always covered by a protective sheath which appears as a ring with a certain width dependent on the manufacturer and catheter type. During the image acquisition, the imaging catheter moves sideways inside the protective sheath, thus the protective sheath position varies during the pullback and therefore must be detected frame by frame. First, a ROI was defined for the detection. It started from the outer wall of the imaging catheter and was wide enough to cover the protective sheath. As the protective sheath diameter and the image resolution are known, a proper width of the ROI can be computed. Next, the Prewitt compass edge filter with a kernel sensitive to vertical edges [22] was applied to the image, so that the outer (bright-to-dark) edge of the protective sheath was

#205761 - $15.00 USD Received 31 Jan 2014; revised 5 Aug 2014; accepted 13 Aug 2014; published 12 Sep 2014

represent by strong negative values. The gradient image was used as a cost matrix to which Dijkstra's algorithm [23] was applied to detect the minimum cost path dynamically. This path is the outer boundary of the protective sheath. An example of the detection results of the imaging catheter, the protective sheath and the guide wire shadow region is given in Fig. 3(a). To avoid creating new dark to bright edges that may influence the lumen contour detection, the image region inside the protective sheath was masked using the background intensity value. It was computed based on a fixed percentile of the histogram of the entire image sequence. An example of the preprocessed image is presented in Fig. 3(b).

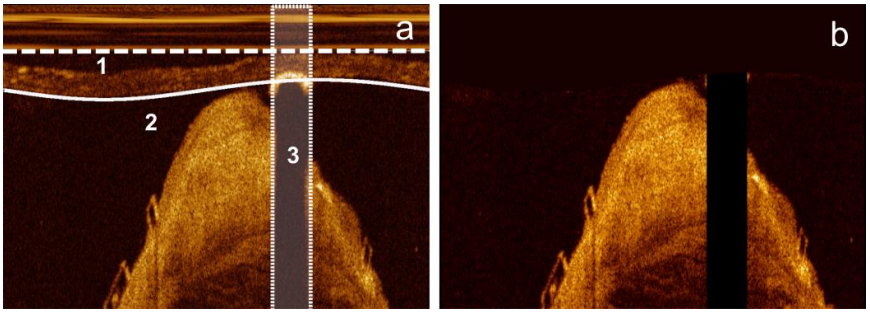

Fig. 3. The detected imaging catheter (dashed straight line "1"), protective sheath (solid curve "2") and guide wire shadow region (area "3") are given in figure (a). The masked image is given in figure (b). Inside the protective sheath, it is masked with the background intensity value, while the guide wire shadow region is masked as 0.

2.2 Image transformation

Our BVS strut detection is applied to polar images. However, the box-shape BVS struts are usually distorted like parallelograms in the original polar images, since they are converted from Cartesian images based on the catheter center instead of the stent contour center. To improve the BVS strut appearance, new polar images should be created from Cartesian images based on the stent contour center. As lumen contour is similar to the stent contour in most of the cases, its center was used as an approximation of the stent contour center.

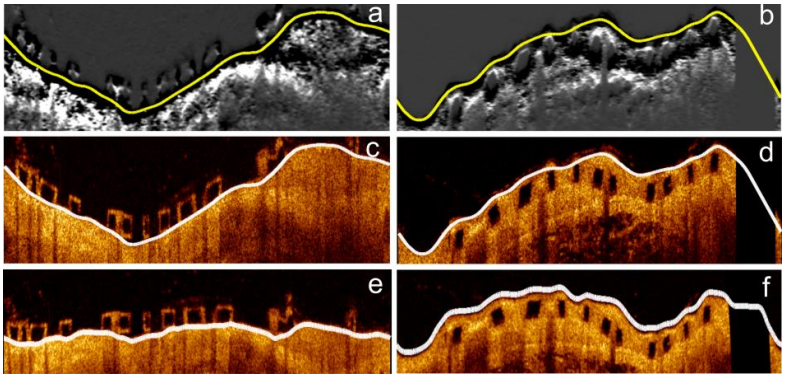

Fig. 4. The gradient images of a baseline image and a follow-up image are given in figures (a) and (b). They are used for lumen detection. Yellow curves indicate the detected minimal cost paths. In figures (c) and (d), the original polar images are presented with lumen contours (white curves). The new polar images transformed based on the lumen center are shown in figures (e) and (f) in which most of the BVS struts are more rectangular than in original polar images.

#205761 - $15.00 USD Received 31 Jan 2014; revised 5 Aug 2014; accepted 13 Aug 2014; published 12 Sep 2014

The lumen boundary was detected in the original polar images. First, the images were denoised using a median filter [24] to smooth the lumen boundary. Next, a gradient image was generated by applying the Prewitt compass edge filter with the kernel for vertical edges to the smoothed image. Two examples are given in Figs. 4(a) and 4(b). In the gradient image, the lumen boundary is represented by strong negative values and hence Dijkstra's minimum cost path detected in it was treated as the lumen boundary as Figs. 4(c) and 4(d) demonstrate. The detected lumen boundary was converted into the Cartesian coordinates system and its center was detected using a distance transformation method presented in [25]. Based on the lumen center, a Cartesian image can be transformed into a new polar image like Fig. 4(e). Compared with the original polar images, the shapes of most BVS strut are more rectangular. However, in some cases, the lumen contour is highly irregular, so that BVS struts are still not rectangular after the image transformation as Fig. 4(f) shows. They have irregular shapes and different thickness in the vertical direction. The proposed method contains procedures to detect these irregular struts in the further steps, but in the worst situation, these struts cannot be detected.

2.3 Candidate strut detection

In the new transformed polar images, candidate BVS struts were detected. As mentioned in the beginning, the presented method has two different strategies to detect baseline and follow-up struts, separately. There are three main differences between them:

1. Different ROI for strut detection. For baseline data sets, the struts are usually aligned with the lumen boundary or malapposed, which means most of the struts are inside the lumen contour as Fig. 4(e) demonstrates. However, the lumen detection may be affected by confluent struts or struts placed inside the tissue, so that the detected lumen contour may follow the front wall of these struts instead of the back wall. To cover all the baseline struts, the detected lumen contour needs to be extended with an offset equal to BVS strut thickness. The ROI of baseline strut detection is between this extended contour and the previously detected protective sheath contour. In contrast, in the follow-up data sets, most of the BVS struts are outside the lumen contour as Fig. 4(f) shows, but when some struts are not covered by tissue, the detected lumen contour could pass behind them mistakenly. To include all the follow-up struts, we need to shrink the lumen contour to the lumen center direction with an offset equal to BVS strut thickness. Therefore, the ROI for follow-up strut detection is between the shrunken lumen contour and the image boundary.

2. Different thickness threshold. After implantation, BVS struts start to be degenerated and covered by healing tissue. Hence, the boundaries of the follow-up struts are less sharp than newly implanted struts. Consequently, the method uses a slightly bigger thickness threshold to detect follow-up struts than the newly implanted struts. This parameter is set based on the image resolution and will be described later in this section.

3. Different degree of the boundary completeness. The boundary of a newly implanted strut usually contains many small gaps as Fig. 4(c) shows. Because a baseline strut is not covered by tissue, its box-shape boundary is mostly created by the backscattering at the strut surfaces which could be affected by the strut position and orientation. Parts of the boundary could be blurred or even missing. Moreover, the residual blood and other artifacts also can affect the completeness of the box-structure. At follow-up stage, struts are usually covered by tissue which helps to generate bright boundaries as Fig. 4(d) shows. Compared with the newly implanted struts, the follow-up struts have a more complete box-shape boundary and hence the method is stricter with regard to their boundary shape and completeness.

In the ROI, we first detected the candidate line segments between the front and back walls of BVS struts scan-line by scan-line and later clustered these segments into candidate struts. To detect candidate segments, both original and gradient images were used. Again, the Prewitt compass edge filter for vertical edges was applied to generate gradient images in which dark-to-bright edges are represented by negative values and bright-tot-dark edges are

#205761 - $15.00 USD Received 31 Jan 2014; revised 5 Aug 2014; accepted 13 Aug 2014; published 12 Sep 2014

positive values. The intensity profile and the gradient profile of a scan-line that passes through a BVS strut are given in Fig. 5. According to these profiles, one can state that the BVS region starts with a relatively high intensity (front wall) followed by a certain low intensity region (black core) and it ends with another relatively high intensity (back wall). As a result, candidate segments constituting BVS struts were detected with four main rules:

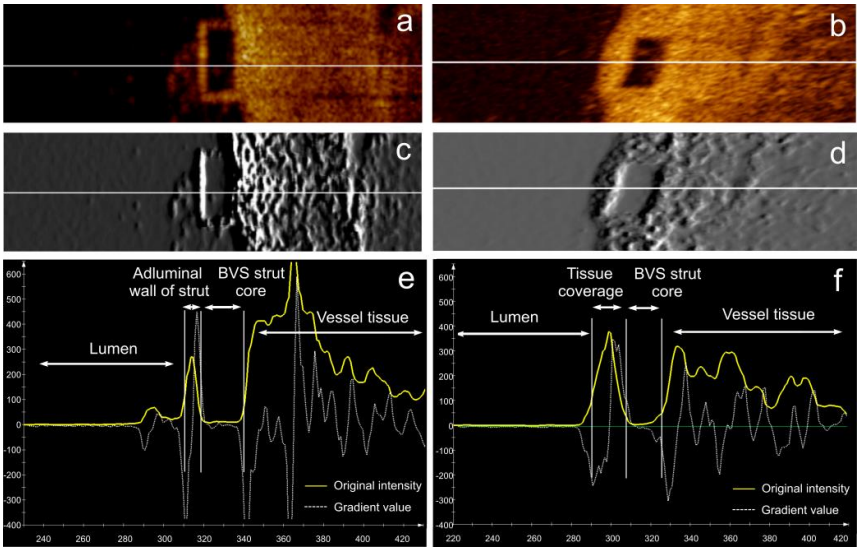

Fig. 5. Figures (a) and (b) show a scan-line (white line) passing through a BVS strut in a baseline image and a follow up image, respectively. The corresponding gradient images are presented in figures (c) and (d). The intensity profile (yellow curve) and the gradient profile (white curve) are given in figures (e) and (f). A BVS strut always has low intensity values in the black core region and strong gradient values along the boundary.

1. It has low intensity black core region. In this method, the low black core intensity threshold was calculated based on a fixed percentile of the histogram of the pullback run.

2. It has a strong positive gradient value in the beginning and a strong negative gradient value in the end. Both the gradient value thresholds were computed according to fixed percentiles of the histogram of the gradient images.

3. It has a reasonable length. Segment length represents the strut thickness in scan-line direction. Ideally, the thickness of BVS struts in a pullback run should be the same in each scan-line. However, BVS struts could still appear distorted after the image transformation in section 2.2, since the lumen is not always circular. Moreover, the strut boundary thickness can be influenced by the distance and orientation of the struts. Struts close to the imaging catheter or uncovered by tissue usually are characterized by a wider boundary. Therefore, the thickness of the strut cores in a single pullback run can be different from the standard thickness. In our approach, a range of acceptable thicknesses of BVS strut cores was set based on the standard thickness.

4. Candidate segments should not be overlaid in the same scan-line. In case the noise has stronger edge than real struts, the algorithm allows more than one candidate segment in the same scan-line. However, when two candidate segments were found overlaid in the same scan-line, only the one having the highest intensity sum of the front and back walls was selected. If they both had the same intensity sum, the longest one was saved.

#205761 - $15.00 USD Received 31 Jan 2014; revised 5 Aug 2014; accepted 13 Aug 2014; published 12 Sep 2014

For example, the candidate segment results for Figs. 6(a) and 6(b) are presented in Figs. 6(c) and 6(d), which still contain some false candidate segments. They are generated due to the residual blood, micro-vessels, plaques and weak signal region deep in the tissue.

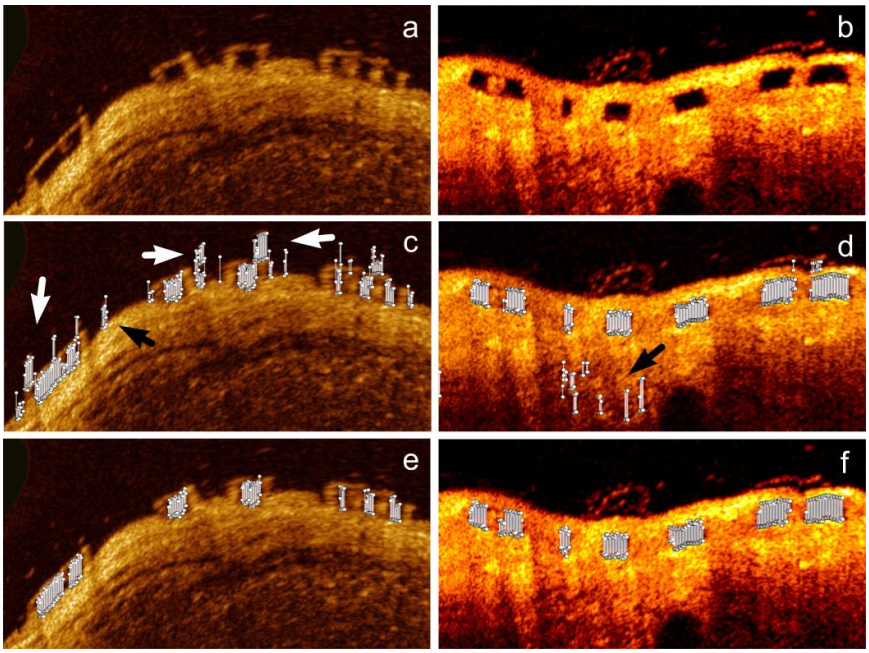

Fig. 6. Figure (a) shows a new polar baseline image that is transformed based on the center of a highly irregular lumen contour. The BVS struts in figure (a) still appear distorted and their thickness in the vertical direction is very different. Figure (b) demonstrates a follow-up image transformed based on the center of a circular lumen contour. The BVS struts are less distorted than these in figure (a). The detected candidate line segments (short white lines) are presented in both figures (c) and (d). Both white and black arrows point out the candidate segments caused by residual blood or noise in tissue. These candidates will be clustered as false candidate strut during the clustering. After the false positive removal, only real struts are left as figures (e) and (f) shows.

After having obtained the BVS candidate segments, a clustering method was applied to merge these segments into candidate struts. As Figs. 6(c) and 6(d) show, the candidate segments belonging to the same BVS strut are connected, while the false positives are usually randomly distributed. In this method, the segments were clustered according to their position. It started from the first un-clustered candidate segment and searched for the next segment close to it. A candidate segment can be added to the cluster if it is connected with the last segment in the cluster. The searching continues until no more segments can be attached. Next, we checked if a cluster has top and bottom boundaries as BVS struts should have box-shape boundaries. The follow-up BVS strut boundary is usually complete due to the tissue coverage so that only clusters having both top and bottom edges were saved. In baseline data sets, the BVS strut could have an incomplete box-structure, so that the method allows a cluster to miss its top or bottom boundaries.

2.4 False positive removal

During the clustering, many false candidate struts were generated from false candidate segments as presented in Figs. 6 (c) and 6(d). Therefore, a series of false positive filters were

#205761 - $15.00 USD Received 31 Jan 2014; revised 5 Aug 2014; accepted 13 Aug 2014; published 12 Sep 2014

applied to the clustering results to remove them. First, the strut size was used for filtering. A BVS strut should contain a certain number of candidate segments. Small clusters are usually caused by random noise or artifacts in the images. In our research, clusters containing less than 3 candidate segments were removed as false positives. A second filter was applied to search for overlaid struts in each scan-line, because there should be at most one strut in any radial direction, but some false positives can share parts of the boundary with real struts. As a result, when two clusters were overlaid in the radial direction, only the one with complete box-structure was saved. If both clusters had complete box-structures, the bigger cluster was kept.

The third filter is only applicable for follow-up data sets. After the first two filters, a few false positives may still exist in the deep tissue region which contains much random noise due to the weak signal. Compared with the true positives, these false positives were commonly located deeper in the tissue; therefore, a filter was applied to remove outliers based on the thickness of tissue coverage (the distance between struts and the lumen boundary) for each candidate strut, so that a candidate strut having a very different thickness of tissue coverage with the majority was considered as a false positive, since the thickness of tissue coverage changes smoothly in the follow-up data sets. After the previous filtering, the majority of current results should be true positives. Therefore, the median coverage thickness was computed for outlier detection. To be accurate, the clusters in the neighboring frames were used to estimate the median coverage thickness as well. This filter also removed most of the false positives caused by micro vessels and plaques. However, it is not applicable for baseline data sets, as the malapposed struts could have very different distances to the lumen boundary. Examples of the false positive removal results are given in Figs. 6(e) and 6(f).

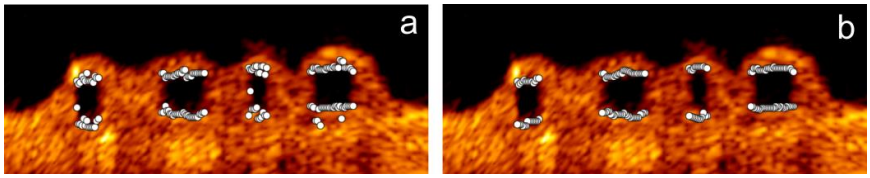

Fig. 7. The original boundaries of clusters formed by white points in figure (a) and the smoothed boundaries in figure (b).

2.5 Strut contour refining

After false positive removal, the main bodies of the strut black cores were detected. As the candidate segments were always selected with the strongest boundary intensity, the detected adluminal and abluminal walls of BVS struts were usually rough. Besides, the original boundary could be fluctuating because of the noise, inside fractures and low image quality. Examples of the unsmoothed BVS strut contours are shown in Fig. 7(a). Therefore, the front wall and back wall of each detected strut were smoothed using a median filter. Any outliers were replaced by the interpolated point between the nearest neighboring points. The smoothing results are show in Fig. 7(b).

The main bodies of the strut cores were formed by line segments with a range of acceptable thickness. However, an irregular shape strut could contain sharp tips in one or both ends as Fig. 8(a) shows. The core regions in the sharp tips have smaller thickness than the acceptable thickness and usually contain more noise than the main body. As a result, the sharp tip regions might be missed during the detection. To recover these tip regions, a post-processing was applied. First, the adluminal and abluminal boundaries were fitted into lines using the least-square error method and the fitted lines specify the ROI for tip refining. Due to the irregular lumen contour, a long BVS strut could be curved, so its front and back walls cannot be fitted into one single line. To be accurate, we fitted two separated lines for the top and bottom boundary of the struts containing more than 20 candidate segments as Fig. 8(b)

#205761 - $15.00 USD Received 31 Jan 2014; revised 5 Aug 2014; accepted 13 Aug 2014; published 12 Sep 2014

presents. Next, along the fitted lines, the adluminal and abluminal walls for the missed sharp tip regions were recovered by searching continuous boundaries in the Prewitt edge filtered polar images. The searching ended when the fitted line met the top or bottom edges. The recovered boundary can be seen in Fig. 8(c). In the end, a spline contour was generated for each BVS strut based on the refined boundary as Fig. 8(d) shows. At the same time, the center of each BVS strut was calculated.

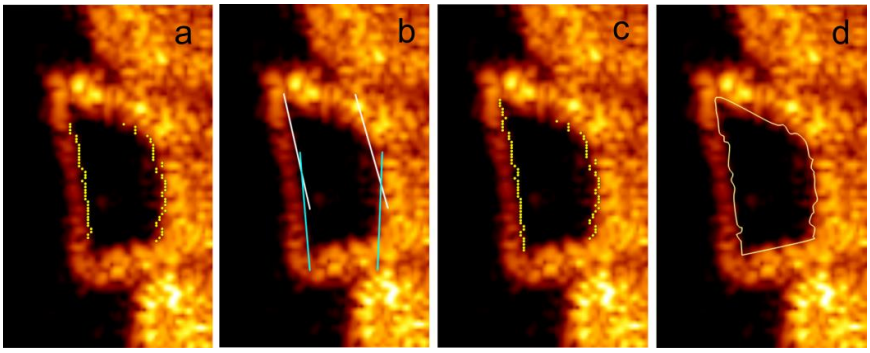

Fig. 8. Figure (a) shows the smoothed boundaries of a cluster in yellow dots. In figure (b), two white lines are fitted to the top part of the strut boundary and two light blue lines are fitted to the bottom part of the strut boundary. Along the fitted lines, the missed boundaries in the sharp tip regions are recovered as figure (c) demonstrated and the final refined strut contour is generated as (d) presents.

3. Validation and results

The automatic BVS strut detection and measurement method was developed using the MeVisLab toolbox (Fraunhofer MeVis, Bremen, Germany) together with in-house developed C++ modules. For validation purposes, 6 pullback runs were used which were acquired using a C7-XR FD-OCT intravascular imaging system together with a C7 Imaging catheter (St. Jude Medical Inc., St. Paul, MN, USA). The automated pullback speed was 20 mm/s with a data frame rate of 100 frames per second. All the pullback runs are in the original 16-bit polar format and each contains 271 frames. Three pullback runs were acquired at baseline, while the other three at 6 to 24 months, respectively. In both baseline and follow-up groups, one pullback run contains no guide wire and the other two contain a standard 0.014 inch steerable guide wire. Temporary blood flushing was performed with a contrast infusion. All the stents are the ABSORB 1.1 bioresorbable vascular scaffold (Abbott Vascular, Santa Clara, CA, USA). Overtime struts are absorbed. According to the trails for the ABSROB BVS [15], there is about 9% reduction of struts in IVOCT images over 6 months and 35% reduction over 24 months. Already due to the difference in position of the IVOCT catheter for the same scaffold at the same time point, there could be a difference in the number of struts. In our study, the baseline and follow up data sets are from different patients and therefore the number of struts is different. Part of the BVS struts could become undetectable after 24 months, but every visible strut in the 6 in-vivo IVOCT pullback runs were used for validation purposes, including struts without box-shape and the struts partly blocked by guide wire shadows.

To generate the ground truth, one observer manually drew all 4691 black cores of BVS struts in the 6 pullback runs, 2183 cores from the baseline group and 2508 from the follow-up group. A second independent observer manually drew all the struts in a subset containing one baseline data set and one follow-up data set. The second observer drew one contour for a strut with big fractures. These struts contain more than one black core, and have similar appearance as confluent struts. Therefore, the ground truth from the second observer contains some bright regions between black cores compared with that from the first observer as Figs.

#205761 - $15.00 USD Received 31 Jan 2014; revised 5 Aug 2014; accepted 13 Aug 2014; published 12 Sep 2014

9(a) and 9(b) shows. For incomplete struts, both observers marked the contour based on experience. In total, 726 newly implanted struts and 795 follow-up struts were marked by the second observer. In the same subset, the first observer marked 783 baseline cores and 819 follow-up strut cores. The agreements for BVS strut were given in Sensitivity and the core area agreements were computed using the Dice's coefficient. The inter-observer agreement of the BVS struts was 98.8% for baseline struts and 99.6% for follow-up struts. The strut area similarity was both 0.83 in the baseline group and the follow-up group. The area difference is mainly because the first observer did not include the bright region caused by big fractures.

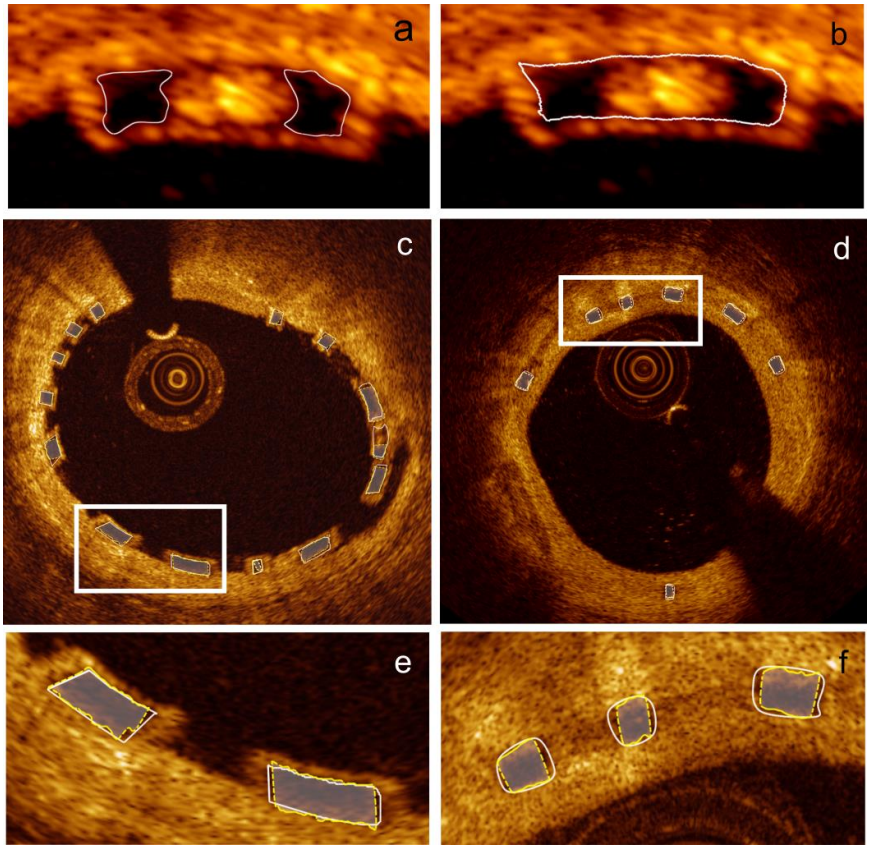

Fig. 9. Figure (a) shows two black cores marked by the first observer and they were marked as a big strut by the second observer as figure (b) presents. A comparison of the ground truth (solid white contours) from the second observer and the algorithmic results (dashed yellow contour with white translucent mask) in a baseline image is presented in figure (c) and another comparison of the ground truth from the first observer and the algorithmic results in a follow-up image is given in figure (d). The enlarged images of the white rectangle regions are given in figures (e) and (f).

During the evaluation, if a detected strut overlays the area of a ground truth, it was counted as a true positive. Otherwise, it is a false positive. The accuracy of black core area was measured by Dice's coefficient as well. According to the first observer, on average, the method correctly detected 90.0 ± 3.2% struts with 3.1 ± 0.7% false positives in every baseline data set and the Precision was 97.0 ± 0.1%. The Dice's coefficient for the BVS strut area was

#205761 - $15.00 USD Received 31 Jan 2014; revised 5 Aug 2014; accepted 13 Aug 2014; published 12 Sep 2014

0.83 ± 0.02. If we measure only the area of the correctly detected struts, the Dice's coefficient was 0.86 ± 0.01. For the follow-up group, the method detected 96.6 ± 2.0% struts correctly with only 0.8 ± 0.8% false positives and the Precision was 99.2 ± 0.1%. The Dice's coefficient for the strut area was 0.85 ± 0.02. For only the true positive struts, the number was 0.86 ± 0.01. According to the second observer, the method successfully detected 90.8% of baseline struts with 4.3% false positives and the Precision was 95.9%. 92.6% of follow-up struts were detected with 2.2% false positives and the Precision was 97.7%. The Dice's coefficient for baseline and follow-up strut areas was 0.76 and 0.75, separately. Counting only true positive areas, the Dice's coefficient was 0.79 and 0.77. Some examples of the ground truth from both observers and algorithmic results are given in Figs. 9(c)–9(f). The strut detection and the area measurement performance for each individual pullback run are presented in Table 1 and Table 2, separately.

The center position error of the correctly detected strut was computed as well. The average distance error of the strut centers was 17.0 ± 22.5 μm for newly implanted struts, 13.9 ± 11.1 μm for follow-up struts and 15.3 ± 21.0 μm for all struts. The median distance errors for two groups were both 11.1 μm.

Table 1. The strut detection results of the presented method for each validation data set. For each data set, the number of frames containing struts (Frame No.), the numbers of struts in the ground truth (GT), the percentages of true positive (TP) and false positive (FP) are given

Strut status	Data set	Frame No. (with struts)	No. of GT	TP (%)	FP (%)
Baseline	1	89	630	85.5	3.8
	2	94	770	92.2	3.3
	3	93	783	92.5	2.0
Follow-up	4	97	868	93.7	0.0
	5	91	819	98.0	0.6
	6	97	821	90.4	1.8
Total	-	561	4691	93.7	1.8

Table 2. The strut area measurement performance of the present method in each validation data set. The area of the ground truth (GT) and the Dice's coefficient between the ground truth and the algorithmic results are given for all struts and only successfully detected struts

Strut status	Data set	Area of all struts		Area of only true positives	
		GT area (mm^2)	Dice	GT area (mm^2)	Dice
Baseline	1	16.4	0.81	15.0	0.86
	2	14.3	0.82	13.7	0.85
	3	15.9	0.85	15.4	0.87
Follow-up	4	20.1	0.87	19.9	0.88
	5	19.8	0.83	19.0	0.85
	6	18.3	0.84	18.0	0.85
Total	-	104.8	0.84	101.0	0.86

4. Discussion

According to the validation results, the algorithm successfully detected 96.6 ± 2.0% follow-up struts with only 0.8 ± 0.8% false positives and 90.0 ± 3.2% newly implanted struts with

#205761 - $15.00 USD Received 31 Jan 2014; revised 5 Aug 2014; accepted 13 Aug 2014; published 12 Sep 2014

3.1 ± 0.7% false positives. The strut center error was 15.3 ± 21.0 μm. Generally, the presented method is accurate and robust under different image circumstances. The performance for the follow-up group is slightly better than the baseline group, because follow-up BVS struts have more complete box-shape boundaries due to the tissue coverage. Backscattering on the interface between struts and tissue creates strong bright boundaries. By checking the boundary completeness during the clustering, the algorithm can easily remove most of the false positive from the follow-up pullback runs. In contrast, the contour of newly implanted struts can be influenced by noise in the lumen, such as residual blood, and hence contains many gaps. The algorithm keeps the clusters that have mild incomplete boundaries to avoid removing too many true positives, but fails to keep the real struts having severe incomplete boundaries. On the other hand, it also leaves more false positives in the results than the follow-up data set. Most of these false positives can be later removed by the filters, but still a few could leave as they are difficult to distinguish. Actually, most of the final false positives are from the baseline group. Similarly, the strut area performance in the follow-up pullback runs (0.85 ± 0.02) is also better than in the baseline pullback runs (0.83 ± 0.02).

When a BVS strut fractures, it generates bright scattering regions that separate the strut into several black cores as Fig. 9(a) shows. In this case, the first observer marked each cores separately, while the second observer drew one big contour for all the cores including the bright fractures as Fig. 9(b) presents. Hence, the manual results from the second observer contain fewer struts but more strut areas than those from the first observer, and the false positive rate according the second observer is 3.2% and the Dice's coefficient for the strut area is 0.75. However, if we count only the agreed areas between two observers, 95.1% and 96.9% of these areas were correctly detected for baseline and follow-up groups, separately. It suggests that the algorithmic results have a good agreement with the black core regions from both observers. The area errors in the baseline data sets are largely caused by incomplete boundaries, because the strut areas may be overestimated or underestimated. The area errors for follow-up struts are mainly due to the blurred boundary edges, because struts are slowly bioresorbed after implantation. Tissue coverage also weakens the sharpness of strut boundaries. As this method prefers strong edges when detecting struts, the final follow-up strut contours could be distorted.

The strut detection also replies on the proper preprocessing. The imaging catheter, the guide wire and the protective sheath should be removed to facilitate the lumen detection. Besides, these bright components also can negatively impact the baseline strut detection. The lumen center is used as an approximation of the stent contour center. After transforming the Cartesian image to a new polar image based on the lumen center, we could get more rectangular strut contours. However, when the lumen contour is highly irregular, the BVS strut in the transformed polar image could be still distorted like a parallelogram and in many cases, the strut edges are not straight. Therefore, the thickness and the shape of these struts could vary a lot during in the pullback run. To handle this situation, the presented method allows a range of acceptable thickness instead of only the standard thickness to detect as many candidate segments as possible, and in the end, refines irregular strut contours to be more accurate. In a rare case, a strut can be highly distorted in the new polar image and therefore, cannot be detected by this method.

Most of the parameters used in the presented method are related to the image size and image resolution, while the remaining three parameters were set based on the histogram of the original images or the gradient images. These parameters are the minimum intensity threshold for strut boundary, the minimum absolute gradient threshold for edges and the maximum intensity threshold for black core regions. One data set from each group was used for parameter tuning. The same parameter setting was applied to all the pullback runs during the validation.

The presented method also has limitations. The BVS struts can have four different appearances: preserved box, open box, dissolved black box and dissolved bright box [15].

#205761 - $15.00 USD Received 31 Jan 2014; revised 5 Aug 2014; accepted 13 Aug 2014; published 12 Sep 2014

This method can only detect the majority of the cases, being the preserved box, which has a closed high intensity boundary and a low intensity core. All other three types cannot be detected. It also has limitations to handle struts with an incomplete boundary. Moreover, in a few cases, BVS struts can be overlaid after the implantation, but our method cannot detect the overlapping BVS struts, because a false positive filter checks all the overlapping results in radial direction. Only one of these struts could be left in the results. This research is based on the ABSORB 1.1 BVS struts; hence our results cannot be directly generalized to other type of BVS struts which may have different appearance with ABSORB 1.1 BVS after implantation and during the follow up.

5. Conclusion and future work

In conclusion, with the ongoing development of BVS technology, automated BVS strut detection methods become important as they can simplify and speed the quantitative analysis for both clinical research and medical care. In this paper, we implemented an automatic method to detect and measure BVS struts based on the black core region in both baseline and follow-up IVOCT image sequences. The validation results suggest that the proposed algorithm is very accurate and robust, which could be a helpful tool for tissue coverage thickness measurement, strut distribution analysis, 3D visualization, BVS bioresorption validation and vascular response research. In future, we plan to improve the current detection method and to detect BVS struts without box-shape contours.

Acknowledgments

Ancong Wang appreciates the financial support from the China Scholarship Council.

#205761 - $15.00 USD Received 31 Jan 2014; revised 5 Aug 2014; accepted 13 Aug 2014; published 12 Sep 2014

1.2 Light intensity analysis of polymeric struts

Temporal evolution of strut light intensity after implantation of bioresorbable polymeric intracoronary scaffolds in the ABSORB cohort B trial-an application of a new quantitative method based on optical coherence tomography.

Circ J. 2014;78(8):1873-81.
[Original research paper, Impact Factor : 3.94]

Nakatani S, Onuma Y, Ishibashi Y, Eggermont J, Zhang YJ, Campos CM, Cho YK, Liu S, Dijkstra J, Reiber JH, Perkins L, Sheehy A, Veldhof S, Rapoza R, van Es GA, Garcia-Garcia HM, van Geuns RJ, Serruys PW; ABSORB Cohort B investigators.

Temporal Evolution of Strut Light Intensity After Implantation of Bioresorbable Polymeric Intracoronary Scaffolds in the ABSORB Cohort B Trial

– An Application of a New Quantitative Method Based on Optical Coherence Tomography –

Shimpei Nakatani, MD; Yoshinobu Onuma, MD, PhD; Yuki Ishibashi, MD, PhD; Jeroen Eggermont, PhD; Yao-Jun Zhang, MD, PhD; Carlos M. Campos, MD; Yun Kyeong Cho, MD, PhD; Shengnan Liu; Jouke Dijkstra, PhD; Johan H.C. Reiber, PhD; Laura Perkins, PhD; Alexander Sheehy, PhD; Susan Veldhof, BSc; Richard Rapoza, PhD; Gerrit-Anne van Es, PhD; Hector M. Garcia-Garcia, MD, PhD; Robert-Jan van Geuns, MD, PhD; Patrick W. Serruys, MD, PhD on behalf of the ABSORB Cohort B investigators

Background: Quantitative light intensity analysis of the strut core by optical coherence tomography (OCT) may enable assessment of changes in the light reflectivity of the bioresorbable polymeric scaffold from polymer to provisional matrix and connective tissues, with full disappearance and integration of the scaffold into the vessel wall. The aim of this report was to describe the methodology and to apply it to serial human OCT images post procedure and at 6, 12, 24 and 36 months in the ABSORB cohort B trial.

Methods and Results: In serial frequency-domain OCT pullbacks, corresponding struts at different time points were identified by 3-dimensional foldout view. The peak and median values of light intensity were measured in the strut core by dedicated software. A total of 303 corresponding struts were serially analyzed at 3 time points. In the sequential analysis, peak light intensity increased gradually in the first 24 months after implantation and reached a plateau (relative difference with respect to baseline [%Dif]: 61.4% at 12 months, 115.0% at 24 months, 110.7% at 36 months), while the median intensity kept increasing at 36 months (%Dif: 14.3% at 12 months, 75.0% at 24 months, 93.1% at 36 months).

Conclusions: Quantitative light intensity analysis by OCT was capable of detecting subtle changes in the bioresorbable strut appearance over time, and could be used to monitor the bioresorption and integration process of polylactide struts. (*Circ J* 2014; **78:** 1873–1881)

Key Words: Bioresorbable vascular scaffold; Bioresorption; Coronary artery disease; Light intensity analysis; Optical coherence tomography

Fully bioresorbable scaffolds (BRS) are a novel approach to interventional treatment of coronary artery disease, and this new era has been dubbed the fourth revolution in percutaneous coronary revascularization.[1,2] The biological advantages of a transient device include late lumen enlargement with wall thinning, restoration of vasomotion and return of pulsatility, which are important in effecting optimal repair of the vessel wall, potentially reducing adverse events such as late/very late neoatherosclerosis and stent/scaffold thrombosis.[2–4]

Received February 5, 2014; revised manuscript received April 11, 2014; accepted April 27, 2014; released online June 18, 2014 Time for primary review: 18 days

Thoraxcenter, Department of Cardiology, Erasmus MC (S.N., Y.O., Y.I., Y.-J.Z., C.M.C., Y.K.C., H.M.G.-G., R.-J.v.G., P.W.S.), Cardialysis (G.-A.v.E., H.M.G.-G., P.W.S.), Rotterdam; Leiden University Medical Center, Leiden (J.E., S.L., J.D., J.H.C.R.); Medis Medical Imaging Systems BV, Leiden (J.H.C.R.), The Netherlands; Abbott Vascular, Santa Clara, CA (L.P., A.S., S.V., R.R.), USA; and International Centre for Circulatory Health, NHLI, Imperial College London, London (P.W.S), UK

Appendix lists the investigators who contributed to OCT image acquisition in the ABSORB cohort B trial.

Mailing address: Yoshinobu Onuma, MD, Thoraxcenter, Ba-583 's Gravendijkwal 230 3015, CE Rotterdam, The Netherlands. E-mail: yoshinobuonuma@gmail.com

ISSN-1346-9843 doi:10.1253/circj.CJ-14-0143

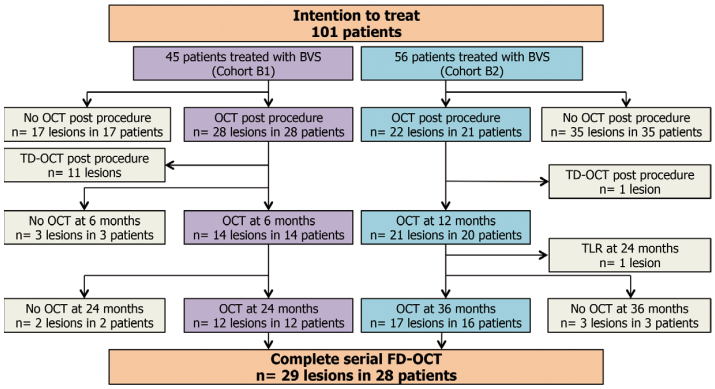

Figure 1. Flow chart of serial FD-OCT investigation in Cohort B of the ABSORB clinical trial. OCT, optical coherence tomography; FD-OCT, frequent-domain OCT; TD-OCT, time-domain OCT.

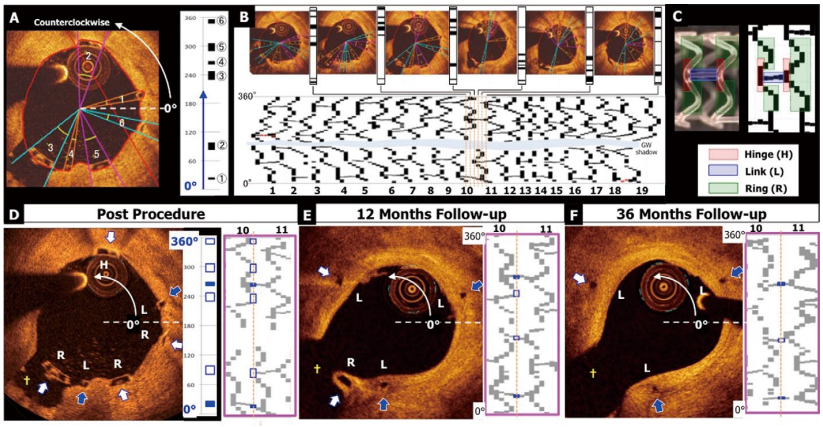

Figure 2. Strut core matching at serial time points confirmed by 3D foldout view. Lumen contour is drawn and the strut angle defined as the angle created by 2 lines originating from the center of gravity of the lumen to the edges of the visualized struts. By taking the position at 3 o'clock as the 0° reference angle, the angular orientation of each strut can be visualized in the 2D cross-section as indicated in the 3D foldout view. (**A**) By correlating the cross-sectional angular position with the longitudinal distance from the distal edge of the scaffold (defined as at least 1 strut detected in a cross-section) for each visualized strut, the 3D foldout view of a scaffold can be constructed.[16] (**B**) Foldout view of a 3×18 mm scaffold with 19 circular rings connected by 54 longitudinal links. The 3D foldout view confirms the location of matched or unmatched struts in a ring (R in white), link (L in white) or a hinge (H in white) in (**C**) and (**D**). The corresponding cross-sections were identified post procedure (**D**) and at 12 (**E**) and 36 months (**F**) by using a side branch (yellow cross) as an anatomical landmark. The corresponding struts were then selected by identifying those with a similar angular orientation in the corresponding cross-sections. However, some struts need confirmation on the 3D foldout view. For example, in (**D**), post procedure, in the cross-sections there are 2 visualized struts close in their angular orientations (350° and 20°), while at 12 (**E**) and 36 (**F**) months there is only one small strut visualized at 20°. The 3D foldout views at 12 and 36 months demonstrate that this small strut is located in a link connecting the 10th and 11th rings, and the 3D foldout view post procedure shows that the strut at 20° is also located in a link connection; thus, this strut is confirmed as correctly matched. Accordingly, the blue arrows show the corresponding struts and the white arrows show the non-corresponding struts.

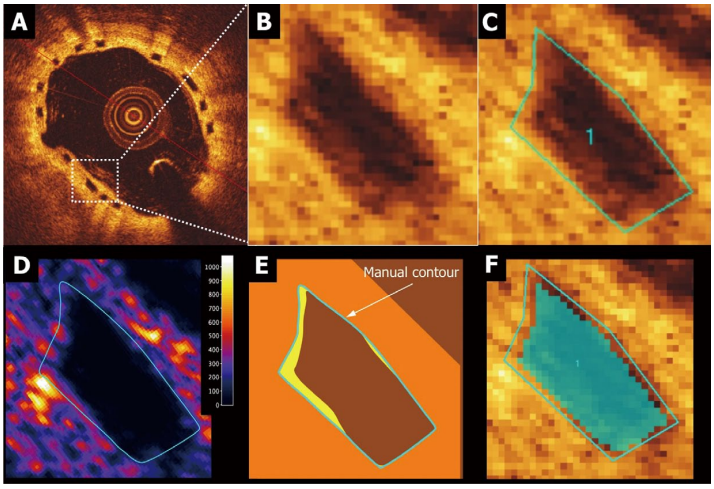

Figure 3. Strut core for light intensity assessment (region of interest, ROI). (**A**,**B**) OCT visualization of Absorb BVS strut consisting of a core area surrounded by reflective borders that are the interfaces between strut core and lumen or strut core and neointima/vessel wall. The struts "frame" can only be assessed unequivocally post procedure.[12] (**C**–**F**). Contours at follow-up of a strut core of interest visually delineated by manually drawn contours (**C**) and light intensity mapping around the strut core (**D**). The manually drawn borders of a strut core at follow-up often includes the reflective strut frame borders, so that part of the bright reflective frame can be misclassified as strut core region (**E**). Strut core region after automatic subtraction of 2 pixels inside the manual contours (**F**).

The current-generation BRS are constructed of either a polymer or a metallic alloy.[5] A variety of polymers with different chemical compositions and bioresorption times are in the preclinical and/or clinical stages of investigation. The most frequently used polymer is poly-L-lactide (PLLA).[2]

After implantation of a PLLA scaffold in vivo, the polymeric struts are progressively hydrolyzed and replaced by a provisional matrix; as it is released, the monomeric component, lactic acid, is metabolized via the Krebs cycle into carbon dioxide and water, with complete resorption occurring within approximately 24–36 months.[6] The duration of bioresorption is influenced by the initial molecular weight (MW) of the main component and the presence of oligomer, monomer and/or solvents.[6] After completion of bioresorption, the provisional matrix becomes cellularized with connective tissue; the struts eventually become fully integrated into the surrounding vessel wall and their OCT "footprint" becomes undetectable.[7]

In previous preclinical and clinical studies of the first-generation Absorb scaffold, 4 subgroups of strut appearance on OCT were visually categorized: "black box, dissolved bright box, dissolved black box or open box".[7] However, in those studies, the categorization showed only moderate reproducibility (k=0.58); therefore, more reproducible and/or quantitative methods were warranted. Quantitative light intensity analysis of the strut core is a method that could enable assessment of the light reflectivity of the resorbing polymer, its replacement by a provisional matrix and its vessel wall integration after cellularization by de novo connective tissue.[8–10] The aim of this report was to describe the methodology of light intensity analysis, to demonstrate the reproducibility of the assessment and to apply the method in serial OCT images collected post procedure and at 6, 12, 24 and 36 months follow-up in the ABSORB cohort B studies.[11]

Methods

Study Population

The OCT data used in the current analysis were obtained in the ABSORB Cohort B trial, a multicenter single-arm trial assessing the safety and performance of the Absorb™ everolimus-eluting bioresorbable vascular scaffold (BVS; Abbott Vascular, Santa Clara, CA, USA) in the treatment of 101 patients with a maximum of 2 de novo native coronary artery lesions.[12] The Absorb BVS consists of a semicrystalline PLLA backbone, coated with a thin amorphous layer of poly-D,L-lactide containing the antiproliferative agent everolimus. The details of inclusion and exclusion criteria have been described previously.[12] In this trial, 23 lesions in 23 patients were serially imaged by OCT post procedure and at 6 and 24 months (Cohort B1), and 19 lesions in 18 patients were serially investigated post procedure and at 12 and 36 months (Cohort B2).[11] Per study protocol, all patients were treated uniformly with a 3×18 mm BVS. To avoid variation in light intensity because of different types of the light imaging system used (ie, time-domain OCT [TD-OCT] vs. frequency-domain OCT [FD-OCT]), cases of investigation by TD-OCT were excluded from the analysis (n=12). In total, 87 pullbacks in 29 cases of truly serial FD-OCT were included in this study (**Figure 1**).

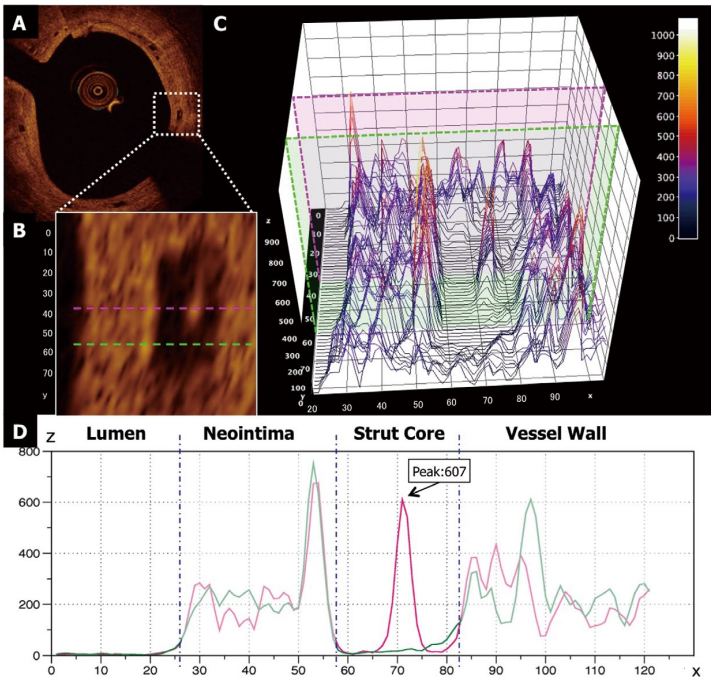

Figure 4. Two-dimensional and three-dimensional presentations of light intensity of the strut core. (**A**,**B**) Single strut located at 3 o'clock (0° reference angle) on this single cross-section of a scaffold implanted 36 months before. Inside the core region (**B**), there is a focus of high light intensity. The pink dotted line passes through this focus. The green dotted line crosses the strut core without passing the high-intensity spot. (**C**) 3D mapping of light intensity with 2 individual light profiles corresponding to the pink and green dotted (**B**) and continuous lines (**D**). The dotted blue lines in (**D**) indicate the region of interest (ROI). X and Y axis scales are in pixels, the *Z* axis has a dimensionless intensity value.

Method of Strut Matching

Preclinical studies suggest that the speed at which struts integrate into the arterial wall could vary within a single device depending on the location of the struts.[7] Therefore, in our analysis, strut-by-strut matching was performed to ascertain that the light intensity was repeatedly measured at the same site in the scaffold.[13–16] Using landmarks such as metallic markers or side branches, the corresponding cross-sections were identified at the different time points of follow-up. In corresponding OCT cross-sections, visualized struts' cores were matched by identifying struts with similar angular orientation in the 2D cross-section. This strut level matching was further confirmed by using a 3-D foldout view of the scaffold (**Figures 2C–E**).[13–16]

In every cross-section with at least 1 scaffold strut, the lumen contour was drawn, and the strut angle was defined as the angle created by 2 lines originating from the center of the gravity of the lumen to the edges of the struts, taking the position at 3 o'clock as the 0° angle of reference (**Figure 2A**).[13] By correlating the cross-sectional angular position of the struts with the longitudinal distance of each strut from the distal edge of the scaffold, a 3D foldout view of a scaffold can be constructed and thereby confirms the location of a matched or unmatched struts in a ring, link or a hinge (**Figure 2C**).[16]

Light Intensity Analysis

Light intensity analysis was performed using dedicated software (QCU-CMS v4.69 research version, Leiden, The Netherlands). Raw images in original polar format were used to ensure that interpolation, dynamic range compression or other image processing did not alter the signal and bias the analysis. The OCT image of an Absorb BVS strut consists of a "black core" area, surrounded by reflective borders created by the following interfaces because of differences in refraction index: at baseline, the lumen-polymer interface and the abluminal polymer-vessel wall interface and at follow-up, a neointima-strut core interface and an abluminal strut core-vessel wall interface. These interfaces are depicted in **Figure 3**.

The contours of the strut core of interest were delineated manually by visual inspection in a Cartesian image that were created from the raw polar images. The manually drawn bor-

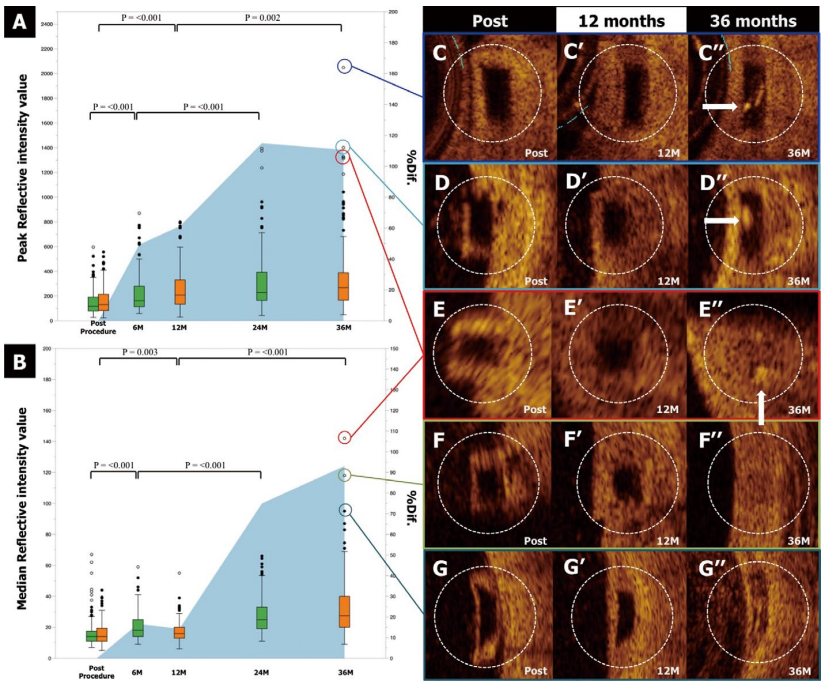

Figure 5. Change in peak and median intensity values over time with examples of serial highest peak or median intensity changes. (**A**,**B**) Whisker plots of peak and median intensity values (dimensionless) of corresponding strut cores in peak and median light intensities. Blue shadow curves depict the average of relative changes from baseline to follow-up (right vertical axis scale in percent, % difference). (**C″**–**E″**) Struts with the highest peak intensity values at 36 months. Corresponding struts post procedure (**C**–**E**) and 12 months (**C′**–**E′**) after implantation. (**C″**,**D″**) At 36 months, the corresponding struts on visual inspection still have a "black box" appearance but now include a high-intensity spot (arrows). (**E″**–**G″**) Struts with the highest median intensity values at 36 months. Corresponding struts post procedure (**E**–**G**) and 12 months (**E′**–**G′**) after implantation. These strut cores with high median values show increased light reflection of the entire core, which according to our previous categorized nomenclature could have been visually categorized as dissolved bright (**E″**), dissolved black (**F″**) or open (**G″**) box.[19]

ders of a strut core region often included complex reflective interfaces between the strut core and the surroundings, so that part of the bright reflective OCT frame of the strut (easily discernable at baseline) could become included in the strut core area at follow-up (**Figures 3C–E**) The interobserver manual delineation of the region of interest (ROI) could vary by 1 or 2 pixels (10–20 micron). To substantially reduce such a variability in ROI contours, 2 pixels inside of the manual contour were automatically subtracted (**Figure 3F**).

Although the strut borders at follow-up were no longer detectable because of changes in strut appearance, the contours at baseline were manually superimposed on the follow-up images (**Figure 5F″**). In addition, the malapposed struts and struts located at the ostium of the side branch post procedure were excluded in the current analysis. Furthermore, struts with post-procedure scattering center, which is a focal hyperintense signal in the strut core without apparent contact with either the axial or transversal strut edge and derived from polymer crazing caused by mechanical deformation of scaffold during crimping and deployment, were excluded in this analysis.[16,17]

The peak and median intensity values (dimensionless) of the strut core were then measured by the dedicated software (**Figure 4**). To evaluate interobserver reproducibility, 2 readers (S.N. and Y.I.) independently analyzed 400 struts randomly selected from the total number of investigated struts (n=909). To determine intraobserver reproducibility, 1 reader (S.N.) analyzed the struts twice, with the second reading occurring 3 months later. The inter- and intraobserver reproducibility were good according to the conventional norms[18] (peak intensity value: interobserver ICCa=0.92, intraobserver ICCc=0.89, median intensity value: interobserver ICCa=0.91, intraobserver ICCc=0.93; **Table S1**, **Figure S1**).

Table. Peak and Median Intensity Values at Several Time Points After Implantation of Bioresorbable Polymeric Intracoronary Scaffolds in the ABSORB Cohort B Trial

	Peak intensity value		Median intensity value	
	Cohort B1 (n=141)	Cohort B2 (n=162)	Cohort B1 (n=141)	Cohort B2 (n=162)
Post procedure, median [IQR]/ mean (SD)	117.0 [79.0 to 194.0]/ 149.5 (100.2)	131.0 [81.5 to 214.3]/ 157.4 (95.48)	14.0 [11.0 to 17.8]/ 17.1 (10.4)	14.0 [11.0 to 19.9]/ 15.8 (7.8)
M, median [IQR]/mean (SD)				
6	162.0 [112.5 to 279.5]/ 221.5 (162.2)	–	18.0 [14.0 to 25.0]/ 20.7 (9.4)	–
12	–	206.5 [133.5 to 330.3]/ 254.1 (178.4)	–	16.0 [13.0 to 20.0]/ 17.2 (7.4)
24	228.0 [162.0 to 393.5]/ 322.9 (247.0)	–	25.0 [19.0 to 33.0]/ 28.2 (12.3)	–
36	–	265.0 [163.5 to 386.0]/ 347.7 (302.8)	–	27.5 [20.0 to 40.3]/ 32.5 (19.4)
Dif., median [IQR]				
6M-Post	48.0 [–36.5 to 147.5]	–	3.0 [–1.0 to 9.5]	–
12M-Post	–	72.5 [–21.5 to 194.0]	–	1.8 [–2.0 to 6.0]
24M-6M	72.0 [38.5 to 108.5]	–	6.0 [0.8 to 15.0]	–
36M-12M	–	32.0 [–69.5 to 201.5]	–	11.0 [4.4 to 22.0]
P value				
Post-1st FUP	<0.001	<0.001	<0.001	0.003
1st–2nd FUP	<0.001	0.002	<0.001	<0.001
Post-2nd FUP	<0.001	<0.001	<0.001	<0.001

All P-values are calculated by Wilcoxon paired test. Continuous variables are presented as the mean±standard deviation (SD) or median with interquartile range (IQR). FUP, follow up; M, months.

Statistical Analysis

All statistical analyses were performed using the statistical software package SPSS version 21.0 (SPSS Inc, Chicago, IL, USA). Continuous variables are presented as the mean±standard deviation or median with interquartile ranges. Paired comparisons between post procedure and follow-up were done by Wilcoxon's signed rank test. Values of P<0.05 were considered statistically significant.

Results

In 87 serial pullbacks (19 lesions) performed either at 6 and 24 months (cohort B1) or at 12 and 36 months (cohort B2), 423 cross-sections were matched using anatomical landmarks. After strut level matching, a total of 303 corresponding struts (141 struts in cohort B1, 162 struts in cohort B2) were serially analyzed at 3 time points (909 strut images). Both peak and median intensity values over time are tabulated in **Table**, and the whisker plots of peak and median intensity values of the corresponding struts with the blue shadow curves representing the average relative change from baseline to follow-up are shown in **Figure 5**. The changes in absolute values for both parameters in the serial paired analysis are highly significant. In a relative difference analysis, the peak light intensity value increased gradually in the first 24 months after implantation (relative difference [%Dif.]: 49.4% at 6 months, 61.4% at 12 months, 115.0% at 24 months) and reached a plateau (%Dif.: 110.7% at 36 months), while the median intensity value increased significantly at 24 months (%Dif: 14.3% at 12 months, 75.0% at 24 months) and kept increasing at 36 months (93.1% at 36 months).

Mean plus 1 standard deviation of the measurement of the parameters was used as arbitrary threshold criteria for defining 4 groups: (1) struts with low peak and median light intensity values, (2) struts with high peak and low median intensity values, (3) struts with low peak and high median intensity values, and (4) struts with high peak and median intensity values.

The categorization into 4 groups helps in evaluating the changes of the strut appearance over time. At 36 months, 16.6% of the strut cores no longer has the appearance of those with low median and low peak intensities. This percentage is expected to rise dramatically at 5 years.

Struts with the highest peak or median intensity values at 3 years are exemplified in **Figure 5**. In 2 out of 3 struts with the highest peak intensity value, the strut core still appeared as a "black box" but contained isolated bright spots (arrows in **Figures 5C",D"**), Three struts with high median intensity values showed an increase in the light reflection of the entire strut (**Figures 5E"–G"**).

Discussion

The main findings of this study using the new methodology of light intensity assessment are: (1) serial quantification of light intensity in matched strut cores is feasible and reproducible when using dedicated software and (2) the peak and median intensity values increase gradually in the serial light intensity analysis, a phenomenon presumably related to bioresorption and/or the integration process of the resorbable device.

Bioresorption Process Monitoring by Light Intensity

Preclinical studies have demonstrated that the MW of the first-generation Absorb BVS becomes undetectable by gel permeation chromatography 24 months after implantation, and the polylactide is replaced by a provisional matrix that gradually integrates into the arterial wall.[7] Using visual qualitative assessment only, OCT is unable to monitor MW loss or to detect replacement of the polymer by this provisional matrix. In the current study using a quantitative method, there was an overall

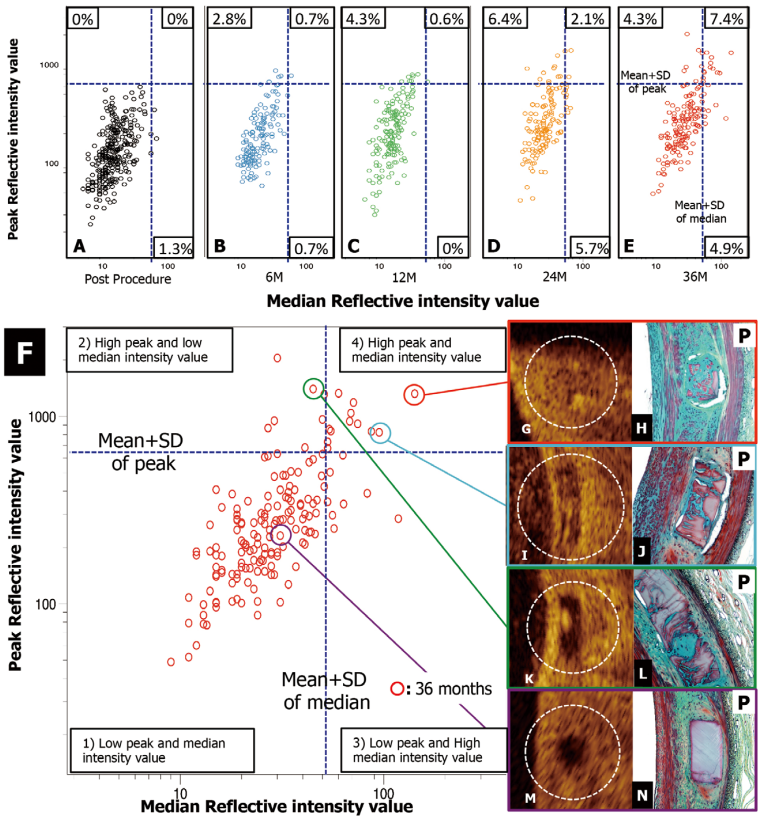

Figure 6. Quantitative light intensity assessment of strut integration on optical coherence tomography (OCT). (**A**–**E**) Scatter plots of the peak and median values post procedure and at 6, 12, 24 and 36 months. (**F**) Scatter diagram of the peak and median intensity values of each individual strut core at 36 months (dotted blue lines represent the light intensity values of the mean+1 SD for both parameters. According to these 2 threshold criteria, the strut cores are classified into 4 groups: (1) struts with low peak and low median light intensity values, (2) struts with high peak and low median intensity values, (3) struts with low peak and high median intensity values, and (4) struts with high peak and high median intensity values. The majority of struts are still categorized as having low peak/low median intensity value (M), which could correspond to struts without cellularization, but presumably occupied by provisional matrix (N). This panel also includes histological examples obtained from Absorb BVS implanted porcine coronary arteries at 36 moths after implantation and stained by Movat's pentachrome staining (red: smooth muscle cell/protein; blue-green: provisional matrix with staining characteristics comparable to that of proteoglycan; yellow: collagen). Strut cores with high median intensity value could (**G**,**I**) correspond to those that have been substantially cellularized with homogeneous connective tissue infiltration (**H**) such that the integration into the vessel wall is almost complete. (**I**) Strut core with high median and peak intensities suggesting that connective tissue infiltration is more modest (**J**). The strut cores with high peak/low median intensities (**K**) could correspond to struts that are focally cellularized with infiltration of connective tissue on histology (**L**).

increase in peak light intensity values from baseline to 24 months, followed by a plateau; these changes could reflect early connective tissue infiltration forming foci of cellularization in the provisional matrix; preliminary investigations (data not shown) in a porcine model suggest that specific interpretation (**Figure 6L**).

Integration Process on OCT

In previous preclinical studies, OCT assessment by visual inspection was sensitive enough to monitor the integration process after bioresorption ("strut footprint" becoming undetectable on OCT).[7] In the present study, by using peak and median intensity values (**Figure 6**), the struts could be categorized into

4 groups (see above).

In the current follow-up (36 months), the majority of struts (83.6%) still retained low peak and low median intensity values (**Figure 6M**), an observation that could correspond to strut cores without cellularization, but exclusively replaced by provisional matrix in the porcine model (**Figure 6N**). The strut cores with high peak intensity but low median intensity values (**Figure 6K**) could correspond to struts with focal cellularization according to histology in the porcine model (**Figure 6L**), whereas strut cores with high median intensity values (**Figures 6G,I**) could correspond to struts that have been fully cellularized in the porcine model (**Figures 6H,J**). Indeed, high median light intensity might reflect a more homogeneous replacement of struts with connective tissue whereby it is no longer possible to detect a demarcation between the de novo tissue replacing the pre-existing strut and the surrounding arterial wall, ultimately rendering the foci of the pre-existing struts undetectable by OCT (**Figure 6H**).

However, these hypothetical correlations between light intensity and histological changes need to be further cross-validated in the porcine model and investigated in patients with a follow-up of 5 years (March–November 2014). It is our expectation that most of these sites at 5 years will have high median intensity values and therefore will be no longer be detectable on OCT. In summary, categorization by peak/median light intensity value could be used to quantify the integration process of struts made of polylactide.

Clinical Implication of Light Intensity Analysis

The preclinical investigation of scaffolded porcine coronary artery models at 2, 3 and 4 years, combining OCT and histology, indicated that the last process in the integration of struts involves their complete replacement with connective tissue and maturation (shrinkage) of this tissue. This same process of cellularization and contracture also occurs clinically and may correspond to vessel wall thinning, the latter of which could contribute to lumen enlargement with/without adaptive remodeling. The current method of light intensity analysis could be applied clinically to assess the degree of strut/scaffold integration after implantation. Therefore, by using the classification of struts based on quantitative light intensity values, clinicians could assess the stage of scaffold integration that heralds late lumen enlargement.

From the regulatory perspective, it is mandatory to investigate the rate of biodegradation/bioresorption of each device, because the rate can vary according to the manufacturing process of PLLA (extrusion, molding, microfiber braiding etc), even in devices made of the same MW PLLA with an identical scaffold design.[19,20] Moreover, the rate at which a device becomes integrated into the tissue can also vary according to its anatomical placement, the nature of the tissue underlying the scaffold (normal or pathological) and the location of each strut against the wall (apposition, malapposition or side-branch ostium).[21] Considering the fact that the translucent polymeric scaffold initially does not interfere with imaging of the underlying plaque, the interaction between strut integration and underlying plaque could be also assessed with OCT.

Study Limitations

In the current study, OCT imaging was optional per protocol and cases of events were excluded, so only 28 of 101 patients (27.7%) with truly serial OCT were analyzed, which might under-represent the total cohort and relevant outcomes. Using the dedicated software algorithm, automatic exclusion of the outer circumferential pixels from the strut core could overlook changes around the border of a strut core. Theoretically, neointimal tissue on the endoluminal side of a strut core might influence the light intensity value of the strut cores; however, the median light intensity value of a strut core had no significant correlation with the thickness and median light intensity value of the neointimal tissue covering the endoluminal side of struts (**Figures S2,S3**).

Conclusions

The current analysis demonstrated that strut-by-strut serial light intensity analysis of the bioresorbable strut core is feasible and reproducible. The changes in peak intensity values at early time points may be related to focal cellularization, whereas the evolution of peak/median intensity values at later time points could reflect the integration process. Ongoing analysis of a porcine model up to 42 months will help in the interpretation of the 60-month (March–November 2014) OCT analysis of the sequential cohort of patients in the ABSORB cohort B1 and B2 trials.

Acknowledgments

The authors thank Renu Virmani for her preparation and interpretation of the preclinical histological samples from which the images were taken.

Disclosures

Conflict of Interest Statement: L. Perkins, A. Sheehy, S. Veldhof and R. Rapoza are full-time employees of Abbott Vascular, which sponsored the Cohort B trial.

References

1. Serruys PW, Garcia-Garcia HM, Onuma Y. From metallic cages to transient bioresorbable scaffolds: Change in paradigm of coronary revascularization in the upcoming decade? *Eur Heart J* 2012; **33:** 16–25b.
2. Onuma Y, Serruys PW. Bioresorbable scaffold: The advent of a new era in percutaneous coronary and peripheral revascularization? *Circulation* 2011; **123:** 779–797.
3. Raber L, Magro M, Stefanini GG, Kalesan B, van Domburg RT, Onuma Y, et al. Very late coronary stent thrombosis of a newer-generation everolimus-eluting stent compared with early-generation drug-eluting stents: A prospective cohort study. *Circulation* 2012; **125:** 1110–1121.
4. Nakazawa G, Otsuka F, Nakano M, Vorpahl M, Yazdani SK, Ladich E, et al. The pathology of neoatherosclerosis in human coronary implants bare-metal and drug-eluting stents. *J Am Coll Cardiol* 2011; **57:** 1314–1322.
5. Iqbal J, Onuma Y, Ormiston J, Abizaid A, Waksman R, Serruys P. Bioresorbable scaffolds: Rationale, current status, challenges, and future. *Eur Heart J* 2014; **35:** 765–776.
6. Vorpahl M, Finn AV, Nakano M, Virmani R. The bioabsorption process: Tissue and cellular mechanisms and outcomes. *EuroIntervention* 2009; **5**(Suppl F)**:** F28–F35.
7. Onuma Y, Serruys PW, Perkins LE, Okamura T, Gonzalo N, Garcia-Garcia HM, et al. Intracoronary optical coherence tomography and histology at 1 month and 2, 3, and 4 years after implantation of everolimus-eluting bioresorbable vascular scaffolds in a porcine coronary artery model: An attempt to decipher the human optical coherence tomography images in the ABSORB trial. *Circulation* 2010; **122:** 2288–2300.
8. Tearney GJ, Bouma BE. Shedding light on bioabsorbable stent struts seen by optical coherence tomography in the ABSORB trial. *Circulation* 2010; **122:** 2234–2235.
9. Sheehy A, Gutierrez-Chico JL, Diletti R, Oberhauser JP, Glauser T, Harrington J, et al. In vivo characterisation of bioresorbable vascular scaffold strut interfaces using optical coherence tomography with Gaussian line spread function analysis. *EuroIntervention* 2012; **7:** 1227–1235.
10. Templin C, Meyer M, Muller MF, Djonov V, Hlushchuk R, Dimova I, et al. Coronary optical frequency domain imaging (OFDI) for in vivo evaluation of stent healing: Comparison with light and electron microscopy. *Eur Heart J* 2010; **31:** 1792–1801.
11. Serruys PW, Onuma Y, Garcia-Garcia HM, Muramatsu T, van

Geuns RJ, de Bruyne B, et al. Dynamics of vessel wall changes following the implantation of the Absorb everolimus-eluting bioresorbable vascular scaffold: A multi-imaging modality study at 6, 12, 24 and 36 months. *EuroIntervention* 2014; **9:** 1271–1284.
12. Serruys PW, Onuma Y, Ormiston JA, de Bruyne B, Regar E, Dudek D, et al. Evaluation of the second generation of a bioresorbable everolimus drug-eluting vascular scaffold for treatment of de novo coronary artery stenosis: Six-month clinical and imaging outcomes. *Circulation* 2010; **122:** 2301–2312.
13. Okamura T, Garg S, Gutierrez-Chico JL, Shin ES, Onuma Y, Garcia-Garcia HM, et al. In vivo evaluation of stent strut distribution patterns in the bioabsorbable everolimus-eluting device: An OCT ad hoc analysis of the revision 1.0 and revision 1.1 stent design in the ABSORB clinical trial. *EuroIntervention* 2010; **5:** 932–938.
14. Gutierrez-Chico JL, van Geuns RJ, Regar E, van der Giessen WJ, Kelbaek H, Saunamaki K, et al. Tissue coverage of a hydrophilic polymer-coated zotarolimus-eluting stent vs. a fluoropolymer-coated everolimus-eluting stent at 13-month follow-up: An optical coherence tomography substudy from the RESOLUTE All Comers trial. *Eur Heart J* 2011; **32:** 2454–2463.
15. Gomez-Lara J, Radu M, Brugaletta S, Farooq V, Diletti R, Onuma Y, et al. Serial analysis of the malapposed and uncovered struts of the new generation of everolimus-eluting bioresorbable scaffold with optical coherence tomography. *JACC Cardiovasc Interv* 2011; **4:** 992–1001.
16. Gutierrez-Chico JL, Radu MD, Diletti R, Sheehy A, Kossuth MB, Oberhauser JP, et al. Spatial distribution and temporal evolution of scattering centers by optical coherence tomography in the poly(L-lactide) backbone of a bioresorbable vascular scaffold. *Circ J* 2012; **76:** 342–350.
17. Radu MD, Onuma Y, Rapoza RJ, Diletti R, Serruys PW. In vivo visualisation by three-dimensional optical coherence tomography of stress crazing of a bioresorbable vascular scaffold implanted for treatment of human coronary stenosis. *EuroIntervention* 2012; **7:** 1461–1463.
18. Fleiss J. The design and analysis of clinical experiments. New York: Wiley, 1986.
19. Serruys PW, Ormiston JA, Onuma Y, Regar E, Gonzalo N, Garcia-Garcia HM, et al. A bioabsorbable everolimus-eluting coronary stent system (ABSORB): 2-year outcomes and results from multiple imaging methods. *Lancet* 2009; **373:** 897–910.
20. Ormiston JA, Serruys PW, Onuma Y, van Geuns RJ, de Bruyne B, Dudek D, et al. First serial assessment at 6 months and 2 years of the second generation of ABSORB everolimus-eluting bioresorbable vascular scaffold: A multi-imaging modality study. *Circ Cardiovasc Interv* 2012; **5:** 620–632.
21. Gutierrez-Chico JL, Gijsen F, Regar E, Wentzel J, de Bruyne B, Thuesen L, et al. Differences in neointimal thickness between the adluminal and the abluminal sides of malapposed and side-branch struts in a polylactide bioresorbable scaffold: Evidence in vivo about the abluminal healing process. *JACC Cardiovasc Interv* 2012; **5:** 428–435.

Appendix

The list of investigators who contributed to OCT image acquisition in the ABSORB cohort B trial.

Robert-Jan van Geuns, MD, PhD (n=14), Evald Christiansen, MD (n=12), Dariusz Dudek, MD (n=8), Dougal McClean, MD (n=7), Jacques Koolen, MD, PhD (n=7), John A Ormiston, MB, ChB, PhD (n=7), Bernard Chevalier, MD (n=7), Stefan Windecker, MD (n=6), Pieter C. Smits, MD, PhD (n=6), Bernard de Bruyne, MD, PhD (n=5), Robert Whitbourn, MD (n=3).

Supplementary Files

Supplementary File 1

Inter- and intraobserver reproducibility of the light intensity value analysis of strut core

Influence of neointimal tissue on the endoluminal side of a strut core for the light intensity value of strut cores

Table S1. Inter- and intraobserver variability of peak and median intensity values

Figure S1. Inter- and intraobserver reproducibility analysis.

Figure S2. Neointimal thickness and the median light intensity value of the neointimal tissue covering the endoluminal side of struts.

Figure S3. Influence of neointimal tissue for the light intensity value of strut cores.

Please find supplementary file(s);
http://dx.doi.org/10.1253/circj.CJ-14-0143

1.3 Attenuation analysis of the light signal for calcified plaque

Impact of the orbital atherectomy system on a coronary calcified lesion: quantitative analysis by light attenuation in optical coherence tomography.

EuroIntervention. 2015;11(5):e1.
[Case report, Impact Factor : 3.77]

Sotomi Y, Shlofmitz RA, Nakatani S, Onuma Y, Serruys PW.

Impact of the orbital atherectomy system on a coronary calcified lesion: quantitative analysis by light attenuation in optical coherence tomography

Yohei Sotomi[1], MD; Richard A. Shlofmitz[2], MD; Shimpei Nakatani[3], MD; Yoshinobu Onuma[3], MD, PhD; Patrick W. Serruys[4]*, MD, PhD

1. Academic Medical Center, University of Amsterdam, Amsterdam, The Netherlands; 2. St. Francis Hospital, The Heart Center, Roslyn, New York, NY, USA; 3. Thoraxcenter, Erasmus Medical Center, Rotterdam, The Netherlands; 4. International Centre for Circulatory Health, NHLI, Imperial College London, London, United Kingdom

GUEST EDITOR: Antonio Colombo, MD; *Interventional Cardiology Unit, EMO-GVM Centro Cuore Columbus and San Raffaele Scientific Institute, Milan, Italy*

A 64-year-old female with chronic kidney disease was scheduled to undergo stenting of a severely calcified lesion in the left anterior descending coronary artery following "preparation" of the lesion by orbital atherectomy performed with the Diamondback 360® Coronary Orbital Atherectomy System (OAS), 1.25 mm Classic Crown (Cardiovascular Systems, Inc., St. Paul, MN, USA) **(Figure 1A)** (pre- and post-OAS angiography: **Figure 1B-1C** and **Figure 1B'-1C'**, respectively). The first run was performed at 80,000 rpm for 25 s followed by the second run at 120,000 rpm for 25 s. A 2.75×38 mm everolimus-eluting stent (XIENCE; Abbott Vascular, Santa Clara, CA, USA) was successfully implanted. Optical coherence tomography (C7-XR system, C7 Dragonfly™ catheter; LightLab Imaging, St. Jude, Minneapolis, MN, USA) was performed before and after OAS. **Figure 1D** and **Figure 1D'** show the thinning of a mixed calcified plaque (cross-sections corresponding to the dotted line in **Figure 1C** and **Figure 1C'**) (*wire artefact). In order to characterise changes in tissue components better, light attenuation was quantified circumferentially at different depths from the lumen surface using QCU-CMS software (Medis, Leiden, The Netherlands). Spread-out maps of tissue layers every 100 µm in the vessel wall are colour-coded according to their attenuation coefficient µt (**Figure 1E-1G** and **Figure 1E'-1G'**; *wire artefact) in an attempt to differentiate the mixed calcified plaque from the relatively low light-attenuating layer underlying it. Changes in light attenuation of the most superficial layer **(Figure 1F-1F')** suggest the ablation of the light-attenuating tissue (yellow and red area decreased, and blue area appeared). At deeper levels, no significant change was observed **(Figure 1G-1G')**.

Guest Editor

This paper was Guest Edited by Antonio Colombo, MD; Interventional Cardiology Unit, EMO-GVM Centro Cuore Columbus and San Raffaele Scientific Institute, Milan, Italy.

Conflict of interest statement

R. Shlofmitz has received speaker's honoraria from Cardiovascular Systems Inc. and St. Jude Medical. The other authors have no conflicts of interest to declare. The Guest Editor has no conflicts of interest to declare.

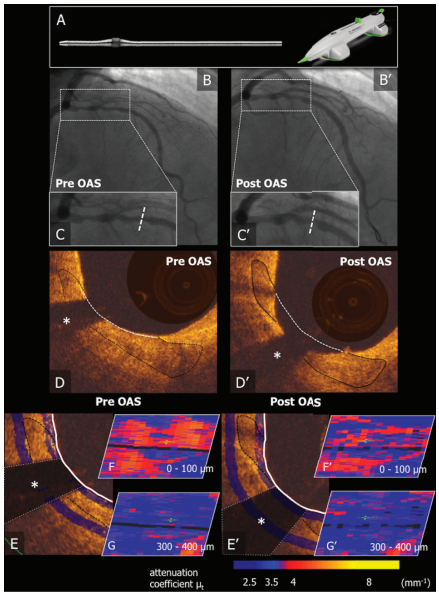

Figure 1. *Impact of the orbital atherectomy system on a coronary calcified lesion. A) Diamondback 360 OAS, 1.25 mm Classic Crown. B) and C) Pre- and post-OAS angiography. D) Corresponding OCT cross-sections. E-G) Light attenuation analysis.*

1.4 Discernment of metallic markers from calcification on MSCT

Fate of Bioresorbable Vascular Scaffold Metallic Radio-Opaque Markers at the Site of Implantation After Bioresorption.

JACC Cardiovasc Interv. 2015;8(8):1130-2.
[Letter to the editor Impact Factor : 7.35]

Suwannasom P, Onuma Y, Campos CM, Nakatani S, Ishibashi Y, Tateishi H, Grundeken MJ, Stanetic B, Nieman K, Jonker H, Garcia-Garcia HM, Serruys PW; investigators of ABSORB Cohort A, B and EXTEND trials.

Fate of Bioresorbable Vascular Scaffold Metallic Radio-Opaque Markers at the Site of Implantation After Bioresorption

The use of bioresorbable vascular scaffolds (BRS) is increasing in patients with coronary artery disease undergoing percutaneous coronary interventions. Because the devices are radiolucent on fluoroscopy, 2 adjacent cylindrical platinum markers are incorporated in the proximal and distal edges of the polymeric devices for precise scaffold deployment and post-dilation during the procedure. In addition, the metallic radio-opaque markers (MRMs) also provide anatomic landmarks for long-term follow-up when all the polymeric struts have been bioresorbed. There has been concern about the potential risk of MRM beads becoming dislodged from the device and embolized into the coronary bed after complete bioresorption of the polymeric struts. Beyond the biological hazard of MRMs embolization, the additional inconvenience is that the embolization may result in the incapacity to locate the coronary segment where the fully bioresorbed scaffold was implanted. Invasive assessment of BRS such as quantitative coronary angiography (QCA), intravascular ultrasound (IVUS), or optical coherence tomography (OCT) may be unable to detect the precise location of the MRMs either because of the resolution of the imaging technique (QCA) or as a result of wire artifact (IVUS, OCT) or mimicry by heavy calcium (IVUS). Multislice computed tomography coronary angiography (MSCT) has provided reliable assessment of the angiographic results up to 3 to 5 years (1,2) after scaffold implantation with accurate detection of the position of MRMs and their blooming effect without being dependent on the rate of image acquisition and wire artifact. In order to dispel the question of embolization of MRMs, we evaluated the persistent presence and location at 18 months of the MRMs following implantation of these fully bioresorbable scaffolds.

We retrospectively pooled data from the ABSORB trials (ABSORB Cohort A, ABSORB Cohort B, and ABSORB EXTEND) in which 943 patients with de novo native coronary artery lesions were treated with the fully resorbable everolimus-eluting Absorb scaffold (Abbott Vascular, Santa Clara, California); the details and primary outcome of each trial have been published (2-4). Of these 943 patients, 165 patients with 168 lesions underwent MSCT at 18 months. A list of the MSCT scanners, the acquisition protocol, and the MSCT analysis are described in the Online Appendix.

To establish the persistent presence of the MRMs in MSCT, both qualitative and quantitative evidence were required. The qualitative evidence was the ability to identify both proximal and distal MRMs position. Because calcified nodules (CN) could mimic MRMs, 4 criteria were used to identify the position of the radio-opaque markers: 1) typical location and orientation of the MRMs; 2) marker-to-marker length; 3) topographical relationship of the radio-opaque markers with anatomic landmarks visualized on MSCT and conventional coronary angiography; and 4) blooming artifact and its peak attenuation. The description of criteria and examples of MSCT images by using these 4 criteria are provided in Online Figure 1. The quantitative evidence is the MSCT scaffold length compared with its nominal length.

The statistical analysis is detailed in the Online Appendix.

A total of 168 lesions (12 lesions in ABSORB Cohort A, 61 lesions in ABSORB Cohort B, and 95 lesions in the ABSORB EXTEND study) were analyzed, and the study profile is shown in Online Figure 2. A total of 348 MRMs were evaluated by both quantitative and qualitative analyses; all MRMs were detected at the implantation site; and there was no evidence of marker embolization to distal vascular beds. The median MSCT scaffold length was 18.0 mm (ranging from 12 mm to 36 mm; interquartile range [IQR]: 17 to 19 mm) as well as the median nominal scaffold length was 18.0 mm (ranging from 12 mm to 28 mm) (**Figure 1**). The median difference in length between MSCT scaffold length and nominal scaffold length was 0.0 mm (IQR: −1.0 to 1.0 mm). There was a moderate correlation between MSCT mean lumen area (Mean LA) and QCA Mean LA ($r = 0.54$, $p < 0.0001$). A good correlation was observed between MSCT Mean LA and IVUS Mean LA, and between MSCT Mean LA and OCT Mean LA ($r = 0.74$ and $r = 0.73$, respectively; $p < 0.0001$) (Online Figure 3). The Mean LA measured by MSCT was comparable to QCA, but statistically lower than IVUS and OCT (Online Table 1). The reproducibility of the 4 criteria to identify MRMs from CN was good, $r = 0.97$; $p < 0.0001$ (Online Figure 4).

The attenuation of MRMs was approximately 30% higher than dense CN attenuation, but there was nevertheless a modest overlap of the attenuation values; MRM attenuation was sometimes lower than 1,000 HU as a result of the partial volume effect. The median peak density of MRMs was 1,368 HU (IQR: 1,158 to 1,715 HU) in contrast to the median peak density of CN that was 946 HU (IQR: 844 to 1,133 HU).

The main findings of this study are the following: 1) according to the criteria, all MRMs were identified and located at the site of the initial implantation; 2) the MSCT Mean LA was comparable to the Mean LA measured by QCA but lower than OCT and IVUS; and 3) the reproducibility in detecting of MRMs by using 4 criteria was high.

However, the distinction between calcified spots and metallic markers with computed tomography is also not easy to determine compared with OCT. The possible advantages of OCT are the ability to: 1) distinguish the MRMs from underlying calcium more clearly than MSCT; 2) measure the embedment of the struts; and 3) evaluate the thickness of neo-

intima because of a higher axial resolution of around 10 to 15 μm as compared with MSCT.

The limitation in this study is that the study result was able to confirm the persistent presence of MRMs only at medium-term follow-up, and the long-term results still require investigation.

In conclusion, MRM recognition by MSCT is critical for precise noninvasive assessment of the coronary location of all MRMs. On the basis of our study criteria, there was no evidence of MRMs dislodgement and embolization 18 months after scaffold implantation.

Pannipa Suwannasom, MD
Yoshinobu Onuma, MD, PhD
Carlos M. Campos, MD
Shimpei Nakatani, MD
Yuki Ishibashi, MD, PhD
Hiroki Tateishi, MD, PhD
Maik J. Grundeken, MD
Bojan Stanetic, MD
Koen Nieman, MD, PhD
Hans Jonker, BSc
Hector M. Garcia-Garcia, MD, PhD
***Patrick W. Serruys, MD, PhD**
on behalf of the investigators of ABSORB Cohort A, B and EXTEND trials
*International Center for Circulatory Health
NHLI, Imperial College London
London, United Kingdom

P.O. box 2125
Rotterdam 3000CC
the Netherlands
E-mail: patrick.w.j.c.serruys@gmail.com

http://dx.doi.org/10.1016/j.jcin.2015.04.010

Please note: The ABSORB trials were sponsored by Abbott Vascular. Dr. Nieman has received institutional research support from Siemens Medical Solutions, GE Healthcare, and Bayer HealthCare. Mr. Jonker is an employee of Cardialysis. Drs. Garcia-Garcia, Onuma, and Serruys are members of the Advisory Board of Abbott Vascular. All other authors have reported that they have no relationships relevant to the contents of this paper to disclose.

REFERENCES

1. Onuma Y, Dudek D, Thuesen L, et al. Five-year clinical and functional multislice computed tomography angiographic results after coronary implantation of the fully resorbable polymeric everolimus-eluting scaffold in patients with de novo coronary artery disease: the ABSORB cohort A trial. J Am Coll Cardiol Intv 2013;6:999–1009.

2. Serruys PW, Onuma Y, Garcia-Garcia HM, et al. Dynamics of vessel wall changes following the implantation of the absorb everolimus-eluting bioresorbable vascular scaffold: a multi-imaging modality study at 6, 12, 24 and 36 months. EuroIntervention 2014;9:1271–84.

3. Ormiston JA, Serruys PW, Regar E, et al. A bioabsorbable everolimus-eluting coronary stent system for patients with single de-novo coronary artery lesions (ABSORB): a prospective open-label trial. Lancet 2008;371:899–907.

4. Abizaid A, Ribamar Costa J Jr., Bartorelli AL, et al. The ABSORB EXTEND study: preliminary report of the twelve-month clinical outcomes in the first 512 patients enrolled. EuroIntervention 2014;10:1396–401.

APPENDIX For supplemental methods, statistical analysis, table, and figures, please see the online version of this article.

FIGURE 1 MSCT Scaffold Length Compared With Nominal Scaffold Length

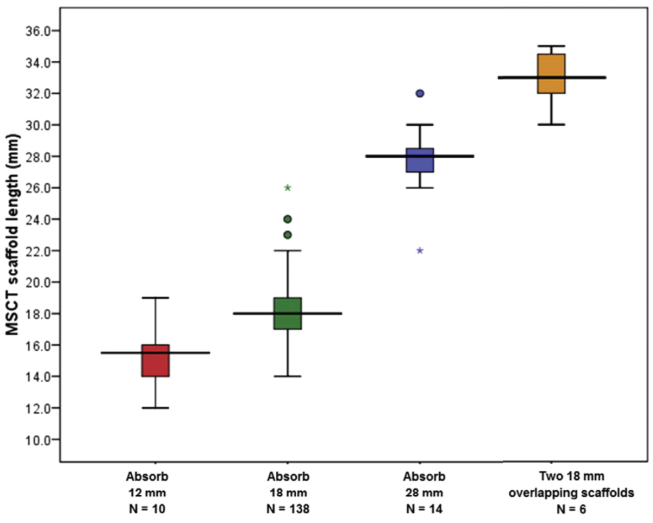

The median and the 1st and 3rd quartiles of each multislice computed tomography (MSCT) scaffold length corresponding to its nominal length are shown in **boxes**, and the minimum and maximum values as whiskers. The **asterisks and the dots above/below** indicate the outlier cases.

Chapter 2

Comparative analysis method between a metallic and a bioresorbable device

---

2.1. "Apple and Apple" comparison on OCT

Comparative analysis method of permanent metallic stents (XIENCE) and bioresorbable poly-L-lactic (PLLA) scaffolds (Absorb) on optical coherence tomography at baseline and follow-up.

EuroIntervention. 2015;11(6). pii: 20150528-02.
[Original research paper, Impact Factor : 3.77]

Nakatani S, Sotomi Y, Ishibashi Y, Grundeken MJ, Tateishi H, Tenekecioglu E, Zeng Y, Suwannasom P, Regar E, Radu MD, Räber L, Bezerra H, Costa MA, Fitzgerald P, Prati F, Costa RA, Dijkstra J, Kimura T, Kozuma K, Tanabe K, Akasaka T, Di Mario C, Serruys PW, Onuma Y.

Comparative analysis method of permanent metallic stents (XIENCE) and bioresorbable poly-L-lactic (PLLA) scaffolds (Absorb) on optical coherence tomography at baseline and follow-up

Shimpei Nakatani[1], MD; Yohei Sotomi[2], MD; Yuki Ishibashi[1], MD, PhD; Maik J. Grundeken[2], MD; Hiroki Tateishi[1], MD, PhD; Erhan Tenekecioglu[1], MD; Yaping Zeng[1], MD, PhD; Pannipa Suwannasom[1], MD; Evelyn Regar[1], MD, PhD; Maria D. Radu[3], MD, PhD; Lorenz Räber[4], MD, PhD; Hiram Bezerra[5], MD, PhD; Marco A. Costa[5], MD, PhD; Peter Fitzgerald[6], MD, PhD; Francesco Prati[7,8], MD, PhD; Ricardo A. Costa[9], MD, PhD; Jouke Dijkstra[10], PhD; Takeshi Kimura[11], MD, PhD; Ken Kozuma[12], MD, PhD; Kengo Tanabe[13], MD, PhD; Takashi Akasaka[14], MD, PhD; Carlo Di Mario[15], MD, PhD; Patrick W. Serruys[16]*, MD, PhD; Yoshinobu Onuma[1,17], MD, PhD

1. Thoraxcenter, Erasmus Medical Center, Rotterdam, The Netherlands; 2. Academic Medical Center, University of Amsterdam, Amsterdam, The Netherlands; 3. Department of Cardiology, The Heart Center, Rigshospitalet, Copenhagen University Hospital, Copenhagen, Denmark; 4. University Hospital Bern, Bern, Switzerland; 5. Harrington Heart and Vascular Institute, University Hospitals Case Medical Center, and Case Western Reserve University, Cleveland, OH, USA; 6. Stanford University, Stanford, CA, USA; 7. San Giovanni Addolorata Hospital, Rome, Italy; 8. Centro per la Lotta Contro L'Infarto - CLI Foundation, Rome, Italy; 9. Instituto Dante Pazzanese de Cardiologia, Sao Paulo, Brazil; 10. Leiden University Medical Center, Leiden, The Netherlands; 11. Kyoto University, Kyoto, Japan; 12. Teikyo University School of Medicine, Tokyo, Japan; 13. Mitsui Memorial Hospital, Tokyo, Japan; 14. Wakayama Medical University, Wakayama, Japan; 15. National Institute of Health Research Cardiovascular BRU, Royal Brompton & Harefield Foundation Trust & National Heart & Lung Institute, Imperial College, London, United Kingdom; 16. International Centre for Circulatory Health, NHLI, Imperial College London, London, United Kingdom; 17. Cardialysis B.V., Rotterdam, The Netherlands

S. Nakatani and Y. Sotomi contributed equally to this work.

GUEST EDITOR: Giulio Guagliumi, MD; *Cardiovascular Department, Ospedali Riuniti di Bergamo, Bergamo, Italy*

KEYWORDS

- comparative analysis method
- metallic stent
- optical coherence tomography
- PLLA scaffold

Abstract

Aims: Fully bioresorbable Absorb poly-L-lactic-acid (PLLA) scaffolds (Abbott Vascular, Santa Clara, CA, USA) are a novel approach for the treatment of coronary narrowing. Due to the translucency of the material (PLLA), the optical coherence tomography (OCT) measurement methods used in the ABSORB trials were unique but not applicable for permanent metallic stents. When the Absorb scaffold and metallic stents are compared in the context of randomised trials, it is challenging to compare the two devices using the conventional methods. The primary purpose of this report is to explain the biases in conventional methodologies applied for metallic stents and for PLLA scaffolds at baseline and follow-up, and to propose a new standard methodology that enables us to compare two different devices using an almost identical and methodological language.

Methods and results: A consensus amongst multiple core labs and expert researchers of OCT was reached on a new standard OCT measurement methodology that enables us to compare these two different devices. In brief, the proposed OCT methods are summarised as follows. 1) Both endoluminal and abluminal scaffold/stent contours should be traced. 2) Consistently, endoluminal and abluminal incomplete stent apposition areas should be measured. 3) The area occupied by scaffold/stent struts should be quantified directly or virtually. 4) The strut area should be systematically excluded from the flow area as well as the neointimal area. 5) Additional information on the degree of embedment could be reported using the interpolated lumen contour. Interobserver variability of the proposed method was excellent (intraclass correlation 0.89-100).

Conclusions: A standardised OCT measurement methodology is proposed. This should be implemented in ongoing and future trials comparing the Absorb scaffolds and metallic stents.

Introduction

The implantation of a bioresorbable scaffold (BRS) is a new approach that provides transient vessel support with drug delivery capability, potentially without the limitations of permanent metallic implants[1]. The potential short- and long-term performance of this technology has been repeatedly investigated with optical coherence tomography (OCT)[2-7]. However, images acquired by OCT after implantation of BRS are different from those with metallic stents due to the translucency of polymeric materials compared to the opacity of metallic compounds[8] **(Figure 1)**. Metallic struts appear on OCT as a reflective leading structure with abluminal shadowing, while polymeric struts appear as a "black box" area surrounded by bright reflecting frames without abluminal shadowing. As a consequence, in polymeric scaffolds the vessel wall behind the struts and the luminal area can easily be imaged and assessed, contributing to several advantages in quantitative analysis: i) capability of measuring the lumen vessel wall interface at baseline; ii) accurate assessment of malapposed struts; iii) measurement of strut/strut core area; iv) precise measurements of flow area; v) measurement of neointimal area between and on top of the struts, resembling very much the histomorphometric analysis of the animal models at follow-up.

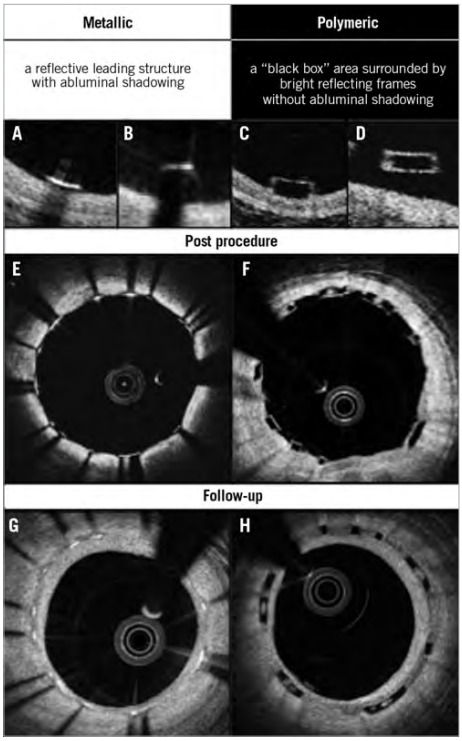

Figure 1. *The inherent differences between metallic stents and polymeric scaffolds on OCT. Representative appearance of metallic and polymeric struts is shown in A-D. Cross-sections post procedure with well-apposed struts (E and F) and those at follow-up (G and H) are illustrated.*

In previous ABSORB studies of polymeric scaffolds without comparison with metallic stents, OCT methods were developed to take advantage of the optical properties of poly-L-lactic-acid (PLLA); however, some of these were not applicable to metallic stents. For example, strut core area is not directly measurable in metallic stents. Taking into account the fact that many randomised trials comparing BRS and metallic stents with imaging endpoints are still ongoing[9] **(Online Table 1)**, it is important to establish a standardised and comparative method for quantitative analysis on OCT.

The primary purpose of this report is to explain differences in the conventional methodologies applied to metallic stents and PLLA scaffolds (specifically for the Absorb scaffold; Abbott Vascular, Santa Clara, CA, USA) at various time points, and to present the consensus of multiple core labs and OCT experts on a new standard methodology that enables us to compare two different devices using an almost identical, methodological language.

Potential biases caused by application of conventional methods

The basic differences in the two OCT measurement methods for polymeric struts and metallic stents stem from the translucency of the polymeric device. The conventional bioresorbable methodology provides more parameters than metallic methods: the area occupied by the struts and tracing of the back of struts. These parameters influence the measurement and calculation of the scaffold area, lumen area, total strut area, flow area, and malapposition area. In some parameters (e.g., flow area), the conventional metallic methods are incomplete in that the strut area is ignored. When the conventional methods **(Online Table 2-Online Table 4)** are applied for the comparison of the polymeric bioresorbable scaffold and the permanent metallic stents, the following methodological discrepancies lead to biased results post procedure and at follow-up **(Table 1)**.

STENT (ENDOLUMINAL)/SCAFFOLD (ABLUMINAL) AREA

Post procedure **(Figure 2)**, in metallic stents, the stent area is typically measured by interpolated contours connecting the endoluminal edge of the reflective border[10-14]. In polymeric scaffolds, the scaffold area is measured by interpolated contours connecting the abluminal side of black strut cores[6]. The scaffold area of polymeric devices (abluminal) is expected to be systematically larger than the stent area of metallic devices (endoluminal).

Theoretically speaking, when a 3.0 mm Absorb device with a strut thickness of 150 µm is deployed perfectly at the nominal size, endoluminal device area and abluminal device area are 7.07 mm^2 and 8.54 mm^2, respectively. In the clinical cases where the endoluminal stent area and endoluminal scaffold area are

Table 1. Biased results post procedure and at follow-up caused by methodological discrepancies.

	Metallic stent	Bias	PLLA scaffold
Post procedure			
Stent/scaffold area	Endoluminal	<	Abluminal
Lumen area	Embedded area of the struts is excluded	<	Total area of struts is included
Strut area	Not measured	<	Measured
Flow area	Protruding and malapposed areas of struts are included	>	The area occupied by struts is excluded
Malapposed strut assessment	Partially malapposed struts are defined as malapposed struts	>	Partially malapposed struts are defined as apposed struts
Incomplete stent apposition area	Difference between endoluminal stent contour and lumen contour at malapposed struts	>	Difference between abluminal scaffold contour and lumen contour at malapposed struts
At follow-up			
Stent/scaffold area	Endoluminal	<	Abluminal
Neointimal area	Neointimal area on top of struts	<	Neointimal area on top of struts and growing between struts
Lumen area	Protruding part of the uncovered struts is included	<	Total area of struts is excluded
Strut (core) area	Not measured	<	Measured
Flow area	Area of struts without any tissue is included	>	Area of struts is excluded
Malapposed strut assessment	Struts with reflective bridge to vessel wall are defined as malapposed struts when the distance from the midpoint of the bright leading edge to the lumen contour exceeds the strut thickness	>	Struts with reflective bridge to vessel wall are defined as apposed struts
Incomplete stent apposition area	Difference between endoluminal stent contour and lumen contour at malapposed struts	>	Difference between abluminal scaffold contour and lumen contour at malapposed struts

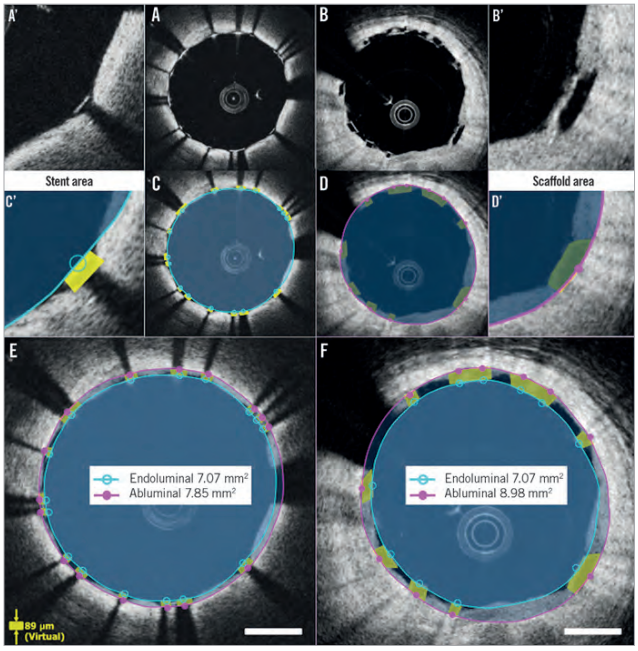

Figure 2. *Differences in endoluminal and abluminal stent area between metallic and polymeric struts. Metallic struts and polymeric struts post procedure are shown in A and B. Conventional measurements of stent/scaffold area are indicated in C and D. A'-D' show magnified views of A-D. In the cases where the endoluminal stent area and endoluminal scaffold area are identical (7.07 mm²), conventional stent area is measured as 7.07 mm² (E), while abluminal scaffold area is measured as 8.98 mm² (F).*

identical (7.07 mm^2), the conventional stent area is measured on OCT as 7.07 mm^2, while the abluminal scaffold area is measured as 8.98 mm^2 **(Figure 2)**. This causes the difference in reporting the stent/scaffold area of approximately 2 mm^2. The same is applicable to the follow-up up to three years. At a very long-term follow-up (>4 years), the scaffold area becomes difficult to measure due to the complete integration (disappearance) of the polymeric struts.

LUMEN AREA

The lumen area measured with BRS methods includes the entire strut area, while the lumen area with metallic methods excludes some of the strut area. Therefore, the lumen area by BRS methods tends to be larger than that by metallic methods (0.42 mm^2 on average)[6].

Post procedure **(Figure 3)**, the luminal contour of metallic stents is generally traced somewhat behind the apposed strut and interpolated through the struts virtually[10-14]. The embedded part of the metallic strut is excluded from the lumen area measurement. In polymeric devices, the embedded part of the polymeric strut (struts not buried) is fully included in the lumen area measurement.

At follow-up **(Figure 4)**, the two methods do not cause discrepancy as long as all struts are apposed and covered. In the presence of uncovered metallic struts, the metallic lumen area tends to be smaller since the uncovered struts are excluded from the lumen.

TOTAL STRUT AREA

The abluminal edge of metallic struts cannot be visualised on OCT imaging due to the outer shadow. Therefore, the area occupied by metallic struts has not been quantified and taken into account in any measurements. In polymeric scaffolds, two areas have been measured for individual struts: i) total strut area (tracing the outer boundary of the bright reflective frame), and ii) strut core area (tracing the black core)[6]. This inconsistency affects the lumen and flow area measurement both post procedure **(Figure 3)** and at follow-up **(Figure 4)**.

FLOW AREA

The flow area of metallic methods tends to be larger than that of BRS methods in the presence of malapposed struts[6,15]. Flow area is defined as the cross-sectional area where the blood flows. This excludes any intraluminal structures (such as thrombus, malapposed struts, and their surrounding neointimal tissue). In metallic struts, due to the lack of direct measurement of metallic strut areas, the malapposed struts and surrounding tissues are typically included **(Figure 3)**.

MALAPPOSED STRUT ASSESSMENT

Post procedure **(Figure 3)** and at follow-up **(Figure 4)**, the frequency of malapposed struts is potentially overestimated with the metallic methods compared to BRS methods. In the metallic stents, the struts are judged as malapposed when the distance from the midpoint of the bright leading edge to the interpolated lumen contour exceeds the strut thickness (including polymer, if present) as provided by the manufacturer[10-14,16-18]. In this method, partially malapposed struts (a part of the strut is in contact with the vessel wall, which is invisible due to outer shadow) are counted as malapposed struts. In polymeric devices, the contact of struts with the vessel wall is directly visible[6,19]. When any part of the struts is touching the vessel wall, the struts are judged as apposed.

At follow-up **(Figure 4)**, with polymeric devices, when any part of the struts is connected to the vessel wall by an abluminal connecting bridge, a lateral connecting bridge or a bilateral connecting bridge (directly visible), the struts are judged as apposed[6]. With metallic stents, the back of the struts is invisible, so that, in the presence or absence of an abluminal connecting bridge, the struts are always judged as malapposed.

INCOMPLETE STENT APPOSITION AREA

Due to the discrepancy of the methods, the incomplete stent apposition (ISA) area in the polymeric scaffold is expected to be systematically smaller than that in the metallic stent both post procedure **(Figure 3)** and at follow-up **(Figure 4)**. Post procedure, in metallic stents, the ISA area is defined as the area between the endoluminal leading edge of the metallic struts and the lumen contour at the site of malapposed struts[20]. In polymeric scaffolds, this is defined as the area between the scaffold (abluminal) and the lumen contour[6,21].

NEOINTIMAL AREA

The neointimal area measurement in metallic stents is expected to be systematically smaller than that of polymeric scaffolds **(Figure 4)**. Metallic methods quantify the neointima on top of the struts, but ignore the neointima growing between the struts as well as the neointima surrounding the malapposed strut. In polymeric devices[6,21], the neointima growing between the strut and the neointima surrounding the malapposed strut are included in the neointimal area measurement.

Proposed comparative measurement methods

To minimise/eliminate the discrepancy in measurement and reporting due to the difference in measurement, the following measurement methods are proposed in consensus amongst core labs and expert researchers. The most important changes are: standardisation of device area measurement (abluminal or endoluminal) and the direct or virtual measurement of the area occupied by struts.

STENT/SCAFFOLD AREA

ABLUMINAL STENT/SCAFFOLD AREA

The measurement of abluminal device area represents the area of the device that interacts with the vessel wall. Furthermore, it will give the baseline landmark in measurement of a neointimal hyperplasia between and on top of the struts. In polymeric scaffolds, the abluminal scaffold contour is drawn by joining the midpoint of the abluminal side of the black core in the apposed struts **(Figure 5, Figure 6)**, or the abluminal edge of the reflective frame borders of malapposed struts **(Online Figure 1)**.

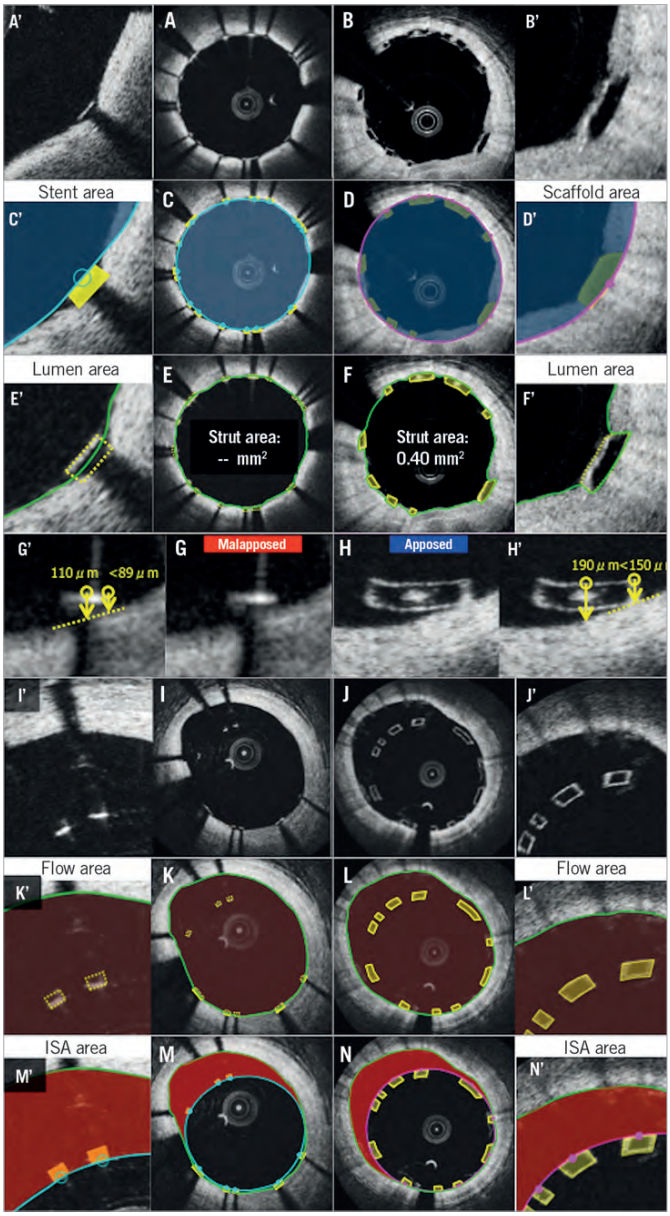

Figure 3. *Potential biases caused by application of conventional methods post procedure. Representative cross-sections of apposed struts, stent/scaffold area measurement, lumen area measurement, apposition of struts, ISA, flow area measurement, and ISA area measurement are shown in A, C, E, G, I, K, M (metallic stents) and B, D, F, H, J, L, N (polymeric struts), respectively. A'-N' are magnified views of A-N.*

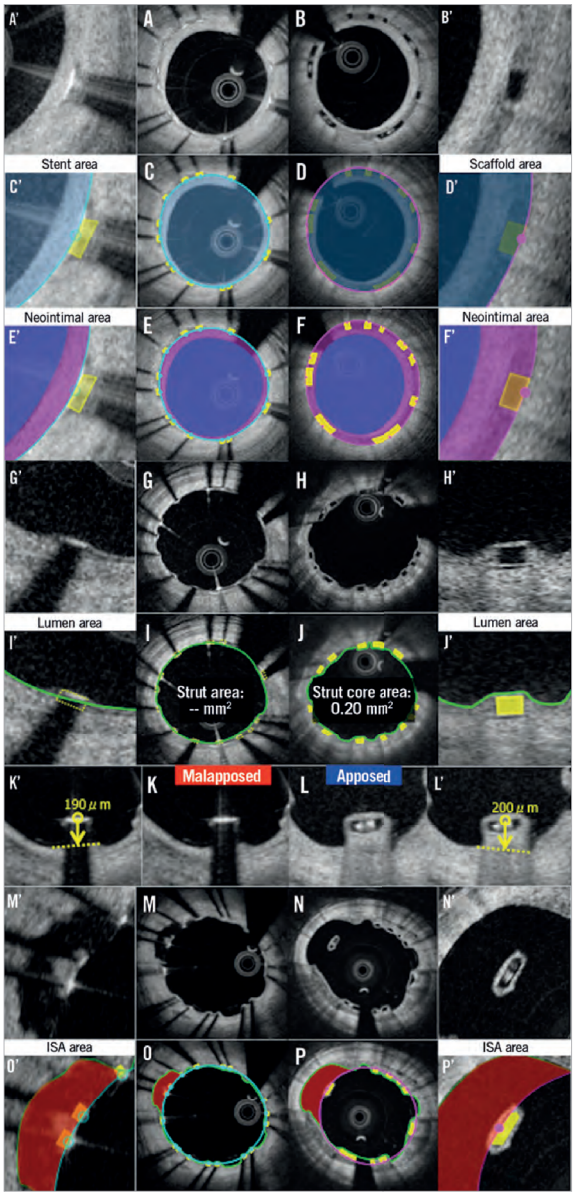

Figure 4. *Potential biases caused by application of conventional methods at follow-up. Representative cross-sections of covered struts, stent/scaffold area measurement, neointimal area measurement, uncovered struts, strut area or strut core area measurement, apposition of struts, ISA, ISA area measurement are shown in A, C, E, G, I, K, M, O (metallic stents) and B, D, F, H, J, L, N, P (polymeric struts), respectively. A'-P' are magnified views of A-P.*

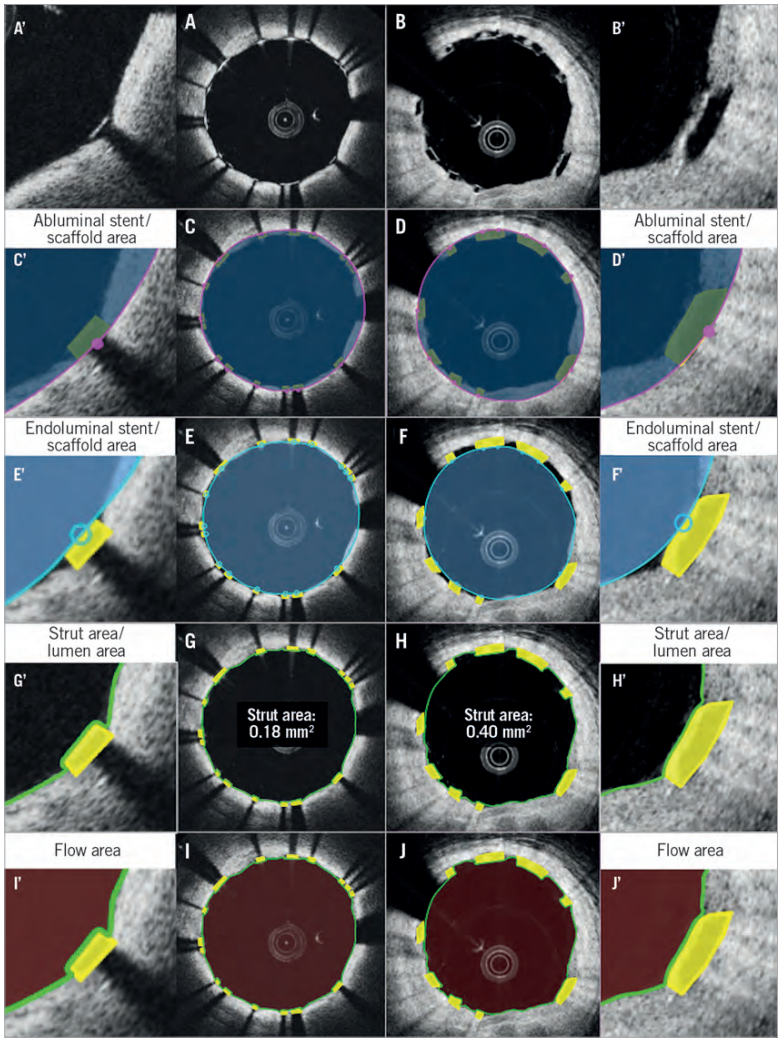

Figure 5. *Proposed comparative analysis methods post procedure in the cross-section without malapposed struts. Representative cross-sections with well-apposed metallic struts and polymeric struts are shown in A and B. Comparative methods of abluminal stent/scaffold area, endoluminal stent/scaffold area, strut area/lumen area, and flow area are illustrated in C, E, G, I (metallic strut), and D, F, H, J (polymeric strut), respectively. A'-J' are magnified views of A-J.*

Post procedure **(Figure 5)** and at follow-up **(Figure 6)**, in metallic stents, the abluminal stent contour cannot be directly delineated; however, this can be automatically drawn by simulating the virtual contour of the struts. After identifying all struts in a cross-section, the abluminal stent contour is delineated by a curvilinear interpolation connecting the middle points of the abluminal edge of virtual metallic struts.

ENDOLUMINAL STENT/SCAFFOLD AREA

Measurement of the endoluminal device area enables a direct comparison of the internal dimensions of the device. The endoluminal

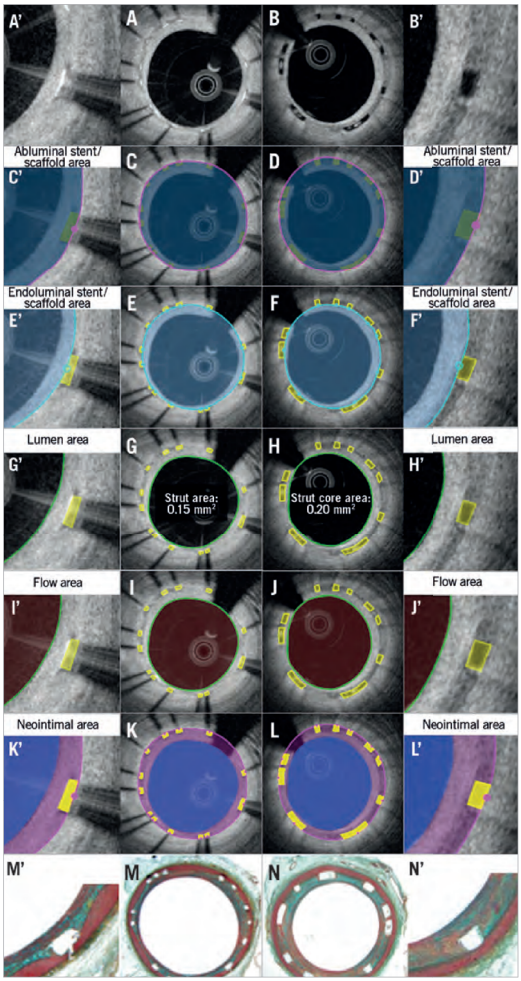

Figure 6. *Proposed comparative analysis methods at follow-up in the cross-section of covered struts without malapposed struts. Representative cross-sections with well-covered metallic and polymeric struts at follow-up are shown in A and B, respectively. Abluminal stent/scaffold area, endoluminal stent/scaffold area, lumen area, flow area, and neointimal area are shown in C, E, G, I, K (metallic strut), and D, F, H, J, L (polymeric strut), respectively. Histomorphometric analyses of the animal models are shown in M (metallic strut) and N (polymeric strut). A'-N' are magnified views of A-N.*

metallic stent contour is delineated by a curvilinear interpolation connecting the midpoints of the endoluminal leading edge of the reflective border **(Figure 5)**. At follow-up, the bright leading edge of the metallic strut is generally still detectable in the neointima **(Figure 6)**.

The endoluminal polymeric scaffold contour is delineated by a curvilinear interpolation connecting the midpoint of the endoluminal side of the reflective frame. Whenever the polymeric reflective frame is not discernible, such as with buried struts in the vessel wall post procedure or struts at follow-up, there is no other alternative and the leading edge of the black box in polymeric struts has to be compared with the bright leading edge of the metallic struts **(Figure 6)**.

LUMEN AREA

Lumen contour is defined as the continuous interface between a blood and non-blood structure. Since any intraluminal structures isolated in the blood area are measured separately, the lumen area does not primarily exclude them (intraluminal mass and isolated malapposed struts not connected to the vessel wall by a bridge) **(Figure 5, Online Figure 1)**.

At follow-up, when the side-to-side bridge divides the vessel into a double channel lumen, the second lumen behind the bridge should be included in flow area measurement **(Figure 6, Online Figure 2, Online Figure 3)**.

MALAPPOSED STRUTS

In general, when the distance between the endoluminal surfaces of struts with respect to the interpolated lumen contour is more than the strut thickness, either metallic or polymeric, the strut is considered as a malapposed strut. It is measured at the midpoint of the endoluminal reflective border of metallic stents or the endoluminal side of the reflective frame of polymeric scaffolds **(Online Figure 4)**.

Post procedure, the malapposition distance is the distance between the interpolated (made necessary by the metal shadowing) lumen contour and the back of the completely malapposed metallic or polymeric struts (abluminal reflective frame in polymeric struts and virtual back [=89 μm from the bright leading edge] in metallic [XIENCE®; Abbott Vascular] struts) at the midpoint of the endoluminal edge of the strut. A malapposition distance greater than zero is the criterion of malapposition. Whenever the back of polymeric or metallic struts (virtual back) is in contact with the (interpolated) lumen contour, the malapposition is characterised as partial. Even in case of partial malapposition, the malapposition distance can be measured.

At follow-up, in polymeric scaffolds, the abluminal side of the black core is used for the measurement of malapposed distance, since the abluminal reflective bright frame cannot be distinguished from the neointima coverage.

In recent core lab experiences, we have observed on follow-up OCT that malapposed struts are sometimes connected with the vessel wall by tissue created behind the struts or between the struts and vessel wall unilaterally or bilaterally. This aspect should be described and classified according to the type of connecting bridge **(Online Figure 4)**: i) malapposed struts without connecting bridge (isolated malapposed strut), ii) malapposed struts with a potentially thin abluminal connecting bridge, which could be masked by the shadow in metallic struts, iii) malapposed struts with an abluminal connecting bridge, iv) malapposed struts with a lateral connecting bridge, v) malapposed struts with a bilateral connecting bridge.

INCOMPLETE STENT APPOSITION AREA

The ISA area is a part of the blood flow area located behind the malapposed struts. The delineation of the abluminal side of the ISA area is usually drawn as the same as the scaffold/stent area. As described above, when the scaffold/stent area is drawn using the endoluminal and/or abluminal contours, the same principle should be applied for measurement of the ISA area.

ABLUMINAL INCOMPLETE STENT APPOSITION AREA

Abluminal ISA area is the difference between the abluminal stent/scaffold area and the lumen area at the site of malapposed metallic/polymeric struts **(Online Figure 1, Online Figure 3)**. Although we could use endoluminal/abluminal ISA area, we favour the use of abluminal ISA area for consistency with the measurement of the flow area.

ENDOLUMINAL INCOMPLETE STENT APPOSITION AREA

Endoluminal ISA area is the difference between the endoluminal scaffold/stent area (see previous definition) and the lumen area at the site of malapposed polymeric/metallic struts **(Online Figure 1, Online Figure 3)**.

PROLAPSE AREA

Post procedure, prolapse is a protrusion of the vessel wall structure between or on top of adjacent stent struts beyond the endoluminal stent/scaffold contour without disruption of the continuity of the lumen vessel surface[22] (modified from the previously published methodology[23]). At follow-up, this area is measured as a part of the neointima.

INTRALUMINAL DEFECT AREA

An irregularly shaped structure in contact with the luminal contour is defined as an intraluminal defect attached to the vessel wall. The area of defect can be measured. An isolated structure in the lumen distant from the vessel wall is defined as a free intraluminal defect.

FLOW AREA

In order systematically to exclude the intraluminal structures attached to or free from the vessel wall, the measurement of malapposed struts with surrounding tissue is mandatory, either with direct measurement or by virtual simulation of the metallic strut area. The flow area can be calculated using the following formula: (lumen area [see the previous definition]) (second lumen area [if any]) - (intraluminal structures area [e.g., isolated intraluminal defect area, strut area of malapposed strut without surrounding tissue and malapposed strut with surrounding tissues not connected to the vessel wall including strut area, if any]) **(Figure 5, Figure 6, Online Figure 1-Online Figure 3)**.

ASSESSMENT OF THE INTERACTION BETWEEN THE STRUTS AND VESSEL WALL USING THE INTERPOLATED LUMEN CONTOUR

In order to assess the strut-vessel wall interaction, the interpolated contour should be drawn at the site where the metallic or polymeric struts are embedded inside the vessel wall level. In case of a single protruding or malapposed strut, a short linear interpolation between the two edges should be used. In case of multi-strut extensive malapposition, a curvilinear interpolation should be used **(Online Figure 4)**.

Post procedure, this contour interpolates through the protruding metallic or polymeric struts. At follow-up, this contour should keep circularity and interpolate through the uncovered struts and the connecting reflective bridge of malapposed struts. However, it should be noted that the interpolated contour is the line of the lumen vessel wall virtually interpolated through the struts. Therefore, the area measurement according to this contour has no meaning from the biological point of view, but reflects the vessel wall injury.

Using the interpolated lumen contour, malapposition and the degree of embedment are assessed per strut **(Figure 7)**. The degree of embedment could be the parameter of the vessel injury caused by the implantation of the scaffold/stent struts. Notably, the current BRS has a larger surface (Absorb: 26%) area compared to metallic stents (XIENCE: 12%). When the same force is applied, BRS struts create less pressure compared to metallic struts, which could result in less embedment of BRS struts[24]. Therefore, the reporting of the degree of embedment could be important to describe the difference in device-vessel interaction.

The degree of embedment (in percentage) could be calculated using the following formula: (1 – [the distance between the midpoint of the endolumnal strut surface to the interpolated lumen contour]/[the thickness of the strut (as indicated by the manufacturer)])×100 (%). Complete protruding is defined as the (virtual) abluminal surface of metallic or polymeric struts being aligned with the interpolated lumen contour line (i.e., 0% embedment). When the degree of the embedment is between 0% and 50%, the strut is classified as partially protruding. When the degree is between 50% and 100%, such struts are categorised as partially embedded. Complete embedment is defined as the endoluminal

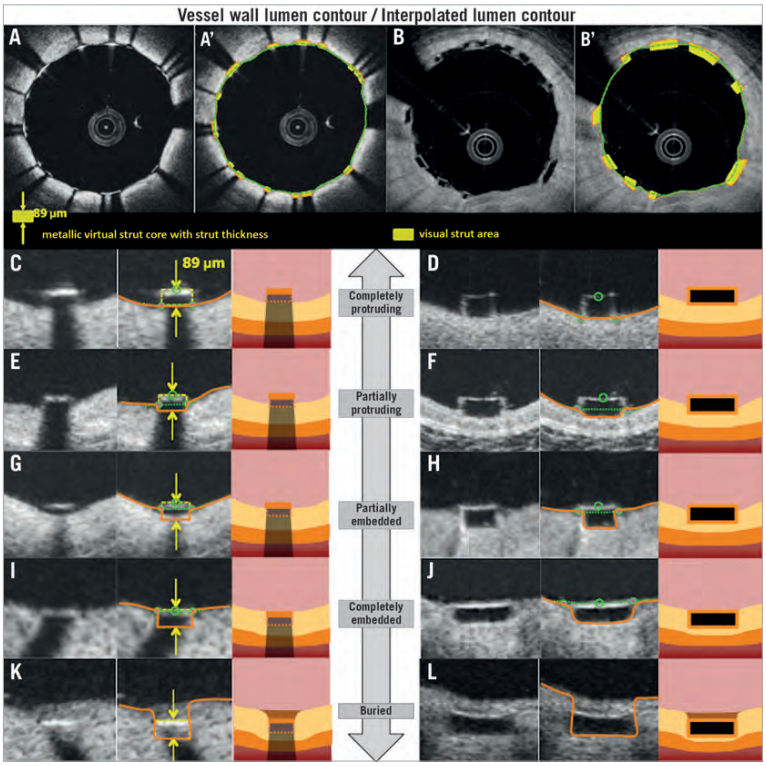

Figure 7. *Assessment of the interaction between the struts and the vessel wall. Representative cross-sections with well-apposed metallic struts and polymeric struts are shown in A and B. A' and B' show the strut area measurement and interpolated lumen contour. Definitions of embedment based on the distance between strut and interpolated lumen contour are shown in C-L. Completely protruding, partially protruding, partially embedded, completely embedded, and buried struts are shown in C, E, G, I, K (metallic struts), and D, F, H, J, L (polymeric struts), respectively.*

surface of metallic or polymeric struts being aligned with the interpolated lumen contour line (i.e., 100% embedment). When the tissue is covering the endoluminal surface of struts, the struts are considered as buried.

Vessel wall lumen contour implicates the whole vessel wall which consists of a three-layer structure (intima, media, adventitia); these structures are deformed during stent/scaffold implantation, and therefore the vessel wall lumen contour should be drawn behind the abluminal side of metallic struts (virtual contour, taking into account the strut thickness) or the scaffold strut (visible contour of black core) at the site of apposed struts.

NEOINTIMAL AREA

After an implantation of a coronary device, neointimal tissue grows not only on top of the struts but also between the struts as a response to the acute injury. In histomorphometry, the amount of neointimal tissue between the struts is quantified using the internal elastic membrane (IEM). On OCT, the abluminal scaffold/stent contour measured directly or virtually could serve as a landmark indicating the original lumen border (surrogate for an IEM), which enables quantification of a neointimal hyperplasia as in histomorphometry **(Figure 6)**.

When all struts are apposed, the neointimal area is calculated as: (abluminal stent/scaffold area) - (lumen area+strut/strut core area). With this comparative method, the areas occupied by the metallic or polymeric struts are excluded, and the neointima between and on top of the struts is quantified. In the presence of any malapposed struts, there is a need to introduce the concept of a hybrid area, consisting of a combination of scaffold contour and lumen contour **(Online Figure 3)**. The hybrid area is delineated by the abluminal side of the struts (abluminal stent/scaffold contour) of the apposed struts and by the interpolated lumen contour at malapposed struts (interpolated contour). According to these measurements, the neointimal area is calculated as: ([hybrid area] – [lumen area] – [apposed strut/strut core area])+([isolated malapposed strut with surrounding tissues area] – [malapposed strut/strut core area]).

The presence of neointima between struts could be described (covered strut with complete inter-strut neointima, covered strut with incomplete inter-strut neointima, uncovered strut with complete inter-strut neointima and uncovered strut with incomplete inter-strut neointima) **(Online Figure 5)**.

STRUT COVERAGE

Coverage of polymeric struts and metallic stents should be assessed using different criteria. Typically, on OCT the polymeric struts look like black boxes surrounded by a bright frame, which is the interface between the blood and PDLLA/PLLA. Immediately after the implantation *in vivo* of BRS, the thickness of the endoluminal bright border is measured as 30 μm on average[4]. The light intensity of neointimal tissue is similar to the bright border, and they are indistinguishable on visual assessment. Any tissue coverage on top of the struts should result in an increase of the thickness of the bright border: therefore, the threshold of coverage thickness ≥30 μm should be used to assess the coverage of the polymeric struts.

Regarding metallic struts, the coverage thickness of >0 μm (tissue can be identified above the struts) should be used to classify covered and uncovered struts.

In malapposed struts without an abluminal connecting bridge, the coverage of the abluminal strut side should be assessed. The neointimal abluminal coverage at the back of the metallic or polymeric strut does not reflect the initial degree of malapposition, but reflects a biological attempt to create a connecting bridge between the struts and the lumen interface.

The coverage thickness (neointimal thickness on top of struts) is defined as the distance between the luminal surface of the covering tissue and endoluminal reflective edge in metallic struts or endoluminal side of the black core in polymeric struts. In malapposed struts, it is possible to measure the thickness of the abluminal neointima.

In malapposed struts without an abluminal connecting bridge, the neointimal thickness should be measured on both the abluminal and endoluminal sides. The endoluminal neointimal thickness is defined as the distance from the abluminal side of the strut (abluminal side of the black core in a polymeric strut or that of a virtual strut in a metallic stent) to the neointima-lumen interface, following a straight line connecting the midpoint of the longitudinal axis of the strut with the centre of gravity of the lumen. The reason why we use the back of metallic or polymeric struts is to take into account the initial degree of malapposition post procedure.

The reproducibility data of the proposed method are additionally presented in terms of mean abluminal stent area, mean endoluminal stent area, mean lumen area, mean flow area, and mean total strut area. The interobserver variability showed excellent correlation of the two measurements with an ICC ranging from 0.89 to 1.00 **(Online Table 5, Online Figure 6)**.

Discussion

In short, the proposed OCT methods are summarised as follows. 1) Both endoluminal and abluminal scaffold/stent contours should be traced. 2) Consistently, endoluminal and abluminal ISA area should be measured. 3) The area occupied by scaffold/stent struts should be quantified directly or virtually. 4) The strut area should be systematically excluded from the flow area as well as the neointimal area. 5) Additional information on the degree of embedment could be reported using the interpolated lumen contour.

The proposed new method is applicable specifically for the Absorb scaffolds, and in general for metallic stents. Amongst PLLA-based scaffolds, there is considerable variance in the initial molecular weight, the presence of a copolymer, the purity of PLLA (monomer, solvent) and post-processing methods (extrusion, annealing, microbraiding, etc.), which could influence the bioresorption time and optical properties of struts (OCT imaging). For example, the same methods could be used at baseline for the other PLLA devices such as ART® BRS (Arterial Remodeling

Technologies, Noisy-le-Roi, France), Amaranth FORTITUDE® (Amaranth Medical, Inc., CA, USA), and DESolve® (Elixir Medical, Sunnyvale, CA, USA) but not for the Mirage PLLA scaffold (ManLi Cardiology, Singapore). On OCT, the strut of the Mirage scaffold is bright at implantation, and therefore OCT cannot measure its dimensions. Regarding the ART, Amaranth and DESolve scaffolds, the proposed methods may not be applicable at follow-up due to the different resorption times. The general concept of measuring endoluminal and abluminal scaffold contours and strut area should be applied for the other PLLA technologies, but the details of analysis (follow-up method) should be fine-tuned for each individual device.

In metallic stents, it could be challenging to simulate the area occupied by a strut and the location of the abluminal surface of the strut by drawing a virtual square with a length that is equivalent to the known strut plus polymer (if present) thickness. To the best of our knowledge, we do not have commercially available software that enables us to depict the abluminal metallic stent contour with the strut thickness automatically, which could result in limited reproducibility in the measurements. In addition, the virtual metallic struts should be drawn considering the limitations of OCT images in the following cross-sections: i) in the cross-section with suboptimal flushing, the stent struts are illustrated as blurred and enlarged due to the low lateral resolution, ii) in the cross-section when the OCT catheter is located towards one side of the vessel, the stent struts appear to face the catheter (strut orientation artefact)[13].

After the integration of a bioresorbable scaffold to the vessel wall, we can no longer use the measurement of scaffold area, neointimal area and ISA area (if present), and at long-term follow-up we can only compare the flow area between metallic stents and bioresorbable scaffolds. We therefore emphasise the accurate measurement of flow area in the currently proposed methods. In the conventional analysis method of metallic stents, the flow area is calculated based on the lumen contour, which is the virtually interpolated contour through the struts, resulting in inaccurate measurement of flow area. In the currently proposed method, this interpolated contour enables us to assess the malapposed or apposed struts.

Limitations

In other BRS made of magnesium or iron, the proposed method for metallic stents could be applied post procedure but not at follow-up. In BRS made of a fully bioresorbable polymer with a different optical property due to the different material or post-processing such as microbraiding, some proposed methods cannot be applied. However, even in BRS where the abluminal side of the struts is not discernible, some interpolation (abluminal side is drawn virtually to simulate the thickness of the strut) could be applied. The bright reflective border of the polymeric struts is not distinguishable from the vessel neointima at the follow-up phase, so that measuring the black core area might slightly underestimate the strut area. In the presence of the blooming and/or sunflower artefact[13] of metallic struts, it remains challenging for technology to measure accurately the metallic stent area.

Conclusion

When conventional methods are applied for the comparison of polymeric scaffolds and permanent metallic stents, the different methodological approaches lead to biased results post procedure and at follow-up. By introducing the virtual square of metallic struts, the proposed method enables us to compare topologically the two different devices.

Impact on daily practice

In the ABSORB first-in-man trials testing an everolimus-eluting bioresorbable scaffold, the optical coherence tomography analysis was performed with a unique methodology taking advantage of the translucency of the material (PLLA); however, such methods could not be applied to permanent metallic stents. In this report, the authors describe differences in conventional methodologies applied for metallic stents and PLLA scaffolds at various time points, assess a potential impact on measurement by applying heterogeneous methods, and propose a new standard methodology that enables us to compare two different devices using an almost identical, methodological language. This standardised OCT measurement methodology should be implemented in the ongoing and future trials comparing the Absorb scaffolds and metallic stents, enabling us to make a fair evaluation of the performance of both devices.

Guest Editor

This paper was guest edited by Giulio Guagliumi, MD; Cardiovascular Department, Ospedali Riuniti di Bergamo, Bergamo, Italy.

Conflict of interest statement

E. Regar receives research support from St. Jude Medical to the institution. M.D. Radu receives speaker honoraria from St. Jude Medical. L. Räber receives speaker bureau and an unrestricted research grant to the institution from St. Jude Medical. F. Prati is a consultant of St. Jude Medical. T. Kimura is a member of the Advisory Board for Abbott Vascular and receives a research grant. K. Kozuma is a member of the Advisory Board for Abbott Vascular Japan and receives lecture fees. K. Tanabe is a member of the Advisory Board for Abbott Vascular Japan, a consultant of Terumo, Kaneka and Zeon, and receives remuneration from St. Jude Medical. C. Di Mario receives a research grant from Abbott Vascular to the institution. P.W. Serruys is a member of the Advisory Board for Abbott Vascular. Y. Onuma is a member of the Advisory Board for Abbott Vascular. The other authors have no conflicts of interest to declare. The Guest Editor is a consultant for St. Jude Medical and Boston Scientific and received research grants through the hospital from Abbott Vascular, Boston Scientific and St. Jude Medical.

References

1. Serruys PW, Garcia-Garcia HM, Onuma Y. From metallic cages to transient bioresorbable scaffolds: change in paradigm of coronary revascularization in the upcoming decade? *Eur Heart J.* 2012;33:16-25b.

2. Karanasos A, Simsek C, Gnanadesigan M, van Ditzhuijzen NS, Freire R, Dijkstra J, Tu S, Van Mieghem N, van Soest G, de Jaegere P, Serruys PW, Zijlstra F, van Geuns RJ, Regar E. OCT assessment of the long-term vascular healing response 5 years after everolimus-eluting bioresorbable vascular scaffold. *J Am Coll Cardiol.* 2014;64:2343-56.

3. Ormiston JA, Serruys PW, Onuma Y, van Geuns RJ, de Bruyne B, Dudek D, Thuesen L, Smits PC, Chevalier B, McClean D, Koolen J, Windecker S, Whitbourn R, Meredith I, Dorange C, Veldhof S, Hebert KM, Rapoza R, Garcia-Garcia HM. First serial assessment at 6 months and 2 years of the second generation of absorb everolimus-eluting bioresorbable vascular scaffold: a multi-imaging modality study. *Circ Cardiovasc Interv.* 2012;5:620-32.

4. Serruys PW, Onuma Y, Dudek D, Smits PC, Koolen J, Chevalier B, de Bruyne B, Thuesen L, McClean D, van Geuns RJ, Windecker S, Whitbourn R, Meredith I, Dorange C, Veldhof S, Hebert KM, Sudhir K, Garcia-Garcia HM, Ormiston JA. Evaluation of the second generation of a bioresorbable everolimus-eluting vascular scaffold for the treatment of de novo coronary artery stenosis: 12-month clinical and imaging outcomes. *J Am Coll Cardiol.* 2011;58:1578-88.

5. Serruys PW, Onuma Y, Garcia-Garcia HM, Muramatsu T, van Geuns RJ, de Bruyne B, Dudek D, Thuesen L, Smits PC, Chevalier B, McClean D, Koolen J, Windecker S, Whitbourn R, Meredith I, Dorange C, Veldhof S, Hebert KM, Rapoza R, Ormiston JA. Dynamics of vessel wall changes following the implantation of the absorb everolimus-eluting bioresorbable vascular scaffold: a multi-imaging modality study at 6, 12, 24 and 36 months. *EuroIntervention.* 2014;9:1271-84.

6. Serruys PW, Onuma Y, Ormiston JA, de Bruyne B, Regar E, Dudek D, Thuesen L, Smits PC, Chevalier B, McClean D, Koolen J, Windecker S, Whitbourn R, Meredith I, Dorange C, Veldhof S, Miquel-Hebert K, Rapoza R, Garcia-Garcia HM. Evaluation of the second generation of a bioresorbable everolimus drug-eluting vascular scaffold for treatment of de novo coronary artery stenosis: six-month clinical and imaging outcomes. *Circulation.* 2010;122:2301-12.

7. Serruys PW, Ormiston JA, Onuma Y, Regar E, Gonzalo N, Garcia-Garcia HM, Nieman K, Bruining N, Dorange C, Miquel-Hebert K, Veldhof S, Webster M, Thuesen L, Dudek D. A bioabsorbable everolimus-eluting coronary stent system (ABSORB): 2-year outcomes and results from multiple imaging methods. *Lancet.* 2009;373:897-910.

8. Gomez-Lara J, Brugaletta S, Farooq V, Onuma Y, Diletti R, Windecker S, Thuesen L, McClean D, Koolen J, Whitbourn R, Dudek D, Smits PC, Chevalier B, Regar E, Veldhof S, Rapoza R, Ormiston JA, Garcia-Garcia HM, Serruys PW. Head-to-head comparison of the neointimal response between metallic and bioresorbable everolimus-eluting scaffolds using optical coherence tomography. *JACC Cardiovasc Interv.* 2011;4:1271-80.

9. Serruys PW, Chevalier B, Dudek D, Cequier A, Carrie D, Iniguez A, Dominici M, van der Schaaf RJ, Haude M, Wasungu L, Veldhof S, Peng L, Staehr P, Grundeken MJ, Ishibashi Y, Garcia-Garcia HM, Onuma Y. A bioresorbable everolimus-eluting scaffold versus a metallic everolimus-eluting stent for ischaemic heart disease caused by de-novo native coronary artery lesions (ABSORB II): an interim 1-year analysis of clinical and procedural secondary outcomes from a randomised controlled trial. *Lancet.* 2015;385:43-54.

10. Gonzalo N, Garcia-Garcia HM, Serruys PW, Commissaris KH, Bezerra H, Gobbens P, Costa M, Regar E. Reproducibility of quantitative optical coherence tomography for stent analysis. *EuroIntervention.* 2009;5:224-32.

11. Terashima M, Rathore S, Suzuki Y, Nakayama Y, Kaneda H, Nasu K, Habara M, Katoh O, Suzuki T. Accuracy and reproducibility of stent-strut thickness determined by optical coherence tomography. *J Invasive Cardiol.* 2009;21:602-5.

12. Okamura T, Gonzalo N, Gutierrez-Chico JL, Serruys PW, Bruining N, de Winter S, Dijkstra J, Commossaris KH, van Geuns RJ, van Soest G, Ligthart J, Regar E. Reproducibility of coronary Fourier domain optical coherence tomography: quantitative analysis of in vivo stented coronary arteries using three different software packages. *EuroIntervention.* 2010;6:371-9.

13. Tearney GJ, Regar E, Akasaka T, Adriaenssens T, Barlis P, Bezerra HG, Bouma B, Bruining N, Cho JM, Chowdhary S, Costa MA, de Silva R, Dijkstra J, Di Mario C, Dudek D, Falk E, Feldman MD, Fitzgerald P, Garcia-Garcia HM, Gonzalo N, Granada JF, Guagliumi G, Holm NR, Honda Y, Ikeno F, Kawasaki M, Kochman J, Koltowski L, Kubo T, Kume T, Kyono H, Lam CC, Lamouche G, Lee DP, Leon MB, Maehara A, Manfrini O, Mintz GS, Mizuno K, Morel MA, Nadkarni S, Okura H, Otake H, Pietrasik A, Prati F, Raber L, Radu MD, Rieber J, Riga M, Rollins A, Rosenberg M, Sirbu V, Serruys PW, Shimada K, Shinke T, Shite J, Siegel E, Sonoda S, Suter M, Takarada S, Tanaka A, Terashima M, Thim T, Uemura S, Ughi GJ, van Beusekom HM, van der Steen AF, van Es GA, van Soest G, Virmani R, Waxman S, Weissman NJ, Weisz G; International Working Group for Intravascular Optical Coherence Tomography (IWG-IVOCT). Consensus standards for acquisition, measurement, and reporting of intravascular optical coherence tomography studies: a report from the International Working Group for Intravascular Optical Coherence Tomography Standardization and Validation. *J Am Coll Cardiol.* 2012;59:1058-72.

14. Prati F, Guagliumi G, Mintz GS, Costa M, Regar E, Akasaka T, Barlis P, Tearney GJ, Jang IK, Arbustini E, Bezerra HG, Ozaki Y, Bruining N, Dudek D, Radu M, Erglis A, Motreff P, Alfonso F, Toutouzas K, Gonzalo N, Tamburino C, Adriaenssens T, Pinto F, Serruys PW, Di Mario C; Expert's OCT Review Document. Expert review document part 2: methodology, terminology and clinical applications of optical coherence tomography for the assessment of interventional procedures. *Eur Heart J.* 2012;33:2513-20.

15. Onuma Y, Thuesen L, van Geuns RJ, van der Ent M, Desch S, Fajadet J, Christiansen E, Smits P, Holm NR, Regar E, van Mieghem N, Borovicanin V, Paunovic D, Senshu K, van Es GA, Muramatsu T, Lee IS, Schuler G, Zijlstra F, Garcia-Garcia HM, Serruys PW; TROFI Investigators. Randomized study to assess the effect of thrombus aspiration on flow area in patients with ST-elevation myocardial infarction: an optical frequency domain imaging study--TROFI trial. *Eur Heart J.* 2013;34:1050-60.

16. Foin N, Gutierrez-Chico JL, Nakatani S, Torii R, Bourantas CV, Sen S, Nijjer S, Petraco R, Kousera C, Ghione M, Onuma Y, Garcia-Garcia HM, Francis DP, Wong P, Di Mario C, Davies JE, Serruys PW. Incomplete stent apposition causes high shear flow disturbances and delay in neointimal coverage as a function of strut to wall detachment distance: implications for the management of incomplete stent apposition. *Circ Cardiovasc Interv.* 2014;7:180-9.

17. Tanigawa J, Barlis P, Di Mario C. Intravascular optical coherence tomography: optimisation of image acquisition and quantitative assessment of stent strut apposition. *EuroIntervention.* 2007;3:128-36.

18. Radu M, Jorgensen E, Kelbaek H, Helqvist S, Skovgaard L, Saunamaki K. Strut apposition after coronary stent implantation visualised with optical coherence tomography. *EuroIntervention.* 2010;6:86-93.

19. Farooq V, Onuma Y, Radu M, Okamura T, Gomez-Lara J, Brugaletta S, Gogas BD, van Geuns RJ, Regar E, Schultz C, Windecker S, Lefevre T, Brueren BR, Powers J, Perkins LL, Rapoza RJ, Virmani R, Garcia-Garcia HM, Serruys PW. Optical coherence tomography (OCT) of overlapping bioresorbable scaffolds: from benchwork to clinical application. *EuroIntervention.* 2011;7:386-99.

20. Amoroso G, van Geuns RJ, Spaulding C, Manzo-Silberman S, Hauptmann KE, Spaargaren R, Garcia-Garcia HM, Serruys PW, Verheye S. Assessment of the safety and performance of the STENTYS self-expanding coronary stent in acute myocardial infarction: results from the APPOSITION I study. *EuroIntervention.* 2011;7:428-36.

21. Gomez-Lara J, Brugaletta S, Diletti R, Garg S, Onuma Y, Gogas BD, van Geuns RJ, Dorange C, Veldhof S, Rapoza R, Whitbourn R, Windecker S, Garcia-Garcia HM, Regar E, Serruys PW. A comparative assessment by optical coherence tomography of the performance of the first and second generation of the everolimus-eluting bioresorbable vascular scaffolds. *Eur Heart J.* 2011;32:294-304.

22. Muramatsu T, Garcia-Garcia HM, Onuma Y, Zhang YJ, Bourantas CV, Diletti R, Iqbal J, Radu MD, Ozaki Y, Serruys PW. Intimal flaps detected by optical frequency domain imaging in the proximal segments of native coronary arteries: an innocent bystander? Insights from the TROFI Trial. *Circ J.* 2013;77:2327-33.

23. Gonzalo N, Serruys PW, Okamura T, Shen ZJ, Onuma Y, Garcia-Garcia HM, Sarno G, Schultz C, van Geuns RJ, Ligthart J, Regar E. Optical coherence tomography assessment of the acute effects of stent implantation on the vessel wall: a systematic quantitative approach. *Heart.* 2009;95:1913-9.

24. Serruys PW, Suwannasom P, Nakatani S, Onuma Y. Snowshoe Versus Ice Skate for Scaffolding of Disrupted Vessel Wall. *JACC Cardiovasc Interv.* 2015;8:910-3.

Supplementary data

Online Table 1. Ongoing randomised trials comparing BRS with their metallic counterparts.

Online Table 2. Summary of OCT analysis methods used in previous trials without comparison between BRS and permanent metallic stents at post procedure.

Online Table 3. Summary of OCT analysis methods used in previous trials without comparison between BRS and permanent metallic stents at follow-up.

Online Table 4. Summary of OCT analysis methods used in previous trials without comparison between BRS and permanent metallic stents at very long-term follow-up.

Online Table 5. Interobserver variability.

Online Figure 1. Proposed comparative analysis methods post procedure in the presence of malapposed struts.

Online Figure 2. Proposed comparative analysis methods at follow-up in cross-section in the presence of uncovered struts.

Online Figure 3. Proposed comparative analysis methods at follow-up in the presence of malapposed struts.

Online Figure 4. Proposed assessment of malapposed struts at follow-up.

Online Figure 5. Assessment of strut coverage.

Online Figure 6. Interobserver variability.

Supplementary data

Online Table 1. Ongoing randomised trials comparing BRS with their metallic counterparts.

Study title	Design	No. of patients (N)	FUP (yrs)	Primary endpoint	Secondary endpoints	Intravascular imaging endpoint	Status	NCT Number
ABSORB II	RCT (2:1) Absorb vs. EES	501	3	Vessel motion at 3 yrs	Clinical, procedural, anginal, and disease-related QOL	IVUS; LA, PA, SA, and neointimal area	Enrolment completed	01425281
ABSORB III	RCT (2:1) Absorb vs. EES	2,000	5	TLF at 1 yr	Clinical, procedural, anginal, diabetic indication, and disease-related QOL outcome	IVUS; in-stent/scaffold mean LA change up to 3 yrs OCT; neointimal coverage, ISA up to 3 yrs, and jailed SB analyses from 3D	Enrolment completed	01751906
ABSORB Japan	RCT (2:1) Absorb vs. EES	400	5	TLF at 1 yr	Vessel motion at 2 yrs and 4 yrs	IVUS; change in average LA from post procedure to 2 yrs OCT; neointimal coverage, ISA	Enrolment completed	01844284
TROFI II	STEMI RCT (1:1) Absorb vs. EES	190	3	6-month neointimal healing score	Device and procedural success, MACE and angina class	OFDI; presence of filling defect, both malapposed and uncovered struts, neointimal hyperplasia area/volume, mean flow area/volume, intraluminal defect area/volume, thickness of neointimal tissue developed over lipid-rich plaque	Enrolment ongoing	01986803
AIDA	All-comers (1:1) RCT Absorb vs. EES	2,194	5	2-yr TVF	Device and procedural success, ST, TLF, MACE and QOL	IVUS or OCT can be performed at the discretion of the operator	Enrolment completed	01858077
ABSORB China	RCT (1:1) Absorb vs. EES	480	5	In-segment LL at 1 yr	Device success, MACE	NA	Enrolment completed	01923740
ABSORB IV	RCT (1:1) Absorb vs. EES	3,000 (landmark analysis; 5,000)	5	Angina at 1 yr, TLF between 1 and 5 yrs (landmark analysis)	Repeat angiography up to 5 yrs, landmark analysis on MACE and TVF up to 5 yrs	NA	Enrolment ongoing	02173379
VANISH	RCT (1:1) Absorb vs. EES	60	3	Myocardial blood flow over time	Restenosis, and lumen dimensions	NA (using $H_2{}^{15}O$ PET)	Enrolment ongoing	01876589
EVERBIO II	RCT EES, vs. BES, vs. Absorb	240	5	LLL at 9 mo	DoMACE, PoMACE	NA	Enrolment completed	01711931
ISAR ABSORB MI	RCT (1:1) Absorb vs. EES	260	5	%DS at 6-8 months	DoCE, PoCE, ST and composite of MI/death	NA	Enrolment ongoing	01942070
PROSPECT ABSORB*	ACS RCT (1:1), Absorb vs. GDMT in VP	900	3	2-yr IVUS MLA	The utility of low-risk IVUS and NIRS	IVUS and NIRS; identify plaques prone to future rupture and clinical events	Enrolment ongoing	02171065

Online Table 2. Summary of OCT analysis methods used in previous trials without comparison between BRS and permanent metallic stents at post procedure.

Post procedure	Metallic stents	PLLA scaffolds
Strut-vessel wall interaction	Malapposition: malapposed struts Struts with the axial distance (the strut's surface to the luminal surface) being greater than the strut thickness (including polymer, if present). Apposition: protruding and embedded struts – protruding; the endoluminal strut boundary is located above the level of the luminal surface – embedded; the endoluminal strut boundary is below the level of the luminal surface The clinical significance of this classification is, however, unclear[12].	Malapposition: malapposed struts Struts with a clear separation between the abluminal side of the strut and the vessel wall by flash. Apposition: aligned (protruding) and apposed (embedded) struts – aligned (protruding); a distance between the vessel wall and strut abluminal surface less than the thickness of the strut – apposed (embedded); embedded within the vessel wall
Lumen area	The vessel lumen can be traced at the boundary between the lumen and the leading edge of the intima using automatic, semiautomatic, or manual means. Care should be taken to avoid interpreting artefacts such as shadowing as being part of the artery lumen[12].	…
Lumen vessel wall area	So far not done (impossible to calculate directly due to shadow)	Delineated at the back (abluminal) side of the apposed struts, or at the endoluminal contour of the vessel wall behind the malapposed struts (if any)[6]
Stent/scaffold area	Trace the leading edge and axial centre of the stent strut surface reflection. Contour interpolation such as polynomial and spline interpolation of the lines between the strut anchors has been used.	– Join the middle point of the black core abluminal side of the apposed struts, or the abluminal edge of the frame borders of malapposed struts (if any)[6]. – Manually join the middle point of each consecutive strut around the circumference. In frames with only a few struts, the BVS area was adjusted to follow the lumen area in the regions where its contour was outside the lumen area[19].
Strut core area	So far not done (impossible to calculate directly due to shadow)	Area consists of a central black core and a light-scattering frame border[6]
Prolapse area	Convex-shaped protrusion of tissue between or on top of adjacent stent struts towards the lumen without disruption of the continuity of the luminal vessel surface	Between the prolapsed contour (lumen contour) and the scaffold area
ISA area	The space between the lumen contour and the stent contour at the location of malapposed struts[18]	The abluminal side of the frame border of the malapposed strut and the endoluminal contour of the vessel wall[6]
Flow area	(Stent area + ISA area [if any]) – (Tissue protrusion + isolated intraluminal defect area)[15]	(Scaffold area + ISA area [if any]) – (Intraluminal strut areas + Tissue prolapse area + Intraluminal defect area)[6]
ISA distance	Distance between the abluminal surface of the strut and the luminal surface of the artery wall[12].	So far not done
Detachment distance/ ISA thickness	Detachment distance: (ISA distance) – (strut thickness [including polymer, if present])[16]	ISA thickness: Distance from the abluminal side of the white frame zone to the lumen area boundary[17]

Online Table 3. Summary of OCT analysis methods used in previous trials without comparison between BRS and permanent metallic stents at follow-up.

At follow-up	Metallic stents	PLLA scaffolds
Strut-vessel wall interaction	Malapposition: the axial distance between the strut's surface and the luminal surface is greater than the strut thickness (including polymer, if present).	Malapposition: struts with a clear separation between the abluminal side of the strut and the vessel wall by flash.
Strut coverage	Covered strut: tissue can be identified above the struts[12]	Covered strut: – the thickness of the coverage (between the abluminal side of the strut core and the lumen) is above 150 microns[6] – the thickness of the coverage (between the endoluminal side of the strut core and the lumen) is above 30 microns[4] – one of the strut corners preserved the right angle shape without signs of neointimal tissue[8]
Lumen area	Lumen border is bounded by the luminal border automatically with a dedicated software and additional manual corrections are performed if necessary[12]	Following the endoluminal contour of the neointima between and on top of the apposed struts and the endoluminal contour of the vessel wall behind the malapposed struts[6]
Stent/scaffold area	Trace the leading edge and axial centre of the stent strut surface reflection. Contour interpolation such as polynomial and spline interpolation of the lines between the strut anchors has been used.	– Delineate the abluminal side of the black box-shaped core[6] – Join the middle point of the struts[19]
Strut core area	So far not done (impossible to calculate directly due to shadow)	Embedding, coverage and thickening of the frame borders; the strut (core) area is defined only by its black core
ISA area	The space between the lumen contour and the stent contour at the location of malapposed struts[18]	The abluminal side of the frame border of the malapposed strut (covered or uncovered) and the endoluminal contour of the vessel wall[6]
Flow area	(Stent area + ISA area [if any]) – (Tissue protrusion + Isolated intraluminal defect area)[15]	(Scaffold area + ISA area [if any]) – (Intraluminal strut areas + Tissue prolapse area + Intraluminal defect area)[6]
Neointimal hyperplasia area	(Stent area + ISA area [if any]) – (Lumen area)	When all struts are apposed: Scaffold area – (Lumen area + Black core area) When malapposed: (Scaffold area + ISA area + Malapposed strut with surrounding tissue) – (Lumen area + Strut core area)
Stent area stenosis	Stent area stenosis (stent percent area obstruction, neointimal burden): (Stent area minus lumen area)/stent area	Lumen area stenosis: (Scaffold area minus lumen area)/scaffold area
Neointimal thickness	Distance between the luminal surface of the covering tissue and the luminal surface of the strut[12]	Thickness from the endoluminal border of the black strut core to the lumen[19]
ISA distance	Distance between the abluminal surface of the strut and the luminal surface of the artery wall[12]	So far not done
Detachment distance/ ISA thickness	Detachment distance: (ISA distance) – (strut thickness [including polymer, if present])[16]	ISA thickness: Distance from the abluminal side of the white frame zone to the lumen area boundary

Online Table 4. Summary of OCT analysis methods used in previous trials without comparison between BRS and permanent metallic stents at very long-term follow-up.

At very long-term follow-up	Metallic stents	PLLA scaffolds
Strut-vessel wall interaction	Malapposition: the axial distance between the strut's surface and the luminal surface is greater than the strut thickness (including polymer, if present). Apposition: – protruding, where the endoluminal strut boundary is located above the level of the luminal surface – embedded, where the endoluminal strut boundary is below the level of the luminal surface The clinical significance of this classification is, however, unclear.	So far not done (impossible to calculate due to indiscernibility of struts)
Strut coverage	Tissue can be identified above the struts	So far not done (impossible to calculate due to indiscernibility of struts)
Lumen area	Lumen border is bounded by the luminal border automatically with a dedicated software and additional manual corrections are performed if necessary	Following the endoluminal contour of the neointima between and on top of the apposed struts. In case of malapposed struts, the analyst uses the endoluminal contour of the vessel wall behind the malapposed struts.
Stent/scaffold area	Trace the leading edge and axial centre of the stent strut surface reflection. Contour interpolation, such as polynomial and spline interpolation of the lines between the strut anchors, has been used.	So far not done (impossible to calculate due to indiscernibility of struts)
Strut core area	So far not done (impossible to calculate directly due to shadow)	So far not done (impossible to calculate due to indiscernibility of struts)
Flow area	(Stent area + ISA area [if any]) – (Tissue protrusion + Isolated intraluminal defect area)[15]	(Lumen area) – (Intraluminal defect area)
Neointimal hyperplasia area	(Stent area + ISA area [if any]) – (Lumen area)	So far not done (impossible to calculate due to indiscernibility of struts)
Neointimal thickness	Distance between the luminal surface of the covering tissue and the luminal surface of the strut.	So far not done (impossible to calculate due to indiscernibility of struts)

Online Table 5. Interobserver variability.

	Observer A	Observer B	Absolute difference	ICC (95% CI)
Metallic stent (n=106 cross-sections)				
Abluminal stent area (mm^2)	8.54±2.14	8.51±2.15	0.03±0.15	0.9983 (0.9975-0.9988)
Endoluminal stent area (mm^2)	7.68±2.01	7.66±2.02	0.02±0.13	0.9985 (0.9979-0.9990)
Lumen area (mm^2)	7.65±2.06	7.58±2.04	0.07±0.04	0.9998 (0.9997-0.9998)
Total strut area (mm^2)	0.12±0.04	0.14±0.05	–0.02±0.02	0.8912 (0.8442-0.9246)
Flow area (mm^2)	7.64±2.05	7.57±2.03	0.07±0.04	0.9998 (0.9997-0.9998)
Polymeric scaffold (n=131 cross-sections)				
Abluminal scaffold area (mm^2)	7.55±1.85	7.50±1.84	0.05±0.17	0.9956 (0.9939-0.9969)
Endoluminal scaffold area (mm^2)	6.01±1.63	6.15±1.65	–0.14±0.19	0.9937 (0.9911-0.9955)
Lumen area (mm^2)	6.88±2.11	6.88±2.11	–0.00±0.01	1.0000 (1.0000-1.0000)

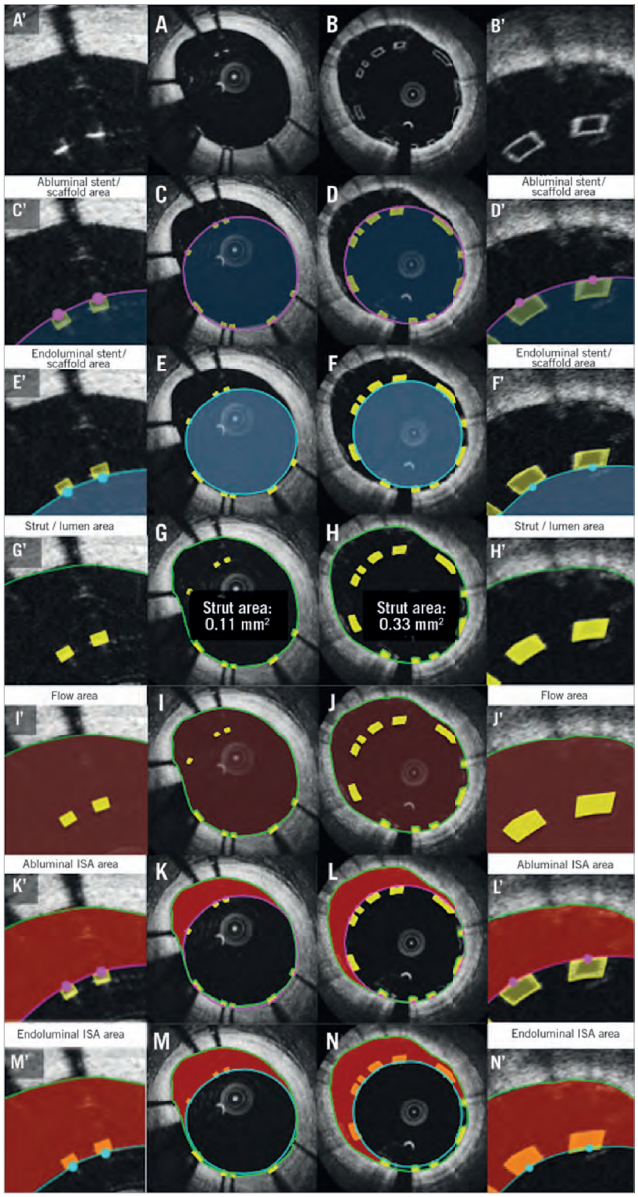

Online Figure 1. *Proposed comparative analysis methods post procedure in the presence of malapposed struts. Representative cross-sections with malapposed metallic struts and polymeric struts are shown in A and B. Comparative methods of abluminal stent/scaffold area, endoluminal stent/scaffold area, strut area/lumen area, flow area, endoluminal ISA area, and abluminal ISA area are illustrated in C, E, G, I, K, M (metallic strut), and D, F, H, J, L, N (polymeric strut), respectively. A'-N' are magnified views of A-N.*

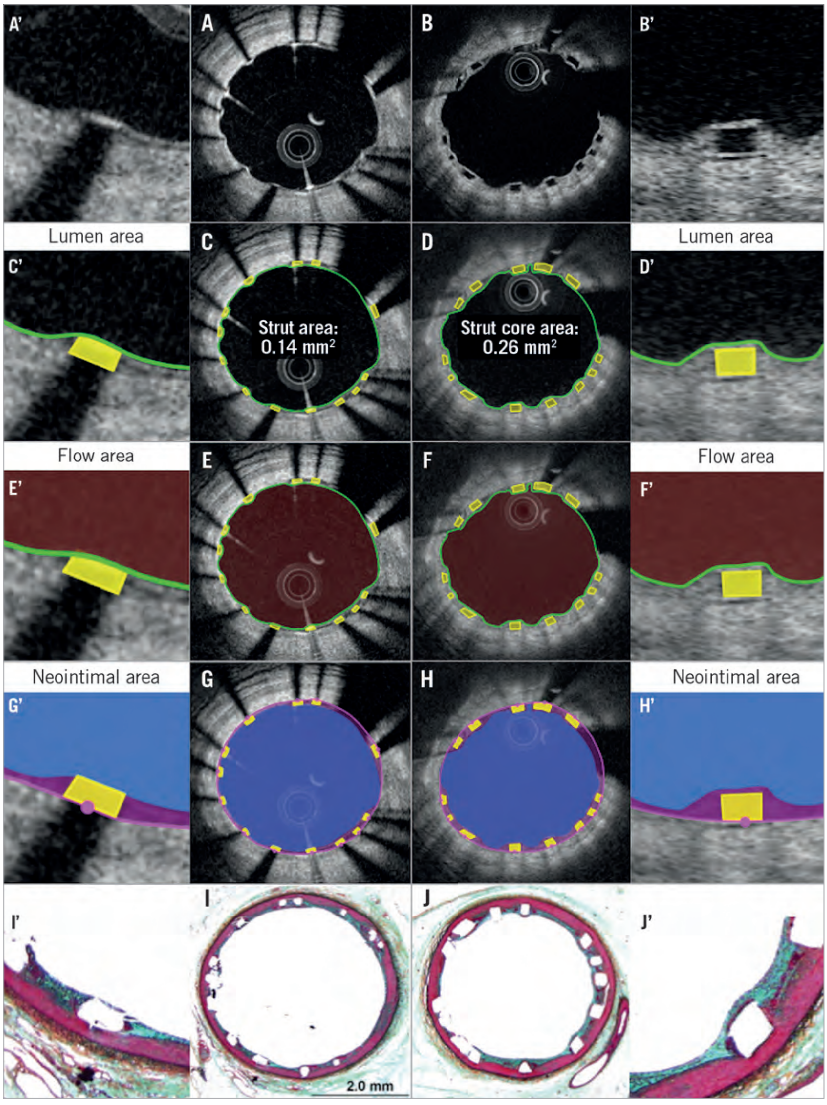

Online Figure 2. *Proposed comparative analysis methods at follow-up in cross-section in the presence of uncovered struts. Representative cross-sections with uncovered metallic and polymeric struts at follow-up are shown in A and B, respectively. Lumen area, flow area, and neointimal area are shown in C, E, G (metallic strut) and D, F, H (polymeric strut), respectively. Histomorphometric analyses of the animal models are shown in I (metallic strut) and J (polymeric strut). A'-J' are magnified views of A-J.*

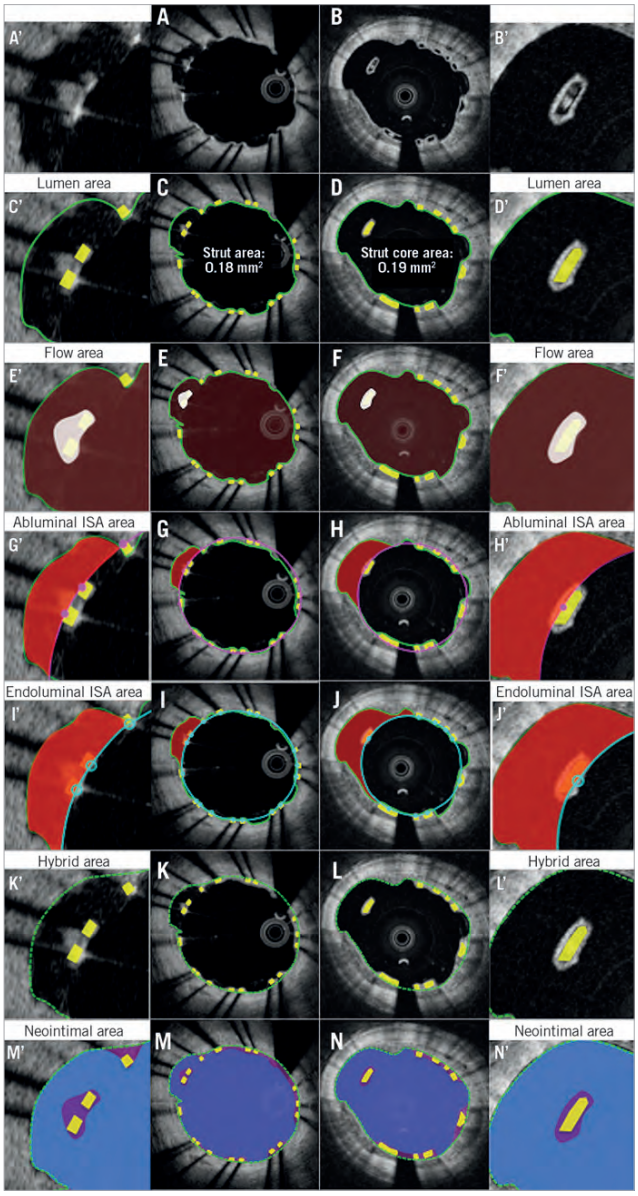

Online Figure 3. *Proposed comparative analysis methods at follow-up in the presence of malapposed struts. Representative cross-sections with malapposed metallic and polymeric struts at follow-up are shown in A and B, respectively. Lumen area, flow area, abluminal ISA area, endoluminal ISA area, hybrid area, neointimal area are shown in C, E, G, I, K, M (metallic strut) and D, F, H, J, L, N (polymeric strut), respectively. A'-N' are magnified views of A-N.*

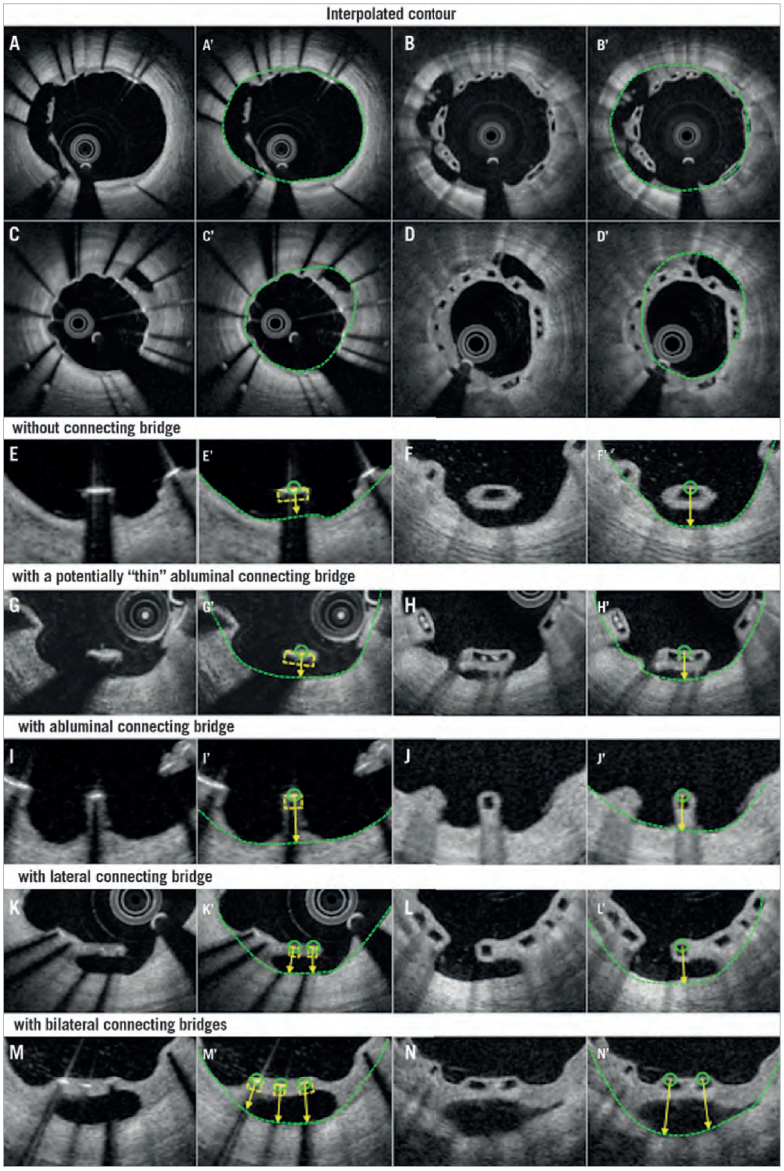

Online Figure 4. *Proposed assessment of malapposed struts at follow-up. Representative cross-sections with malapposed metallic and polymeric struts at follow-up are shown in A and B, respectively. Classifications of malapposed struts are displayed in E-N. Malapposed struts without connecting bridge, those with a potentially thin abluminal connecting bridge, those with an abluminal connecting bridge, those with a lateral connecting bridge, and those with bilateral connecting bridges are shown in E, G, I, K, M (metallic strut), and F, H, J, L, N (polymeric strut), respectively. A'-N' display interpolated contours of A-N.*

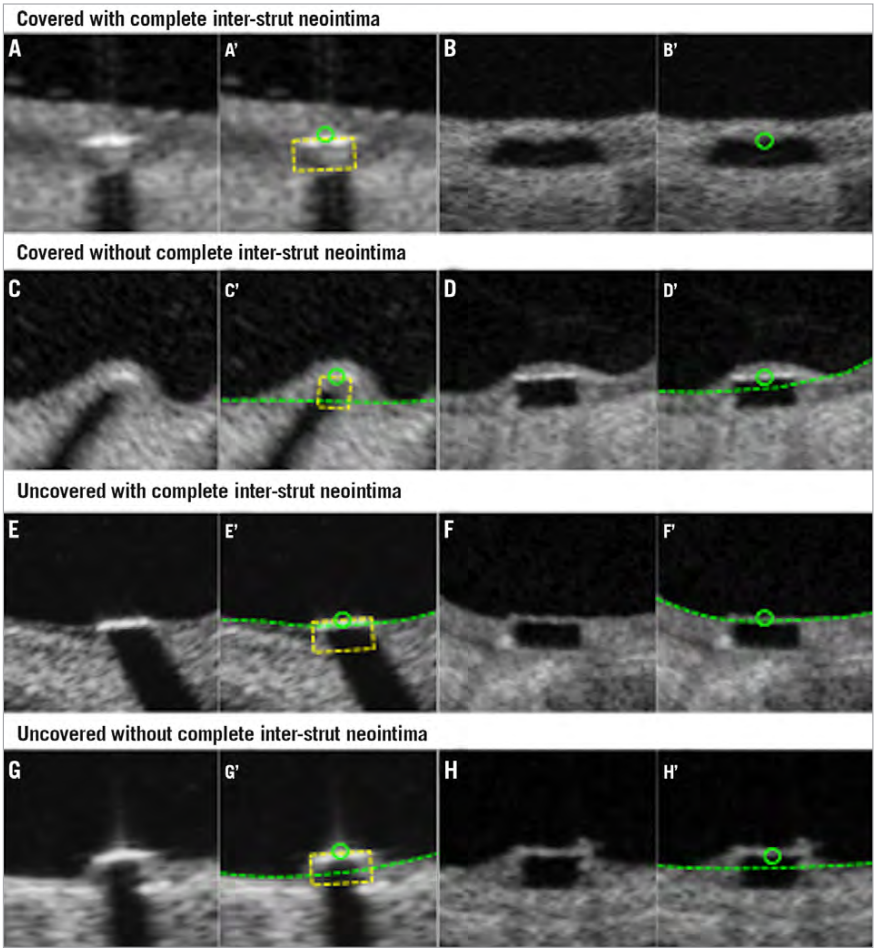

Online Figure 5. *Assessment of strut coverage. Covered strut with complete inter-strut neointima (A and B), covered strut with incomplete inter-strut neointima (C and D), uncovered strut with complete inter-strut neointima (E and F), and uncovered strut with incomplete inter-strut neointima (G and H) are displayed. A'-H' display interpolated contours of A-H.*

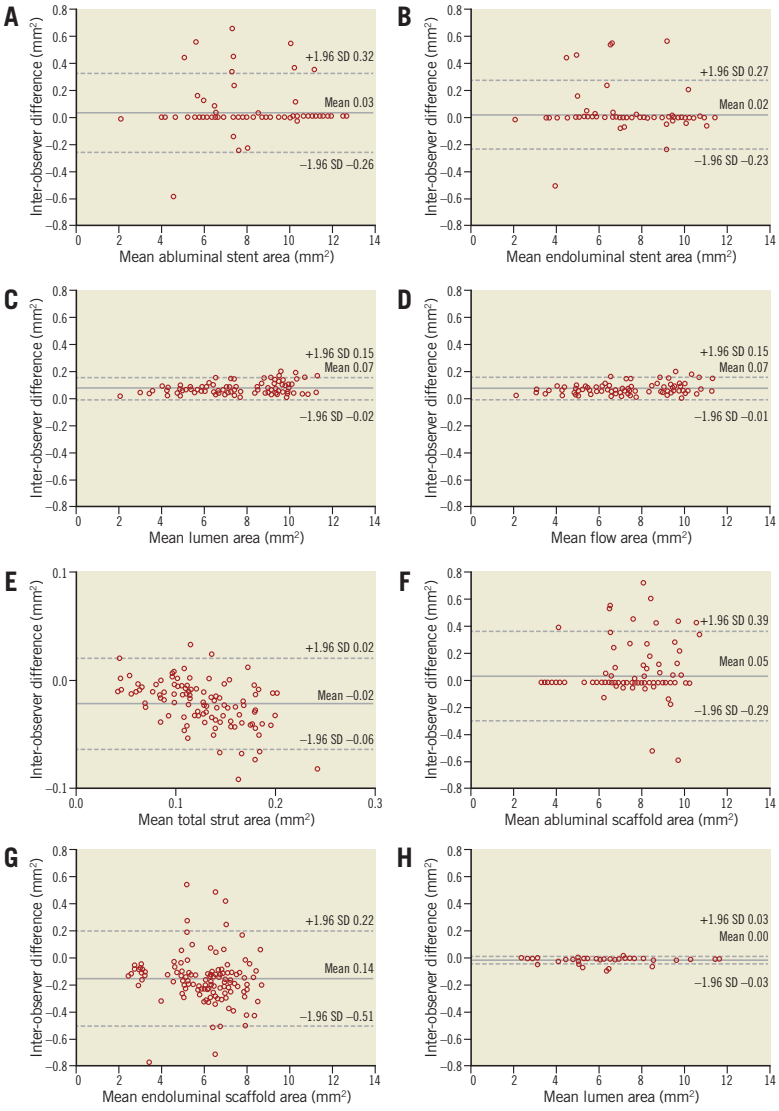

Online Figure 6. *Interobserver variability. Bland-Altman analysis was performed for parameters in a metallic stent and a polymeric scaffold. In a metallic stent, mean abluminal stent area (A), mean endoluminal stent area (B), mean lumen area (C), mean flow area (D), and mean total strut area (E) were analysed. In a polymeric scaffold, mean abluminal scaffold area (F), mean endoluminal scaffold area (G), and mean lumen area (H) were analysed.*

Chapter 3

Validation of the invented methods of coronary imaging

3.1 Validation of light intensity analysis of polymeric struts on OCT

Bioresorption and Vessel Wall Integration of a Fully Bioresorbable Polymeric Everolimus-Eluting Scaffold: Optical Coherence Tomography (OCT), Intravascular Ultrasound (IVUS) and Histological Study in Porcine Model with Four Years Follow-up

JACC Cardiovasc Interv. 2016:838-51.
[Original research paper, Impact Factor : 7.35]

Nakatani S, Ishibashi Y, Perkins L, Eggermont J, Sotomi Y, Grundeken M, Dijkstra J, Richard R, Virmani R, Serruys PW, Onuma Y

Bioresorption and Vessel Wall Integration of a Fully Bioresorbable Polymeric Everolimus-Eluting Scaffold

Optical Coherence Tomography, Intravascular Ultrasound, and Histological Study in a Porcine Model With 4-Year Follow-Up

Shimpei Nakatani, MD,[a] Yuki Ishibashi, MD, PhD,[a] Yohei Sotomi, MD,[b] Laura Perkins, DVM, PhD,[c] Jeroen Eggermont, PhD,[d] Maik J. Grundeken, MD,[b] Jouke Dijkstra, PhD,[d] Richard Rapoza, PhD,[c] Renu Virmani, MD,[e] Patrick W. Serruys, MD, PhD,[f] Yoshinobu Onuma, MD, PhD[a]

ABSTRACT

OBJECTIVES The aim of the present study was to investigate the relationship between the integration process and luminal enlargement with the support of light intensity (LI) analysis on optical coherence tomography (OCT), echogenicity analysis on intravascular ultrasound, and histology up to 4 years in a porcine model.

BACKGROUND In pre-clinical and clinical studies, late luminal enlargement has been demonstrated at long-term follow-up after everolimus-eluting poly-L-lactic acid coronary scaffold implantation. However, the time relationship and the mechanistic association with the integration process are still unclear.

METHODS Seventy-three nonatherosclerotic swine that received 112 Absorb scaffolds were evaluated in vivo by OCT, intravascular ultrasound, and post-mortem histomorphometry at 3, 6, 12, 18, 24, 30, 36, 42, and 48 months.

RESULTS The normalized LI, which is the signal densitometry on OCT of a polymeric strut core normalized by the vicinal neointima, was able to differentiate the degree of connective tissue infiltration inside the strut cores. Luminal enlargement was a biphasic process at 6 to 18 months and at 30 to 42 months. The latter phase occurred with vessel wall thinning and coincided with the advance integration process demonstrated by the steep change in normalized LI (0.26 [interquartile range (IQR): 0.20 to 0.32] at 30 months versus 0.68 [IQR: 0.58 to 0.83] at 42 months, $p < 0.001$).

CONCLUSIONS In this pre-clinical model, late luminal enlargement relates to strut integration into the arterial wall. Quantitative LI analysis on OCT could be used as a surrogate method for monitoring the integration process of poly-L-lactic acid scaffolds, which could provide insight and understanding on the imaging-related characteristics of the bioresorption process of polylactide scaffolds in human. (J Am Coll Cardiol Intv 2016;9:838–51)

From the [a]ThoraxCenter, Erasmus Medical Center, Rotterdam, the Netherlands; [b]Academic Medical Center, University of Amsterdam, Amsterdam, the Netherlands; [c]Abbott Vascular, Santa Clara, California; [d]Leiden University Medical Center, Leiden, the Netherlands; [e]CVPath Institute, Gaithersburg, Maryland; and the [f]International Centre for Circulatory Health, National Heart and Lung Institute, Imperial College London, London, United Kingdom. This study was funded by Abbott Vascular. Drs. Perkins and Rapoza are full-time employees of Abbott Vascular. Drs. Serruys and Onuma are members of the advisory board of Abbott Vascular. Dr Virmani receives research support from Abbott Vascular, BioSensors International, Biotronik, Boston Scientific, Medtronic, MicroPort Medical, OrbusNeich Medical, SINO Medical Technology, and Terumo Corporation; has speaking engagements with Merck; receives honoraria from Abbott Vascular, Boston Scientific, Lutonix, Medtronic, and Terumo Corporation; and is a consultant for 480 Biomedical, Abbott Vascular, Medtronic, and W.L. Gore. All other authors have reported that they have no relationships relevant to the contents of this paper to disclose.

Manuscript received December 22, 2015; accepted January 15, 2016.

As an alternative approach to metal drug-eluting stents, fully bioresorbable polymeric drug-eluting scaffolds provide transient vessel support with drug-delivery capability. As the scaffold begins to resorb, the vessel is no longer caged, and therefore luminal area as well as vessel area could increase simultaneously without creating evagination (1-5). The everolimus-eluting scaffold (Absorb; Abbott Vascular, Santa Clara, California) consists of a semicrystalline poly-L-lactic acid (PLLA) backbone coated by a thin amorphous layer of poly-D,L-lactic acid containing the antiproliferative agent everolimus. After implantation, the polylactide strut progressively degrades by hydrolysis, and its molecular weight starts to decrease from its initial molecular

SEE PAGE 852

weight of around 100 kDa (molecular weight loss) (6). The PLLA molecules remain at the implanted site until the polymeric chains become small enough to diffuse from the site into the surrounding tissue (mass loss). As small oligomers or monomers gradually leave the site, there is progressive replacement by a provisional matrix initially composed of a milieu of extracellular matrix components. This initially acellular provisional matrix is gradually cellularized with connective tissues, and the struts and footprints eventually become fully integrated into the surrounding neointimal tissue of the vessel wall (6,7).

It is well-established that the scaffolding efficacy of the device is related to the timing of molecular weight reduction and the loss of mechanical integrity (8). However, at a late phase, it is still unclear whether the integration of strut footprints is associated with the late luminal enlargement. In the pre-clinical assessment of fully bioresorbable scaffolds, it is therefore important to assess the processes of molecular weight loss and integration in vivo. In humans, intravascular imaging has been used in vivo as a surrogate marker to understand the bioresorption and integration process, but the correlation between the surrogate assessment and the true bioresorption process needs to be established.

On intravascular ultrasound (IVUS), quantitative echogenicity has been demonstrated to correlate with the molecular weight of PLLA (9). On optical coherence tomography (OCT), the visual categorizations of strut appearance have previously been demonstrated to correlate with the integration process (10). However, this visual categorization was limited by its moderate reproducibility (k = 0.58). Recently, log-transformed optical coherence tomographic signal measurement (light intensity analysis) of strut cores was introduced as a feasible and reproducible method to assess the degree of strut integration after scaffold implantation (11). In humans, the median intensity value of strut cores increased significantly at 24 months and kept increasing up to 36 months, and most of pre-existing struts were indiscernible at 60 months on OCT (**Figure 1**). It was hypothesized

ABBREVIATIONS AND ACRONYMS

IQR = interquartile range

IVUS = intravascular ultrasound

OCT = optical coherence tomography

PLLA = poly-L-lactic-acid

TD = time-domain

FIGURE 1 Strut Appearance on Optical Coherence Tomography of Revision 1.0 (Used in the ABSORB Cohort A Study) and Revision 1.1 (Used in the ABSORB Cohort B Study) of the Absorb Device

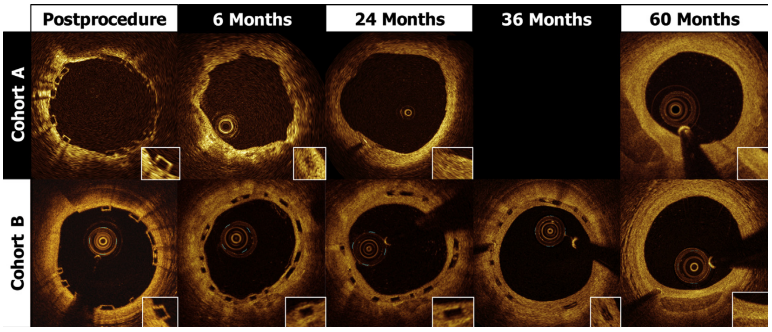

The time to complete degradation of the Absorb A device was approximately 2 years, whereas that for the Absorb B device was approximately 3 years, resulting in the different appearance of strut cores on optical coherence tomography over time in Absorb B devices compared with that of Absorb A devices in humans (5,26).

print & web 4C/FPO

that light reflectivity is correlated with connective tissue infiltration of the strut cores. However, this hypothetical correlation between light intensity and histological changes has so far not been demonstrated with strut histology-matched light intensity.

The aim of this study was to demonstrate the relationship between light intensity and histological changes with regard to strut integration at 3, 6, 12, 18, 24, 30, 36, 42, and 48 months in a porcine coronary artery model. In addition, IVUS echogenicity analysis was also assessed to monitor early changes in molecular weight.

METHODS

The present study was conducted from 2009 to 2013. Eight nonatherosclerotic juvenile domestic crossbred farm swine and 65 Yucatan mini-swine underwent Absorb scaffold implantation with a targeted balloon-to-artery ratio of 1.0:1.1. Each animal received a single everolimus-eluting scaffold (Absorb; 3.0 × 18 mm for 1, 3, and 6 months and 3.0 × 12 mm for 12 to 48 months) in 1 or 2 main coronary arteries. The Absorb scaffold used in the present study is the same as the device used in cohort B of the ABSORB clinical trials. Seventy-three pigs with 112 Absorb scaffolds implanted were examined by OCT at baseline and anesthetized at the designated endpoints with the optical coherence tomographic and IVUS examinations at 3 months (n = 10 Absorb scaffolds in 8 farm swine), as well as 6 (n = 10 Absorb scaffolds in 8 Yucatan mini-swine), 12 (n = 11 in 7), 18 (n = 12 in 7), 24 (n = 12 in 7), 30 (n = 12 in 8), 36 (n = 12 in 8), 42 (n = 13 in 8), and 48 (n = 20 in 12) months (**Figure 2**).

Optical coherence tomographic acquisition was executed by the frequency-domain optical coherence tomographic imaging system (C7 Dragonfly or Dragonfly Duo, St. Jude Medical, St. Paul, Minnesota), with the exception of a few early investigations performed with the time-domain (TD) OCT imaging system in 2 animals. IVUS runs were acquired with 40-MHz mechanical systems, using Galaxy version 2.02 or iLab (Boston Scientific, Natick, Massachusetts). After performing intravascular imaging studies (OCT and IVUS), animals were humanely euthanized. Hearts were excised and pressure perfused with 0.9% saline solution, followed by pressure perfusion fixation with 10% neutral buffered formalin overnight in preparation for histology. Embedded arteries were divided into a minimum of 3 blocks representing the proximal, medial, and distal regions of the scaffold. Duplicate 4- to 6-mm sections from each of the

FIGURE 2 Study Flowchart of the Pigs Receiving Absorb Scaffolds Evaluated by Optical Coherence Tomography, Intravascular Ultrasound, and Histology

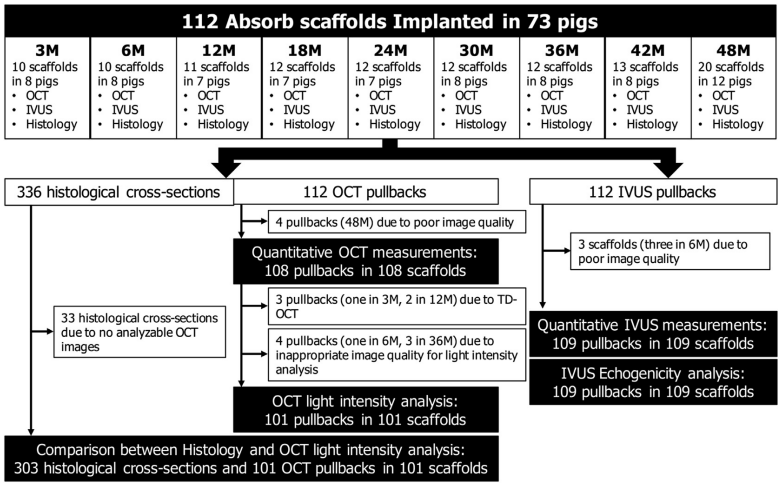

IVUS = intravascular ultrasound; M = month; OCT = optical coherence tomography.

3 blocks were collected, and each was stained with Movat's pentachrome and hematoxylin and eosin for evaluation by light microscopy.

Experimental studies received protocol approval from the Institutional Animal Care and Use Committee and were conducted in accordance with American Heart Association guidelines for pre-clinical research and the Guide for the Care and Use of Laboratory Animals (National Institutes of Health, 1996).

HISTOLOGICAL CATEGORIZATION OF STRUT AND STRUT FOOTPRINT. On histology, the integration grade of each strut was semiquantitatively classified into 6 groups according to the connective tissue composition within a strut core in Movat's pentachrome-stained sections: 0) acellular, no connective tissue composition; 1) hypointegration, 1% to 10% connective tissue composition; 2) low integration, 11% to 25% connective tissue composition; 3) moderate integration, 26% to 50% connective tissue composition; 4) moderate to high integration, 51% to 75% connective tissue composition; and 5) high integration, >75% connective tissue composition. **Figure 3** shows examples of strut appearance on the basis of histological classification of integration (10).

OPTICAL COHERENCE TOMOGRAPHIC QUANTITATIVE MEASUREMENTS. Cross sections with unacceptable image quality for measurements due to suboptimal flushing (4 scaffolds at 48 months) were excluded from the quantitative analysis and light intensity analysis. Quantitative measurements (scaffold area, incomplete scaffold apposition area, and neointimal area) were performed in the scaffolded segment and periscaffolded segments (within 5 mm proximal and distal to the stent edge) at 1-mm intervals according to previously published methods (12). As the porcine coronary artery grows, the luminal area in the periscaffolded segment (reference luminal area) is enlarged (2,13). To compare the time-dependent changes, the normalized scaffold and luminal area was calculated as the ratio of the scaffold and lumen to the reference luminal area (2).

OPTICAL COHERENCE TOMOGRAPHIC LIGHT INTENSITY ANALYSIS OF STRUT CORES. Because the light intensity values vary between TD and frequency-domain OCT, images obtained by TD OCT (1 scaffold at 3 months and 2 at 12 months) were excluded from the light intensity analysis. Pull-backs with high intraluminal signal intensity with shadows

FIGURE 3 Light Intensity Analysis on Optical Coherence Tomography and Categorization on Histology

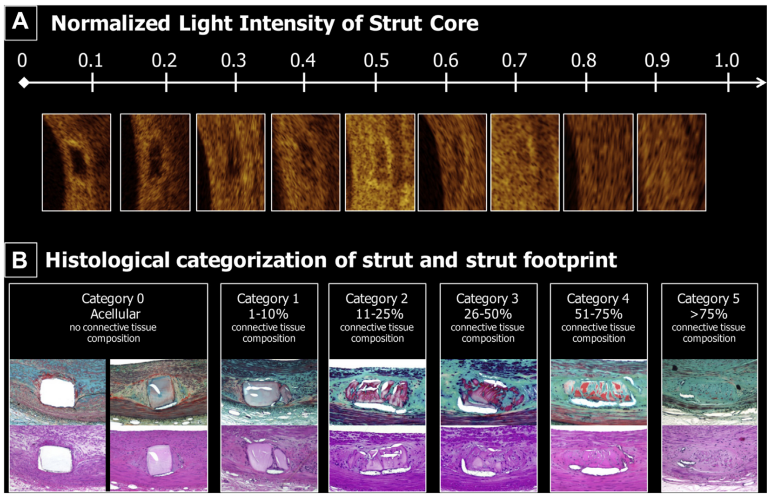

Representative strut appearance according to the normalized light intensity on optical coherence tomography **(A)** and histological categorization **(B)** of the strut core and footprint.

TABLE 1 Light Intensity Analysis in Matched Struts Over Time

Time Point (months)	Matched Struts	Accellular Struts	Integrated Struts					p Value
		0. Acellular: No connective Tissue Composition	1. Hypointegration: 1%–10% Connective Tissue Composition	2. Low Integration: 11%–25% Connective Tissue Composition	3. Moderate Integration: 26%–50% Connective Tissue Composition	4. Moderate to High Integration: 51%–75% Connective Tissue Composition	5. High Integration: >75% Connective Tissue Composition	
3	228	220 (96.5%)	8 (3.5%)	–	–	–	–	
6	255	231 (90.6%)	24 (9.4%)	–	–	–	–	
12	219	194 (88.6%)	20 (9.1%)	4 (1.8%)	1 (0.5%)	–	–	
18	310	256 (82.6%)	37 (11.9%)	16 (5.2%)	1 (0.3%)	–	–	
24	251	199 (79.3%)	38 (15.1%)	14 (5.5%)	–	–	–	
30	294	222 (75.5%)	46 (15.6%)	24 (8.2%)	2 (0.7%)	–	–	
36	214	29 (13.6%)	38 (17.8%)	85 (4.0%)	34 (15.9%)	13 (6.1%)	15 (7.0%)	
42	334	–	1 (3.0%)	14 (4.2%)	158 (47.3%)	92 (27.5%)	69 (20.7%)	
48	350	–	1 (2.9%)	29 (8.3%)	106 (30.3%)	124 (35.4%)	90 (25.7%)	
Normalized light intensity		0.16 [0.11–0.23]	0.25 [0.17–0.38]*	0.43 [0.32–0.61]†	0.65 [0.54–0.77]‡	0.72 [0.58–0.88]	0.80 [0.67–0.96]	<0.001

*p < 0.05 versus category 0, †p < 0.05 versus category 1, and ‡p < 0.05 versus category 2, performed by performed by post hoc multiple comparison.

due to suboptimal flushing were excluded from the light intensity analysis (1 scaffold at 6 months, 3 at 36 months, and 4 at 48 months).

Light intensity analysis of the strut cores was performed using dedicated software (QCU-CMS version 4.69 [research version]; Leiden, the Netherlands). Raw images with 16 bits in original polar format were used to ensure that interpolation, dynamic range compression, or other image processing did not alter the signal and bias the analysis. The contours of strut cores were delineated manually with "box-shape" by visual inspection in Cartesian images (Online Figure 1) (11). According to the strut contours, the median light intensity values were computed with the subtraction of 2 pixels inside of the manual strut core contour by the software automatically, as described previously (11).

To minimize bias in light intensity measurement caused by the variation in optical signal due to eccentric location of the optical coherence tomographic catheter or the uneven distribution of neointima on top of the strut, the light intensity values of strut cores were normalized by the median light intensity value of the interstrut neointima in the vicinity (bilaterally 22.5° wide originating from the strut center) of each strut (referred to as the normalized light intensity of strut cores) (Online Figure 1).

The light intensity analysis was performed in cross sections at intervals of 1 mm and additionally in the OCT-imaged struts matched with histology. **Figure 3** shows examples of strut appearance on the basis of normalized light intensity of strut cores on OCT.

MATCHING OF STRUTS ON HISTOLOGY AND OCT. To correlate strut cores and histology at a strut level, 1 observer (Y.O.) aware of the histological image selected the matched OCT-histology cross sections at each time point using landmarks such as side branches, metallic radiopaque markers, or the appearance of neointima and media (Online Appendix). In the selected cross sections of OCT and histology, individual struts were further matched by identifying struts with similar angular orientation and peculiar appearance of struts (strut-level matching) (Online Figure 2). To ensure accurate identification of the strut areas by OCT and histology, especially at later time points (36, 42, and 48 months), when struts are more integrated and thus more difficult to identify, strut contours drawn on optical coherence tomographic analysis were superimposed on histology to match the strut core regions and to calculate the percentage of infiltration by connective tissue normalized for the strut footprint area.

These matched strut images were sent to the independent optical coherence tomographic analyst (S.N.) and the pathologist (L.P.). The normalized light intensity of the OCT-imaged strut and the histological categorization of integration of this strut into the surrounding neointimal tissue was blinded to the observer who had performed the matching.

ECHOGENICITY ANALYSIS IN IVUS GRAYSCALE. IVUS quantitative analysis (vessel, scaffold, and luminal area) was performed in 0.5-mm intervals in the scaffolded segment and periscaffolded segments (defined by a length 5 mm proximal and distal to the stent edge). The normalized vessel area was calculated as the ratio of the vessel to the reference vessel area, and the normalized scaffold and luminal area was calculated as the ratio to the reference luminal area.

According to the contours of lumen and vessel, the dedicated software (QCU-CMS version 4.69 [research

FIGURE 4 Normalized Light Intensity and Histological Findings in Matched Strut Cores

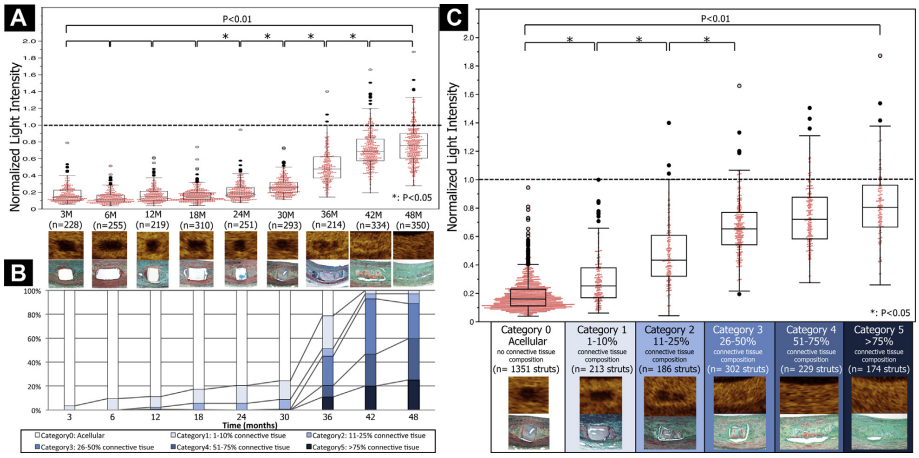

(A) Whisker plots combined with scatterplots of matched strut cores in normalized light intensity (dimensionless) over time. Normalized light intensity increased gradually between 18 and 30 months, then surged between 30 and 42 months and approached 1.0 at 48 months. **(B)** Changes in histological categories of struts over time. The rate of acellular struts decreased gradually during the first 30 months, then abruptly decreased from 75.5% at 30 months to 13.6% at 36 months. Spontaneously, the frequency of moderately to highly integrated struts (histological grade ≥3) increased from 0.7% to 94% between 30 and 42 months. After 42 months, there was no strut without integration. **(C)** Correlation between normalized light intensity on optical coherence tomography and histological categorization on whisker plots in combination with scatterplots. Normalized light intensity was significantly different between categories 0 and 1 ($p < 0.05$), between categories 1 and 2 ($p < 0.05$), and between categories 2 and 3 ($p < 0.05$). There were no significant differences in normalized light intensity among categories 3, 4, and 5. M = month.

version]) calculates the areas of 5 tissue types categorized by using the median brightness of the adventitia as a reference in the lumen-vessel compartments automatically: 1) hypoechogenic, 2) hyperechogenic, 3) calcified, 4) upper echogenic, and 5) unknown (9).

STATISTICAL ANALYSIS. All statistical analyses were performed using the SPSS version 23.0 (SPSS, Chicago, Illinois). Normality of distributions was tested with the Kolmogorov-Smirnov statistic. Continuous variables are presented as mean ± SD or median (interquartile range [IQR]), as indicated in the tables. Generalized estimating equations modeling was performed to take into an account the clustered nature of >1 scaffold analyzed from the same pig, which might result in unknown correlations among measurements within these scaffold clusters. Categorical variables are presented as absolute values and percentages. Relations between histological categories and normalized light intensity of strut cores were analyzed by Spearman's rank-order correlation. Bayesian analysis of normalized light intensity included estimation of area under the receiver-operating characteristic, curve with the optimal cut-off value for the detection of the onset of "strut integration" into the neointimal surrounding and the shift to "moderate to high filtration into the strut core," with associated sensitivity and specificity. A modification of the classification of Swets (13) was used to classify diagnostic efficiency of normalized light intensity according to the values of the area under the curve as low (<0.70), moderate (0.70 to 0.90), or high (>0.90).

RESULTS

In total, 336 histological cross sections and 112 optical coherence tomographic pull-backs were available (Figure 2). After excluding 4 optical coherence tomographic pull-backs because of impaired image quality, 108 pull-backs were analyzed for quantitative measurements. Of 108 pull-backs, 7 were excluded from the light intensity analysis for

TABLE 2 Optical Coherence Tomographic Quantitative Measurements

Quantitative Measurement	3 months (n = 10)	6 months (n = 10)	12 months (n = 11)	18 months (n = 12)	24 months (n = 12)	30 months (n = 12)	36 months (n = 12)
Mean scaffold area (mm^2)	7.05 ± 0.64	7.33 ± 0.51	7.82 ± 1.98	9.47 ± 2.39	9.90 ± 2.33	11.72 ± 2.97	10.49 ± 1.58
Minimum scaffold area (mm^2)	5.96 ± 1.24	6.42 ± 0.46	6.71 ± 1.61	8.33 ± 2.45	8.95 ± 2.21	10.81 ± 2.77	9.32 ± 1.45
Normalized scaffold area	0.95 ± 0.17	1.08 ± 0.23	1.08 ± 0.24	1.07 ± 0.24	1.10 ± 0.19	1.07 ± 0.07	1.35 ± 0.22
Mean luminal area (mm^2)	4.04 ± 0.62	4.37 ± 0.64	5.28 ± 1.12	6.49 ± 2.33	6.96 ± 2.25	8.45 ± 2.63	7.27 ± 1.48
Minimum luminal area (mm^2)	3.30 ± 0.96	3.33 ± 0.71	4.37 ± 0.85	5.56 ± 2.43	5.99 ± 1.95	7.47 ± 2.53	6.31 ± 1.54
Normalized luminal area	0.54 ± 0.13	0.65 ± 0.16	0.73 ± 0.13	0.72 ± 0.19	0.76 ± 0.16	0.77 ± 0.20	0.93 ± 0.17
Mean neointimal area (mm^2)	2.76 ± 0.60	2.69 ± 0.39	2.38 ± 0.98	2.71 ± 0.34	2.71 ± 0.31	3.00 ± 0.55	2.90 ± 0.54
Neointimal thickness on top of struts (μm)	218 ± 73	208 ± 15	151 ± 72	165 ± 47	162 ± 42	159 ± 38	179 ± 47
Area stenosis (%)	29.9 ± 8.8	27.8 ± 7.1	19.4 ± 6.5	20.7 ± 8.0	19.6 ± 6.7	17.9 ± 6.0	20.2 ± 5.4
Mean reference luminal area (mm^2)	7.69 ± 1.69	7.03 ± 1.49	7.29 ± 1.03	8.97 ± 1.92	9.11 ± 2.08	11.21 ± 2.39	7.97 ± 1.77
	n = 1,369 struts in 9 pigs	n = 1,646 struts in 9 pigs	n = 904 struts in 9 pigs	n = 1,364 struts in 12 pigs	n = 1,030 struts in 12 pigs	n = 1,134 struts in 12 pigs	n = 1,365 struts in 9 pigs
Normalized light intensity	0.17 (0.15–0.19)	0.15 (0.14–0.18)	0.14 (0.12–0.15)	0.19 (0.18–0.22)	0.25 (0.21–0.29)	0.3 (0.28–0.32)	0.55 (0.55–0.64)

Continued on the next page

technical reasons (3 because of TD OCT and 4 because of inappropriate image quality for light intensity analysis), resulting in 101 OCT pull-backs available for light intensity analysis. After excluding 33 histological cross sections because of lack of analyzable OCT pull-backs, 2,979 struts were identified in 303 histological cross sections. Using sectorial approximate locations and landmarks such as metallic radiopaque markers, side branches, and neointimal formation, a total of 2,455 struts were matched between OCT and histology.

LIGHT INTENSITY ANALYSIS OVER TIME. The light intensity analysis in 2,455 matched struts over time is summarized in Table 1 and Figure 4A. There was no significant difference in the normalized light intensity of strut cores until 18 months after scaffold implantation: 0.14 (IQR: 0.11 to 0.22) at 3 months, 0.12 (IQR: 0.08 to 0.17) at 6 months, 0.15 (IQR: 0.10 to 0.21) at 12 months, and 0.15 (IQR: 0.11 to 0.19) at 18 months. The normalized light intensity increased gradually between 18 and 30 months (0.19 [IQR: 0.14 to 0.26] at 24 months; $p = 0.001$ vs. 18 months; 0.26 [IQR: 0.20 to 0.32] at 30 months; $p < 0.001$ vs. 24 months). After 30 months, the normalized light intensity surged until 42 months: 0.48 (IQR: 0.37 to 0.62) at 36 months ($p < 0.001$ vs. 30 months) and 0.68 (IQR: 0.58 to 0.83) at 42 months ($p < 0.001$ vs. 36 months) and was close to 1.0 at 48 months (0.76 [IQR: 0.61 to 0.90]; $p = 1.00$ vs. 42 months), suggesting that the strut cores were completely integrated into the surrounding tissue.

HISTOLOGICAL FINDINGS. The categorization of histological integration of 2,455 matched struts over time is summarized in Table 1 and Figure 4B. From 3 to 12 months, the struts were completely separated from the lumen by a thin, fibromuscular neointima and had well-defined, squared appearances. Most of the struts were classified as acellular (96.5% at 3 months, 90.6% at 6 months, and 88.6% at 12 months). From 18 to 30 months, the strut footprints maintained their discrete borders but began to appear blue with Movat's pentachrome. The percentage of acellular struts decreased gradually (82.6% at 18 months, 79.3% at 24 months, and 75.5% at 30 months). Six months later (at 36 months), the percentage of acellular struts has abruptly decreased to 13.6%, and the strut footprints were generally colonized by connective tissue. These strut footprints further progressed up to the point at which the strut footprint was only poorly discernible. Twenty-nine percent of matched struts were classified as grade ≥3 (>25% of cellularization and connective tissue composition). After 42 months, there was no strut without integration, and the rate of highly integrated struts increased gradually up to 48 months. At 48 months, 61.1% of matched struts showed >50% of connective tissue composition.

COMPARISON BETWEEN OPTICAL COHERENCE TOMOGRAPHIC LIGHT INTENSITY ANALYSIS AND HISTOLOGICAL CLASSIFICATION. The correlation between the normalized light intensity on OCT and histological categorization of 2,455 matched struts is summarized in Table 1 and Figure 4C. There were significant differences among the histological categories with respect to normalized light intensity: 0.16 (IQR: 0.11 to 0.23) in category 0 (acellular), 0.25 (IQR: 0.17 to 0.38) in category 1 (1% to 10%), 0.43 (IQR: 0.32 to 0.61) in category 2 (11% to 25%), 0.65 (IQR: 0.54 to 0.77) in category 3 (26% to 50%), 0.72 (IQR: 0.58 to

TABLE 2 Continued

42 months (n = 13)	48 months (n = 16)	p Value: Overall	6 vs. 3 months	12 vs. 3 months	18 vs. 3 months	24 vs. 3 months	30 vs. 3 months	36 vs. 3 months	42 vs. 3 months	48 vs. 3 months
12.14 ± 2.00	12.64 ± 1.72	<0.001	0.182	0.238	0.002	<0.001	<0.001	<0.001	<0.001	<0.001
11.02 ± 2.31	11.60 ± 1.76	<0.001	0.138	0.209	0.004	<0.001	<0.001	<0.001	<0.001	<0.001
1.22 ± 0.18	1.20 ± 0.15	0.001	0.137	0.244	0.246	0.044	0.189	<0.001	0.001	<0.001
9.27 ± 2.02	9.69 ± 1.61	<0.001	0.116	<0.001	0.001	<0.001	<0.001	<0.001	<0.001	<0.001
8.41 ± 2.30	8.81 ± 1.80	<0.001	0.924	<0.001	0.005	<0.001	<0.001	<0.001	<0.001	<0.001
0.93 ± 0.16	0.92 ± 0.13	<0.001	0.098	0.002	0.022	<0.001	0.002	<0.001	<0.001	<0.001
2.57 ± 0.22	2.63 ± 0.24	0.241	0.714	0.352	0.802	0.766	0.345	0.562	0.284	0.48
138 ± 34	140 ± 19	<0.001	0.689	0.056	0.04	0.021	0.016	0.128	<0.001	<0.001
15.0 ± 5.0	14.6 ± 2.2	<0.001	0.476	0.002	0.007	0.001	<0.001	0.001	<0.001	<0.001
10.09 ± 2.01	10.68 ± 1.80	<0.001	0.346	0.485	0.128	0.051	<0.001	0.703	0.004	<0.001
n = 1,335 struts in 13 pigs	n = 1,894 struts in 16 pigs									
0.8 (0.77–0.87)	0.82 (0.79–0.83)	<0.001	0.296	0.426	0.565	0.001	<0.001	<0.001	<0.001	<0.001

0.88) in category 4 (51% to 75%), and 0.80 (IQR: 0.67 to 0.96) in category 5 (>75%) ($p < 0.01$). In paired comparison, normalized light intensity was significantly different between categories 0 and 3, whereas there were no significant differences between categories 3 and 5 (**Table 1**, **Figure 4C**). In Spearman rank-order correlation analysis, there was a significant positive correlation between histological category of integration and normalized light intensity of strut cores ($r = 0.791$; $p < 0.01$).

Receiver-operating characteristic curves demonstrated that the diagnostic efficiency of the normalized light intensity of strut cores for the detection of the onset of the "strut integration" into the surrounding neointima (histological category ≥1, area under the curve 0.924, cutoff value 0.326) and for the detection of the shift to "moderate to high filtration into the strut core" (histological category ≥3, area under the curve 0.965, cutoff value 0.413) were excellent (Online Figure 3).

QUANTITATIVE MEASUREMENTS ON OCT. The optical coherence tomographic quantitative measurements and light intensity analysis of strut cores performed in 1-mm interval cross sections are summarized in **Table 2** and Online Figure 4. At baseline, there were no significant difference in scaffold and flow area among all time-point groups (scaffold area, $p = 0.113$; flow area, $p = 0.124$). Compared with 3 months (0.54 ± 0.13), the normalized luminal area was significantly larger after 12 months ($p < 0.05$). The neointimal thickness on top of struts decreased significantly at 48 compared with 3 months (218 ± 73 μm at 3 months vs. 140 ± 19 μm at 48 months, $p < 0.001$).

The light intensity analysis of strut core in 1-mm intervals was in line with the matched struts, showing a surge between 30 and 42 months.

QUANTITATIVE MEASUREMENTS AND ECHOGENICITY CHANGES ON IVUS. The IVUS quantitative measurements and echogenicity analysis on the basis of 0.5-mm-interval cross sections are summarized in **Table 3**. The area of vessel wall (including media and neointima) did not change over time, whereas the thickness of vessel wall significantly decreased at 48 months (0.33 ± 0.06 mm) compared with 3 months (0.41 ± 0.05 mm) ($p < 0.001$).

The hyperechogenicity plus upper echogenicity area, a surrogate parameter for the molecular weight of PLLA (9), significantly decreased during the first 24 months (0.42 [IQR: 0.29 to 0.56] at 24 months vs. 1.10 [IQR: 1.07 to 1.48] at 3 months, $p < 0.001$).

DISCUSSION

The main findings of the present analysis are as follows (**Figures 5 and 6A**). First, following polymeric scaffold implantation, the normalized light intensity of strut cores did not change between 3 and 18 months; thereafter it gradually increased from 18 to 30 months, but the change in light intensity significantly surged between 30 and 42 months. Second, the histological evaluation showed that the frequency of acellular strut cores (absence of tissue infiltration) remained the same up to 12 months and then gradually decreased up to 30 months and began to dramatically change between 30 and 42 months, virtually disappearing at 48 months. Third, in matched struts for OCT and histology, the normalized

TABLE 3 Intravascular Ultrasound Quantitative Measurements

Quantitative Measurement	3 months (n = 10)	6 months (n = 7)	12 months (n = 11)	18 months (n = 12)	24 months (n = 12)	30 months (n = 12)
Mean vessel area, mm^2	8.30 ± 1.12	8.66 ± 1.34	8.86 ± 1.93	10.79 ± 2.46	11.86 ± 2.53	11.81 ± 3.31
Normalized vessel area by reference vessel area	0.94 ± 0.19	1.06 ± 0.18	0.99 ± 0.12	1.04 ± 0.12	1.05 ± 0.13	0.99 ± 0.17
Mean scaffold area, mm^2	5.81 ± 1.17	6.12 ± 1.20	6.39 ± 1.82	8.16 ± 2.30	8.74 ± 2.06	9.13 ± 3.00
Normalized scaffold area by reference luminal area	0.76 ± 0.15	0.92 ± 0.16	0.82 ± 0.14	0.93 ± 0.15	0.86 ± 0.13	0.84 ± 0.17
Mean luminal area, mm^2	4.59 ± 0.88	4.96 ± 1.02	5.01 ± 1.18	6.73 ± 2.23	7.11 ± 2.01	7.89 ± 2.79
Normalized luminal area by reference luminal area	0.60 ± 0.10	0.74 ± 0.13	0.65 ± 0.12	0.76 ± 0.16	0.70 ± 0.12	0.72 ± 0.16
Mean neointimal area + media	3.73 ± 0.73	3.70 ± 0.45	4.01 ± 1.20	4.03 ± .0.60	4.75 ± 0.67	3.95 ± 0.61
Vessel wall thickness (thickness between lumen and vessel)	0.41 ± 0.05	0.40 ± 0.03	0.35 ± 0.11	0.39 ± .0.08	0.44 ± 0.04	0.36 ± 0.02
Mean reference vessel area, mm^2	8.96 ± 1.54	8.30 ± 1.63	8.93 ± 1.53	10.46 ± .2.60	11.39 ± 2.65	12.06 ± 3.18
Mean reference luminal area, mm^2	6.08 ± 1.29	5.60 ± 1.27	6.56 ± 1.07	8.06 ± .2.24	8.74 ± 2.08	9.61 ± 2.68
Echogenicity analysis						
Mean upper, mm^2	0.4 (0.30-0.46)	0.3 (0.17-0.34)	0.22 (0.16-0.29)	0.26 (0.17-0.29)	0.26 (0.16-0.28)	0.25 (0.16-0.27)
Mean hyper, mm^2	0.73 (0.64-1.04)	0.78 (0.74-0.84)	0.46 (0.38-0.65)	0.65 (0.23-0.83)	0.24 (0.10-0.35)	0.24 (0.16-0.32)
Mean upper + hyper, mm^2	1.10 (1.07-1.48)	0.98 (0.90-1.16)	0.8 (0.68-0.87)	0.91 (0.47-1.10)	0.42 (0.35-0.60)	0.46 (0.43-0.54)

Continued on the next page

light intensity was able to differentiate the degree and intensity of connective tissue infiltration inside the strut cores. Using a cutoff value of 0.413, the normalized light intensity could detect the advanced process of integration of the strut cores (histological grade ≥3) with an accuracy of 0.922. Fourth, the optical coherence tomographic quantitative measurements demonstrated that the scaffold and luminal area normalized to the reference luminal area increased between 30 and 36 months. The neointimal thickness on top of the struts and the black core strut thickness (if visible) decreased concurrently between 36 and 42 months. Fifth, the IVUS quantitative measurements were in line with the results of optical coherence tomographic measurements but were not as discrete as those of OCT. The area of neointima plus media in absolute value did not show a significant change over time, whereas there was a thinning of the vessel wall (thickness between lumen and vessel) due to the late luminal enlargement. Finally, the upper echogenicity plus hyperechogenicity area steadily decreased during the first 24 months, reflecting the early loss of molecular weight.

LUMINAL ENLARGEMENT IN THE FIRST 2 YEARS: LOSS OF MECHANICAL INTEGRITY AND ADAPTIVE EXPANSION TO THE INHERENT ARTERIAL GROWTH OF THE MODEL. One of the most important findings of the present study is that there are 2 phases of vessel and luminal growth in 4 years after implantation of the Absorb bioresorbable scaffold. On IVUS and OCT, the first significant luminal and scaffold enlargement occurs between 6 to 18 months, whereas the second occurs between 30 and 42 months (**Figure 6A**). Of note, these luminal gains were not observed following permanent metallic stent implantation, because of the permanent mechanical caging (2,14).

The first growth of the scaffold and luminal area seems to be related to the loss of mechanical integrity and the natural growth of coronary artery. The Absorb device loses its mechanical strength 6 months after implantation (15,16). On OCT, at 3 months, luminal and scaffold area is normalized by the reference lumen smaller than the reference area (0.54), but after 6 months, and coinciding with the loss of mechanical integrity, the scaffold and lumen started to follow the enlargement of reference area (normalized lumen area at 12 to 30 months: 0.72 to 0.77). The current animal study was performed in the Yucatan pig model, which is known to have inherent coronary arterial growth over time (2,17).

SECOND-PHASE LUMINAL ENLARGEMENT: INTEGRATION OF STRUT CORE. The second phase of vessel remodeling, which occurred between 30 and 42 months, is presumably due to the integration process. During this period, the normalized luminal area further increased from 0.77 to 0.93. On histology, rapid integration of the struts in the surrounding neointima was observed. The frequency of moderately to highly integrated struts (histological grade ≥3) increased from 0.7% to 94%, which was clearly illustrated by the surge of light intensity inside the strut core void on OCT.

During the infiltration of connective tissue into the provisional matrix, the thickness of the neointima on top of struts decreased. It is still unclear whether maturation from a provisional matrix to collagen-rich connective tissue may further influence

TABLE 3 Continued

36 months (n = 12)	42 months (n = 13)	48 months (n = 20)	p Value								
			Overall	6 vs. 3 months	12 vs. 3 months	18 vs. 3 months	24 vs. 3 months	30 vs. 3 months	36 vs. 3 months	42 vs. 3 months	48 vs. 3 months
11.21 ± 1.65	13.37 ± 1.83	13.43 ± 1.64	<0.001	0.596	0.478	0.002	<0.001	0.004	<0.001	<0.001	<0.001
1.08 ± 0.10	1.07 ± 0.08	0.97 ± 0.06	0.005	0.203	0.521	0.135	0.124	0.552	0.042	0.048	0.734
8.50 ± 1.26	10.47 ± 1.44	10.14 ± 1.28	<0.001	0.57	0.396	0.001	<0.001	0.002	<0.001	<0.001	<0.001
0.94 ± 0.11	0.96 ± 0.07	0.86 ± 0.07	0.001	0.07	0.429	0.012	0.109	0.282	0.003	<0.001	0.041
7.04 ± 1.22	9.21 ± 1.26	9.45 ± 1.18	<0.001	0.428	0.391	0.002	<0.001	0.001	<0.001	<0.001	<0.001
0.78 ± 0.10	0.85 ± 0.07	0.81 ± 0.08	<0.001	0.033	0.341	0.007	0.06	0.055	<0.001	<0.001	<0.001
4.19 ± 0.61	4.13 ± 0.72	3.99 ± 0.16	0.005	0.925	0.48	0.274	0.001	0.469	0.085	0.2	0.365
0.39 ± 0.05	0.35 ± 0.05	0.33 ± 0.06	<0.001	0.824	0.056	0.666	0.176	0.019	0.385	0.006	<0.001
10.50 ± 1.97	12.57 ± 2.18	13.96 ± 1.79	<0.001	0.347	0.959	0.061	0.004	0.003	0.027	<0.001	<0.001
7.98 ± 1.62	9.79 ± 1.63	10.57 ± 1.45	<0.001	0.436	0.369	0.007	<0.001	<0.001	0.003	<0.001	<0.001
0.18 (0.12–0.20)	0.18 (0.11–0.20)	0.11 (0.07–0.14)	<0.001	0.056	0.001	<0.001	<0.001	<0.001	<0.001	<0.001	<0.001
0.25 (0.14–0.34)	0.19 (0.17–0.31)	0.10 (0.07–0.16)	<0.001	0.688	0.003	0.022	<0.001	<0.001	<0.001	<0.001	<0.001
0.42 (0.29–0.56)	0.38 (0.32–0.50)	0.22 (0.15–0.29)	<0.001	0.197	<0.001	0.001	<0.001	<0.001	<0.001	<0.001	<0.001

mechanotransduction by improving the transmission of mechanical signal (18). The stimulation of initial smooth muscle cells can induce matrix metalloproteinase release, which plays a key role in matrix deposition and reorganization by collagen type I deposition that leads to negative arterial remodeling and potential neointimal shrinkage (18–21).

CLINICAL IMPLICATIONS. The present analysis confirms that 1) OCT light intensity correlated with the integration process and that 2) IVUS echogenicity can detect early changes in molecular weight. By using IVUS echogenicity, molecular weight loss could be monitored, and the timing of loss of mechanical integrity could be predicted. Without any reference to gel permeate chromatography in vivo, it would be clinically useful to judge by echogenicity the degree of biodegradation related to the loss of mechanical strength and subsequent restoration of mechanotransduction.

Optical coherence tomographic light intensity is more sensitive for the integration process, which is associated with the thinning of the vessel wall as well as very late luminal enlargement. By using the classification of strut (using a proposed cutoff of 0.413 for infiltration greater than 25%), clinicians can assess the stage of integration that heralds late luminal enlargement.

When the quantitative light intensity analysis is applied to the human data obtained from ABSORB cohort B (**Figure 6B**), the light intensity surge had not yet been detected at 36 months (the average of normalized light intensity was 0.22 in 161 sequentially matched struts). This suggests that the integration process in humans is somewhat slower than that in animals and that either late luminal enlargement could commence later than 3 years or that the underlying plaque fails to allow positive remodeling because it is rich in type I collagen.

The influence of the underlying plaque on the integration process remains unclear. In previous clinical studies, the Absorb scaffold was associated with a decrease of the plaque area on IVUS in the long term when compared with post-implantation (22). It was questioned whether this is due to the disappearance of struts or the real reduction of atherosclerotic plaque. In the present animal study, the area of neointima plus media remained unchanged throughout the 4-year follow-up period, whereas vessel wall thickness was reduced as a result of the very late luminal expansion or conversion of type III collagen to type I with cross-linking of collagen (**Figure 6A**). This suggests that the integration of the struts does not significantly affect the area of neointima plus media but induces the expansion of the lumen and the vessel, which could be mediated by the mechanotransduction and the restoration of shear stress (1).

FROM VISUAL CATEGORIZATION TO QUANTITATIVE MEASUREMENT OF LIGHT INTENSITY. In the present analysis, we used quantitative assessment of light intensity, which is more reproducible than visual assessment. The method has been applied to optical coherence tomographic analysis of struts in humans. The intraclass correlation coefficient for interobserver variability was as high as 0.91 (11).

The present OCT analysis using the second iteration of the Absorb device showed that using a cutoff of 0.413, the measured light intensity can

FIGURE 5 Change of Strut Core on Histology, Optical Coherence Tomography, and Intravascular Ultrasound From 3 to 48 Months

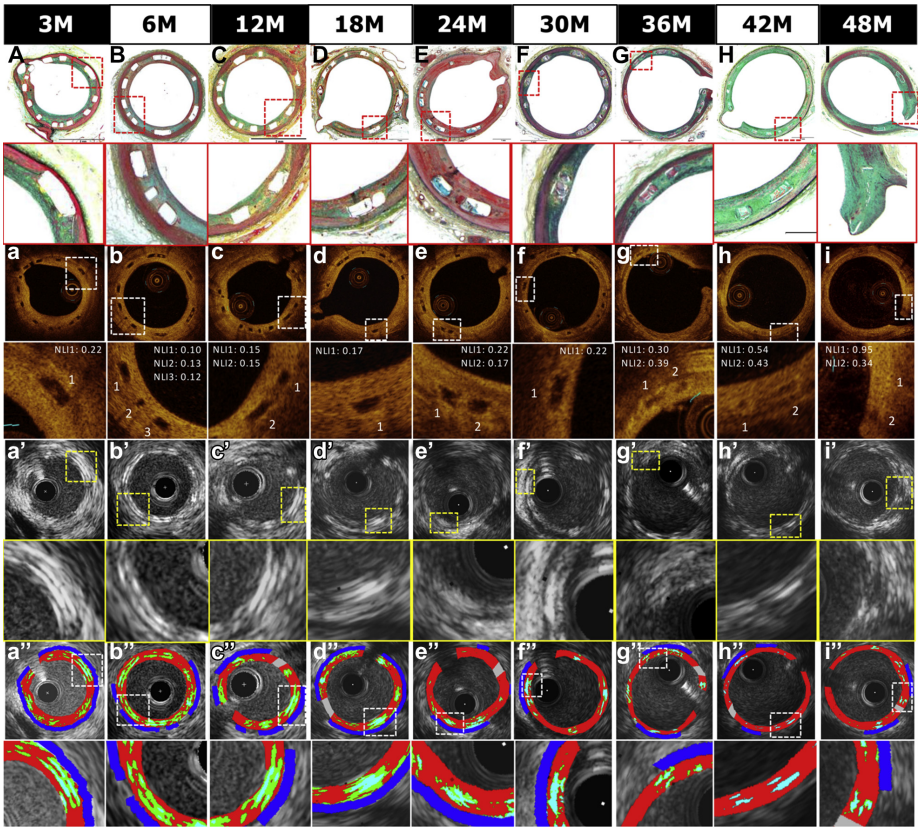

The figure summarizes the changes in strut cores from 3 to 48 months in the matched struts between histology **(A-I)**, optical coherence tomography (OCT) **(a-i)**, intravascular ultrasound (IVUS) grayscale **(a'-i')**, and IVUS echogenicity **(a''-i'')**. During the first 18 months, the struts were completely sequestered from the lumen by a thin and fibromuscular neointima with well-defined and squared edge on histology. **(A-D)** Although the normalized light intensity (NLI) on OCT showed low values **(a-d)**, the echogenicity of struts on IVUS decreased gradually (light blue area plus green area in **a''-d''**). At 24 and 30 months, the strut footprints had discrete borders but started to be replaced by provisional matrix **(E)**, followed by infiltration by connective tissue on histology **(F-I)**. The NLI slightly increased **(e,f)**, whereas the echogenicity of struts reached to plateau **(e'',f'')**. On histology, the filtration inside of strut void rapidly advanced between 30 and 42 months **(G,H)**. Correspondingly, the normalized intensity on OCT surged **(g,h)**. At 48 months, the integration of strut cores was almost complete **(I)**, and the NLI reached a plateau **(i')**. Light blue indicates upper echogenicity, and light green indicates hyperechogenicity.

differentiate moderately to highly integrated struts from low-integrated struts with an accuracy of 0.922. This integration progressively occurs between 30 and 42 months after implantation, which seems to be the critical timing for maximal vessel remodeling.

The other possible optical coherence tomographic methods to evaluate the bioresorption process include the refractive index or dispersion to differentiate the provisional matrix and polymer, or birefringence analysis using polarization-sensitive

FIGURE 6 Relationships Among Quantitative Light Intensity Analysis, Luminal Area, and Echogenicity in Animal and Human Models

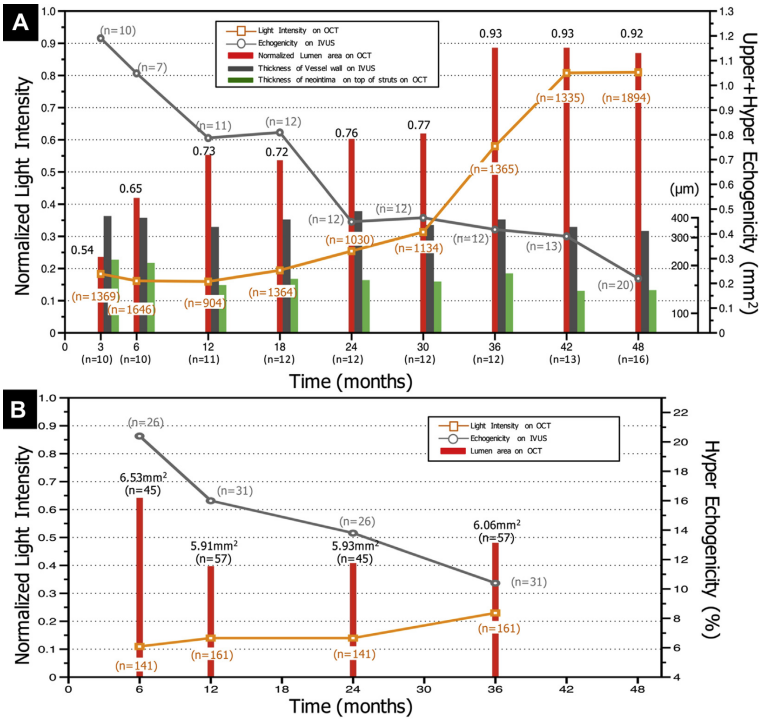

(A) The relationships among quantitative light intensity, normalized luminal area, and echogenicity with superimposed wall thickness and neointimal thickness on top of struts in swine. There are 2 periods of facilitated enlargement of normalized luminal area **(red bar)**. The first enlargement of lumen occurs during the first 30 months, which could be related to the loss of mechanical integrity and the natural growth of the coronary artery. During this period, the upper echogenicity plus hyperechogenicity area on intravascular ultrasound (IVUS) echogenicity decreased and reached a plateau **(gray line)**. The second luminal enlargement occurred between 30 and 42 months. During this period, the normalized light intensity on optical coherence tomography (OCT) surged **(orange line)**. In addition, the vessel wall thickness **(gray bar)** was reduced with the thinning of the neointima on top of struts **(green bar)**. **(B)** The relationships among quantitative light intensity, luminal area, and echogenicity in humans. In the ABSORB cohort B trial, at 36 months IVUS echogenicity had decreased **(gray line)**, whereas the normalized light intensity on OCT had not yet surged (the average of normalized light intensity was 0.22 at 36 months; orange line). Luminal area did not change significantly from 12 to 36 months.

OCT (23). In terms of quantitative measurement, OCT is presumably more close to the in vivo dimension than histomorphometric measurement, because of the absence of vessel shrinkage from histological preparation (24).

On histology, we used a semiquantitative scale to classify the degree of integration. Theoretically, the infiltration rate of connective tissues into the strut footprint could also be quantifiable on histology; however, because of tissue shrinkage due to formalin fixation and dehydration with tissue processing, it is unclear which segment of the vessel may be most affected. It is likely to be proteoglycans, which are water rich, and dehydration affects water-rich areas more than other regions. It was also possible that the strut footprint could deform during the histological

processing; after 4 years, the original area occupied by the polymeric strut is poorly discernible by light microscopy, which made quantitative measurement on histology difficult. The use of time-of-flight secondary iron mass spectroscopic analysis might facilitate future pre-clinical studies to quantify the degrees of degradation and integration (25).

STUDY LIMITATIONS. The present study was performed in a healthy porcine model without atherosclerosis, so the generalizability of the concepts to human is therefore limited. The methodology for normalization is not necessarily applicable to humans, because homogeneity of neointima is different between human and porcine models. The expected complex relationships among plaque burden, mechanotransduction, luminal enlargement and vascular remodeling, and natural coronary artery growth are not yet elucidated in the current models, although the initial molecular weight loss due to depolymerization is not different between human and pigs, because the process is purely chemical via hydrolysis.

From a regulatory perspective, it is mandatory to investigate the process of bioresorption of each fully bioresorbable scaffold, because the rate can vary according to the manufacturing process. The current assessment for monitoring bioresorption and integration process by echogenicity on IVUS and light intensity on OCT could be applied only to scaffolds made of PLLA, with similar molecular weights and similar manufacturing processes, but it could not be applied to other scaffolds made of different materials (e.g., magnesium), with different molecular weights (e.g., Igaki-Tamai) or different manufacturing processes (e.g., Mirage).

CONCLUSIONS

In this pre-clinical model, luminal enlargement is a biphasic process in which the latter phase likely relates, at least in part, to strut integration of the Absorb scaffold into the arterial wall. The quantitative light intensity analysis of strut cores on OCT could be used as a surrogate method for monitoring matrix infiltration and integration of collagen-rich connective tissue within the polymeric struts that coincide with the time of late luminal enlargement. These intravascular methods may provide insight and understanding of the imaging-related characteristics of the bioresorption process of various polylactide scaffolds in human.

REPRINT REQUESTS AND CORRESPONDENCE: Dr. Yoshinobu Onuma, Thoraxcenter, Ba-583, 's Gravendijkwal 230, 3015 CE Rotterdam, the Netherlands. E-mail: yoshinobuonuma@gmail.com.

PERSPECTIVES

WHAT IS KNOWN? Visual categorizations of strut appearance of bioresorbable scaffolds on OCT have previously been demonstrated to correlate with the integration process with limited reproducibility. Light intensity analysis of strut cores has been introduced as a feasible and reproducible method for a quantitative assessment of strut integration after scaffold implantation.

WHAT IS NEW? In a porcine pre-clinical model, IVUS echogenicity analysis and light intensity analysis on OCT were well correlated with the depolymerization process of the strut and the integration process after the complete bioresorption, respectively. The late luminal enlargement observed between 3 and 4 years seems to be related to strut integration.

WHAT IS NEXT? Further studies are needed to evaluate the generalizability of the concepts to human and to elucidate the expected complex relationships among plaque burden, mechanotransduction, luminal enlargement and vascular remodeling, and natural coronary artery growth.

REFERENCES

1. Serruys PW, Garcia-Garcia HM, Onuma Y. From metallic cages to transient bioresorbable scaffolds: change in paradigm of coronary revascularization in the upcoming decade? Eur Heart J 2012;33:16-25.

2. Lane JP, Perkins LE, Sheehy AJ, et al. Lumen gain and restoration of pulsatility after implantation of a bioresorbable vascular scaffold in porcine coronary arteries. J Am Coll Cardiol Intv 2014;7:688-95.

3. Onuma Y, Dudek D, Thuesen L, et al. Five-year clinical and functional multislice computed tomography angiographic results after coronary implantation of the fully resorbable polymeric everolimus-eluting scaffold in patients with de novo coronary artery disease: the ABSORB cohort A trial. J Am Coll Cardiol Intv 2013;6:999-1009.

4. Radu MD, Raber L, Kalesan B, et al. Coronary evaginations are associated with positive vessel remodelling and are nearly absent following implantation of newer-generation drug-eluting stents: an optical coherence tomography and intravascular ultrasound study. Eur Heart J 2014;35:795-807.

5. Serruys PW, Onuma Y, Garcia-Garcia HM, et al. Dynamics of vessel wall changes following the implantation of the absorb everolimus-eluting bioresorbable vascular scaffold: a multi-imaging modality study at 6, 12, 24 and 36 months. Eurointervention 2014;9:1271-84.

6. Otsuka F, Pacheco E, Perkins LE, et al. Long-term safety of an everolimus-eluting bioresorbable vascular scaffold and the cobalt-chromium XIENCE V stent in a porcine coronary artery model. Circ Cardiovasc Interv 2014;7:330-42.

7. Vorpahl M, Finn AV, Nakano M, Virmani R. The bioabsorption process: tissue and cellular mechanisms and outcomes. Eurointervention 2009;5 Suppl F:F28–35.

8. Middleton JC, Tipton AJ. Synthetic biodegradable polymers as orthopedic devices. Biomaterials 2000;21:2335–46.

9. Campos CM, Ishibashi Y, Eggermont J, et al. Echogenicity as a surrogate for bioresorbable everolimus-eluting scaffold degradation: analysis at 1-, 3-, 6-, 12-18, 24-, 30-, 36- and 42-month follow-up in a porcine model. Int J Cardiovasc Imaging 2015;31:471–82.

10. Onuma Y, Serruys PW, Perkins LE, et al. Intracoronary optical coherence tomography and histology at 1 month and 2, 3, and 4 years after implantation of everolimus-eluting bioresorbable vascular scaffolds in a porcine coronary artery model: an attempt to decipher the human optical coherence tomography images in the ABSORB trial. Circulation 2010;122:2288–300.

11. Nakatani S, Onuma Y, Ishibashi Y, et al. Temporal evolution of strut light intensity after implantation of bioresorbable polymeric intracoronary scaffolds in the ABSORB cohort B trial. Circ J 2014;78:1873–81.

12. Serruys PW, Onuma Y, Ormiston JA, et al. Evaluation of the second generation of a bioresorbable everolimus drug-eluting vascular scaffold for treatment of de novo coronary artery stenosis: six-month clinical and imaging outcomes. Circulation 2010;122:2301–12.

13. Swets JA. Measuring the accuracy of diagnostic systems. Science 1988;240:1285–93.

14. Strandberg E, Zeltinger J, Schulz DG, Kaluza GL. Late positive remodeling and late lumen gain contribute to vascular restoration by a non-drug eluting bioresorbable scaffold: a four-year intravascular ultrasound study in normal porcine coronary arteries. Circ Cardiovasc Interv 2012;5:39–46.

15. Oberhauser JP, Hossainy S, Rapoza RJ. Design principles and performance of bioresorbable polymeric vascular scaffolds. Eurointervention 2009;5 Suppl F:F15–22.

16. Onuma Y, Serruys PW. Bioresorbable scaffold: the advent of a new era in percutaneous coronary and peripheral revascularization? Circulation 2011; 123:779–97.

17. Lowe HC, Schwartz RS, Mac Neill BD, et al. The porcine coronary model of in-stent restenosis: current status in the era of drug-eluting stents. Catheter Cardiovasc Interv 2003;60:515–23.

18. Chien S. Mechanotransduction and endothelial cell homeostasis: the wisdom of the cell. Am J Physiol Heart Circ Physiol 2007;292:H1209–24.

19. Deguchi JO, Aikawa E, Libby P, et al. Matrix metalloproteinase-13/collagenase-3 deletion promotes collagen accumulation and organization in mouse atherosclerotic plaques. Circulation 2005; 112:2708–15.

20. Galis ZS, Khatri JJ. Matrix metalloproteinases in vascular remodeling and atherogenesis: the good, the bad, and the ugly. Circ Res 2002;90: 251–62.

21. Nagase H, Visse R, Murphy G. Structure and function of matrix metalloproteinases and TIMPs. Cardiovasc Res 2006;69:562–73.

22. Sarno G, Bruining N, Onuma Y, et al. Morphological and functional evaluation of the bioresorption of the bioresorbable everolimus-eluting vascular scaffold using IVUS, echogenicity and vasomotion testing at two year follow-up: a patient level insight into the ABSORB A clinical trial. Int J Cardiovasc Imaging 2012;28:51–8.

23. Tearney GJ, Bouma BE. Shedding light on bioabsorbable stent struts seen by optical coherence tomography in the ABSORB trial. Circulation 2010;122:2234–5.

24. Gogas BD, Radu M, Onuma Y, et al. Evaluation with in vivo optical coherence tomography and histology of the vascular effects of the everolimus-eluting bioresorbable vascular scaffold at two years following implantation in a healthy porcine coronary artery model: implications of pilot results for future pre-clinical studies. Int J Cardiovasc Imaging 2012;28:499–511.

25. Ninomiya S, Ichiki K, Yamada H, et al. Precise and fast secondary ion mass spectrometry depth profiling of polymer materials with large Ar cluster ion beams. Rapid Commun Mass Spectrom 2009; 23:1601–6.

26. Simsek C, Karanasos A, Magro M, et al. Long-term invasive follow-up of the everolimus-eluting bioresorbable vascular scaffold: five-year results of multiple invasive imaging modalities. Eurointervention 2016;11:996–1003.

KEY WORDS **biodegradable polymer, bioresorbable scaffold, coronary intervention, intravascular ultrasound, optical coherence tomography, pathology**

APPENDIX **For additional methods and supplemental figures, please see the online version of this article.**

3.2 Validation of echogenicity analysis of polymeric struts on IVUS

Echogenicity as a surrogate for bioresorbable everolimus-eluting scaffold degradation: analysis at 1-, 3-, 6-, 12- 18, 24-, 30-, 36- and 42-month follow-up in a porcine model.

Int J Cardiovasc Imaging. 2015;31(3):471-82.
[Original research paper, Impact Factor : 1.81]

Campos CM, Ishibashi Y, Eggermont J, Nakatani S, Cho YK, Dijkstra J, Reiber JH, Sheehy A, Lane J, Kamberi M, Rapoza R, Perkins L, Garcia-Garcia HM, Onuma Y, Serruys PW.

Echogenicity as a surrogate for bioresorbable everolimus-eluting scaffold degradation: analysis at 1-, 3-, 6-, 12- 18, 24-, 30-, 36- and 42-month follow-up in a porcine model

Carlos M. Campos · Yuki Ishibashi · Jeroen Eggermont · Shimpei Nakatani · Yun Kyeong Cho · Jouke Dijkstra · Johan H. C. Reiber · Alexander Sheehy · Jennifer Lane · Marika Kamberi · Richard Rapoza · Laura Perkins · Hector M. Garcia-Garcia · Yoshinobu Onuma · Patrick W. Serruys

Received: 27 November 2014 / Accepted: 10 January 2015 / Published online: 28 January 2015

Abstract The objective of the study is to validate intravascular quantitative echogenicity as a surrogate for molecular weight assessment of poly-l-lactide-acid (PLLA) bioresorbable scaffold (Absorb BVS, Abbott Vascular, Santa Clara, California). We analyzed at 9 time points (from 1- to 42-month follow-up) a population of 40 pigs that received 97 Absorb scaffolds. The treated regions were analyzed by echogenicity using adventitia as reference, and were categorized as more (hyperechogenic or upperechogenic) or less bright (hypoechogenic) than the reference. The volumes of echogenicity categories were correlated with the measurements of molecular weight (Mw) by gel permeation chromatography. Scaffold struts appeared as high echogenic structures. The quantification of grey level intensity in the scaffold-vessel compartment had strong correlation with the scaffold Mw: hyperechogenicity (correlation coefficient = 0.75; $P < 0.01$), upperechogenicity (correlation coefficient = 0.63; $P < 0.01$) and hyper + upperechogenicity (correlation coefficient = 0.78; $P < 0.01$). In the linear regression, the R^2 for high echogenicity and Mw was 0.57 for the combination of hyper and upper echogenicity. IVUS high intensity grey level quantification is correlated to Absorb BVS residual molecular weight and can be used as a surrogate for the monitoring of the degradation of semi-crystalline polymers scaffolds.

Keywords Absorb · Bioresorbable vascular scaffold · Degradation · Echogenicity · IVUS · Porcine

Abbreviations

IVUS	Intravascular ultrasound
BRS	Bioresorbable scaffolds
PLLA	Poly-l-lactide-acid
PDLLA	Poly-D, L-lactide
Mw	Molecular weight
Absorb	Poly-l-lactide-acid everolimus eluting
BVS	bioresorbable scaffold
CAD	Coronary artery disease

Impact on daily practice

Changes in bioresorbable vascular scaffolds (BRS), design and compositions may affect their degradation and loss of

Electronic supplementary material The online version of this article (doi:10.1007/s10554-015-0591-4) contains supplementary material, which is available to authorized users.

C. M. Campos · Y. Ishibashi · S. Nakatani · Y. K. Cho · H. M. Garcia-Garcia · Y. Onuma · P. W. Serruys (✉)
Department of Interventional Cardiology, Thoraxcenter, Erasmus University Medical Centre, s-Gravendijkwal 230, 3015 CE Rotterdam, The Netherlands
e-mail: p.w.j.c.serruys@erasmusmc.nl

C. M. Campos
Heart Institute (InCor), University of São Paulo Medical School, Sao Paulo, Brazil

J. Eggermont · J. Dijkstra · J. H. C. Reiber
Leiden University Medical Center, Leiden, The Netherlands

A. Sheehy · J. Lane · M. Kamberi · R. Rapoza · L. Perkins
Abbott Vascular, Santa Clara, CA, USA

H. M. Garcia-Garcia
Cardialysis, Rotterdam, The Netherlands

P. W. Serruys
International Centre for Circulatory Health, NHLI, Imperial College London, London, UK

biomechanical characteristics (with the risk of late recoil) and may be associated with a second wave of arterial wall inflammation. Therefore, studying the BRS degradation is crucial to fully understand this technology. The present work validates echogenicity as a surrogate for polylactide scaffold degradation.

Introduction

Bioresorbable vascular scaffolds (BRS) are a novel approach to the interventional treatment of coronary artery disease (CAD), providing short-term vascular scaffolding combined with drug-delivery capability. They may offer potential advantages compared to metallic drug-eluting stents (e.g. adaptive remodeling, restoration of vasomotion and late luminal enlargement). The so called 4th revolution in coronary artery disease revascularization steered extensive scientific research in BRS developments [1–3].

It has been shown that the designs and materials of BRS platforms—either metallic or polymeric—influence the resorption process [3–5]. Considering the variety of possible platforms, it is necessary to establish tools capable of monitoring the degradation process and its correlated mechanical characteristics.

Intravascular ultrasound-derived parameters have shown to be useful to assess the BRS resorption of metallic and polymeric scaffolds in humans [6–8]. One of the most studied intravascular ultrasound (IVUS) techniques to evaluate the resorption process is called differential echogenicity [8, 9]. This method consists in an automated and quantitative three-dimensional analysis of coronary tissue components scored for echogenicity using as reference the mean level of the adventitia brightness [9] where scaffold struts appear as bright hyperechogenic structures. In clinical studies, a continuous decrease of echogenicity over time has been shown in regions treated with BRS, being putatively correlated to BRS degradation [7, 8]. However, in serial human assessments, changes in the adventitia and plaque-media compartment of the treated regions during the follow-up period could possibly affect these interpretations [10–14].

The objectives of the current study were: (1) to describe a novel method of echogenicity for tissue analysis; (2) to evaluate its reproducibility; and (3) to assess its aptitude to assess the BRS degradation process through a direct correlation with the molecular weight (Mw) in a preclinical model using a drug-eluting poly-l-lactide-acid (PLLA) bioresorbable scaffold (Absorb BVS, Abbott Vascular, Santa Clara, California).

Methods

Study devices

The device used in the present preclinical study is the same used in Cohort B of the ABSORB clinical trial [15, 16]. Absorb is a balloon-expandable BRS that consists of a polymer backbone of Poly (L-lactide) (PLLA) coated with a thin layer of a 1:1 mixture of Poly-D, L-lactide (PDLLA) polymer with the antiproliferative drug everolimus to form an amorphous drug-eluting coating matrix containing 100 μg of everolimus/cm^2 of scaffold [17].

Experimental model

For validation purposes, we analyzed non-atherosclerotic Yorkshire-Landrace swine which had been implanted with Absorb BVS via femoral access according to published procedures [18]. Absorb sizes were matched to the vessel size at a target balloon-to-artery ratio of 1.0–1.1 (10 % overstretch). Each animal received a single Absorb (3.0 × 18 mm for 1-, 3-, and 6-month and 3.0x12 mm for 12- to 42-month) in 2 or 3 main coronary arteries. Forty pigs (98 arteries) underwent IVUS acquisition and were then euthanized at 1-month (n = 12 scaffolds), 3-(n = 12), 6-(n = 14), 12-(n = 12), 18-(n = 12), 24-(n = 12), 30-(n = 8), 36-(n = 8) or 42-months (n = 8). Each scaffold had quantification of polymer degradation by gel permeation chromatography (GPC). Experimental studies received protocol approval from the institutional animal care and use committee and were conducted in accordance with American Heart Association guidelines for pre-clinical research and the Guide for the Care and Use of Laboratory Animals (National Institutes of Health 2010).

Gel permeation chromatography (GPC)

A previously reported GPC method, with a slightly modified sample extraction/purification process, was employed to investigate the degradation of polymer over time by evaluating the number-average molecular weight (Mn) of polymer in the Absorb [19]. In the present method, the extraction and purification of the polymer was repeated up to five times until the polymer was fully extracted from the tissue (i.e., the polymer signal in the last extract below the quantitation limit of 0.3 mg/mL). The samples were analyzed prior at 1-, 3-, 6-, 12-, 18-, 24-, 30-, 36- and 42-months after implantation.

IVUS acquisition and analysis

All IVUS runs were acquired with 40 MHz mechanical systems, using Galaxy V2.02 (Boston Scientific, MA,

USA) at 1-, 3-, 6- and 12-month follow-ups and iLab at 18-, 24-, 30-, 36- and 42-month (Boston Scientific, MA, USA). We used motorized pullback of 0.5 mm/s with a frame rate of 30 frames/second. The regions of interest were restrict to the scaffolded areas, identified by the first and the last cross-sectional IVUS frame in which scaffold struts could be identified and/or where the proximal or distal metallic markers could be identified. Vessel, scaffold and lumen contours were delimited every 0.5 mm blind to molecular weight results. We analysed four compartments by IVUS: the luminal, scaffold, vessel and the neointimal volume (vessel volume-lumen volume). The scaffold was delineated semiautomatically at the luminal leading edge of the struts and the lumen was delineated at the inner detectable tissue (Fig. 1).

To evaluate inter-observer reproducibility, 2 readers (C.C. and Y.I.) independently analyzed 30 segments randomly selected from the total number of the investigated segments. To determine intra-observer reproducibility, one reader (C.C.) analyzed these segments twice, with the second reading occurring 3 months later. The inter- and intra-observer reproducibility were good according to the conventional norms [20] (hyperechogenicity inter-observer interclass correlation coefficient [ICC] = 0.80, intra-observer ICC = 0.95; hypoechogenicity: inter-observer ICC = 0.78, intra-observer ICC = 0.97; upperechogenicity: inter-observer ICC = 0.92, intra-observer ICC = 0.97) (Supplementary material).

Automatic quantitative echogenicity analysis

The principle of echogenicity has been previously described elsewhere [9, 21, 22]. Echogenicity aims to classify the vessel wall components located between the luminal boundary and the external elastic membrane (EEM) into categories based on their grey-level intensity in B-mode IVUS images rather than based on radiofrequency ultrasound signal analysis [23–26] (Fig. 1). Here we quantified 5 tissue types: hypoechogenic, hyperechogenic, calcified, upperechogenic and unknown.

Comparison with the adventitia allows for normalization with respect to transducer variability, gain settings and across populations [21]. However, in the analysis of atherosclerotic tissue, the adventitia can be partially obscured or darkened as a result of the guide-wire shadowing or the presence of dense tissue (e.g. calcium) which reduces the average grey-level values of the adventitia. Therefore, these parts need to be excluded from the reference adventitial area. To determine the reference adventitia area in each frame, the full adventitial area located just outside the EEM is first determined based on a minimum (0.01 mm) and maximum (0.21 mm) distance from the EEM contour (Fig. 1). To remove the low echogenic parts of the adventitia an adaptive threshold value for the entire adventitia area is determined based on Otsu's method [27]. Otsu's method is a classic automatic non-parametric threshold selection method which maximizes the between-class variance. Next, the adventitial area is divided into 2-degree wide sectors. If more than half of the pixels inside of a sector is below the adaptive threshold, the sector is excluded from the reference adventitia area. Finally, the histograms of the reference adventitial areas of the individual frames are combined into a global adventitia grey-level intensity histogram and the median value is computed as a threshold. Cross-section pixels with an intensity lower than the median value are classified as hypoechogenic, pixels with an intensity higher than the median value threshold are classified as hyperechogenic.

Calcified plaque is typically identified in B-mode IVUS images as a highly echogenic area creating an acoustic shadow [21]. To determine the high-intensity grey-level threshold for highly echogenic components we use the adaptive threshold selection method described in [28]. First Otsu's method is applied to the entire grey-level histogram of an image resulting in an optimal threshold value. In the next 2 iterations, Otsu's method is applied to the histogram of all intensities above the threshold found in the previous step. Next, we apply an in-house developed acoustic shadow detection algorithm. Highly echogenic areas with a grey-level intensity higher than the high-intensity threshold but without acoustic shadow behind them are classified as upperechogenic, while highly echogenic areas with acoustic shadow are classified as calcified and the shadow itself is classified as unknown. The entire method has been implemented and tested in QCU-CMS-Research v4.69 (research version of QIvus, developed by the Leiden University Medical Center) [29].

Data analysis

Continuous variables are presented as mean ± SD or medians (interquartile range). The ANOVA test was used to compare continuous variables. As we had different scaffold lengths we normalized all measurements by the mean length for all pigs as described previously [30]. This adjusts for differing segment lengths across animals, thereby providing equal weighting of each individual in the calculation of echogenicity volumes. The residual scaffold molecular weight by GPC was compared to the echogenicity findings and the correlation coefficient was used as a measure of the degree of relationship (Pearson's correlation coefficient). A linear regression was used to evaluate if hyper and/or upperechogenicity were able to predict the residual molecular weight. A

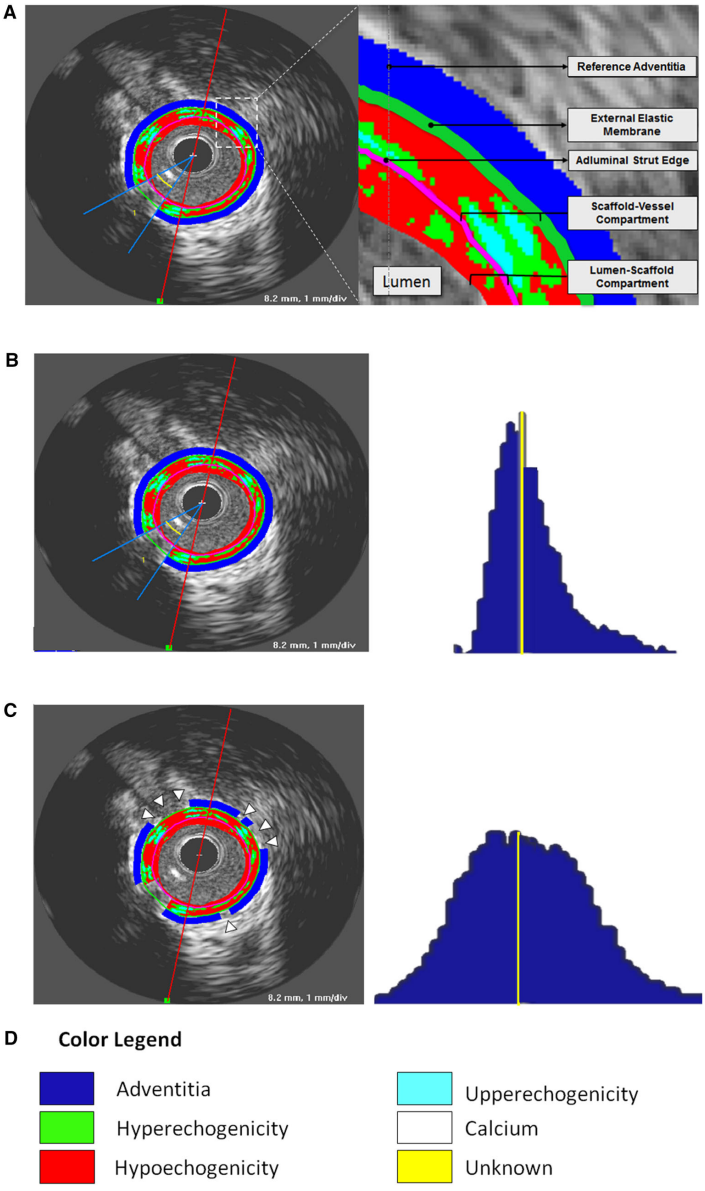

Fig. 1 Differential echogenicity methodology. **a** The first step was to determine the lumen-scaffold and scaffold-vessel compartments by defining the vessel, lumen and luminal scaffold contours in every 0.5 mm. After guidewire masking, the software identifies the adventitia as a ring between 0.01 and 0.21 mm outside vessel contours. **b** However, if the software uses as reference the whole layer around the vessel contour, it will include low intensity structures (e.g., pericardium, side branches, low attenuated tissues, etc.) resulting in a histogram with a non-normal distribution (*right panel*). **c** The present software detects automatically high signal adventitia as reference, excluding low intensity structures (*arrow heads*). The *right panel* shows that the combination of high signal adventitia in all frames obtains a bell shaped normally distributed histogram. The yellow line represents the referential adventitial median value. **d** The color legend of each echogenicity classification is provided. As we used a non-atherosclerotic porcine model there was no calcification and unknown tissue. Nevertheless, the present software is able to detect theses tissues

hierarchical cluster analysis using Ward's method (Squared Euclidean distance) was applied for hyper + upperechogenicity and hypoechogenicity volumes. The differences were regarded significant when $P < 0.05$ (two-tailed). SPSS version 21.0 (SPSS Inc., Chicago, Illinois) was used for all statistical analyses.

Results

The main grey scale IVUS volumetric findings are shown in Fig. 2 and the comparisons between each group are given in the supplementary material (Tables 2-5). The mean scaffold length was 16.5 mm. Compared with 1-month follow-up, the vessel, scaffold and lumen volumes had a trend to be larger after 18-month follow-up. These three aforementioned volumes were significantly larger at 36- and 42-month. Additionally, the neointima had the biggest volume at 1-month follow-up, being similar among groups thereafter (Fig. 3).

Differential echogenicity and molecular weight

Table 1 summarizes the main findings on differential echogenicity and mean Mw at each time point. The highest total hypoechogenicity volume was found at 1-month follow-up, the time point with also the highest neointimal hyperplasia as aforementioned. The lumen-scaffold compartment had an increase in hyper + upperechogenic volumes up to 12-month and subsequently a decrease until 42-month. Using the as reference the 1-month group, the hyper + upperechogenic decreased significantly in the scaffold vessel compartment after 12 months (supplementary material).

The GPC results indicated a continuous decrease in molecular weight over time. The rate of reduction was slower during the first 6-months of scaffold implantation followed by a more rapid decline thereafter, being fully resorbed 36-months after implantation (Fig. 2).

To validate the scaffold degradation by echogenicity we took into consideration the hyper- and upperechogenicity in

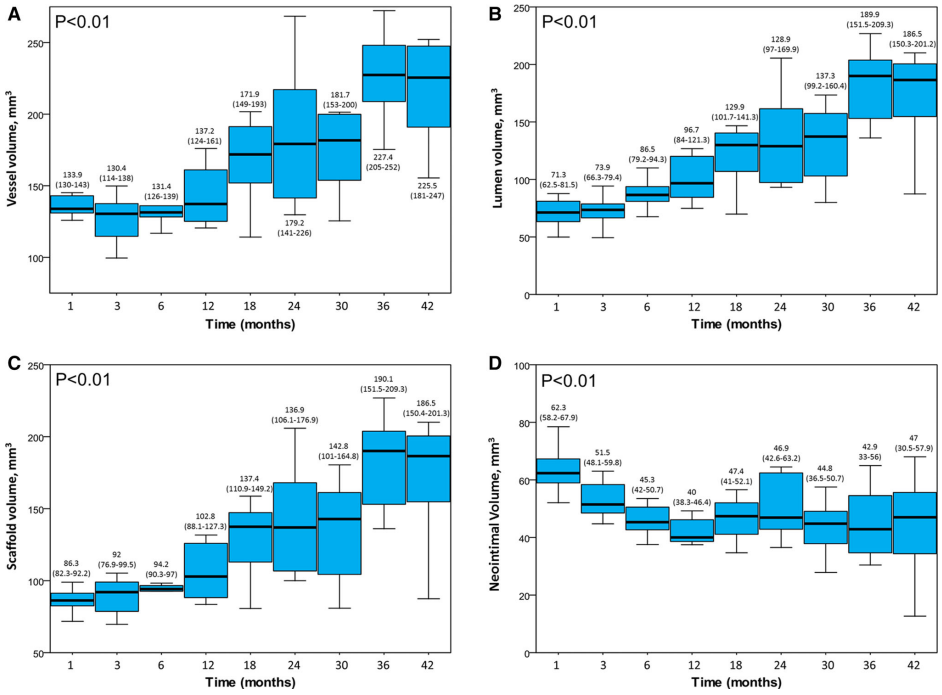

Fig. 2 Grey Scale intravascular ultrasound volumetric findings at different time points. **a** Vessel volume; **b** Lumen Volume; **c** Scaffold Volume and **d** Neointimal Volume. Values are median and interquartile range

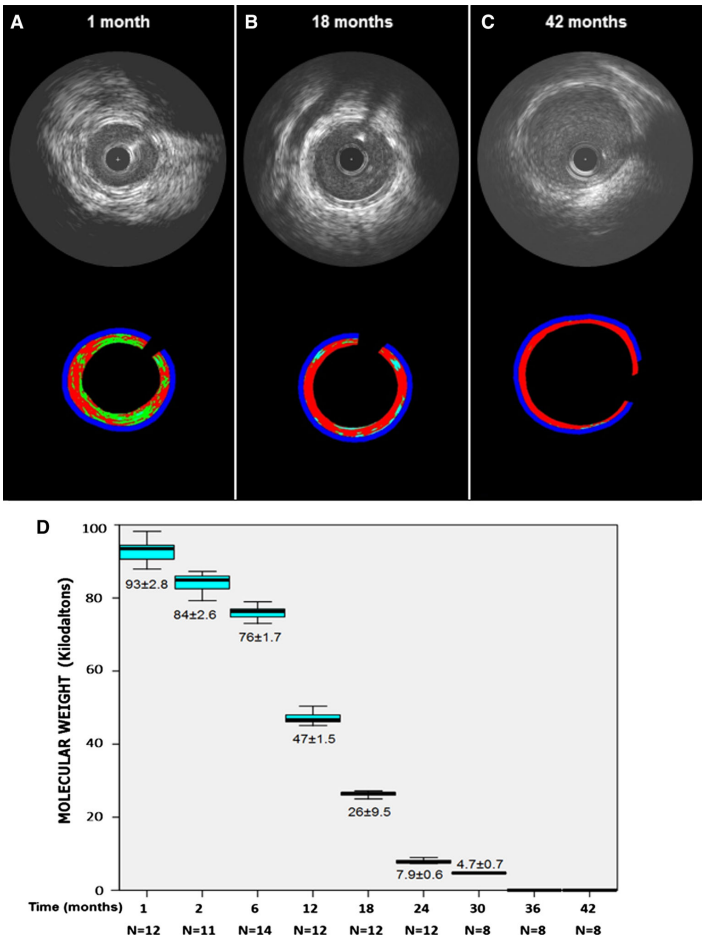

Fig. 3 IVUS echogenicity analysis at 1- (**a**), 18- (**b**) and 42-month (**c**). The high echogenic (including hyper = *light green* and upper = *light blue*) parameters decrease over time. **d** Gel permeation chromatography (GPC) for the assessment of degradation of Absorb showing the in vivo degradation of polymer of Absorb over time

the scaffold-vessel compartment (Fig. 1). As shown in Table 1, the earlier IVUS were more likely to present higher grey-level intensity (hyper + upperechogenicity). The scaffold-vessel hyperechogenicity (Pearson correlation coefficient = 0.75; $P < 0.01$), upperechogenicity (Pearson correlation coefficient = 0.63; $P < 0.01$) and hyper + upperechogenicity (Pearson correlation coefficient = 0.78; $P < 0.01$) had strong correlation with the scaffold molecular weight. As shown in Fig. 4, in linear regression, the best correlation found in linear regression model for molecular weight was scaffold-vessel hyper + upperechogenicity (R squared = 0.57; $P < 0.01$); i.e., all grey-level intensity higher than median adventitia in the scaffold-vessel compartment should be considered for monitoring the degradation process of this semi-crystalline polymers scaffold. Post-Hoc comparisons between each group are given in the supplementary material (Tables 6-8).

Additionally, a cluster analysis was run for scaffold-vessel hyper + upperechogenicity and hypoechogenicity. It produced five clusters, among which the variables were significantly different in the main (Fig. 5). The comparison among clusters of hyper + upperechogenicity showed a clear positive association scaffold-vessel hyper + upperechogenicity and molecular weight (Fig. 5).

Table 1 Differential echogenicity findings and polymer molecular weight by gel permeation chromatography

	1 Month (n = 12)	3 Months (n = 12)	6 Months (n = 14)	12 Months (n = 12)	18 Months (n = 12)	24 Months (n = 12)	30 Months (n = 8)	36 Months (n = 8)	42 Months (n = 8)	*P* value for overall comparison
Total hypoechogenicity Volume (mm^3)	49.3 ± 6.9	34.7 ± 6.8	31.4 ± 5.5	28.7 ± 4.5	33.3 ± 6.2	42.2 ± 8	28.4 ± 7	38.6 ± 12.2	37.6 ± 14.3	<0.01
% Total hypoechogenicity	79.4 ± 4.9	68.3 ± 7.8	70.3 ± 6.5	71.6 ± 6.7	80.5 ± 5.0	86.8 ± 5.4	78.1 ± 6.1	89.7 ± 4.3	92.0 ± 3.4	<0.01
Total hyperechogenicity volume (mm^3)	8.5 ± 2.7	8.7 ± 4	6.6 ± 1	6.5 ± 2.8	4.8 ± 1	3.9 ± 1.5	4.3 ± 1.3	2.8 ± 1.2	2.2 ± 1.1	<0.01
% Total Hyperechogenicity	13.6 ± 3.6	17.2 ± 7.0	15.5 ± 2.7	16.1 ± 6.1	11.8 ± 2.4	8.0 ± 2.6	12.0 ± 2.9	6.7 ± 2.5	5.3 ± 1.9	<0.01
Total upperechogenicity volume (mm^3)	6.3 ± 3.5	13.7 ± 5	12.9 ± 3.6	14.1 ± 7.1	9.5 ± 5.5	6.1 ± 3.6	11.3 ± 4.3	3.9 ± 2.1	2.9 ± 1.9	<0.01
% Total upperechogenicity	7.0 ± 3.9	14.5 ± 5.5	14.1 ± 5.3	12.3 ± 5.3	7.7 ± 4.0	5.2 ± 2.9	9.9 ± 3.4	3.7 ± 1.9	2.8 ± 1.6	<0.01
Total hyper and upperechogenicity volumes (mm^3)	14.9 ± 4.5	22.4 ± 5.2	19.6 ± 4.4	20.6 ± 6.8	14.4 ± 6.1	10 ± 4.9	15.6 ± 5.3	6.7 ± 3.16	5.1 ± 3	<0.01
% Total hyper and upperechogenicity	20.6 ± 4.9	31.7 ± 7.8	29.7 ± 6.5	28.4 ± 6.7	19.5 ± 5.1	13.2 ± 5.4	21.9 ± 6.1	10.3 ± 4.3	8.1 ± 3.4	<0.01
Lumen-scaffold hypoechogenicity Volume (mm^3)	13.6 ± 5.5	13.4 ± 4.3	7.7 ± 7.5	3.9 ± 1.9	6.7 ± 2.5	7.8 ± 4.1	2.9 ± 2	0 ± 0.1	0 ± 0.1	<0.01
% Lumen-scaffold hypoechogenicity	91.9 ± 4.3	88.8 ± 4.5	88.4 ± 4.1	80.5 ± 11.6	89.3 ± 3.7	92.3 ± 2.9	86.1 ± 4.5	22.0 ± 41.3	44.5 ± 48.3	<0.01
Lumen-scaffold hyperechogenicity volume (mm^3)	1.25 ± 0.9	1.5 ± 0.8	1.2 ± 1.8	0.8 ± 0.5	0.4 ± 0.2	0.3 ± 0.2	0.3 ± 0.2	0	0	<0.01
% Lumen-scaffold hyperechogenicity	8.1 ± 4.4	10.7 ± 4.7	11.0 ± 3.8	19.0 ± 11.6	6.5 ± 3.0	4.0 ± 2.0	9.9 ± 3.5	1.8 ± 5.0	3.7 ± 8.7	<0.01
Lumen-scaffold upperechogenicity volume (mm^3)	1.9 ± 1.3	6.6 ± 2.8	6.6 ± 2.8	9.3 ± 5.1	6.6 ± 3.9	3.8 ± 2.2	7.7 ± 3.22	2.4 ± 1.4	1.8 ± 1.3	<0.01
% Lumen-scaffold upperechogenicity	0.1 ± 0.1	0.5 ± 0.7	0.5 ± 0.7	0.4 ± 0.5	4.2 ± 0.9	3.1 ± 1.2	4.0 ± 1.7	1.2 ± 3.4	1.8 ± 51	<0.01
Lumen-scaffold hyper and upperechogenicity Volumes (mm^3)	3.2 ± 1.5	8.1 ± 3.1	7.9 ± 2.6	10.1 ± 5.4	7.1 ± 4	4.1 ± 2.4	8 ± 3.3	2.4 ± 1.4	1.8 ± 1.3	<0.01
% Lumen-scaffold hyper and upperechogenicity	8.1 ± 4.3	11.2 ± 4.5	11.6 ± 4.1	19.5 ± 11.6	10.7 ± 37	7.1 ± 2.9	13.9 ± 4.5	3.0 ± 8.4	5.5 ± 10.3	<0.01
Scaffold-vessel hypoechogenicity volume (mm^3)	35.7 ± 4	21.3 ± 5.1	23.8 ± 9.3	24.9 ± 4.6	26.6 ± 4.9	34.4 ± 7.9	25.5 ± 7.9	38.5 ± 12.2	37.7 ± 14.3	<0.01
% Scaffold-vessel hypoechogenicity	75.5 ± 6.0	59.6 ± 8.6	66.9 ± 8.3	70.1 ± 6.9	78.4 ± 6.2	85.3 ± 6.3	77.0 ± 6.3	89.7 ± 4.3	91.9 ± 3.4	<0.01
Scaffold-vessel hyperechogenicity volume (mm^3)	7.3 ± 2	7.2 ± 4.2	5.4 ± 2.3	5.7 ± 2.5	4.4 ± 0.9	3.5 ± 1.3	4 ± 1.4	2.8 ± 1.1	2.2 ± 1.2	<0.01
% Scaffold-vessel hyperechogenicity	15.4 ± 4.1	19.5 ± 7.3	16.3 ± 2.9	15.9 ± 5.7	13.1 ± 2.8	8.9 ± 3.0	12.3 ± 3.0	6.7 ± 2.5	5.3 ± 1.9	<0.01
Scaffold-vessel upperechogenicity volume (mm^3)	4.4 ± 2.6	7.1 ± 2.5	6.3 ± 1.8	4.8 ± 2.1	2.9 ± 1.7	2.3 ± 1.4	3.5 ± 1.5	1.5 ± 0.8	1.1 ± 0.8	<0.01
% Scaffold-vessel upperechogenicity	9.2 ± 5.3	20.8 ± 8.3	16.7 ± 6.7	14.4 ± 6.4	8.5 ± 4.9	5.8 ± 3.5	10.7 ± 3.7	3.7 ± 1.9	2.8 ± 1.6	<0.01

Table 1 continued

	1 Month (n = 12)	3 Months (n = 12)	6 Months (n = 14)	12 Months (n = 12)	18 Months (n = 12)	24 Months (n = 12)	30 Months (n = 8)	36 Months (n = 8)	42 Months (n = 8)	*P* value for overall comparison
Scaffold-vessel hyper and upperechogenicity volumes (mm^3)	11.7 ± 3.4	14.3 ± 3.8	11.7 ± 3.8	10.5 ± 2.4	7.3 ± 2.3	5.8 ± 2.7	7.5 ± 2.7	4.3 ± 1.9	3.2 ± 1.9	<0.01
% Scaffold-vessel hyper and Upperechogenicity	24.6 ± 6.0	40.4 ± 8.6	33.1 ± 8.3	29.9 ± 6.9	21.7 ± 6.2	14.7 ± 6.3	23.0 ± 6.3	10.4 ± 4.3	8.1 ± 3.4	<0.01
Molecular weight (kDa)	92.9 ± 2.8	84.2 ± 2.5	76 ± 1.7	47.1 ± 1.5	26.2 ± 0.9	7.9 ± 0.6	4.7 ± 73.9	0	0	<0.01

Discussion

In the present study, using IVUS grey scale derived parameters we attempted to assess the degradation process of the Absorb poly-L-lactide bioresorbable everolimus-eluting scaffold at multiple time points in a porcine model. The major findings of this study can be summarized as follows: (1) hyperechogenic and upperechogenic thresholds had strong and positive correlations with the scaffold molecular weight assessment; (2) the combination of hyper and upperechogenicity could be used as a surrogate for the chromatographic assessment of scaffold molecular weight and (3) echogenicity demonstrated good inter- and intra-observer reproducibility (Supplementary Material).

The present manuscript describes a new software designed to assess the differential echogenicity and, for the first time, ascertained the correlation between IVUS grey scale intensities and quantitative assessment of Mw by GPC. The first novelty is that it was not necessary to use ECG gating and therefore, it is not needed a dedicated IVUS console or post-processing correction. The robustness of this method and the aforementioned good reproducibility demonstrate, for the first time, good correlation of echogenicity with the degradation of the scaffold without being mandatory correction for motion artifacts [30].

Image resolution can be defined as the capability of making distinguishable the individual parts of an object. Therefore, the use of 40 MHz IVUS catheter in the present study has potential to be more precise to detect scaffold degradation than the previous methodology with the 20 MHz ultrasound [7, 31]. Ultrasound at a center frequency of 10 MHz has demonstrated to detect decline in the acoustic impedance of PLA when molecular weight varied from 60 to 24 kDa, but further decrease in molecular weight to 15 kDa did not result in discernible change [32]. In the present study, working with the higher resolution of the 40 MHz IVUS catheter, we were able to detect acoustic differences in 150 m thick samples degrading from $\sim$100 to <4 kDa.

The use of ultrasound to monitor the degradation process of polymers has been initially proposed with a wave pulse-echo method in an in vitro essay [31]. Wu succeeded to monitor by ultrasound the degradation process of three biodegradable polymers: poly(glycolic acid) (PGA), poly(L-lactic acid) (PLLA) and 50:50 poly(D, L-lactide-co-glycolide) (PDLLG) [33]. Another IVUS based approach to detect the resorption process in human is virtual histology [6]. The spectral analysis of the raw backscattered ultrasound misrepresents polymeric struts as dense calcium (DC) and necrotic core (NC). As these parameters are shown to decrease over time after implantation, they have been correlated putatively with resorption [6, 16, 34, 35].

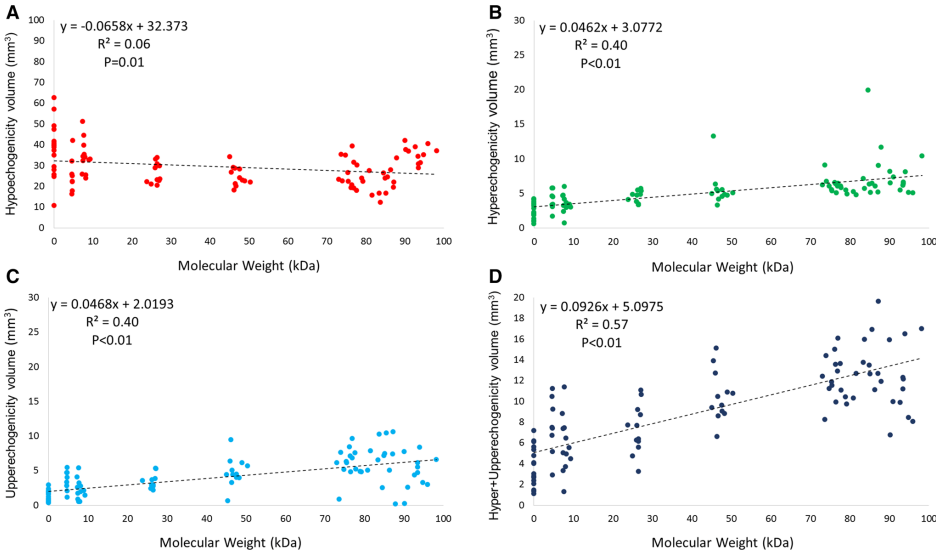

Fig. 4 Linear regressions between molecular weight and echogenicity derived parameters in the scaffold-vessel compartment

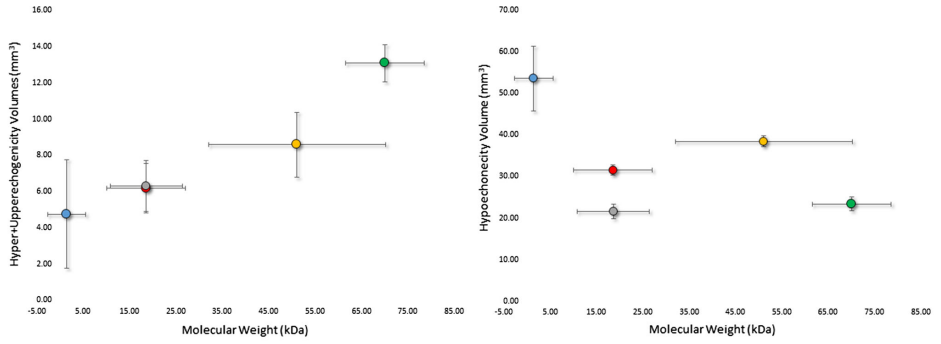

Cluster	1 (n=22)	2 (n=34)	3 (n=19)	4 (n=18)	5 (n=5)	P
Parameter						
Hyper+Upperechogenicity Volume, (mm^3)	4.75±2.41	6.19±2.93	6.31±2.75	8.59±4.02	13.08±2.92	<0.01
Hypoechogenicity Volume, (mm^3)	53.58±6.31	31.56±2.46	21.56±3.60	38.43±2.97	23.37±4.75	<0.01
Molecular Weight, (kDa)	1.48±3.30	18.54±17.09	18.63±17.09	51.13±43.10	70.08±24.42	<0.01

Fig. 5 A hierarchical cluster analysis labeled by animal was run for scaffold-vessel hyper + upperechogenicity and hypoechogenicity. Cluster 2 and 3 had similar hyper + upperechogenicity but statistically significant greater hypoechogenicity volumes in the cluster 2. Cluster 3 and 5 had similar hypoechogenicity but markedly higher hyper + upperechogenicity volumes in cluster 5. There was a clear positive association between scaffold-vessel hyper + upperechogenicity and molecular weight. The sample sizes are number of scaffolds included in each pig cluster. The values are mean ± standard deviation and the errors bars are 95 % confidence interval

Previously, echogenicity has been used to assess paired serial acoustic properties of coronary plaques in BRS-treated segments in the clinical setting [7, 8, 35]. It has been shown that these segments had an increase in hyperechogenic tissue after implantation which decreased over time [7, 8, 35]. The aforementioned methodology succeeds to document the progressive decrease of high intensity grey level tissues in both metallic and polymeric BRS [8, 35].

However, until now, the link between echogenicity and the degradation process has been hypothetically assumed. The pending question was whether temporal plaque changes could interfere with the multistage degradation of the polymer and confound the echogenicity analysis. It has been shown that coronary atherosclerosis is a dynamic phenomenon and numerous factors can influence the atherosclerotic changes as detected by IVUS-derived parameters. For instance, statin treatment may reduce the percentage lipid volume index over time [13] and may increase the calcified plaque component [11]. Additionally, there is a significant decrease in NC (16 %) and DC (30 %) content in coronary plaque located behind the struts of the everolimus-eluting bioresorbable vascular scaffold [36]. All the above-mentioned confounding factors might influence the acoustic properties in the lumen-vessel compartment and hinder the clinical relevance of echogenicity for BRS degradation assessment.

As we have used a porcine non-atherosclerotic model, we did not have the confounding presence of coronary artery disease, thus enabling the evaluation of Poly-L-Lactide's echogenic characteristics over time. Hyperechogenic, upperechogenenic and hyper + upperechogenic tissues had strong and positive correlations between echogenicity and the degradation process. Echogenicity is determined by the difference in acoustic impedance between two mediums, which is proportional to density and acoustic velocity. The acoustic velocity is proportional to the square root of the stiffness (bulk and shear moduli). Many factors impact the stiffness of PLA, including molecular weight, polydispersity, crystallinity, orientation of crystalline microstructure, and other environmental conditions [37]. As a result, one would expect to change the impedance of PLA as it degrades and molecular weight to have a generalized relationship to this decline.

Qualitatively, the correlation was however not perfectly linear. For instance, at 1-month the combination hyper + upper tended (without statistical significance; Table 6, supplementary material), in average, to be lower than at 3-months whereas the molecular weight had a continuous decrease in the same period. From the ultrasonic point of view, the significantly higher neointimal hyperplasia (Fig. 2) at 1-month might have affected the ultrasound penetration and therefore the echogenicity interpretation. Additionally, the scaffold-vessel hyper + upperechogenicity at 30-months was numerically comparable to that at 18-month. However, the degradation process may be influenced by individual biological factors and it has to be emphasized that these assessments were not serial. However, we showed a consistent individual positive correlation between the molecular weight and echogenicity (Figs. 4 and 5).

Limitations

Arteries used for molecular weight assessment could not be evaluated histologically. Therefore, changes in the observed echogenicity (both lumen-scaffold and scaffold-vessel) could not be related to the histologic changes over time [19, 38]. As this study has been performed in a non-atherosclerotic model, it should be acknowledged that the rate of degradation has not been confirmed in atherosclerotic coronary arteries. However, as the degradation of PLLA is a hydrolytically driven and not enzymatically driven process, it is expected that the rates would be largely equivalent.

We could not test the reproducibility of the echogenicity IVUS findings in the two different consoles. However as we worked at the same ultrasound frequency (40 MHz) and the tissue classifications were normalized by the individual adventitia grey scale intensity we could show a robust correlation between scaffold degradation and high echogenic parameters. It has been shown that the comparison with the adventitia allows for normalization with respect to transducer variability, gain settings and across populations [21].

The changes in vessel, lumen, scaffold and neointima volumes over time are in line with the serial IVUS findings in the pre-clinical model and clinical setting showing progressive increase in vessel, lumen area and scaffold area [16, 18, 39, 40]. However, in the porcine model the somatic growth can influence our findings [39]. As we do not have the IVUS at baseline we could not normalize these geometrical changes for the increase in the reference vessel size. Nevertheless, this information has been described in the literature and are beyond the main scope of the current manuscript.

Conclusion

IVUS high intensity grey level quantification is correlated to Absorb scaffold residual molecular weight assessment. Echogenicity is a reproducible technique which could be considered as a surrogate assessment of polylactide molecular weight decrease as assessed by chromatography and allows for monitoring of the degradation of semi-crystalline polymeric scaffolds.

Acknowledgments The authors acknowledge Dave Pinson and Katherine Fu (Abbott Vascular) for their technical contributions in GPC analysis. The authors also acknowledge Michael Frie and the staff of American Preclinical Services (Minneapolis, MN) for their care and attention in successful completion of the in life phase of this study. The present study was sponsored by Abbott Vascular, Santa Clara, California.

Conflict of interest Alexander Sheehy, Marika Kamberi, Richard Rapoza and Laura Perkins are full-time employee of Abbott Vascular, Santa Clara, California, and at the time of this work, Jennifer Lane also was a full-time employee of Abbott Vascular. The others authors have no conflict of interest and did not receive grants or financial support from industry or from any other source to prepare this manuscript.

References

1. Iqbal J, Onuma Y, Ormiston J, Abizaid A, Waksman R, Serruys P (2013) Bioresorbable scaffolds: rationale, current status, challenges, and future. Eur Heart J
2. Wykrzykowska JJ, Onuma Y, Serruys PW (2009) Vascular restoration therapy: the fourth revolution in interventional cardiology and the ultimate "rosy" prophecy. EuroIntervention 5 Suppl F:F7-F8
3. Garcia-Garcia HM, Serruys PW, Campos CM, Muramatsu T, Nakatani S, Zhang YJ, Onuma Y, Stone GW (2014) Assessing Bioresorbable Coronary Devices: Methods and Parameters. JACC Cardiovasc Imaging 7:1130–1148
4. Campos CM, Muramatsu T, Iqbal J, Zhang YJ, Onuma Y, Garcia-Garcia HM, Haude M, Lemos PA, Warnack B, Serruys PW (2013) Bioresorbable drug-eluting magnesium-alloy scaffold for treatment of coronary artery disease. Int J Mol Sci 14:24492–24500
5. Campos CM, Lemos PA (2014) Bioresorbable vascular scaffolds: novel devices, novel interpretations, and novel interventions strategies. Catheter Cardiovasc Interv 84:46–47
6. Garcia-Garcia HM, Gonzalo N, Pawar R, Kukreja N, Dudek D, Thuesen L, Ormiston JA, Regar E, Serruys PW (2009) Assessment of the absorption process following bioabsorbable everolimus-eluting stent implantation: temporal changes in strain values and tissue composition using intravascular ultrasound radiofrequency data analysis. A substudy of the ABSORB clinical trial. EuroIntervention 4:443–448
7. Bruining N, de Winter S, Roelandt JR, Regar E, Heller I, van Domburg RT, Hamers R, Onuma Y, Dudek D, Webster MW, Thuesen L, Ormiston JA, Cheong WF, Miquel-Hebert K, Veldhof S, Serruys PW (2010) Monitoring in vivo absorption of a drug-eluting bioabsorbable stent with intravascular ultrasound-derived parameters a feasibility study. JACC Cardiovasc Interv 3:449–456
8. Waksman R, Prati F, Bruining N, Haude M, Bose D, Kitabata H, Erne P, Verheye S, Degen H, Vermeersch P, Di Vito L, Koolen J, Erbel R (2013) Serial observation of drug-eluting absorbable metal scaffold: multi-imaging modality assessment. Circ Cardiovasc Interv 6:644–653
9. Bruining N, Verheye S, Knaapen M, Somers P, Roelandt JR, Regar E, Heller I, de Winter S, Ligthart J, Van Langenhove G, de Feijter PJ, Serruys PW, Hamers R (2007) Three-dimensional and quantitative analysis of atherosclerotic plaque composition by automated differential echogenicity. Catheter Cardiovasc Interv 70:968–978
10. Puri R, Libby P, Nissen SE, Wolski K, Ballantyne CM, Barter PJ, Chapman MJ, Erbel R, Raichlen JS, Uno K, Kataoka Y, Tuzcu EM, Nicholls SJ (2014) Long-term effects of maximally intensive statin therapy on changes in coronary atheroma composition: insights from SATURN. Eur Heart J Cardiovasc Imaging 15:380–388
11. Nozue T, Fukui K, Yamamoto S, Kunishima T, Umezawa S, Onishi Y, Tohyama S, Hibi K, Sozu T, Terashima M, Michishita I (2013) Time course of statin-induced changes in coronary atherosclerosis using intravascular ultrasound with virtual histology. Coron Artery Dis 24:481–486
12. Zhao Z, Witzenbichler B, Mintz GS, Jaster M, Choi SY, Wu X, He Y, Margolis MP, Dressler O, Cristea E, Parise H, Mehran R, Stone GW, Maehara A (2013) Dynamic nature of nonculprit coronary artery lesion morphology in STEMI: a serial IVUS analysis from the HORIZONS-AMI trial. JACC Cardiovasc Imaging 6:86–95
13. Hattori K, Ozaki Y, Ismail TF, Okumura M, Naruse H, Kan S, Ishikawa M, Kawai T, Ohta M, Kawai H, Hashimoto T, Takagi Y, Ishii J, Serruys PW, Narula J (2012) Impact of statin therapy on plaque characteristics as assessed by serial OCT, grayscale and integrated backscatter-IVUS. JACC Cardiovasc Imaging 5:169–177
14. Lee IS, Bourantas CV, Muramatsu T, Gogas BD, Heo JH, Diletti R, Farooq V, Zhang Y, Onuma Y, Serruys PW, Garcia-Garcia HM (2013) Assessment of plaque evolution in coronary bifurcations located beyond everolimus eluting scaffolds: serial intravascular ultrasound virtual histology study. Cardiovasc Ultrasound. 11:25
15. Serruys PW, Onuma Y, Dudek D, Smits PC, Koolen J, Chevalier B, de Bruyne B, Thuesen L, McClean D, van Geuns RJ, Windecker S, Whitbourn R, Meredith I, Dorange C, Veldhof S, Hebert KM, Sudhir K, Garcia-Garcia HM, Ormiston JA (2011) Evaluation of the second generation of a bioresorbable everolimus-eluting vascular scaffold for the treatment of de novo coronary artery stenosis: 12-month clinical and imaging outcomes. J Am Coll Cardiol 58:1578–1588
16. Serruys PW, Onuma Y, Garcia-Garcia HM, Muramatsu T, van Geuns RJ, de Bruyne B, Dudek D, Thuesen L, Smits PC, Chevalier B, McClean D, Koolen J, Windecker S, Whitbourn R, Meredith I, Dorange C, Veldhof S, Hebert KM, Rapoza R, Ormiston JA (2013) Dynamics of vessel wall changes following the implantation of the Absorb everolimus-eluting bioresorbable vascular scaffold: a multi-imaging modality study at 6, 12, 24 and 36 months. EuroIntervention
17. Serruys PW, Onuma Y, Ormiston JA, de Bruyne B, Regar E, Dudek D, Thuesen L, Smits PC, Chevalier B, McClean D, Koolen J, Windecker S, Whitbourn R, Meredith I, Dorange C, Veldhof S, Miquel-Hebert K, Rapoza R, Garcia-Garcia HM (2010) Evaluation of the second generation of a bioresorbable everolimus drug-eluting vascular scaffold for treatment of de novo coronary artery stenosis: six-month clinical and imaging outcomes. Circulation 122:2301–2312
18. Lane JP, Perkins LE, Sheehy AJ, Pacheco EJ, Frie MP, Lambert BJ, Rapoza RJ, Virmani R (2014) Lumen gain and restoration of pulsatility after implantation of a bioresorbable vascular scaffold in porcine coronary arteries. JACC Cardiovasc Interv
19. Onuma Y, Serruys PW, Perkins LE, Okamura T, Gonzalo N, Garcia-Garcia HM, Regar E, Kamberi M, Powers JC, Rapoza R, van Beusekom H, van der Giessen W, Virmani R (2010) Intracoronary optical coherence tomography and histology at 1 month and 2, 3, and 4 years after implantation of everolimus-eluting bioresorbable vascular scaffolds in a porcine coronary artery

model: an attempt to decipher the human optical coherence tomography images in the ABSORB trial. Circulation 122:2288–2300
20. Fleiss JL (ed) (1986) The design and analysis of clinical experiments. Wiley, New York
21. Rasheed Q, Dhawale PJ, Anderson J, Hodgson JM (1995) Intracoronary ultrasound-defined plaque composition: computer-aided plaque characterization and correlation with histologic samples obtained during directional coronary atherectomy. Am Heart J 129:631–637
22. Schartl M, Bocksch W, Koschyk DH, Voelker W, Karsch KR, Kreuzer J, Hausmann D, Beckmann S, Gross M (2001) Use of intravascular ultrasound to compare effects of different strategies of lipid-lowering therapy on plaque volume and composition in patients with coronary artery disease. Circulation 104:387–392
23. Sathyanarayana S, Carlier S, Li W, Thomas L (2009) Characterisation of atherosclerotic plaque by spectral similarity of radiofrequency intravascular ultrasound signals. EuroIntervention 5:133–139
24. Nair A, Kuban BD, Tuzcu EM, Schoenhagen P, Nissen SE, Vince DG (2002) Coronary plaque classification with intravascular ultrasound radiofrequency data analysis. Circulation 106:2200–2206
25. Nair A, Margolis MP, Kuban BD, Vince DG (2007) Automated coronary plaque characterisation with intravascular ultrasound backscatter: ex vivo validation. EuroIntervention 3:113–120
26. Okubo M, Kawasaki M, Ishihara Y, Takeyama U, Kubota T, Yamaki T, Ojio S, Nishigaki K, Takemura G, Saio M, Takami T, Minatoguchi S, Fujiwara H (2008) Development of integrated backscatter intravascular ultrasound for tissue characterization of coronary plaques. Ultrasound Med Biol 34:655–663
27. Otsu N (1979) A threshold selection method from gray-level histograms. IEEE Transactions on Systems, Man and Cybernetics 9:62–66
28. Santos Filho ESY, Tanaka A, Yoshizawa M (2008) Detection and quantification of calcifications in intravascular ultrasound images by automatic thresholding. Ultrasound Med Biol 34:160–165
29. Koning G, Dijkstra J, von Birgelen C, Tuinenburg JC, Brunette J, Tardif JC (2002) Advanced contour detection for three-dimensional intracoronary ultrasound: a validation–in vitro and in vivo. Int J Cardiovasc Imag 18:235–248
30. Mintz GS, Garcia-Garcia HM, Nicholls SJ, Weissman NJ, Bruining N, Crowe T, Tardif JC, Serruys PW (2011) Clinical expert consensus document on standards for acquisition, measurement and reporting of intravascular ultrasound regression/progression studies. EuroIntervention 6(1123–30):9
31. Wu HC, Shen FW, Hong X, Chang WV, Winet H (2003) Monitoring the degradation process of biopolymers by ultrasonic longitudinal wave pulse-echo technique. Biomaterials 24:3871–3876
32. Parker NG, Mather ML, Morgan SP, Povey MJ (2010) Longitudinal acoustic properties of poly(lactic acid) and poly(lactic-co-glycolic acid). Biomed Mater 5:055004
33. Chen S, Hong Y, Scherer SJ, Schartl M (2001) Lack of ultraviolet-light inducibility of the medakafish (Oryzias latipes) tumor suppressor gene p53. Gene 264:197–203
34. Sarno G, Onuma Y, Garcia Garcia HM, Garg S, Regar E, Thuesen L, Dudek D, Veldhof S, Dorange C, Ormiston JA, Serruys PW (2010) IVUS radiofrequency analysis in the evaluation of the polymeric struts of the bioabsorbable everolimus-eluting device during the bioabsorption process. Catheter Cardiovasc Interv 75:914–918
35. Brugaletta S, Gomez-Lara J, Serruys PW, Farooq V, van Geuns RJ, Thuesen L, Dudek D, Koolen J, Chevalier B, McClean D, Windecker S, Smits PC, de Bruyne B, Whitbourn R, Meredith I, van Domburg RT, Sihan K, de Winter S, Veldhof S, Miquel-Hebert K, Rapoza R, Garcia-Garcia HM, Ormiston JA, Bruining N (2011) Serial in vivo intravascular ultrasound-based echogenicity changes of everolimus-eluting bioresorbable vascular scaffold during the first 12 months after implantation insights from the ABSORB B trial. JACC Cardiovasc Interv 4:1281–1289
36. Brugaletta S, Gomez-Lara J, Garcia-Garcia HM, Heo JH, Farooq V, van Geuns RJ, Chevalier B, Windecker S, McClean D, Thuesen L, Whitbourn R, Meredith I, Dorange C, Veldhof S, Rapoza R, Ormiston JA, Serruys PW (2012) Analysis of 1 year virtual histology changes in coronary plaque located behind the struts of the everolimus eluting bioresorbable vascular scaffold. Int J Cardiovasc Imaging 28:1307–1314
37. Henton DE, Gruber P, Lunt J, Randall J (2005) Polylactic acid technology. CRC Press, Boca Raton
38. Vorpahl M, Finn AV, Nakano M, Virmani R (2009) The bioabsorption process: tissue and cellular mechanisms and outcomes. EuroIntervention 5(Suppl F):F28–F35
39. Strandberg E, Zeltinger J, Schulz DG, Kaluza GL (2012) Late positive remodeling and late lumen gain contribute to vascular restoration by a non-drug eluting bioresorbable scaffold: a four-year intravascular ultrasound study in normal porcine coronary arteries. Circ Cardiovasc Interv 5:39–46
40. Durand E, Sharkawi T, Leclerc G, Raveleau M, van der Leest M, Vert M, Lafont A (2013) Head-to-head comparison of a drug-free early programmed dismantling polylactic acid bioresorbable scaffold and a metallic stent in the porcine coronary artery: six-month angiography and optical coherence tomographic follow-up study. Circ Cardiovasc Interv

3.3 Validation of shear flow disturbances around malapposed struts

Incomplete stent apposition causes high shear flow disturbances and delay in neointimal coverage as a function of strut to wall detachment distance: implications for the management of incomplete stent apposition.

Circ Cardiovasc Interv. 2014;7(2):180-9.
[Original research paper, Impact Factor: 6.32]

Foin N, Gutiérrez-Chico JL, Nakatani S, Torii R, Bourantas CV, Sen S, Nijjer S, Petraco R, Kousera C, Ghione M, Onuma Y, Garcia-Garcia HM, Francis DP, Wong P, Di Mario C, Davies JE, Serruys PW.

Incomplete Stent Apposition Causes High Shear Flow Disturbances and Delay in Neointimal Coverage as a Function of Strut to Wall Detachment Distance

Implications for the Management of Incomplete Stent Apposition

Nicolas Foin, MSc, PhD*; Juan Luis Gutiérrez-Chico, MD, PhD*; Shimpei Nakatani, MD*; Ryo Torii, MSc, PhD*; Christos V. Bourantas, MD, PhD; Sayan Sen, MD, PhD; Sukhjinder Nijjer, MD; Ricardo Petraco, MD; Chrysa Kousera, MSc; Matteo Ghione, MD; Yoshinobu Onuma, MD; Hector M. Garcia-Garcia, MD, PhD; Darrel P. Francis, MD, PhD; Philip Wong, MD; Carlo Di Mario, MD, PhD; Justin E. Davies, MD, PhD; Patrick W. Serruys, MD, PhD

Background—Lack of re-endothelialization and neointimal coverage on stent struts has been put forward as the main underlying mechanism leading to late stent thrombosis. Incomplete stent apposition (ISA) has been observed frequently in patients with very late stent thrombosis after drug eluting stent implantation, suggesting a role of ISA in the pathogenesis of this adverse event. The aim of this study was to evaluate the impact of different degrees of ISA severity on abnormal shear rate and healing response with coverage, because of its potential implications for stent optimization in clinical practice.

Methods and Results—We characterized flow profile and shear distribution in different cases of ISA with increasing strut-wall detachment distance (ranging from 100 to 500 μm). Protruding strut and strut malapposed with moderate detachment (ISA detachment distance <100 μm) have minimal disturbance to blood flow as compared with floating strut that has more significant ISA distance. In vivo impact on strut coverage was assessed retrospectively using optical coherence tomography evaluation on 72 stents (48 patients) sequentially at baseline and after 6-month follow-up. Analysis of coverage revealed an important impact of baseline strut-wall ISA distance on the risk of incomplete strut coverage at follow-up. Malapposed segments with an ISA detachment <100 μm at baseline showed complete strut coverage at follow-up, whereas segments with a maximal ISA detachment distance of 100 to 300 μm and >300 μm had 6.1% and 15.7% of their struts still uncovered at follow-up, respectively (P<0.001).

Conclusions—Flow disturbances and risk of delayed strut coverage both increase with ISA detachment distance. Insights from this study are important for understanding malapposition as a quantitative, rather than binary phenomenon (present or absent) and to define the threshold of ISA detachment that might benefit from optimization during stent implantation. **(*Circ Cardiovasc Interv*. 2014;7:180-189.)**

Key Words: angioplasty ■ blood flow velocity ■ stents ■ thrombosis

Drug eluting stents (DESs) have significantly reduced the incidence of stent restenosis and target vessel revascularization from 20.0% to 50.3% in the bare metal stent (BMS) era[1] to 7.9% to 8.9%.[2–4] However, these promising early results of DES have been undermined by concerns over a possible increase in late and very late stent thrombosis (LST, VLST) as compared with BMS.[5–8] Pathological studies have revealed that delayed healing[9–14] and incomplete re-endothelialization[13] are common morphological findings in fatal cases of LST after DES.[9–14] DES can interfere with this physiological healing process through different mechanisms: first, the antiproliferative drug released by the device prevents the cellular mitosis required to restore the endothelial continuity; second, the polymer carrying the drug exerts a proinflammatory effect itself[15]; finally, in

Received July 24, 2013; accepted February 7, 2014.

From the International Centre for Circulatory Health, NHLI, Imperial College London, London, United Kingdom (N.F., S.S., S.N., R.P., C.K., D.P.F., J.E.D., P.W.S.); National Heart Centre Singapore, Singapore (N.F., P.W.); ThoraxCenter, Erasmus Medical Center, Rotterdam, The Netherlands (J.L.G.-C., S.N., C.V.B., Y.O., H.M.G.-G., P.W.S.); Ludwig-Maximilian Universität, München, Germany (J.L.G.-C.); Department of Mechanical Engineering, University College London, London, United Kingdom (R.T.); NIHR, BRU, Royal Brompton and Harefield NHS Trust, London, United Kingdom (M.G., C.D.M.); and Cardialysis, Rotterdam, The Netherlands (H.M.G.-G., P.W.S.).

*Drs Foin, Gutiérrez-Chico, Nakatani, and Torii contributed equally to this work.

Correspondence to Patrick W. Serruys, MD, PhD, or Nicolas Foin, MSc, PhD, ThoraxCenter, Erasmus University Medical Center, Ba-583, 's Gravendijkwal 230, 3015 CE Rotterdam, The Netherlands. E-mail p.w.j.c.serruys@erasmusmc.nl or nicolas.foin@gmail.com

WHAT IS KNOWN

- In rheology studies, flow disturbances and high shear rates have been shown to influence biological processes and platelet activation.
- Incomplete stent apposition is observed frequently by intravascular imaging in patients affected with late stent thrombosis.
- Neointimal formation can reduce stent malapposition and the number of uncovered stent struts.

WHAT THE STUDY ADDS

- This study shows that the shear rate value and the area of blood affected by a high shear rate increase dramatically with increasing distance between a stent strut and vessel wall incomplete stent apposition distance.
- A 4-level grading scheme is outlined for the assessment of malapposition severity based on the impact on flow and a refined sequential optical coherence tomographic assessment of the healing process.
- Mildly malapposed struts affect flow patterns to a lesser extent and, in addition, neointimal healing process tends to completely correct for the malapposition, resulting in full integration of these struts within a year.
- More severely malapposed segments with maximal incomplete stent apposition distance >300 μm represent a greater concern as they affect not only larger areas of blood flow with higher shear but also have a higher likelihood of delayed healing.

some cases, the polymer may trigger a hypersensitivity reaction resulting in endothelial denudation and risk of VLST.[11,16] The association between lack of stent strut coverage and LST/VLST has been revealed by histopathology studies,[12,13] as well as in clinical setting by in vivo imaging studies.[17]

Several clinical and pathological studies have also shown an association between ISA and stent thrombosis in DES.[11,17–19] Incidence of ISA has been reported in ≤77% of the cases of VLST and explained as the consequence of a delayed hypersensitivity reaction mediated by eosinophils and resulting in weakening of the vessel wall, positive remodeling of the vessel, late-acquired ISA, endothelial denudation, and VLST.[11,16–20] Based on these observations, ISA has been suggested to be an important predisposing factor to stent thrombosis[21–24]: asymptomatic incidentally discovered ISA at 8th month follow-up was shown to be associated with higher major adverse cardiac event and definite late stent thrombosis rates at 5-year follow-up.[24] ISA struts exhibit delayed neointimal coverage as compared with well-apposed struts.[21–23]

Shear rate, defined as the local gradient in velocity between adjacent flow streamlines, affects biological arterial response[25–28] and is a known modulator of platelet activation and thrombosis.[29–32] Normal human shear rate (shear rate in large-to-medium–sized arteries) usually varies from 100 to 1000/s.[32,33] However, protruding and malapposed stent struts create back-facing steps, which disturb the blood flow and produce flow separation with eddies and larger shear rates.[34–36] The aim of the present study was to investigate the influence of increasing malapposition severity on intracoronary flow disturbances and biological response in vivo.

Methods

Computational Fluid Dynamic Simulation

We created models of stent strut malapposition: the models were based on a 2-dimensional midsection representative of a 3-mm-diameter straight coronary artery with parabolic steady inflow and peak velocity 50 cm/s (representative of the flow velocity in the human coronary circulation). We characterized blood flow patterns in different cases (Figure 1A) simulated using computational fluid dynamics (CFD) with finite volume method (CFX 12.1, ANSYS, Inc). Blood was assumed to be a Newtonian fluid. Apposed struts were defined as struts in contact with the underlying vessel wall. Two different categories of apposed struts were considered in the simulation: (1) embedded struts, defined as those with ≥50% of the strut thickness inlaid into the vessel wall,[37] (2) protruding struts, defined as those with <50% of the strut thickness inlaid into the vessel wall.[37] Malapposed ISA struts were defined as struts detached from the vessel wall; ISA detachment distance was defined as the distance between the abluminal face of the strut and the vessel wall. Different levels of ISA were considered in the simulation with increasing maximal strut-wall ISA distances (distance from the abluminal side of malapposed strut to the vessel wall), ranging from 100 up to 500 μm.

Shear rate represents a measure of the local gradient of velocity in a flowing material (measured in inverse seconds). Velocity profiles, plot of shear rate, as well as quantification of the maximal shear and area of blood flow affected by abnormal shear rate were calculated from postprocessing of the CFD data for each case of ISA (Figures 1A and 2).

Computational mesh for the CFD studies was tested for its accuracy by comparing the velocity profiles around the 500-μm malapposed strut–computed meshes at various refinement levels. As a result of the sensitivity test, a 19 604-node mesh provided 0.03% difference in velocity and 2.85% difference in maximum shear rate compared with a refined mesh with 78 009 nodes.

Clinical Optical Coherence Tomographic Study

Vascular healing response in ISA regions was evaluated by sequential optical coherence tomographic (OCT) analysis. Such an approach to assess natural healing of malapposed segments has been described previously by Gutierrez-Chico et al.[23] OCT data from 3 different randomized trials were pooled and specifically reanalyzed to test the effect baseline ISA distance on strut coverage at follow-up. The trials combined were A Randomized Comparison of a Zotarolimus-Eluting Stent With an Everolimus-Eluting Stent for Percutaneous Coronary Intervention (RESOLUTE-all comers) trial (NCT00617084),[38,39] De Novo Pilot Study (NCT00934752),[40] and Direct Implantation of a Rapamycin-Eluting Stent With Bio-Eroding Carrier Technology Using an Integrated Delivery System (DIRECT) study (ACTRN12611001131943).[41] Detailed description of the OCT substudies and method for baseline-follow-up sequential analysis have been described previously.[23,39–41] Briefly, the RESOLUTE-All comers trial (NCT00617084) compared a zotarolimus-eluting stent with hydrophilic-polymer coating (Resolute, Medtronic Cardio Vascular, Santa Rosa, CA) versus an everolimus-eluting stent with fluoropolymer (Xience V, Abbott Vascular, Santa Clara, CA) in a nonselected all-comers population,[38] with angiographic and OCT follow-up scheduled at 13th month in a subgroup of patients.[39] The De Novo Pilot Study (NCT00934752) assessed the performance of a paclitaxel-coated balloon (Moxy, Lutonix Inc, Maple Grove, MN) in combination with a bare metal stent (Multi-link Vision/MiniVision, Abbott Vascular, Santa Clara, CA) for the treatment of de novo coronary lesions, with angiographic and OCT follow-up scheduled at the 6th month.[40] The DIRECT study assessed the efficacy of the Svelte sirolimus-eluting coronary cobalt-chromium stent with fully

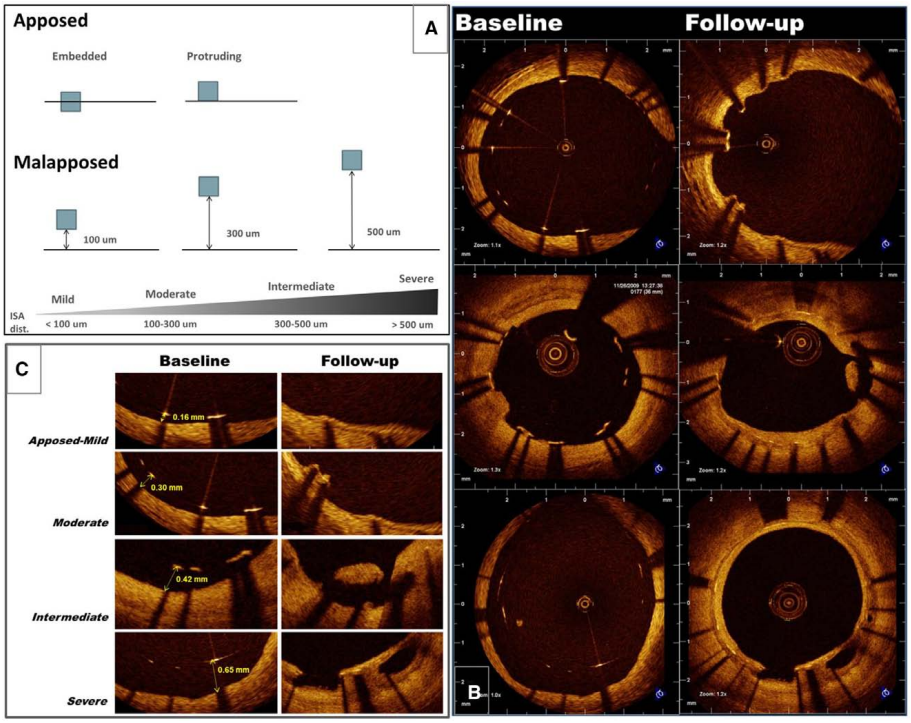

Figure 1. A, Definition and classification of strut apposition. **Upper**, Illustration of embedded and protruding but apposed struts. **Lower**, Illustration of progressive stent strut malapposition with increasing strut to wall incomplete stent apposition (ISA) detachment distance (ISA classification: mild, <100 μm; moderate, 100–300 μm; intermediate, 300–500 μm; and severe, > 500 μm). **B**, Examples of ISA segments immediately post implantation (baseline, **left**) and at follow-up (**right**) in 3 clinical samples. Notice the different vascular healing patterns intended to cover the detached metallic struts with a neointimal layer. **C**, Closed-up from examples of **B** with ISA segments immediately post implantation (baseline, **left**) and at follow-up (**right**) illustrating cases of different ISA severity. The more severe is the strut detachment to the wall, the more likely is ISA to be still persistent at follow-up. Despite rims of neointimal tissue bridging between unapposed struts, remaining gaps can be observed at follow-up between ISA segments and the wall.

bioabsorbable amino acid coating mounted on a fixed-wire, all-in-one integrated delivery system in patients with de novo coronary artery lesions (Svelte Medical Systems, New Providence, NJ). Angiographic and OCT follow-up were scheduled after 6-month follow-up.[41]

OCT pullbacks were obtained with M2, M3, or C7 systems (Lightlab Imaging, Westford, MA), according to the availability at the participating sites, using occlusive or nonocclusive technique where appropriate. All studies were approved by the institutional review board (Thoraxcentre, Rotterdam, The Netherlands). Tables 1 and 2 summarize the patients studied and the corresponding technical specifications.

OCT pullbacks were analyzed offline in a core laboratory (Cardialysis BV, Rotterdam, NL) by independent operators blinded to stent-type allocation and clinical and procedural characteristics of the patients, using a dedicated OCT software (Lightlab Imaging) or Q-IVUS (version 2.1; Medis, Leiden, The Netherlands). Cross-sections were analyzed at 1-mm longitudinal intervals within the stented segment. The assessment of apposition and coverage was performed at baseline (apposition) and at the time of follow-up (apposition and coverage) according to previously described methodology.[23,39–41] ISA distance was measured for each strut as the distance from the luminal leading edge of the strut reflection, at the midpoint of the strut long axis, to the vessel wall. To be consistent with the computational simulation models, detachment distances, defined as the distances between the abluminal leading edge of the strut and the vessel wall, were derived from OCT measures by subtracting the strut (and polymer) thickness for each device, namely: 89 μm for everolimus-eluting stent, 97 μm for zotarolimus-eluting stent, 81 μm for BMS in combination with drug-coated balloon, and 87 μm for sirolimus-eluting coronary cobalt-chromium stent (integrated delivery system).

ISA segments were defined as segments with ≥2 consecutive cross-sections containing ISA struts immediately post implantation (baseline). In summary, ISA segments extended proximally and distally to fiduciary landmarks in the vicinity of the ISA cross-sections. Fiduciary landmarks enabled the matching of the ISA segments with the follow-up studies. Reproducibility of such methodology for matching baseline and follow-up segments has been described previously[23] (Figure 1B).

However, a previous study using this sequential OCT assessment reported that ISA segments with maximal ISA detachment <300 μm were covered completely in 98% of cases and spontaneously resolved in 93% of cases, whereas maximal ISA detachment distances ≥750 μm remained incompletely covered and persistently malapposed at follow-up in 100% of cases.[23]

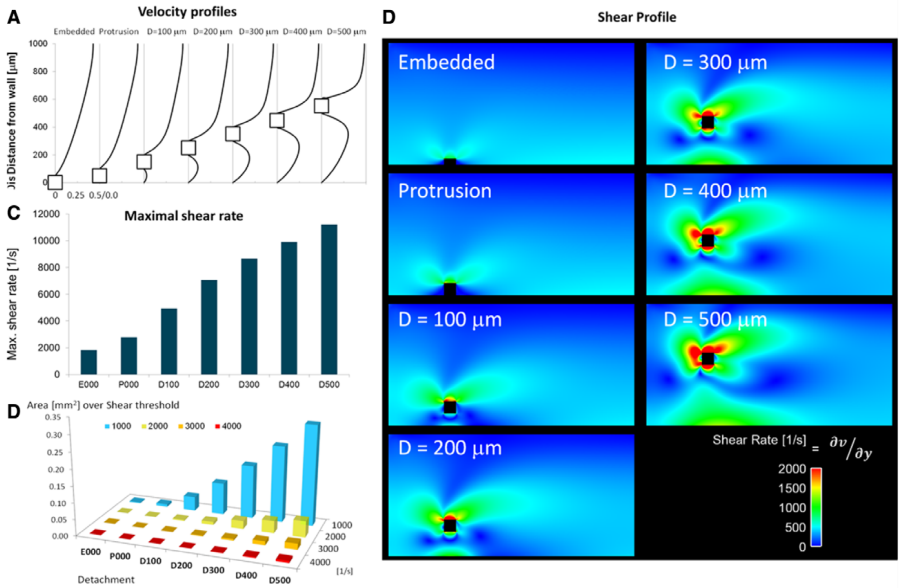

Strut apposition	Case	Shear_max [1/s]	Area > shear threshold [mm2]				
			> 500	> 1000	> 2000	> 3000	> 4000
Apposed	E000	1828	0.76	0.00	0.00	0.00	0.00
	P000	2778	0.79	0.01	0.00	0.00	0.00
ISA	D100	4934	0.90	0.04	0.00	0.00	0.00
	D200	7062	1.04	0.10	0.01	0.00	0.00
	D300	8653	1.12	0.16	0.02	0.00	0.00
	D400	9910	1.20	0.23	0.04	0.01	0.00
	D500	11213	1.11	0.31	0.05	0.02	0.01

Figure 2. Impact of strut-wall malapposition distance on blood flow velocity profiles (**A**) and shear rate patterns (**B**). **A**, Blood flow velocity profiles for the different cases of strut apposition (embedded and protrusion) and strut malapposition considered in the computational simulation with increasing maximal strut-wall incomplete stent apposition (ISA) distances, ranging from *D*=100 µm up to *D*=500 µm. **B**, Corresponding shear profile in blood flow around stent strut for each cases. High shear rate values (red) correspond to blood flow disturbance with highest velocity gradients. **C**, Absolute maximal shear rate [1/s] and (**D**) area of blood (mm²) affected by abnormal shear above the preset threshold computed for each cases. E000, embedded; P000, protrusion; D100–D500, malapposition cases with ISA detachment distance ranging from 100 to 500 µm.

Statistical Analysis

Continuous variables are presented as the mean and SD or median with interquartile ranges. The association between ISA severity (detachment distance in the ISA segments at baseline) and the percentage of uncovered struts at follow-up was explored as the primary objective. Secondary objectives were the association between shear profile in the different malapposition categories at baseline with the presence of persistent malapposed struts at follow-up and thickness of coverage. Malapposition was categorized as mild (≤100 µm), moderate (>100, ≤300 µm), intermediate (>300, ≤500 µm), or severe (>500 µm) based on their maximal ISA detachment distance. The corresponding average values of the target variables were compared between categories by means of the Kruskal–Wallis nonparametric test, and a linear trend among the ranked categories was explored with the Jonckheere–Terpstra test (*P* value testing hypothesis that each ISA category results have the same distribution). Calculations were done with PASW version 17.0 (Chicago, IL).

Results

CFD Simulation

Figure 3 shows the impact of strut-wall malapposition distance on blood flow velocity profiles (Figure 3A) and shear rate patterns (Figure 3B). CFD reconstruction showed that protruding struts and struts mildly malapposed (detachment ≤100 µm) only minimally disturb blood flow as compared with floating struts with larger detachment distance. Maximal shear rate (Figure 3C) and areas affected by abnormal shear rate (Figure 3D) were found to both increase with detachment distance.

Table 1. Patients' and Procedural Baseline Characteristics

	Patients (n=48)
Age, y	59.3 (10.7)
Men	39 (81.3%)
Cardiovascular risk factors	
Hypertension	24 (50.0%)
DM	10 (20.8%)
Insulin-requiring	1 (2.1%)
Hypercholesterolemia	36 (75.0%)
Smoking	18 (37.5%)
Current smoker (<30 d)	9 (18.8%)
Antecedents	
Previous MI	18 (37.5%)
Previous PCI	6 (12.5%)
Previous CABG	2 (4.2%)
Clinical presentation	
Silent ischemia	4 (8.3%)
Stable angina	28 (58.3%)
Unstable angina	12 (25.0%)
Myocardial infarction	4 (8.3%)
Procedural characteristics	
No. of vessels treated	1.31 (0.59)
No. of lesions treated	1.21 (0.41)
No. of stents implanted	1.56 (1.24)
Total stented length, mm	29.6 (28.5)
Small vessel (<2.5 mm diameter)	14 (29.2%)
Overlap	4 (8.3%)
Type of stent	
EES	8 (16.7%)
ZES	6 (12.5%)
SES (IDS)	13 (27.1%)
DCB-BMS	21 (43.8%)

CABG indicates coronary artery by-pass graft; DCB-BMS, combination of drug-coated balloon with bare metal stent; DM, diabetes mellitus; EES, everolimus-eluting stent; MI, myocardial Infarction; PCI, percutaneous coronary intervention; SES (IDS), sirolimus-eluting stent on integrated delivery system; and ZES, zotarolimus-eluting stent.

Shear rate profiles calculated for an embedded or protruding strut remain <3000/s with the high shear values confined to the edge of the strut. Maximal shear rate increases with malapposition distance; rates >10 000/s were reached for a detachment distance >300 μm. Area of blood stream affected by the highest shear values (>1000/s threshold) increased gradually with ISA detachment distance (Figure 2D), revealing a critical difference between opposing or mildly malapposed struts close to the vessel wall as compared with ISA struts floating in the middle of the lumen.

Clinical OCT Study

A total of 48 patients (8 everolimus-eluting stent, 6 zotarolimus-eluting stent, 13 sirolimus-eluting coronary cobalt-chromium stent [integrated delivery system], and 21 drug-coated balloon), 52 lesions, and 72 stents from the 3 trials included in this study were analyzed sequentially at baseline and follow-up (Figure 3). Tables 1 and 2 summarize the baseline clinical and procedural characteristics of the patients and angiographic characteristics of the lesions, respectively. Seventy-eight segments with acute ISA were identified in the baseline OCT images. Matching with the OCT at follow-up was not possible in 6 segments, because of lack of fiduciary landmarks (2 cases), out-of-image artifacts (3 cases), or incomplete follow-up pullbacks not including the ISA segment (1 case). Five ISA segments were excluded from the quantitative analysis because the quality of the acquisition was deemed insufficient to yield reliable results, thus resulting in a total of 67 ISA segments included in the final quantitative analysis.

Table 2. Angiographic Characteristics of the Lesions

	Lesions (n=52)
Target vessel	
LAD	23 (44.2%)
LCX	7 (13.5%)
RCA	22 (42.3%)
TO	3 (5.8%)
Bifurcation	13 (25.0%)
Moderate or severe calcific	8 (15.4%)
QCA characteristics	
Lesion length, mm	12.5 (7.4)
Prestenting	
RVD, mm	2.62 (0.44)
MLD, mm	0.90 (0.42)
Percentage of diameter stenosis	66 (15)
Poststenting in-stent	
RVD, mm	2.76 (0.39)
MLD, mm	2.33 (0.43)
Percentage of diameter stenosis	14 (7)

LAD indicates left anterior descending; LCX, left circumflex; MLD, minimal lumen diameter; QCA, quantitative coronary angiography; RCA, right coronary artery; RVD, reference vessel diameter; and TO, total occlusion.

Table 3 and Figure 4 show the results of the quantitative OCT analysis. Seven ISA segments at baseline had maximal detachment distances ≤100 μm immediately post implantation (mild), 38 ISA segments had maximal detachment distances between 100 and 300 μm (moderate), 17 ISA segments between 300 and 500 μm (intermediate), and in 5 ISA segments the maximal detachment distances were >500 μm (severe), corresponding to the largest disturbances and shear value in the blood stream. The percentage of uncovered struts and persistent ISA struts at follow-up showed significant differences between the categories (P value=0.010 and 0.001, respectively) and a statistically significant linear trend (P value=0.001 and <0.001, respectively), with values increasing from 0% to 18% uncovered struts and from 0% to 13% persistent ISA struts over the different categories of malapposition. As shear rate increases with malapposition distance, so does the rate of uncovered struts and incidence of persistent ISA at follow-up. Correlation between baseline shear rate (lower boundary obtained from the idealized responses in Figure 2) and mean percentage of uncovered struts and rate of persistent ISA at follow-up in each ISA category is shown in Figure 5.

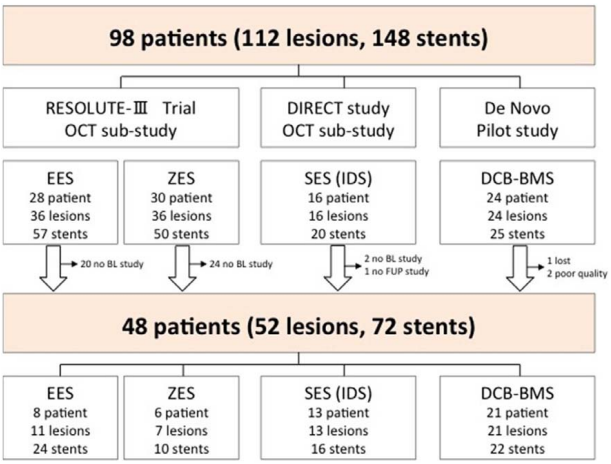

Figure 3. Flow chart summarizing the patients and stents included in the present study, pooled from 3 different trials with optical coherence tomography (OCT). BL indicates baseline study after stent implantation; DCB-BMS, combination of drug-coated balloon with bare metal stent; DIRECT, Direct Implantation of a Rapamycin-Eluting Stent With Bio-Eroding Carrier Technology Using an Integrated Delivery System; EES, everolimus-eluting stent; RESOLUTE, A Randomized Comparison of a Zotarolimus-Eluting Stent With an Everolimus-Eluting Stent for Percutaneous Coronary Intervention; SES (IDS), cobalt-chromium stent with fully bioabsorbable amino acid coating mounted on integrated delivery system; and ZES, zotarolimus-eluting stent.

The association with the thickness of coverage is less clear: either considering the mean thickness of coverage or the maximal thickness of coverage measured in each ISA segment; there seems to be an inverse relation between detachment distance and thickness of coverage along the 3 inferior ISA categories. However, coverage in the category of >500 μm detachment is thicker than in the precedent categories, resulting in a u-shaped distribution and no significant linear association (Table 3; Figures 1C and 4).

Discussion

The main findings of this study are as follows: (1) protrusion and detachment of stent struts from the vessel wall create disturbances in the coronary flow, translated into higher shear rates around the strut boundaries. (2) The magnitude and area affected by higher shear augment gradually with the degree of malapposition. (3) The delay in neointimal healing is related to the degree of ISA severity measured immediately post implantation by OCT, meaning that the more severely a strut is detached, the less likely it is to heal and integrate within the artery wall.

Our analysis indicates that shear rate is affected by the degree of malapposition. The parallel between shear and delayed coverage as a function of the detachment distance might be interpreted in terms of a causative relation. Flow disturbances and high shear rates are present in the coronary artery from the moment of stent implantation, therefore they precede the neointimal healing process and might determine its progress to some extent. Previous work showed that shear stress modulates the neointimal healing after stenting, and the thickness of the neointimal hyperplasia layer covering the struts is inversely related to the local level of shear stress.[25–28] The similarity in dose–response relations suggests that the more detached the strut, the larger its distance from the existing endothelial layer and the higher the shear stress on the strut wall, and subsequently the more hampered the neointimal reaction intended to cover the detached struts.

Shear Stress as a Mechanism to Explain the Delayed Healing of Acute ISA Regions

Several investigators have described previously how protruding or detached struts can alter normal coronary flow and affect drug distribution and recirculation,[35,42,43] and the larger the strut, the more severe its impact on flow,[35] but the intrinsic dependence of shear rate on the detachment distance and

Table 3. Optical Coherence Tomographic Analysis of the Matched ISA Segments

	ISA Categories According to the Maximal Detachment Distance in the Segment at Baseline					
	≤100 μm	>100 μm ≤300 μm	>300 μm ≤500 μm	>500 μm	KW (*P* Value)	JT (*P* Value)
No. of ISA segments	7	38	17	5		
Percentage of uncovered struts	0 (0–0)	6 (0–9)	15 (0–24)	18 (8–25)	0.010	0.001
Percentage of persistent ISA struts	0 (0–0)	1 (0–0)	11 (0–17)	13 (11–19)	0.001	<0.001
Mean thickness coverage, μm	143 (73–198)	132 (68–188)	91 (52–95)	106 (65–157)	0.342	0.101
Maximal thickness coverage, μm	357 (290–445)	243 (163–310)	196 (110–280)	370 (280–390)	0.011	0.372

Descriptive results presented as mean (interquartile range). Differences among categories explored by means of Kruskal–Wallis nonparametric test; lineal trend explored by means of Jockheere–Terpstra test. ISA indicates incomplete stent apposition; JT, Jonckheere–Terpstra; and KW, Kruskal–Wallis.

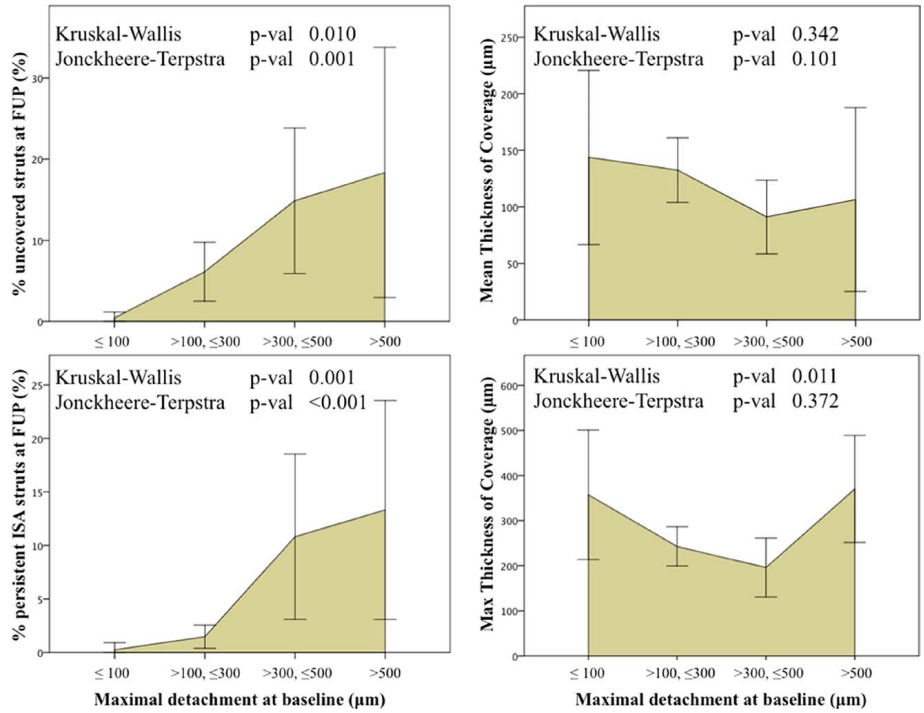

Figure 4. Impact of detachment distance on neointimal coverage in a clinical setting. Mean values of percentage of uncovered struts at follow-up (FUP; primary objective), percentage of persistent malapposed (incomplete stent apposition [ISA]) struts at follow-up, mean and maximal thickness of coverage measured in the ISA segment. Bars, 95% confidence intervals.

its effect on coverage has not been shown previously hitherto. This information is relevant to understand the problem of acute ISA properly, that is, ISA that appears as a consequence of suboptimal stent implantation during the coronary intervention, therefore at the moment when optimization is still possible. The results of our current study are consistent with previous evidences and propose increase in shear rate as a plausible mechanism to explain the incomplete coverage of malapposed struts with ISA. Shear stress has been shown to modulate the neointimal healing after stenting in BMS[25]and DES.[26,27] It has also been advocated to explain the differences in coverage between the luminal and abluminal sides of the struts in bioresorbable scaffolds.[44] The increase in shear rate as a function of the detachment distance might well explain the incomplete coverage of ISA regions and why the risk of incomplete coverage is also a function of the detachment distance (Figures 4 and 5). In a confluent model of healing, with active endothelial restoration starting from the noninjured margins of the stented segment and from the remnant endothelium in peri-strut spaces, the more detached a strut is, the higher the likelihood of delay and suboptimal healing until the confluence with tissue intended to cover is achieved. These concepts are important to understand malapposition as a quantitative phenomenon, rather than as merely qualitative (present or absent), and to define the threshold of ISA detachment that might benefit from optimization during stent implantation.

Shear as a Mechanism to Explain the Thrombogenicity of Acute ISA Regions

The delayed coverage of acute ISA regions, leaving metallic surfaces on the stent exposed to the blood stream, has raised concerns about an eventual higher risk of stent thrombosis, but this suspicion has not been confirmed clinically hitherto. Several studies have suggested an association between late ISA with stent thrombosis in DES,[11,17–19] and this association has been explained as the consequence of a delayed hypersensitivity reaction triggered by the polymer, mediated by eosinophils and resulting in vascular inflammation, weakening of the vessel wall, positive remodeling, late-acquired ISA, endothelial denudation, and finally VLST.[11,16–20]

A recent study reported that incidentally detected ISA at the 8th month after stent implantation in asymptomatic patients was associated with higher risk of VLST and myocardial infarction as compared with well-apposed stents.[24] Although this finding does not properly confirm the clinical

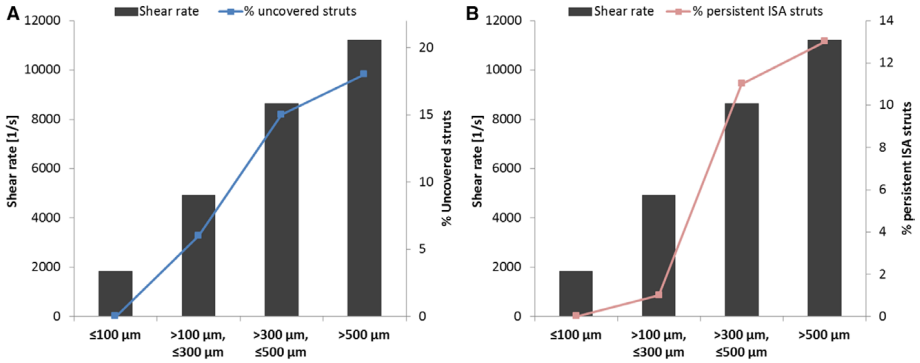

Figure 5. Correlation between baseline shear rate and mean percentage uncovered strut (**A**) and percentage persistent incomplete stent apposition (ISA; **B**) at follow-up in each ISA category. Baseline shear rate (lower boundary for each ISA category computed in Figure 2) compared with mean percentage of uncovered struts and rate of persistent ISA at follow-up. As shear increases with malapposition distance, so does the rate of uncovered struts (linear regression: r=0.99; P=0.006) and incidence of persistent ISA (linear regression: r=0.92; P=0.04) at follow-up.

consequences of acute ISA, it is consistent with the suspicion that ISA entails a higher risk of stent thrombosis because incidentally discovered ISA in asymptomatic patients is unlikely to be the consequence of a hypersensitivity reaction.

The mechanism underlying the link between ISA struts and thrombosis is not fully understood yet. The increase in shear rate at ISA struts surfaces might partially explain its propensity to thrombotic phenomena. In addition to impairing the neointimal coverage of ISA struts, shear is known in rheology to activate platelets.[29–33] High shear rate activates platelets (>1000/s) in a dose-dependent manner through von Willebrand factor binding to glycoprotein Ib and glycoprotein IIb/IIIa receptors.[29–33] Several experiments have shown in vitro the influence of shear on clot formation and high shear rate is actually a prerequisite to reproduce the mechanisms of thrombus formation in both in vitro and in vivo models.[29–32] In a recent study relevant to stent malapposition, Kolandaivelu et al[35] showed an increased amount of clot with underdeployed bare stent versus well deployed bare stent using an in vitro chandler loop system perfused with porcine blood. Therefore, the detachment of a strut from the vessel wall not only leads to higher levels of shear stress on the strut surface, potentially affecting neointimal coverage process, but the higher flow disturbances around its edges also increase the risk of platelet activation and thrombi aggregation. Under the shear rate hypothesis, the thrombogenicity of malapposed struts is a function of the detachment distance as well, which may warrant further exploration in future studies. This flow hypothesis has been only rarely considered in previous studies about ISA and stent thrombosis. Nonetheless, there are no compelling in vivo evidences yet about different thrombosis propensity in ISA regions depending on their detachment distance hitherto. This point must be specifically addressed in the future.

Practical Implications

Recent OCT studies have demonstrated consistently higher risk of delayed (or incomplete) coverage in acute ISA regions as compared with well-apposed struts,[21–23] thus raising concerns about an eventual higher risk of stent thrombosis. In this series, we did not observe cases of late-acquired ISA, which has been suggested to be one of the hallmarks of VLST. In contrary to acute ISA, late-acquired ISA cannot be optimized during the interventional procedure because it usually happens in stents optimally deployed and apposed to the vessel wall, getting subsequently malapposed and thrombosed as a consequence of the inflammatory process. Evidence about the consequences of acute ISA on neointimal healing and clinical outcome is still scarce, and the question about whether it is worth spending time and resources in the optimization of apposition remains an open issue for the interventional cardiologist. Still, correction of ISA documented at the time of a DES deployment can be justified not only on the grounds of preventing risk of delayed coverage but also for ensuring adequate drug delivery to the vessel wall.

Extent of acute ISA has been shown to be the only independent predictor of persistent ISA and delayed coverage at follow-up.[23] If shear is one of the key mechanisms for delayed coverage and higher thrombogenicity associated with malapposition, then the clinical relevance of acute ISA might depend directly on how distant the strut is from the vessel wall. According to this model, the classical question of whether we should optimize acute ISA might be reformulated as to what degree of acute ISA should we optimize. We are still far from a definite answer to this question. In this study, we used OCT series in exploring predicators of the lack of coverage at follow-up with 4 different grades of ISA severity. Data were analyzed to test consistency with the shear stress hypothesis, and sequential OCT quantitative analysis could be performed on 67 ISA stent segments. Results from this shear calculation and sequential OCT analysis using the classification proposed here suggest that the optimization of malapposition when the ISA detachment distance is <300 µm (moderate ISA) and particularly when the ISA distance is <100 µm (mild ISA) might be less critical as ISA in this case will be corrected over

time by the vascular healing reaction, restoring smooth laminar flow with complete strut coverage as evidenced in >98% of cases within a year. Severely malapposed segments with maximal ISA distance >300 μm represent a greater concern as these segments are affecting not only larger areas of blood flow with high shear rate but also have a higher likelihood of delayed healing with ISA struts persistent at follow-up.

Although this strategy has not been evaluated clinically hitherto, future research on this topic would certainly benefit from this approach.

Limitations

This study is only hypothesis generating: shear values have been simulated based on a simple idealized computational model and the correspondence between the computed shear rate and the coverage measured by OCT in a clinical scenario only suggests the differences in the local flow patterns as a plausible mechanism to explain the incomplete coverage of ISA and a possible link to stent thrombogenicity. These findings on the evolution of acute ISA, and its relationship with disturbed rheology, have to be therefore interpreted with caution and results must be replicated in different and larger series. Although these results suggest shear alterations as a mechanism underlying the delayed coverage, this hypothesis still needs to be demonstrated on a large clinical population. Thrombogenicity is a complex biological process involving a mixture of the persistent flow disruption (stagnant flow or high shear rate), platelet activation, and vessel surface injury/inflammation. Also, although shear is known to augment some thrombotic effects (ie, platelet activation), it can also reduce others through increased transport (ie, wash out of thrombin).

OCT has consistently shown good correlation with histology for the assessment of neointimal coverage after stenting in different studies, so it should be considered a valid in vivo proxy for neointimal coverage.[45–49] Nonetheless, its sensitivity and specificity for this aim are <100% and still poorly known.[50] In particular, OCT can hardly be used to discriminate whether healthy endothelium is present at its surface. We have considered the coverage assessed by OCT as a reliable estimate for the neointimal coverage, but this approach entails some degree of inaccuracy.

Conclusions

This study shows that flow disturbances and risk of delayed strut coverage both increase with ISA detachment distance. Risk of persistent malapposed struts in a clinical scenario also depends on their detachment from the vessel wall. These insights are important for understanding malapposition as a quantitative phenomenon and to define threshold of ISA detachment that might benefit from optimization during stent implantation. Additional studies are required to determine the exact impact of ISA severity on patient outcomes.

Disclosures

The study pools optical coherence tomographic data from 3 different clinical trials sponsored by Medtronic (Santa Rosa, CA), Lutonix Inc (Maple Grove, MN), and Svelte Medical Systems (New Providence, NJ), respectively. The core laboratory and clinical research organization responsible for the analysis (Cardialysis BV, Rotterdam, The Netherlands) received grants from the corresponding sponsors to run the trials, but the content of this article is an investigator-driven independent post hoc analysis.

References

1. Kastrati A, Mehilli J, Dirschinger J, Pache J, Ulm K, Schühlen H, Seyfarth M, Schmitt C, Blasini R, Neumann FJ, Schömig A. Restenosis after coronary placement of various stent types. *Am J Cardiol*. 2001;87:34–39.
2. Morice MC, Serruys PW, Sousa JE, Fajadet J, Ban Hayashi E, Perin M, Colombo A, Schuler G, Barragan P, Guagliumi G, Molnàr F, Falotico R; RAVEL Study Group. Randomized Study with the Sirolimus-Coated Bx Velocity Balloon-Expandable Stent in the Treatment of Patients with de Novo Native Coronary Artery Lesions. A randomized comparison of a sirolimus-eluting stent with a standard stent for coronary revascularization. *N Engl J Med*. 2002;346:1773–1780.
3. Moses JW, Leon MB, Popma JJ, Fitzgerald PJ, Holmes DR, O'Shaughnessy C, Caputo RP, Kereiakes DJ, Williams DO, Teirstein PS, Jaeger JL, Kuntz RE; SIRIUS Investigators. Sirolimus-eluting stents versus standard stents in patients with stenosis in a native coronary artery. *N Engl J Med*. 2003;349:1315–1323.
4. Stone GW, Ellis SG, Cox DA, Hermiller J, O'Shaughnessy C, Mann JT, Turco M, Caputo R, Bergin P, Greenberg J, Popma JJ, Russell ME; TAXUS-IV Investigators. A polymer-based, paclitaxel-eluting stent in patients with coronary artery disease. *N Engl J Med*. 2004;350:221–231.
5. Iakovou I, Schmidt T, Bonizzoni E, Ge L, Sangiorgi GM, Stankovic G, Airoldi F, Chieffo A, Montorfano M, Carlino M, Michev I, Corvaja N, Briguori C, Gerckens U, Grube E, Colombo A. Incidence, predictors, and outcome of thrombosis after successful implantation of drug-eluting stents. *JAMA*. 2005;293:2126–2130.
6. Ong AT, McFadden EP, Regar E, de Jaegere PP, van Domburg RT, Serruys PW. Late angiographic stent thrombosis (LAST) events with drug-eluting stents. *J Am Coll Cardiol*. 2005;45:2088–2092.
7. Pfisterer M, Brunner-La Rocca HP, Buser PT, Rickenbacher P, Hunziker P, Mueller C, Jeger R, Bader F, Osswald S, Kaiser C; BASKET-LATE Investigators. Late clinical events after clopidogrel discontinuation may limit the benefit of drug-eluting stents: an observational study of drug-eluting versus bare-metal stents. *J Am Coll Cardiol*. 2006;48:2584–2591.
8. Lagerqvist B, James SK, Stenestrand U, Lindbäck J, Nilsson T, Wallentin L; SCAAR Study Group. Long-term outcomes with drug-eluting stents versus bare-metal stents in Sweden. *N Engl J Med*. 2007;356:1009–1019.
9. Farb A, Heller PF, Shroff S, Cheng L, Kolodgie FD, Carter AJ, Scott DS, Froehlich J, Virmani R. Pathological analysis of local delivery of paclitaxel via a polymer-coated stent. *Circulation*. 2001;104:473–479.
10. Farb A, Burke AP, Kolodgie FD, Virmani R. Pathological mechanisms of fatal late coronary stent thrombosis in humans. *Circulation*. 2003;108:1701–1706.
11. Virmani R, Guagliumi G, Farb A, Musumeci G, Grieco N, Motta T, Mihalcsik L, Tespili M, Valsecchi O, Kolodgie FD. Localized hypersensitivity and late coronary thrombosis secondary to a sirolimus-eluting stent: should we be cautious? *Circulation*. 2004;109:701–705.
12. Joner M, Finn AV, Farb A, Mont EK, Kolodgie FD, Ladich E, Kutys R, Skorija K, Gold HK, Virmani R. Pathology of drug-eluting stents in humans: delayed healing and late thrombotic risk. *J Am Coll Cardiol*. 2006;48:193–202.
13. Finn AV, Joner M, Nakazawa G, Kolodgie F, Newell J, John MC, Gold HK, Virmani R. Pathological correlates of late drug-eluting stent thrombosis: strut coverage as a marker of endothelialization. *Circulation*. 2007;115:2435–2441.
14. Finn AV, Nakazawa G, Joner M, Kolodgie FD, Mont EK, Gold HK, Virmani R. Vascular responses to drug eluting stents: importance of delayed healing. *Arterioscler Thromb Vasc Biol*. 2007;27:1500–1510.
15. van der Giessen WJ, Lincoff AM, Schwartz RS, van Beusekom HM, Serruys PW, Holmes DR Jr, Ellis SG, Topol EJ. Marked inflammatory sequelae to implantation of biodegradable and nonbiodegradable polymers in porcine coronary arteries. *Circulation*. 1996;94:1690–1697.
16. Cook S, Ladich E, Nakazawa G, Eshtehardi P, Neidhart M, Vogel R, Togni M, Wenaweser P, Billinger M, Seiler C, Gay S, Meier B, Pichler WJ, Jüni P, Virmani R, Windecker S. Correlation of intravascular ultrasound findings with histopathological analysis of thrombus aspirates in patients with very late drug-eluting stent thrombosis. *Circulation*. 2009;120:391–399.
17. Guagliumi G, Sirbu V, Musumeci G, Gerber R, Biondi-Zoccai G, Ikejima H, Ladich E, Lortkipanidze N, Matiashvili A, Valsecchi O, Virmani R, Stone GW. Examination of the in vivo mechanisms of late drug-eluting

stent thrombosis: findings from optical coherence tomography and intravascular ultrasound imaging. *JACC Cardiovasc Interv*. 2012;5:12–20.
18. Cook S, Wenaweser P, Togni M, Billinger M, Morger C, Seiler C, Vogel R, Hess O, Meier B, Windecker S. Incomplete stent apposition and very late stent thrombosis after drug-eluting stent implantation. *Circulation*. 2007;115:2426–2434.
19. Hassan AKM, Bergheanu SC, Stijnen T, van der Hoeven BL, Snoep JD, Plevier JWM, Schalij MJ, Wouter Jukema J. Late stent malapposition risk is higher after drug-eluting stent compared with bare-metal stent implantation and associates with late stent thrombosis. *Eur Heart J*. 2010;31:1172–1180.
20. Siqueira DA, Abizaid AA, Costa Jde R, Feres F, Mattos LA, Staico R, Abizaid AA, Tanajura LF, Chaves A, Centemero M, Sousa AG, Sousa JE. Late incomplete apposition after drug-eluting stent implantation: incidence and potential for adverse clinical outcomes. *Eur Heart J*. 2007;28:1304–1309.
21. Ozaki Y, Okumura M, Ismail TF, Naruse H, Hattori K, Kan S, Ishikawa M, Kawai T, Takagi Y, Ishii J, Prati F, Serruys PW. The fate of incomplete stent apposition with drug-eluting stents: an optical coherence tomography-based natural history study. *Eur Heart J*. 2010;31:1470–1476.
22. Gutiérrez-Chico JL, Regar E, Nüesch E, Okamura T, Wykrzykowska J, di Mario C, Windecker S, van Es GA, Gobbens P, Jüni P, Serruys PW. Delayed coverage in malapposed and side-branch struts with respect to well-apposed struts in drug-eluting stents: in vivo assessment with optical coherence tomography. *Circulation*. 2011;124:612–623.
23. Gutiérrez-Chico JL, Wykrzykowska J, Nüesch E, van Geuns RJ, Koch KT, Koolen JJ, di Mario C, Windecker S, van Es GA, Gobbens P, Jüni P, Regar E, Serruys PW. Vascular tissue reaction to acute malapposition in human coronary arteries: sequential assessment with optical coherence tomography. *Circ Cardiovasc Interv*. 2012;5:20–29, S1.
24. Cook S, Eshtehardi P, Kalesan B, Räber L, Wenaweser P, Togni M, Moschovitis A, Vogel R, Seiler C, Eberli FR, Lüscher T, Meier B, Jüni P, Windecker S. Impact of incomplete stent apposition on long-term clinical outcome after drug-eluting stent implantation. *Eur Heart J*. 2012;33:1334–1343.
25. Wentzel JJ, Krams R, Schuurbiers JC, Oomen JA, Kloet J, van Der Giessen WJ, Serruys PW, Slager CJ. Relationship between neointimal thickness and shear stress after Wallstent implantation in human coronary arteries. *Circulation*. 2001;103:1740–1745.
26. Tanabe K, Gijsen FJ, Degertekin M, Ligthart JM, Oortman RM, Serruys PW, Slager CJ. Images in Cardiovascular Medicine. True three-dimensional reconstructed images showing lumen enlargement after sirolimus-eluting stent implantation. *Circulation*. 2002;106:e179–e180.
27. Gijsen FJ, Oortman RM, Wentzel JJ, Schuurbiers JC, Tanabe K, Degertekin M, Ligthart JM, Thury A, de Feyter PJ, Serruys PW, Slager CJ. Usefulness of shear stress pattern in predicting neointima distribution in sirolimus-eluting stents in coronary arteries. *Am J Cardiol*. 2003;92:1325–1328.
28. Thury A, Wentzel JJ, Vinke RV, Gijsen FJ, Schuurbiers JC, Krams R, de Feyter PJ, Serruys PW, Slager CJ. Images in cardiovascular medicine. Focal in-stent restenosis near step-up: roles of low and oscillating shear stress? *Circulation*. 2002;105:e185–e187.
29. Holme PA, Orvim U, Hamers MJ, Solum NO, Brosstad FR, Barstad RM, Sakariassen KS. Shear-induced platelet activation and platelet microparticle formation at blood flow conditions as in arteries with a severe stenosis. *Arterioscler Thromb Vasc Biol*. 1997;17:646–653.
30. Strony J, Beaudoin A, Brands D, Adelman B. Analysis of shear stress and hemodynamic factors in a model of coronary artery stenosis and thrombosis. *Am J Physiol*. 1993;265(5 pt 2):H1787–H1796.
31. Badimon L, Badimon JJ, Turitto VT, Vallabhajosula S, Fuster V. Platelet thrombus formation on collagen type I. A model of deep vessel injury. Influence of blood rheology, von Willebrand factor, and blood coagulation. *Circulation*. 1988;78:1431–1442.
32. Hanson SR, Sakariassen KS. Blood flow and antithrombotic drug effects. *Am Heart J*. 1998;135(5 pt 2 suppl):S132–S145.
33. Moake JL, Turner NA, Stathopoulos NA, Nolasco L, Hellums JD. Shear-induced platelet aggregation can be mediated by vWF released from platelets, as well as by exogenous large or unusually large vWF multimers, requires adenosine diphosphate, and is resistant to aspirin. *Blood*. 1988;71:1366–1374.
34. Duraiswamy N, Schoephoerster RT, Moreno MR, Moore JE. Stented artery flow patterns and their effects on the artery wall. *Annu Rev Fluid Mech*. 2006;39:357–382
35. Kolandaivelu K, Swaminathan R, Gibson WJ, Kolachalama VB, Nguyen-Ehrenreich KL, Giddings VL, Coleman L, Wong GK, Edelman ER. Stent thrombogenicity early in high-risk interventional settings is driven by stent design and deployment and protected by polymer-drug coatings. *Circulation*. 2011;123:1400–1409.
36. Foin N, Torii R, Mortier P, De Beule M, Viceconte N, Chan PH, Davies JE, Xu XY, Krams R, Di Mario C. Kissing balloon or sequential dilation of the side branch and main vessel for provisional stenting of bifurcations: lessons from micro-computed tomography and computational simulations. *JACC Cardiovasc Interv*. 2012;5:47–56.
37. Tanigawa J, Barlis P, Di Mario C. Intravascular optical coherence tomography: optimisation of image acquisition and quantitative assessment of stent strut apposition. *EuroIntervention*. 2007;3:128–136.
38. Serruys PW, Silber S, Garg S, van Geuns RJ, Richardt G, Buszman PE, Kelbaek H, van Boven AJ, Hofma SH, Linke A, Klauss V, Wijns W, Macaya C, Garot P, DiMario C, Manoharan G, Kornowski R, Ischinger T, Bartorelli A, Ronden J, Bressers M, Gobbens P, Negoita M, van Leeuwen F, Windecker S. Comparison of zotarolimus-eluting and everolimus-eluting coronary stents. *N Engl J Med*. 2010;363:136–146.
39. Gutiérrez-Chico JL, van Geuns RJ, Regar E, van der Giessen WJ, Kelbæk H, Saunamäki K, Escaned J, Gonzalo N, di Mario C, Borgia F, Nüesch E, García-García HM, Silber S, Windecker S, Serruys PW. Tissue coverage of a hydrophilic polymer-coated zotarolimus-eluting stent vs. a fluoropolymer-coated everolimus-eluting stent at 13-month follow-up: an optical coherence tomography substudy from the RESOLUTE All Comers trial. *Eur Heart J*. 2011;32:2454–2463.
40. Gutiérrez-Chico JL, van Geuns RJ, Koch KT, Koolen JJ, Duckers H, Regar E, Serruys PW. Paclitaxel-coated balloon in combination with bare metal stent for treatment of de novo coronary lesions: an optical coherence tomography first-in-human randomised trial, balloon first vs. stent first. *EuroIntervention*. 2011;7:711–722.
41. Webster M, Harding S, McClean D, Jaffe W, Ormiston J, Aitken A, Watson T. First-in-human evaluation of a sirolimus-eluting coronary stent on an integrated delivery system: the DIRECT study. *EuroIntervention*. 2013;9:46–53.
42. Chen HY, Hermiller J, Sinha AK, Sturek M, Zhu L, Kassab GS. Effects of stent sizing on endothelial and vessel wall stress: potential mechanisms for in-stent restenosis. *J Appl Physiol (1985)*. 2009;106:1686–1691.
43. Chen HY, Sinha AK, Choy JS, Zheng H, Sturek M, Bigelow B, Bhatt DL, Kassab GS. Mis-sizing of stent promotes intimal hyperplasia: impact of endothelial shear and intramural stress. *Am J Physiol Heart Circ Physiol*. 2011;301:H2254–H2263.
44. Gutiérrez-Chico JL, Gijsen F, Regar E, Wentzel J, de Bruyne B, Thuesen L, Ormiston J, McClean DR, Windecker S, Chevalier B, Dudek D, Whitbourn R, Brugaletta S, Onuma Y, Serruys PW. Differences in neointimal thickness between the adluminal and the abluminal sides of malapposed and side-branch struts in a polylactide bioresorbable scaffold: evidence in vivo about the abluminal healing process. *JACC Cardiovasc Interv*. 2012;5:428–435.
45. Suzuki Y, Ikeno F, Koizumi T, Tio F, Yeung AC, Yock PG, Fitzgerald PJ, Fearon WF. In vivo comparison between optical coherence tomography and intravascular ultrasound for detecting small degrees of in-stent neointima after stent implantation. *JACC Cardiovasc Interv*. 2008;1:168–173.
46. Deuse T, Erben RG, Ikeno F, Behnisch B, Boeger R, Connolly AJ, Reichenspurner H, Bergow C, Pelletier MP, Robbins RC, Schrepfer S. Introducing the first polymer-free leflunomide eluting stent. *Atherosclerosis*. 2008;200:126–134.
47. Prati F, Zimarino M, Stabile E, Pizzicannella G, Fouad T, Rabozzi R, Filippini A, Pizzicannella J, Cera M, De Caterina R. Does optical coherence tomography identify arterial healing after stenting? An in vivo comparison with histology, in a rabbit carotid model. *Heart*. 2008;94:217–221.
48. Murata A, Wallace-Bradley D, Tellez A, Alviar C, Aboodi M, Sheehy A, Coleman L, Perkins L, Nakazawa G, Mintz G, Kaluza GL, Virmani R, Granada JF. Accuracy of optical coherence tomography in the evaluation of neointimal coverage after stent implantation. *JACC Cardiovasc Imaging*. 2010;3:76–84.
49. Templin C, Meyer M, Müller MF, Djonov V, Hlushchuk R, Dimova I, Flueckiger S, Kronen P, Sidler M, Klein K, Nicholls F, Ghadri JR, Weber K, Paunovic D, Corti R, Hoerstrup SP, Lüscher TF, Landmesser U. Coronary optical frequency domain imaging (OFDI) for in vivo evaluation of stent healing: comparison with light and electron microscopy. *Eur Heart J*. 2010;31:1792–1801.
50. Gutiérrez-Chico JL, Alegría-Barrero E, Teijeiro-Mestre R, Chan PH, Tsujioka H, de Silva R, Viceconte N, Lindsay A, Patterson T, Foin N, Akasaka T, di Mario C. Optical coherence tomography: from research to practice. *Eur Heart J Cardiovasc Imaging*. 2012;13:370–384.

Chapter 4

Clinical Application of coronary imaging after a polymeric device implantation

---

4.1 Coronary artery aneurysm after a PLLA scaffold implantation

Development and receding of a coronary artery aneurysm after implantation of a fully bioresorbable scaffold.

Circulation. 2015;131(8):764-7.
[Original research paper, Impact Factor: 15.07]

Nakatani S, Ishibashi Y, Suwannasom P, Grundeken MJ, Høj Christiansen E, Onuma Y, Serruys PW; ABSORB Cohort B Investigators.

Development and Receding of a Coronary Artery Aneurysm After Implantation of a Fully Bioresorbable Scaffold

Shimpei Nakatani, MD; Yuki Ishibashi, MD, PhD; Pannipa Suwannasom, MD; Maik J. Grundeken, MD; Evald Høj Christiansen, MD, PhD; Yoshinobu Onuma, MD, PhD; Patrick W. Serruys, MD, PhD; on behalf of the ABSORB Cohort B Investigators

A 83-year-old man included in the ABSORB cohort B trial underwent successful percutaneous coronary intervention of the middle left anterior descending artery with a 3.0×18-mm bioresorbable scaffold (Absorb, Abbott Vascular, CA) that was postdilated with a 3.0-mm noncompliant balloon at 24 atm (Figure 1A and 1B). The 2-dimensional and 3-dimensional (3D) optical coherence tomography (OCT) confirmed the absence of structural discontinuity after the procedure (Figure 2B and Figure 3A'). At 6 months, the planned angiography showed the absence of restenosis but an ectasia in the scaffolded segment (Figure 1C). Intravascular ultrasound revealed a focal vessel and lumen enlargement (17.93 mm^2 [Δ+20.5%] and 6.99 mm^2 [Δ+9.6%], respectively, in the matched cross-section analysis; Figure 2C), whereas 3D OCT suggested a deformation of the scaffold in the 2-mm segment of the ectasia (Figure 3B'). At 18 months, the planned multislice computed tomography showed lumen dilatation in the scaffolded segment (Figure 1D). At 2 years, on angiography, the ectatic lesion in the scaffold became aneurysmal (50% increase compared with the adjacent reference vessel; Figure 1E). Intravascular imaging revealed the increase in the vessel area and lumen area (20.90 mm^2 [Δ+40.5%] on intravascular ultrasound and 10.91 mm^2 [Δ+35.7%] on OCT, respectively, from baseline; Figure 1E and 1F), whereas 3D OCT showed a focal cleavage of the scaffold rings and a bulge of the vessel in the segment free from the scaffold struts (Figure 3C and C'). Five years after implantation, angiography revealed that the aneurysm was still present but had become smaller compared with the previous time points (Figure 1F). Intravascular ultrasound and OCT demonstrated the diminished vessel and lumen area (17.11 mm^2 [Δ−18.1%] and 8.78 mm^2 [Δ−19.5%], respectively, from 2 years; Figure 2G and 2H), making the scaffold indiscernible on OCT.

In general, aneurysm after drug-eluting device implantation is attributed to residual dissection and deep arterial wall injury and to inflammatory and allergic reactions to the drug, polymer, or device such as metal. In rare cases, a fully bioresorbable poly(L-lactide) acid prosthesis can cause inflammation.[1] Further insight can be obtained from the 3D reconstructions of the OCT signal (Figure 3A', 3B', and 3C'), in which the pattern of the struts can qualitatively outline the time history of the aneurysmal expansion. From implantation to 6 months, the wall distended and displaced the strut pattern without an apparent change in intracrown angulations, indicating a wall distention that occurred while the strut material was still continuous and minimally degraded. Further expansion from 6 to 24 months occurred in part after substantial polymer degradation had already occurred, as evidenced by the widening of intracrown angulations or complete separation of strut segments, indicating that strut migration follows wall migration entirely and continuity of struts has diminished to subpattern levels. Cross-sectional and longitudinal reconstructions of these segments appear to show that, although diameter is substantially distended, the arterial wall thickness over and under the struts is uniform in nature, an appearance inconsistent with severe inflammatory reactions to polymer.

Disclosures

Dr Serruys is a member of Advisory Board of Abbott Vascular.

References

1. Katsuragi YT, Gomi A, Sunaga A, Miyazaki K, Kamochi H, Arai F, Fukushima N, Sugawara Y. Intracerebral foreign body granuloma caused by a resorbable plate with passive intraosseous translocation after cranioplasty. *J Neurosurg Pediatr*. 2013;12:622–625. doi: 10.3171/2013.9.PEDS13187.

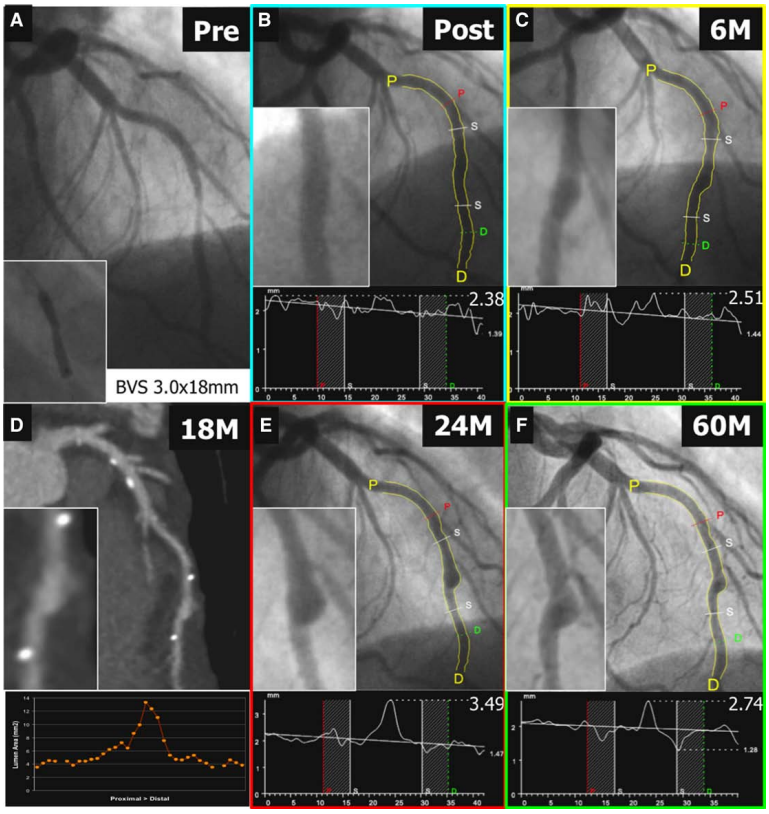

Figure 1. Coronary angiography of the left anterior descending artery before (**A**) and after (**B**) intervention at baseline. At 6 months, the planned angiography showed an ectasia in the scaffolded segment (**C**). The planned multislice computed tomography showed lumen dilatation in the scaffolded segment at 18 months (**D**). Repeat angiography demonstrated that the ectatic lesion in the scaffold became aneurysmal at 2 years (**E**) and diminished at 5 years (**F**).

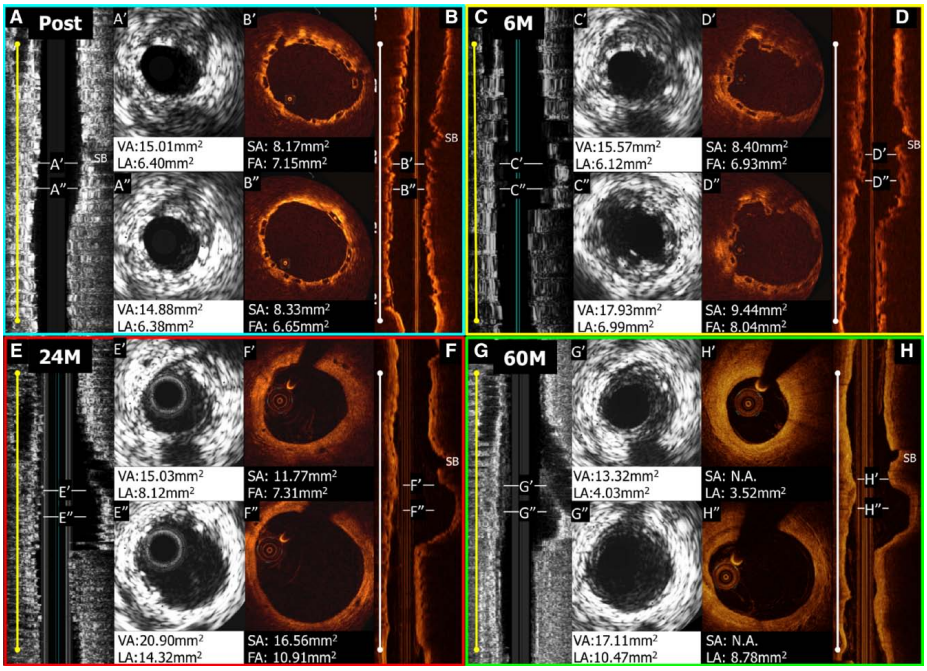

Figure 2. Intravascular ultrasound (IVUS) and optical coherence tomography (OCT) images from matched sites (aneurysm site and near proximal site) after the procedure (**A** and **B**), at 6 months (**C** and **D**), at 2 years (**E** and **F**), and at 5 years (**G** and **H**) after scaffold implantation. The white lines in the longitudinal view indicate the sites corresponding to the cross sections of **A'** to **H"**. Postprocedural OCT showed some malapposed struts but confirmed the absence of structural discontinuity. At 6 months, IVUS revealed a focal vessel and lumen enlargement (**C"**). IVUS and OCT revealed the increase in the vessel and the lumen area at 2 years (**E"** and **F"**) and the subsequent decrease in the aneurysm, with the scaffold becoming indiscernible on OCT at 5 years (**G"** and **H"**). FA indicates flow area; LA, lumen area; SA, scaffold area; and VA, vessel area.

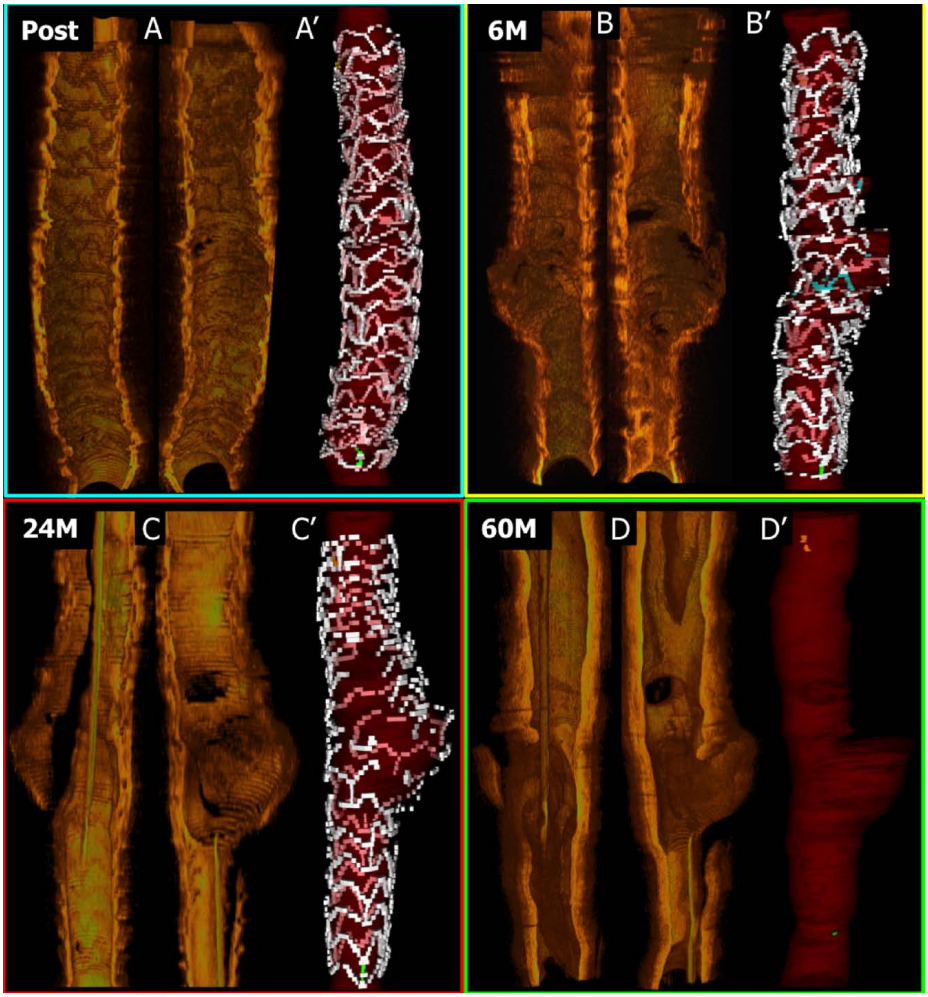

Figure 3. Three-dimensional (3D) reconstruction of cross-sectional images corresponding to the scaffold segment. **A'** through **D'** are reconstructed for emphasizing the scaffold structure. 3D optical coherence tomography (OCT) confirmed the absence of structural discontinuity after the procedure. At 6 months, 3D OCT suggested a deformation of the scaffold in the 2-mm segment corresponding to the ectasia (**B** and **B'**). At 2 years, 3D OCT showed a focal cleavage of the scaffold rings and a bulge of the vessel in the segment free from the scaffold struts (**C** and **C'**). At 5 years, the aneurysm started to reduce, with the scaffold becoming indiscernible on OCT (**D** and **D'**). In **A'** to **D'**, the yellow and green dots indicate the proximal and distal radiopaque makers. The blue struts indicate malapposed struts.

4.2 Disruption and late discontinuity after a PLLA scaffold implantation

Incidence and imaging outcomes of acute scaffold disruption and late structural discontinuity after implantation of the Absorb everolimus-eluting fully bioresorbable vascular scaffold: optical coherence tomography assessment in the ABSORB Cohort B trial.

JACC Cardiovasc Intv. 2014;7:1400-11.
[Original research paper, Impact Factor : 7.35]

Onuma Y, Serruys PW, Muramatsu T, Nakatani S, van Geuns RJ, de Bruyne B, Dudek D, Christiansen E, Smits PC, Chevalier B, McClean D, Koolen J, Windecker S, Whitbourn R, Meredith I, Garcia-Garcia HM, Veldhof S, Rapoza R, Ormiston JA.

.

Incidence and Imaging Outcomes of Acute Scaffold Disruption and Late Structural Discontinuity After Implantation of the Absorb Everolimus-Eluting Fully Bioresorbable Vascular Scaffold

Optical Coherence Tomography Assessment in the ABSORB Cohort B Trial (A Clinical Evaluation of the Bioabsorbable Everolimus Eluting Coronary Stent System in the Treatment of Patients With De Novo Native Coronary Artery Lesions)

Yoshinobu Onuma, MD,* Patrick W. Serruys, MD, PhD,* Takashi Muramatsu, MD, PhD,* Shimpei Nakatani, MD,* Robert-Jan van Geuns, MD, PhD,* Bernard de Bruyne, MD, PhD,† Dariusz Dudek, MD,‡ Evald Christiansen, MD,§ Pieter C. Smits, MD, PhD,‖ Bernard Chevalier, MD,¶ Dougal McClean, MD,# Jacques Koolen, MD, PhD,** Stephan Windecker, MD,†† Robert Whitbourn, MD,‡‡ Ian Meredith, MD, PhD,§§ Hector M. Garcia-Garcia, MD, PhD,‖‖ Susan Veldhof, RN,¶¶ Richard Rapoza, PhD,## John A. Ormiston, MBChB, PhD***

ABSTRACT

OBJECTIVES This study sought to describe the frequency and clinical impact of acute scaffold disruption and late strut discontinuity of the second-generation Absorb bioresorbable polymeric vascular scaffolds (Absorb BVS, Abbott Vascular, Santa Clara, California) in the ABSORB (A Clinical Evaluation of the Bioabsorbable Everolimus Eluting Coronary Stent System in the Treatment of Patients With De Novo Native Coronary Artery Lesions) cohort B study by optical coherence tomography (OCT) post-procedure and at 6, 12, 24, and 36 months.

BACKGROUND Fully bioresorbable scaffolds are a novel approach to treatment for coronary narrowing that provides transient vessel support with drug delivery capability without the long-term limitations of metallic drug-eluting stents. However, a potential drawback of the bioresorbable scaffold is the potential for disruption of the strut network when over-expanded. Conversely, the structural discontinuity of the polymeric struts at a late stage is a biologically programmed fate of the scaffold during the course of bioresorption.

METHODS The ABSORB cohort B trial is a multicenter single-arm trial assessing the safety and performance of the Absorb BVS in the treatment of 101 patients with de novo native coronary artery lesions. The current analysis included 51 patients with 143 OCT pullbacks who underwent OCT at baseline and follow-up. The presence of acute disruption or late discontinuities was diagnosed by the presence on OCT of stacked, overhung struts or isolated intraluminal struts disconnected from the expected circularity of the device.

RESULTS Of 51 patients with OCT imaging post-procedure, acute scaffold disruption was observed in 2 patients (3.9%), which could be related to overexpansion of the scaffold at the time of implantation. One patient had a target lesion revascularization that was presumably related to the disruption. Of 49 patients without acute disruption, late discontinuities were observed in 21 patients. There were no major adverse cardiac events associated with this finding except for 1 patient who had a non-ischemia-driven target lesion revascularization.

CONCLUSIONS Acute scaffold disruption is a rare iatrogenic phenomenon that has been anecdotally associated with anginal symptoms, whereas late strut discontinuity is observed in approximately 40% of patients and could be viewed as a serendipitous OCT finding of a normal bioresorption process without clinical implications. (ABSORB Clinical Investigation, Cohort B [ABSORB B]; NCT00856856) (J Am Coll Cardiol Intv 2014;7:1400–11) © 2014 by the American College of Cardiology Foundation.

Fully bioresorbable scaffolds are a novel approach for treatment of coronary narrowing that provides transient vessel support with drug delivery capability without the long-term limitations of metallic drug-eluting stents, such as permanent caging with either outward bulging (evagination) of the luminal wall outside of the "cage," or intracage neoatherosclerosis (1,2). By freeing the coronary artery from metallic caging, the vessel thereby recovers its pulsatility, and vasomotion becomes again responsive without any constraint to the biochemical milieu, the endothelial shear stress, and the physiological cyclic strain (3,4). The technology has the potential to overcome many of the safety concerns associated with metallic drug-eluting stents and could possibly even provide further clinical benefit (5).

In the ABSORB (A Clinical Evaluation of the Bioabsorbable Everolimus Eluting Coronary Stent System in the Treatment of Patients With De Novo Native Coronary Artery Lesions) cohort A trial, the first generation of the Absorb everolimus-eluting fully bioresorbable polymeric vascular scaffolds (Absorb BVS, Abbott Vascular, Santa Clara, California) showed a low event rate with a late lumen enlargement from 6 months to 2 years. At 5 years, the absence of metallic material allowed the noninvasive anatomical as well as functional assessment by multislice computed tomography of arteries previously treated with a bioresorbable scaffold (4,6,7). In the subsequent ABSORB cohort B trial, the second generation of the Absorb BVS showed a low late loss of 0.19 mm without any reduction of the scaffold area at 6 months by intravascular ultrasound (IVUS) and optical coherence tomography (OCT) (8,9). At 12-month follow-up, the angiographic late loss was 0.27 ± 0.32 mm, with an unchanged scaffold area. In addition, vasomotion induced by ergonovine and acetylcholine followed by intracoronary nitrate became detectable again, suggesting that the scaffolds mechanical integrity had subsided. At 24-month follow-up, the angiographic late loss remained stable (0.27 ± 0.20 mm) with a late enlargement of the scaffold that compensated for the neointimal growth as detected by OCT (10–12).

However, a potential drawback of this new technology is the risk for disruption of the strut network when it is overexpanded. Historically, the phenomenon was documented for the first time in an anecdotal case from the ABSORB cohort A trial. A 3.0-mm scaffold was overexpanded with a 3.5-mm balloon, resulting in scaffold disruption as documented by OCT (7). Due to the recurrence of anginal symptoms at 40 days, this patient underwent repeat revascularization despite an angiographically nonsignificant stenosis by quantitative coronary angiography (QCA) (diameter stenosis of 42%) (13). It is important that this acute mechanical disruption, is distinguished from the structural discontinuity of the polymeric struts at a later stage, a biologically programmed process during the course of bioresorption (13–15).

ABBREVIATIONS AND ACRONYMS

BVS = bioresorbable polymeric vascular scaffolds

Dmax = maximum diameter

IVUS = intravascular ultrasound

OCT = optical coherence tomography

QCA = quantitative coronary angiography

TLR = target lesion revascularization

From the *Department of Interventional Cardiology, ThoraxCenter, Erasmus Medical Center, Rotterdam, the Netherlands; †Department of Interventional Cardiology, Cardiovascular Center, Aalst, Belgium; ‡Department of Cardiology and Cardiovascular Interventions, Jagiellonian University, Krakow, Poland; §Department of Cardiology, Skejby Sygehus University Hospital, Aarhus, Denmark; ‖Department of Interventional Cardiology, Maasstad Hospital, Rotterdam, the Netherlands; ¶Institut Cardiovasculaire Paris Sud, Institut Jacques Cartier, Massy, France; #Department of Interventional Cardiology, Christchurch Hospital, Christchurch, New Zealand; **Department of Interventional Cardiology, Catharina Hospital, Eindhoven, the Netherlands; ††Department of Interventional Cardiology, Bern University Hospital, Bern, Switzerland; ‡‡Cardiac Investigation Unit, St. Vincents Hospital, Fitzroy, Australia; §§Department of Medicine, Cardiology, Monash Cardiovascular Research Centre, Melbourne, Australia; ‖‖Department of Interventional Cardiology, Cardialysis, Rotterdam, the Netherlands; ¶¶Department of Clinical Research, Abbott Vascular, Diegem, Belgium; ##Research and Development, Abbott Vascular, Santa Clara, California; and the ***Department of Interventional Cardiology, Auckland City Hospital, Auckland, New Zealand. This study was sponsored by Abbott Vascular. Dr. van Geuns has consulted for Abbott Vascular. Dr. Dudek has received consulting and lecture fees from Abbott, Adamed, Adyton Medical Polska, Abiomed Europe, AstraZeneca, Biotronik, Balton, Bayer, BBraun, BioMatrix, Boston Scientific, Boehringer Ingleheim, Bracco, Bristol-Myers Squibb, Comesa Polska, Cordis, Cook, Covidien Polska Sp. z o. o., DRG MedTek, Eli Lilly, EuroCor, Hammermed, GE Healthcare, GlaxoSmithKline, Inspire-MD, Iroko Cardio International, Medianet Sp. z o. o., Medtronic, Medicines Company, Meril Life Sciences, MSD, Orbus-Neich, Pfizer Inc., Possis, ProCardia Medical, Promed, REVA Medical, Sanofi-Aventis, Siemens, Solvay, Stentys, St. Jude Medical, Terumo, Tyco, and Volcano. Dr. Smits has received speaking and travel fees from Abbott Vascular; and research grants from Abbott Vascular, St. Jude Medical, and Terumo. Dr. Chevalier has consulted for Abbott Vascular. Dr. Whitbourn has been awarded institutional grants from Abbott Vascular. Ms. Veldhof and Dr. Rapoza are full-time employees of Abbott Vascular. Dr. Ormiston has served on the advisory boards of Abbott Vascular and Boston Scientific; and has received honoraria from Abbott Vascular and Boston Scientific. All other authors have reported that they have no relationships relevant to the contents of this paper to disclose. Drs. Ormiston and Serruys are coprincipal and principal investigators. The other investigators are listed as coauthors according to the recruitment of their respective centers.

Manuscript received January 21, 2014; revised manuscript received May 20, 2014, accepted June 2, 2014.

The purpose of the present report therefore is to describe the frequency and clinical impact of acute scaffold disruption and late strut discontinuity of the second-generation Absorb BVS in the ABSORB cohort B study. The frequency and impact are documented in a serial or nonserial manner by OCT post-procedure and at 6, 12, 24, and 36 months.

METHODS

STUDY POPULATION. The ABSORB cohort B trial is a multicenter single-arm trial assessing the safety and performance of the second-generation Absorb BVS in the treatment of 101 patients with a maximum of 2 de novo native coronary artery lesions. The inclusion and exclusion criteria have been described previously (8,12). The first 45 patients (B1) had an invasive imaging follow-up at 6 and 24 months, whereas the latter 56 patients (B2) had an imaging follow-up at 12 months and at 36 months.

The current analysis included 51 patients who underwent OCT at baseline as an optional investigation. The details of the follow-up are presented in Online Figure 1. In total, the analysis included 143 OCT pullbacks performed at baseline and follow-up. The details of the study device and study procedure are described in the Online Appendix.

OPTICAL COHERENCE TOMOGRAPHY. As an optional investigation, intravascular OCT imaging using either time-domain OCT (M3 system, LightLab Imaging, Westford, Massachusetts) or frequency-domain OCT (C7XR system, LightLab Imaging) was performed at baseline and at follow-up (15-19). The OCT measurements were performed with proprietary software for offline analysis (LightLab Imaging). To search for the presence of scaffold disruption, the analysis of continuous cross sections was performed in all frames within the treated segment. The main quantitative measurements (strut core area, strut area, lumen area, scaffold area, incomplete scaffold apposition area, and neointimal area) required different analysis rules than metallic stents (8,9,12,20). The thickness of the neointimal coverage was measured for every strut between the abluminal side of the strut core and the lumen. Because the strut thickness is approximately 150 μm, the strut was considered as covered whenever the thickness of the coverage was above this threshold value (8,12).

DEFINITION OF ACUTE SCAFFOLD DISRUPTION OR LATE DISCONTINUITY ON OCT. Ex vivo experiments were performed to identify OCT findings of disrupted struts. In a silicon phantom with a diameter of 3.5 mm, a 3.0-mm Absorb BVS (maximal labeled diameter expansion of 3.5 mm) was deployed and expanded with a 4.0-mm compliant balloon (21). After disrupting the scaffold, OCT pullback was performed and analyzed (**Figure 1**). Acute (periprocedural) structural scaffold disruption or late strut discontinuities were diagnosed by at least 1 of the following: 1) if 2 struts overhung each other in the same angular sector of the lumen perimeter, without close contact (overhung strut) or with contact (stacked strut) in at least 1 cross section; or 2) if there was isolated (malapposed) struts that could not be integrated in the expected circularity of the device in at least 1 cross section. "Isolated strut" was defined as a strut located at a distance from the vessel wall (>1/3 of span between the center of gravity and the luminal border) (8,12,21).

If acute scaffold disruption was persistently observed at follow-up, the case was classified as persistent scaffold disruption. Late discontinuity at follow-up was diagnosed when no initial procedural scaffold disruption could be documented post-procedure. In the case of iterative follow-up, late discontinuities could be classified as resolved or persistent (**Table 1**). Using the new criteria, the OCT image was reanalyzed for the presence of acute disruption or late discontinuities. The details of 3-dimensional OCT analysis, IVUS grayscale analysis, and definition of clinical events are described in the Online Appendix.

STATISTICAL ANALYSIS. Continuous variables are presented as mean ± SD, whereas categorical variables are expressed as percent. Categorical variables were compared using Pearson chi-square test or Fisher exact test and continuous variables were compared using *F* test for analysis of variance. As no formal hypothesis testing was planned for assessing the success of the study, no statistical adjustment was applied. The p values presented are exploratory analyses only and therefore should be interpreted cautiously. Statistical analysis was performed with SPSS (version 20 for Macintosh, SPSS Inc., Chicago, Illinois).

RESULTS

Baseline characteristics are presented in Online Table 1. All patients received 1 Absorb scaffold except for 1 patient who received 2. Post-dilation was performed in 57% of lesions.

ACUTE PROCEDURAL SCAFFOLD DISRUPTION AT BASELINE. Of 51 patients with OCT imaging post-procedure (52 scaffolded lesions), acute scaffold disruption was observed in 2 patients (3.9%). **Table 2**

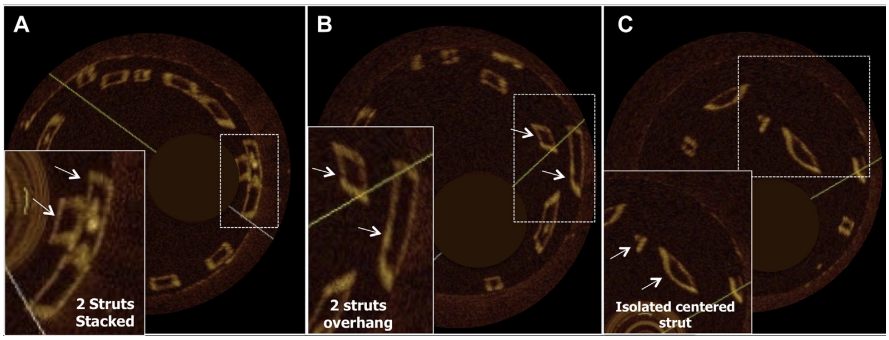

FIGURE 1 **OCT Criteria to Diagnose Acute Scaffold Disruption (Phantom Assessment)**

In a silicon phantom, a 3.0-mm Absorb BVS scaffold was disrupted through inflation of a semicompliant balloon up to 4.3 mm in diameter. Optical coherence tomography (OCT) showed the following: more than 2 struts in the same angular sector with close contact (2 struts stacked) **(A)** or without any contact (overhung struts) **(B)**. The other presentation of disrupted scaffold is the detection of an isolated malapposed strut located at the center of the lumen with loss of circularity of the scaffold **(C)**. The distance from the abluminal side of the strut to the luminal border should be more than one-third of the distance from the center of gravity to the lumen border in the corresponding angular sector.

tabulates the details of the procedures and imaging by OCT, IVUS, and QCA. Scaffold disruption at baseline was detectable on IVUS in 1 of these 2 cases.

Notably, 1 patient had a target lesion revascularization (TLR) presumably associated with the acute disruption and its worsening at 1 month. In this case (**Figure 2**), an Absorb BVS 3.0 mm × 18 mm scaffold was implanted in an obtuse marginal branch with a reference diameter of 3.26 mm (13). After post-dilation with a 3.25-mm noncompliant balloon at 24 atm, malapposition remained at the proximal part of the scaffold on OCT. To correct the malapposition, an additional post-dilation was performed with a compliant 3.5-mm balloon at 16 atm (expected diameter, approximately 4.0 mm). The repeat OCT and IVUS demonstrated acute scaffold disruption in the scaffolded segment. At 1 month, the patient experienced 5 episodes of recurrent angina at rest. Despite the fact that the exercise tolerance test was negative, the patient underwent recatheterization because of

TABLE 1 **Classification of OCT Findings**

		Time of OCT Observation	
	Etiology	**Post-Procedure**	**Late**
Scaffold disruption	Procedure-related		Late persistent*/Late procedural†
		• Stacked struts • Overhung struts • Isolated intraluminal strut(s)	• Stacked struts with/without coverage, with/without malapposition • Overhung struts with/without coverage, with/without malapposition • Isolated malapposed struts with‡/without coverage
Scaffold discontinuities	Resorption-related	NA	Late acquired* • Stacked/overhung/isolated or intraluminal strut(s) with or without coverage or malapposition

Artifacts such as nonuniform rotational deformation and noncoaxial positioning of the catheter should be excluded with caution (21). *Late persistent or late acquired can be only diagnosed when serial OCT is available (baseline/follow-up). If serial imaging cannot determine the etiology, the absence of a circular strut configuration at a late imaging time point may support a procedural disruption etiology, whereas the presence of a circular strut configuration may support the etiology of a resorption-related discontinuity. †Late procedural is related to the diagnostic procedure at follow-up, which either aggravates or creates the disruption. ‡Isolated malapposed struts can be detected as neointimal bridge where the struts are thickly covered with homogenous tissue.

NA = not applicable; OCT = optical coherence tomography.

TABLE 2 Details of Patients With Acute Disruption

	Case #1	Case #2
Sex	Male	Male
Age, yrs	78	83
Pre-procedural QCA		
Minimal lumen diameter, mm	1.61	0.87
Reference vessel diameter, mm	3.26	2.24
Angulation, °	35.54	2.97
Curvature, cm^{-1}	0.04	0.005
Procedural details		
Size of implanted BVS, mm	3.0 × 18	3.0 × 18
Post-dilation	Performed	Performed
Size of post-dilation balloon, mm	3.5 × 9 mm (compliant)	3.0 × 10 (noncompliant)
Maximal pressure at post-dilation, atm	16	24
Expected diameter of balloon at maximal pressure according to the chart,* mm	>3.96	>3.22
Maximal balloon diameter by QCA, mm	3.87	2.98
OCT findings at baselines		
Total CS with strut disruption	6	5
CS with isolated struts	1	1
CS with overhung struts	5	4
CS with stacked struts	0	0
Minimal lumen area, mm	5.82	3.59
Minimal scaffold area, mm^2	7.83	5.23
IVUS at baselines		
Visibility of strut disruption on IVUS	Yes	No
Minimal lumen area, mm^2	6.04	4.68
Minimal scaffold area, mm^2	6.04	4.68
QCA at baselines		
Percent of diameter stenosis, %	20	1.3
Minimal lumen diameter, mm	2.7	1.94
Timing of 1st follow-up	1 months	6 months
OCT findings at 1st follow-up		
Total CS with strut disruptions	22	8
CS with isolated struts	2	4
CS with overhang struts	20	6
CS with stacked struts	1	0
Minimal lumen area, mm^2	NA†	4.82
Minimal scaffold area, mm^2	NA†	6.01
IVUS at 1st follow-up		
Visibility of strut disruption on IVUS	Yes	No
Minimal lumen area, mm^2	5.23	4.21
Minimal scaffold area, mm^2	5.23	4.21
QCA at 1st follow-up		
Percent of diameter stenosis, %	23	23
Minimal lumen diameter, mm	2.47	1.84
Late loss, mm	0.23	0.1
OCT findings at 2 yrs		
Total CS with strut disruptions	0	25
CS with isolated struts	0	14
CS with overhang struts	0	12
CS with stacked struts	0	0
Minimal lumen area, mm^2	NA‡	5.15
Minimal scaffold area, mm^2	NA‡	7.46
Findings in 3-dimensional reconstruction	NA‡	Tissue arch
IVUS at 2 yrs		
Visibility of strut disruption on IVUS	No	Yes
Minimal lumen area, mm^2	NA	5.87
Minimal scaffold area, mm^2	NA	6.15
QCA at 2 yrs		
Percent of diameter stenosis, %	14.5	25.5
Minimal lumen diameter, mm^2	2.74	1.8
Late loss, mm	-0.4	0.11
Clinical events up to 2 yrs	Non-ischemia-driven target lesion revascularization	None

Values are n unless otherwise indicated. *The balloon diameter at maximal pressure is in a chart provided by the balloon manufacturer. †The quantitative assessment was not performed because in many cross sections, the complete luminal border was not visualized. ‡The quantitative assessment was not performed because the segment was covered by a metallic stent after non-ischemia-driven revascularization.

CS = cross section(s); IVUS = intravascular ultrasound; NA = not available; QCA = quantitative coronary angiography.

Continued in the next column

persisting symptoms. The angiography revealed a patent scaffold segment with a TIMI (Thrombolysis In Myocardial Infarction) flow grade 3; however, OCT, compared with baseline images, showed a deterioration of scaffold disruption. There was no tissue observed around the struts. A metallic Xience V stent (Abbott Vascular) was placed inside the Absorb scaffold, which eliminated the symptoms. After this nonischemic TLR, there was a rise in troponin (0.09 μl/g with an upper limit of normal of 0.03 μl/g), which would be adjudicated as a non-Q-wave myocardial infarction according to the Academic Research Consortium definition.

In the second case, a 3.0-mm scaffold was implanted in a small vessel with a reference vessel diameter

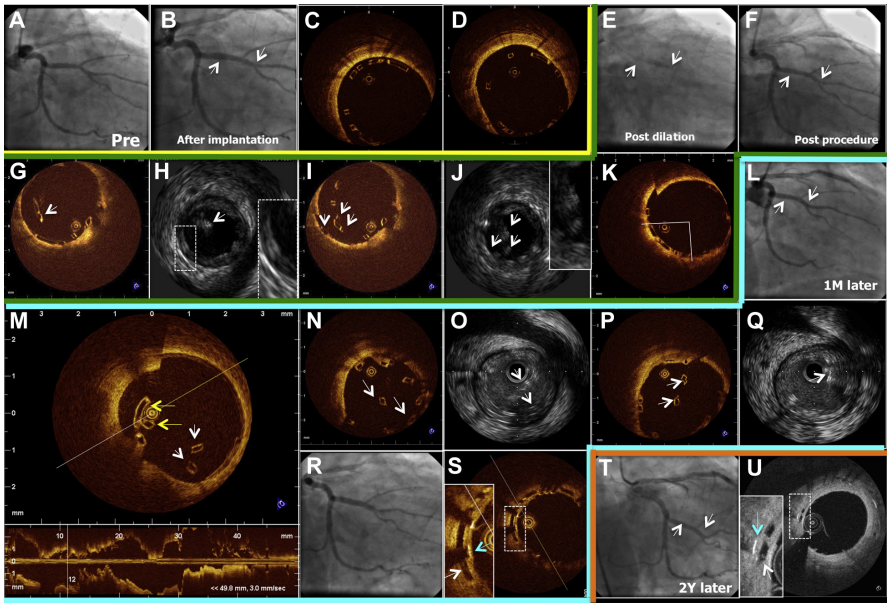

FIGURE 2 A Case of Acute Disruption

Each series of framed illustrations (**yellow, green, blue, and orange**) represents the observation at different time points (before post-dilation, after post-dilation, at 1 month [M] and at 2 years [Y]). An Absorb BVS 3.0 mm × 18 mm scaffold was implanted in an obtuse marginal branch **(A)** (pre-procedural angiography) with a reference diameter of 3.26 mm. After the first post-dilation by a 3.25-mm noncompliant balloon at 24 atm **(B),** malapposition remained at the proximal part of the scaffold on optical coherence tomography (OCT) (**C**, **D**). To correct the malapposition, an additional post-dilation was performed with a compliant 3.5-mm balloon at 16 atm (expected diameter, approximately 4.0 mm) **(E)**. The angiographic result was successful **(F)** but the post-procedural OCT (**G** and **I**) and intravascular ultrasound (IVUS) demonstrated acute strut disruption (**H** and **J**) in the scaffolded segment. Presence of a long strut extending greater than 90 degree suggests overexpansion of scaffold **(K)**. On both OCT and IVUS, isolated intraluminal struts (**white arrow**: OCT in **G** and IVUS in **H**) and overhung struts (**white arrow**: OCT in **I** and IVUS in **J**) were observed. At 1 month, the patient had 5 episodes of recurrent angina at rest. The angiography **(L)** revealed a patent scaffold segment with a TIMI (Thrombolysis In Myocardial Infarction) flow grade 3; however, OCT **(M, N, P)** showed a deterioration of strut discontinuity (**white arrows**: isolated intraluminal or overhung struts). In the corresponding IVUS frames (**O** and **Q**), the disrupted struts were also visible. A metallic Xience V stent was placed inside the Absorb BVS scaffold **(R)**. Post-target lesion revascularization OCT **(S)** showed the metallic struts, with shadows behind **(blue arrows),** are located inside of a polymeric strut **(white arrow)**. At 2 years, the planned repeat angiography showed a patent stented segment **(T),** whereas OCT **(U)** showed in some cross sections the presence of covered polymeric struts **(white arrow)** inside the metallic struts **(light blue arrow)**.

of 2.24 mm followed by a post-dilation with a 3.0-mm noncompliant balloon at 24 atm. Immediately after procedure, overhung struts were observed on OCT at baseline in 5 cross sections (Figure 3). According to the protocol, this asymptomatic patient underwent repeat angiography at 6 months with IVUS and OCT imaging. After the IVUS acquisition, the operator experienced difficulty recrossing the scaffold segment with the OCT catheter. After rewiring the scaffolded vessel, OCT was successfully acquired, which demonstrated extremely malapposed struts close to the OCT catheter (see the noncircularity of struts). The irregularity of the strut structure might have been caused by advancing the wire outside of the scaffold and pushing the OCT catheter under the abluminal side of the struts. At 2-year imaging follow-up, OCT revealed detached struts densely encapsulated with homogeneous tissue, forming an arch attached proximally and distally to the vessel wall. On IVUS, it was documented as a

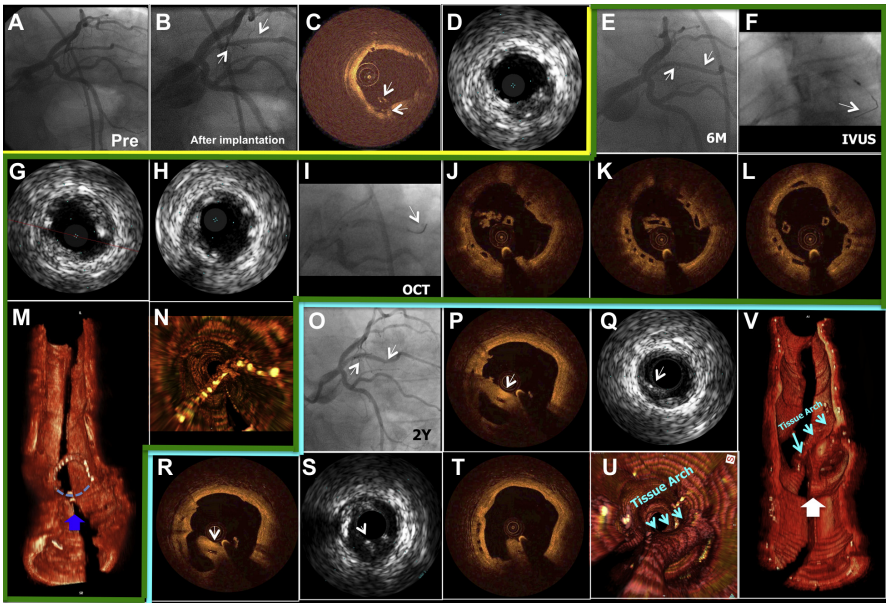

FIGURE 3 **An Example of Acute Disruption**

Each series of framed illustrations (**yellow, green, and blue**) represents the observation at different time points (post-procedure, at 6 months, and at 2 years). An Absorb BVS scaffold was implanted in a small circumflex (reference vessel diameter 2.42 mm) **(A)** followed by post-dilation with a 3.0-mm noncompliant balloon at a maximal pressure of 24 atm **(B)**. Post-procedural OCT detected overhung struts or isolated struts in 5 cross sections **(C),** which were not detected by IVUS **(D)**. At 6-month follow-up, the patient underwent repeat angiography that revealed low angiographic late loss of 0.10 mm **(E)**. According to the protocol, IVUS **(F)** and OCT were performed. IVUS did not detect any abnormality **(G, H)**. After IVUS, the operator experienced difficulty crossing the scaffolded segment with the OCT catheter **(I)**. After rewiring the scaffolded segment, OCT was successfully acquired and showed isolated struts close to the OCT catheter with loss of circularity of the scaffold (**J, K, L**: corresponding frames with **G** and **H**). On 3-dimensional OCT, it was evident that 1 ring of the scaffold was detached from the vessel wall **(M)** and divided the coronary flow **(N)** (endoscopic view). The late disruption of the scaffold might have been induced by advancing the wire outside of the scaffold, pushing the OCT catheter under the abluminal side of the struts during the first crossing attempt. Despite the abnormal OCT findings, the patient remained asymptomatic up to 2 years. At 2-year angiographic follow-up **(O),** OCT revealed detached struts **(P, R, T),** which were fully covered by thick homogeneous tissue extending as an endoluminal arch connected proximally and distally to the vessel wall (3-dimensional) **(U, V)**. On IVUS, it was documented as a "dissection" in a scaffold segment **(Q, S)**. **P**, **R**, and **Q, S** are the corresponding frames on OCT and IVUS, respectively. Abbreviations as in **Figure 2**.

dissection in the scaffold segment. Despite the abnormal imaging findings, the patient remains asymptomatic to date.

LATE STRUT DISCONTINUITIES AT FOLLOW-UP. Follow-up OCT images were obtained in all but 2 patients (at 6 months, 1 year, 2 years, or 3 years) (Online Figure 1). Of 50 scaffolded lesions (49 patients) without acute scaffold disruption, late acquired structural discontinuity was observed in 21 scaffolds (n = 21, 42%). The cases are detailed in Online Table 2 and **Figure 4**. There were no differences in baseline characteristics between patients with or without late discontinuities except for the pre-procedural minimal lumen diameter and diameter stenosis, which could be a play of chance. On IVUS, late discontinuities were detected only in 3 cases.

In the series with 6- and 24-month follow-up, late discontinuities were observed in 3 cases at 6 months and were persistently observed at the second follow-up at 24 months (Online Figure 2). In 8 cases, late discontinuities were observed only at 2 years.

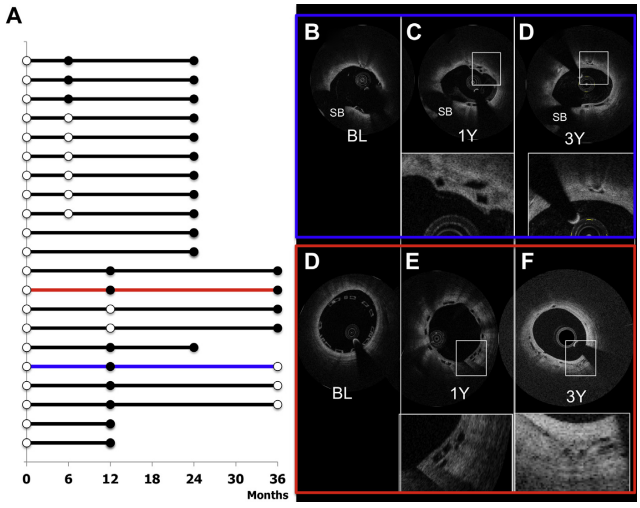

FIGURE 4 Late Discontinuities

(A) The development of late discontinuities is shown; each line represents a scaffold with late discontinuities at various time points of follow-up (post-procedure, 6, 12, 24, and 36 months). **Open circles** indicate OCT investigation without late strut discontinuities, whereas **solid circles** represent OCT observation with late discontinuities at that time point. Framed illustrations in **blue** (**B, C, D**) correspond to scaffolds with resolution at 36 months of late acquired discontinuity originally detected at 12 months. Framed illustrations in **red** (**D, E, F**) correspond to a scaffold with persistent (at 36 months) late discontinuities detected at 12 months. In both cases, the stacked struts were already covered at 12 months. BL = baseline, SB = side-branch; other abbreviations as in Figures 1 and 2.

In the series with 1- and 3-year follow-up, late structural discontinuities were observed at 1 year in 8 cases. Two discontinuities were persistently observed in serial OCT images at 3 years, whereas in 3 cases, discontinuities were resolved at 3 years. In 2 cases, no follow-up was performed after 1 year, so the outcomes of these discontinuities remained unknown. One patient underwent unscheduled OCT at 2 years, revealing persistent discontinuities. Two scaffolds had late structural discontinuities only at 3 years. Figure 4 illustrates the complex timing and outcome of these serial or nonserial investigations.

There were no events associated with these late discontinuities observed on OCT at follow-up except for 1 patient who underwent a non-ischemia-driven repeat TLR (Online Figure 3). The 45-year-old man received a 3.0 mm × 18 mm Absorb BVS scaffold in the mid-left anterior descending artery. Post-procedural OCT did not show malapposition. At 1 year, the patient underwent a planned repeat angiography, which showed an enlargement of the lumen. OCT showed late discontinuity with malapposed overhanging struts over a length of 4 mm. Due to the pronounced malapposition, clopidogrel treatment was continued after 1 year. The patient had stable angina of Canadian Cardiovascular Society class 2 to 3 and underwent a repeat angiography on day 722. On angiography, the lumen was found to become ectatic (QCA maximal diameter: 3.6 mm) without any significant stenosis in the scaffolded segment, whereas on OCT, 1 ring of scaffold showed persistent discontinuity with malapposition. Despite the absence of evidence of ischemia, it was thought that the anginal symptoms were somewhat related to the malapposition. A 3.0 mm × 28 mm metallic Xience Prime stent was placed in the scaffolded segment. After post-dilation with a 3.5-mm balloon, retention of angiographic contrast medium was observed along the new stent and diagnosed as malapposed struts on OCT. The segment was further dilated with a 4.5-mm

balloon. Following the dilation, contrast retention was resolved.

DISCUSSION

The main findings of the current analysis are the following: 1) acute disruption induced by the procedure was observed in 2 of 51 patients (52 pullbacks, 3.9%), with 1 patient, it was presumably related to the TLR; 2) late resorption-related discontinuity was observed in 21 patients with 1, presumably nonrelated, non-ischemia-driven TLR; 3) QCA was unable to detect these structural changes, whereas IVUS was able to detect some of the major acute disruptions/late discontinuities (4 of 23 cases).

ACUTE SCAFFOLD DISRUPTION AND SIZING. Although both acute scaffold disruption and late discontinuity can be diagnosed as stacked/overhung struts or isolated struts on OCT, the 2 phenomena should be categorized differently: 1 as an accidental occurrence; and 1 as a programmed biological process. At the time of implantation, the bioresorption process does not influence the mechanical integrity of the scaffold at all, so that any disrupted struts observed immediately after the procedure are the result of a mechanical disruption caused by extreme overexpansion of the scaffold. The radial force of the polymeric device is comparable with a metallic scaffold as long as the device is expanded within certain restricted limits; however, the mechanical force yields quickly if expanded over the pre-determined boundary of expansion.

The tensile strength of the poly-L-lactide is 50 to 70 MPa, whereas that of cobalt-chrome alloy or stainless steel is in the range of 668 to 1,449 MPa. Percent of elongation at break is 2% to 10 % for poly-L-lactide, whereas it is more than 40% for cobalt chromium or stainless steel. The expansion range of the polymeric device is therefore inherently limited (12).

The relationship between the diameter of expansion and likelihood of device disruption was investigated ex vivo in 30,000 scaffolds. After inflating a 3.0-mm balloon in a phantom, the presence of acute scaffold disruption was examined. Up to a size of 3.65 mm, no scaffold disruption was observed. However, when a 3.0-mm scaffold was expanded to 3.70, 3.76, 3.83, and 3.92 mm in diameter, the likelihood of acute disruption increased by 3%, 24%, 58%, and 80%. The expansion capability is, however, one of multiple attributes related to the performance of the scaffold, such as radial strength, vessel support time, flexibility, fatigue, and acute recoil. To ensure an optimal performance of the drug-eluting scaffold, the scaffold should be expanded within its indicated range, so that the scaffold will not become disrupted and will still perform as expected. This expansion capacity should also be maintained during the entire shelf life of the device. The manufacturer accordingly recommends the maximal limits of expansion of the 3.0-mm device examined in this study as 3.5 mm.

To prevent overexpansion, it is important to implant the scaffold in a properly sized vessel using angiography or intravascular imaging in order to avoid severe mismatch between the device and vessel size. In a previously published study, QCA was used to detect the maximal diameter (Dmax) of the vessel in the landing zone proximal or distal to the stenosis. Three vessel-size groups according to Dmax (small: <2.5 mm, middle: 2.5 to 3.3 mm, large: >3.3 mm) were investigated by OCT post-procedure. The small vessel group presented with a higher percent of lesions with any degree of edge dissections visually detected on OCT (small: 61.5% vs. middle: 33.3% vs. large: 11.1%; $p = 0.05$). Lesions with >5% of incomplete scaffold apposition were significantly higher in the large vessel group with a Dmax >3.3 mm (7.7% vs. 36.7% vs. 66.7%; $p = 0.02$). Thus, sizing according to Dmax seems to be useful in optimizing the acute OCT outcomes (22).

Although the incidence of acute scaffold disruption is low (2 cases, 3.9%), 1 of these 2 cases was associated with a clinical event of non-ischemia-driven TLR at 1 month, followed by a rise of troponin after repeat intervention. On OCT, from baseline to 1 month, more struts became malapposed and isolated toward the lumen center, suggesting that the degree of scaffold disruption may have become worse over time. Although the presence of ischemia was not proven, the fact that chest pain vanished after repeat intervention suggests a relationship between the acute disruption and the symptoms. This could be due to the vasomotion disturbance triggered by the intraluminal presence of struts, or due to small thrombus formation around the malapposed struts with subsequent embolization. Both explanations are hypothetical as objective proof was not observed. Although ex vivo analysis showed that the thrombogenicity of polymeric struts is less than that of bare-metal struts, the possibility exists that a small thrombus could form around the isolated and malapposed struts. This is also suggested by 1 of the cases of acute disruption in cohort A of the ABSORB trial. The patient presented with chest pain at rest with OCT showing intraluminal masses with irregular contour around the disrupted strut (7).

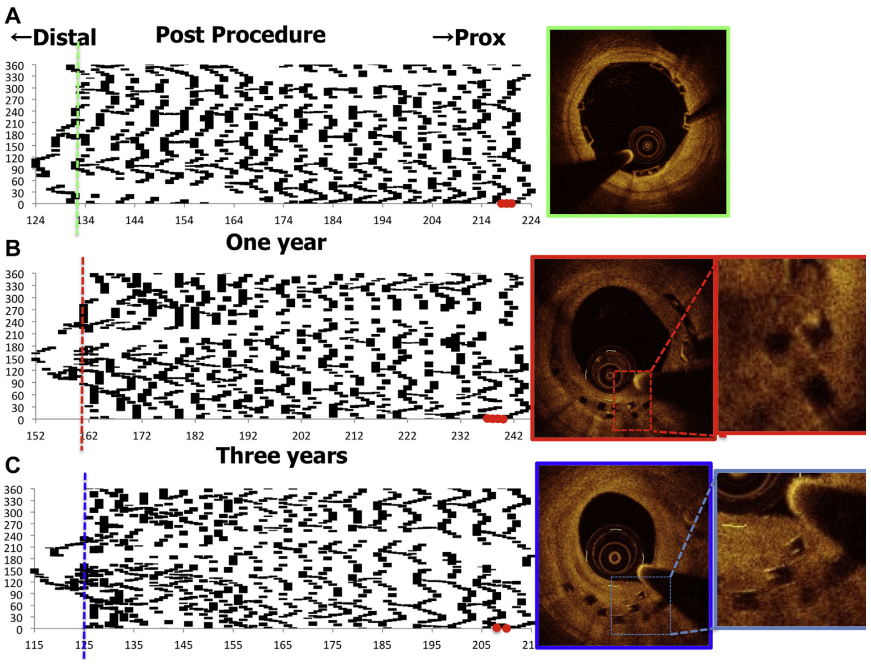

FIGURE 5 **Serial Assessment of Late Discontinuities Using Spread-Out-Vessel Graphics**

(A to C) The foldout views represent spread-out-vessel graphics created by correlating the longitudinal distance from the distal scaffold edge to the individual s detected in a single cross section (abscissa) with on the ordinate the angle where the individual strut was located in the circular cross section with respect to the cent gravity of the vessel (ordinates). In each cross section (axial resolution of 200 μm), the circumferential length of each individual strut was depicted in an angular fas The resultant graphic represented the scaffolded vessel, as if it had been cut longitudinally along the reference angle and spread out on a flat surface. The spreac view post-procedure **(A)** showed that the scaffold consisted of 19 rings interconnected by 3 links. At 1 year **(B)** and 3 years **(C),** mechanical integrity has gradual subsided and the distal part of the scaffold was starting to show signs of dismantling, along which late discontinuities were observed. At baseline, in the distal ed the scaffold (**green dotted line** in the foldout view), 2-dimensional optical coherence tomography (OCT) **(green frame)** revealed well apposed struts. At 1 year, i distal edge (**red dotted line** in the foldout view), 2-dimensional OCT **(red frame)** showed overhung and apposed struts. At 3 years, these struts remained overhung **line** in the foldout view, corresponding to 2-dimensional OCT with a **blue frame**). The phenomenon is considered benign because the struts are mostly covered at 1 years. **Red dots** represent the proximal metallic markers.

LATE, RESORPTION-RELATED STRUCTURAL DISCONTINUITIES. The hydrolysis of polymeric strut starts immediately after the device comes in contact with water, whereas the decrease in mechanical support of the scaffold starts approximately 6 months after implantation. The process of restenosis is a time-limited phenomenon due to negative remodeling of the vessel and neointimal hyperplasia inside of the stent, which occurs 3 to 6 months after implantation in the coronary artery. During this time, the maintenance of the mechanical structure as well as the elution of everolimus is critical to prevent restenosis. Beyond this critical period, however, the mechanical support of the scaffold, as well as the active neointimal inhibition are no longer necessary, because the restenosis process is no longer ongoing. In fact, after 6 months, the polymeric scaffold starts losing its mechanical integrity and that can lead to

expected late discontinuity. Figure 5 shows the progression of structural disintegration over time due to bioresorption. The spread-out view showed that post-procedure, the scaffold consisted of 19 rings connected to each other with 3 links, as manufactured. As shown in Figure 5, at 1 year, mechanical integrity had partially subsided and the distal part of the scaffold has started to dismantle, which corresponds to late discontinuities of individual struts. This phenomenon is considered benign because the struts are mostly covered at 1 and 3 years.

Among the 21 cases with late strut discontinuity, 20 cases had no clinical consequences during the entire follow-up. In 1 case, non-ischemia-driven- TLR with a metallic stent was performed at 2 years to remediate an abnormal outward bulging of the vessel wall, resulting in major malapposition and late strut discontinuities already detected by OCT at 1-year follow-up. Although a huge malapposition could increase a risk of scaffold thrombosis, the microscopic resolution of OCT imaging may have triggered a new kind of "occulo-OCT" reflex because, on angiography, this was inconspicuous.

SINGLE OR SERIAL OBSERVATION. In the current analysis, post-procedural OCT was available in all cases, which enabled us to distinguish the persistent acute disruption from late discontinuities. Whenever OCT was not available post-procedure, differentiation of persistent acute disruption from late discontinuities was speculative (Table 1). Stacked, overhung, or isolated malapposed struts with circular structure that were observed later than 6 months, especially when covered and apposed, could likely be attributed to late resorption-related discontinuities.

OCT AND IVUS. The current analysis showed that IVUS is less sensitive than OCT in the detection of acute strut disruption or late strut discontinuity. IVUS was able to detect major disruptions or discontinuities, but overlooked some disruptions or could not differentiate them from malapposition (23). Because acute scaffold disruption could be associated with anginal symptoms, OCT might be recommended as an additional diagnostic technique when the scaffolded vessel angiographically appears patent, and oversizing and/or overexpansion is suspected.

IMAGING PROCEDURE AT FOLLOW-UP. The anecdotal cases presented in this report highlight the fact that imaging procedures at follow-up can worsen pre-existing scaffold disruptions at late follow-up. The mechanical strength of the device starts to subside 6 months after implantation so that intravascular imaging follow-up occurring later than 6 months post-implantation has to be performed cautiously. Introducing a guidewire into the scaffolded segment should be carried out carefully in cases of known malapposition post-procedure. The operator should not reinvestigate the vessel if any resistance in advancing the imaging device into the scaffolded segment is experienced.

STUDY LIMITATIONS. The current study has a limited number of patients who underwent OCT at the different time points. However, it is the largest series of patients investigated with serial OCT over a follow-up period of 3 years. The "snapshot" nature of the OCT investigations precludes any dynamic interpretation of the ongoing and intended mechanical dismantling of the scaffold. For instance, the longitudinal polymeric links rather than the rings may be the first structures to degrade and the longitudinal mechanical stress might be more intense along the outer epicardial border of the vessel rather than at the inner myocardial side. These speculations should be the focus of further preclinical investigations involving other techniques such as a permanently implanted sono-micrometer. The OCT criteria used in this analysis (stacked struts or overhung struts) will not be applicable to the overlapped segment, because these strut dispositions are normally seen in such segments.

CONCLUSIONS

Acute scaffold disruptions are rare procedural phenomena that have been anecdotally associated with angina symptoms, although pathological correlation between disrupted struts and angina remain elusive. They can be generally avoided by respecting the stated expansion limits for each scaffold diameter. In case of recurrent angina without angiographic stenosis, OCT might be recommended as an additional diagnostic technique, whereas the imaging follow-up later than 6 months needs a careful advance of the imaging device. Late discontinuities as a result of the expected resorption process are observed in approximately 40% of patients who experienced, at the time of follow-up, the struts fully covered or embedded in tissue and should be viewed as a serendipitous OCT finding of a normal bioresorption process without clinical implication.

REPRINT REQUESTS AND CORRESPONDENCE: Prof. Patrick W. Serruys, ThoraxCenter, Ba-583, 's Gravendijkwal 230, 3015 CE Rotterdam, the Netherlands. E-mail: patrick.w.j.c.serruys@gmail.com.

REFERENCES

1. Nakazawa G, Otsuka F, Nakano M, et al. The pathology of neoatherosclerosis in human coronary implants bare-metal and drug-eluting stents. J Am Coll Cardiol 2011;57: 1314–22.

2. Räber L, Baumgartner S, Garcia HM, et al. Long-term vascular healing in response to sirolimus- and paclitaxel-eluting stents: an optical coherence tomography study. J Am Coll Cardiol Intv 2012;5: 946–57.

3. Farooq V, Vergouwe Y, Räber L, et al. Combined anatomical and clinical factors for the long-term risk stratification of patients undergoing percutaneous coronary intervention: the Logistic Clinical SYNTAX score. Eur Heart J 2012; 33:3098–104.

4. Gonzalo N, Serruys PW, Garcia-Garcia HM, et al. Quantitative ex vivo and in vivo comparison of lumen dimensions measured by optical coherence tomography and intravascular ultrasound in human coronary arteries. Rev Esp Cardiol 2009;62: 615–24.

5. Serruys PW, Garcia-Garcia HM, Onuma Y. From metallic cages to transient bioresorbable scaffolds: change in paradigm of coronary revascularization in the upcoming decade? Eur Heart J 2012;33:16–25b.

6. Ormiston JA, Serruys PW, Regar E, et al. A bioabsorbable everolimus-eluting coronary stent system for patients with single de-novo coronary artery lesions (ABSORB): a prospective open-label trial. Lancet 2008;371: 899–907.

7. Onuma Y, Serruys PW, Ormiston JA, et al. Three-year results of clinical follow-up after a bioresorbable everolimus-eluting scaffold in patients with de novo coronary artery disease: the ABSORB trial. EuroIntervention 2010;6:447–53.

8. Serruys PW, Onuma Y, Ormiston JA, et al. Evaluation of the second generation of a bioresorbable everolimus drug-eluting vascular scaffold for treatment of de novo coronary artery stenosis: six-month clinical and imaging outcomes. Circulation 2010;122:2301–12.

9. Gomez-Lara J, Brugaletta S, Diletti R, et al. A comparative assessment by optical coherence tomography of the performance of the first and second generation of the everolimus-eluting bioresorbable vascular scaffolds. Eur Heart J 2011;32: 294–304.

10. Serruys PW, Luijten HE, Beatt KJ, et al. Incidence of restenosis after successful coronary angioplasty: a time-related phenomenon. A quantitative angiographic study in 342 consecutive patients at 1, 2, 3, and 4 months. Circulation 1988;77:361–71.

11. Nobuyoshi M, Kimura T, Nosaka H, et al. Restenosis after successful percutaneous transluminal coronary angioplasty: serial angiographic follow-up of 229 patients. J Am Coll Cardiol 1988; 12:616–23.

12. Onuma Y, Serruys PW. Bioresorbable scaffold: the advent of a new era in percutaneous coronary and peripheral revascularization? Circulation 2011; 123:779–97.

13. Ormiston JA, De Vroey F, Serruys PW, Webster MW. Bioresorbable polymeric vascular scaffolds: a cautionary tale. Circ Cardiovasc Interv 2011;4:535–8.

14. Serruys PW, Onuma Y, Dudek D, et al. Evaluation of the second generation of a bioresorbable everolimus-eluting vascular scaffold for the treatment of de novo coronary artery stenosis: 12-month clinical and imaging outcomes. J Am Coll Cardiol 2011;58:1578–88.

15. Okamura T, Garg S, Gutiérrez-Chico J, et al. In vivo evaluation of stent strut distribution patterns in the bioabsorbable everolimus-eluting device: an OCT ad hoc analysis of the revision 1. 0 and revision 1.1 stent design in the ABSORB clinical trial. EuroIntervention 2010;5:932–8.

16. Sihan K, Botha C, Post F, et al. Fully automatic three-dimensional quantitative analysis of intracoronary optical coherence tomography: method and validation. Catheter Cardiovasc Interv 2009; 74:1058–65.

17. Prati F, Regar E, Mintz GS, et al. Expert review document on methodology, terminology, and clinical applications of optical coherence tomography: physical principles, methodology of image acquisition, and clinical application for assessment of coronary arteries and atherosclerosis. Eur Heart J 2010;31:401–15.

18. Gonzalo N, Serruys PW, Okamura T, et al. Optical coherence tomography assessment of the acute effects of stent implantation on the vessel wall: a systematic quantitative approach. Heart 2009;95:1913–9.

19. Regar E, van Leeuwen AMGJ, Serruys PW. Optical Coherence Tomography in Cardiovascular Research. London: Informa Healthcare, 2007.

20. Gomez-Lara J, Radu M, Brugaletta S, et al. Serial analysis of the malapposed and uncovered struts of the new generation of everolimus-eluting bioresorbable scaffold with optical coherence tomography. J Am Coll Cardiol Intv 2011;4: 992–1001.

21. Radu MD. The Clinical Atlas of Intravascular Optical Coherence Tomography for iPad. Eur Heart J 2012;33:1174–5.

22. Gomez-Lara J, Diletti R, Brugaletta S, et al. Angiographic maximal luminal diameter and appropriate deployment of the everolimus-eluting bioresorbable vascular scaffold as assessed by optical coherence tomography: an ABSORB cohort B trial sub-study. EuroIntervention 2012;8: 214–24.

23. Gomez-Lara J, Brugaletta S, Diletti R, et al. Agreement and reproducibility of gray-scale intravascular ultrasound and optical coherence tomography for the analysis of the bioresorbable vascular scaffold. Catheter Cardiovasc Interv 2012; 79:890–902.

KEY WORDS atherosclerosis, biodegradable polymer, bioresorbable scaffold, everolimus, stent

APPENDIX For supplemental methods, figures, and tables, please see the online version of this article.

4.3 In-Scaffold Restenosis (ISR)

Early (before 6 months), late (6-12 months) and very late (after 12 months) angiographic scaffold restenosis in the ABSORB Cohort B trial.

Eurointervention. 2015;10(11):1288-98.
[Original research paper, Impact Factor : 3.77]

Nakatani S, OnumaY, Ishibashi Y, Muramatsu T, Iqbal J, Zhang YJ, van Geuns RJ, Ormiston JA, Serruys PW; on behalf of the ABSORB Cohort B investigators.

Early (before 6 months), late (6-12 months) and very late (after 12 months) angiographic scaffold restenosis in the ABSORB Cohort B trial

Shimpei Nakatani[1], MD; Yoshinobu Onuma[1]*, MD; Yuki Ishibashi[1], MD, PhD; Takashi Muramatsu[1], MD, PhD; Javaid Iqbal[1], MRCP, PhD; Yao-Jun Zhang[1], MD, PhD; Robert-Jan van Geuns[1], MD, PhD; John A. Ormiston[2], MBChB, PhD; Patrick W. Serruys[1], MD, PhD; on behalf of the ABSORB Cohort B investigators

1. Thoraxcenter, Erasmus Medical Center, Rotterdam, The Netherlands; 2. Auckland City Hospital, Auckland, New Zealand

GUEST EDITOR: Rafael Beyar, MD, DSc, MPH, Director; *Rambam Health Care Campus, Women's Division/Dr Phillip and Sara Gotlieb Chair, Department of Medicine and Biomedical Engineering, Technion, Israel*

KEYWORDS

- bioresorbable scaffold
- everolimus
- intravascular imaging
- long-term follow-up
- restenosis

Abstract

Aims: The long-term follow-up of the first-in-man ABSORB Cohort B trial showed that angiographic binary restenosis can occur early, late or very late after implantation of the Absorb everolimus-eluting bioresorbable vascular scaffold (Absorb BVS). Since the mechanical support of the scaffold decreases during bioresorption, the mechanism of in-segment restenosis (ISR) of the Absorb BVS might be different from that of metallic stents. The objective of the current analysis was to review the multimodality imaging of cases with binary restenosis to elucidate the mechanism of ISR after Absorb BVS implantation.

Methods and results: The ABSORB Cohort B trial enrolled 101 patients with a maximum of two *de novo* coronary lesions. At the three-year imaging and clinical follow-up, there were six cases of in-segment binary restenosis: two early ISR (<6 months), one late ISR (6-12 months) and three very late ISR (>12 months). Three of these ISR cases seemed to be induced by anatomical or procedural factors. In the other three cases, intravascular imaging (IVUS/OCT) demonstrated that the main mechanism of restenosis was significant intra-scaffold tissue growth, while the structural circularity and diameter of the scaffold were not affected.

Conclusions: Early and late restenosis after implantation of the Absorb bioresorbable scaffold could be related to anatomical or procedural factors. In this small cohort of patients late or very late restenosis seems to be attributed to pure intra-scaffold tissue growth without extrinsic encroachment of the scaffold.

**Corresponding author: Thoraxcenter, Ba-583, 's Gravendijkwal 230, 3015 CE Rotterdam, The Netherlands. E-mail: yoshinobuonuma@gmail.com*

SUBMITTED ON 29/08/2013 - REVISION RECEIVED ON 09/12/2013 - ACCEPTED ON 08/01/2014

Introduction

The Absorb everolimus-eluting bioresorbable vascular scaffold (Absorb BVS; Abbott Vascular, Santa Clara, CA, USA) shows unique potential in vascular repair, such as late lumen enlargement, restoration of vasomotion and plaque media reduction[1-4]. However, in-scaffold restenosis may occur as frequently as with metallic drug-eluting stents (DES). Since the Absorb BVS loses its mechanical strength during bioresorption, unlike metallic stents, the mechanism of in-scaffold restenosis might be unique and different from DES and bare metal stents (BMS).

The process of lumen loss (LL) is a "time limited phenomenon" due to negative remodelling of the vessel and neointimal hyperplasia inside the stent, which occurs three to six months after implantation[5,6]. Beyond this critical period, the mechanical support of the scaffold and the active pharmacological inhibition of the neointima are no longer necessary. According to this concept, mechanical support of the scaffold could decrease approximately six months after implantation. Actually, it has been established in humans that the mechanical integrity is maintained over a period of six months but subsides afterwards[7]. However, one could speculate that the plaque behind the struts of the scaffold might progress and narrow the lumen once the scaffold has lost its mechanical strength.

Timing of restenosis and its potential mechanism after implantation of the Absorb BVS have not been investigated. We report six cases of ISR (quantitative coronary angiography [QCA] diameter stenosis ≥50% within the scaffolded segment and 5 mm proximal and distal to the scaffolded segment) observed in the ABSORB Cohort B trial (101 patients, 102 lesions) according to the timing, and describe in detail the intravascular findings in an attempt to elucidate the mechanism of this complication. Two cases were early ISR (<6 months), one case was late ISR (6-12 months), and three cases were very late ISR (>12 months) **(Table 1, Figure 1)**.

Case histories

CASE 1. EARLY ISR DUE TO MYOCARDIAL BRIDGE

A 57-year-old man with a history of hypertension, dyslipidaemia, smoking and COPD presented with stable angina. The coronary angiography showed a type B2 lesion in the mid left anterior descending (LAD) artery with severe stenosis in systole (percentage diameter stenosis [%DS]: 84%), but without significant stenosis in diastole (%DS: 26%), thus with typical evidence of a myocardial bridge **(Figure 2A-Figure 2C)**[8]. After predilatation with a 2.75 mm semi-compliant balloon, a 3.0×18 mm Absorb BVS was deployed and post-dilated with a 3.5 mm non-compliant balloon at 16 atm **(Figure 2D)**. On day 89, the patient experienced recurrent angina and underwent re-catheterisation. The angiography revealed a focal ISR at the site of the myocardial bridge (QCA minimum lumen diameter [MLD]: 1.20 mm, %DS: 59.0%, LL: 0.90 mm) **(Figure 2E)**. This ISR was treated by implantation of a 3.5×15 mm XIENCE V stent (Abbott Vascular) inside the Absorb BVS **(Figure 2F)**. At three years, angiography revealed a significant re-ISR of this XIENCE V stent (QCA MLD: 1.20 mm, %DS: 59.0%, LL: 0.90 mm) **(Figure 2G)**.

Table 1. Case summary.

	Case 1	Case 2	Case 3	Case 4	Case 5	Case 6
Timing	Early	Early	Late	Very late	Very late	Very late
Day	89	168	354	383	567	833
Age	57	69	57	76	62	42
Sex	Male	Male	Male	Male	Male	Female
History of DM	no	no	no	no	no	no
Pre procedure						
RVD (mm)	2.51	2.05	2.64	2.82	2.97	2.24
Lesion length	10.3	5.9	12.0	8.1	15.4	10.2
%DS (%)	71.5	72.5	70.0	71.0	64.5	52.5
MLD (mm)	0.72	0.58	0.79	0.82	1.05	1.06
Post procedure						
%DS (%)	16.7	27.0	16.0	24.5	23.5	9.0
MLD (mm)	1.91	1.94	2.08	2.10	1.95	1.93
At TLR						
Clinical presentation	Stable angina	No angina	Stable angina	Unstable angina	Unstable angina	Stable angina
Examination for ischaemia	–	FFR: 0.72	Asynergy on echo.	–	–	Myocardial scintigram positive
%DS (%)	59.0	63.5	64.0	67.0	71.0	63.7
MLD (mm)	1.20	0.89	0.79	0.90	0.81	0.72
LL (mm)	0.90	0.50	1.58	1.20	1.47	1.38

DM: diabetes mellitus; RVD: reference vessel diameter; %DS: % diameter stenosis; MLD: minimum lumen diameter; LL: lumen loss; FFR: fractional flow reserve; TLR: target lesion revascularisation

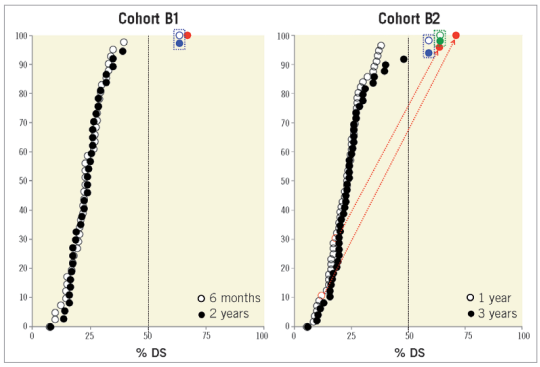

Figure 1. *Cumulative frequency distribution curves of angiographic % diameter stenosis (%DS). A) %DS at 6 (circle) and 24 months (dot) of Cohort B1. B) %DS at 12 (circle) and 36 months (dot) of Cohort B2. If the patient had TLR before the planned angiography, %DS at the time of TLR (before repeat revascularisation) was used for the %DS at the later time point. Blue dots (●) and blue circles (○) represent %DS in TLR patients who experienced early ISR (<6 months). Green dots (●) and green circles (○) represent %DS in TLR patients who experienced late ISR (6-12 months). Red dots (●) and red circles (○) represent %DS in TLR patients who experienced very late ISR.*

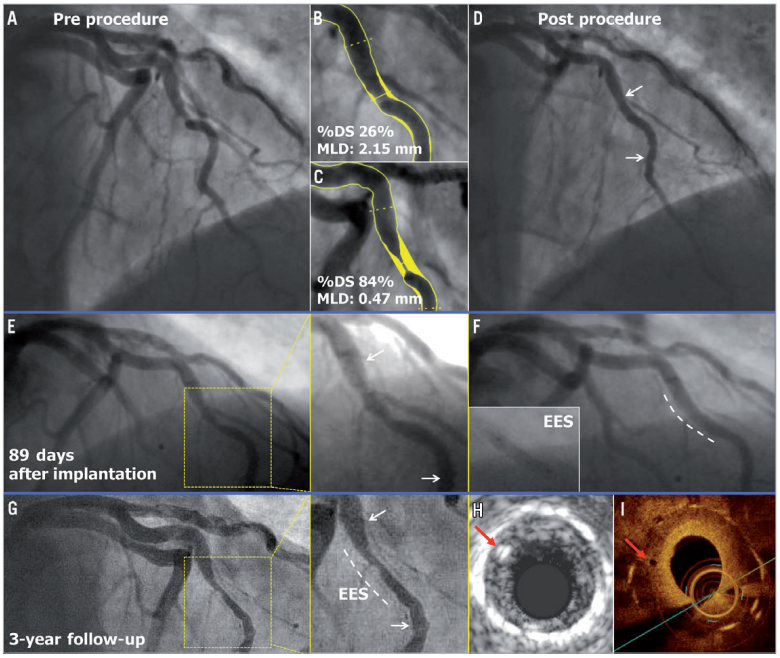

Figure 2. *Early ISR due to myocardial bridge. The white arrows indicate the metallic markers of the implanted scaffold, while the white dotted line illustrates the implanted EES. The red arrows show the scaffold struts of the previously implanted Absorb BVS located inside the metal stent on IVUS (H) and OCT (I).*

Optical coherence tomography (OCT) revealed intra-scaffold tissue growth with homogeneous light reflectivity. Of interest, OCT and intravascular ultrasound (IVUS) showed that some struts of the previously implanted Absorb BVS were located inside the metal stent (**Figure 2H**, **Figure 2I**). Finally, this re-ISR lesion was treated by a coronary artery bypass graft (CABG).

CASE 2. EARLY ISR AT PROXIMAL EDGE

A 69-year-old male with a history of dyslipidaemia and previous coronary intervention of the left circumflex (LCX) artery presented with stable angina. Coronary angiography showed a type B1 severe stenosis in the mid right coronary artery (RCA) **(Figure 3A)**. After predilatation with a 2.5 mm semi-compliant balloon, a 3.0×18 mm Absorb BVS was deployed and post-dilated with a 3.0 mm balloon at 15 atm (expected diameter according to the manufacturer was 3.3 mm) **(Figure 3B)**. As the IVUS catheter failed to pass through the implanted scaffold, the guiding catheter was changed from JR4 to AL1. After repeated attempts to cross the IVUS catheter through the scaffold by seating the guiding catheter deeply up to the proximal edge of the scaffold in order to perform the protocol-related imaging, the operator was unable to cross the scaffold and the procedure was ended **(Figure 3C)**. On day 168, the patient underwent a planned repeat angiography, which showed a type 1B ISR at the proximal edge of the scaffold (QCA MLD: 0.89 mm, %DS: 63.5%, LL: 0.50 mm) without significant restenosis in the scaffold itself **(Figure 3D)**[9]. Greyscale IVUS (IVUS-GS) showed a high-echoic intra-scaffold tissue growth in the segment proximal to the scaffold, with maintained circularity of the scaffold (**Figure 3E**, **Figure 3F**). This ISR was treated by implantation of a 3×28 mm XIENCE V stent with full coverage of the previously implanted Absorb BVS.

CASE 3. LATE ISR WITH HOMOGENEOUS INTRA-SCAFFOLD TISSUE ON OCT

In a 57-year-old man with a history of dyslipidaemia and smoking, and presenting with unstable angina, coronary angiography showed a severe type B1 stenosis in the proximal LAD with TIMI grade 2 flow **(Figure 4A)**. After predilatation with a 2.5 mm

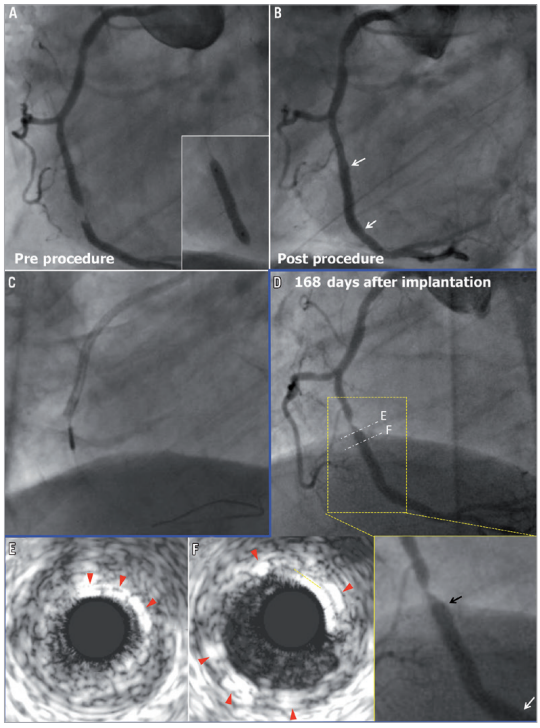

Figure 3. *Early ISR at proximal edge. The white and black arrows indicate the metallic markers of the implanted scaffold. In panels E and F, the red arrows show the polymeric strut on IVUS.*

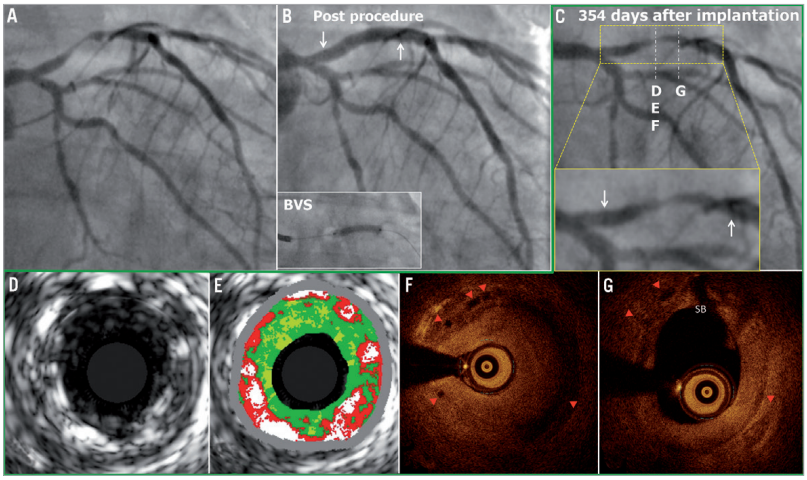

Figure 4. *Late ISR with homogeneous intra-scaffold tissue on OCT. The white arrows show the metallic marker of the implanted scaffold. In panels F and G, the red triangles show the scaffold struts on OCT (case 3).*

semi-compliant balloon, a 3.0×18 mm Absorb BVS was deployed and post-dilated with a 3.0 mm non-compliant balloon at 20 atm **(Figure 4B)**. On day 348, the patient had recurrence of angina pectoris. On day 354, the patient underwent a planned repeat angiography, which showed a significant type 1C ISR (QCA MLD: 0.79 mm, %DS: 64.0%, LL: 1.58 mm) in the body of the scaffold **(Figure 4C)**[9]. OCT showed that the circularity of the scaffold was maintained throughout the pullback (the mean scaffold area was 5.67 mm^2 and the minimum scaffold area was 4.73 mm^2) and all the struts were completely apposed and covered. At the site of the minimal lumen area (MLA), OCT revealed homogeneous signal-rich intra-scaffold tissue (**Figure 4D-Figure 4G**). On virtual histology IVUS (IVUS-VH), intra-scaffold tissue was documented as fibrous **(Figure 4E)**. A XIENCE V stent was implanted to cover the previously implanted Absorb BVS.

CASE 4. VERY LATE ISR AT THE PROXIMAL EDGE

A 76-year-old gentleman with a history of dyslipidaemia, chronic kidney failure and coronary intervention to the mid LAD (non-target lesion) presented with stable angina. The coronary angiography showed a type B1 moderate stenosis in the mid LAD **(Figure 5A)**. After predilatation with a 2.5 mm semi-compliant balloon, a 3.0×18 mm Absorb BVS was deployed. However, the Absorb BVS did not cover the proximal part of the predilated segment, resulting in geographical miss **(Figure 5B)**. After implantation of the scaffold, the jailed diagonal branch became occluded. Since this closure resulted in chest pain, bradycardia and hypotension, the side branch was dilated with a 1.5 mm balloon **(Figure 5C)**. OCT post procedure revealed a small dissection in the proximal edge of the scaffold, presumably due to the geographical miss during the procedure **(Figure 5D, Figure 5E)**. The patient refused the scheduled follow-up angiography at six months. One year later, the patient presented with recurrence of angina pectoris, and repeat angiography showed a type 1B ISR in the segment proximal to the scaffold (QCA MLD: 0.90 mm, %DS: 67.0%, LL: 1.20 mm) **(Figure 5F)**, while the scaffolded segment was free from significant restenosis[9]. A 3.0×15 mm XIENCE V stent was implanted to overlap the proximal part of the previously implanted Absorb BVS.

CASE 5. VERY LATE ISR WITH HOMOGENEOUS INTRA-SCAFFOLD TISSUE ON OCT

A 62-year-old man with a history of hypertension, smoking and COPD presented with stable angina. Coronary angiography showed a type B1 severe stenosis in the proximal LAD **(Figure 6A)**. Although the proximal maximum luminal diameter (Dmax) on QCA was 3.90 mm, a 3.0 mm Absorb BVS was planned **(Figure 6B, Figure 6C)**. After predilatation with a 2.5 mm semi-compliant balloon, this 3.0×18 mm Absorb BVS was implanted and post-dilated with a 3.5 mm non-compliant balloon at 12 atm **(Figure 6F)**. Post-procedural OCT showed large incomplete stent apposition (ISA) (max ISA area: 11.89 mm^2, max ISA distance 1.63 mm, the number of cross-sections with ISA: 25 frames) at the proximal edge of the scaffold, but additional dilatation was not performed **(Figure 6D, Figure 6E)**. At one year, the planned follow-up coronary angiography showed patency of the scaffold (QCA MLD: 1.99 mm, %DS: 10.0%, LL: -0.04 mm) **(Figure 6G)**. OCT showed persistent numerous malapposed struts with intraluminal mass attached to or free from the vessel wall at the proximal edge of the previously

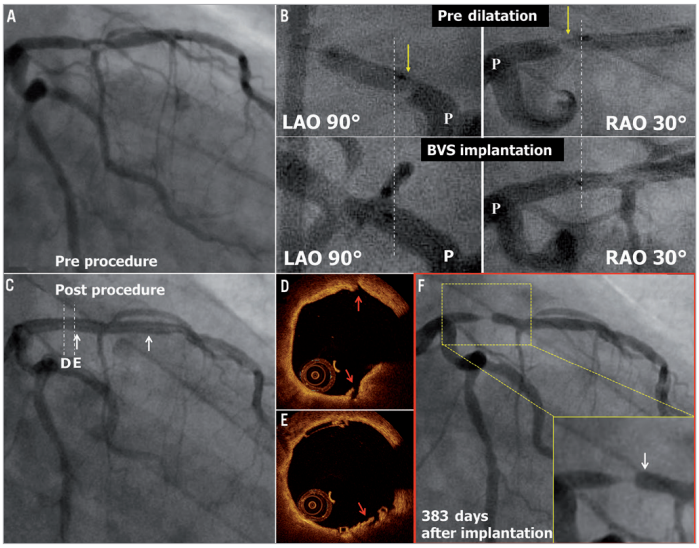

Figure 5. *Very late ISR at the proximal edge. The white arrows show the metallic marker of the implanted scaffold. In panel B, the yellow arrows show the proximal edge of the predilatation balloon. The angiograms are matched anatomically between predilatation and scaffold implantation, and the white dotted lines show the proximal edge of the implanted scaffold. The red arrows show the small dissection observed post procedure on OCT in panels D and E.*

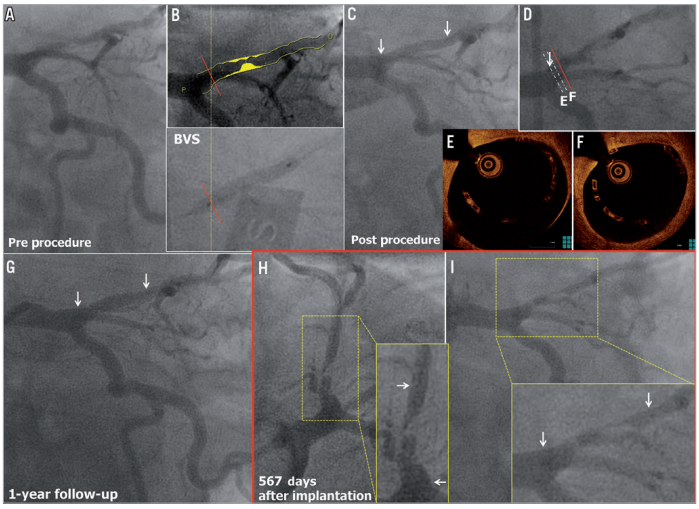

Figure 6. *Very late ISR with homogeneous intra-scaffold tissue on OCT. The white arrows show the metallic marker of the implanted scaffold. The red line shows the point of Dmax on QCA, which is superimposed on the angiogram at scaffold implantation in panel B. The red line is superimposed on the angiogram at OCT study in panel D (case 5).*

implanted scaffold **(Figure 7a)**. On the three-dimensional OCT image, the intraluminal masses were interlinked to the malapposed struts and connected proximally to the vessel wall **(Figure 7a')**. On day 564 the patient was hospitalised with unstable angina and underwent a repeat angiography on day 567, which showed a type 1C ISR in the body of the scaffold (QCA MLD: 0.81 mm, %DS: 71.0% and LL: 1.47 mm)[9]. OCT showed homogeneous signal-rich intra-scaffold tissue in the middle of the scaffold segment with persistent malapposed struts at the proximal edge **(Figure 7B-E)**[10]. After predilatation, repeat OCT revealed an extensive tissue protrusion with maintained circularity of the scaffold **(Figure 7B'-E')**. On OCT analysis, the mean scaffold area was 8.32 mm^2, and the minimum scaffold area was 6.23 mm^2 **(Figure 7A)**. This ISR was treated by implantation of a 3.0×18 mm XIENCE V stent which overlapped the proximal part of the previously implanted Absorb BVS.

CASE 6. VERY LATE ISR WITH ISO-ECHOIC INTRA-SCAFFOLD TISSUE ON IVUS-GS

In a 42-year-old female with a history of smoking presenting with stable angina, coronary angiography demonstrated a type B1 moderate stenosis in the mid LAD **(Figure 8A)**. After predilatation with a 2.5 mm semi-compliant balloon, a 3.0×18 mm Absorb BVS was implanted. After post-dilatation with a 3.0 mm non-compliant balloon at 20 atm, post-procedural angiography showed a residual stenosis of 9.0% **(Figure 8B)**. At one year, a planned repeat angiography showed patency of the previously implanted scaffold (QCA MLD was 1.73 mm, %DS was 18.0% and LL was 0.35 mm) **(Figure 8C)**. On day 833, the patient underwent a repeat angiography because of stable angina with ischaemia on a myocardial scintigraphy: the angiogram showed a type 1B ISR at the distal margin of the scaffold segment (QCA MLD: 0.72 mm, %DS: 63.7% and LL:

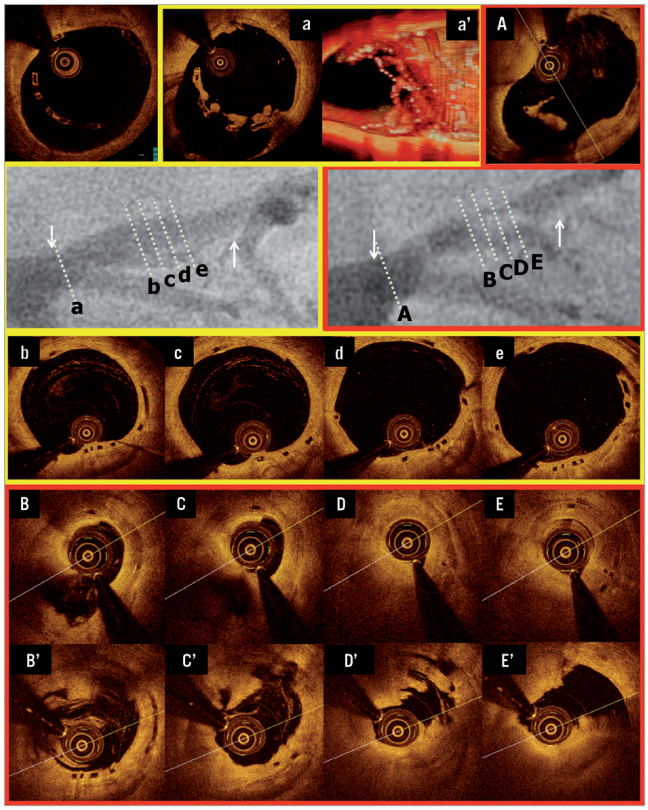

Figure 7. *Very late ISR with homogeneous intra-scaffold tissue on OCT. The white arrows show the metallic marker of the implanted scaffold. OCT images pre TLR before ballooning are shown in panels B to E, and those after ballooning are shown in panels B' to E'. In panels b to e, the corresponding cross-sections to ISR site are shown at 12-month follow-up.*

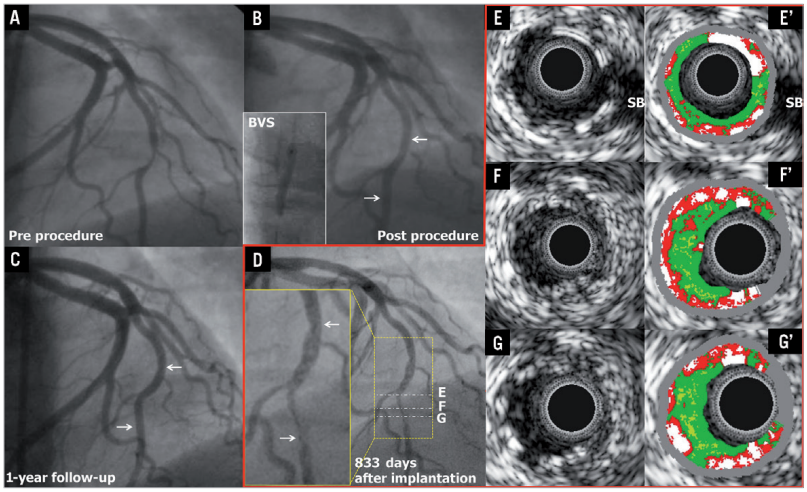

Figure 8. *Very late ISR with iso-echoic intra-scaffold tissue on IVUS-GS. The white arrows show the metallic marker of the implanted scaffold.*

1.38 mm) **(Figure 8D)**[9]. IVUS-GS showed that the scaffold circularity was maintained and that the eccentric intra-scaffold tissue was iso-echoic **(Figure 8E-G)**. On IVUS-VH, small necrotic core and dense calcium were detected in the intra-scaffold tissue **(Figure 8E'-G')**. In this case, the ISR lesion was treated by the implantation of a 3.0×23 mm XIENCE V which overlapped the distal part of the previously implanted Absorb BVS.

Discussion

The main findings of the current report are the following: 1) out of 101 patients enrolled in the ABSORB trial, at three years early restenosis occurred in two cases (2.0%), late ISR in one case (1.0%), and very late ISR in three cases (3.0%); 2) the early ISR was associated with a myocardial bridge (case 1); 3) two of the three late ISR cases may have been caused by procedural edge injury at the index procedure (one case was due to the injury caused by deep insertion of the guiding catheter [case 2], while the other case could be attributed to proximal geographical miss [case 4]); 4) in three cases (one late ISR and two very late ISR), the mechanism of ISR could not be identified (case 3, case 5, and case 6) , but in all cases the circularity of the scaffold was maintained.

It is noteworthy that ISR occurred in patients without diabetes, with relatively large vessels (reference vessel diameter 3 or more mm) and short lesion length (less than 10 mm).

ISR ASSOCIATED WITH MYOCARDIAL BRIDGE

Myocardial bridging (MB) is a potential cause of myocardial ischaemia and in such cases medical therapy, with beta-blockers or calcium channel blockers, is recommended as a first-line strategy[8,11]. Although intracoronary stent implantation is another therapeutic approach to prevent external systolic compression and ischaemia caused by the MB, this therapy is still controversial because of concerns regarding high restenosis rates, plaque prolapse and stent fracture[12,13]. In the current series, one early TLR occurred in a myocardial bridge at three months after implantation of an Absorb BVS, followed by a second failure occurring after implantation of a metallic drug-eluting stent. This case suggests that scaffold implantation for a myocardial bridge treatment should be discouraged. Myocardial bridges generate compressive pressure (up to 300 mmHg) capable of fully closing the vessel in systole. Although the initial radial strength of an Absorb BVS is approximately 900 mmHg and superior to this compressive pressure, this systolic external compression occurs at least 100,000 times/day, and in the course of bioresorption a bioresorbable transient scaffold might yield to such a mechanical stress[3,14].

In this case, at three years, OCT and IVUS detected one scaffold strut inside the area of the metal stent, while post procedure no disrupted strut had been detected on IVUS. The location of a polymeric strut inside the metallic stent may suggest that the discontinued strut could protrude between the metallic mesh of the stent after TLR at three months.

ISR PRESUMABLY TRIGGERED BY PROCEDURAL INJURY

It has been shown that procedural vessel injury might lead to late intra-scaffold tissue growth[15]. In one case in the current series, the deeply inserted AL1 guide catheter might have injured the edge of the scaffold at baseline and led to proximal edge ISR at six months.

Geographical miss is also a known cause of restenosis[16,17]. In one case, the predilatation might have caused "barotrauma" to the proximal plaque and the Absorb BVS did not cover the injured edge segment. Actually, a proximal edge dissection not scaffolded by the Absorb BVS was observed on OCT. The edge ISR could therefore be related to the proximal plaque injury associated with geographical miss[18].

MAINTAINED CIRCULARITY OF SCAFFOLD AREA IN LATE/VERY LATE ISR

As previously described, the radial strength of the fully bioresorbable scaffold declines following polymer hydrolysis at six months, and this device becomes malleable without any supportive properties at 12 months. One could therefore speculate that the scaffold might become encroached by plaque growth behind the struts. In the balloon angioplasty era, Serruys et al demonstrated that the incidence of restenosis reaches a plateau at four months[6]. Ormiston et al demonstrated that the late loss in response to balloon injury reached a maximum before six months and then regressed, while some cases with an intermediate stenosis at six months showed very late lumen narrowing at five years[19].

In this study, we observed three ISR cases without any possible causal relationship with procedural or anatomical factors: one case presented a late ISR and two cases a very late ISR. As shown in **Figure 9**, the circularity of the Absorb BVS, especially at MLA cross-section, was preserved post procedure in all cases. In addition, there were no changes in mean/minimum scaffold area.

This report suggests that the perceived relative weakness of the scaffold related to its polymeric nature does not seem to have any direct impact on the restenosis phenomenon, and late lumen loss seems to be the result of intra-scaffold tissue growth rather than late scaffold recoil.

Late and very late restenosis have also been reported with metallic drug-eluting stents. In the SPIRIT II trial, the rate of ischaemia-driven TLR steadily increased from 1.8% at one year to 3.8% at two years and 4.6% at three years[20-22]. In the ABSORB Cohort B trial, the rate of ischaemia-driven TLR beyond one year increased similarly (4.0% at one year, 5.0% at two years, and 5.9% at three years). These data suggest that ISR with the Absorb BVS occurs as frequently as with metallic DES, and a reduced mechanical strength of the scaffold cannot be implicated in the occurrence of ISR.

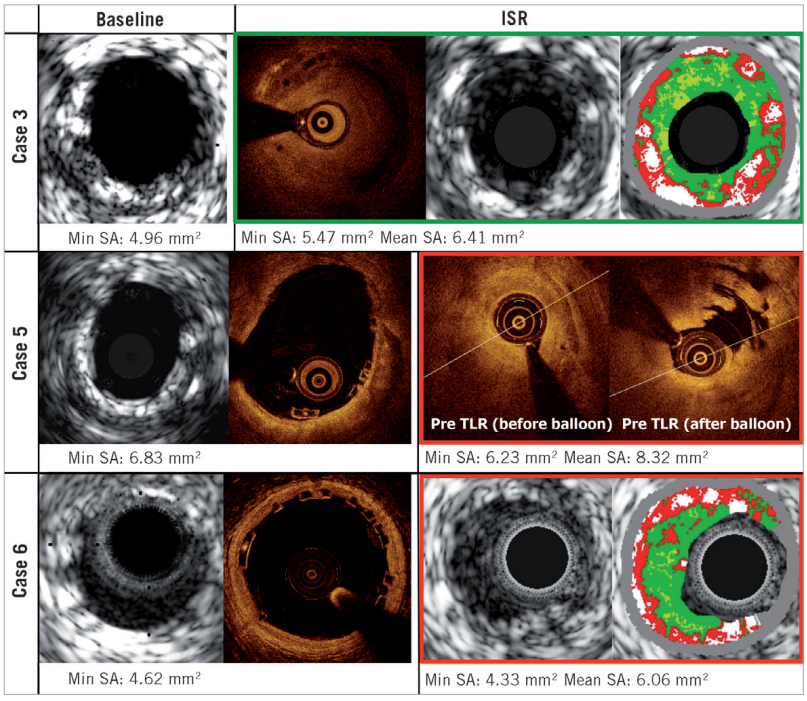

Figure 9. *Intravascular imaging of the late and very late restenosis.*

MORPHOLOGICAL CHARACTERISTICS OF INTRA-SCAFFOLD TISSUE IN LATE/VERY LATE ISR

On IVUS-VH, a typical neointimal restenosis within one year after BMS implantation appears as fibrous or fibro-fatty tissue (green or green-yellow)[23]. Neointima after DES implantation or beyond one year after BMS implantation is sometimes detected as necrotic core tissue (red and red-white) on IVUS-VH[23]. It should be noted that intramural thrombus also has the appearance of fibrous or fibro-fatty tissue[24]. In the current series, two IVUS-VH images were available: one was a late ISR and the other was a very late ISR. In the late ISR case, the intra-scaffold tissue appeared as fibrous tissue, while, in the very late ISR case, the small necrotic core and dense calcium were interspersed in fibrous tissue **(Figure 9)**.

OCT has been used to evaluate the efficacy of stenting by analysing tissue characteristics of in-stent intima[25]. Goto et al demonstrated that homogeneous high-signal band is a typical in-stent intima within one year after BMS implantation, while heterogeneous mixed-signal band is observed at all timing points after DES implantation[24]. In the current series, two OCT images were available: both of them were late ISR. In these cases, the intra-scaffold tissue appeared as a homogeneous tissue **(Figure 9)**.

Limitations

The sample size was small and the first-in-man trial had no control arm. The current findings therefore need to be confirmed in a large randomised trial.

Conclusion

The current analysis suggests that early and late restenosis after implantation of the Absorb bioresorbable scaffold could be related to anatomical or procedural factors. Late or very late restenosis could be attributed to intra-scaffold tissue growth but not to the encroachment of the scaffold.

Impact on daily practice

Since the Absorb everolimus-eluting bioresorbable vascular scaffold (BVS) loses its mechanical strength during bioresorption, the mechanism of in-scaffold restenosis (ISR) could be different from metallic stents. In the ABSORB Cohort B trial, at three years, ISR with the BVS occurs as frequently as with drug-eluting metallic stents. By investigating the ISR according to the time line of the mechanical change of the BVS, the perceived relative weakness of the scaffold does not seem to have any direct impact on the restenosis phenomenon, and seems to be the result of intra-scaffold tissue growth rather than late scaffold recoil and extrinsic encroachment of the scaffold. The disappearance of the device was not found to be a disadvantage in relation to ISR in the current study.

Guest Editor

This paper was guest edited by Rafael Beyar, MD, DSc, MPH, Director, Rambam Health Care Campus, Women's Division/Dr Phillip and Sara Gotlieb Chair, Department of Medicine and Biomedical Engineering, Technion, Israel.

Funding

The ABSORB trial was sponsored by Abbott Vascular.

Conflict of interest statement

The authors have no conflicts of interest to declare. The Guest Editor has no conflicts of interest to declare.

References

1. Ormiston JA, Serruys PW, Onuma Y, van Geuns RJ, de Bruyne B, Dudek D, Thuesen L, Smits PC, Chevalier B, McClean D, Koolen J, Windecker S, Whitbourn R, Meredith I, Dorange C, Veldhof S, Hebert KM, Rapoza R, Garcia-Garcia HM. First serial assessment at 6 months and 2 years of the second generation of absorb everolimus-eluting bioresorbable vascular scaffold: a multi-imaging modality study. *Circ Cardiovasc Interv.* 2012;5:620-32.

2. Serruys PW, Ormiston JA, Onuma Y, Regar E, Gonzalo N, Garcia-Garcia HM, Nieman K, Bruining N, Dorange C, Miquel-Hebert K, Veldhof S, Webster M, Thuesen L, Dudek D. A bioabsorbable everolimus-eluting coronary stent system (ABSORB): 2-year outcomes and results from multiple imaging methods. *Lancet.* 2009;373:897-910.

3. Serruys PW, Onuma Y, Dudek D, Smits PC, Koolen J, Chevalier B, de Bruyne B, Thuesen L, McClean D, van Geuns RJ, Windecker S, Whitbourn R, Meredith I, Dorange C, Veldhof S, Hebert KM, Sudhir K, Garcia-Garcia HM, Ormiston JA. Evaluation of the second generation of a bioresorbable everolimus-eluting vascular scaffold for the treatment of de novo coronary artery stenosis: 12-month clinical and imaging outcomes. *J Am Coll Cardiol.* 2011;58:1578-88.

4. Onuma Y, Serruys PW, Ormiston JA, Regar E, Webster M, Thuesen L, Dudek D, Veldhof S, Rapoza R. Three-year results of clinical follow-up after a bioresorbable everolimus-eluting scaffold in patients with de novo coronary artery disease: the ABSORB trial. *EuroIntervention.* 2010;6:447-53.

5. Nobuyoshi M, Kimura T, Nosaka H, Mioka S, Ueno K, Yokoi H, Hamasaki N, Horiuchi H, Ohishi H. Restenosis after successful percutaneous transluminal coronary angioplasty: serial angiographic follow-up of 229 patients. *J Am Coll Cardiol.* 1988;12:616-23.

6. Serruys PW, Luijten HE, Beatt KJ, Geuskens R, de Feyter PJ, van den Brand M, Reiber JH, ten Katen HJ, van Es GA, Hugenholtz PG. Incidence of restenosis after successful coronary angioplasty: a time-related phenomenon. A quantitative angiographic study in 342 consecutive patients at 1, 2, 3, and 4 months. *Circulation.* 1988;77:361-71.

7. Onuma Y, Serruys PW, Gomez J, de Bruyne B, Dudek D, Thuesen L, Smits P, Chevalier B, McClean D, Koolen J, Windecker S, Whitbourn R, Meredith I, Garcia-Garcia H, Ormiston JA; ABSORB Cohort A and B investigators. Comparison of in vivo acute stent

recoil between the bioresorbable everolimus-eluting coronary scaffolds (revision 1.0 and 1.1) and the metallic everolimus-eluting stent. *Catheter Cardiovasc Interv.* 2011;78:3-12.

8. Ge J, Erbel R, Rupprecht HJ, Koch L, Kearney P, Gorge G, Haude M, Meyer J. Comparison of intravascular ultrasound and angiography in the assessment of myocardial bridging. *Circulation.* 1994;89:1725-32.

9. Mehran R, Dangas G, Abizaid AS, Mintz GS, Lansky AJ, Satler LF, Pichard AD, Kent KM, Stone GW, Leon MB. Angiographic patterns of in-stent restenosis: classification and implications for long-term outcome. *Circulation.* 1999;100:1872-8.

10. Tearney GJ, Regar E, Akasaka T, Adriaenssens T, Barlis P, Bezerra HG, Bouma B, Bruining N, Cho JM, Chowdhary S, Costa MA, de Silva R, Dijkstra J, Di Mario C, Dudek D, Falk E, Feldman MD, Fitzgerald P, Garcia-Garcia HM, Gonzalo N, Granada JF, Guagliumi G, Holm NR, Honda Y, Ikeno F, Kawasaki M, Kochman J, Koltowski L, Kubo T, Kume T, Kyono H, Lam CC, Lamouche G, Lee DP, Leon MB, Maehara A, Manfrini O, Mintz GS, Mizuno K, Morel MA, Nadkarni S, Okura H, Otake H, Pietrasik A, Prati F, Raber L, Radu MD, Rieber J, Riga M, Rollins A, Rosenberg M, Sirbu V, Serruys PW, Shimada K, Shinke T, Shite J, Siegel E, Sonoda S, Suter M, Takarada S, Tanaka A, Terashima M, Thim T, Uemura S, Ughi GJ, van Beusekom HM, van der Steen AF, van Es GA, van Soest G, Virmani R, Waxman S, Weissman NJ, Weisz G; International Working Group for Intravascular Optical Coherence Tomography (IWG-IVOCT). Consensus standards for acquisition, measurement, and reporting of intravascular optical coherence tomography studies: a report from the International Working Group for Intravascular Optical Coherence Tomography Standardization and Validation. *J Am Coll Cardiol.* 2012;59:1058-72.

11. Schwarz ER, Klues HG, vom Dahl J, Klein I, Krebs W, Hanrath P. Functional, angiographic and intracoronary Doppler flow characteristics in symptomatic patients with myocardial bridging: effect of short-term intravenous beta-blocker medication. *J Am Coll Cardiol.* 1996;27:1637-45.

12. Tandar A, Whisenant BK, Michaels AD. Stent fracture following stenting of a myocardial bridge: report of two cases. *Catheter Cardiovasc Interv.* 2008;71:191-6.

13. Arora P, Bhatia V, Parida AK, Kaul U. Myocardial bridge in association with fixed atherosclerotic lesions treated with drug-eluting stents: a follow-up report with quantitative coronary analysis. *Indian Heart J.* 2008;60:594-6.

14. Oberhauser JP, Hossainy S, Rapoza RJ. Design principles and performance of bioresorbable polymeric vascular scaffolds. *EuroIntervention.* 2009;5:F15-22.

15. Lee JH, Kim EM, Ahn KT, Kim MS, Kim KS, Jung IS, Park JH, Choi SW, Seong IW, Jeong JO. Significant left main coronary artery disease from iatrogenic dissection during coronary angiography. *Int J Cardiol.* 2010;138:e35-7.

16. Costa MA, Angiolillo DJ, Tannenbaum M, Driesman M, Chu A, Patterson J, Kuehl W, Battaglia J, Dabbons S, Shamoon F, Flieshman B, Niederman A, Bass TA; STLLR Investigators. Impact of stent deployment procedural factors on long-term effectiveness and safety of sirolimus-eluting stents (final results of the multicenter prospective STLLR trial). *Am J Cardiol.* 2008;101:1704-11.

17. Sabate M, Costa MA, Kozuma K, Kay IP, van der Giessen WJ, Coen VL, Ligthart JM, Serrano P, Levendag PC, Serruys PW. Geographic miss: a cause of treatment failure in radio-oncology applied to intracoronary radiation therapy. *Circulation.* 2000;101:2467-71.

18. Gogas BD, Onuma Y, van Geuns RJ, Serruys PW. The edge vascular response following implantation of a fully bioresorbable device: 'a miss always counts'. *Int J Cardiol.* 2012;158:455-7.

19. Ormiston JA, Stewart FM, Roche AH, Webber BJ, Whitlock RM, Webster MW. Late regression of the dilated site after coronary angioplasty: a 5-year quantitative angiographic study. *Circulation.* 1997;96:468-74.

20. Claessen BE, Beijk MA, Legrand V, Ruzyllo W, Manari A, Varenne O, Suttorp MJ, Tijssen JG, Miquel-Hebert K, Veldhof S, Henriques JP, Serruys PW, Piek JJ. Two-year clinical, angiographic, and intravascular ultrasound follow-up of the XIENCE V everolimus-eluting stent in the treatment of patients with de novo native coronary artery lesions: the SPIRIT II trial. *Circ Cardiovasc Interv.* 2009;2:339-47.

21. Garg S, Serruys P, Onuma Y, Dorange C, Veldhof S, Miquel-Hebert K, Sudhir K, Boland J, Huber K, Garcia E, te Riele JA; SPIRIT II Investigators. 3-year clinical follow-up of the XIENCE V everolimus-eluting coronary stent system in the treatment of patients with de novo coronary artery lesions: the SPIRIT II trial (Clinical Evaluation of the Xience V Everolimus Eluting Coronary Stent System in the Treatment of Patients with de novo Native Coronary Artery Lesions). *JACC Cardiovasc Interv.* 2009;2:1190-8.

22. Ruygrok PN, Desaga M, Van Den Branden F, Rasmussen K, Suryapranata H, Dorange C, Veldhof S, Serruys PW. One year clinical follow-up of the XIENCE V Everolimus-eluting stent system in the treatment of patients with de novo native coronary artery lesions: the SPIRIT II study. *EuroIntervention.* 2007;3:315-20.

23. Wakabayashi K, Mintz G, Delhaye C, Choi YJ, Doh JH, Ben-Dor I, Gaglia M Jr, Pakala R, Suddath W, Satler L, Kent K, Pichard A, Weissman N, Waksman R. In vivo virtual histology intravascular ultrasound comparison of neointimal hyperplasia within drug-eluting versus bare metal stents. *J Invasive Cardiol.* 2011;23:262-8.

24. Nasu K, Tsuchikane E, Katoh O, Vince DG, Margolis PM, Virmani R, Surmely JF, Ehara M, Kinoshita Y, Fujita H, Kimura M, Asakura K, Asakura Y, Matsubara T, Terashima M, Suzuki T. Impact of intramural thrombus in coronary arteries on the accuracy of tissue characterization by in vivo intravascular ultrasound radiofrequency data analysis. *Am J Cardiol.* 2008;101:1079-83.

25. Gonzalo N, Serruys PW, Okamura T, van Beusekom HM, Garcia-Garcia HM, van Soest G, van der Giessen W, Regar E. Optical coherence tomography patterns of stent restenosis. *Am Heart J.* 2009;158:284-93.

4.4 Edge vascular response at mid-term follow-up

Scaffold and edge vascular response following implantation of everolimus-eluting bioresorbable vascular scaffold: a 3-year serial optical coherence tomography study.

JACC Cardiovasc Interv. 2014;7(12):1361-9.
[Original research paper, Impact Factor: 7.35]

Zhang YJ, Iqbal J, Nakatani S, Bourantas CV, Campos CM, Ishibashi Y, Cho YK, Veldhof S, Wang J, Onuma Y, Garcia-Garcia HM, Dudek D, van Geuns RJ, Serruys PW; ABSORB Cohort B Study Investigators.

Scaffold and Edge Vascular Response Following Implantation of Everolimus-Eluting Bioresorbable Vascular Scaffold

A 3-Year Serial Optical Coherence Tomography Study

Yao-Jun Zhang, MD, PhD,*† Javaid Iqbal, PhD,*‡ Shimpei Nakatani, MD,* Christos V. Bourantas, MD, PhD,* Carlos M. Campos, MD,* Yuki Ishibashi, MD, PhD,* Yun-Kyeong Cho, MD,* Susan Veldhof, RN,§ Jin Wang,§ Yoshinobu Onuma, MD, PhD,* Hector M. Garcia-Garcia, MD, PhD,* Dariusz Dudek, MD,‖ Robert-Jan van Geuns, MD, PhD,* Patrick W. Serruys, MD, PhD,*¶
on behalf of the ABSORB Cohort B Study Investigators

ABSTRACT

OBJECTIVES This study sought to investigate the in-scaffold vascular response (SVR) and edge vascular response (EVR) after implantation of an everolimus-eluting bioresorbable scaffold (BRS) using serial optical coherence tomography (OCT) imaging.

BACKGROUND Although studies using intravascular ultrasound have evaluated the EVR in metal stents and BRSs, there is a lack of OCT-based SVR and EVR assessment after BRS implantation.

METHODS In the ABSORB Cohort B (ABSORB Clinical Investigation, Cohort B) study, 23 patients (23 lesions) in Cohort B1 and 17 patients (18 lesions) in Cohort B2 underwent truly serial OCT examinations at 3 different time points (Cohort B1: post-procedure, 6 months, and 2 years; B2: post-procedure, 1 year, and 3 years) after implantation of an 18-mm scaffold. A frame-by-frame OCT analysis was performed at the 5-mm proximal, 5-mm distal edge, and 2-mm in-scaffold margins, whereas the middle 14-mm in-scaffold segment was analyzed at 1-mm intervals.

RESULTS The in-scaffold mean luminal area significantly decreased from baseline to 6 months or 1 year (7.22 ± 1.24 mm^2 vs. 6.05 ± 1.38 mm^2 and 7.64 ± 1.19 mm^2 vs. 5.72 ± 0.89 mm^2, respectively; both $p < 0.01$), but remained unchanged from then onward. In Cohort B1, a significant increase in mean luminal area of the distal edge was observed (5.42 ± 1.81 mm^2 vs. 5.58 ± 1.53 mm^2; $p < 0.01$), whereas the mean luminal area of the proximal edge remained unchanged at 6 months. In Cohort B2, the mean luminal areas of the proximal and distal edges were significantly smaller than post-procedure measurements at 3 years. The mean luminal area loss at both edges was significantly less than the mean luminal area loss of the in-scaffold segment at both 6-month and 2-year follow-up in Cohort B1 or at 1 year and 3 years in Cohort B2.

CONCLUSIONS This OCT-based serial EVR and SVR evaluation of the Absorb Bioresorbable Vascular Scaffold (Abbott Vascular, Santa Clara, California) showed less luminal loss at the edges than luminal loss within the scaffold. The luminal reduction of both edges is not a nosologic entity, but an EVR in continuity with the SVR, extending from the in-scaffold margin to both edges. (ABSORB Clinical Investigation, Cohort B [ABSORB B]; NCT00856856) (J Am Coll Cardiol Intv 2014;7:1361–9) © 2014 by the American College of Cardiology Foundation.

From the *Thoraxcenter, Erasmus Medical Center, Rotterdam, the Netherlands; †Nanjing First Hospital, Nanjing Medical University, Nanjing, China; ‡Department of Cardiovascular Science, University of Sheffield, Sheffield, United Kingdom; §Abbott Vascular, Diegem, Belgium; ‖Jagiellonian University, Krakow, Poland; and the ¶International Centre for Circulatory Health, NHLI, Imperial College London, London, United Kingdom. This study was sponsored by Abbott Vascular, Santa Clara, California. Dr. Geuns has received speaker honoraria from Abbott Vascular. S. Veldhof and J. Wang are full-time employees of Abbott Vascular. All other authors have reported that they have no relationships relevant to the contents of this paper to disclose.

Manuscript received February 3, 2014; revised manuscript received April 30, 2014, accepted June 19, 2014.

ABBREVIATIONS AND ACRONYMS

BMS = bare-metal stent(s)

BRS = bioresorbable scaffold(s)

BVS = bioresorbable vascular scaffold(s)

CI = confidence interval

DES = drug-eluting stent(s)

EVR = edge vascular response

IVUS = intravascular ultrasound

OCT = optical coherence tomography

SVR = in-scaffold vascular response

Restenosis in the segments adjacent to the proximal and distal edges of a permanent or transient coronary implant has been a concern for many years (1–5). In the metal drug-eluting stent (DES) era, studies demonstrated effective inhibition of neointimal hyperplasia reducing the risk of edge restenosis and the need for repeat intervention on the edges (6,7). Our group, using intravascular ultrasound (IVUS) imaging, previously investigated the edge vascular response (EVR) after implantation of fully bioresorbable scaffold (BRS) and reported a luminal area reduction at the proximal edge at 2-year follow-up (8).

SEE PAGE 1370

Optical coherence tomography (OCT) offers substantially superior resolution that allows a precise evaluation of luminal dimensions, edge dissections, and relevant vessel wall pathology (9–12). To date, no study has used serial OCT imaging to examine the EVR and its relationship with in-scaffold vascular response (SVR) at 3-year follow-up after BRS implantation. We hypothesized that the local changes in luminal dimensions at the edge of the Absorb Bioresorbable Vascular Scaffold (Absorb BVS) (Abbott Vascular, Santa Clara, California) are simply the extension of the changes in luminal dimension observed at the in-scaffold margins and not a separate pathological entity. This study aimed to evaluate the OCT-based SVR and EVR after Absorb BVS (Abbott Vascular) implantation in the ABSORB Cohort B (ABSORB Clinical Investigation, Cohort B) trial.

METHODS

STUDY DESIGN AND POPULATION. The ABSORB Cohort B trial was described in detail previously (12). Briefly, this was a nonrandomized, multicenter, single-arm trial that enrolled 101 patients (102 lesions) treated with the second-generation Absorb BVS (Abbott Vascular) (A complete list of the members of the ABSORB Cohort B Study appears in the Online Appendix). The participants were divided into 2 groups according to the pre-defined invasive follow-up: Cohort B1 at post-procedure, 6 months, and 2 years and Cohort B2 at post-procedure, 1 year, and 3 years. OCT was an optional examination conducted at selected centers with OCT capability and previous experience. The registry was approved by the ethics committee at each participating institution, and each patient gave written informed consent before inclusion.

STUDY DEVICE AND TREATMENT PROCEDURE. The Absorb BVS (Abbott Vascular) is a balloon-expandable scaffold consisting of a polymer backbone of poly-L-lactide coated with a thin layer of a 1:1

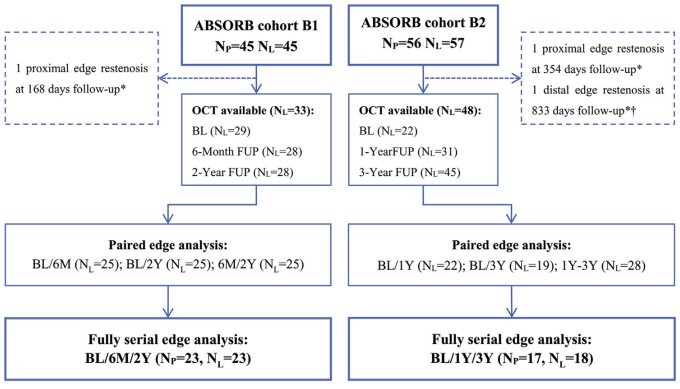

FIGURE 1 Flowchart of the Patients Included in the Current Analysis

*Edge restenoses in Cohort B that mandated repeat revascularization. †This case had in-segment restenosis at the distal margin of the scaffolded segment and distal edge. 1Y = 1 year; 2Y = 2 years; 3Y = 3 years; BL = baseline; FUP = follow-up; N_L = number of lesions; N_P = number of patients; OCT = optical coherent tomography.

mixture of amorphous poly-D,L-lactide polymer and the antiproliferative drug everolimus to form a drug-eluting coating matrix that contains 100 μg of everolimus per square centimeter of scaffold (13-15).

Target lesions were treated with routine interventional techniques, and pre-dilation was mandatory. The Absorb BVS (Abbott Vascular) inflation pressure did not exceed 16 atm, the burst pressure according to the product chart. Post-dilation with a balloon shorter than the implanted scaffold was at the discretion of the operator. OCT imaging was performed after optimal Absorb BVS (Abbott Vascular) implantation and at follow-up.

OCT ACQUISITIONS AND DATA ANALYSIS. OCT acquisitions were performed using 3 different commercially available systems: the M2 and M3 Time-Domain Systems and the C7XR Fourier-Domain System (LightLab Imaging, Westford, Massachusetts). OCT images were acquired at frame rates of 15.6, 20, and 100 frames/s with pullback speeds of 2, 3, and 20 mm/s in the M2 Time-Domain System (n = 11), M3 Time-Domain System (n = 11), and C7XR Fourier-Domain System (n = 101) (LightLab Imaging), respectively. All recordings were performed according to the recommended procedure for each OCT system (16). The OCT images acquired post-procedure and at follow-up were analyzed off-line, using proprietary LightLab Imaging software (St. Jude Medical Inc., St. Paul, Minnesota). Truly serial OCT data were defined as the patient undergoing OCT examinations at all 3 time points.

The SVR analysis included all 18-mm scaffold segments, analyzed at 1-mm intervals by an independent core laboratory (Cardialysis, Rotterdam, the Netherlands). The EVR analysis included the 5-mm proximal and distal edges, analyzed in a frame-by-frame fashion (128-μm interval for the M2, 150-μm interval for the M3, 200-μm interval for the C7). In addition, we performed a frame-by-frame analysis of changes in the lumen area at the 2-mm margins of the scaffold to explore the relationship between in-scaffold margins and the edges. The scaffold edge was defined as the first cross section exhibiting visible struts in a circumference <270° (10). If the 5-mm edge had a side branch with a vessel diameter ≥1.5 mm, the analysis included only frames between the scaffold's margin and the ostium of the side branch. If the vessel diameter of the side branch was <1.5 mm, only the frames at the ostium of the side branch were excluded. In addition, we excluded the cases that needed a bailout stent as well as the frames with insufficient assessment of the entire luminal circumference due to inadequate blood clearance or incomplete scanning perimeter. Edge dissection was defined as disruption of the endoluminal vessel surface at the proximal and distal edges (17).

TABLE 1 Baseline and Lesion Characteristics of Fully Serial OCT Available Patients

	Cohort B1 (n = 23)	Cohort B2 (n = 17)	Difference (95% CI)
Age, yrs	63.4 ± 9.8	61.6 ± 8.0	1.8 (−3.9 to 7.5)
Male	82.6	64.7	17.9 (−8.8 to 43.5)
Diabetes mellitus	4.3	5.9	−1.5% (−22.9 to 15.8)
Hypertension	52.2	70.6	−18.4 (−43.5 to 11.7)
Hypercholesterolemia	95.7	76.5	19.2 (−2.6 to 43.2)
Current smoker	21.7	29.4	−7.7% (−34.3 to 18.2)
Family history of CAD	52.2	66.7	−14.5% (−40.9 to 16.6)
Previous MI	43.5	12.5	31.0 (1.5-52.7)
History of PCI	26.1	11.8	14.3 (−12.0 to 36.4)
Unstable angina	17.4	5.9	11.5 (−12.0 to 31.8)
Target-lesion vessel, %			
LAD	26.1	11.1	15.0 (−10.6 to 36.9)
LCX	26.1	33.3	−7.3 (−33.9 to 19.3)
RCA	47.8	55.6	−7.7 (−35.0 to 21.4)
RVD before intervention	2.59 ± 0.40	2.57 ± 0.26	0.02 (−0.19 to 0.23)
Maximal balloon artery ratio	1.01 ± 0.15	1.05 ± 0.11	−0.04 (−0.12 to 0.05)
Maximal inflation pressure	18.4 ± 3.0	16.6 ± 5.3	1.8 (−1.1 to 4.7)

Values are mean ± SD or %.

CAD = coronary artery disease; CI = confidence interval; LAD = left anterior descending artery; LCX = left circumflex artery; MI = myocardial infarction; OCT = optical coherent tomography; PCI = percutaneous coronary intervention; RCA = right coronary artery; RVD = reference vessel diameter.

STATISTICAL ANALYSIS. Continuous variables are presented as mean ± SD or median (interquartile range). Binary variables are presented as count and percent. Absolute difference and 95% confidence interval (CI) of baseline characteristics was generated by normal approximation for continuous variables and Newcombe score method for binary variables. A paired *t* test or Wilcoxon signed rank test was used to compare SVR and EVR within groups at different time points. The normality of the data was determined with the D'Agostino Pearson test and verified by histogram plots. To evaluate the relationship of the lumen area

TABLE 2 In-Scaffold Vascular Response Analysis

	In-Scaffold Vascular Response (18 mm)			
Luminal Area Changes	Distal Subsegment (6 mm)	Middle Subsegment (6 mm)	Proximal Subsegment (6 mm)	p Value
Cohort B1				
6 months vs. baseline	−1.21 ± 0.79	−0.98 ± 0.68	−1.34 ± 0.79	0.27
2 yrs vs. 6 months	−0.44 ± 0.91	0.05 ± 1.46	0.12 ± 1.29	0.25
2 yrs vs. baseline	−1.65 ± 0.99	−0.94 ± 1.62	−1.22 ± 1.24	0.18
Cohort B2				
1 yr vs. baseline	−1.91 ± 1.24	−1.77 ± 1.10	−2.06 ± 0.87	0.73
3 yrs vs. 1 yr	−0.18 ± 0.93	0.26 ± 0.84	0.05 ± 0.72	0.29
3 yrs vs. baseline	−2.10 ± 1.59	−1.51 ± 1.23	−2.00 ± 1.03	0.36

Values are mean ± SD.

TABLE 3 Edge Vascular Response Analysis

Luminal Area	Cohort B1		Cohort B2	
Distal edge, 5 mm	6M	2Y	1Y	3Y
Baseline	5.42 ± 1.81		5.78 ± 2.04	
FUP (6M/2Y, 1Y/3Y)	5.58 ± 1.53	5.26 ± 1.40	5.63 ± 1.45	5.29 ± 1.77
Difference	0.19 ± 1.05	−0.16 ± 1.24	−0.14 ± 1.25	−0.49 ± 1.17
p value (BL vs. FUP)	<0.01	0.03	0.11	<0.01
Proximal edge, 5 mm	6M	2Y	1Y	3Y
Baseline	6.84 ± 2.86		7.27 ± 2.01	
FUP (6M/2Y, 1Y/3Y)	6.76 ± 2.63	6.75 ± 2.60	6.66 ± 1.74	6.51 ± 1.63
Difference	−0.07 ± 1.14	−0.08 ± 1.13	−0.61 ± 1.33	−0.76 ± 1.57
p value (BL vs. FUP)	0.31	0.25	<0.01	<0.01

Values are mean ± SD.
6M = 6 months; 1Y = 1 year; 2Y = 2 years; 3Y = 3 years; BL = baseline; FUP = follow-up.

within different segments of the scaffold (3 subsegments: proximal, middle, and distal), multilevel generalized estimating equation model fitting, with the mean lumen area as the response and the subsegments and the follow-up visits as categorical variables, were nested within each patient. Multiple comparisons were conducted without adjustment. Statistical significance was assumed at $p < 0.05$. All statistical analyses were performed with SAS version 9.1.3 (SAS Institute Inc., Cary, North Carolina).

RESULTS

STUDY POPULATION AND OCT ACQUISITION. A flowchart of the subjects included in the current

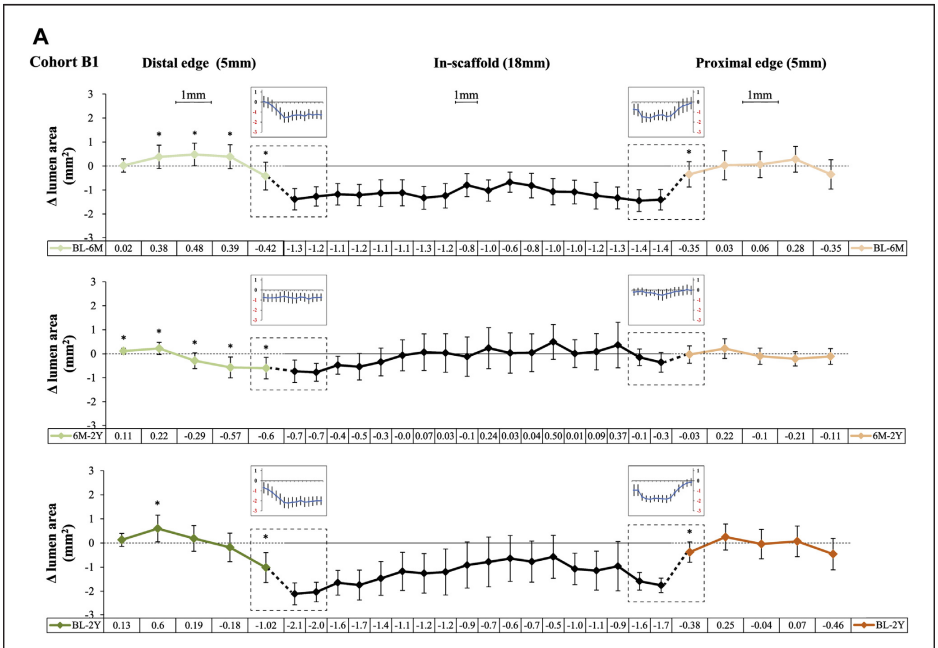

FIGURE 2 Scaffold and Its EVR

The images present the global mean luminal area changes including in-scaffold, 5-mm proximal and distal edges at follow-up. **(A)** Cohort B1. **(B)** Cohort B2. Mean luminal area of the 18-mm in-scaffold segment significantly decreased from baseline to 6-month or 1-year follow-up, but no change from 6 months to 2 years or 1 year to 3 years. The EVR analysis showed an increase in mean luminal area at the distal edge at 6 months and a reduction at both the proximal and distal edges at long-term follow-up. The transitional regions with a 200-μm interval analysis are presented in the embedded panels, indicating a continuous pattern of luminal reduction extending from the in-scaffold margins to the first 1 mm of proximal and distal edges. *Indicates a significant change in mean luminal area in each 1-mm interval at the proximal or distal edge ($p < 0.05$). EVR = edge vascular response; other abbreviations as in Figure 1.

analysis is shown in Figure 1. A total of 183 OCT pullbacks at baseline and follow-up were performed in 80 patients (81 lesions). Twenty-three patients (23 lesions) in Cohort B1 and 17 patients (18 lesions) in Cohort B2 had truly serial OCT examinations at 3 different time points. Three patients who had a target lesion revascularization did not undergo OCT examination before the reintervention.

Baseline characteristics of the patients with truly serial OCT pullbacks are shown in Table 1. There was a greater prevalence of patients with previous myocardial infarction (43.5% vs. 12.5%; difference: 31.0%; 95% CI: 1.5% to 52.7%) and lesions in the left anterior descending artery in Cohort B1 (26.1% vs. 11.1%; difference: 15.0%; 95% CI: −10.6% to 36.9%) than in Cohort B2.

SVR ANALYSIS. In Cohort B1, there was a significant reduction in mean in-scaffold luminal area at 6 months (7.22 ± 1.24 mm^2 vs. 6.05 ± 1.38 mm^2, $p < 0.01$). However, the mean luminal area remained unchanged from 6 months to 2 years (5.97 ± 1.61 mm^2, $p = 0.75$). Similarly, in Cohort B2, there was a significant reduction in mean in-scaffold luminal area from baseline to 1 year (7.64 ± 1.19 mm^2 vs. 5.72 ± 0.89 mm^2, $p < 0.01$), but no change from 1 year to 3 years (5.81 ± 1.29 mm^2, $p = 0.60$).

At 3-year follow-up, there was no significant difference in behavior of the 3 in-scaffold subsegments (proximal, middle, and distal) (Table 2). The mean luminal area of proximal and middle subsegments numerically increased from 6 months to 2 years or 1 year to 3 years (B1: 0.12 ± 1.29 mm^2, 0.05 ± 1.46 mm^2; B2: 0.05 ± 0.72 mm^2, 0.26 ± 0.84 mm^2; respectively), whereas the mean luminal area of the distal segment numerically decreased (B1: −0.44 ± 0.91 mm^2, −0.18 ± 0.93 mm^2).

EVR ANALYSIS. The changes in mean luminal area of the proximal and distal edges at different time points are shown in Table 3. In Cohort B1, a significant increase in mean luminal area at the distal edge (5-mm

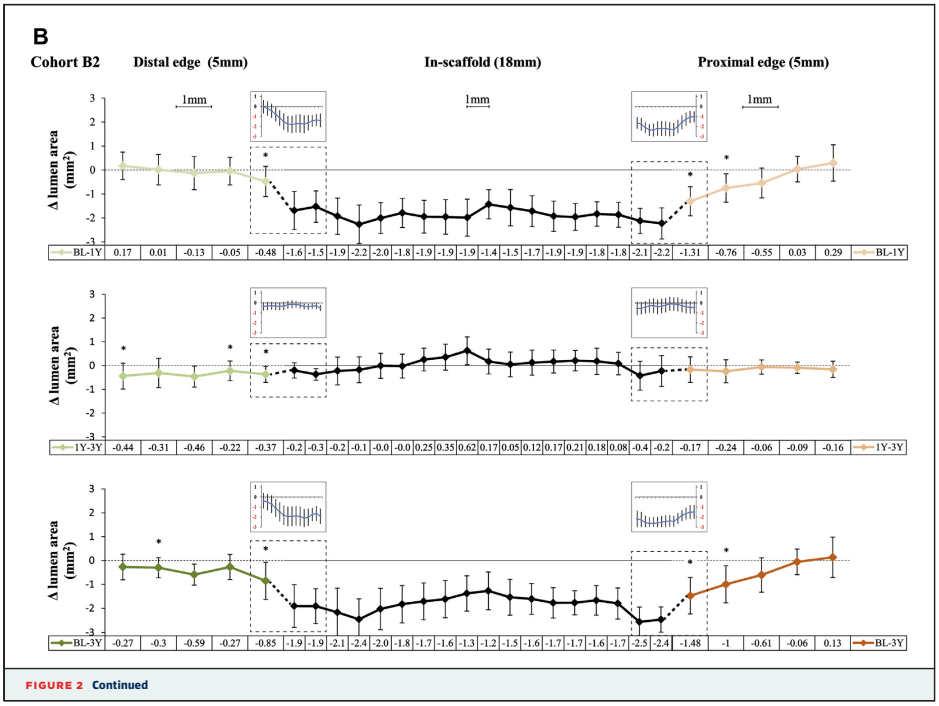

FIGURE 2 Continued

TABLE 4 Overall Vascular Response Analysis

Luminal Area Changes	Distal Edge, 5 mm	In-Scaffold, 18 mm	Proximal Edge, 5 mm	p Value (Distal vs. In-Scaffold)	p Value (Proximal vs. In-Scaffold)
Cohort B1					
6 months vs. baseline, mm^2	0.16 ± 1.05	−1.18 ± 1.06	−0.07 ± 1.14	<0.01	<0.01
2 years vs. baseline, mm^2	−0.16 ± 1.24	−1.23 ± 1.64	−0.08 ± 1.13	<0.01	<0.01
Cohort B2					
1 year vs. baseline, mm^2	−0.14 ± 1.25	−1.88 ± 1.29	−0.61 ± 1.33	<0.01	<0.01
3 years vs. baseline, mm^2	−0.49 ± 1.17	−1.85 ± 1.50	−0.76 ± 1.56	<0.01	<0.01

Values are mean ± SD.

segment) was observed at 6 months (5.42 ± 1.81 mm^2 vs. 5.58 ± 1.53 mm^2, $p < 0.01$) (Figure 2A), whereas at the proximal edge (5-mm segment), the mean luminal area remained unchanged (6.84 ± 2.86 mm^2 vs. 6.76 ± 2.63 mm^2, $p = 0.31$). In Cohort B2, the mean luminal area at the distal edge was unchanged at 1-year follow-up (5.78 ± 1.45 mm^2 vs. 5.63 ± 1.45 mm^2, $p = 0.11$) (Figure 2B). At 3-year follow-up, a significant reduction in the mean luminal area was observed at both edges (distal: 5.78 ± 2.04 mm^2 vs. 5.29 ± 1.77 mm^2; proximal: 7.27 ± 2.01 mm^2 vs. 6.51 ± 1.63 mm^2; both $p < 0.01$).

PATTERN OF CHANGES IN LUMINAL DIMENSIONS FROM IN-SCAFFOLD MARGINS TO EDGES. At all time points, reduction in the luminal area was observed in the first 1 mm of the edges, both proximally and distally, indicating a continuous pattern of luminal reduction extending from the scaffold margin to the proximal or distal edge (Figure 2). The overall reduction in mean luminal area at both edges was significantly less than the in-scaffold segments (all $p < 0.05$) (Table 4).

EDGE RESTENOSIS, EDGE DISSECTION, AND STENT THROMBOSIS. Of 101 patients in the entire ABSORB Cohort B trial, 2 patients (2.0%) had proximal edge restenosis and 1 patient (1%) had distal edge restenosis. Patients with the proximal edge restenosis had a repeat revascularization at day 168 and day 383, respectively. The patient with the distal edge restenosis had a repeat revascularization at day 833. These 3 patients were treated without previous OCT to examine edge restenosis. In 2 of these patients, a geographic miss (injured or diseased segment not covered by the device, balloon-artery ratio <0.9 or >1.3) was previously reported (15).

In total, 12 proximal (24%) and 21 distal (42%) edge dissection flaps were observed post-procedure. In the truly serial OCT analysis, 9 proximal (21%) and 16 distal (38%) edge dissection flaps were identified post-procedure, which decreased to 1 proximal (2%) and 2 distal (5%) at 6 months, only proximal 1 (2%) at 1-year follow-up, and none at 2- and 3-year follow-up (Figure 3). No scaffold thrombosis was reported in this trial.

DISCUSSION

This study, for the first time, reported OCT-derived EVR and SVR evaluation after Absorb BVS (Abbott Vascular) implantation at mid- and long-term follow-up. The primary findings are the following: 1) an increase in mean luminal area at the distal edge at 6 months; 2) a reduction in the mean luminal area at both edges at long-term (2- or 3-year) follow-up; 3) reduction in luminal area at the in-scaffold segment from baseline to 6 or 12 months, but no change from then onward. A uniform pattern of luminal reduction extending from the in-scaffold margins to the first 1-mm of the proximal and distal edges of the scaffold is also demonstrated, suggesting that the edge changes in luminal dimension is not a nosologic entity, but a progressive transition in luminal dimension from the in-scaffold margin to the edges.

EVOLUTION OF DEVICES AND EVR. The introduction of coronary metal stents has markedly reduced the risk of restenosis (14). The EVR in the era of bare metal stents (BMS) was mainly due to an increase in plaque and medial area and reduction in luminal area within the first 1 to 2 mm of the device (15,18). Radioactive stents, developed to reduce restenosis, were proved to be safe in initial studies (19,20), but led to a profound edge effect defined angiographically as a diameter stenosis of >50% at the proximal and distal stent edges (2,3). In the DES era, the EVR can also be influenced by the drug and polymer incorporated into the stent (21). A high degree of variability in EVR was identified among the different DES types (5). In the TAXUS II trial, paired-edge analyses with IVUS showed a significant increase in luminal area at the distal edge of paclitaxel-eluting stent compared with the BMS at 6 months, whereas a significant decrease in the luminal area was observed at the proximal edge (22). The beneficial effect of the paclitaxel-eluting stent was most notable in the area closest to its distal edge (23). Trials with the Endeavor stent (Medtronic, Minneapolis, Minnesota) demonstrated a reduction in the luminal area at both the proximal and distal edges, mainly due to negative remodeling, plaque growth, and rapid elution of zotarolimus (24,25). However, serial IVUS

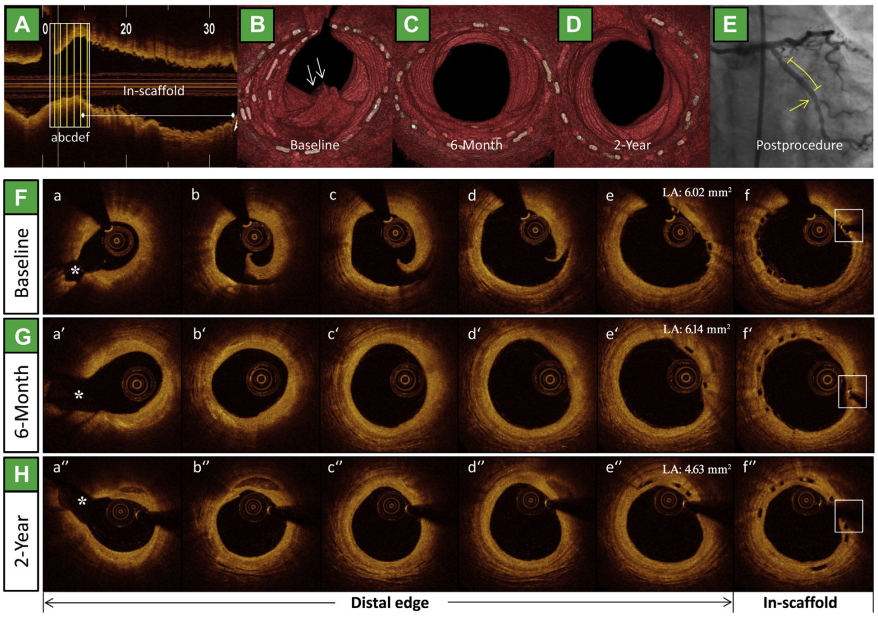

FIGURE 3 **Dissections at the Distal Edge**

(A) Longitudinal view of patients with distal dissection. **(B)** Three-dimensional reconstruction of optical coherence tomography pullbacks show that dissection is visible at distal edge **(double white arrow)**. **(C, D)** Three-dimensional reconstruction at 6-month and 2-year follow-up showed that dissection has healed. **(E)** No distal edge dissection **(arrow)** is visible from the post-procedure angiograms. The **curved line** indicates the scaffolded segment. **(F)** Dissection extends into at least the media from multiple cross-sectional views. **(G)** Increased luminal area without visible dissection at 6-month follow-up. **(H)** The luminal area decreased with detected calcific tissue at 2-year follow-up. LA = lumen area. *Indicates a side branch.

examination in sirolimus- and everolimus-eluting stents revealed an enlargement of the luminal area at the distal edge (26-28). Our results are in agreement with those of previous reports on metal everolimus-eluting stents (28), with a significant increase in the distal-edge luminal area and a nonsignificant decrease in the proximal edge at 6-month follow-up. The difference in behavior of the 2 edges can partially be explained by downstream diffusion of antiproliferative drug to the distal edge (21).

IN-DEPTH ANALYSIS OF EVR AND SVR. IVUS imaging has contributed to our understanding of EVR after BRS implantation. However, this approach has inherent limitations (e.g., poor resolution, cardiac motion artifacts) and makes it difficult to assess EVR precisely (29-31). The present study, performed with OCT, for the first time evaluated EVR in frame-by-frame (≤200 μm) fashion after Absorb BVS (Abbott Vascular) implantation and provided additional insights into the changes in luminal dimensions at the proximal and distal edges.

Our previous IVUS-based study demonstrated a nonsignificant reduction in luminal area at the distal edge at 6 months (32); however, accurate assessment with OCT has documented it to be a significant change. By the virtue of the high resolution of OCT, we also demonstrated that the pattern of in-scaffold luminal reduction extended progressively from the in-scaffold margins to the contiguous first 1 mm of the edges outside the scaffold, both proximally and distally, presumably related to neointimal

hyperplasia or neoatherosclerosis (33). In addition, the discrepancy with previous IVUS observations can also be attributed to the nonserial nature of the data in previous IVUS studies. Thus, we believe that OCT-based EVR evaluation with truly serial data can provide more reliable and precise information.

Finally, the SVR analysis presented here is consistent with the previous final 3-year report of the ABSORB Cohort B study (32). The analysis of changes in mean luminal area of different in-scaffold subsegments using a generalized estimating equation model did not show any significant difference in vascular response; however, there was a numerical increase in luminal area in the middle subsegment from 1 year to 3 years. Preclinical studies of the BRS have demonstrated that late luminal positive remodeling was observed at late follow-up (34). It will be interesting to re-evaluate this subsegment behavior at 5-year follow-up of the ABSORB Cohort B study.

CLINICAL IMPLICATIONS. The Absorb BVS (Abbott Vascular) does not produce a pathological edge effect that was seen with BMS or notoriously with radioactive stents. The stable luminal area after 6 to 12 months without late catch-up is a potential superiority of BRS over metal DES. In the ABSORB Cohort B trial, there were only 3 cases of edge restenosis, and 2 of them could be attributed to longitudinal geographic miss (13). Edge dissections, considered to be a trigger for early stent thrombosis, were often detected by post-procedure OCT in the present study; however, most of these dissections healed within 6 months, without any clinical adverse events.

STUDY LIMITATIONS. First, the number of patients in the current study is small; however, it is the largest and longest series available to date, and due to the truly serial OCT data, potential patient-to-patient variability was minimized. Second, OCT examination was not available for patients undergoing repeat revascularization, and, therefore, we decided to exclude these patients from this analysis. Finally, OCT cannot visualize external elastic lamina due to its low penetration, and, hence, changes in plaque media or vessel area cannot be assessed adequately.

CONCLUSIONS

In this study, truly serial OCT imaging was used to assess the EVR and SVR after Absorb BVS (Abbott Vascular) implantation up to 3-year follow-up. We found a significant increase in the luminal area at the distal edge at 6-month follow-up. However, at longer term (1, 2, and 3 years), the luminal area decreased at both edges, resulting in a repeat revascularization rate of 3%. In-scaffold luminal area significantly decreased from post-procedure to 6 months or 1 year, but remained unchanged from then onward. A continuous pattern of luminal loss extending from the in-scaffold margins to the first 1-mm of scaffold edges has suggested that the changes in luminal area at the edge of a BRS is not a nosologic entity in itself, but an extension of the in-scaffold response to the edges.

REPRINT REQUESTS AND CORRESPONDENCE: Dr. Patrick W. Serruys, International Centre for Circulatory Health, NHLI, Imperial College London, Royal Brompton Campus, London SW7 2AZ, United Kingdom. E-mail: p.w.j.c.serruys@gmail.com.

REFERENCES

1. Albiero R, Nishida T, Adamian M, et al. Edge restenosis after implantation of high activity (32)P radioactive beta-emitting stents. Circulation 2000;101:2454–7.

2. van Der Giessen WJ, Regar E, Harteveld MS, et al. "Edge Effect" of (32)p radioactive stents is caused by the combination of chronic stent injury and radioactive dose falloff. Circulation 2001;104:2236–41.

3. Serruys PW, Kay IP. I like the candy, I hate the wrapper: the (32)P radioactive stent. Circulation 2000;101:3–7.

4. Serruys PW, Ormiston JA, Sianos G, et al. Actinomycin-eluting stent for coronary revascularization: a randomized feasibility and safety study: the ACTION trial. J Am Coll Cardiol 2004;44:1363–7.

5. Gogas BD, Garcia-Garcia HM, Onuma Y, et al. Edge vascular response after percutaneous coronary intervention: an intracoronary ultrasound and optical coherence tomography appraisal: from radioactive platforms to first- and second-generation drug-eluting stents and bioresorbable scaffolds. J Am Coll Cardiol Intv 2013;6:211–21.

6. Serruys PW, Silber S, Garg S, et al. Comparison of zotarolimus-eluting and everolimus-eluting coronary stents. N Engl J Med 2010;363:136–46.

7. Windecker S, Serruys PW, Wandel S, et al. Biolimus-eluting stent with biodegradable polymer versus sirolimus-eluting stent with durable polymer for coronary revascularisation (LEADERS): a randomised non-inferiority trial. Lancet 2008;372:1163–73.

8. Gogas BD, Bourantas CV, Garcia-Garcia HM, et al. The edge vascular response following implantation of the Absorb everolimus-eluting bioresorbable vascular scaffold and the XIENCE V metallic everolimus-eluting stent. First serial follow-up assessment at six months and two years: insights from the first-in-man ABSORB Cohort B and SPIRIT II trials. EuroIntervention 2013;9:709–20.

9. Ormiston JA, Serruys PW, Onuma Y, et al. First serial assessment at 6 months and 2 years of the second generation of absorb everolimus-eluting bioresorbable vascular scaffold: a multi-imaging modality study. Circ Cardiovasc Interv 2012;5:620–32.

10. Gogas BD, Onuma Y, van Geuns RJ, Serruys PW. The edge vascular response following implantation of a fully bioresorbable device: 'a miss always counts'. Int J Cardiol 2012;158:455–7.

11. Gogas BD, Muramatsu T, Garcia-Garcia HM, et al. In vivo three dimensional optical coherence tomography. A novel imaging modality to visualize the edge vascular response. Int J Cardiol 2013;164:e35–7.

12. Serruys PW, Onuma Y, Dudek D, et al. Evaluation of the second generation of a bioresorbable everolimus-eluting vascular scaffold for the treatment of de novo coronary artery stenosis: 12-month clinical and imaging outcomes. J Am Coll Cardiol 2011;58:1578–88.

13. Nakatani S, Onuma Y, Ishibashi Y, et al. Early (before 6 months), late (6-12 months) and very late (after 12 months) angiographic scaffold restenosis in the ABSORB Cohort B trial. EuroIntervention 2014 Feb 27 [E-pub ahead of print].

14. Iqbal J, Gunn J, Serruys PW. Coronary stents: historical development, current status and future directions. Br Med Bull 2013;106:193–211.

15. Weissman NJ, Wilensky RL, Tanguay JF, et al. Extent and distribution of in-stent intimal hyperplasia and edge effect in a non-radiation stent population. Am J Cardiol 2001;88:248–52.

16. Tearney GJ, Regar E, Akasaka T, et al. Consensus standards for acquisition, measurement, and reporting of intravascular optical coherence tomography studies: a report from the International Working Group for Intravascular Optical Coherence Tomography Standardization and Validation. J Am Coll Cardiol 2012;59:1058–72.

17. Muramatsu T, Garcia-Garcia HM, Onuma Y, et al. Intimal flaps detected by optical frequency domain imaging in the proximal segments of native coronary arteries. Circ J 2013;77:2327–33.

18. Popma JJ, Leon MB, Moses JW, et al. Quantitative assessment of angiographic restenosis after sirolimus-eluting stent implantation in native coronary arteries. Circulation 2004;110:3773–80.

19. King SB 3rd, Williams DO, Chougule P, et al. Endovascular beta-radiation to reduce restenosis after coronary balloon angioplasty: results of the beta energy restenosis trial (BERT). Circulation 1998;97:2025–30.

20. Condado JA, Waksman R, Gurdiel O, et al. Long-term angiographic and clinical outcome after percutaneous transluminal coronary angioplasty and intracoronary radiation therapy in humans. Circulation 1997;96:727–32.

21. Wakabayashi K, Waksman R, Weissman NJ. Edge effect from drug-eluting stents as assessed with serial intravascular ultrasound: a systematic review. Circ Cardiovasc Interv 2012;5:305–11.

22. Serruys PW, Degertekin M, Tanabe K, et al. Vascular responses at proximal and distal edges of paclitaxel-eluting stents: serial intravascular ultrasound analysis from the TAXUS II trial. Circulation 2004;109:627–33.

23. Weissman NJ, Ellis SG, Grube E, et al. Effect of the polymer-based, paclitaxel-eluting TAXUS Express stent on vascular tissue responses: a volumetric intravascular ultrasound integrated analysis from the TAXUS IV, V, and VI trials. Eur Heart J 2007;28:1574–82.

24. Sakurai R, Hongo Y, Yamasaki M, et al. Detailed intravascular ultrasound analysis of Zotarolimus-eluting phosphorylcholine-coated cobalt-chromium alloy stent in de novo coronary lesions (results from the ENDEAVOR II trial). Am J Cardiol 2007;100:818–23.

25. Waseda K, Miyazawa A, Ako J, et al. Intravascular ultrasound results from the ENDEAVOR IV trial: randomized comparison between zotarolimus- and paclitaxel-eluting stents in patients with coronary artery disease. J Am Coll Cardiol Intv 2009;2:779–84.

26. Jimenez-Quevedo P, Sabate M, Angiolillo DJ, et al. Vascular effects of sirolimus-eluting versus bare-metal stents in diabetic patients: three-dimensional ultrasound results of the Diabetes and Sirolimus-Eluting Stent (DIABETES) Trial. J Am Coll Cardiol 2006;47:2172–9.

27. Jensen LO, Maeng M, Mintz GS, et al. Serial intravascular ultrasound analysis of peri-stent remodeling and proximal and distal edge effects after sirolimus-eluting or paclitaxel-eluting stent implantation in patients with diabetes mellitus. Am J Cardiol 2009;103:1083–8.

28. Shimohama T, Ako J, Yamasaki M, et al. SPIRIT III JAPAN versus SPIRIT III USA: a comparative intravascular ultrasound analysis of the everolimus-eluting stent. Am J Cardiol 2010;106:13–7.

29. Arbab-Zadeh A, DeMaria AN, Penny WF, Russo RJ, Kimura BJ, Bhargava V. Axial movement of the intravascular ultrasound probe during the cardiac cycle: implications for three-dimensional reconstruction and measurements of coronary dimensions. Am Heart J 1999;138:865–72.

30. von BC, de Vrey EA, Mintz GS, et al. ECG-gated three-dimensional intravascular ultrasound: feasibility and reproducibility of the automated analysis of coronary lumen and atherosclerotic plaque dimensions in humans. Circulation 1997;96:2944–52.

31. Bruining N, von BC, de Feyter PJ, et al. ECG-gated versus nongated three-dimensional intracoronary ultrasound analysis: implications for volumetric measurements. Cathet Cardiovasc Diagn 1998;43:254–60.

32. Gogas BD, Serruys PW, Diletti R, et al. Vascular response of the segments adjacent to the proximal and distal edges of the ABSORB everolimus-eluting bioresorbable vascular scaffold: 6-month and 1-year follow-up assessment: a virtual histology intravascular ultrasound study from the first-in-man ABSORB cohort B trial. J Am Coll Cardiol Intv 2012;5:656–65.

33. Serruys PW, Onuma Y, Garcia-Garcia HM, et al. Dynamics of vessel wall changes following the implantation of the Absorb everolimus-eluting bioresorbable vascular scaffold: a multi-imaging modality study at 6, 12, 24 and 36 months. EuroIntervention 2014;9:1271–84.

34. Strandberg E, Zeltinger J, Schulz DG, Kaluza GL. Late positive remodeling and late lumen gain contribute to vascular restoration by a non-drug eluting bioresorbable scaffold: a four-year intravascular ultrasound study in normal porcine coronary arteries. Circ Cardiovasc Interv 2012;5:39–46.

KEY WORDS **Absorb BVS, bioresorbable scaffold, edge vascular response, in-scaffold vascular response, optical coherence tomography**

APPENDIX **For a complete list of the ABSORB Cohort B study investigators, please see the online version of this article.**

4.5 Edge vascular response at long-term follow-up

Edge Vascular Response After Resorption of the Everolimus-Eluting Bioresorbable Vascular Scaffold: A 5-Year Serial Optical Coherence Tomography Study

Circ J. 2016 Mar 3. [Epub ahead of print]
[Original research paper, Impact Factor : 3.94]

Tateishi H, Suwannasom P, Sotomi Y, Nakatani S, Ishibashi Y, Tenekecioglu E, Abdelgani M, Cavalcante R, Zeng Y, Grundeken M, Albuquerque FN, Veldhof S, Onuma T, Serruys PW, On behalf of the investigators of the ABSORB Cohort B study Investigators.

Edge Vascular Response After Resorption of the Everolimus-Eluting Bioresorbable Vascular Scaffold

– A 5-Year Serial Optical Coherence Tomography Study –

Hiroki Tateishi, MD, PhD; Pannipa Suwannasom, MD; Yohei Sotomi, MD; Shimpei Nakatani, MD; Yuki Ishibashi, MD, PhD; Erhan Tenekecioglu, MD; Mohammad Abdelgani, MD; Rafael Cavalcante, MD, PhD; Yaping Zeng, MD, PhD; Maik J. Grundeken, MD; Felipe N. Albuquerque, MD; Susan Veldhof; Yoshinobu Onuma, MD, PhD; Patrick W. Serruys, MD, PhD on behalf of the investigators of the ABSORB Cohort B study

Background: The edge vascular response (EVR) has been linked to important prognostic implications in patients treated with permanent metallic stents. We aimed to investigate the relationship of EVR with the geometric changes in the everolimus-eluting bioresorbable scaffold using serial optical coherence tomography (OCT) analysis.

Methods and Results: In the first-in-man ABSORB trial, 28 patients (29 lesions) underwent serial OCT at 4 different time points (Cohort B1: post-procedure, 6, 24, and 60 months [n=13]; Cohort B2: post-procedure, 12, 36, and 60 months [n=15]) following implantation of the scaffold. In Cohort B1, there was no significant luminal change at the distal or proximal edge segment throughout the entire follow-up. In contrast, there was a significant reduction of the lumen flow area (LFA) of the scaffold between post-procedure and 6 months (−1.03±0.49 mm^2 [P<0.001]), whereas between 6 and 60 months the LFA remained stable (+0.31±1.00 mm^2 [P=0.293]). In Cohort B2, there was a significant luminal reduction of the proximal edge between post-procedure and 12 months (−0.57±0.74 mm^2 [P=0.017]), whereas the lumen area remained stable (−0.26±1.22 mm^2 [P=0.462]) between 12 and 60 months. The scaffold LFA showed a change similar to that observed in Cohort B1.

Conclusions: Our study demonstrated a reduction in the scaffold luminal area in the absence of major EVR, suggesting that the physiological continuity of the lumen contour is restored long term.

Key Words: Coronary artery disease; Optical coherence tomography; Percutaneous coronary intervention

The advent of the metallic stent has been a major breakthrough in the treatment of patients with ischemic coronary artery disease. In the era of the bare-metal stent (BMS), the edge vascular response (EVR) was defined as a reduction in the lumen area mainly from an increase in plaque/media and lumen area within the first 1–2 mm of the device.[1,2] In the era of radioactive stents, EVR became a more prominent effect.[3] In the drug-eluting stent (DES) era, although several studies have demonstrated effective inhibition of neointimal hyperplasia, the EVR was mostly focal and located at the proximal stent edge.[4–7] The rigidity of the metal encaging the vessel can potentially lead to a life-long loss of pulsatility and distensibility of the coronary arterial wall in the stented segment and a compliance mismatch between the stented and adjacent segments of the vessel. In the bioresorbable scaffold (BRS) era, a variety of polymers with different chemical compositions, mechanical properties, and bioresorption duration became available. The polymer most frequently used is poly-L-lactide (PLLA).[8] After completion of the bioresorption process, the struts become integrated into the surrounding vessel wall,[9,10] and the strut voids are no longer visible on optical coherence tomography (OCT) at 5 years after implantation.[11] Our group has previously demonstrated no major changes in lumen area at both the distal and proximal

Received December 13, 2015; revised manuscript received January 20, 2016; accepted February 4, 2016; released online March 3, 2016 Time for primary review: 22 days

Thoraxcenter, Erasmus Medical Center, Rotterdam (H.T., P.S., S.N., Y.I., E.T., R.C., Y.Z., Y.O.); Academic Medical Center, Amsterdam (P.S., Y.S., M.A., M.J.G.), The Netherlands; Montefiore Medical Center/Albert Einstein College of Medicine, NY (F.N.A.), USA; Abbott Vascular, Diegem (S.V.), Belgium; and International Centre for Circulatory Health, NHLI, Imperial College London, London (P.W.S.), UK

A list of the investigators of the ABSORB Cohort B study is provided in the **Appendix**.

Mailing address: Patrick W. Serruys, MD, PhD, FESC, FACC, Proffessor of Cardiology, Cardiovascular Science Division, NHLI, Imperial College of Science, Technology and Medicine, London, UK. Westblaak 98, 3012KM, Rotterdam, The Netherlands. Email: patrick.w.j.c.serruys@gmail.com

ISSN-1346-9843 doi:10.1253/circj.CJ-15-1325

edges of the scaffold at 6 months using intravascular ultrasound (IVUS) analysis. However, at long-term follow-up (1 and 2 years), especially at the proximal edge, there was a slight but statistically significant lumen loss (LL) without any significant change in the lumen area of the distal edge.[12,13]

The aim of the present study was to describe the EVR and its relationship with the scaffold throughout the entire follow-up period of 60 months using serial OCT analysis.

Methods

Study Design and Study Device

The ABSORB Cohort B trial (clinicaltrials.gov NCT00856856, Study Sponsor Abbott Vascular) is a non-randomized, multicenter, single-arm prospective, open-label trial that included 101 patients (102 lesions) treated with the 2nd-generation Absorb scaffold. The first 45 patients (Cohort B1) underwent intravascular imaging follow-up with OCT at 6, 24, and 60 months, whereas the other 56 patients (B2) underwent the same at 12, 36, and 60 months follow-up.

The Absorb scaffold (Abbott Vascular, Santa Clara, CA, USA) consists of a PLLA scaffold, a coating layer of poly-D,L-lactide (PDLLA) and the antiproliferative drug everolimus, a pair of radiopaque platinum markers at the proximal and distal ends of the scaffold, and a balloon catheter delivery system.[14] The details of the study and treatment procedure have been previously described.[15–18]

OCT Image Acquisition

Over the past 5 years OCT techniques have evolved. OCT acquisition in this study was performed using 4 different commercially available systems: the M2 and M3 Time-Domain Systems and the C7 and C8 Fourier-Domain Systems (LightLab Imaging, Westford, MA, USA). OCT images were acquired at a frame rate of 15.6, 20, 100, 180 frames/s with a pullback speed of 2, 3, 20, 18 mm/s in the M2 (n=11), M3 (n=11), C7 (n=174), and C8 (n=39), respectively. All image acquisition was performed according to the recommended procedure for each OCT system.[19] None of the OCT images was acquired with the occlusion technique.[16–18] If the 5-mm edge segment had a side branch with an ostium diameter ≥1.5 mm, the analysis included only those frames between the scaffold margin and the ostium of the side branch. If the ostium diameter of the side branch was less than 1.5 mm, the frames at the ostium of the side branch were excluded. In addition, we excluded subjects who required a bailout stent, subjects with a scaffold implantation adjacent to a previously deployed stent, subjects in whom the edge segment was not fully documented, and frames with insufficient assessment of the entire lumen circumference because of inadequate blood clearance, air bubbles or contrast filling the extremity of the OCT catheter.[20]

OCT Data Analysis

The OCT images acquired post-procedure and at follow-up were analyzed off-line, using proprietary LightLab software (St. Jude Medical Inc, MA, USA) and Q-IVUS 3.0 (Medis Medical Imaging systems, Leiden, The Netherlands). Truly serial OCT data were used in patients who underwent OCT examinations at all 4 time points. Lumen flow area (LFA) of the scaffold segment and the 5-mm segments adjacent to both edges were analyzed at 1-mm intervals by an independent core laboratory (Cardialysis, Rotterdam, The Netherlands). Adjusting for the pullback speed, the analysis of continuous cross-sections was performed at each 1-mm longitudinal interval.[16–18]

As a specific additional approach, frame-by-frame analyses were performed for the 5-mm edge segment and the transitional region between the edge and scaffold segment. The transitional region was defined as a 4-mm region including both the 2 mm of the lumen vessel adjacent to the scaffold edge and the 2-mm margins of the scaffold. The LFA (ie, the effective lumen filled by circulating blood) was defined as the lumen area minus the strut area.[16,21] At follow-up, LFA was equal to the lumen area if no malapposed struts were found. Details of the LFA measurements have been previously described.[21]

Definition of the Scaffolded Segment

At 3 years, most of the scaffold struts remained visible as a black core, so the scaffold edges were defined as the first and last cross-sections with circumferentially visible struts.[13] At 5 years, the struts are no longer visible, so only the platinum marker was visualized as evidence and location of the bioresorbed scaffold. However, in a few patients visualization of the marker was masked by the guidewire shadow. Furthermore, poor image acquisition because of inadequate blood clearance, contrast filling the OCT catheter, artifact from tangential signal drop out, or other reflective structures (eg, mineralization) was a limiting factor. Accordingly, in the present study localization of the edges of the scaffold was performed as follows: (1) when both the proximal and distal markers could be identified, the scaffold segment was defined as the segment between the first cross-section of the distal marker and the last cross-section of the proximal marker; (2) when the marker could not be clearly identified, we used anatomical landmarks on previous OCT images and another imaging modality, such as coronary angiography or IVUS, to localize the edge of the bioresorbed body of the scaffold; (3) when the marker could be identified only on one side, the scaffold length (18 mm) was used to assume the localization of the other edge of the scaffold.

IVUS Greyscale Analysis

Treated vessels post-procedure were examined with phased array IVUS catheters (EagleEye™; Volcano Corporation, Rancho Cordova, CA, USA) using a pullback speed of 0.5 mm/s.[16–18,22] The region of interest, beginning 5 mm distal to and extending 5 mm proximal to the treated segment, was examined. Lumen area, vessel area, plaque burden at the edge segment, and significant residual reference segment stenosis,[23] defined as a reference minimum lumen (CSA <4 mm^2) plus plaque burden <70%, are shown in **Table 1**.

Assessment of Procedural Performance and Postprocedural Findings on OCT

According to the IVUS-MUSIC criteria,[24] we calculated the expansion index (=minimum scaffold area/reference lumen area), the percentage of residual area stenosis (%RAS: =[reference lumen area-minimum scaffold area]/reference lumen area×100), and the scaffold-artery ratio (the ratio of nominal scaffold diameter to the mean reference diameter, the ratio of the post-dilatation balloon nominal diameter to the mean reference diameter, and the ratio of expected scaffold diameter from pressure to mean reference diameter). The procedural details are summarized in **Table 1** and the adequacy of expansion was evaluated based on the MUSIC criteria.

The frequency of non-flow-limiting edge dissection, which was identified on postprocedural OCT, is shown in **Table 1**, as well as intra-scaffold dissection, tissue protrusion, and thrombus, which were identified in the 2-mm margin of the scaffold segment in accordance with previous reports.[25,26]

Table 1. Lesion Characteristics and Procedural Parameters at the Lesion Level in Patients With Serial OCT Analysis

Variable	B1+B2 (n=29)	B1 (n=13)	B2 (n=16)	P value (B1 vs. B2)
Target-lesion vessel (LAD/LCx/RCA)	15/6/8	6/4/3	9/2/5	0.87
AHA classification (A/B1/B2/C)	0/20/8/0	0/10/3/0	0/10/5/0	0.56
Stent implantation				
Scaffold size diameter, mm	3.0	3.0	3.0	–
Scaffold inflation pressure, atm	13.17±2.90	14.15±2.51	12.37±3.03	0.51
Expected scaffold diameter, mm	3.30±0.11	3.32±0.90	3.26±0.13	0.40
Expected scaffold area, mm^2	8.58±0.55	8.67±0.47	8.38±0.65	0.41
Post-dilatation				
Balloon dilatation after device implantation, n (%)	19/29 (65.5)	9/13 (69.2)	10/16 (62.5)	0.71
Maximal diameter of post-dilatation balloon (nominal pressure), mm	3.18±0.19	3.22±0.23	3.15±0.17	0.49
Post-dilatation balloon area (nominal pressure), mm^2	7.98±0.82	8.31±0.90	7.61±0.64	0.09
Length of post-dilatation balloon inflation, mm	11.70±3.13	11.22±3.11	12.09±3.23	0.55
Maximal post-dilatation balloon inflation, atm	17.79±5.32	18.00±6.00	17.60±4.95	0.86
No. of inflations performed	2.26±2.00	2.22±1.99	2.44±2.19	0.94
Ratio of post-dilatation balloon nominal diameter to nominal stent diameter	1.06±0.05	1.08±0.06	1.04±0.04	0.09
Scaffold-artery ratio on postprocedural OCT				
Ratio of nominal scaffold diameter to mean reference diameter	1.10±0.14	1.11±0.17	1.10±0.11	0.77
Ratio of post-dilatation balloon nominal diameter to mean reference diameter	1.16±0.13	1.20±0.16	1.14±0.09	0.27
Ratio of expected scaffold diameter according to dilatation pressure to mean reference diameter	1.21±0.15	1.22±0.15	1.20±0.10	0.56
Postprocedural OCT findings				
Mean reference lumen area, mm^2	6.20±1.65	6.14±2.06	6.31±1.51	0.71
Mean reference diameter, mm	2.76±0.34	2.77±0.43	2.75±0.27	0.94
Mean scaffold area, mm^2	7.56±0.98	7.59±1.38	7.66±0.91	0.79
Minimal scaffold area, mm^2	6.19±0.93	6.23±1.28	6.33±0.76	0.72
Expansion index	1.04±0.21	1.05±0.16	1.04±0.20	0.74
Percentage of residual area stenosis (%RAS)	–4.16±21.20	–5.35±16.06	–3.80±19.95	0.73
Edge segment after procedure				
Proximal non-flow-limiting edge dissection, number (%)	7/26 (26.9)	2/10 (20.0)	5/16 (31.3)	0.53
Distal non-flow-limiting edge dissection, number (%)	6/27 (22.2)	3/13 (23.1)	3/14 (21.4)	0.92
2-mm scaffold margin after procedure				
Proximal intra-scaffold dissection, n (%)	8/29 (27.6)	3/13 (23.1)	5/16 (31.3)	0.62
Distal intra-scaffold dissection, n (%)	3/28 (10.7)	0/13	3/15 (20.0)	0.09
Proximal intra-scaffold thrombus, n (%)	3/29 (10.3)	1/13 (7.7)	2/16 (12.5)	0.67
Distal intra-scaffold thrombus, n (%)	2/28 (7.1)	1/13 (7.7)	1/15 (6.7)	0.92
Tissue prolapse at proximal 2-mm margin of scaffold, n (%)	22/29 (75.9)	11/13 (84.6)	11/16 (75.9)	0.32
Tissue prolapse at distal 2-mm margin of scaffold, n (%)	23/28 (82.1)	12/15 (80.0)	11/13 (84.6)	0.75
Greyscale IVUS findings at the reference segment				
Proximal mean reference lumen area, mm^2	7.55±2.10	7.62±2.64	7.50±1.66	0.89
Distal mean reference lumen area, mm^2	6.37±1.36	5.98±0.98	6.64±1.56	0.28
Proximal mean vessel area, mm^2	14.15±3.48	14.03±4.64	14.24±2.41	0.89
Distal mean vessel area, mm^2	11.10±3.51	10.26±3.78	11.69±3.33	0.36
Residual plaque burden at proximal edge segment, %	46.05±10.26	44.65±11.93	47.16±9.06	0.56
Residual plaque burden at distal edge segment, %	38.83±17.40	36.66±18.46	40.34±17.22	0.64
Significant residual stenosis at the proximal edge segment, n (%)	1/23 (4.3)	1/11 (9.1)	0	–
Significant residual stenosis at the distal edge segment, n (%)	1/22 (4.5)	0	1/13 (7.7)	–

IVUS, intravascular ultrasound; LAD, left anterior descending; LCx, left circumflex artery; OCT, optical coherence tomography; RCA, right coronary artery.

Statistical Analysis

Continuous variables are presented as mean±standard deviation (SD) or median and interquartile range. Normality of the data was determined with the Shapiro-Wilk test and verified by histogram. For the overall assessment, Wilcoxon signed-rank test adjusted by the Bonferroni correction was used to compare EVR within groups at different time points, while for the truly serial follow-up assessment, paired t-test or Wilcoxon signed-rank test was used to compare EVR within groups at different time points without adjustment. A P-value <0.05 was

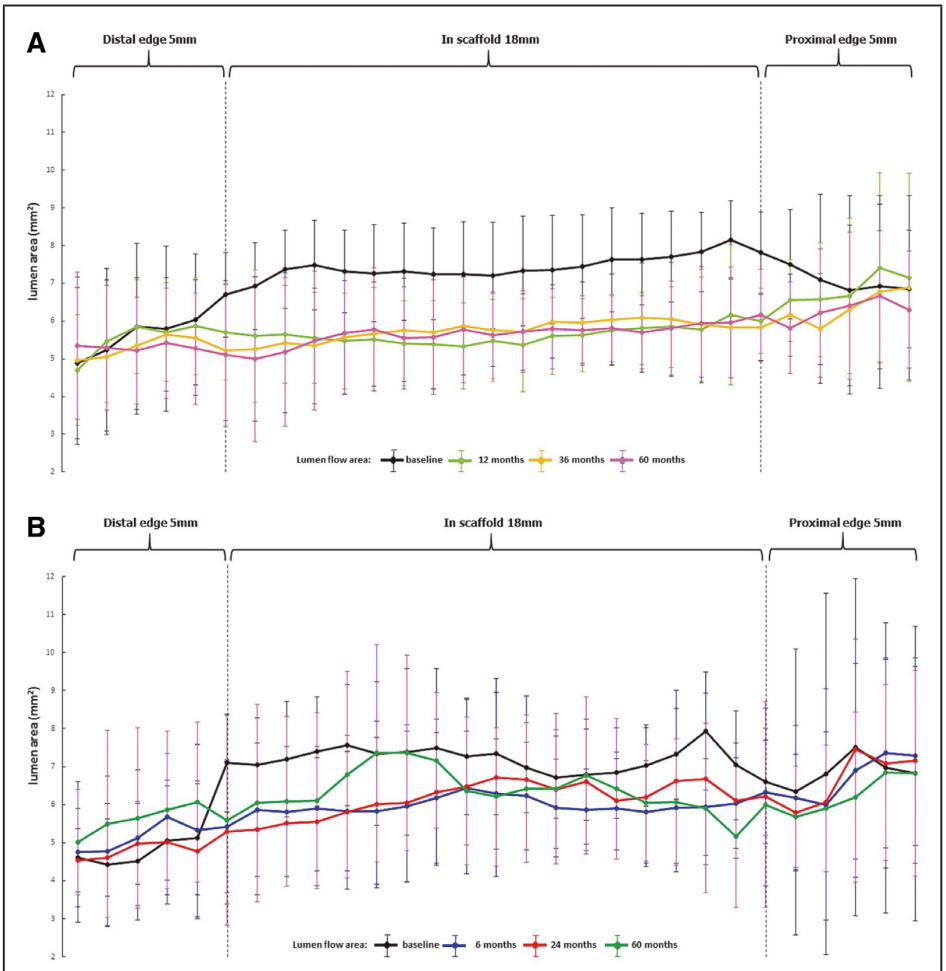

Figure 1. Mean values of the lumen area of the target segment with every 1-mm analysis. Lumen area of the entire scaffold segment as well as the proximal and distal 5-mm edges. The 4 time points are illustrated by lines of different colors. (**A**) Cohort B2 at 12, 36 and 60 months; (**B**) Cohort B1 at 6, 24 and 60 months. The respective absolute values and the delta changes as well as the statistical significance are tabulated in **Tables 2A**,**B**.

considered statistically significant. All statistical analyses were performed with IBM SPSS Statistics 22 (IBM Co, NY, USA) and MedCalc (ver. 14.12.0, MedCalc Software, Ostend, Belgium).

Results

Study Population and OCT Image Acquisition

A total of 235 OCT pullbacks were analyzed in 90 patients (Cohort B1: 40 patients, 40 lesions; Cohort B2: 50 patients, 51 lesions). At 5-year follow-up, OCT was performed in 52 patients (53 lesions) [Cohort B1: 22 patients (22 lesions); Cohort B2: 30 patients (31 lesions)] (**Figures S1A**,**B**). According to the criteria described in the Methods section, we excluded a total of 14 distal edges and 15 proximal edges for the following reasons: 4 edges were not documented on the pullback; 2 edges had overlap with a previously deployed DES; 4 edges had been treated with bailout DES deployment;

Table 2. Changes in Lumen Area at Both the Distal and Proximal Edges on Serial OCT Analysis (A) Cohort B2 at 12, 36 and 60 Months, (B) Cohort B1 at 6, 24 and 60 Months

(A)	BL (n)	1Y (n)	3Y (n)	5Y (n)	1Y-BL Difference P value	3Y-1Y Difference P value	5Y-3Y Difference P value	5Y-1Y Difference P value	3Y-BL Difference P value	5Y-BL Difference P value
Distal edge 5 mm (mm^2)	5.71±1.82 (n=13)	5.70±1.21 (n=14)	5.41±1.59 (n=14)	5.41±1.41 (n=13)	+0.07±1.09 0.821	−0.29±0.79 0.191	0.00±0.78 0.985	−0.29±0.82 0.209	−0.15±0.92 0.591	−0.22±1.34 0.584
Distal scaffold (mm^2)	7.35±1.02 (n=16)	5.75±1.26 (n=16)	5.73±1.77 (n=16)	5.45±1.75 (n=16)	−1.60±1.21 <0.001	−0.02±0.89 0.926	−0.28±1.04 0.301	−0.30±1.13 0.307	−1.62±1.77 0.002	−1.90±1.72 <0.001
Mid-scaffold (mm^2)	7.13±1.31 (n=16)	5.48±0.83 (n=16)	5.84±1.12 (n=16)	5.69±1.14 (n=16)	−1.66±1.21 <0.001	+0.37±0.78 0.079	−0.15±0.70 0.394	+0.21±0.84 0.331	−1.29±1.47 0.003	−1.45±1.53 0.002
Proximal scaffold (mm^2)	7.51±1.17 (n=16)	5.80±0.67 (n=16)	5.93±1.07 (n=16)	5.88±1.01 (n=16)	−1.70±1.16 <0.001	+0.13±0.90 0.584	−0.05±0.66 0.782	+0.08±0.90 0.727	−1.58±1.46 0.001	−1.62±1.38 <0.001
Whole scaffold (mm^2)	7.32±0.89 (n=16)	5.68±0.74 (n=16)	5.75±1.06 (n=16)	5.66±1.10 (n=16)	−1.63±1.00 <0.001	+0.07±0.76 0.724	−0.09±0.43 0.418	−0.02±0.81 0.917	−1.57±1.07 <0.001	−1.65±1.10 <0.001
Proximal edge 5 mm (mm^2)	7.20±1.75 (n=13)	6.70±1.53 (n=13)	6.36±1.61 (n=12)	6.22±1.83 (n=13)	−0.57±0.74 0.017	−0.12±0.73 0.564	−0.14±0.94 0.596	−0.26±1.22 0.462	−0.84±1.27 0.027	−0.98±1.66 0.047
(B)	**BL (n)**	**6M (n)**	**2Y (n)**	**5Y (n)**	**6M-BL Difference P value**	**2Y-6M Difference P value**	**5Y-2Y Difference P value**	**5Y-6M Difference P value**	**2Y-BL Difference P value**	**5Y-BL Difference P value**
Distal edge 5 mm (mm^2)	4.94±1.23 (n=12)	5.39±1.83 (n=12)	4.95±1.26 (n=10)	5.61±2.08 (n=11)	+0.59±0.89 0.0520	−0.21±1.09 0.542	+0.21±0.78 0.391	+0.22±1.03 0.479	+0.22±0.86 0.433	+0.74±1.31 0.088
Distal scaffold (mm^2)	7.27±1.40 (n=13)	5.78±1.61 (n=13)	5.58±1.73 (n=13)	6.30±2.14 (n=13)	−1.50±0.69 <0.001	−0.20±0.98 0.477	+0.72±0.73 0.004	+0.52±1.57 0.253	−1.70±0.95 <0.001	−0.97±1.51 0.039
Mid-scaffold (mm^2)	7.19±1.48 (n=13)	6.16±1.29 (n=13)	6.44±1.80 (n=13)	6.67±1.72 (n=13)	−1.03±0.74 <0.001	+0.28±1.80 0.589	+0.23±1.34 0.544	−0.52±1.56 0.222	0.51±1.43 0.201	−0.75±2.01 0.251
Proximal scaffold (mm^2)	7.42±1.11 (n=13)	6.12±0.95 (n=13)	6.52±1.67 (n=13)	6.12±1.47 (n=13)	−1.31±0.83 <0.001	+0.40±1.64 0.396	−0.40±1.51 0.361	+0.00±1.05 0.996	−0.91±1.46 0.045	−1.31±0.73 <0.001
Whole scaffold (mm^2)	7.06±1.23 (n=13)	6.04±1.19 (n=13)	6.17±1.44 (n=13)	6.34±1.51 (n=13)	−1.03±0.49 <0.001	+0.13±1.28 0.716	+0.17±0.63 0.338	+0.31±1.00 0.293	−0.90±1.16 0.016	−0.72±0.96 0.019
Proximal edge 5 mm (mm^2)	6.37±3.18 (n=11)	6.63±2.68 (n=11)	6.73±2.70 (n=11)	6.69±2.61 (n=10)	+0.32±1.33 0.488	+0.09±0.66 0.612	−0.04±0.72 0.855	−0.06±0.80 0.801	−0.43±0.91 0.191	−0.22±1.31 0.625

Values are presented as mean±standard deviation. The edge segments were evaluated by Wilcoxon signed-rank test, while the subsegments of scaffold were evaluated by paired t-test. A significant level for each paired comparison is 0.05. BL, baseline; OCT, optical coherence tomography; 6M, 6 months; 1Y, 1 year; 2Y, 2 years; 3Y, 3 years; 5Y, 5 years.

1 edge because of DES overlapping the scaffold segment for target lesion revascularization (TLR), and the remaining 18 edges because of a large side branch (≥1.5 mm), insufficient assessment of the entire lumen, or inadequate contrast clearance.

During the 5-year follow-up, of the entire cohort of 101 patients, 11 patients underwent TLR, and 1 of them underwent TLR twice during the entire follow-up. Of these 11 patients (12 TLR), only 3 patients had preprocedural OCT images and were noted to have TLR for edge restenosis (2 proximal, 1 distal). These 3 cases were excluded and thus the study reports exclusively the evolution of the edges in patients who had an uneventful follow-up.

Over the entire follow-up period, 13 patients (13 lesions) of Cohort B1 and 15 patients (16 lesions) of Cohort B2 had serial OCT follow-up images (**Figures S2A**,**B**).

Assessment of Procedural Performance on Postprocedural OCT

The scaffold-artery ratio, which indicates the adequate and appropriate ratio for optimal scaffold expansion, was 1.10±0.14 for the ratio of nominal scaffold diameter to the mean reference diameter, and 1.16±0.13 for the ratio of the post-dilatation balloon nominal diameter to the mean reference diameter (**Table 1**).

Table 1 shows the procedural details and OCT performance parameters that were used to evaluate the stent expansion and scaffold-artery ratio. The expansion index was 1.04±0.21 and the %RAS was −4.16±21.20, suggesting that optimal scaffold expansion was achieved in this population.

Edge dissections were identified at the proximal edge segment (26.9%), and at the distal edge segment (22.2%) immediately post-procedure. Tissue prolapse was identified in most of the lesions; however, there was no more than 500 μm of tissue prolapse (data not shown). Greyscale IVUS analysis showed no large plaque burden of the edge segment (proximal: 46.05±10.26%, distal: 38.83±17.40%). Only 1 significant residual stenosis at the proximal edge segment and 1 significant residual stenosis at the distal edge segment were identified.

Change in the LFA of the Scaffold Segment

Figure 1A shows the LFA of the entire scaffold segment as well as the proximal and distal 5-mm edges. The 4 time points are illustrated by the different lines: the black line illustrates the postprocedural contour of the edge and scaffold, which is over-expanded with respect to the edge with a "step-up" and a "step down" at the site of the scaffold implantation. The major change in the first 12 months was a reduction in flow area without any further change in the luminal dimensions after 12 months, so the LFA curves of 12, 36, and 60 months are more or less superimposed in **Figure 1A**. **Figure 1B** shows similar profile for the patients who had serial OCT at 6, 24, and 60 months.

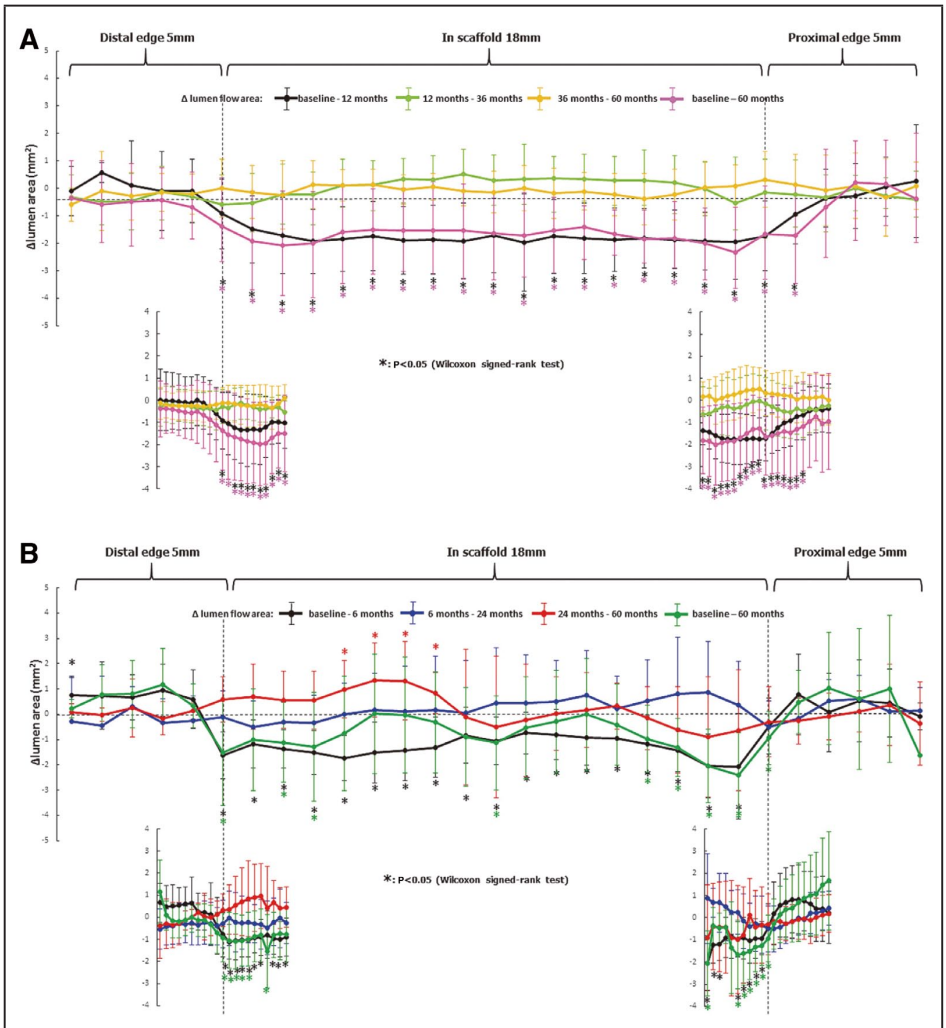

Figure 2. Change in lumen area of both edges and in-scaffold through the entire follow-up. (**A**) Cohort B2 at 12, 36 and 60 months: mean lumen area of the 18-mm in-scaffold segment decreased from baseline to 12-month (black line), extending into the first 1-mm proximal edge. There is a continuous pattern of luminal reduction extending from the in-scaffold margin to the first 1-mm of both the distal and proximal edges from baseline to 12 months; however, significant luminal reduction in-scaffold extends into only the first 1-mm proximal edge. (**B**) Cohort B1 at 6, 24 and 60 months: mean lumen area of the 18-mm in-scaffold segment decreased from baseline to 6-month (black line); however, there is no further significant change in the following 54 months. There is a trend toward an increase at the 5-mm distal edge in the first 6 months following device implantation without a following significant change from 6 to 60 months. In contrast, there is no significant change in lumen area at the proximal edge segment throughout the entire follow-up in this cohort. The 200-μm analysis at the transitional region reveals that although there is a continuous pattern of luminal reduction extending from the in-scaffold margin to the first 1-mm of both the distal and proximal edges in the first 6 months, significant lumen reduction is observed only at the in-scaffold margin.

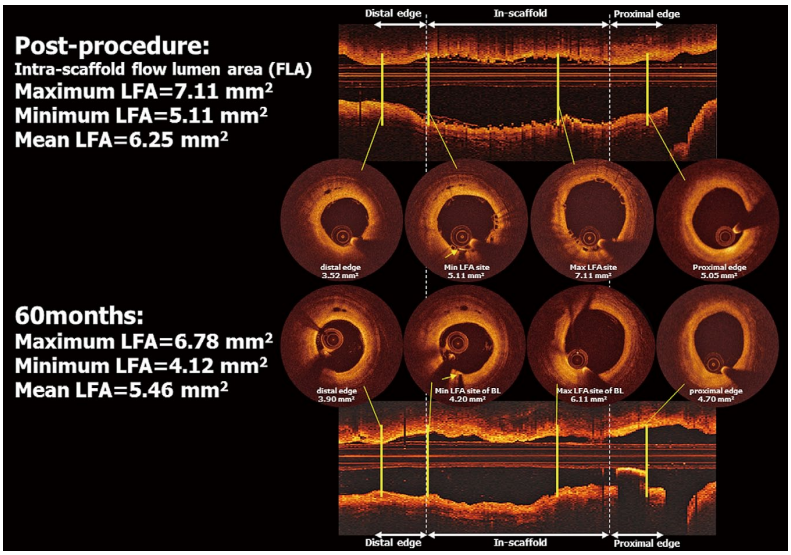

Figure 3. Representative longitudinal images at both edges and in-scaffold at post-procedure and 60 months. The longitudinal image shows both the edges and the postprocedural scaffold, with a "step-up and step-down" at the site of the scaffold implantation. In the following 48 months, the target vessel evolves to resemble a "straight tube" because of the filling of the gap between the initial expansion of the scaffold and the final lumen at 60 months. BL, baseline; LFA, lumen flow area.

EVR and the Change in Lumen Area of the Scaffold Subsegment

The mean LFA, minimal LFA, as well as the changes in the mean LFA over time for both edges and scaffolds at all the time points in the 2 cohorts are shown in the **Table S1**. The lumen area of the distal edges did not change significantly throughout the entire follow-up period, but there was a trend toward a decrease in the lumen area of the proximal edges over the same period (7.17±2.45 mm^2 post-procedure vs. 6.05±1.80 mm^2 at 60 months [P=0.214] for Cohort B1; 7.95±3.50 mm^2 post-procedure vs. 6.12±1.71 mm^2 at 60 months [P=0.022] for Cohort B2). After the initial and significant decreases in the mean and minimal LFA of the scaffold documented at either 6 months or 12 months, no further significant changes in these parameters were observed.

To further assess the changes in the lumen area of the edge segment, truly serial assessment was performed at 6, 24 and 60 months (Cohort B1) and at 12, 36 and 60 months (Cohort B2) (**Tables 2A**,**B**; **Figures 2A**,**B**).

At 12, 36 and 60 months (B2), there was a significant reduction of the LFA at the distal margin between post-procedure and 12 months (at the 1-mm margin: 6.92±1.15 mm^2 vs. 5.60±1.75 mm^2, and 2-mm margin: 7.36±1.04 mm^2 vs. 5.64±1.30 mm^2, both P-values=0.001) (**Table 2A**; **Figure 2A**). However, there were no significant changes of the LFA at either the 1-mm or 2-mm distal margins of the scaffold between 12 months and 60 months (at the 1-mm margin: 5.60±1.75 mm^2 vs. 4.99±2.19 mm^2 [P=0.116]; at the 2-mm margin: 5.64±1.30 mm^2 vs. 5.18±1.96 mm^2 [P=0.211]) (**Figure 2A**).

At 6, 24 and 60 months (B1), there was a trend toward an increase in the lumen area of the distal edge (4.94±1.23 mm^2 post-procedure vs. 5.39±1.83 mm^2 at 6 months [P=0.052]; 5.61±2.08 mm^2 at 60 months [P=0.088, vs. post-procedure]) (**Table 2B**; **Figure 2B**). There was also a significant reduction of the LFA at both the 1-mm and 2-mm distal margins of the scaffold between post-procedure and 6 months (at the 1-mm margin: 7.05±1.23 mm^2 vs. 5.86±1.76 mm^2 [P=0.005], and at the 2-mm margin: 7.20±1.52 mm^2 vs. 5.82±1.71 mm^2 [P=0.001]) (**Figure 2B**).

At 12, 36 and 60 months (B2), the proximal edge lumen area of the first 1-mm edge decreased significantly between post-procedure and 12 months (7.49±1.45 mm^2 vs. 6.55±1.08 mm^2 [P=0.019]). In contrast there was no significant change of the lumen area at the first 1-mm edge between 12 months and 60 months (6.55±1.08 mm^2 vs. 5.81±1.22 mm^2 [P=0.508]) (**Figure 2A**).

At 6, 24 and 60 months (B1), no significant change was observed in the lumen of the proximal edge segment (6.37±3.18 mm^2 post-procedure, 6.63±2.68 mm^2 at 6 months, 6.73±2.70 mm^2 at 24 months, 6.69±2.61 mm^2 at 60 months, P=0.889) (**Table 2B**; **Figure 2B**).

In this cohort (B1), the 2-mm proximal margin of the scaffold segment also showed a significant reduction of LFA at the 2-mm proximal margin of the scaffold between post-procedure and 6 months (at the 1-mm margin: 7.05±1.43 mm^2 vs.

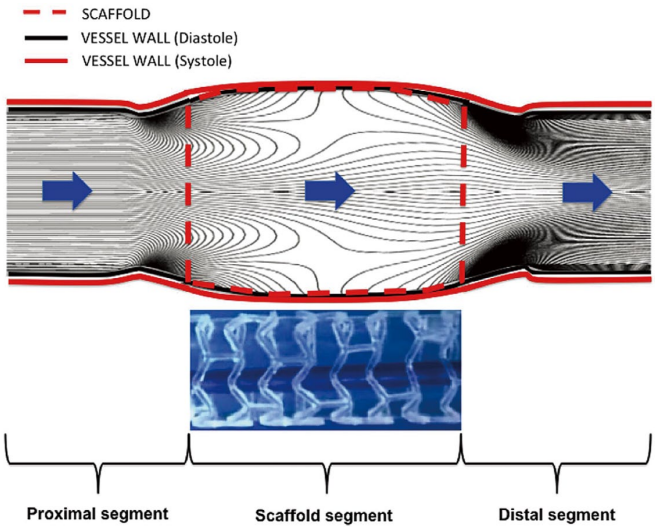

Figure 4. Compliance mismatch after scaffold implantation with alteration in flow. In this diagram the mismatch in compliance created by the scaffold (red dotted line) is indicated as a "bump" in the vessel wall compared with the proximal and distal segments. Instantaneous vortices fields calculated by a mathematical model are also shown, indicating the presence of turbulence at the proximal and distal edges. Instantaneous vorticity fields reconstructed according to Tortoriello A, et al.[31] (Reproduced with permission from Brugaletta S, et al.[30])

6.04±1.19 mm^2 [P=0.003]; at the 2-mm margin: 7.94±1.54 mm^2 vs. 5.94±1.28 mm^2 [P=0.002]) (**Figure 2B**). A similar change was observed at 12, 36 and 60 months (B2) between post-procedure and 12 months (at the 1-mm margin: 8.15±1.04 mm^2 vs. 6.17±1.85 mm^2 [P=0.002]; at the 2-mm margin: 7.83±1.06 mm^2 vs. 5.78±1.38 mm^2 [P=0.001]) (**Figure 2A**). However, there was no change in the LFA in the 2-mm proximal margin of the scaffold between 12 months and 60 months (at the 1-mm margin: 6.17±1.85 mm^2 vs. 5.95±1.47 mm^2 [P=0.638]; at the 2-mm margin: 5.78±1.38 mm^2 vs. 5.94±1.42 mm^2 [P=0.532]) (**Figure 2A**).

Discussion

The main findings of the present study are: (1) in the first 12 months following device implantation, there was a significant reduction of the lumen of the scaffold, while in the following 48 months no significant change was demonstrated; (2) the change in lumen area at the edge segment within the first year can be more precisely localized in the so-called transitional region and the lumen reduction at the edges seems to be geometric prolongation of the scaffold reduction; (3) the scaffold segment and the lumen area in the transitional region no longer change after the first year of follow-up and the lumen contour of the edges aligned with the contour of the scaffold after 1 year; (4) no cases of TLR for either proximal or distal edge restenosis occurred after 3 years.

Because of the long-term follow-up and serial follow-up, this study was limited to a small number of observations. In view of the limited number of patients documented so far worldwide, we believed that Cohorts B1 and B2 should be pooled because both have follow-up at 5 years. Although some cases of aneurysmal changes were responsible for some heterogeneity of the lumen contours in Cohort B1 and there are some differences in the temporal changes of lumen area measurements between the 2 cohorts, the lumen contours of both cohorts presented a similar profile through the entire period (**Figures 1A**,**B**).

In order to fully document and evaluate the temporal changes in luminal contours, we deliberately selected cases of patients with truly serial OCT analyses. Furthermore, from a nosologic point of view, EVR and edge restenosis have to be differentiated. EVR is a general observation made at the scaffold edges, whereas edge restenosis is a truly pathologic phenomenon resulting from focal exuberance of neointima eventually combined with constrictive remodeling and progression of the atherosclerotic process.[2] For this reason and to fully understand EVR we excluded the 3 cases of edge restenosis that could be related to other pathologic mechanisms such as the presence of active plaque at the edge of the scaffold, defect in the manufacturing process and coating of the scaffold edge or intense barotrauma during post-dilatation outside the scaffold. All these specific phenomena could induce true restenosis of the edge.[27]

The present study describes a frame interval of 200 μm, the transition between the native vessel wall and the neointima

that has fully integrated the polymeric material.

Previously, a late vascular response to DES was primarily attributed to a delay in strut healing because of subsequent drug toxicity and polymer-induced inflammation followed by hypersensitivity reactions.[27,28] A preclinical study in non-atherosclerotic pigs treated with the Absorb scaffold showed the disappearance of inflammatory response associated with the scaffold after 2, 3, or 4 years, as evidenced by the absence of the polylactide at 3 years and its replacement by malleable proteoglycan, which was demonstrated by gel permeation chromatography.[9] However, those findings were derived from a non-diseased vessel, and could be at variance with the inflammatory response observed in a diseased vessel.

In clinical studies, we have demonstrated the return of vasomotion of the scaffold segment at 12 months, which indicates that the device has lost its mechanical integrity at around 12 months.[17] Other clinical studies have shown that the malleable matrix of proteoglycan, which fills the strut void of the scaffold, can be pushed outward and expanded; the expansion of the scaffold matrix compensates for the continuing growth of neointimal hyperplasia between and on the top of the struts.[22]

In the present study, the postprocedural luminal dimensions of the scaffold and edge were characterized by a "step-up and step-down" in luminal area measurements (**Figure 3**) that implies excellent deployment and expansion of the device without systematic OCT or IVUS guidance, as performed by Mattesini et al[29] or according to the MUSIC Study criteria.[24] Although non-flow-limiting edge dissection occurred frequently, these 2 cohorts have good long-term OCT results that were presumably related to the small residual plaque burden at the edge segment immediately post-procedure.

We show that the growth of neointimal tissue between baseline and 12 months fills almost perfectly the gap between the initial expansion of the strut and the final lumen at 60 months, because the dimension of the lumen did not change between 12, 36, and 60 months (**Figure 3**).

Previously, using the first iteration of the device with a faster bioresorption we demonstrated that scaffold implantation transiently reduced vascular compliance, which disappeared after 24 months.[15,30] After completion of bioresorption, unlike a metal cage, the disappearance of the "step up-step down" in vascular compliance and the cyclic strain at the scaffold edges might theoretically correct the early disturbances in shear stress at the edges and finally lead to laminar flow in the scaffold segment, including the transitional region, and the distal and proximal edge segments (**Figure 4**).[30,31] Moreover, exposing the endothelial cells to a homogeneous shear stress can potentially prevent neointimal growth and neoatherosclerosis in the late phase in all regions (scaffold, transitional region, and edge segment).[32–35]

According to the results from the late phase (between 2–3 and 5 years), the favorable lumen evolution of the scaffold itself apparently abrogated the EVR phenomenon. At the present time there is no comparable late observation of metallic DES.

Clinical Implications

Although metallic stented segments showed positive vessel remodeling up to 2 years,[36,37] and no late analysis is available, in contrast the latest report of the ABSORB Cohort B trial at 5 years demonstrated a decrease in plaque media together with adaptive, constrictive remodeling of the vessel area on IVUS analysis at 5 years.[38] Our study demonstrated a reduction of the scaffold luminal area in the absence of major EVR, suggesting that the physiological continuity of the lumen contour is restored long term. Loss of the mechanical property of the scaffold allows restoration of the endothelial shear stress, which is the frictional force on the vessel lining as blood flows through it, and cyclic strain, which is the force generated by the stretching of the vessel wall during systole and is affected by vessel distensibility. Furthermore, the interaction of shear stress and cyclic strain controls cell signaling. Cyclic strain stimulates eNOS gene regulation and steady-state levels of prostacyclin are increased when the shear stress force is applied in a pulsatile fashion.[39] The present study showed no late LL, so we could expect fewer cases of late TLR.

Study Limitations

This was an observational study and the OCT assessment was limited to a small number of observations, which were, however, serial and performed long term. We used 2 different OCT systems (TD- and FD-OCT) because OCT techniques evolved over the study period. Validity of the OCT measurements between 2 different systems has been established.[40] Regarding size discrepancy between the 2 modalities, we minimized it because none of the OCT images was acquired using the occlusion technique.[16–18,22]

An inherent limitation of a first-in-man trial is that the lesion subset may be relatively simple and likely not reflective of "real-world lesions". The postprocedural luminal dimensions of the scaffold and edge were characterized by a "step-up and step-down" in luminal area measurements (**Figure 3**), which implied excellent deployment and expansion of the device that in itself may constitute a favorable selection bias bound to the "first in man" nature of the study; Mattesini et al have reported a similar luminal area increase when a metallic DES or BRS was implanted under OCT guidance.[29] In the BMS era the IVUS-MUSIC criteria for optimal BMS implantation resulted in the lowest binary restenosis rate (9.7%) ever observed.[24]

In order to fully document and evaluate the temporal changes in luminal contour, we deliberately selected cases of patients with truly serial OCT analyses. To fully understand EVR, we excluded the 3 cases of edge restenosis (see **Discussion**).

There were some differences in the sequential and temporal changes of OCT area measurements between Cohorts B1 and B2 which may raise a concern about the potential patient heterogeneity. The small sample size precludes a formal univariate or multivariable analysis of the differences between cohorts.

Conclusions

The key observation was global reduction of the scaffolded lumen in the absence of major EVR, suggesting that the physiological continuity of the lumen boundaries after bioresorption of the scaffold are restored long term.

Disclosures

S.V. is an employee of Abbott Vascular. P.W.S. and Y.O. are members of the advisory board of Abbott Vascular. All other authors report no conflicts of interest in relation to this manuscript.

References

1. Weissman NJ, Wilensky RL, Tanguay JF, Bartorelli AL, Moses J, Williams DO, et al. Extent and distribution of in-stent intimal hyperplasia and edge effect in a non-radiation stent population. *Am J Cardiol* 2001; **88:** 248–252.
2. Serruys PW, Degertekin M, Tanabe K, Russell ME, Guagliumi G, Webb J, et al. Vascular responses at proximal and distal edges of

paclitaxel-eluting stents: Serial intravascular ultrasound analysis from the TAXUS II trial. *Circulation* 2004; **109:** 627–633.
3. Serruys PW, Kay IP. I like the candy, i hate the wrapper: The (32)P radioactive stent. *Circulation* 2000; **101:** 3–7.
4. Popma JJ, Leon MB, Moses JW, Holmes DR Jr, Cox N, Fitzpatrick M, et al. Quantitative assessment of angiographic restenosis after sirolimus-eluting stent implantation in native coronary arteries. *Circulation* 2004; **110:** 3773–3780.
5. Windecker S, Serruys PW, Wandel S, Buszman P, Trznadel S, Linke A, et al. Biolimus-eluting stent with biodegradable polymer versus sirolimus-eluting stent with durable polymer for coronary revascularisation (LEADERS): A randomised non-inferiority trial. *The Lancet* 2008; **372:** 1163–1173.
6. García-García HM, Gonzalo N, Tanimoto S, Meliga E, de Jaegere P, Serruys PW. Characterization of edge effects with paclitaxel-eluting stents using serial intravascular ultrasound radiofrequency data analysis: The BETAX (BEside TAXus) study. *Rev Esp Cardiol (English Version)* 2008; **61:** 1013–1019.
7. Serruys PW, Silber S, Garg S, van Geuns RJ, Richardt G, Buszman PE, et al. Comparison of zotarolimus-eluting and everolimus-eluting coronary stents. *N Engl J Med* 2010; **363:** 136–146.
8. Onuma Y, Serruys PW. Bioresorbable scaffold: The advent of a new era in percutaneous coronary and peripheral revascularization? *Circulation* 2011; **123:** 779–797.
9. Onuma Y, Serruys PW, Perkins LE, Okamura T, Gonzalo N, Garcia-Garcia HM, et al. Intracoronary optical coherence tomography and histology at 1 month and 2, 3, and 4 years after implantation of everolimus-eluting bioresorbable vascular scaffolds in a porcine coronary artery model: An attempt to decipher the human optical coherence tomography images in the ABSORB trial. *Circulation* 2010; **122:** 2288–2300.
10. Nakatani S, Onuma Y, Ishibashi Y, Eggermont J, Zhang YJ, Campos CM, et al. Temporal evolution of strut light intensity after implantation of bioresorbable polymeric intracoronary scaffolds in the ABSORB Cohort B trial: An application of a new quantitative method based on optical coherence tomography. *Circ J* 2014; **78:** 1873–1881.
11. Karanasos A, Simsek C, Serruys P, Ligthart J, Witberg K, van Geuns RJ, et al. Five-year optical coherence tomography follow-up of an everolimus-eluting bioresorbable vascular scaffold: Changing the paradigm of coronary stenting? *Circulation* 2012; **126:** e89–e91, doi:10.1161/circulationaha.1112.110122.
12. Gogas BD, Bourantas CV, Garcia-Garcia HM, Onuma Y, Muramatsu T, Farooq V, et al. The edge vascular response following implantation of the Absorb everolimus-eluting bioresorbable vascular scaffold and the XIENCE V metallic everolimus-eluting stent: First serial follow-up assessment at six months and two years: Insights from the first-in-man ABSORB Cohort B and SPIRIT II trials. *EuroIntervention* 2013; **9:** 709–720.
13. Gogas BD, Serruys PW, Diletti R, Farooq V, Brugaletta S, Radu MD, et al. Vascular response of the segments adjacent to the proximal and distal edges of the ABSORB everolimus-eluting bioresorbable vascular scaffold: 6-month and 1-year follow-up assessment: A virtual histology intravascular ultrasound study from the first-in-man ABSORB cohort B trial. *JACC Cardiovasc Interv* 2012; **5:** 656–665.
14. Oberhauser J, Hossainy S, Rapoza R. Design principles and performance of bioresorbable polymeric vascular scaffolds. *EuroIntervention* 2009; **5:** F15–F22.
15. Serruys PW, Ormiston JA, Onuma Y, Regar E, Gonzalo N, Garcia-Garcia HM, et al. A bioabsorbable everolimus-eluting coronary stent system (ABSORB): 2-year outcomes and results from multiple imaging methods. *Lancet* 2009; **373:** 897–910.
16. Serruys PW, Onuma Y, Ormiston JA, de Bruyne B, Regar E, Dudek D, et al. Evaluation of the second generation of a bioresorbable everolimus drug-eluting vascular scaffold for treatment of de novo coronary artery stenosis: Six-month clinical and imaging outcomes. *Circulation* 2010; **122:** 2301–2312.
17. Serruys PW, Onuma Y, Dudek D, Smits PC, Koolen J, Chevalier B, et al. Evaluation of the second generation of a bioresorbable everolimus-eluting vascular scaffold for the treatment of de novo coronary artery stenosis: 12-month clinical and imaging outcomes. *J Am Coll Cardiol* 2011; **58:** 1578–1588.
18. Ormiston JA, Serruys PW, Onuma Y, van Geuns RJ, de Bruyne B, Dudek D, et al. First serial assessment at 6 months and 2 years of the second generation of absorb everolimus-eluting bioresorbable vascular scaffold: A multi-imaging modality study. *Circ Cardiovasc Interv* 2012; **5:** 620–632.
19. Tearney GJ, Regar E, Akasaka T, Adriaenssens T, Barlis P, Bezerra HG, et al. Consensus standards for acquisition, measurement, and reporting of intravascular optical coherence tomography studies: A report from the International Working Group for Intravascular Optical Coherence Tomography Standardization and Validation. *J Am Coll Cardiol* 2012; **59:** 1058–1072.
20. Zhang YJ, Iqbal J, Nakatani S, Bourantas CV, Campos CM, Ishibashi Y, et al. Scaffold and edge vascular response following implantation of everolimus-eluting bioresorbable vascular scaffold: A 3-year serial optical coherence tomography study. *JACC Cardiovasc Interv* 2014; **7:** 1361–1369.
21. Nakatani S, Sotomi Y, Ishibashi Y, Grundeken MJ, Tateishi H, Tenekecioglu E, et al. Comparative analysis method of permanent metallic stents (XIENCE) and bioresorbable poly-L-lactic (PLLA) scaffolds (Absorb) on optical coherence tomography at baseline and follow-up. *EuroIntervention* 2015 Octber 9, doi:10.4244/EIJY15M10_03.
22. Serruys PW, Onuma Y, Garcia-Garcia HM, Muramatsu T, van Geuns RJ, de Bruyne B, et al. Dynamics of vessel wall changes following the implantation of the absorb everolimus-eluting bioresorbable vascular scaffold: A multi-imaging modality study at 6, 12, 24 and 36 months. *EuroIntervention* 2014; **9:** 1271–1284.
23. Fujii K, Carlier SG, Mintz GS, Yang YM, Moussa I, Weisz G, et al. Stent underexpansion and residual reference segment stenosis are related to stent thrombosis after sirolimus-eluting stent implantation: An intravascular ultrasound study. *J Am Coll Cardiol* 2005; **45:** 995–998.
24. de Jaegere P, Mudra H, Figulla H, Almagor Y, Doucet S, Penn I, et al. Intravascular ultrasound-guided optimized stent deployment: Immediate and 6 months clinical and angiographic results from the Multicenter Ultrasound Stenting in Coronaries Study (MUSIC Study). *Eur Heart J* 1998; **19:** 1214–1223.
25. Gonzalo N, Serruys PW, Okamura T, Shen ZJ, Onuma Y, Garcia-Garcia HM, et al. Optical coherence tomography assessment of the acute effects of stent implantation on the vessel wall: A systematic quantitative approach. *Heart* 2009; **95:** 1913–1919.
26. Radu MD, Räber L, Heo JH, Gogas BD, Jørgensen E, Kelbæk H, et al. Natural history of optical coherence tomography-detected non-flow-limiting edge dissections following drug-eluting stent implantation. *EuroIntervention* 2014; **9:** 1085–1094.
27. Gogas BD, Samady H. Shedding light on scaffold vascular response. *JACC Cardiovasc Interv* 2014; **7:** 1370–1373.
28. Hiranuma N, Shinke T, Nakazawa G, Otake H, Matsumoto D, Ijichi T, et al. Optical coherence tomography and histopathology assessment after implantation of first- and second-generation drug-eluting stents in a porcine coronary model. *Circ J* 2014; **78:** 2665–2673.
29. Mattesini A, Secco GG, Dall'Ara G, Ghione M, Rama-Merchan JC, Lupi A, et al. ABSORB biodegradable stents versus second-generation metal stents: A comparison study of 100 complex lesions treated under OCT guidance. *JACC Cardiovasc Interv* 2014; **7:** 741–750.
30. Brugaletta S, Gogas BD, Garcia-Garcia HM, Farooq V, Girasis C, Heo JH, et al. Vascular compliance changes of the coronary vessel wall after bioresorbable vascular scaffold implantation in the treated and adjacent segments. *Circ J* 2012; **76:** 1616–1623.
31. Tortoriello A, Pedrizzetti G. Flow-tissue interaction with compliance mismatch in a model stented artery. *J Biomech* 2004; **37:** 1–11.
32. Wentzel JJ, Whelan DM, van der Giessen WJ, van Beusekom HM, Andhyiswara I, Serruys PW, et al. Coronary stent implantation changes 3-D vessel geometry and 3-D shear stress distribution. *J Biomech* 2000; **33:** 1287–1295.
33. Schwarzacher SP, Tsao PS, Ward M, Hayase M, Niebauer J, Cooke JP, et al. Effects of stenting on adjacent vascular distensibility and neointima formation: Role of nitric oxide. *Vasc Med* 2001; **6:** 139–144.
34. Benard N, Coisne D, Donal E, Perrault R. Experimental study of laminar blood flow through an artery treated by a stent implantation: Characterisation of intra-stent wall shear stress. *J Biomech* 2003; **36:** 991–998.
35. Nakazawa G, Otsuka F, Nakano M, Vorpahl M, Yazdani SK, Ladich E, et al. The pathology of neoatherosclerosis in human coronary implants bare-metal and drug-eluting stents. *J Am Coll Cardiol* 2011; **57:** 1314–1322.
36. Wilson GJ, Nakazawa G, Schwartz RS, Huibregtse B, Poff B, Herbst TJ, et al. Comparison of inflammatory response after implantation of sirolimus- and paclitaxel-eluting stents in porcine coronary arteries. *Circulation* 2009; **120:** 141–149, 141–142.
37. Garcia-Garcia HM, Serruys PW, Campos CM, Onuma Y. Differential impact of five coronary devices on plaque size: Insights from the ABSORB and SPIRIT trials. *Int J Cardiol* 2014; **175:** 441–445.
38. Serruys PW, Ormiston J, van Geuns RJ, de Bruyne B, Dudek D, Christiansen E, et al. A polylactide bioresorbable scaffold eluting everolimus for treatment of coronary stenosis: 5-year follow-up. *J Am Coll Cardiol* 2016; **67:** 766–776.

39. Serruys PW, Garcia-Garcia HM, Onuma Y. From metallic cages to transient bioresorbable scaffolds: Change in paradigm of coronary revascularization in the upcoming decade? *Eur Heart J* 2012; **33:** 16–25.
40. Takarada S, Imanishi T, Liu Y, Ikejima H, Tsujioka H, Kuroi A, et al. Advantage of next-generation frequency-domain optical coherence tomography compared with conventional time-domain system in the assessment of coronary lesion. *Catheter Cardiovasc Interv* 2010; **75:** 202–206.

Appendix

List of Investigators Contributing to OCT Image Acquisition in the ABSORB Cohort B Trial

Robert-Jan van Geuns, MD, PhD (n=14); Evald Christiansen, MD (n=12); Dariusz Dudek, MD (n=8); Dougal McClean, MD (n=7); Jacques Koolen, MD, PhD (n=7); John A Ormiston, MB, ChB, PhD (n=7); Bernard Chevalier, MD (n=7); Stefan Windecker, MD (n=6); Pieter C. Smits, MD, PhD (n=6); Bernard de Bruyne, MD, PhD (n=5); Robert Whitbourn, MD (n=3).

Supplementary Files

Supplementary File 1

Figure S1. (**A**) Study profile through the entire follow-up.

Figure S2. Study profile of the serial OCT analysis.

Table S1. Mean lumen area and changes over time at both edges and in-scaffold (**A**) cohort B2 at 12, 36 and 60 months, (**B**) cohort B1 at 6, 24 and 60 months

Please find supplementary file(s);
http://dx.doi.org/10.1253/circj.CJ-15-1325

4.6 Shielding the underlying plaque after a PLLA scaffold implantation

Bioresorbable vascular scaffold treatment induces the formation of neointimal cap that seals the underlying plaque without compromising the luminal dimensions: a concept based on serial optical coherence tomography data.

EuroIntervention. 2015;11(8):746-56.
[Original research paper, Impact Factor : 3.77]

Bourantas CV, Serruys PW, Nakatani S, Zhang YJ, Farooq V, Diletti R, Ligthart J, Sheehy A, van Geuns RJ, McClean D, Chevalier B, Windecker S, Koolen J, Ormiston J, Whitbourn R, Rapoza R, Veldhof S, Onuma Y, Garcia-Garcia HM.

Bioresorbable vascular scaffold treatment induces the formation of neointimal cap that seals the underlying plaque without compromising the luminal dimensions: a concept based on serial optical coherence tomography data

Christos V. Bourantas[1], MD, PhD; Patrick W. Serruys[1]*, MD, PhD; Shimpei Nakatani[1], MD; Yao-Jun Zhang[1], PhD; Vasim Farooq[1], MBChB, MRCP; Roberto Diletti[1], MD; Jurgen Ligthart[1], BSc; Alexander Sheehy[2], MSc; Robert-Jan M. van Geuns[1], MD, PhD; Dougal McClean[3], MD; Bernard Chevalier[4], MD; Stephan Windecker[5], MD; Jacques Koolen[6], MD, PhD; John Ormiston[7], MBChB; Robert Whitbourn[8], MD; Richard Rapoza[2], PhD; Susan Veldhof[9], RN; Yoshinobu Onuma[1], MD; Hector M. Garcia-Garcia[1], MD, PhD

1. Thoraxcenter, Erasmus Medical Center, Rotterdam, The Netherlands; 2. Abbott Vascular, Santa Clara, CA, USA; 3. Christchurch Hospital, Christchurch, New Zealand; 4. Institut Cardiovasculaire Paris Sud, Massy, France; 5. Bern University Hospital, Bern, Switzerland; 6. Catharina Hospital, Eindhoven, The Netherlands; 7. Auckland City Hospital, Auckland, New Zealand; 8. St Vincent's Hospital, Fitzroy, VIC, Australia; 9. Abbott Vascular, Diegem, Belgium

GUEST EDITOR: Giulio Guagliumi, MD; *Department of Interventional Cardiology, Ospedale Papa Giovanni XXIII, Bergamo, Italy.*

The accompanying supplementary data are published online at: http://www.pcronline.com/eurointervention/ahead_of_print/201410-06

KEYWORDS

- bioresorbable vascular scaffold
- high-risk plaque
- neointimal formation
- optical coherence tomography

Abstract

Aims: To evaluate the implications of an Absorb bioresorbable vascular scaffold (Absorb BVS) on the morphology of the superficial plaques.

Methods and results: Forty-six patients who underwent Absorb BVS implantation and 20 patients implanted with bare metal stents (BMS) who had serial optical coherence tomographic examination at baseline and follow-up were included in this analysis. The thin-capped fibroatheromas (TCFA) were identified in the device implantation regions and in the adjacent native coronary segments. Within all regions, circumferential locations of TCFA and calcific tissues were identified, and the neointimal thickness was measured at follow-up. At six to 12-month follow-up, only 8% of the TCFA detected at baseline were still present in the Absorb BVS and 27% in the BMS implantation segment (p=0.231). Sixty percent of the TCFA in native segments did not change their phenotype at follow-up. At short-term follow-up, significant reduction in the lumen area of the BMS was noted, which was higher compared to that reported in the Absorb BVS group (–2.11±1.97 mm^2 vs. –1.34±0.99 mm^2, p=0.026). In Absorb BVS, neointima tissue continued to develop at midterm follow-up (2.17±0.48 mm^2 vs. 1.38±0.52 mm^2, p<0.0001) and covered the underlying tissues without compromising the luminal dimensions (5.93±1.49 mm^2 vs. 6.14±1.49 mm^2, p=0.571) as it was accommodated by the expanded scaffold (8.28±1.74 mm^2 vs. 7.67±1.28 mm^2, p<0.0001).

Conclusions: Neointimal tissue develops following either Absorb BVS or BMS implantation and shields lipid tissues. The neointimal response in the BMS causes a higher reduction of luminal dimensions compared to the Absorb BVS. Thus, Absorb BVS may have a value in the invasive re-capping of high-risk plaques.

**Corresponding author: Erasmus MC, 's-Gravendijkwal 230, 3015 CE Rotterdam, The Netherlands. E-mail: p.w.j.c.serruys@erasmusmc.nl*

Introduction

Bioresorbable vascular scaffolds (BVS) are a novel technology that introduces a unique potential in the treatment of coronary atherosclerosis as they provide transient scaffolding which temporarily safeguards the patency of the vessel and, once resorbed, they allow the vessel to restore its physiological integrity[1-3]. The mechanisms involved in BVS degradation depend on the composition of the scaffold. In the case of the Absorb BVS, degradation implies hydrolysis of the two polymers (poly-L-lactide and poly-D,L-lactide) which, along with the end-stage phagocytosis of crystals, ultimately form lactic acid molecules that can be fully catabolised. In the first year after implantation, degradation progresses steadily without the appearance of mass loss. The protruded struts of the scaffold create a neointima-promoting haemodynamic environment that triggers neointimal proliferation[4]. The final outcome of these processes is the development of neointima, which consists of connective tissue and smooth muscle cells, that covers the underlying plaque[5]. The neointima that develops post Absorb BVS implantation has features that have been shown to be potentially associated with plaque stability, and has been hypothesised to be able to shield high-risk plaques[6].

The aim of the current analysis was to examine the implications of the Absorb BVS on the phenotype of the plaque and compare the changes in plaque morphology with those occurring after bare metal stent (BMS) implantation. For this purpose, we analysed serial optical coherence tomographic (OCT) data obtained from patients implanted with an Absorb BVS or a BMS and we used spread-out vessel plots to portray the spatial distribution of the different plaque types and to measure the thickness of the neointima at follow-up.

Methods

INCLUDED PATIENTS AND STUDY DESIGN

This study is an observational *post hoc* analysis of the data acquired in the ABSORB cohort B trial (A Clinical Evaluation of the Everolimus Eluting Bioresorbable Vascular Scaffold System in the Treatment of Patients with *de Novo* Native Coronary Artery Lesions), the Svelte Coronary Stent Integrated Delivery System (IDS) first-in-man trial and the vShield Evaluated at Cardiac hospital in Rotterdam for Investigation and Treatment of thin-cap fibroatheromas (SECRITT) study. The design and results of each study have been described in detail elsewhere[7-9]. In brief, the ABSORB cohort B study was a prospective multicentre single-arm trial which examined for the first time the safety and efficacy of the second-generation Absorb BVS (Abbott Vascular, Santa Clara, CA, USA) (dimensions: 3.0×18 mm) in 101 patients with a single or two-vessel *de novo* lesions[8]. The Svelte Coronary Stent IDS first-in-man trial was a multicentre, prospective, single-arm study designed to assess the safety and short-term performance of the Svelte Coronary IDS stent (a balloon-expandable, cobalt-chromium, thin-strut fixed wire BMS) in 47 patients with *de novo* coronary lesions, whereas the SECRITT study was a pilot prospective single-centre randomised control trial that aimed to assess the feasibility and safety of shielding non-obstructive high-risk plaques with a self-expanding thin-strut vascular shield (vProtect™ system; Prescient Medical, Inc., Doylestown, PA, USA)[7,9].

The patients recruited in the ABSORB cohort B study were divided into two groups (cohort B1 and cohort B2). Cohort B1 underwent coronary angiography, greyscale intravascular ultrasound (IVUS), IVUS virtual histology (IVUS-VH) and OCT evaluation at baseline (post-procedure), and at six-month and two-year follow-up. Cohort B2 underwent the same investigations at baseline, one-year and three-year follow-up. OCT examination was an optional study and thus some patients did not have this investigation. The patients recruited in the Svelte Coronary Stent IDS first-in-man trial and the SECRITT study had OCT examination at baseline and repeat invasive assessment and OCT re-evaluation at six-month follow-up. All the patients recruited in our analysis had serial OCT evaluation at baseline (post scaffold or BMS implantation), and any follow-up time point. The ABSORB cohort B study was sponsored and financially supported by Abbott Vascular. The protocol of the three studies was approved by the human research committee of the institutions that participated. Informed consent was obtained from all patients.

QUANTITATIVE CORONARY ANGIOGRAPHY

Quantitative coronary angiography (QCA) was performed in corresponding end-diastolic angiographic images acquired pre and post device deployment and at follow-up using dedicated software (CAAS II; Pie Medical Imaging BV, Maastricht, The Netherlands, or QCA-CMS; Medis, Leiden, The Netherlands). For each treated lesion the following metrics were obtained: reference vessel diameter (RVD), estimated using an interpolated approach, minimum lumen diameter (MLD), diameter stenosis (DS), and late lumen loss (LLL), defined as the difference between the MLD post-procedure and the MLD at follow-up.

OPTICAL COHERENCE TOMOGRAPHY

OCT images were acquired using either an M3 time-domain, or a C7-XR Fourier-domain system (LightLab Imaging Inc., Westford, MA, USA). Pullback in all systems was performed with the use of an automated pullback device at a speed of 3 mm/s for the M3, and 20 mm/s for the C7-XR system, while the frame rates were 20 frames/s and 100 frames/s, respectively. The OCT data acquired post scaffold implantation and at follow-up were analysed by two operators (Cardialysis BV, Rotterdam, The Netherlands) blinded to the examination time and patients' procedural and clinical characteristics, using dedicated off-line software (St. Jude Medical Inc., St. Paul, MN, USA). In the segments implanted with an Absorb BVS or a BMS the two operators selected the frames portraying the scaffolded/stented segment (defined by the most distal and most proximal frames that showed at least one strut of the devices) and analysed one frame every three frames (0.43 mm interval) in the sequences acquired with the M3 system, and one frame every two frames (0.4 mm interval) in the sequences obtained by the C7-XR system[10].

Lumen and scaffold border detection was performed using the methodology described by Serruys et al[8]. In brief, at baseline the lumen area was delineated by the endoluminal border of the vessel

wall and the abluminal side of the scaffold struts if these were embedded or well apposed in the vessel wall. In case of malapposed struts, the lumen border was defined by the endoluminal contour of the vessel wall behind the malapposed struts. At follow-up, the lumen was delineated by the endoluminal border of the neointima tissue. At all time points, the scaffold borders were defined by the abluminal side of the scaffold's struts. In the segments treated with a BMS, the lumen border was defined by the endoluminal border of the vessel wall and the stent border by a curve connecting the hyperintense signal of the metallic struts. The detected borders were used to calculate the lumen area, the scaffold/stent area and the neointima area (given as: scaffold/stent area - lumen area).

In the selected cross-sections, the operators identified vessel wall discontinuities post-procedure and assessed the composition of the plaque **(Online Appendix, Online Figure 1-Online Figure 5)**. These data were then used to construct spread-out scaffold/stent plots which allowed comprehensive visualisation and quantification of the composition of the superficial plaque as well as estimation of the mean and minimum thickness of the neointima over different tissues **(Online Appendix, Online Figure 1-Online Figure 5)**.

In addition, the two observers reviewed the OCT images, acquired post scaffold implantation, and identified thin-cap fibroatheromas (TCFA) in the native segments located proximal and distal to the scaffold **(Online Appendix, Online Figure 1-Online Figure 5)**. Anatomical landmarks proximal and distal to the TCFA (i.e., the origin of a side branch or the proximal or distal end of the scaffold) were used to define the segment of interest and to identify correspondence between baseline and follow-up examinations. These segments were used as control segments to examine the natural evolution of the TCFA in patients implanted with an Absorb BVS.

STATISTICAL ANALYSIS

Continuous variables are reported as mean and standard deviation whereas categorical values are presented as absolute values and percentages. Comparison between continuous variables at different time points was performed using the Wilcoxon signed-rank test while the Mann-Whitney U test was used for independent two-sample comparisons of the continuous variables. Comparison between categorical variables was performed using the Fisher's exact test. To control for patient effect, mixed models with random intercept were used to estimate the overall association between thickness, stent type, plaque type and follow-up time. A p-value <0.05 was considered statistically significant. Data analysis was performed using the Statistical Package for Social Sciences (SPSS) version 16.0 (SPSS Inc., Chicago, IL, USA) and SAS version 9.2 (SAS Institute Inc., Cary, NC, USA).

Results

PATIENT CHARACTERISTICS

Data from 47 segments (46 patients) implanted with an Absorb BVS and 20 segments (20 patients) treated with a BMS (12 with a single Svelte Coronary IDS stent, seven with a single and one with two vProtect™ devices) were included in the current analysis. At baseline in the patients implanted with an Absorb BVS, 10 TCFAs were detected in nine native coronary segments (six located proximally to the scaffolded segment and three distally): three of these segments had follow-up imaging at short-term (six- to 12-month) follow-up and six at midterm (24- to 36-month) follow-up. There were no differences in age and sex between the Absorb BVS and the BMS group; however, the patients implanted with a BMS were more likely to be diabetics and to have a history of coronary artery disease **(Table 1)**.

QUANTITATIVE CORONARY ANGIOGRAPHY ANALYSIS

Segments treated with a BMS had a larger RVD compared to those implanted with an Absorb BVS **(Table 2)**. At post-procedure, the MLD was smaller in the segments treated with an Absorb BVS but there were no differences in the DS between the two groups. There were no statistically significant differences in the QCA measurements between the two groups at short-term follow-up, although the LLL was numerically higher and had a broader standard deviation in the BMS arm. At midterm follow-up, there was a small but statistically significant reduction in the MLD in the Absorb BVS group.

OPTICAL COHERENCE TOMOGRAPHIC ANALYSIS

The total number of analysed frames was 9,007, of which 6,586 portrayed scaffolded segments, 1,714 stented segments and 697 native segments **(Online Table 1)**. All the scaffolded segments had

Table 1. Baseline characteristics of the studied population.

	Patients with TCFA in native segments	Patients implanted with an Absorb BVS	Patients implanted with a BMS	*p*
Baseline characteristics	**(n=9)**	**(n=46)**	**(n=20)**	
Age (years)	57±8	61±10	60±10	0.499
Male	7 (78%)	34 (73.9%)	14 (70%)	0.770
Hypertension	6 (67%)	28 (60.9%)	17 (85%)	0.084
Hypercholesterolaemia	7 (78%)	39 (84.8%)	17 (85%)	1.000
Diabetes mellitus	0 (0%)	3 (6.5%)	6 (30%)	0.018
Prior PCI	1 (11%)	9 (19.6%)	10 (50%)	0.018
Prior myocardial infarction	2 (22%)	14 (31.1%)	14 (70%)	0.006
Stable angina	9 (100%)	36 (78.3%)	12 (60%)	0.144
Unstable angina	0 (0%)	5 (10.9%)	3 (15%)	0.690
Myocardial infarction	0 (0%)	0 (0%)	5 (25%)	0.002
Treated vessel	**(n=9)**	**(n=47)**	**(n=20)**	
Left anterior descending artery	4 (44%)	25 (53.2%)	5 (25%)	0.059
Left circumflex artery	2 (22%)	7 (14.9%)	4 (20%)	0.721
Right coronary artery	3 (33%)	14 (29.8%)	11 (55%)	0.060
Ramus intermedius	0 (0%)	1 (2.1%)	0 (0%)	1.000
Medications	**(n=9)**	**(n=46)**	**(n=20)**	
ß-blockers	4 (44%)	30 (65%)	16 (80%)	0.262
RAAS inhibitors	5 (56%)	22 (48%)	14 (70%)	0.114
Statins	9 (100%)	42 (91%)	19 (95%)	1.000

PCI: percutaneous coronary intervention; RAAS: renin-angiotensin-aldosterone system; *p* by Fisher's exact test for binary variables and Mann-Whitney U test for continuous variables denotes the significance of difference between the Absorb BVS and the BMS group.

Table 2. QCA measurements at pre procedure, post-procedure, short-term and midterm follow-up in patients implanted with an Absorb BVS or a BMS.

	Pre procedure			Post-procedure			Short-term follow-up			Midterm follow-up	
	Absorb BVS (n=46)	BMS (n=20)	p_1	Absorb BVS (n=47)	BMS (n=20)	p_2	Absorb BVS (n=47)	BMS (n=19)	p_3	Absorb BVS (n=44)	p_4
Reference vessel diameter (mm)	2.59±0.34	2.89±0.43	0.010	2.66±0.30	3.02±0.41	0.001	2.55±0.30	2.77±0.45	0.105	2.53±0.35	0.375
Minimum lumen diameter (mm)	1.08±0.26	1.37±0.70	0.192	2.27±0.27	2.52±0.41	0.013	2.06±0.30	2.04±0.74	0.949	1.96±0.40	0.044
Diameter stenosis (%)	57.62±10.52	53.29±22.90	0.933	14.26±5.19	16.41±7.68	0.233	19.14±8.33	26.82±22.21	0.423	22.64±12.90	0.110
Late lumen loss (mm)							0.21±0.24	0.47±0.74	0.440	0.31±0.34	0.077

p_1: the significance of difference of the QCA measurements in the scaffolded and the stented segments at baseline before device implantation; p_2: the significance of difference for the QCA measurements between the scaffolded and the stented segments immediately after device deployment; p_3: the significance of difference between the QCA estimations in the Absorb BVS and BMS at short-term follow-up; p_4: the significance of difference of the QCA estimations in the scaffolded segments at short-term and midterm follow-up.

OCT imaging at short-term follow-up while at midterm follow-up 42 scaffolded segments underwent OCT examination.

The mean length of the scaffolded segments was 19.38±1.18 mm at baseline, 19.31±1.09 mm at short-term and 19.12±1.09 mm at midterm follow-up, (p=0.390); the length of the segments implanted with a Svelte Coronary IDS stent was 17.49±0.94 mm at baseline and 17.83±1.54 mm at short-term follow-up (p=0.594); the length of the segments treated with a vProtect stent was 16.80±4.16 mm and 16.43±3.25 mm, respectively (p=0.500); while the length of the studied native segments was 15.33±3.44 mm at baseline and 15.73±3.77 mm at follow-up (p=0.352).

The mean lumen area decreased in the scaffolded and stented segments between baseline and short-term follow-up, while the scaffold/stent area remained unchanged. The reduction of the lumen area in the scaffolded segments was considerably smaller than that observed in the stented segments (–1.34±0.99 mm^2 vs. –2.11±1.97 mm^2, p=0.026), a finding that was attributed to the increased neointima in the BMS group **(Table 3)**. At midterm follow-up the scaffold expanded (7.67±1.28 mm^2 vs. 8.28±1.74 mm^2, p<0.001) and accommodated the increased neointima (1.38±0.52 mm^2 vs. 2.17±0.48 mm^2, p<0.001) so that the lumen area remained unchanged. No evidence of neoatherosclerosis was seen in the scaffolded and stented segments. In the native segments there were no differences in the luminal dimensions between baseline and follow-up.

At baseline, 12 TCFA were detected in the scaffolded segments, 11 in the stented segments (three TCFA in patients implanted with a Svelte Coronary IDS stent and eight in patients implanted with a vProtect stent), and 10 TCFA in the nine native segments. There was no difference in the minimum cap thickness in TCFA identified at baseline in the scaffolded, stented and native segments (50±12 µm vs. 53±11 µm vs. 47±11 µm, p=0.595). At short-term follow-up, only one TCFA in the scaffolded and three TCFA in the stented segments were still present (p=0.231). At midterm follow-up, all TCFA detected at baseline in the scaffolded segment were

Table 3. OCT analysis at post-procedure, short-term and midterm follow-up in patients implanted with an Absorb BVS or a BMS.

	Post-procedure			Short-term follow-up					Midterm follow-up	
	Absorb BVS (n=47)	BMS (n=20)	p_1	Absorb BVS (n=47)	p'	BMS (n=20)	p''	p_2	Absorb BVS (n=42)	p'''
Lumen area in the scaffolded/stented segment (mm^2)	7.49±1.26	8.12±2.59	0.551	6.14±1.49	<0.001	6.00±3.06	<0.001	0.384	5.93±1.49	0.571
Scaffold/stent area (mm^2)	7.59±1.12	8.08±2.58	0.706	7.67±1.28	0.708	8.44±2.81	0.756	0.225	8.28±1.74	<0.001
Neointima area (mm^2)				1.38±0.52		2.29±1.39		0.002	2.17±0.48	<0.001
TCFA										
TCFA per patient in the scaffolded/stented segments	0.26±0.44	0.55±0.51	0.022	0.02±0.15	0.001	0.15±0.37	0.008	0.045	0	1.000
LPBI in scaffolded/stented segments (%)	4.90±10.12	15.38±19.70	0.010	4.40±10.16	0.519	15.90±19.45	0.638	0.007	4.62±11.23	0.700
Minimum thickness of the neointima tissue (µm)	–	–	–	23±28	–	85±118	–	0.324	85±72	0.016
Mean thickness of the neointima tissue (µm)	–	–	–	116±64	–	227±140	–	0.034	233±78	0.005
Calcific spots										
Spots per patient in the scaffolded/stented segments	3.19±2.20	3.15±2.37	0.917	3.17±2.32	0.944	2.45±2.58	0.105	0.125	3.38±2.14	0.518
CPBI in the scaffolded/stented segments (%)	5.23±4.90	4.15±3.33	0.442	4.12±4.12	0.017	2.85±4.26	0.100	0.066	4.51±4.44	0.349
Minimum thickness of the neointima tissue (µm)	–	–	–	101±94	–	195±132	–	<0.001*	168±90	<0.001*
Mean thickness of the neointimal tissue (µm)	–	–	–	180±301	–	281±195	–	0.045*	220±87	0.110*

p_1: the significance of difference between the OCT measurements in the scaffolded and stented segments at baseline post device implantation; p': the significance of difference for the OCT measurements in the scaffolded segment between baseline and short-term follow-up; p'': the significance of difference for the OCT measurements in the BMS between baseline and short-term follow-up; p_2: the significance of difference between the Absorb BVS and BMS at short-term follow-up; p''': the significance of difference between the OCT estimations in the Absorb BVS at short-term and midterm follow-up. * Calculated by mixed model considering several plaques per patient. CPBI: calcific plaque burden index; LPBI: lipid plaque burden index; TCFA: thin-cap fibroatheromas

fully covered. In native segments, six TCFA were still present after a follow-up period of 24±12 months. The minimum thickness of the tissue covering the TCFA in native segments increased compared to baseline but in all cases it was <150 μm (79±27 μm vs. 47±11 μm, p=0.013). The neointima thickness that developed over TCFA and calcific spots was higher in the segments implanted with a BMS at short-term follow-up compared to the neointima thickness measured in the Absorb BVS at the same time point. At midterm follow-up neointima continued to develop in the Absorb BVS. When we compared the mean neointima thickness over TCFA and calcific spots in the Absorb BVS at midterm follow-up, and in the BMS at six-month follow-up, there were no significant differences (p=0.948 and p=0.109, respectively). The lipid plaque burden index (LPBI) did not change at follow-up in the scaffolded, stented and native segments **(Table 3, Table 4, Figure 1-Figure 3)**.

One hundred and fifty calcific spots were detected post-procedure in the Absorb BVS, 63 in the BMS group and 10 in the native segments. Although there were no differences in the calcific spots detected at baseline and follow-up, there was a significant reduction in the calcific plaque burden index (CPBI) in both devices at short-term follow-up **(Figure 4)**, while in native segments the CPBI was significantly increased at follow-up (**Table 3**, **Table 4**).

The full mixed model, including the underlying tissue, follow-up time and stent type, for the mean neointima thickness showed a significant effect for follow-up time (lower at short-term, p=0.040) and stent type (lower in Absorb BVS, p=0.006) but not for the plaque type. A more restricted mixed model conducted using only the short-term data showed only a significant effect of the stent type for the mean thickness (p=0.023). When the mixed model was conducted using the short-term data from the BMS group and the midterm

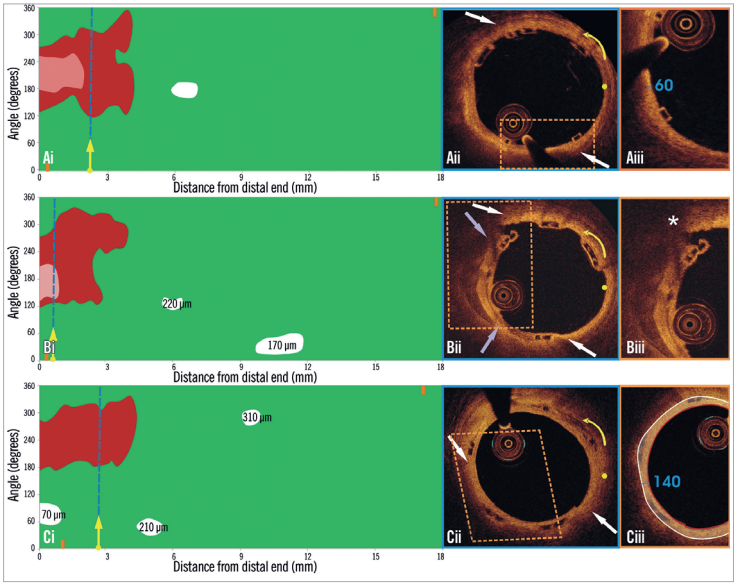

Figure 1. *Spread-out plots of a scaffolded coronary segment at baseline and at 12 and 36-month follow-up. The X axis represents the distance from the distal end of the scaffold, while the Y axis represents the circumferential segment (angle) where the different plaque components are located. The axial position of the metallic, non-translucent to light markers seen at the borders of the scaffold is shown with orange markers. The red colour corresponds to TCFA, the white to calcific, and the green to fibrous tissue. A mixed lipid/calcific plaque is detected at baseline (Ai) and at 12-month follow-up (Bi) at the distal end of the scaffold, and the calcific tissue is portrayed in a semi-transparent fashion. The calcific spots are fully covered by neointima at 12-month follow-up but not the TCFA detected at baseline. At three-year follow-up (Ci) the neointima has covered both lipid and calcific tissue. The measured minimum thickness is provided. The blue dashed lines indicate the location of the frames portrayed in panels Aii, Bii and Cii. The yellow spot in panels Aii, Bii and Cii denotes the 0 degree location in the spread-out scaffold plot, while the yellow arrow denotes the anticlockwise direction followed to evaluate the circumferential location of the detected tissues. The white arrows correspond to the lateral extremities of the lipid tissue and the grey to the lateral extremities of the calcific tissue. Panels Bii and Cii illustrate the frame with the minimum thickness of the neointima developed over the TCFA. The segments defined by the parallelograms with the dashed orange contour are portrayed in panels Aiii, Biii and Ciii. The minimum thickness of the cap in panel Aiii was measured as 60 μm using Sheehy's method. As is shown in panel Biii, there is vessel wall disruption and strut protrusion at 12 months and thus the TCFA detected at baseline is uncovered. At 36 months, the minimum neointimal thickness over the TCFA detected at baseline was estimated at 140 μm (panel Ciii).*

Table 4. Luminal dimensions, amount of the lipid cores and calcific spots and thickness of the overlaying tissue in native segments (n=9) with a TCFA phenotype.

	Baseline	Follow-up	*p*
Lumen area native segment (mm²)	7.09±1.84	7.24±1.96	0.594
TCFA			
TCFA per patient in the native segments	1.11±0.33	0.67±0.70	0.296
LPBI in native segment (%)	28.47±20.87	28.12±22.00	0.767
Calcific spots			
Spots per patient in the native segments	1.44±2.60	1.44±1.70	0.705
CPBI in the native segment (%)	4.43±9.51	6.84±12.89	0.043

data from the Absorb BVS group, neither the stent type nor the tissue type had an effect on the mean thickness (p=0.090 and p=0.080, respectively).

LESION-RELATED CARDIOVASCULAR EVENTS

Within the studied follow-up period, three lesion-related events were reported in the Absorb BVS group (two non-Q-wave myocardial infarctions occurred at short-term follow-up, of which one was periprocedural, and one target lesion revascularisation occurred at midterm follow-up). In the BMS arm, two target lesion revascularisations were reported at short-term follow-up.

Discussion

In this analysis we introduced a novel approach, the spread-out vessel plots, to visualise and assess changes in the composition of the superficial plaque in native segments and in segments implanted with Absorb BVS or BMS. We found that: 1) in contrast to native coronary segments where the morphology of most of the plaques remained unchanged, the neointima that developed in treated segments altered the phenotype of the plaque by covering the calcific spots and TCFA with neointima, thus transforming the TCFA to thick-cap fibroatheromas; 2) the increased neointima reported in BMS caused a significantly higher reduction in the luminal dimensions; 3) in Absorb BVS neointima continued to develop after the short-term follow-up and sealed the underlying plaques without compromising the luminal dimensions, since the scaffold was shown to expand: and 4) the type of the underlying tissue did not appear to affect neointimal formation with either the BMS or the Absorb BVS.

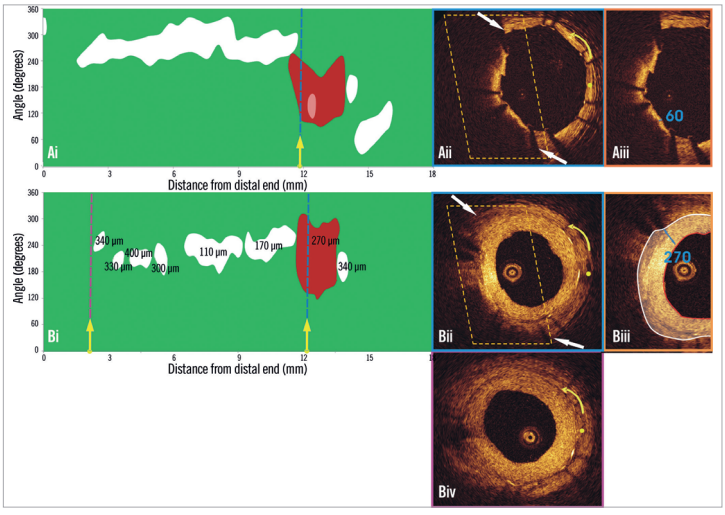

Figure 2. *Spread-out plot of a stented segment at baseline and at six-month follow-up. The blue dashed lines indicate the location of the frames portrayed in panels Aii and Bii, while the purple dashed line indicates the frame portrayed in panel Biv. The yellow spot in panels Aii, Bii and Biv denotes the 0 degree location in the spread-out scaffold plot, while the yellow arrow denotes the anticlockwise direction followed to evaluate the circumferential location of the detected tissues. A TCFA is detected at baseline (Aii). Panel Bii illustrates the frame with the minimum thickness of the neointima developed over the TCFA. The segments defined by the parallelograms with the dashed orange contour are portrayed in panels Aiii and Biii. The minimum thickness of the cap in panel Aiii was measured at 60 µm. As is shown in panel Biii, the minimum thickness of the neointima that has covered the TCFA was estimated at 270 µm (panel Ciii). The excessive neointima resulted in a significant reduction of the lumen area and did not allow visualisation of the calcific tissue in some OCT frames at follow-up. The minimum lumen area at follow-up was measured 1.86 mm² (Biv) while the CPBI was reduced from 12.00% to 5.35%.*

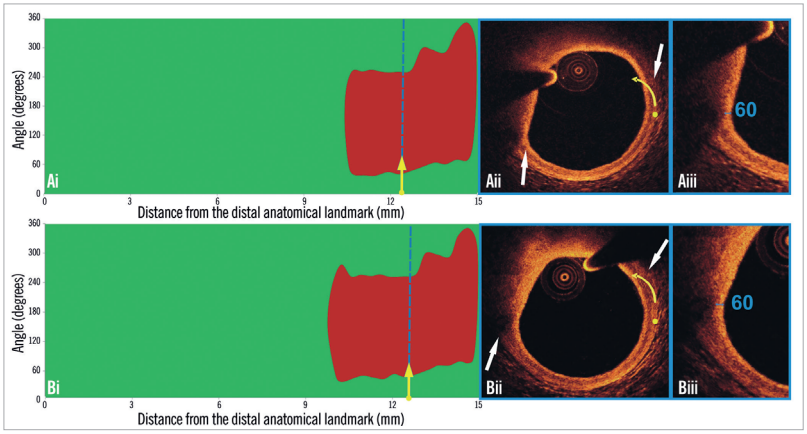

Figure 3. *Spread-out plots of a native coronary segment at baseline and at 12-month follow-up. The X axis represents the distance from the distal end of the segment of interest, while the Y axis represents the circumferential segment (angle) where the different plaque components are located. At baseline (Ai) and follow-up examination (Bi) a TCFA is detected at the distal end of the segment of interest. The blue dashed lines indicate the location of the minimum thickness of the fibrous cap, and the corresponding frames are portrayed in panels Aii and Bii. The yellow spot in panels Aii and Bii denotes the 0 degree location in the spread-out scaffold plot, while the yellow arrow denotes the anticlockwise direction followed to evaluate the circumferential location of the detected tissues. The white arrows denote the lateral extremities of the lipid tissue. The minimum thickness of the cap in panel Aii was 60 μm (Aiii) and was unchanged at follow-up (Biii).*

SPREAD-OUT VESSEL PLOTS FOR THE QUANTIFICATION OF THE COMPOSITION OF THE PLAQUE

IVUS and IVUS-VH cannot be used to detect changes in the composition of the superficial plaque following an Absorb BVS implantation, since the polymeric struts appear as bright hyperechogenic shadows with acoustic fingerprints, similar to calcific tissue, leading to false estimations[11,12]. Since OCT has a substantially higher resolution compared to IVUS, it can overcome these limitations and permit a more accurate characterisation of the superficial plaque, and assessment of neointima thickness over different tissues. The low intra- and inter-observer variability for the characterisation of different tissues, the circumferential location and the extent of the detected lipid and calcific tissue indicates that the use of spread-out vessel plots allows not only for a comprehensive and reproducible visualisation of the superficial plaque, but also for an accurate quantification of each plaque component **(Online Table 2)**[13,14].

STENT TYPE AND NEOINTIMAL PROLIFERATION

We found that, in both the Absorb BVS and BMS groups, at short-term follow-up the developed neointima covered most of the TCFA and calcific spots. The neointima was increased in the BMS arm (although this group included non-flow-limiting plaques that were treated with a self-expanding stent, something which is anticipated to cause less vessel wall trauma) compared to the Absorb BVS group, and it reduced considerably the luminal dimensions at follow-up. The difference in the neointima burden is likely to be attributed to the antiproliferative properties of everolimus in the Absorb BVS, which controlled the vessel wall healing process. Moreover, in contrast to BMS where it has been shown that the neointima formation is completed within the first six months post device implantation, in Absorb BVS the neointima continues to develop beyond 12 months[15].

In contrast to the metallic stents in Absorb BVS, the delayed neointima proliferation did not compromise luminal dimensions, as the loss of the scaffold's structural integrity allowed the device to expand and accommodate the developed tissue that re-capped the underlying high-risk plaques[5,15,16]. This unique ability of the Absorb BVS, in combination with the fact that it disappears at long-term follow-up and thus allows for the restoration of vessel wall physiologic function, renders the Absorb BVS a potentially useful tool for the invasive treatment of high-risk, i.e., prone to rupture, plaques[2]. Of note, there is no evidence to support the use of any endovascular device for this purpose, and it is too premature to advocate an invasive sealing of vulnerable plaques based on the findings of this analysis. Although intravascular imaging studies have allowed us to identify plaque characteristics associated with increased vulnerability, and provided unique insights into atherosclerotic evolution, robust evidence from randomised control trials and further research are required in order to identify more accurately future culprit lesions and the timing of the event before advocating the use of BVS to re-cap vulnerable plaques[17].

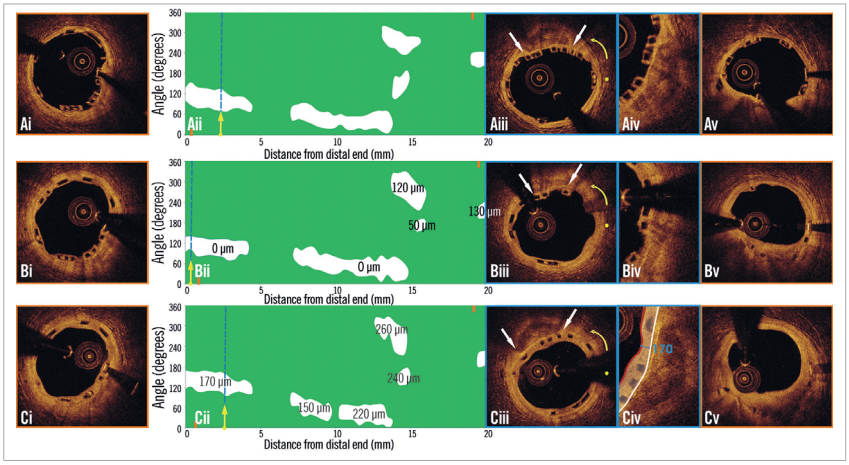

Figure 4. *Spread-out plot of a scaffolded segment at baseline and at 12 and 36-month follow-up. The orange markers, shown on the spread-out plots at baseline (Aii) and follow-up (Bii, Cii), correspond to the axial position of the metallic non-translucent to light markers. The proximal markers are shown in panels Ai, Bi, Ci, and the distal markers in panels Av, Bv, and Cv. The blue dashed lines indicate the location of the frames portrayed in panels Aiii, Biii and Ciii. The yellow spot in panels Aiii, Biii, and Ciii denotes the 0 degree location in the spread-out scaffold plots, while the yellow arrow denotes the anticlockwise direction followed to evaluate the circumferential location of the detected tissues. The white arrows correspond to the lateral extremities of the detected calcific tissue. As is shown in panels Aiii, Aiv, Biii, Biv, Ciii and Civ, the neointima (minimum thickness: 110 µm at six-month and 210 µm at 24-month follow-up) developed after scaffold implantation sealed the calcific tissue at follow-up.*

COMPOSITION OF THE PLAQUE AND NEOINTIMAL PROLIFERATION

Plaque composition is likely to influence vessel wall response after scaffold or stent implantation, as neointima formation is based on pathophysiological mechanisms (e.g., local inflammation, migration and proliferation of smooth muscle cells, etc.) which involve the underlying vessel wall[18-21]. In a recent report, Kubo et al found no association between the amount of the lipid core component at baseline and the neointimal formation in BMS and drug-eluting stents at follow-up, while Shimada et al showed that calcific-rich plaques were associated with less neointimal proliferation in BMS but did not affect the healing process in drug-eluting stents[22,23].

We found a similar distribution of the neointimal tissue over TCFA and calcific spots in both the Absorb BVS and the BMS groups. The discrepancy between our findings and the results reported by Shimada et al in BMS may be attributed to the different imaging modality used to measure neointimal thickness (Shimada et al used greyscale IVUS and not OCT), as well as to the fact that the BMS group included two different types of stent with a different mechanical behaviour (a balloon-expandable and a self-expandable stent which was implanted in non-obstructive lesions). The smaller minimum neointimal thickness reported over TCFA compared to the one measured in the calcific spots in both the Absorb BVS and the BMS groups may be attributed to the larger surface of the TCFA (in the Absorb BVS group each TCFA occupied 17.22±13.82% while each calcific spot occupied 1.33±0.95% of the spread-out at short-term follow-up, whereas in the BMS group each TCFA occupied 28.91±17.47% and each calcific spot occupied 1.25±1.07%, $p<0.001$).

In contrast to the native segments where the calcific plaque burden index (CPBI) appears to increase at follow-up, in the scaffolded/stented segments the CPBI decreased. The reduction of the CPBI in the treated segments (which is not in agreement with computed tomographic calcium screening studies that showed an increase in calcium burden over time) should be attributed to the developed neointima which masked deeply embedded calcific spots that were visible in the baseline OCT examination, resulting in the false impression that the calcific tissue is reduced at follow-up. On the other hand, there were no differences in the LPBI as this referred to lipid tissue which was located in the superficial plaque.

Limitations

A significant limitation of the current analysis is the fact that the characterisation of the superficial plaque was performed in the scaffolded and stented segments post device implantation. To minimise erroneous estimations, we identified vessel wall discontinuities and we did not measure the thickness of the cap in these segments. It is plausible that micro-disruptions which could not be identified by the naked eye may have led to erroneous assessments of plaque morphology.

Another limitation of this study is that the quantification of the composition of the superficial plaque depended on the expertise of the two observers. OCT may often fail to discriminate lipid from macrophages or calcific tissue, especially when the lipid/calcific tissue is deeply embedded in the vessel wall[24]. However, since the reproducibility and the agreement of the observers were high, we believe that these erroneous estimations did not affect our findings.

Moreover, although it is evident that the neointima develops in BMS within the first six months post device implantation and thus we did not expect to have different findings in the BMS arm at midterm follow-up, there was a lack of midterm follow-up data in the BMS group which would have allowed a direct comparison of the neointima and luminal dimensions between the Absorb BVS and the BMS at this time point[25]. The lack of a drug-eluting stent group can be considered as another limitation of this analysis. Neointima formation appears to be reduced in drug-eluting stents at short-term follow-up, and thus the changes in the luminal dimensions and the phenotype of the underlying plaque are anticipated to be small at this time point[26]. However, at midterm follow-up the tissue response in drug-eluting stents is similar to the BMS, as the neointima tissue continues to develop and compromises the luminal dimensions[27].

Finally, the difference in the demographics and clinical presentation of the patients implanted with an Absorb BVS and those treated with a BMS is another limitation of this study.

Conclusions

The implementation of spread-out vessel plots allowed us to evaluate changes in the composition of the superficial plaque in segments implanted with an Absorb BVS or a BMS and to compare these changes with the alterations noted in native segments that were used as a control group. We found that, in contrast to the native segments, in the scaffolded and stented segments a thick layer of tissue developed over both lipid and calcific tissues that modifies the morphology of the plaque to more stable phenotypes. The neointima tissue in BMS considerably compromised the luminal dimensions, whereas in the Absorb BVS the neointima developed slowly and was accommodated by the expanded device. This unique ability of the Absorb BVS renders it more appropriate than a BMS for the re-capping of high-risk plaques.

Impact on daily practice

A novel methodology is presented for the processing of serial optical coherence tomographic data and the assessment of the changes in the morphology of the superficial plaque following bioresorbable scaffold or bare metal stent implantation. In both devices, the developed neointima re-caps the underlying plaque, covers tissues with high-risk characteristics, and modifies the plaque morphology to more stable phenotypes. In contrast to bare metal stents, in bioresorbable scaffolds the developed neointima does not compromise the luminal dimensions as it is accommodated by the expanded device. Therefore bioresorbable scaffolds may have a value in the future for the invasive sealing of high-risk, prone to rupture plaques.

Guest Editor

This paper was guest edited by Giulio Guagliumi, MD; Department of Interventional Cardiology, Ospedale Papa Giovanni XXIII, Bergamo, Italy.

Acknowledgements

The first author would like to acknowledge the funding support of the Hellenic Heart Foundation (ELIKAR), Athens, Greece.

Conflict of interest statement

A. Sheehy, S. Veldhof and R. Rapoza are employees of Abbott Vascular. None of the other authors has any conflicts of interest to declare. The Guest Editor is a consultant for Boston Scientific and St. Jude Medical and has received institutional research grants from Abbott Vascular, Boston Scientific, St. Jude Medical.

References

1. Brugaletta S, Heo JH, Garcia-Garcia HM, Farooq V, van Geuns RJ, de Bruyne B, Dudek D, Smits PC, Koolen J, McClean D, Dorange C, Veldhof S, Rapoza R, Onuma Y, Bruining N, Ormiston JA, Serruys PW. Endothelial-dependent vasomotion in a coronary segment treated by ABSORB everolimus-eluting bioresorbable vascular scaffold system is related to plaque composition at the time of bioresorption of the polymer: indirect finding of vascular reparative therapy? *Eur Heart J.* 2012;33:1325-33.

2. Serruys PW, Garcia-Garcia HM, Onuma Y. From metallic cages to transient bioresorbable scaffolds: change in paradigm of coronary revascularization in the upcoming decade? *Eur Heart J.* 2012;33:16-25b.

3. Serruys PW, Ormiston JA, Onuma Y, Regar E, Gonzalo N, Garcia-Garcia HM, Nieman K, Bruining N, Dorange C, Miquel-Hebert K, Veldhof S, Webster M, Thuesen L, Dudek D. A bioabsorbable everolimus-eluting coronary stent system (ABSORB): 2-year outcomes and results from multiple imaging methods. *Lancet.* 2009;373:897-910.

4. Bourantas CV, Papafaklis MI, Kotsia A, Farooq V, Muramatsu T, Gomez-Lara J, Zhang YJ, Iqbal J, Kalatzis FG, Naka KK, Fotiadis DI, Dorange C, Wang J, Rapoza R, Garcia-Garcia HM, Onuma Y, Michalis LK, Serruys PW. Effect of the endothelial shear stress patterns on neointimal proliferation following drug-eluting bioresorbable vascular scaffold implantation: an optical coherence tomography study. *JACC Cardiovasc Interv.* 2014;7:315-24.

5. Onuma Y, Serruys PW, Perkins LE, Okamura T, Gonzalo N, Garcia-Garcia HM, Regar E, Kamberi M, Powers JC, Rapoza R, van Beusekom H, van der Giessen W, Virmani R. Intracoronary optical coherence tomography and histology at 1 month and 2, 3, and 4 years after implantation of everolimus-eluting bioresorbable vascular scaffolds in a porcine coronary artery model: an attempt to decipher the human optical coherence tomography images in the ABSORB trial. *Circulation*. 2010;122:2288-300.

6. Brugaletta S, Radu MD, Garcia-Garcia HM, Heo JH, Farooq V, Girasis C, van Geuns RJ, Thuesen L, McClean D, Chevalier B,

Windecker S, Koolen J, Rapoza R, Miquel-Hebert K, Ormiston J, Serruys PW. Circumferential evaluation of the neointima by optical coherence tomography after ABSORB bioresorbable vascular scaffold implantation: can the scaffold cap the plaque? *Atherosclerosis.* 2012;221:106-12.

7. Wykrzykowska JJ, Diletti R, Gutierrez-Chico JL, van Geuns RJ, van der Giessen WJ, Ramcharitar S, Duckers HE, Schultz C, de Feyter P, van der Ent M, Regar E, de Jaegere P, Garcia-Garcia HM, Pawar R, Gonzalo N, Ligthart J, de Schepper J, van den Berg N, Milewski K, Granada JF, Serruys PW. Plaque sealing and passivation with a mechanical self-expanding low outward force nitinol vShield device for the treatment of IVUS and OCT-derived thin cap fibroatheromas (TCFAs) in native coronary arteries: report of the pilot study vShield Evaluated at Cardiac hospital in Rotterdam for Investigation and Treatment of TCFA (SECRITT). *EuroIntervention.* 2012;8:945-54.

8. Serruys PW, Onuma Y, Ormiston JA, de Bruyne B, Regar E, Dudek D, Thuesen L, Smits PC, Chevalier B, McClean D, Koolen J, Windecker S, Whitbourn R, Meredith I, Dorange C, Veldhof S, Miquel-Hebert K, Rapoza R, Garcia-Garcia HM. Evaluation of the second generation of a bioresorbable everolimus drug-eluting vascular scaffold for treatment of de novo coronary artery stenosis: six-month clinical and imaging outcomes. *Circulation*. 2010;122:2301-12.

9. Diletti R, Garcia-Garcia HM, Bourantas CV, van Geuns RJ, Van Mieghem NM, Agostoni P, Muramatsu T, Farooq V, Spencer R, De Schepper J, Pomeranz M, Stella P, Serruys PW. Clinical and angiographic outcomes following first-in-man implantation of a novel thin-strut low-profile fixed-wire stent: the Svelte Coronary Stent Integrated Delivery System first-in-man trial. *EuroIntervention.* 2013;9:125-34.

10. Guagliumi G, Costa MA, Sirbu V, Musumeci G, Bezerra HG, Suzuki N, Matiashvili A, Lortkipanidze N, Mihalcsik L, Trivisonno A, Valsecchi O, Mintz GS, Dressler O, Parise H, Maehara A, Cristea E, Lansky AJ, Mehran R, Stone GW. Strut coverage and late malapposition with paclitaxel-eluting stents compared with bare metal stents in acute myocardial infarction: optical coherence tomography substudy of the Harmonizing Outcomes with Revascularization and Stents in Acute Myocardial Infarction (HORIZONS-AMI) Trial. *Circulation*. 2011;123:274-81.

11. Bruining N, de Winter S, Roelandt JR, Regar E, Heller I, van Domburg RT, Hamers R, Onuma Y, Dudek D, Webster MW, Thuesen L, Ormiston JA, Cheong WF, Miquel-Hebert K, Veldhof S, Serruys PW. Monitoring in vivo absorption of a drug-eluting bioabsorbable stent with intravascular ultrasound-derived parameters a feasibility study. *JACC Cardiovasc Interv.* 2010;3:449-56.

12. Brugaletta S, Gomez-Lara J, Garcia-Garcia HM, Heo JH, Farooq V, van Geuns RJ, Chevalier B, Windecker S, McClean D, Thuesen L, Whitbourn R, Meredith I, Dorange C, Veldhof S, Rapoza R, Ormiston JA, Serruys PW. Analysis of 1 year virtual histology changes in coronary plaque located behind the struts of the everolimus eluting bioresorbable vascular scaffold. *Int J Cardiovasc Imaging.* 2012;28:1307-14.

13. Tearney GJ, Waxman S, Shishkov M, Vakoc BJ, Suter MJ, Freilich MI, Desjardins AE, Oh WY, Bartlett LA, Rosenberg M, Bouma BE. Three-dimensional coronary artery microscopy by intracoronary optical frequency domain imaging. *JACC Cardiovasc Imaging.* 2008;1:752-61.

14. Waxman S, Freilich MI, Suter MJ, Shishkov M, Bilazarian S, Virmani R, Bouma BE, Tearney GJ. A case of lipid core plaque progression and rupture at the edge of a coronary stent: elucidating the mechanisms of drug-eluting stent failure. *Circ Cardiovasc Interv.* 2010;3:193-6.

15. Ormiston JA, Serruys PW, Onuma Y, van Geuns RJ, de Bruyne B, Dudek D, Thuesen L, Smits PC, Chevalier B, McClean D, Koolen J, Windecker S, Whitbourn R, Meredith I, Dorange C, Veldhof S, Hebert KM, Rapoza R, Garcia-Garcia HM. First serial assessment at 6 months and 2 years of the 2nd generation of Absorb everolimus eluting bioresorbable vascular scaffold: a multi-imaging modality study. *Circ Cardiovasc Interv.* 2012;5:620-32.

16. Nishio S, Kosuga K, Igaki K, Okada M, Kyo E, Tsuji T, Takeuchi E, Inuzuka Y, Takeda S, Hata T, Takeuchi Y, Kawada Y, Harita T, Seki J, Akamatsu S, Hasegawa S, Bruining N, Brugaletta S, de Winter S, Muramatsu T, Onuma Y, Serruys PW, Ikeguchi S. Long-term (>10 years) clinical outcomes of first-in-human biodegradable poly-l-lactic acid coronary stents: Igaki-Tamai stents. *Circulation*. 2012;125:2343-53.

17. Bourantas CV, Garcia-Garcia HM, Diletti R, Muramatsu T, Serruys PW. Early detection and invasive passivation of future culprit lesions: a future potential or an unrealistic pursuit of chimeras? *Am Heart J.* 2013;165:869-81.e4.

18. Kornowski R, Hong MK, Tio FO, Bramwell O, Wu H, Leon MB. In-stent restenosis: contributions of inflammatory responses and arterial injury to neointimal hyperplasia. *J Am Coll Cardiol.* 1998;31:224-30.

19. Kibos A, Campeanu A, Tintoiu I. Pathophysiology of coronary artery in-stent restenosis. *Acute Card Care.* 2007;9:111-9.

20. Farb A, Weber DK, Kolodgie FD, Burke AP, Virmani R. Morphological predictors of restenosis after coronary stenting in humans. *Circulation*. 2002;105:2974-80.

21. Farooq V, Gogas BD, Serruys PW. Restenosis: delineating the numerous causes of drug-eluting stent restenosis. *Circ Cardiovasc Interv.* 2011;4:195-205.

22. Shimada Y, Kataoka T, Courtney BK, Morino Y, Bonneau HN, Yock PG, Grube E, Honda Y, Fitzgerald PJ. Influence of plaque calcium on neointimal hyperplasia following bare metal and drug-eluting stent implantation. *Catheter Cardiovasc Interv.* 2006;67: 866-9.

23. Kubo T, Maehara A, Mintz GS, Garcia-Garcia HM, Serruys PW, Suzuki T, Klauss V, Sumitsuji S, Lerman A, Marso SP, Margolis MP, Margolis JR, Foster MC, De Bruyne B, Leon MB, Stone GW. Analysis of the long-term effects of drug-eluting stents on coronary arterial wall morphology as assessed by virtual histology intravascular ultrasound. *Am Heart J.* 2010;159:271-7.

24. Manfrini O, Mont E, Leone O, Arbustini E, Eusebi V, Virmani R, Bugiardini R. Sources of error and interpretation of

plaque morphology by optical coherence tomography. *Am J Cardiol*. 2006;98:156-9.

25. Kimura T, Tamura T, Yokoi H, Nobuyoshi M. Long-term clinical and angiographic follow-up after placement of Palmaz-Schatz coronary stent: a single center experience. *J Interv Cardiol.* 1994;7:129-39.

26. Shiratori Y, Brugaletta S, Alvarez-Contreras L, Azpeitia Y, Ospino N, Gaido S, Delahanty A, Santos A, Martin-Yuste V, Masotti M, Serruys PW, Windecker S, Sabate M. One-year head to head comparison of the neointimal response between sirolimus eluting stent with reservoir technology and everolimus eluting stent: an optical coherence tomography study. *Catheter Cardiovasc Interv.* 2013;82:E428-36.

27. Kim JS, Hong MK, Shin DH, Kim BK, Ko YG, Choi D, Jang Y. Quantitative and qualitative changes in DES-related neointimal tissue based on serial OCT. *JACC Cardiovasc Imaging.* 2012;5: 1147-55.

28. Radu MD, Raber L, Heo J, Gogas BD, Jorgensen E, Kelbaek H, Muramatsu T, Farooq V, Helqvist S, Garcia-Garcia HM, Windecker S, Saunamaki K, Serruys PW. Natural history of optical coherence tomography-detected non-flow-limiting edge dissections following drug-eluting stent implantation. *EuroIntervention.* 2014;9:1085-94.

29. Tearney GJ, Regar E, Akasaka T, Adriaenssens T, Barlis P, Bezerra HG, Bouma B, Bruining N, Cho JM, Chowdhary S, Costa MA, de Silva R, Dijkstra J, Di Mario C, Dudek D, Falk E, Feldman MD, Fitzgerald P, Garcia H, Gonzalo N, Granada JF, Guagliumi G, Holm NR, Honda Y, Ikeno F, Kawasaki M, Kochman J, Koltowski L, Kubo T, Kume T, Kyono H, Lam CC, Lamouche G, Lee DP, Leon MB, Maehara A, Manfrini O, Mintz GS, Mizuno K, Morel MA, Nadkarni S, Okura H, Otake H, Pietrasik A, Prati F, Raber L, Radu MD, Rieber J, Riga M, Rollins A, Rosenberg M, Sirbu V, Serruys PW, Shimada K, Shinke T, Shite J, Siegel E, Sonada S, Suter M, Takarada S, Tanaka A, Terashima M, Troels T, Uemura S, Ughi GJ, van Beusekom HM, van der Steen AF, van Es GA, van Soest G, Virmani R, Waxman S, Weissman NJ, Weisz G; International Working Group for Intravascular Optical Coherence Tomography (IWG-IVOCT). Consensus standards for acquisition, measurement, and reporting of intravascular optical coherence tomography studies: a report from the International Working Group for Intravascular Optical Coherence Tomography Standardization and Validation. *J Am Coll Cardiol.* 2012;59:1058-72.

30. Raber L, Radu MD, Garcia-Garcia HM, Akasaka T, Banz Y, Kume T, Windecker S, Serruys PW. Atherosclerosis. In: Radu MD, Raber L, Garcia-Garcia H, Serruys PW, editors. The clinical atlas of optical coherence tomography. Toulouse, France: Europa Edition; 2012.

31. Sheehy A, Gutierrez-Chico JL, Diletti R, Oberhauser JP, Glauser T, Harrington J, Kossuth MB, Rapoza RJ, Onuma Y, Serruys PW. In vivo characterisation of bioresorbable vascular scaffold strut interfaces using optical coherence tomography with Gaussian line spread function analysis. *EuroIntervention.* 2012;7: 1227-35.

32. Gutierrez-Chico JL, Radu MD, Diletti R, Sheehy A, Kossuth MB, Oberhauser JP, Glauser T, Harrington J, Rapoza RJ, Onuma Y, Serruys PW. Spatial distribution and temporal evolution of scattering centers by optical coherence tomography in the poly(L-lactide) backbone of a bioresorbable vascular scaffold. *Circ J.* 2012;76:342-50.

33. Gutierrez-Chico JL, van Geuns RJ, Regar E, van der Giessen WJ, Kelbaek H, Saunamaki K, Escaned J, Gonzalo N, di Mario C, Borgia F, Nuesch E, Garcia-Garcia HM, Silber S, Windecker S, Serruys PW. Tissue coverage of a hydrophilic polymer-coated zotarolimus-eluting stent vs. a fluoropolymer-coated everolimus-eluting stent at 13-month follow-up: an optical coherence tomography substudy from the RESOLUTE All Comers trial. *Eur Heart J.* 2011;32:2454-63.

34. Gnanadesigan M, van Soest G, White S, Scoltock S, Ughi GJ, Baumbach A, van der Steen AF, Regar E, Johnson TW. Effect of temperature and fixation on the optical properties of atherosclerotic tissue: a validation study of an ex-vivo whole heart cadaveric model. *Biomed Opt Express.* 2014;5:1038-49.

35. Virmani R, Burke AP, Farb A, Kolodgie FD. Pathology of the vulnerable plaque. *J Am Coll Cardiol.* 2006;47:C13-8.

36. Burke AP, Farb A, Malcom GT, Liang YH, Smialek J, Virmani R. Coronary risk factors and plaque morphology in men with coronary disease who died suddenly. *N Engl J Med.* 1997; 336:1276-82.

37. Cohen J. A coefficient of agreement for nominal scales. *Educ Psychol Meas.* 1960;20:37-46.

Online data supplement

Online Appendix. Vessel wall discontinuities.

Online Table 1. Number of frames (total number: 9,907) analysed in segments implanted with a bioresorbable vascular scaffold (Absorb BVS), a bare metal stent (BMS) and in native segments portraying a thin-cap fibroatheroma at baseline, short-term (6 to 12-month) and midterm (24 to 36-month) follow-up.

Online Table 2. Intra- and inter-observer variability for the thickness of the neointima tissue and the circumferential location and extent of the lipid and the calcific tissue.

Online Figure 1. Different types of vessel wall discontinuities seen after Absorb bioresorbable scaffold implantation.

Online Figure 2. Determination of the circumferential distribution of a calcific tissue.

Online Figure 3. Plot of the intensities of the backscatter OCT signals in calcific tissue.

Online Figure 4. Methodology implemented to measure the thickness of the neointima developed over the calcific tissue identified in a segment treated with a bare metal stent.

Online Figure 5. Assessment of observers' agreement.

Online data supplement

Appendix

VESSEL WALL DISCONTINUITIES

Discontinuities of the vessel wall in the scaffolded and stented segments were defined as disruption of the vessel wall and were classified into four categories: flaps, cavities, double lumen and fissures, according to the classification proposed by Radu et al **(Online Figure 1)**[28].

The two observers identified vessel wall discontinuities in 677 (30%) out of the 2,282 frames that portrayed scaffolded segments at baseline. Flaps were detected in 368 (16%) frames, cavities in 126 (6%), double lumen in 35 (2%), and fissures in 221 (10%) frames.

In the segments treated with a BMS, vessel wall discontinuities were detected in 236 (27%) out of the 864 frames. Flaps were detected in 135 (16%) frames, cavities in 37 (4%), double lumen in 12 (1%), and fissures in 87 (10%) frames. As would be expected, the incidence of vessel wall discontinuities was lower in the non-obstructive lesions that were implanted with the self-expanding device than in the stenotic lesions treated with a balloon-expandable metallic stent (13% vs. 36%, p<0.001). There were no differences in the incidence of vessel wall discontinuities in segments treated with a BMS compared with those implanted with an Absorb BVS (p=0.272).

CHARACTERISATION OF THE COMPOSITION OF THE SUPERFICIAL PLAQUE

In the analysed cross-sections, the operators identified the superficial lipid (shown as a signal-poor region with poorly delineated borders, a fast signal drop-off and little or no signal backscattering) and calcific tissue (appearing as a signal-poor heterogeneous region with sharp borders) and marked their location[29,30]. In particular, two markers were placed at the two lateral extremities of the lipid/calcific tissue. Then, their circumferential position was determined with respect to the gravitational centre of the lumen area, and expressed as an angle taking the position at 3 o'clock as the 0° reference **(Online Figure 2)**. Any disagreement between observers was resolved by consensus.

In the segments where there was no disruption, the observers measured the thickness of the fibrous cap over lipid tissue. All the frames portraying lipid tissue that was covered by a thin cap (thickness ≤70 μm – as this was measured with the use of the St. Jude Medical Inc. software which allows calculation of the cap thickness with a resolution of 10 μm) were further processed using the methodology of Sheehy et al to identify more accurately thin-capped fibroatheromas (TCFA)[31]. This approach has been implemented for the *in vivo* evaluation of the thickness of the struts in the Absorb BVS. In brief, the location of the minimum thickness of the fibrous cap was identified by the two observers and then a line was drawn vertical to the lumen border **(Online Figure 3)**. The intensities of the backscatter OCT signal, along that line, were plotted, and two Gaussian curves were drawn to approximate the plotted intensities at the two sides of the

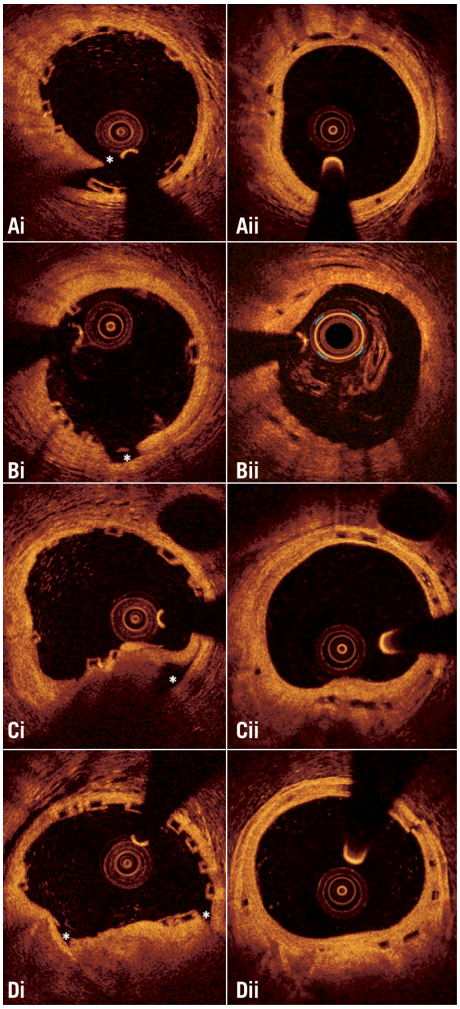

Online Figure 1. *Different types of vessel wall discontinuities seen after Absorb bioresorbable scaffold implantation. (Ai) flap, (Bi) cavity, (Ci) false lumen, and (Di) fissure. The location of the discontinuity is indicated with an asterisk. As is shown in the corresponding frames (panels Aii, Bii, Cii, and Dii) acquired at midterm follow-up, the developed neointima has covered the vessel wall disruptions detected at baseline.*

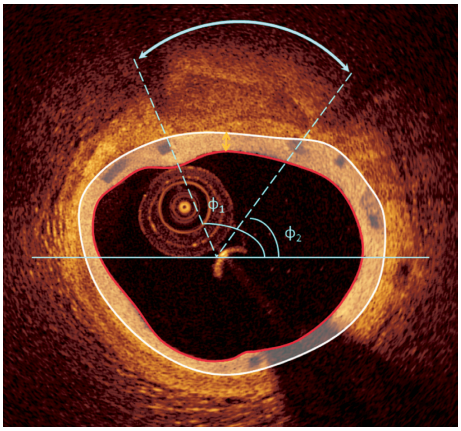

Online Figure 2. *Determination of the circumferential distribution of a calcific tissue. After the detection of the luminal border, the two observers identified the lateral extremities of the calcific tissue. Following the anticlockwise direction the circumferential location of the closest and most remote extremities of the calcific tissue is expressed as the angle defined by each extremity, the gravitational centre of the lumen and a reference horizontal axis at 3 o'clock. The angle difference between the two extremities defines the circumferential extent of the calcific tissue. The yellow arrow indicates the minimum thickness of the neointimal tissue developed over the calcific tissue which was estimated as 200 μm.*

cap (luminal and lipid). The Gaussian fit was determined separately for each side through symmetry of a one-tailed Gaussian fit, with the first peak defining the peak of the Gaussian function. The boundary of the edge of the cap was identified as the half-max of the curve. The width of the cap was determined as the distance from the half-max of one curve to the half-max of the other curve. This approach was restricted to thin fibrous caps, as only in these cases were the optics of the area of interest represented by a Gaussian fit. Deeply embedded lipid tissues exhibited more heterogeneity of signal at the interface and a less clear optical pathway, while the calcium had a heterogeneous appearance and thus the distal interface of the overlaying tissue to the calcific tissue could not be approximated by a Gaussian curve **(Online Figure 3)**. At follow-up examinations the observers estimated the minimum thickness of the neointimal tissue over calcific and lipid tissues that corresponded to the detected TCFA at baseline.

In addition, the two observers reviewed the baseline OCT examinations of the patients implanted with an Absorb BVS and identified the TCFA that were located in native segments proximal and distal to the implanted device. Anatomical landmarks located distally and proximally to the TCFA (i.e., the origin of side branches or the proximal or distal end of the scaffold) were used to define the segment of interest and identify correspondence between baseline and follow-up examinations. The lumen borders were detected in these segments and the circumferential extent of the calcific and lipid tissue was marked as before.

SPREAD-OUT VESSEL PLOTS

The spatial distribution of the TFCA and calcific tissues along the scaffolded/stented and native segments of interest was depicted in spread-out vessel plots[32-34]. These graphs were created by plotting the lateral extremities of the tissue with respect to the angle, which defines their circumferential location, and the longitudinal distance of the analysed frame from the distal end of the studied segment. Extremities with similar circumferential location detected in consecutive frames that delineate the same plaque component (e.g., lipid or calcific tissue) were assumed to define the same plaque type and connected with a Bézier curve. A colour-coded map was used to differentiate plaque components with the red corresponding to TCFA, the white to calcific spots, and the green colour to fibrous tissue. In case of a mixed TCFA-calcific plaque, there was superimposition of the red and white colours. Therefore, to demonstrate mixed plaques, we portrayed the calcific tissue in a semi-transparent fashion **(Figure 1)**. The dimensions of the spread-out plots depended on the length of the scaffolded or native segments (scale in the X axis: 1 mm=200 pixels and in the Y axis: 30°=100 pixels).

We estimated the minimum thickness of the neointimal tissue over TCFA or calcific spots, defined as the minimum thickness of the neointimal tissue amongst all the frames portraying the specific tissue, while the mean thickness over TCFA or calcific spots was defined as the mean value of the minimum thickness measured in all frames portraying the specific tissue. TCFA were defined as necrotic cores with a minimum cap thickness of <65 μm[35,36]. In order to have comparable mean and minimum thickness estimations in the Absorb BVS and BMS groups, the stent borders in the BMS group were extruded towards the outer vessel wall at a distance equal to the thickness of the stent struts (81 μm in the Svelte Coronary IDS stent and 56 μm in the vProtect system) and then the thickness of the neointima developed over the different tissues was estimated as the minimum distance between the extruded stent border and the luminal border **(Online Figure 4)**.

The TCFA burden in each segment was assessed using the lipid plaque burden index (LPBI), defined as the percentage of the number of pixels that corresponded to TFCA/covered TCFA vs. the number of pixels of each spread-out vessel plot. Similarly, the calcific plaque burden index (CPBI) was defined as the percentage of the number of pixels portraying calcific spots vs. the number of pixels of each spread-out vessel plot. Pixels corresponding to mixed plaques were taken into consideration during the computation of both the LPBI and the CPBI.

ASSESSMENT OF OBSERVER VARIABILITY

The reproducibility of the two observers in identifying and classifying the presence of vessel wall discontinuities in the scaffolded segment was examined in 153 frames (three OCT examinations) acquired at baseline. The two observers identified and classified separately

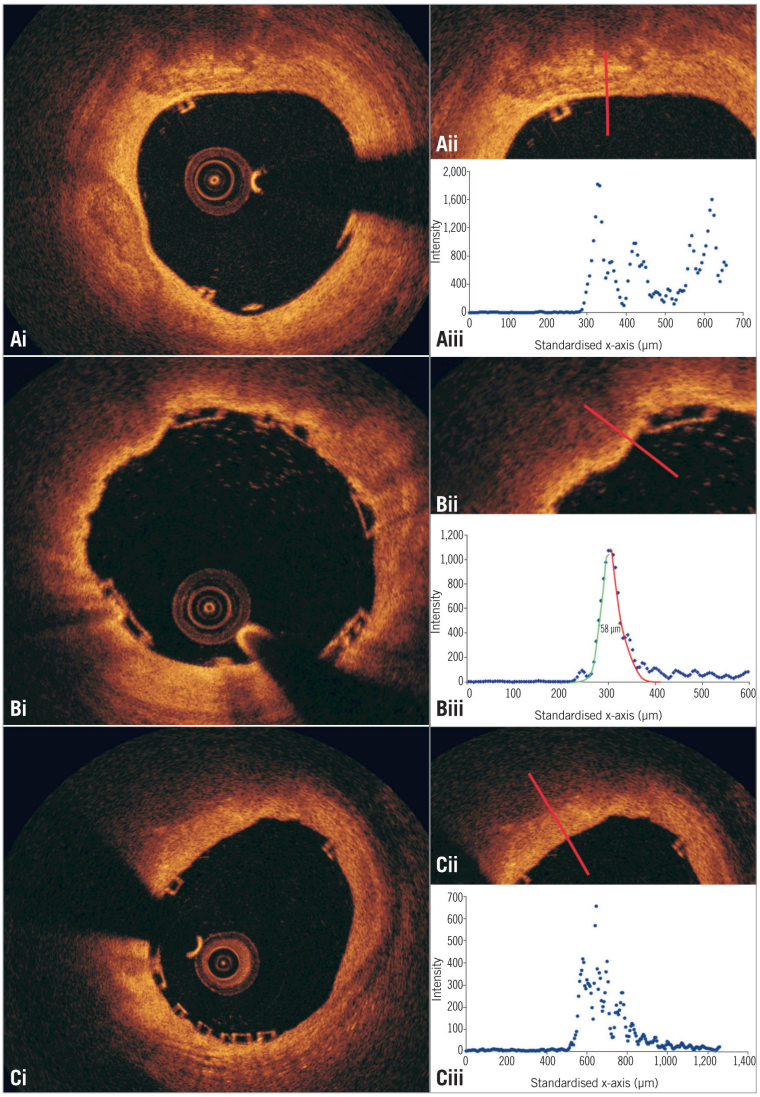

Online Figure 3. *Plot of the intensities of the backscatter OCT signals in calcific tissue (Ai, Aii), in lipid tissue covered by a thin fibrous cap (Bi, Bii), and in lipid tissue covered by a thick cap (Ci, Cii). The calcific tissue has a heterogeneous appearance; therefore, there is an increased scatter at the distal interface of the overlaying tissue to the calcific tissue which cannot be approximated by a Gaussian curve (Aiii). On the other hand, the lipid tissue appears as a signal-poor region resulting in a fast signal drop-off after the signal-rich fibrous cap. Thus, in case of a thin fibrous cap, two Gaussian curves can be fitted over the plotted intensities of the OCT backscatter signal (Biii), the first at the luminal and the second at the lipid border of the cap. The distance between the half-max of the two curves defines the thickness of the fibrous cap, and in the portrayed case this is 58 µm. As is shown in panel Ciii, in thick caps there is signal heterogeneity at the border of the cap with the lipid tissue and a less clear optical pathway which does not allow computation of cap thickness.*

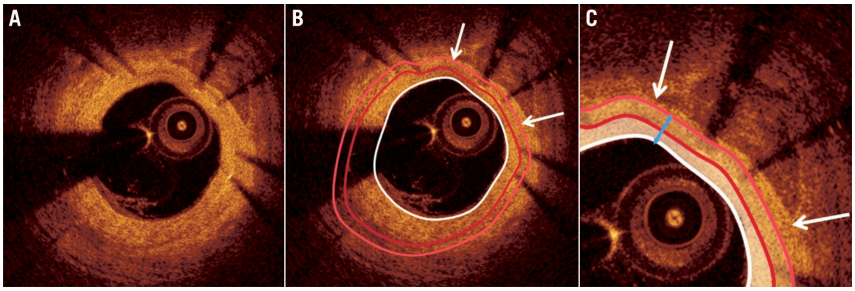

Online Figure 4. *Implementation of methodology to measure the thickness of the neointima developed over the calcific tissue identified in a segment treated with a bare metal stent (A). After the delineation of the luminal (white curve) and the stent (dark red curve) border (B), the neointima is computed (indicated with a white semi-transparent colour in panel C). To calculate the thickness of the neointimal tissue developed over the calcific tissue we extrude the stent border towards the external elastic lamina border at a distance that is equal to the thickness of the stent struts (light red curve). Then we measure the minimum distance (blue arrow) between the lumen and the expanded stent border in the arc defined by the lateral extremities (white arrows) of the detected calcific plaque. This distance (which in this frame was 150 μm) indicates the minimum neointima thickness for the identified calcific tissue at this frame.*

vessel wall discontinuities twice within a one-month period. The κ test of concordance was used to assess observer agreement[37].

The inter- and intra-observer variability of the two observers in characterising the type of plaque was evaluated in 147 frames portraying scaffolded segments (47 frames post scaffold implantation, 100 at follow-up). In these frames, each observer identified the presence of lipid and calcific tissue twice and measured in the follow-up frames the minimum thickness of the neointima overlaying the TCFA detected at baseline or the calcific spots. The κ test of concordance was used to assess observer agreement. To examine the inter- and intra-observer variability in the estimations of the circumferential distribution of the detected lipid/calcific tissue, we calculated the mean and the standard deviation of the differences between the angles that defined the lateral extremities of the tissue **(Online Figure 5)**. In addition, we computed the mean and the standard deviation of the differences between the two estimations of each observer, and the first estimations of the two observers for the minimum thickness of the neointima tissue that covered the detected lipid and calcific tissue. Finally, we calculated the percentage error difference between the two estimations of each observer and the first estimations of the two observers for the circumferential extent (expressed in degrees) of the lipid/calcific tissue.

Results

INTER- AND INTRA-OBSERVER VARIABILITY

A good overall agreement was noted in the detection of the presence of vessel wall discontinuity (κ=0.81), whereas the reproducibility of the two observers in identifying the type of discontinuity was moderate (κ=0.71). The intra-observer variability for the lipid and calcific tissue was κ=0.84 and κ=0.80 for the first observer and κ=0.82 and κ=0.92 for the second observer, respectively, while the inter-observer variability was κ=0.75 and κ=0.71, respectively. The results with regard to the other metrics used to evaluate observer variability are shown in **Online Table 2**.

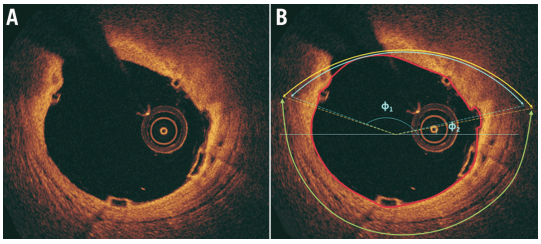

Online Figure 5. *Assessment of observer agreement for the lipid tissue. The estimations of the first observer are denoted with blue and of the second with yellow colour. The green arc indicates the extent of the detected external elastic membrane. It is obvious that there is a good agreement between the two observers.*

Online Table 1. Number of frames (total number: 9,007) analysed in segments implanted with a bioresorbable vascular scaffold (Absorb BVS), a bare metal stent (BMS), and in native segments portraying a thin-cap fibroatheroma at baseline, short-term (6 to 12-month) and midterm (24 to 36-month) follow-up.

Number of analysed frames	Total number of frames	Absorb BVS	BMS		Native segment
			Svelte Coronary IDS stent	vProtect	
Baseline	3,477	2,283	514	331	349
Short-term follow-up	3,256	2,280	544	325	107
Midterm follow-up	2,274	2,033	–	–	241

Online Table 2. Intra- and inter-observer variability for the thickness of the neointima tissue over lipid and calcific tissue and the circumferential location and extent of the lipid and the calcific tissue.

		Mean angle difference for the lateral extremities of the detected tissue	Mean difference for the thickness of the neointima tissue	Mean difference for the circumferential extent of the detected tissue
Lipid tissue (n=55)	1st observer variability	6.8±9.1°	20±21 μm	9.9±9.2%
	2nd observer variability	3.9±4.2°	10±14 μm	5.8±6.3%
	Inter-observer variability	6.1±7.1°	9±14 μm	8.3±11%
Calcific tissue (n=60)	1st observer variability	2.3±3.2°	16±17 μm	6.5±8.7%
	2nd observer variability	2.8±1.9°	9±22 μm	8.2±6.9%
	Inter-observer variability	3.2±4.3°	9±22 μm	8.1±8.9%

4.7 Early performance of a PLLA scaffold in STEMI

Everolimus-eluting bioresorbable vascular scaffolds for treatment of patients presenting with ST-segment elevation myocardial infarction: BVS STEMI first study.

Eur Heart J. 2014;35:777-86.
[Original research paper, Impact Factor: 15.20]

Diletti R, Karanasos A, Muramatsu T, Nakatani S, Van Mieghem NM, Onuma Y, Nauta ST, Ishibashi Y, Lenzen MJ, Ligthart J, Schultz C, Regar E, de Jaegere PP, Serruys PW, Zijlstra F, van Geuns RJ.

Everolimus-eluting bioresorbable vascular scaffolds for treatment of patients presenting with ST-segment elevation myocardial infarction: BVS STEMI first study

Roberto Diletti, Antonios Karanasos, Takashi Muramatsu, Shimpei Nakatani, Nicolas M. Van Mieghem, Yoshinobu Onuma, Sjoerd T. Nauta, Yuki Ishibashi, Mattie J. Lenzen, Jurgen Ligthart, Carl Schultz, Evelyn Regar, Peter P. de Jaegere, Patrick W. Serruys, Felix Zijlstra, and Robert Jan van Geuns*

Thoraxcenter, Erasmus MC, 's-Gravendijkwal 230, 3015 CE Rotterdam, the Netherlands

Received 11 September 2013; revised 6 November 2013; accepted 26 November 2013; online publish-ahead-of-print 6 January 2014

See page 753 for the editorial comment on this article (doi:10.1093/eurheartj/ehu005)

Aims We evaluated the feasibility and the acute performance of the everolimus-eluting bioresorbable vascular scaffolds (BVS) for the treatment of patients presenting with ST-segment elevation myocardial infarction (STEMI).

Methods and results The present investigation is a prospective, single-arm, single-centre study, reporting data after the BVS implantation in STEMI patients. Quantitative coronary angiography and optical coherence tomography (OCT) data were evaluated. Clinical outcomes are reported at the 30-day follow-up. The intent-to-treat population comprises a total of 49 patients. The procedural success was 97.9%. Pre-procedure TIMI-flow was 0 in 50.0% of the patients; after the BVS implantation, a TIMI-flow III was achieved in 91.7% of patients and the post-procedure percentage diameter stenosis was 14.7 $\pm$ 8.2%. No patients had angiographically visible residual thrombus at the end of the procedure. Optical coherence tomography analysis performed in 31 patients showed that the post-procedure mean lumen area was 8.02 $\pm$ 1.92 mm^2, minimum lumen area 5.95 $\pm$ 1.61 mm^2, mean incomplete scaffold apposition area 0.118 $\pm$ 0.162 mm^2, mean intraluminal defect area 0.013 $\pm$ 0.017 mm^2, and mean percentage malapposed struts per patient 2.80 $\pm$ 3.90%. Scaffolds with >5% malapposed struts were 7. At the 30-day follow-up, target-lesion failure rate was 0%. Non-target-vessel revascularization and target-vessel myocardial infarction (MI) were reported. A non-target-vessel non-Q-wave MI occurred. No cases of cardiac death or scaffold thrombosis were observed.

Conclusion In the present series, the BVS implantation in patients presenting with acute MI appeared feasible, with high rate of final TIMI-flow III and good scaffold apposition. Larger studies are currently needed to confirm these preliminary data.

Keywords Bioresorbable vascular scaffolds • ST-segment elevation myocardial infarction • Optical coherence tomography

Introduction

Primary percutaneous coronary intervention has been demonstrated to be superior to thrombolytic strategy and is currently the treatment of first choice for patients presenting with ST-segment elevation myocardial infarction (STEMI) in experienced centres with limited time delay.[1] First-generation drug-eluting stents (DES) have been shown to reduce the need for repeat revascularization compared with bare-metal stents (BMS),[2–4] and the newer-generation DES with improved biocompatibility of polymers may lower the rate of clinical events also in acute patients.[5,6] However, the implantation of metal devices is not devoid of important limitations, such as permanent caging of the vessel with permanent impairment of coronary vasomotion, side branch jailing, impossibility of late lumen

*Corresponding author. Tel: +31 10 4635260(33348), Fax: +31 10 4369154, Email: r.vangeuns@erasmusmc.nl

enlargement, non-invasive imaging and future surgical revascularization of stented segments.[7] Moreover, in spite of the beneficial effect of neointimal inhibition, the antiproliferative drug elution has been shown to interfere with the vascular healing processes providing the background for delayed strut coverage and persistent or acquired malapposition.[8,9] The above-mentioned limitations can be proposed for both stable and acute patients; however, primary stenting has additional specific characteristics that should be highlighted. Stent placement in acute thrombotic lesions has been reported to be an independent predictor of late stent malapposition after the BMS[10] or DES[11] implantation. Possible explanations for this phenomenon could be the thrombus sequestration behind the struts—which subsequently resolves—and the vasoconstriction during the acute phase. Both these factors may predispose to stent underdeployment, malapposition and finally to stent thrombosis. The everolimus-eluting bioresorbable vascular scaffold (BVS) has been designed to overcome the general limitations of the metallic stents and recently has been shown to provide excellent results for the treatment of stable patients.[12,13] However, so far very limited data are available on the use of this novel device in patients with acute coronary syndromes (ACS).[14,15] Given this background, a pilot study investigating the feasibility and acute performance of the BVS for the treatment of patients presenting with STEMI was initiated.

Methods

Rationale

As of 1 September 2012, the BVS (ABSORB; Abbott Vascular, Santa Clara, CA, USA) has been commercially available in the Netherlands. Based on previous experience and available evidence, reported in ABSORB Cohort A and B Trial[13,16] our institution initiated the use of BVS for the treatment of patients presenting for PCI in everyday clinical practice, with a preference for patients with a good life expectancy as demonstrated by the presence of limited co-morbidities. As these patients might have more complex lesions compared with the ABSORB study patients[16,17] the BVS-EXPAND registry was initiated. The BVS-EXPAND also included patients with ACS (unstable angina or non-STEMI). After the first experience with ACS patients and an interim analysis, a decision was made to extend BVS utilization to the treatment of STEMI.

As an additional measure for assessing the safety of a treatment approach with BVS in STEMI, optical coherence tomography (OCT) imaging was performed, according to clinical judgement, for a more comprehensive evaluation of the acute procedural outcome.

Study design

The present report is an investigator initiated, prospective, single-arm, single-centre study to assess feasibility and performance of the second-generation everolimus-eluting BVS for the treatment of patients presenting with STEMI.

Subjects enrolled were patients of $\geq$18-year-old admitted with STEMI, defined as at least 1 mm ST-segment elevation in two or more standard leads or at least 2 mm in two or more contiguous precordial leads or new left bundle branch block within 12 h after the onset of symptoms. Culprit lesions were located in vessels within the upper limit of 3.8 mm and the lower limit of 2.0 mm by online quantitative coronary angiography (QCA). The absorb BVS was implanted according to the manufacturer's indication on target-vessel diameter ranges and absorb BVS diameters to be used. The absorb BVS with a nominal diameter of 2.5 mm was implanted in vessels $\geq$2.0 and $\leq$3.0 mm by online QCA; the 3.0 mm BVS was implanted in vessels $\geq$2.5 and $\leq$3.3 mm by online QCA; the 3.5 mm BVS was implanted in vessels $\geq$3.0 and $\leq$3.8 mm. Given the manufacturer's indication on maximum scaffold expansion, for each nominal diameter a further expansion of 0.5 mm was allowed. Enrolled subjects were willing to comply with specified follow-up evaluation and to be contacted by telephone. Exclusion criteria comprise pregnancy, known intolerance to contrast medium, uncertain neurological outcome after cardiopulmonary resuscitation, previous percutaneous coronary intervention with the implantation of a metal stent, left main (LM) disease previous coronary artery bypass grafting (CABG), age superior to 75 years, and participation to another investigational drug or device study before reaching the primary endpoints. The enrolment period started on 1 November 2012 and ended on 30 March 2013. Dual antiplatelet therapy after the BVS implantation was planned to have a duration of 12 months. Baseline and post-BVS implantation QCA analysis, OCT analyses at post-BVS implantation, and clinical outcomes at the 30-day follow-up were evaluated.

Definitions

Success rates were defined as follows: device success was the attainment of $<$30% final residual stenosis of the segment of the culprit lesion covered by the BVS, by angiographic visual estimation. Procedure success was defined as device success and no major periprocedural complications (Emergent CABG, coronary perforation requiring pericardial drainage, residual dissection impairing vessel flow—TIMI-flow II or less). Clinical success was defined as procedural success and no in-hospital major adverse cardiac events (MACE). All deaths were considered cardiac unless an undisputed non-cardiac cause was identified. Myocardial infarction (MI) and scaffold thrombosis were defined according to the Academic Research Consortium definition.[18] Target-lesion revascularization (TLR) was defined as clinically driven if at repeat angiography the diameter stenosis was $>$70%, or if a diameter stenosis $>$50% was present in association with (i) presence of recurrent angina pectoris, related to the target vessel; (ii) objective signs of ischaemia at rest (ECG changes) or during exercise test, related to the target vessel; and (iii) abnormal results of any functional diagnostic test.

The device-oriented endpoint target-lesion failure was defined as the composite of cardiac death, target-vessel MI, or ischaemia-driven TLR. Major adverse cardiac events defined as the composite of cardiac death, any re-infarction (Q- or non-Q-wave), emergent bypass surgery (CABG), or clinically driven TLR. Target-vessel failure (TVF) was defined as cardiac death, target-vessel MI, or clinically driven TVR.

Ethics

This is an observational study, performed according to the privacy policy of the Erasmus MC and to the Erasmus MC regulations for the appropriate use of data in patient-oriented research, which are based on international regulations, including the declaration of Helsinki. The BVS received the CE mark for clinical use, indicated for improving coronary lumen diameter in patients with ischaemic heart disease due to *de novo* native coronary artery lesions with no

restriction in terms of clinical presentation. Therefore, the BVS can be currently used routinely in Europe in different settings comprising the acute MI without a specific written informed consent in addition to the standard informed consent to the procedure. Given this background, a waiver from the hospital Ethical Committee was obtained for written informed consent, as according to Dutch law written consent is not required, if patients are not subject to acts other than as part of their regular treatment.

Study device

The second-generation everolimus-eluting BVS is a balloon expandable device consisting of a polymer backbone of poly-L-lactide acid (PLLA) coated with a thin layer of amorphous matrix of poly-D and -L-lactide acid (PDLLA) polymer (strut thickness 157 μm). The PDLLA controls the release of the antiproliferative drug everolimus (100 $\mu g/cm^2$), 80% of which is eluted within the first 30 days. Both PLLA and PDLLA are fully bioresorbable. The polymers are degraded via hydrolysis of the ester bonds and the resulting lactate and its oligomers are metabolized by the Krebs cycles. Small particles (<2 μm in diameter) may be also phagocytized and degraded by macrophages.[19] According to preclinical studies, the time for complete bioresorption of the polymer backbone is ~2–3 years.[20] The BVS edges contain two platinum markers for accurate visualization during angiography or other imaging modalities.

Quantitative coronary angiography analysis

Quantitative coronary angiography (QCA) analyses were performed using the Coronary Angiography Analysis System (Pie Medical Imaging, Maastricht, Netherlands).

Analyses were performed at pre-procedure, after thombectomy, after balloon dilatation, and after the BVS implantation with a methodology already reported.[21]

In case of thrombotic total occlusion, pre-procedure QCA analysis was performed as proximally as possible from the occlusion (in case of a side branch distally to the most proximal take off of the side branch). Intracoronary thrombus was angiographically identified and scored in five grades as previously described.[22] Thrombus grade was assessed before procedure and after thombectomy.

The QCA measurements included reference vessel diameter (RVD)—calculated with interpolate method—percentage diameter stenosis, minimal lumen diameter (MLD), and maximal lumen diameter (D_{max}). Acute gain was defined as post-procedural MLD minus pre-procedural MLD (MLD value equal to zero was applied when culprit vessel was occluded pre-procedurally). Complications occurring any time during the procedure, such as dissection, spasm, distal embolization, and no-reflow were reported. As additional information, MI SYNTAX I and MI SYNTAX II scores providing long-term risk stratification for mortality and MACE in patients presenting with STEMI were assessed.[23]

Optical coherence tomography image acquisition and analysis

Optical coherence tomography imaging after the BVS implantation was encouraged in all patients but was not mandatory, subordinated to device availability and left at the operator's discretion.

Therefore, OCT imaging of the culprit lesion after treatment was performed in a subset of the population. The image acquisition was performed with C7XR imaging console and the Dragonfly intravascular imaging catheter (both St. Jude Medical, St. Paul, MN, USA). Image acquisition has been previously described.[24] Briefly, after positioning the OCT catheter distally to the most distal scaffold marker, the catheter is pulled back automatically at 20 mm/s with simultaneous contrast infusion by a power injector (flush rate 3–4 mL/s). In cases where the entire scaffold region was not imaged in one pullback, a second more proximal pullback was performed for complete visualization. Images were stored and analysed offline.

Analysis of the OCT images was performed with the St Jude/Lightlab offline analysis software (St. Jude Medical), using previously described methodology for BVS analysis.[17] Analysis was performed in 1-mm longitudinal intervals within the treated culprit segment, after exclusion of frames with $<75\%$ lumen contour visibility. Lumen, scaffold, and incomplete scaffold apposition (ISA) area were calculated in accordance with standard methodology for analysis of bioresorbable scaffolds[17] (*Figure 1A* and *B*), while in sites with overlapping scaffolds, analysis was performed using previously suggested modifications[25] (*Figure 1D*). Specifically, the lumen contour is traced at the lumen border and in the abluminal (outer) side of apposed struts, while in the case of malapposed struts the contour is traced behind the malapposed struts. In cases where the scaffold struts are completely covered by tissue or thrombus, the lumen contour is traced above the prolapsing tissue (*Figure 1C*). The scaffold area is traced following interpolation of points located in the mid-point of the abluminal border of the black core in apposed struts and the mid-point of the abluminal strut frame border in malapposed or side branch-related struts, so that the scaffold area is identical to the lumen area in the absence of ISA and tissue prolapse. Incomplete scaffold apposition area is traced in the case of malapposed struts as the area delineated between the lumen and scaffold contours (*Figure 1B*).

A special consideration should be mentioned concerning BVS analysis in MI with the presence of increased tissue prolapse and residual thrombus post-implantation[21,26] (*Figures 1C* and *2*). Tissue prolapse area can be quantified as the difference between the scaffold and the lumen area. For the calculation of prolapse area, in the case that one or more scaffold struts are completely covered by thrombus or tissue, the total black core area of these struts is also measured. Prolapse area is then calculated as [scaffold area + ISA area − lumen area − embedded black core area]. The area of non-attached intraluminal defects (e.g. thrombus) is also measured. Atherothrombotic area is then calculated as the sum of prolapse area and intraluminal defect area and normalized as a percent ratio of the scaffold area (atherothrombotic burden, ATB).[21,26] It should be noted that in the case of bioresorbable scaffolds where measurements of the scaffold area are performed using the abluminal side of the scaffold struts, ATB is overestimated compared with metal platform stents where measurements of the stent area are performed from the adluminal (inner) side of the struts. Additionally, flow area was assessed as [scaffold area + ISA area − atherothrombotic area − total strut area] and the minimal flow area was recorded.

A scaffold strut is defined as incompletely apposed when there is no contact between the abluminal border of the strut and the vessel wall. This does not include struts located in front of side branches or their ostium (polygon of confluence region), which are

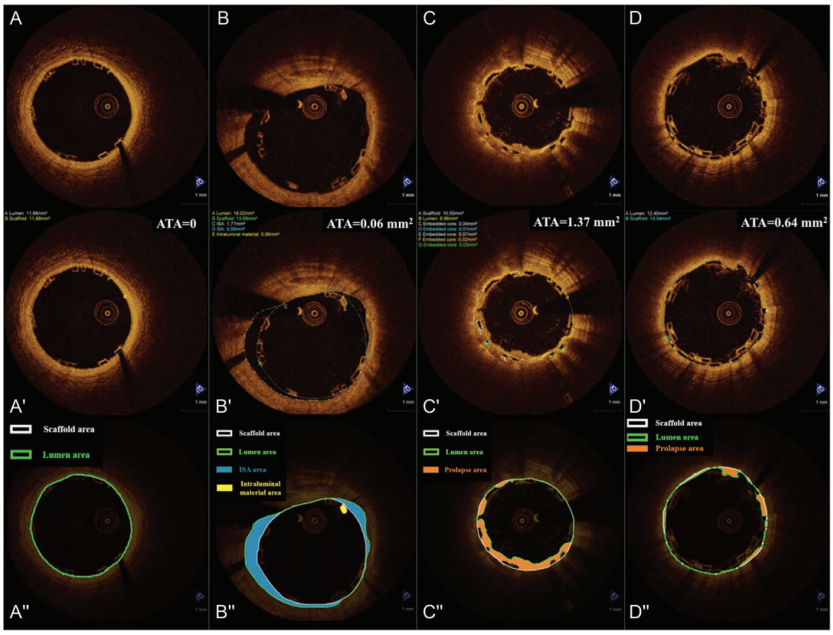

Figure 1 Methodology of optical coherence tomography analysis. (*A*) Good scaffold apposition and absence of incomplete scaffold apposition or tissue prolapse, (*B*) incomplete scaffold apposition, (*C*) sites with high tissue prolapse and struts completely covered by thrombus, and (*D*) overlapping scaffolds. Upper panel shows baseline images, middle panel shows quantitative measurements, and lower panel shows methodology for analysis. ISA, incomplete scaffold apposition; ATA, atherothrombotic area.

defined as side branch-related struts. Intraluminal struts that are part of adjacent clusters of apposed struts in overlapping scaffolds are also not considered malapposed.[25] For illustrative proposes, OCT bi-dimensional images are reported by three-dimensional rendering by dedicated software (Intage Realia, KGT, Kyoto, Japan)[17] (*Figures 2* and *3*).

Statistical analysis

Continuous variables are presented as mean and standard deviation, and categorical variables are reported as count and percentages. Descriptive statistics was provided for all variables. The present study is intended to be a 'first experience investigation' evaluating feasibility and acute performance of the everolimus-eluting BVS for the treatment of patients presenting with STEMI. A patient population of at least 30 patients was planned to be included in the present study. Comparisons among multiple means were performed with analysis of variance (one-way ANOVA). Score (Wilson) confidence intervals were reported for measures of success. Type A intraclass correlation coefficients (ICCs) for absolute agreement were used for assessing intra- and interobserver agreement, while measurement error and 95% limits of agreement were assessed by Bland–Altman analysis. The ICCs were computed with a two-way random effects model (single measures). All statistical tests were performed with SPSS, version 15.0 for windows (IL, USA).

Results

From 1 November 2012 to 30 April 2013, a total of 267 patients presented with acute MI. Twenty-one of those patients were treated percutaneously without any stent implantation (thrombectomy or balloon dilatation alone). Seventy-four had a culprit lesion located in a coronary vessel with a vessel diameter out of the range availability of the BVS (i.e. RVD >4.0 mm). Out of the remaining 172 patients, 125 were meeting the inclusion and none of the exclusion criteria of the present study (47 patients excluded for age, previous PCI or CABG, left main disease). Seventy-six of those patients were treated with metal stents and 49 cases (48 implanted with BVS) were enrolled in the present study (*Figure 4*, *Table 1*). Therefore, the patients implanted with BVS constitute the ~38% of the patients eligible for the present investigation.

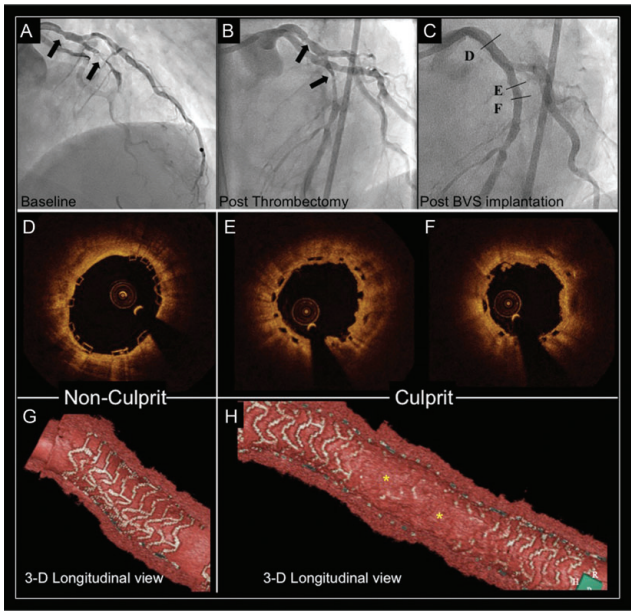

Figure 2 Bioresorbable vascular scaffolds implantation in a culprit and a non-culprit lesion in myocardial infarction. (*A*) Coronary angiography demonstrating a stenotic lesion in proximal LAD (proximal non-culprit lesion) and a total occlusion of the mid-LAD (culprit lesion). (*B*) Angiography following thrombus aspiration. (*C*) Angiography following implantation of a 3.5 × 12 mm bioresorbable vascular scaffolds at the proximal LAD lesion and a 3.0 × 28 mm bioresorbable vascular scaffolds at the mid-LAD lesion. (*D*) Optical coherence tomography image from the proximal non-culprit lesion showing absence of tissue prolapse and thrombus in the 3.5 × 12 mm scaffold. (*E* and *F*) Optical coherence tomography images from the culprit lesion showing complete coverage of the bioresorbable vascular scaffolds by tissue prolapse and presence of small amount of intraluminal defect. (*G*) Three-dimensional optical coherence tomography rendering in the proximal non-culprit lesion with complete scaffold visualization indicating the absence of prolapsing material. (*H*) Conversely, in the three-dimensional rendering of the culprit lesion, the morphology of the bioresorbable vascular scaffolds cannot be fully visualized due to high levels of tissue prolapse (*).

Baseline clinical characteristics of the 172 patients (49 patients included in the intent-to-treat population and 123 patients implanted with metal stents) with vessels size in the range of the BVS availability are reported in *Table 1*. In the intent-to-treat population thirty-eight patients were male (77.6%), mean age was 58.9 $\pm$ 10.5 years. Lesions were distributed as follows: left anterior descending 21 (42.9%), right coronary artery 22 (44.9%), and circumflex 6 (12.2%). Baseline clinical data of the enrolled patients were compared with the general population presenting with acute MI and implanted with a metal stent in vessels theoretically suitable for BVS implantation. Minimal differences were observed between the two groups. Namely, age 58.9 $\pm$ 10.5 vs. 66.4 $\pm$ 12.2, $P < 0.001$ and previous PCI 0% vs. 12.2%, $P = 0.007$. All the other clinical characteristics of the two populations did not show any significant difference.

Mean door-to-balloon time was 31.3 $\pm$ 19.5 min. All patients were treated with unfractionated heparin at the dose of 70–100 UI/kg and dual antiplatelet therapy (aspirin plus, prasugrel in 45 patients or clopidogrel in 4 patients). Manual thrombectomy was performed in 38 patients. In 16 cases, direct stenting was performed; a total of 65 scaffolds were implanted (12 patients received overlapping scaffolds—overlap was systematically intended to be minimal). The scaffolds lengths used were 12, 18, and 28 mm, with scaffolds diameters 2.5, 3.0, and 3.5 mm. Mean scaffold length per-lesion was 26.40 $\pm$ 13.86 mm, mean scaffold diameter per-lesion was 3.2 $\pm$ 34 mm. A highly supportive wire was used in five cases and radial approach was performed in 26 patients (53.0%) (*Table 2*). The procedural success was 97.9% (48/49 patients); in one patient, the delivery of the BVS was unsuccessful (due to the remarkable vessel tortuosity was not

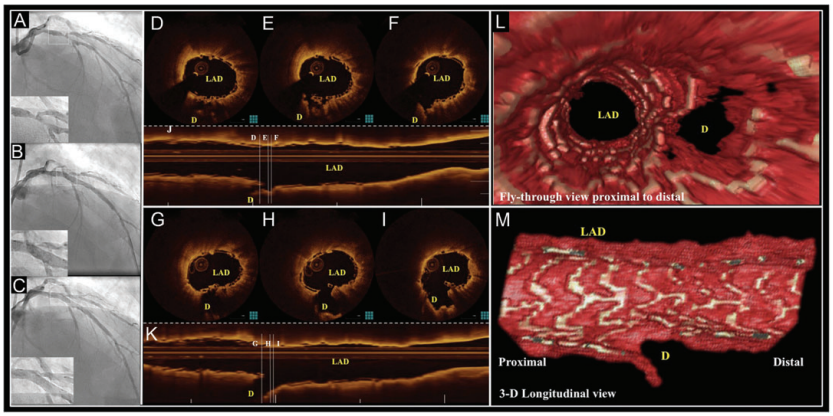

Figure 3 Bioresorbable vascular scaffold implantation in a thrombotic bifurcation lesion treated with provisional approach. (*A*) Coronary angiography pre-intervention. (*B*) Angiography following bioresorbable vascular scaffold implantation in the LAD, showing pinching of the ostium of the diagonal (D). (*C*) Final angiographic result following side branch dilation with 2.0 × 15 mm balloon. (*D–F* and *J*) Optical coherence tomography cross-sectional images and l-mode after bioresorbable vascular scaffolds implantation showing the compromise of the side branch after implantation and presence of thrombus at the side branch ostium. (*G–I* and *K*) Optical coherence tomography cross-sectional images and l-mode after side branch dilation, showing the opening of the carina of the side branch. (*L* and *M*) Three-dimensional reconstructions confirm the opening of the side branch ostium.

possible to advance the BVS at the site of the lesion) and a metallic DES was implanted. Clinical success was 97.9% (48/49 patients).

Quantitative coronary angiography analysis

The QCA is reported only in patients implanted with BVS. In 50.0% of those patients, pre-procedure TIMI-flow was 0 and the RVD was 2.94 ± 0.77 mm. In the non-totally occluded vessels, the RVD was 2.62 ± 0.63 mm, with an MLD of 0.75 ± 0.44 mm and a mean diameter stenosis of 70.8 ± 12.5%. After thrombectomy and balloon dilatation, TIMI-flow grade 0 was present in 2.5 and 0.0% of patients, respectively, and TIMI-flow III in 52.5 and 59.3% of the cases, respectively. After the scaffold implantation, there were no cases of TIMI-flow 0, and a TIMI-flow III was achieved in 91.7% of patients, the mean post-procedure in-scaffold % diameter stenosis was 14.7 ± 8.2%, in-scaffold MLD was 2.44 ± 0.49 mm (*Table 3*). No angiographically visible residual thrombus was observed at post-procedure.

Optical coherence tomography findings

Optical coherence tomography analysis was performed in a subgroup of 31 patients implanted with BVS. Mean lumen area was 8.02 ± 1.92 mm^2, minimum lumen area 5.95 ± 1.61 mm^2, and minimum flow area 5.62 ± 1.66 mm^2. Incomplete scaffold apposition (ISA) was observed in 20 patients with a mean ISA area of 0.118 ± 0.162 mm^2 and a mean percentage of malapposed struts per patients equal to 2.80 ± 3.90%. The mean prolapse area was 0.60 ± 0.26 mm^2, and the mean intraluminal defect area was 0.013 ± 0.017 mm^2. Scaffolds with >5% malapposed struts were 7 (*Table 4*). The OCT analysis stratified by scaffold size (5 BVS 2.5 mm, 13 BVS 3.0 mm, 24 BVS 3.5 mm) showed different lumen, scaffold, and flow areas, but similar amounts of incomplete stent apposition, plaque prolapse, and intraluminal mass areas (*Table 5*). In three cases, the observation of scaffold malapposition by OCT, guided an additional post-dilatation and in one patient the visualization of considerable intraluminal thrombus as assessed by OCT led to a repeated thrombus aspiration.

Intra-observer variability was excellent. Intraclass correlation coefficients were 0.999 for lumen area and 0.999 for scaffold area, and the corresponding measurement errors and limits of agreement were 0.01 mm^2 (−0.12 to 0.15 mm^2) for lumen area and −0.01 mm^2 (−0.20 to 0.17 mm^2) for scaffold area. Similarly, inter-observer intraclass correlation coefficients were 0.997 for lumen area and 0.987 for scaffold area, and the corresponding measurement errors and limits of agreement were −0.01 mm^2 (−0.30 to 0.28 mm^2) for lumen area and −0.22 mm^2 (−0.68 to 0.24 mm^2) for scaffold area.

Clinical outcomes

At the 30-day follow-up, the rate of the device-oriented endpoint, target-lesion failure, was 0%. None of the patients experienced target-vessel re-infarction, emergent bypass surgery, or clinically driven TLR. No cases of cardiac death or scaffold thrombosis were reported. The MACE rate was 2.6% as one patient, after discharge developed a non-Q-wave MI related to a non-target-vessel lesion and underwent a non-target-vessel revascularization within the

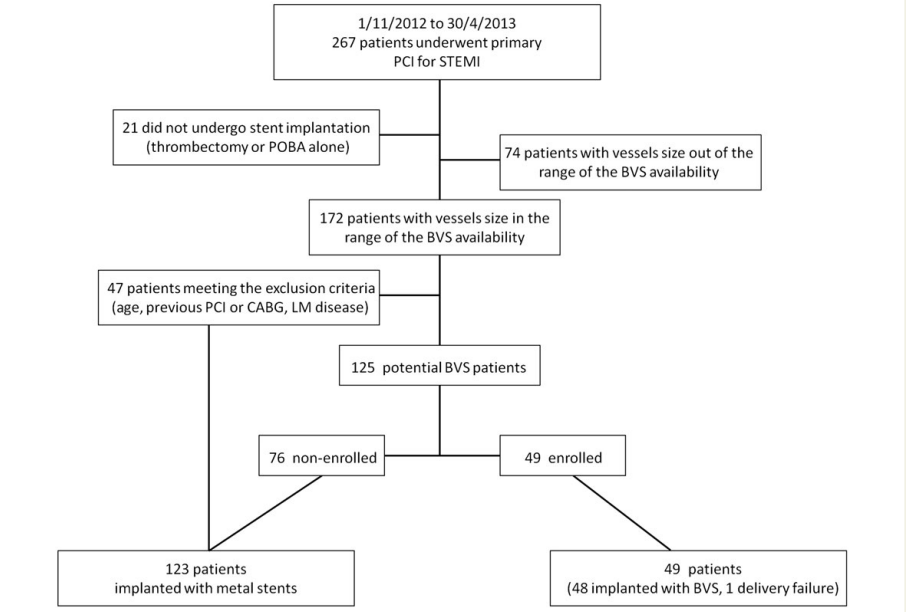

Figure 4 Flow-chart of the study. From 1 November 2012 to 30 April 2013, a total of 267 patients presented with acute myocardial infarction. Twenty-one of those patients were treated percutaneously but without any stent implantation (thrombectomy or balloon dilatation alone). Seventy-four had a culprit lesion located in a coronary vessel with a vessel diameter out of the range availability of the bioresorbable vascular scaffolds (i.e. reference vessel diameter >4.0 mm). Out of the remaining 172 patients, 125 were meeting the inclusion and none of the exclusion criteria of the present study (47 patients excluded for age, previous PCI or CABG, left main disease). Seventy-six of those patients were treated with metal stents and 49 cases (48 implanted with BVS) were included in the present study.

30 days post-procedure. This was the only event reported in the studied population (*Table 6*).

Discussion

The everolimus-eluting BVS has been tested so far only in elective patients with stable, unstable angina, or silent ischaemia;[16,17,27–29] showing promising results up to 4-year follow-up[30] for the first-generation and up to 2 years for the second-generation BVS.[12,13,31] The present study represents an early investigation reporting clinical and angiographic data on the use of the second-generation BVS for the treatment of patients presenting with STEMI and evaluating acute results with high-resolution intracoronary imaging (OCT).

A high device, procedural, and clinical success rates were observed with all the scaffolds achieving a residual stenosis <30% and no in-hospital MACE. Such data are supportive of feasibility and good acute performance of the BVS for the treatment of patients with acute MI.

Angiographic data

The everolimus-eluting BVS was implanted in patients presenting with ST-segment elevation and a thrombus burden 4 or 5 in 63.0% of the cases. A theoretical concern related to the implantation of the BVS in such thrombotic lesions is the fact that scaffold positioning and placement may need a more aggressive lesion preparation (pre-dilatation) compared with standard metal devices, due to its slightly higher profile. We hypothesized that this strategy might be prone to an increase in distal embolization following balloon inflations, favouring no-reflow and reducing the rate of final TIMI-flow III.

However, the analysis of the post-procedural angiographies revealed a TIMI-flow III in 91.7% of the cases; such results are in line with recently reported large trials evaluating the performance of metallic stents in patients presenting with acute MI.[5,6] Less thrombus embolization may result from a different pattern of thrombus dislodgment and compression to the arterial wall after deployment of a device with a larger strut width (157 μm) compared with currently available metallic stents. The percentage of vessel wall area

Table 1 **Baseline clinical characteristics intent-to-treat population and patients treated with metallic stent in the enrolment period**

Clinical characteristics	BVS (*N* = 49)	Metal stents (*N* = 123)	*P*-value
Age (year)	58.9 ± 10.5	66.4 ± 12.2	<0.001
Male, *n* (%)	38 (77.6)	93 (75.6)	0.845
Hypertension, *n* (%)	19 (38.8)	53/105 (50.5)	0.225
Hypercholesterolemia, *n* (%)	11 (22.4)	30/100 (30.0)	0.435
Diabetes, *n* (%)	4 (8.2)	14/116 (12.1)	0.590
Smoke, *n* (%)	27 (69.2)	46/116 (39.7)	0.120
Family history of CAD, *n* (%)	12 (24.5)	31/95 (32.6)	0.343
Peripheral vascular disease, *n* (%)	1 (2.0)	8 (6.5)	0.449
Kidney disease, *n* (%)	1 (2.0)	7 (5.7)	0.442
Prior MI, *n* (%)	1 (2.0)	14 (11.4)	0.070
Prior PCI, *n* (%)	0 (0.0)	15 (12.2)	0.007
Prior CABG, *n* (%)	0 (0.0)	3 (2.4)	0.559
COPD, *n* (%)	2 (4.1)	5 (4.1)	1.000
Culprit vessel			0.624
LM, *n* (%)	0 (0)	2 (1.6)	
LAD, *n* (%)	21 (42.9)	52 (42.3)	
RCA, *n* (%)	22 (44.9)	46 (37.4)	
LCX, *n* (%)	6 (12.2)	21 (17.1)	
SVG, *n* (%)	0 (0)	2 (1.6)	

Patients with vessels diameters not feasible for BVS implantation (i.e. reference vessel diameter ≥4.0 mm) were excluded.
Data are expressed as mean ± SD or number and proportion, *n* (%).
CAD, coronary artery disease; MI, myocardial infarction; PCI, percutaneous coronary intervention; CABG, coronary artery bypass graft; COPD, chronic obstructive pulmonary disease; LM, left main; LAD, left anterior descending; RCA, right coronary artery; LCX, circumflex; SVG, saphenous vein graft.

Table 2 **Procedural data intent-to-treat population**

Procedural data	*N* = 49
Medications	
Aspirin, *n* (%)	49 (100)
Prasugrel, *n* (%)	45 (91.8)
Clopidogrel, *n* (%)	4 (8.2)
Glycoprotein IIb/IIIa antagonists, *n* (%)	17 (34.7)
Unfractionated heparin, *n* (%)	49 (100)
Mean door-to-balloon time (min)	31.3 ± 19.5
Manual thrombectomy, *n* (%)	38 (77.5)
Direct stenting, *n* (%)	16 (32.7)
Pre-dilatation, *n* (%)	33 (67.3)
Mean pre-dilatation balloon diameter per-lesion (mm)	2.6 ± 0.67
Post-dilatation, *n* (%)	10 (20.4)
Mean post-dilatation balloon diameter per-lesion (mm)	3.5 ± 0.47
Overlapping, *n* (%)	12 (24.5)
Overlap scaffolds diameters 3.5 mm–3.5 mm, *n* (%)	5 (10.2)
Overlap scaffolds diameters 3.5 mm – 3 mm *n* (%)	5 (10.2)
Overlap scaffolds diameters 3.5 mm–2.5 mm, *n* (%)	1 (2.0)
Overlap scaffolds diameters, 3 mm–2.5 mm, *n* (%)	1 (2.0)
Total number of scaffolds, *n.*	65
Mean scaffolds per-lesion, *n.*	1.35 ± 0.60
Mean scaffold length per-lesion (mm)	26.40 ± 13.86
Mean scaffold diameter per-lesion (mm)	3.2 ± 34
Supportive wire, *n.* (%)	5 (10.2)
Radial approach, *n.* (%)	26 (53.0)

Data are expressed as mean ± SD or number and proportion, *n* (%).

covered by the BVS polymer (scaffold/vessel ratio) has been previously evaluated to be 26%,[32] a value considerably higher compared with what observed for conventional metallic DES (i.e. EES provides a percentage stent/vessel ratio equal to 12%).[32] This characteristic of the BVS might be associated to an increased capacity of capturing debris and thrombotic material behind the struts before embolization to distal microcirculation. This so-called snow racket concept (entrapment of thrombotic material between the stent and the vessel) is currently the basis for the design of novel devices and clinical studies.[33]

Optical coherence tomography findings

Given its high resolution, OCT allows the assessment of *in vivo* strut apposition and presence of thrombus.[24,34–36]

The present analysis was performed at 1 mm intervals in the OCT pullback. Although, the possibility for a more strict assessment of OCT analysis in thrombotic lesion may be considered,[21] this methodology is the current standard applied in our institution for clinical studies, and the most commonly used in the literature.

Previous reports defined a stent malapposed if at least 5% of struts were observed to be malapposed;[37,38] in the present investigation, only seven scaffolds (22.6%) investigated with OCT showed a strut malapposition of >5%, with an overall mean struts malapposition equal to 2.8 ± 3.90%. A recently reported study using a similar methodology to investigate malapposition after metallic balloon expandable stent implantation in STEMI patients showed a total of 37.1% malapposed stents (stents with >5% malapposition) with a mean percentage of strut malapposition equal to 5.99 ± 7.28%.[38] In addition, the mean ISA area was 0.118 ± 0.162 mm^2, a value in line with data reported for metallic stent implantation in patients presenting with STEMI.[21,38] Similarly, the amount of intraluminal defect after scaffold implantation was minimal and comparable with what is observed in metallic stents.[21] Notably, these results were consistent among different scaffold sizes.

Clinical outcomes

In the present series, none of patients treated with BVS experienced a clinical event related to the treated vessel at the 30-day follow-up. These observations support the feasibility of BVS implantation in patients presenting with acute STEMI.

Table 3 Angiographic analysis in patients implanted with bioresorbable vascular scaffolds

Angiographic data	*N* = 48
Pre-procedure	
TIMI-flow, % (*n*)	
0	50.0% (23/46)
1	15.2% (7/46)
2	21.7% (10/46)
3	13.0% (6/46)
Thrombus burden, % (*n*)	
0	0.0% (0/46)
1	6.5% (3/46)
2	17.4% (8/46)
3	13.0% (6/46)
4	13.0% (6/46)
5	50.0% (23/46)
Total occlusion (*N* = 23)	
RVD (mm)	2.94 ± 0.77
Non-total occlusion (*N* = 23)	
RVD (mm)	2.62 ± 0.63
MLD (mm)	0.75 ± 0.44
Diameter stenosis (%)	70.8 ± 12.5
After thrombectomy	
TIMI-flow, % (*n*)	
0	2.5% (1/40)
1	7.5% (3/40)
2	37.5% (15/40)
3	52.5% (21/40)
Thrombus burden, % (*n*)	
0	0.0% (0/40)
1	30.0% (12/40)
2	35.0% (14/40)
3	22.5% (9/40)
4	10.0% (4/40)
5	2.5% (1/40)
After pre-dilatation	
TIMI-flow, % (*n*)	
0	0.0% (0/27)
1	7.4% (2/27)
2	33.3% (9/27)
3	59.3% (16/27)
Before BVS implantation	
RVD (mm)	2.63 ± 0.53
MLD (mm)	1.21 ± 0.46
Diameter stenosis (%)	53.2 ± 16.1
D_{max} (mm)	3.01 ± 0.52
Post-procedure	
TIMI-flow, % (*n*)	
0	0.0% (0/48)
1	0.0% (0/48)
2	8.3% (4/48)
3	91.7% (44/48)
In-scaffold	
RVD (mm)	2.86 ± 0.52
MLD (mm)	2.44 ± 0.49
Diameter stenosis (%)	14.7 ± 8.2
In-segment	
RVD (mm)	2.74 ± 0.59
MLD (mm)	2.20 ± 0.53
Diameter stenosis (%)	21.8 ± 12.0
MI syntax score I[a]	10.0 (7.0–15.0)
MI syntax score II[a]	7.0 (4.25–10.0)
Dominant right coronary artery, % (*n*)	93.8% (45/48)
Scaffold-to-artery ratio	1.19 ± 0.24
Complications occurring any time during the procedure, % (*n*)	
Dissection	6.3% (3/48)
Spasm	4.2% (2/48)
Distal embolism	14.6% (7/48)
No-reflow	2.1% (1/48)

Data are expressed as mean ± SD or proportion (%).
[a]MI syntax scores I and II are expressed as median (interquartile range).

Table 4 Optical coherence tomography findings post-implantation in patients implanted with bioresorbable vascular scaffolds

OCT variables	*N* = 31
Analysed length (mm)	28.16 ± 13.29
Analysed struts, *n*	245 ± 135
Minimum lumen area (mm^2)	5.95 ± 1.61
Mean lumen area (mm^2)	8.02 ± 1.92
Lumen volume (mm^3)	225.78 ± 113.63
Minimum scaffold area (mm^2)	6.69 ± 1.94
Mean scaffold area (mm^2)	8.54 ± 1.97
Scaffold volume (mm^3)	240.07 ± 118.48
Minimum flow area (mm^2)	5.62 ± 1.66
ISA area (mm^2) (*N* = 20)	0.118 ± 0.162
Mean prolapse area (mm^2)	0.60 ± 0.26
Mean intraluminal defect area (mm^2)	0.013 ± 0.017
Maximum intraluminal defect area (mm^2)	0.094 ± 0.077
Mean atherothrombotic area (mm^2)	0.61 ± 0.27
Mean atherothrombotic burden (%)	7.29 ± 3.12
Malapposed struts per patient (%)	2.80 ± 3.90
Scaffolds with at least 1 malapposed strut, *n* (%)	20 (64.5)
Scaffolds with >5% malapposed struts, *n* (%)	7 (22.6)

ISA, incomplete scaffold apposition.
Data are expressed as mean ± SD or number and proportion, *n* (%).

Table 5 Optical coherence tomography findings post-implantation stratified by scaffold size in patients implanted with bioresorbable vascular scaffolds

OCT variables				
Scaffold size	**2.5 mm (*N* = 5)**	**3.0 mm (*N* = 13)**	**3.5 mm (*N* = 24)**	***P***
Analysed length (mm)	18.80 ± 1.30	22.23 ± 6.46	21.33 ± 7.38	0.628
Minimum lumen area (mm^2)	4.08 ± 0.24	5.60 ± 0.93	7.18 ± 1.58	0.001
Mean lumen area (mm^2)	5.42 ± 0.75	7.18 ± 1.03	9.25 ± 1.72	0.001
Minimum scaffold area (mm^2)	4.53 ± 0.51	6.13 ± 1.02	8.06 ± 1.82	0.001
Mean scaffold area (mm^2)	5.62 ± 0.28	7.66 ± 0.88	9.82 ± 1.70	0.001
Minimum flow area (mm^2)	3.84 ± 0.28	5.17 ± 0.86	6.77 ± 1.60	0.001
ISA area (mm^2) (*N* = 25)	0.190 ± 0.318 (*N* = 3)	0.063 ± 0.072 (*N* = 10)	0.133 ± 0.177 (*N* = 12)	0.429
Mean prolapse area (mm^2)	0.40 ± 0.19	0.54 ± 0.27	0.62 ± 0.29	0.246
Mean intraluminal defect area (mm^2)	0.007 ± 0.008	0.016 ± 0.021	0.012 ± 0.018	0.628
Maximum intraluminal defect area (mm^2)	0.072 ± 0.081	0.102 ± 0.086	0.068 ± 0.065	0.096
Mean atherothrombotic area (mm^2)	0.40 ± 0.19	0.56 ± 0.27	0.64 ± 0.30	0.237
Mean atherothrombotic burden (%)	6.00 ± 4.66	7.42 ± 3.79	6.20 ± 3.39	0.594

ISA, incomplete scaffold apposition.
Data are expressed as mean ± SD or number and proportion, *n* (%).

Table 6 Clinical outcomes at the 30-day follow-up intent-to-treat population

Clinical events	*N* = 49	95% CI
Target-lesion failure	(0/49) 0%	(0–7.41)
TVF	(0/49) 0%	(0–7.41)
Cardiac death	(0/49) 0%	(0–7.41)
Target-vessel MI	(0/49) 0%	(0–7.41)
Q-wave MI	(0/49) 0%	(0–7.41)
Non Q-wave MI	(0/49) 0%	(0–7.41)
Clinically driven target-vessel revascularization	(0/49) 0%	(0–7.41)
Any MI	(1/49) 2.6%	(0–10.69)
Q-wave MI	(0/49) 0%	(0–7.41)
Non Q-wave MI	(1/49) 2.6%	(0–10.69)
Major adverse cardiac events	(1/49) 2.6%	(0–10.69)
Non-target-vessel revascularization	(1/49) 2.6%	(0–10.69)
Definite or probable scaffold thrombosis	(0/49) 0%	(0–7.41)

Data are expressed number and proportion, *n* (%). 95% CI, 95% confidence interval.

Data showed in the present report with optimal acute performance in terms of final TIMI-flow and scaffold apposition may suggest that everolimus-eluting BVS could be considered for the treatment of patients presenting with STEMI, however, due to the limited number of patients and events, caution should be made in reaching firm conclusions. Further larger studies are needed to fully evaluate the performance of the present device in STEMI patients.

Limitations

The present study represents a feasibility study with a limited number of patients. The small sample size does not allow reaching conclusions in terms of clinical outcomes. The lack of a head-to-head comparison with the current standard of care is a major limitation of the present study. A longer follow-up is needed to fully evaluate the performance of this novel device in patients presenting with acute MI. During the enrolment period, the implantation of either metallic stent or BVS in STEMI patients was left to the operator's discretion; this methodology may be prone to selection bias. Therefore, these data should not stimulate at the current state of knowledge the use of BVS in patients presenting with acute MI. Larger randomized studies are needed to confirm these preliminary observations.

Conclusion

In the present investigation, the implantation of the everolimus-eluting BVS was observed to be feasible in patients presenting with STEMI with optimal acute performance. These data are preliminary and need further confirmation in randomized controlled trials to define the true role of BVS for the treatment of patients presenting with acute myocardial infarction.

Funding

Conflict of interest: Dr R.J. van Geuns received speakers fee from Abbott Vascular. Abbott Vascular is providing institution research grant for the Erasmus MC. Antonios Karanasos received funding support from the Hellenic Heart Foundation and St Jude Medical.

References

1. Task Force on Myocardial Revascularization of the European Society of C, the European Association for Cardio-Thoracic S, European Association for Percutaneous

Cardiovascular I, Wijns W, Kolh P, Danchin N, Di Mario C, Falk V, Folliguet T, Garg S, Huber K, James S, Knuuti J, Lopez-Sendon J, Marco J, Menicanti L, Ostojic M, Piepoli MF, Pirlet C, Pomar JL, Reifart N, Ribichini FL, Schalij MJ, Sergeant P, Serruys PW, Silber S, Sousa Uva M, Taggart D. Guidelines on myocardial revascularization. *Eur Heart J* 2010;**31**:2501–2555.

2. Spaulding C, Henry P, Teiger E, Beatt K, Bramucci E, Carrie D, Slama MS, Merkely B, Erglis A, Margheri M, Varenne O, Cebrian A, Stoll HP, Snead DB, Bode C, Investigators T. Sirolimus-eluting versus uncoated stents in acute myocardial infarction. *N Engl J Med* 2006;**355**:1093–1104.
3. Stone GW, Lansky AJ, Pocock SJ, Gersh BJ, Dangas G, Wong SC, Witzenbichler B, Guagliumi G, Peruga JZ, Brodie BR, Dudek D, Mockel M, Ochala A, Kellock A, Parise H, Mehran R, Investigators H-AT. Paclitaxel-eluting stents versus bare-metal stents in acute myocardial infarction. *N Engl J Med* 2009;**360**:1946–1959.
4. Brar SS, Leon MB, Stone GW, Mehran R, Moses JW, Brar SK, Dangas G. Use of drug-eluting stents in acute myocardial infarction: a systematic review and meta-analysis. *J Am Coll Cardiol* 2009;**53**:1677–1689.
5. Raber L, Kelbaek H, Ostojic M, Baumbach A, Heg D, Tuller D, von Birgelen C, Roffi M, Moschovitis A, Khattab AA, Wenaweser P, Bonvini R, Pedrazzini G, Kornowski R, Weber K, Trelle S, Luscher TF, Taniwaki M, Matter CM, Meier B, Juni P, Windecker S, Investigators CAT. Effect of biolimus-eluting stents with biodegradable polymer vs bare-metal stents on cardiovascular events among patients with acute myocardial infarction: the COMFORTABLE AMI randomized trial. *JAMA* 2012; **308**:777–787.
6. Sabate M, Cequier A, Iniguez A, Serra A, Hernandez-Antolin R, Mainar V, Valgimigli M, Tespili M, den Heijer P, Bethencourt A, Vazquez N, Gomez-Hospital JA, Baz JA, Martin-Yuste V, van Geuns RJ, Alfonso F, Bordes P, Tebaldi M, Masotti M, Silvestro A, Backx B, Brugaletta S, van Es GA, Serruys PW. Everolimus-eluting stent versus bare-metal stent in ST-segment elevation myocardial infarction (EXAMINATION): 1 year results of a randomised controlled trial. *Lancet* 2012;**380**:1482–1490.
7. Serruys PW, Garcia-Garcia HM, Onuma Y. From metallic cages to transient bioresorbable scaffolds: change in paradigm of coronary revascularization in the upcoming decade? *Eur Heart J* 2012;**33**:16–25b.
8. Finn AV, Joner M, Nakazawa G, Kolodgie F, Newell J, John MC, Gold HK, Virmani R. Pathological correlates of late drug-eluting stent thrombosis: strut coverage as a marker of endothelialization. *Circulation* 2007;**115**:2435–2441.
9. Joner M, Finn AV, Farb A, Mont EK, Kolodgie FD, Ladich E, Kutys R, Skorija K, Gold HK, Virmani R. Pathology of drug-eluting stents in humans: delayed healing and late thrombotic risk. *J Am Coll Cardiol* 2006;**48**:193–202.
10. Hong MK, Mintz GS, Lee CW, Kim YH, Lee SW, Song JM, Han KH, Kang DH, Song JK, Kim JJ, Park SW, Park SJ. Incidence, mechanism, predictors, and long-term prognosis of late stent malapposition after bare-metal stent implantation. *Circulation* 2004;**109**: 881–886.
11. Hong MK, Mintz GS, Lee CW, Park DW, Park KM, Lee BK, Kim YH, Song JM, Han KH, Kang DH, Cheong SS, Song JK, Kim JJ, Park SW, Park SJ. Late stent malapposition after drug-eluting stent implantation: an intravascular ultrasound analysis with long-term follow-up. *Circulation* 2006;**113**:414–419.
12. Ormiston JA, Serruys PW, Onuma Y, van Geuns RJ, de Bruyne B, Dudek D, Thuesen L, Smits PC, Chevalier B, McClean D, Koolen J, Windecker S, Whitbourn R, Meredith I, Dorange C, Veldhof S, Hebert KM, Rapoza R, Garcia-Garcia HM. First serial assessment at 6 months and 2 years of the second generation of absorb everolimus-eluting bioresorbable vascular scaffold: a multi-imaging modality study. *Circ Cardiovasc Interv* 2012;**5**:620–632.
13. Serruys PW, Onuma Y, Dudek D, Smits PC, Koolen J, Chevalier B, de Bruyne B, Thuesen L, McClean D, van Geuns RJ, Windecker S, Whitbourn R, Meredith I, Dorange C, Veldhof S, Hebert KM, Sudhir K, Garcia-Garcia HM, Ormiston JA. Evaluation of the second generation of a bioresorbable everolimus-eluting vascular scaffold for the treatment of de novo coronary artery stenosis: 12-month clinical and imaging outcomes. *J Am Coll Cardiol* 2011;**58**:1578–1588.
14. Kajiya T, Liang M, Sharma RK, Lee CH, Chan MY, Tay E, Chan KH, Tan HC, Low AF. Everolimus-eluting bioresorbable vascular scaffold (BVS) implantation in patients with ST-segment elevation myocardial infarction (STEMI). *EuroIntervention* 2013;**9**: 501–504.
15. Kocka V, Lisa L, Tousek P, Budesinsky T, Widimsky P. ST elevation myocardial infarction treated with bioresorbable vascular scaffold: rationale and first cases. *Eur Heart J* 2013;**34**:2073.
16. Ormiston JA, Serruys PW, Regar E, Dudek D, Thuesen L, Webster MW, Onuma Y, Garcia-Garcia HM, McGreevy R, Veldhof S. A bioabsorbable everolimus-eluting coronary stent system for patients with single de-novo coronary artery lesions (ABSORB): a prospective open-label trial. *Lancet* 2008;**371**:899–907.
17. Serruys PW, Onuma Y, Ormiston JA, de Bruyne B, Regar E, Dudek D, Thuesen L, Smits PC, Chevalier B, McClean D, Koolen J, Windecker S, Whitbourn R, Meredith I, Dorange C, Veldhof S, Miquel-Hebert K, Rapoza R, Garcia-Garcia HM. Evaluation of the second generation of a bioresorbable everolimus drug-eluting vascular scaffold for treatment of de novo coronary artery stenosis: six-month clinical and imaging outcomes. *Circulation* 2010;**122**:2301–2312.
18. Cutlip DE, Windecker S, Mehran R, Boam A, Cohen DJ, van Es GA, Steg PG, Morel MA, Mauri L, Vranckx P, McFadden E, Lansky A, Hamon M, Krucoff MW, Serruys PW, Academic Research C. Clinical end points in coronary stent trials: a case for standardized definitions. *Circulation* 2007;**115**:2344–2351.
19. Onuma Y, Serruys PW. Bioresorbable scaffold: the advent of a new era in percutaneous coronary and peripheral revascularization? *Circulation* 2011;**123**:779–797.
20. Onuma Y, Serruys PW, Perkins LE, Okamura T, Gonzalo N, Garcia-Garcia HM, Regar E, Kamberi M, Powers JC, Rapoza R, van Beusekom H, van der Giessen W, Virmani R. Intracoronary optical coherence tomography and histology at 1 month and 2, 3, and 4 years after implantation of everolimus-eluting bioresorbable vascular scaffolds in a porcine coronary artery model: an attempt to decipher the human optical coherence tomography images in the ABSORB trial. *Circulation* 2010;**122**:2288–2300.
21. Onuma Y, Thuesen L, van Geuns RJ, van der Ent M, Desch S, Fajadet J, Christiansen E, Smits P, Ramsing Holm N, Regar E, van Mieghem N, Borovicanin V, Paunovic D, Senshu K, van Es GA, Muramatsu T, Lee IS, Schuler G, Zijlstra F, Garcia-Garcia HM, Serruys PW, Investigators T. Randomized study to assess the effect of thrombus aspiration on flow area in patients with ST-elevation myocardial infarction: an optical frequency domain imaging study – TROFI trial. *Eur Heart J* 2013;**34**:1050–1060.
22. Sianos G, Papafaklis MI, Daemen J, Vaina S, van Mieghem CA, van Domburg RT, Michalis LK, Serruys PW. Angiographic stent thrombosis after routine use of drug-eluting stents in ST-segment elevation myocardial infarction: the importance of thrombus burden. *J Am Coll Cardiol* 2007;**50**:573–583.
23. Magro M, Nauta S, Simsek C, Onuma Y, Garg S, van der Heide E, van der Giessen WJ, Boersma E, van Domburg RT, van Geuns RJ, Serruys PW. Value of the SYNTAX score in patients treated by primary percutaneous coronary intervention for acute ST-elevation myocardial infarction: The MI SYNTAXscore study. *Am Heart J* 2011;**161**:771–781.
24. Tearney GJ, Regar E, Akasaka T, Adriaenssens T, Barlis P, Bezerra HG, Bouma B, Bruining N, Cho JM, Chowdhary S, Costa MA, de Silva R, Dijkstra J, Di Mario C, Dudek D, Falk E, Feldman MD, Fitzgerald P, Garcia-Garcia HM, Gonzalo N, Granada JF, Guagliumi G, Holm NR, Honda Y, Ikeno F, Kawasaki M, Kochman J, Koltowski L, Kubo T, Kume T, Kyono H, Lam CC, Lamouche G, Lee DP, Leon MB, Maehara A, Manfrini O, Mintz GS, Mizuno K, Morel MA, Nadkarni S, Okura H, Otake H, Pietrasik A, Prati F, Raber L, Radu MD, Rieber J, Riga M, Rollins A, Rosenberg M, Sirbu V, Serruys PW, Shimada K, Shinke T, Shite J, Siegel E, Sonoda S, Suter M, Takarada S, Tanaka A, Terashima M, Thim T, Uemura S, Ughi GJ, van Beusekom HM, van der Steen AF, van Es GA, van Soest G, Virmani R, Waxman S, Weissman NJ, Weisz G, International Working Group for Intravascular Optical Coherence T. Consensus standards for acquisition, measurement, and reporting of intravascular optical coherence tomography studies: a report from the International Working Group for Intravascular Optical Coherence Tomography Standardization and Validation. *J Am Coll Cardiol* 2012;**59**:1058–1072.
25. Farooq V, Onuma Y, Radu M, Okamura T, Gomez-Lara J, Brugaletta S, Gogas BD, van Geuns RJ, Regar E, Schultz C, Windecker S, Lefevre T, Brueren BR, Powers J, Perkins LL, Rapoza RJ, Virmani R, Garcia-Garcia HM, Serruys PW. Optical coherence tomography (OCT) of overlapping bioresorbable scaffolds: from benchwork to clinical application. *EuroIntervention* 2011;**7**:386–399.
26. Magro M, Regar E, Gutierrez-Chico JL, Garcia-Garcia H, Simsek C, Schultz C, Zijlstra F, Serruys PW, van Geuns RJ. Residual atherothrombotic material after stenting in acute myocardial infarction – an optical coherence tomographic evaluation. *Int J Cardiol* 2013;**167**:656–663.
27. Serruys PW, Ormiston JA, Onuma Y, Regar E, Gonzalo N, Garcia-Garcia HM, Nieman K, Bruining N, Dorange C, Miquel-Hebert K, Veldhof S, Webster M, Thuesen L, Dudek D. A bioabsorbable everolimus-eluting coronary stent system (ABSORB): 2-year outcomes and results from multiple imaging methods. *Lancet* 2009;**373**:897–910.
28. Diletti R, Onuma Y, Farooq V, Gomez-Lara J, Brugaletta S, van Geuns RJ, Regar E, de Bruyne B, Dudek D, Thuesen L, Chevalier B, McClean D, Windecker S, Whitbourn R, Smits P, Koolen J, Meredith I, Li D, Veldhof S, Rapoza R, Garcia-Garcia HM, Ormiston JA, Serruys PW. 6-month clinical outcomes following implantation of the bioresorbable everolimus-eluting vascular scaffold in vessels smaller or larger than 2.5 mm. *J Am Coll Cardiol* 2011;**58**:258–264.
29. Diletti R, Serruys PW, Farooq V, Sudhir K, Dorange C, Miquel-Hebert K, Veldhof S, Rapoza R, Onuma Y, Garcia-Garcia HM, Chevalier B. ABSORB II randomized controlled trial: a clinical evaluation to compare the safety, efficacy, and performance of the absorb everolimus-eluting bioresorbable vascular scaffold system against the XIENCE everolimus-eluting coronary stent system in the treatment of subjects with ischemic heart disease caused by de novo native coronary artery lesions: rationale and study design. *Am Heart J* 2012;**164**:654–663.
30. Dudek D, Onuma Y, Ormiston JA, Thuesen L, Miquel-Hebert K, Serruys PW. Four-year clinical follow-up of the ABSORB everolimus-eluting bioresorbable vascular scaffold in patients with de novo coronary artery disease: the ABSORB trial. *EuroIntervention* 2012;**7**:1060–1061.

31. Diletti R, Farooq V, Girasis C, Bourantas C, Onuma Y, Heo JH, Gogas BD, van Geuns RJ, Regar E, de Bruyne B, Dudek D, Thuesen L, Chevalier B, McClean D, Windecker S, Whitbourn RJ, Smits P, Koolen J, Meredith I, Li X, Miquel-Hebert K, Veldhof S, Garcia-Garcia HM, Ormiston JA, Serruys PW. Clinical and intravascular imaging outcomes at 1 and 2 years after implantation of absorb everolimus eluting bioresorbable vascular scaffolds in small vessels. Late lumen enlargement: does bioresorption matter with small vessel size? Insight from the ABSORB cohort B trial. *Heart* 2013;**99**:98–105.
32. Muramatsu T, Onuma Y, Garcia-Garcia HM, Farooq V, Bourantas CV, Morel MA, Li X, Veldhof S, Bartorelli A, Whitbourn R, Abizaid A, Serruys PW, Investigators A-E. Incidence and short-term clinical outcomes of small side branch occlusion after implantation of an everolimus-eluting bioresorbable vascular scaffold: an interim report of 435 patients in the ABSORB-EXTEND single-arm trial in comparison with an everolimus-eluting metallic stent in the SPIRIT first and II trials. *JACC Cardiovasc Interv* 2013;**6**:247–257.
33. Stone GW, Abizaid A, Silber S, Dizon JM, Merkely B, Costa RA, Kornowski R, Abizaid A, Wojdyla R, Maehara A, Dressler O, Brener SJ, Bar E, Dudek D. Prospective, randomized, multicenter evaluation of a polyethylene terephthalate micronet mesh-covered stent (MGuard) in ST-segment elevation myocardial infarction: the MASTER trial. *J Am Coll Cardiol.* 2012;**60**:1975–1984.
34. Otake H, Shite J, Ako J, Shinke T, Tanino Y, Ogasawara D, Sawada T, Miyoshi N, Kato H, Koo BK, Honda Y, Fitzgerald PJ, Hirata K. Local determinants of thrombus formation following sirolimus-eluting stent implantation assessed by optical coherence tomography. *JACC Cardiovasc Interv* 2009;**2**:459–466.
35. Prati F, Guagliumi G, Mintz GS, Costa M, Regar E, Akasaka T, Barlis P, Tearney GJ, Jang IK, Arbustini E, Bezerra HG, Ozaki Y, Bruining N, Dudek D, Radu M, Erglis A, Motreff P, Alfonso F, Toutouzas K, Gonzalo N, Tamburino C, Adriaenssens T, Pinto F, Serruys PW, Di Mario C, Expert's OCTRD. Expert review document part 2: methodology, terminology and clinical applications of optical coherence tomography for the assessment of interventional procedures. *Eur Heart J* 2012;**33**:2513–2520.
36. Prati F, Regar E, Mintz GS, Arbustini E, Di Mario C, Jang IK, Akasaka T, Costa M, Guagliumi G, Grube E, Ozaki Y, Pinto F, Serruys PW, Expert's OCTRD. Expert review document on methodology, terminology, and clinical applications of optical coherence tomography: physical principles, methodology of image acquisition, and clinical application for assessment of coronary arteries and atherosclerosis. *Eur Heart J* 2010;**31**:401–415.
37. Barlis P, Regar E, Serruys PW, Dimopoulos K, van der Giessen WJ, van Geuns RJ, Ferrante G, Wandel S, Windecker S, van Es GA, Eerdmans P, Juni P, di Mario C. An optical coherence tomography study of a biodegradable vs. durable polymer-coated limus-eluting stent: a LEADERS trial sub-study. *Eur Heart J* 2010;**31**:165–176.
38. van Geuns RJ, Tamburino C, Fajadet J, Vrolix M, Witzenbichler B, Eeckhout E, Spaulding C, Reczuch K, La Manna A, Spaargaren R, Garcia-Garcia HM, Regar E, Capodanno D, Van Langenhove G, Verheye S. Self-expanding versus balloon-expandable stents in acute myocardial infarction: results from the APPOSITION II study: self-expanding stents in ST-segment elevation myocardial infarction. *JACC Cardiovasc Interv* 2012;**5**:1209–1219.

Chapter 5

Clinical Application of coronary imaging after a metallic device implantation

---

5.1 Alteration of malapposed struts at 3-day follow-up in APPOSITON II Study

Incidence and potential mechanism of resolved, persistent and newly acquired malapposition three days after implantation of self-expanding or balloon-expandable stents in a STEMI population: insights from optical coherence tomography in the APPOSITION II study.

EuroIntervention. 2015;11(7). pii: 20150309-10.
[Original research paper, Impact Factor: 3.77]

Nakatani S, Onuma Y, Ishibashi Y, Karanasos A, Regar E, Garcia-Garcia HM, Tamburino C, Fajadet J, Vrolix M, Witzenbichler B, Eeckhout E, Spaulding C, Reczuch K, La Manna A, Spaargaren R, Capodanno D, Van Langenhove L, Verheye S, Serruys PW, van Geuns RJ.

Incidence and potential mechanism of resolved, persistent and newly acquired malapposition three days after implantation of self-expanding or balloon-expandable stents in a STEMI population: insights from optical coherence tomography in the APPOSITION II study

Shimpei Nakatani[1], MD; Yoshinobu Onuma[1], MD, PhD; Yuki Ishibashi[1], MD, PhD; Antonios Karanasos[1], MD; Evelyn Regar[1], MD, PhD; Hector M. Garcia-Garcia[2], MD, PhD; Corrado Tamburino[3], MD, PhD; Jean Fajadet[4], MD; Mathias Vrolix[5], MD; Bernhard Witzenbichler[6], MD; Eric Eeckhout[7], MD, PhD; Christian Spaulding[8,9], MD, PhD; Krzysztof Reczuch[10], MD, PhD; Alessio La Manna[3], MD; René Spaargaren[11], MD; Davide Capodanno[3], MD; Glenn Van Langenhove[12], MD, PhD; Stefan Verheye[12], MD, PhD; Patrick W. Serruys[13], MD, PhD; Robert-Jan van Geuns[1]*, MD, PhD

1. Thoraxcenter, Erasmus Medical Center, Rotterdam, The Netherlands; 2. Cardialysis, Rotterdam, The Netherlands; 3. Division of Cardiology, Ferrarotto Hospital, University of Catania, Catania, Italy; 4. Department of Interventional Cardiology, Clinique Pasteur, Toulouse, France; 5. Department of Cardiology, Ziekenhuis Oost-Limburg, Genk, Belgium; 6. Department of Cardiology, Charité Campus Benjamin Franklin, Berlin, Germany; 7. Cardiology Service, Centre Hospitalier Universitaire Vaudois, Lausanne, Switzerland; 8. Hôpital Européen Georges Pompidou, Assistance Publique Hôpitaux de Paris, Paris Descartes University, Paris, France; 9. Institut National de la Santé et de la Recherche Médicale Unité 970, Paris, France; 10. Military Hospital, Wroclaw, Poland; 11. STENTYS SA, Paris, France; 12. Department of Cardiology, Antwerp Cardiovascular Center, ZNA Middelheim, Antwerp, Belgium; 13. International Centre for Circulatory Health, NHLI, Imperial College London, London, United Kingdom

GUEST EDITOR: Fernando Alfonso, MD; *Cardiac Department, Hospital Universitario de la Princesa, IIS-IP Universidad Autonoma de Madrid, Madrid, Spain*

KEYWORDS

- acute myocardial infarction
- intravascular imaging
- optical coherence tomography
- primary percutaneous coronary intervention
- stent

Abstract

Aims: The aim of the current study was to investigate the frequency and mechanisms of sequential incomplete stent apposition (ISA) changes such as persistent, resolved or newly acquired ISA during the first three days after primary PCI (pPCI) in a matched segment-level analysis, with the comparison between self-expanding and balloon-expandable stents assessed by optical coherence tomography (OCT).

Methods and results: The current analysis is a substudy of the APPOSITION II study that included 69 patients (self-expanding: 35, balloon-expandable: 34) using serial optical coherence tomography (OCT) post procedure and three days after pPCI. In order to evaluate a temporal change in ISA, stented regions were segmented using fiduciary landmarks. In a total of 228 corresponding segments, persistent and newly acquired ISA were less frequently observed in self-expanding stents than in balloon-expandable stents (11.5% vs. 33.9%, $p<0.01$, 2.7% vs. 14.8%, $p<0.01$, respectively). New appearances of ISA were caused by tissue resorption, vasorelaxation and "early" recoil in balloon-expandable stents, and only tissue resorption in self-expanding stents.

Conclusions: Three days after pPCI, tissue resorption and vasorelaxation were biological factors associated with new appearance of ISA while "early" recoil of balloon-expandable stents was a mechanical factor. Both persistent ISA and newly acquired ISA occurred less frequently in self-expanding stents, resulting in a low number of ISA segments compared to balloon-expandable stents. Clinical Trials Registration Information: Randomised Comparison Between the STENTYS Self-expanding Coronary Stent and a Balloon-expandable Stent in Acute Myocardial Infarction (APPOSITION II). ClinicalTrials.gov Identifier: NCT01008085

*Corresponding author: Thoraxcenter, Erasmus MC, 's Gravendijkwal 230, 3015 CE Rotterdam, The Netherlands. E-mail: r.vangeuns@erasmusmc.nl

SUBMITTED ON 09/03/2015 - REVISION RECEIVED ON 10/05/2015 - ACCEPTED ON 13/05/2015

Abbreviations

ACS	acute coronary syndrome
BMS	bare metal stent
DES	drug-eluting stent
ISA	incomplete stent apposition
OCT	optical coherence tomography
pPCI	primary percutaneous coronary intervention
QCA	quantitative coronary angiography
STEMI	ST-elevation myocardial infarction

Introduction

Primary percutaneous coronary intervention (pPCI) is considered to be the optimal approach for the treatment of ST-elevation myocardial infarction (STEMI) due to its superior reperfusion outcome when compared to thrombolysis[1].

Optimal stent deployment in pPCI remains challenging due to the presence of thrombus and vasoconstriction. In the setting of STEMI, a rupture or erosion of vulnerable plaques initiates a series of inflammatory reactions and formation of thrombus. In addition, catecholamine stimulation, inflammatory substances, and the impairment of microcirculation contribute to vasoconstriction[2,3]. At the time of pPCI, this situation could lead to an underestimation of the vessel size and result in underdeployment of stents[4]. A few days after pPCI, the interaction of the struts with the vessel wall can alter dynamically due to vessel condition and/or mechanical changes of devices, for instance: i) disappearance of thrombus trapped between the stent struts and vessel wall, ii) vasorelaxation of initially vasoconstricted vessels, iii) additional formation of thrombus due to stent strut penetration into the necrotic core, iv) stent recoil in balloon-expandable stents or stent enlargement in self-expanding stents. These alterations could subsequently result in the disappearance or the new acquisition of incomplete stent apposition (ISA).

Recently, Nakano et al demonstrated, in an autopsy series of patients who died after receiving bare metal stents (BMS, 49%) or drug-eluting stents (DES, 51%) in a setting of acute coronary syndrome (ACS), that the presence of ISA was one of the primary indicators of early stent thrombosis. Previous studies have demonstrated the dramatic alterations of ISA within three days after pPCI in lesion/patient level analysis. The persistence or disappearance of acute ISA at three days is presumably an important factor related to the occurrence of early stent thrombosis. However, the sequential local changes of ISA and the factors that could influence the temporal evolution of ISA have not been characterised. To enable the assessment of local changes of ISA, the matching of the segments at follow-up by fiduciary landmarks is mandatory with the finest level of matching possible (segment-level analysis)[5,6].

Against this background, the aim of the current study was to investigate the frequency and mechanisms of sequential ISA changes such as persistent, resolved or newly acquired ISA during the first three days after pPCI in a matched segment-level analysis with the comparison between self-expanding and balloon-expandable stents assessed by optical coherence tomography (OCT).

Methods

STUDY POPULATION

The APPOSITION II study is a randomised, international, multicentre, open-label clinical study with blinded assessment of the study endpoints for comparison between self-expanding stents and balloon-expandable stents in the setting of STEMI, with OCT examinations performed both immediately and three days after stent implantation[7]. The study population consisted of patients admitted for STEMI with onset of symptoms <12 hours. The patients who met the study selection criteria were randomly assigned 1:1 to receive treatment with a self-expanding stent (STENTYS SA, Paris, France) or a balloon-expandable stent (MULTI-LINK VISION®; Abbott Vascular, Santa Clara, CA, USA; or Driver®; Medtronic, Minneapolis, MN, USA) using a computer-generated randomisation scheme. Angiographic and OCT assessments were performed immediately after stent implantation and three days after the procedure. The details of the trial are described elsewhere. The study complied with the Declaration of Helsinki. Local institutional ethics committees approved the study protocol and all participating patients provided informed consent.

ANGIOGRAPHIC ASSESSMENT

In the calculation of percent diameter stenosis (%DS), the reference diameter was calculated using the automatic interpolation of the diameter curve at the site of the minimal lumen diameter[8]. For the assessment of vasoconstriction/relaxation, the mean lumen diameter of the remote distal segment (5 to 20 mm distal to the stented segment) was measured using quantitative coronary angiography analysis (QCA)[9]. Details of the methods for QCA are described in the **Online Appendix**.

QUANTITATIVE ANALYSIS ON OCT

OCT acquisition was executed with the C7 XR Fourier-Domain System (LightLab Imaging, Westford, MA, USA) using the flushing technique. The automated pullback speed was 20 mm/s and the frame rate was 100 images/s. The OCT measurements were performed at 1 mm longitudinal intervals or at intervals of 200 microns (ISA analysis) with the QCU-CMS software (Medis medical imaging systems bv, Leiden, The Netherlands). Details of the analysis methods have been previously described[7,10] **(Online Appendix)**.

ISA ANALYSIS ON OCT

Apposition of struts was assessed strut by strut by measuring the distance between the adluminal reflective border of a strut and the lumen contour[7]. If this distance was longer than the strut thickness, it was considered as an ISA strut. The thickness of the STENTYS stent is 112 µm for the small and 146 µm for the medium and large sizes; the strut thickness for the VISION and Driver stents is 84 and 100 µm, respectively. Struts crossing over the ostium of side branches and overlapping stents were excluded from the analysis of apposition.

Whenever any malapposed strut was detected in the initial 1 mm interval analysis, an all-frame analysis (200 µm) was performed in

adjacent cross-sections with ISA to calculate the following ISA parameters: 1) maximum ISA detachment distance, 2) maximum ISA area, and 3) ISA volume in the segment. The ISA detachment distance was defined as the distance between the adluminal leading edge of the strut and vessel wall minus the strut thickness at malapposed struts[5,11]. The ISA area was defined as the space between the lumen contour and stent contour at the location of malapposed struts, which was drawn manually[7]. The ISA volumes were computed by a disc summation method[12].

To summarise the spatial distribution of the malapposed struts along the stents, three "foldout views" were created by correlating the longitudinal distance from the distal edge of the stent to the strut (abscissas) with the angle in which the struts were located in the circular cross-section with respect to the centre of gravity of the vessel (ordinates)[13,14]. In addition, malapposed struts were colour-coded according to the ISA detachment distance. The resulting graphic represented the stented vessel, as if it had been cut longitudinally along the reference angle 0° and spread out on a flat surface **(Figure 1)**.

SEQUENTIAL SEGMENTAL ANALYSIS IN STENTED REGION

The stented regions were segmented by using fiduciary landmarks such as a side branch or overlapping part, which enables the assessment of the sequential change of stented segments (segmental analysis) **(Figure 2A)**. The stented segments were classified into four groups: resolved, persistent, newly acquired ISA and no ISA **(Figure 2B)**. A resolved ISA is a post-procedural ISA that resolves at three-day follow-up. A persistent ISA is a post-procedural ISA that remains present at three days. A newly acquired ISA is a newly developed ISA that is identified at three days despite complete stent apposition during the initial procedure. A no ISA was a segment without malapposed struts post procedure and at three days.

DEFINITION OF VESSEL/LUMEN CHANGE AND MECHANICAL CHANGE OF A STENT

Mechanical change of a stent, stent recoil and enlargement were defined by the sequential difference of mean stent area in corresponding segments. According to the range of reproducibility measurements between inter-/intra-observer and inter-scan[15,16], Tanimoto et al reported that the standard deviation of absolute inter-observer difference in the stent area analysis was 0.68 mm^2. Jamil et al demonstrated that the 95% confidence interval of absolute inter-pullback difference in the stent area analysis was 0.9 mm^2. In the current analysis, the 75% quartile of the delta in stent area analysis in balloon-expandable stents was 0.68 mm^2. Therefore, "early" stent recoil was defined as a reduction of mean stent area greater than 0.7 mm^2 at three days **(Figure 3A, Figure 3B)**, and stent enlargement was defined as an increase in mean stent area greater than 0.7 mm^2 **(Figure 3I, Figure 3J)**[15-18]. Vasorelaxation was defined as an increase in mean lumen diameter greater than 5% in the remote distal segment on QCA **(Figure 3C, Figure 3D)**[9] or a new appearance of an inter-strut dissection flap behind the struts on OCT at three days **(Figure 3E, Figure 3F)**. When strut malapposition was resolved at three days without stent enlargement, it was considered to be due to tissue formation behind the malapposed struts **(Figure 3G, Figure 3H)**. When ISA volume increased at three-day follow-up in the absence of an "early" recoil and/or vasorelaxation, it was judged to be caused by tissue resorption **(Figure 3K, Figure 3L)**.

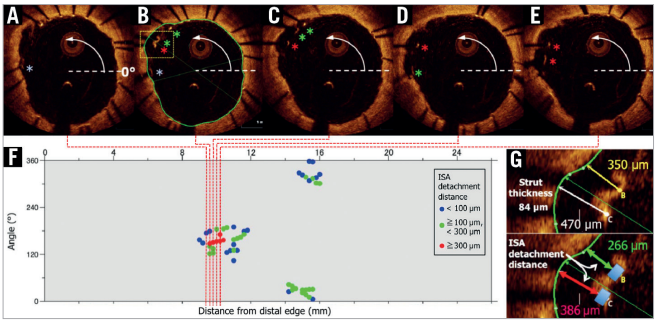

Figure 1. *Foldout view with colour-coded malapposed struts. Apposition of struts was assessed strut by strut in cross-sections with 1 mm intervals. Whenever a malapposed strut was detected, an all-frame analysis (200 µm intervals) was performed for detecting malapposed struts (A-E). By taking the position at 3 o'clock as the 0° reference angle, the malapposed struts could be located in the circular cross-section with respect to the centre of gravity of the vessel. A foldout view of stents can be constructed by correlating the cross-sectional angular position (ordinates) with the longitudinal distance (abscissas) from the distal edge of the stent. The resultant graphic represents the stented vessel, as if it had been cut longitudinally along the reference angle 0° and spread out on a flat surface (F). The malapposed struts were colour-coded according to the ISA detachment distance, which was measured strut by strut, and which was defined as the distance between the adluminal parts of the strut minus the strut thickness of the malapposed strut (G).*

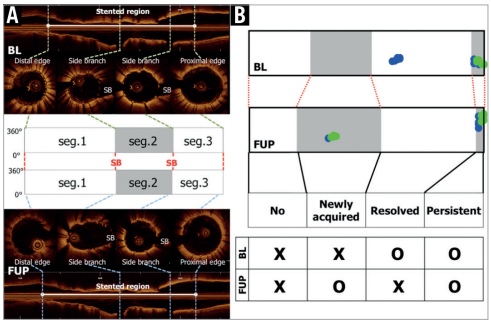

Figure 2. *Segmental analysis and definitions of individual segments. The stented regions were defined as the frames between cross-sections of stent edges in which struts were detected circularly. The stented regions were segmented by using fiduciary landmarks such as side branches or overlaps (A). The corresponding segments were classified into four groups: resolved ISA is a post-procedural ISA segment that resolves at three-day follow-up, persistent ISA is a post-procedural ISA segment that remains present at the three-day follow-up, newly acquired ISA is a newly developed ISA segment that is identified at the three-day follow-up despite complete stent apposition during the initial procedure, and no ISA is a segment without malapposed struts post procedure and at three-day follow-up (B).*

Statistical analysis

All statistical analyses were performed using the statistical software package SPSS, Version 21.0 (IBM Corp., Armonk, NY, USA). Normality of distributions was tested with the Kolmogorov-Smirnov test. Continuous variables are presented as the mean±standard deviation or median with interquartile ranges, as indicated in the Tables. Categorical variables are presented as number (%). Comparisons between the self-expanding and balloon-expandable stents at segment level and between the persistent and resolved ISA were estimated with the Mann-Whitney U test when variables were non-normally distributed and with the Student's t-test when normally distributed. Comparisons of categorical variables were estimated with Fisher's exact test.

Results

From the 80 patients in the APPOSITION II study, 11 were excluded from this analysis because of the lack of OCT imaging data post procedure (n=9) or at three-day follow-up (n=2). A total of 69 lesions in 69 patients had serial OCT images (self-expanding stents: 35, balloon-expandable stents: 34). Baseline clinical and procedural characteristics are summarised in **Online Table 1**. There was no significant difference between groups with respect to baseline clinical characteristics. In the self-expanding group, post-dilation was performed more frequently than in balloon-expandable stents (62.9% [22/35] vs. 23.5% [8/34], p=0.001). The use of post-dilation was recommended if there was a residual stenosis >30% for both treatment groups. However, there were significant differences between study sites in the frequency of post-dilatation. One site never post-dilated, whereas three other sites post-dilated in 100% of the cases in self-expanding stents. On the other hand, four sites never post-dilated balloon-expandable stents.

SEGMENT-LEVEL OCT ANALYSIS

Table 1 summarises the results of OCT analysis in segmental analysis. A total of 228 segments (self-expanding stents: 113, balloon-expandable stents; 115) were assessed sequentially. Mean stent

Table 1. OCT results in segment-level analysis.

	Self-expanding (n=113)	Balloon-expandable (n=115)	*p*-value
Post procedure			
Segment length, mm	7 [4-10]	6 [3-10.5]	0.24
Analysed struts, n	153 [81-214]	60 [36.5-122.5]	<0.001
Mean stent area, mm²	7.33±2.48	9.00±2.25	<0.001
Mean lumen area, mm²	7.73±2.57	9.08±2.34	<0.001
Mean prolapse area, mm²	0.06 [0.01-0.22]	0.23 [0.12-0.48]	<0.001
Mean isolated defect area, mm²	0.00 [0.00-0.00]	0.00 [0.00- 000]	0.93
Isolated defect, n (%)	22 (19.5)	22 (19.1)	1.00
At follow-up			
Segment length, mm²	6 [3-10]	6 [4-11]	0.57
Analysed struts, n	141 [75-226]	65 [34.5-119.5]	<0.001
Mean stent area, mm²	8.53±2.53	8.88±2.04	0.11
Diff. mean stent area, mm²	1.21±1.12	–0.11±0.66	<0.001
Stent enlargement (Diff. mean stent area >0.7 mm²), n (%)	77 (68.1)	0 (0.0)	<0.001
Stent recoil (Diff. mean stent area <–0.7 mm²), n (%)	0 (0.0)	28 (24.3)	<0.001
Mean lumen area, mm²	8.62±2.58	8.96±2.13	0.11
Diff. mean lumen area, mm²	0.88±1.19	–0.12±0.69	<0.001
Mean prolapse area, mm²	0.20 [0.09-0.45]	0.25 [0.15-0.46]	0.11
Diff. mean prolapse area, mm²	0.08 [0.00-0.28]	0.00 [–0.14-0.11]	<0.001
Mean isolated defect area, mm²	0.00 [0.00-0.00]	0.00 [0.00-0.00]	0.15
Isolated defect, n (%)	21 (18.6)	14 (12.2)	0.02

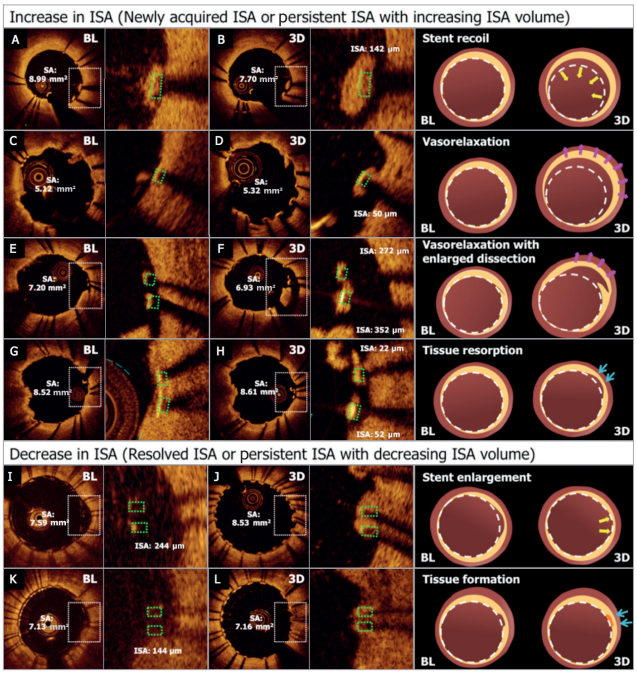

Figure 3. *Mechanisms of ISA changes. The mechanisms of increase and decrease in ISA were defined by the following factors: the difference of stent area on OCT between two time points, inter-strut dissection on OCT and mean lumen diameter of remote distal segments on QCA. A) & B) Newly acquired ISA caused by a stent recoil that is defined by the difference of mean stent area between two time points. C) & D) Newly acquired ISA caused by vasorelaxation that was detected on QCA by the increase of mean lumen diameter in remote distal segments. E) & F) Newly acquired ISA caused by vasorelaxation that is defined by the enlargement of an inter-strut dissection flap behind the struts. G) & H) Newly acquired ISA caused by tissue resorption in which stent enlargement and vasorelaxation are not observed on OCT and QCA. I) & J) The resolved ISA caused by a stent enlargement that is defined by the difference of mean stent area between two time points. K) & L) The resolved ISA caused by tissue formation while stent enlargement is not observed.*

area post procedure was 7.33±2.48 mm^2 in self-expanding stents vs. 9.00±2.25 mm^2 in balloon-expandable stents (p<0.001). Mean stent area at follow-up was 8.53±2.53 mm^2 in self-expanding stents vs. 8.88±2.04 mm^2 in balloon-expandable stents (p=0.11). For the self-expanding stent, the mean stent area was significantly enlarged at three days – by 1.21±1.12 mm^2 (p<0.01). For the balloon-expandable stent, the mean stent area had a tendency to decrease at three-day follow-up – by 0.11±0.66 mm^2 (p=0.07). The difference between mean stent area post procedure and at three-day follow-up was significantly larger in self-expanding stents than in balloon-expandable stents (1.21±1.12 mm^2 vs. –0.11±0.66 mm^2, p<0.001). Although the stent area of a self-expanding stent was smaller than that of a balloon-expandable stent immediately post procedure, there was no difference between the two stents at three days.

SEGMENT-LEVEL ISA ANALYSIS

Table 2 summarises the ISA parameters in segmental analysis, and the foldout views depict the clustering and spread distribution of ISA **(Figure 4)**. ISA segments were more frequently observed in balloon-expandable stents than in self-expanding stents both post procedure and at three days (post procedure: 24.8% vs. 44.3%, p=0.002; at three days: 14.2% vs. 48.7%, p<0.001). Although there was a significant difference in the ISA length and maximum ISA detachment distance, the maximum ISA area and ISA volume were similar between the two groups post procedure. At three days, ISA parameters in the balloon-expandable stents were significantly larger than in the self-expanding stents **(Table 2)**.

In sequential assessment, the incidence of resolved ISA was similar in the self-expanding stents and the balloon-expandable stents (self-expanding: 13.3%, balloon-expandable; 10.4%, p=0.51)

Table 2. Segment-level ISA analysis.

	Self-expanding (n=113)	Balloon-expandable (n=115)	*p*-value
Post procedure			
ISA segment, n (%)	28 (24.8)	51 (44.3)	0.002
ISA length, mm²	0.9 [0.6-1.5]	1.1 [0.8-2.3]	0.02
Max ISA length, mm²	0.6 [0.5-1.2]	1.0 [0.8-2.3]	0.005
Max ISA detachment distance, µm	86 [56-205]	162 [106-293]	0.03
Max ISA area, mm²	0.36 [0.17-0.57]	0.35 [0.20-0.91]	0.34
ISA volume, mm³	0.23 [0.10-0.44]	0.25 [0.11-1.33]	0.17
Malapposed struts >5%, n (%)¶	9 (8.0)	27 (23.5)	0.002
Malapposed struts >30%, n (%)¶	0 (0.0)	6 (5.3)	0.03
3-day follow-up			
ISA segment, n (%)	16 (14.2)	56 (48.7)	<0.001
ISA length, mm	0.7 [0.4-1.0]	1.2 [0.7-2.8]	0.002
Max ISA length, mm	0.6 [0.4-0.9]	1.0 [0.6-2.0]	0.01
Max ISA detachment distance, µm	153 [79-238]	280 [144-396]	0.01
Max ISA area, mm²	0.42 [0.20-0.66]	0.60 [0.28-0.98]	0.01
ISA volume, mm³	0.20 [0.07-0.37]	0.47 [0.19-1.71]	0.01
Malapposed struts >5%, n (%)¶	6 (5.3)	32 (27.8)	<0.001
Malapposed struts >30%, n (%)¶	0 (0.0)	4 (3.5)	0.12
Sequential assessment			
Resolved, n (%)	15 (13.3)	12 (10.4)	0.51
Persistent, n (%)	13 (11.5)	39 (33.9)	<0.001
Newly acquired, n (%)	3 (2.7)	17 (14.8)	0.001
No ISA, n (%)	82 (72.6)	47 (40.9)	<0.001

¶analysed on 1 mm interval cross-sections.

Table 3. Likelihood of persistent versus resolved ISA at three-day follow-up.

	Self-expanding		Balloon-expandable	
	Persistent	Resolved	Persistent	Resolved
Max ISA detachment distance, µm				
<100	…	73.3	…	54.5
<150	…	70.6	…	41.7
<200	…	61.9	…	40.0
<250	…	65.2	…	33.3
≥100	69.2	…	85.0	…
≥150	72.7	…	92.6	…
≥200	71.4	…	100.0	…
≥250	100.0	…	100.0	…
Max ISA area, mm²				
<0.3	…	76.9	…	39.1
<0.5	…	63.2	…	31.0
<0.7	…	60.0	…	29.4
<1.0	…	55.6	…	29.3
≥0.3	66.7	…	89.3	…
≥0.5	66.7	…	86.4	…
≥0.7	100.0	…	88.2	…
≥1.0	100.0	…	100.0	…
ISA volume, mm³				
<0.1	…	71.4	…	50.0
<0.3	…	58.8	…	37.0
<0.5	…	59.1	…	36.4
<0.7	…	55.6	…	34.3
≥0.1	52.4	…	84.6	…
≥0.3	54.5	…	91.7	…
≥0.5	66.7	…	100.0	…
≥0.7	100.0	…	100.0	…

(Table 2, Figure 5). The incidence of persistent and newly acquired ISA in self-expanding stents was significantly lower than in balloon-expandable stents (persistent: 11.5% vs. 33.9%, p<0.001; newly acquired: 2.7% vs. 14.8%, p=0.001) **(Table 2, Figure 5)**. In self-expanding stents, 53.6% (15/28) of the post-procedural ISA was resolved and 46.4% (13/28) was persistent. In balloon-expandable stents, 23.5% (12/51) of post-procedural ISA was resolved and 76.5% (39/51) was persistent **(Table 2, Figure 5)**.

POST-PROCEDURAL ISA SIZE AND PERSISTENCY OR DISAPPEARANCE OF ISA AT THREE DAYS

When comparing post-procedural ISA parameters in persistent and resolved ISA, there was no significant difference in the ISA parameters in self-expanding stents **(Online Table 2)**. In balloon-expandable stents, the maximum ISA detachment distance of persistent ISA was higher than that of resolved ISA (persistent: 237 µm, resolved: 105 µm, p=0.01). **Table 3** shows an estimation of the likelihood at three-day follow-up of resolved versus persistent ISA according to the ISA parameters post procedure. In self-expanding stents, the maximum ISA detachment distance ≥250 µm, the maximum ISA area ≥1.0 mm² and ISA volume ≥0.7 mm³ post procedure resulted in persisting ISA in all cases. In balloon-expandable stents, the maximum ISA detachment distance ≥200 µm, the maximum ISA area ≥1.0 mm² and ISA volume ≥0.5 mm³ post procedure resulted in persisting ISA in all cases.

MECHANISMS OF ISA CHANGE

On QCA, the frequency of vasorelaxation was similar between the two groups (self-expanding: 11 vessels [32.4%], balloon-expandable: 11 vessels [31.4%], p=1.00) **(Online Table 3)**. On OCT, stent recoil was observed in 24.3% of balloon-expandable stent segments and stent enlargement was observed in 68.1% of self-expanding stent segments.

The resolved ISA and persistent ISA with decreasing ISA volume caused by stent enlargement were observed only in self-expanding stents (11 segments [9.7%] in resolved ISA, six segments [5.3%] in persistent ISA with decreasing ISA volume). The persistent ISA with decreasing ISA volume caused by tissue formation was observed less frequently in self-expanding stents than in balloon-expandable stents (self-expanding: two segments [1.8%], balloon-expandable: 13 segments [11.3%], p=0.01) **(Table 4, Online Figure 1)**.

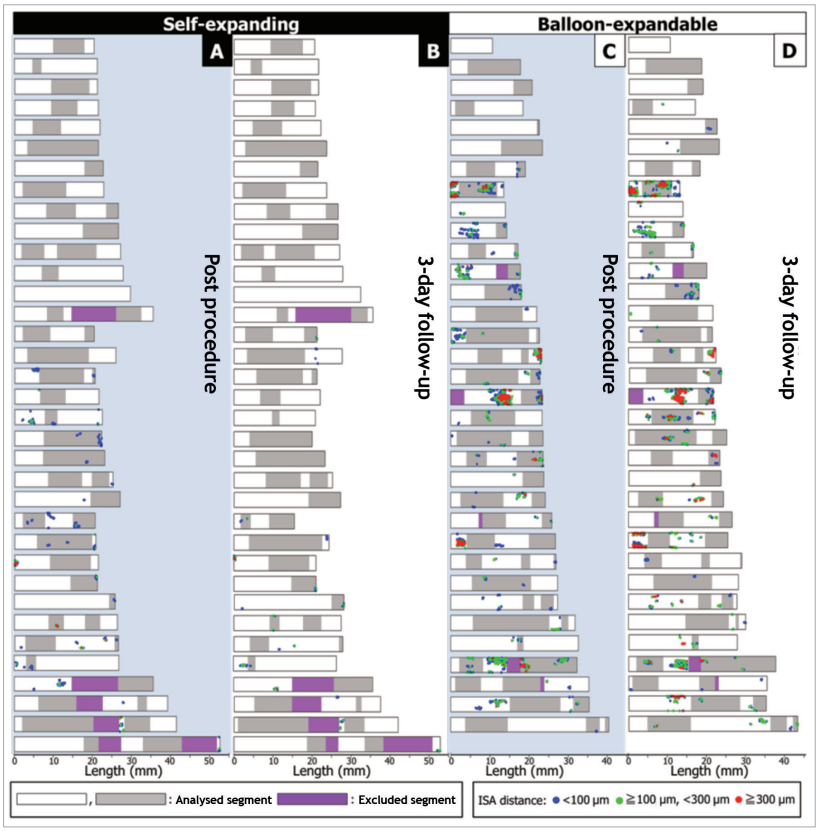

Figure 4. *Sequential foldout views of 228 segments. Foldout views based on frame-by-frame analysis show malapposed struts in 228 segments post procedure and three days after pPCI. The foldout view allows depiction and comparison of the clustering and spread distribution of ISA at two time points. A) & C) Post procedure (A: self-expanding; C: balloon-expandable). B) & D) Three days after pPCI (B: self-expanding; D: balloon-expandable). The blue dots illustrate the malapposed struts with ISA detachment distance <100 microns, the green dots with ISA detachment distance ≥100 microns, and <300 microns, the red dots with ISA detachment distance ≥300 microns. ISA: incomplete stent apposition*

The newly acquired ISA and persistent ISA with increasing ISA volume caused by "early" recoil were observed only in balloon-expandable stents (five segments [4.3%] in newly acquired ISA, six segments [5.2%] in persistent ISA with increasing ISA volume). The persistent ISA with increasing ISA volume caused by tissue resorption was less frequently observed in self-expanding stents than in balloon-expandable stents (two segments [37.4%] vs. 11 segments [7.1%], p=0.02) **(Table 4, Online Figure 1)**.

Discussion

To evaluate the temporal change of ISA and its mechanism, we conducted a matched segment-level analysis and additional QCA analysis with the comparison between self-expanding and balloon-expandable stents assessed by OCT using data from the APPOSITION II study. The main findings of the current analysis are the following. 1) Three days after pPCI in the segmental analysis, persistent and newly acquired ISA segments were less frequently observed in self-expanding stents than in balloon-expandable stents (persistent: 11.5% vs. 33.9%, p<0.001; newly acquired: 2.7% vs. 14.8%, p=0.001). 2) The newly acquired ISA in balloon-expandable stents were caused by tissue resorption, vasorelaxation and "early" recoil while in self-expanding stents it was caused by tissue resorption. 3) Resolved ISA was caused by stent enlargement in self-expanding stents while tissue formation was responsible in balloon-expandable stents.

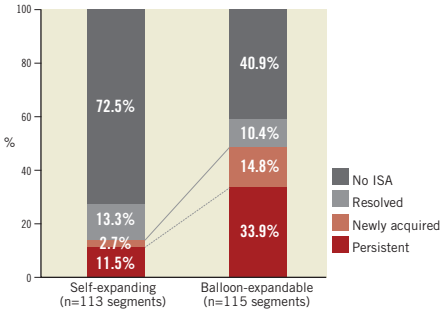

Figure 5. *Summary of ISA changes in three days. In sequential assessment, resolved ISA was observed similarly in the self-expanding stents and the balloon-expandable stents (p=0.51). The rate of persistent and newly acquired ISA in self-expanding stents was significantly less than in balloon-expandable stents (persistent: p<0.001; newly acquired: p=0.001). As a result, ISA was still present at three days in 14.2% of self-expanding stent segments and 48.7% of balloon-expandable stent segments. ISA: incomplete stent apposition*

THE CHANGE OF ISA IN SEGMENTAL ANALYSIS

In the current sub-analysis of the APPOSITION II study, the additional matched segment-level analysis demonstrated the considerable change of ISA in the early phase after pPCI and the difference in temporal ISA change between self-expanding and balloon-expandable stents. ISA is a localised phenomenon in a stented segment, with an average length of 2.0 mm according to the previous literature[5]. Therefore, it is important to match the regions with ISA at different time points in order to assess the temporal changes. A strut-by-strut matching at two time points is ideal; however, this type of analysis is practically impossible to perform due to the rotation of the catheter and limited longitudinal resolution. As a pragmatic approach, segmental level matching using fiduciary landmarks was performed in the current analysis. In addition, foldout views based on frame-by-frame analysis were created to depict the clustering and spread distribution of ISA **(Figure 4)**. In self-expanding stents, ISA had almost uniformly disappeared at three days. In balloon-expandable stents, there was some diversity in ISA distribution, suggesting that there was an influence of mechanical and locoregional factors on ISA.

Table 4. Mechanisms of resolved, persistent and newly acquired ISA.

	Self-expanding n=113	Balloon-expandable n=115	*p*-value
Resolved ISA			
Stent enlargement, n (%)	11 (9.7)	0 (0.0)	<0.001
Tissue formation, n (%)	4 (3.5)	12 (10.4)	0.07
Persistent ISA with decreasing ISA volume			
Stent enlargement, n (%)	6 (5.3)	0 (0.0)	0.01
Tissue formation, n (%)	2 (1.8)	13 (11.3)	0.01
Persistent ISA with increasing ISA volume			
Tissue resorption, n (%)	2 (1.8)	11 (9.6)	0.02
Vasorelaxation, n (%)	3 (2.7)	9 (7.8)	0.14
Vasorelaxation and stent recoil, n (%)	0 (0.0)	4 (3.5)	0.12
Stent recoil, n (%)	0 (0.0)	2 (1.7)	0.50
Newly acquired ISA			
Tissue resorption, n (%)	3 (2.7)	7 (6.1)	0.33
Vasorelaxation, n (%)	0 (0.0)	5 (4.3)	0.06
Vasorelaxation and stent recoil, n (%)	0 (0.0)	2 (1.7)	0.50
Stent recoil, n (%)	0 (0.0)	3 (2.6)	0.25

WORSENING OF ISA WITH VASORELAXATION, STENT RECOIL AND TISSUE RESORPTION IN A STEMI POPULATION

To the best of our knowledge, this is the first OCT report demonstrating the contribution of vasorelaxation to the worsening of ISA three days after STEMI. The self-expanding device expands to its unconstrained size and takes advantage of the vasorelaxation to maintain the contact between struts and the luminal border of the vessel wall. In balloon-expandable stents, the stent dimensions remain the same or get smaller. Therefore, it is critical to select the proper size of stent and to try to anticipate the vessel dimension without vasoconstriction. Alternatively, it is important to eliminate the vasoconstriction as much as possible by administering nitrate before sizing of the vessels and selection of the stent size.

The other novel finding is that the "early" stent recoil (within three days after the procedure) of balloon-expandable stents is one of the aetiologies for the worsening of ISA. There was an average reduction of stent area by 0.11±0.66 mm^2 at three days after implantation of balloon-expandable stents. This could be the result of the inherent recoil of the metallic structure rather than forced constriction by the surrounding tissue, since the reference vessels become more vasorelaxed during the first three days. It would be a technical challenge for a manufacturer to reduce the amount of "early" recoil of balloon-expandable stents.

MALAPPOSED STRUTS AT THREE DAYS AFTER pPCI

Foin et al showed that malapposed struts with maximum ISA detachment distance (the distance between the adluminal strut edge and vessel wall minus strut and polymer thickness) of >300 µm had a likelihood of delayed healing with drug-eluting stents (DES) in the setting of stable angina[11]. Gutiérrez-Chico et al showed that the ISA distance (the distance between the adluminal strut edge and vessel wall) of <270 µm was likely to be again apposed at nine months after DES implantation in the setting of stable angina[5]. In the current analysis of a STEMI population, the post-procedural malapposed struts with ISA detachment distance of >250 µm in self-expanding stents and >200 µm in balloon-expandable stents remained malapposed at three days. A serial OCT examination at long-term follow-up is warranted to create

a threshold value for resolution or persistence of malapposition in the setting of STEMI, which could be helpful to establish the criterion of minimal ISA detachment distance which requires mechanical corrections of acute ISA by post-dilatation.

Limitations

This is a *post hoc* analysis and the population is too small to evaluate the clinical prognostic outcome of ISA. In addition, the influence of acute ISA or temporal ISA change during the first three days on the stent healing at follow-up was unclear since the current study did not have a serial OCT examination at long-term follow-up. The APPOSITION V study will evaluate whether the superior apposition of the STENTYS stent results in at least non-inferior outcome to a balloon-expandable stent[19]. The performance rate of post-dilatation was significantly different between self-expanding stents and balloon-expandable stents. These differences might influence the results of the ISA rate in the post-procedural phase, already reported in the original paper of APPOSITION II. The extent of ISA rather than its mere existence could be the underlying factor as a predictor of thrombosis. Other factors may also play a more relevant role in the risk of early thrombosis.

Conclusion

Three days after pPCI, tissue resorption and vasorelaxation were biological factors associated with new appearance of ISA while "early" recoil of balloon-expandable stents was a mechanical factor. Both persistent ISA and newly acquired ISA occurred less frequently in self-expanding stents, resulting in a lower number of ISA segments when compared to balloon-expandable stents.

Impact on daily practice

In the setting of STEMI, ISA is frequently observed and can be resolved or worsen shortly after pPCI due to several factors correlated with changes of vessel conditions and device performance. The current analysis demonstrated that vasodilatation and dissection were the main contributors to newly acquired ISA, and stent recoil was an important limitation in balloon-expandable stents. The post-procedural ISA detachment distance assessed by OCT could indicate remaining malapposed struts three days after pPCI. Taking into account these acute changes after pPCI, operators should decide on mechanical correction of post-procedural ISA by post-dilatation.

Guest Editor

This paper was guest edited by Fernando Alfonso, MD; Cardiac Department, Hospital Universitario de la Princesa, IIS-IP Universidad Autonoma de Madrid, Madrid, Spain.

Acknowledgements

The authors thank J.L. Gutiérrez-Chico for his interpretation of the methodology of the current substudy.

Conflict of interest statement

B. Witzenbichler received site reimbursement from STENTYS SA for participation in the APPOSITION II study. C. Spaulding is a member of the scientific advisory board for Medpass, Abiomed and Medtronic, has received speaker's honoraria from AstraZeneca, Eli Lilly, Daiichi Sankyo, Servier and Cordis, and has received research grants from Biosensors and Boston Scientific. R. Spaargaren is an employee of STENTYS SA. D. Capodanno has received speaker's honoraria from AstraZeneca, Boston Scientific, and Eli Lilly. RJ.M. van Geuns has received honoraria as a member of the speaker's board from STENTYS SA, Boston Scientific and Abbott Vascular. P.W. Serruys is a member of the Advisory Board for Abbott Vascular. Y. Onuma is a member of the Advisory Board for Abbott Vascular. The other authors have no conflicts of interest to declare. The Guest Editor has no conflicts of interest to declare.

References

1. Keeley EC, Boura JA, Grines CL. Primary angioplasty versus intravenous thrombolytic therapy for acute myocardial infarction: a quantitative review of 23 randomised trials. *Lancet.* 2003;361:13-20.

2. Adlbrecht C, Bonderman D, Plass C, Jakowitsch J, Beran G, Sperker W, Siostrzonek P, Glogar D, Maurer G, Lang IM. Active endothelin is an important vasoconstrictor in acute coronary thrombi. *Thromb Haemost.* 2007;97:642-9.

3. Di Stefano R, Di Bello V, Barsotti MC, Grigoratos C, Armani C, Dell'Omodarme M, Carpi A, Balbarini A. Inflammatory markers and cardiac function in acute coronary syndrome: difference in ST-segment elevation myocardial infarction (STEMI) and in non-STEMI models. *Biomed Pharmacother.* 2009;63:773-80.

4. van Werkum JW, Heestermans AA, Zomer AC, Kelder JC, Suttorp MJ, Rensing BJ, Koolen JJ, Brueren BR, Dambrink JH, Hautvast RW, Verheugt FW, ten Berg JM. Predictors of coronary stent thrombosis: the Dutch Stent Thrombosis Registry. *J Am Coll Cardiol.* 2009;53:1399-409.

5. Gutierrez-Chico JL, Wykrzykowska J, Nuesch E, van Geuns RJ, Koch KT, Koolen JJ, di Mario C, Windecker S, van Es GA, Gobbens P, Jüni P, Regar E, Serruys PW. Vascular tissue reaction to acute malapposition in human coronary arteries: sequential assessment with optical coherence tomography. *Circ Cardiovasc Interv.* 2012;5:20-9, S1-8.

6. Im E, Kim BK, Ko YG, Shin DH, Kim JS, Choi D, Jang Y, Hong MK. Incidences, predictors, and clinical outcomes of acute and late stent malapposition detected by optical coherence tomography after drug-eluting stent implantation. *Circ Cardiovasc Interv.* 2014;7:88-96.

7. van Geuns RJ, Tamburino C, Fajadet J, Vrolix M, Witzenbichler B, Eeckhout E, Spaulding C, Reczuch K, La Manna A, Spaargaren R, Garcia-Garcia HM, Regar E, Capodanno D, Van Langenhove G, Verheye S. Self-expanding versus balloon-expandable stents in acute myocardial infarction: results from the APPOSITION II study: self-expanding stents in

ST-segment elevation myocardial infarction. *JACC Cardiovasc Interv.* 2012;5:1209-19.

8. Serruys PW, Kay IP, Disco C, Deshpande NV, de Feyter PJ. Periprocedural quantitative coronary angiography after Palmaz-Schatz stent implantation predicts the restenosis rate at six months: results of a meta-analysis of the BElgian NEtherlands Stent study (BENESTENT) I, BENESTENT II pilot, BENESTENT II and MUSIC trials. Multicenter Ultrasound Stent In Coronaries. *J Am Coll Cardiol.* 1999;34:1067-74.

9. Maier W, Windecker S, Kung A, Lutolf R, Eberli FR, Meier B, Hess OM. Exercise-induced coronary artery vasodilation is not impaired by stent placement. *Circulation.* 2002;105:2373-7.

10. Onuma Y, Thuesen L, van Geuns RJ, van der Ent M, Desch S, Fajadet J, Christiansen E, Smits P, Holm NR, Regar E, van Mieghem N, Borovicanin V, Paunovic D, Senshu K, van Es GA, Muramatsu T, Lee IS, Schuler G, Zijlstra F, Garcia-Garcia HM, Serruys PW; TROFI Investigators. Randomized study to assess the effect of thrombus aspiration on flow area in patients with ST-elevation myocardial infarction: an optical frequency domain imaging study--TROFI trial. *Eur Heart J.* 2013;34:1050-60.

11. Foin N, Gutierrez-Chico JL, Nakatani S, Torii R, Bourantas CV, Sen S, Nijjer S, Petraco R, Kousera C, Ghione M, Onuma Y, Garcia-Garcia HM, Francis DP, Wong P, Di Mario C, Davies JE, Serruys PW. Incomplete stent apposition causes high shear flow disturbances and delay in neointimal coverage as a function of strut to wall detachment distance: implications for the management of incomplete stent apposition. *Circ Cardiovasc Interv.* 2014;7:180-9.

12. Onuma Y, Serruys P, den Heijer P, Joesoef KS, Duckers H, Regar E, Kukreja N, Tanimoto S, Garcia-Garcia HM, van Beusekom H, van der Giessen W, Nishide T. MAHOROBA, first-in-man study: 6-month results of a biodegradable polymer sustained release tacrolimus-eluting stent in de novo coronary stenoses. *Eur Heart J.* 2009;30:1477-85.

13. Gutierrez-Chico JL, van Geuns RJ, Regar E, van der Giessen WJ, Kelbaek H, Saunamaki K, Escaned J, Gonzalo N, di Mario C, Borgia F, Nuesch E, Garcia-Garcia HM, Silber S, Windecker S, Serruys PW. Tissue coverage of a hydrophilic polymer-coated zotarolimus-eluting stent vs. a fluoropolymer-coated everolimus-eluting stent at 13-month follow-up: an optical coherence tomography substudy from the RESOLUTE all comers trial. *Eur Heart J.* 2011;32:2454-63.

14. Gutierrez-Chico JL, Radu MD, Diletti R, Sheehy A, Kossuth MB, Oberhauser JP, Glauser T, Harrington J, Rapoza RJ, Onuma Y, Serruys PW. Spatial distribution and temporal evolution of scattering centers by optical coherence tomography in the poly(l-lactide) backbone of a bioresorbable vascular scaffold. *Circ J.* 2012;76:342-50.

15. Orii M, Kubo T, Tanaka A, Kitabata H, Ino Y, Shiono Y, Shimamura K, Aoki H, Ohta S, Ozaki Y, Ishibashi K, Yamano T, Tanimoto T, Yamaguchi T, Hirata K, Imanishi T, Akasaka T. Interscan reproducibility of geometric coronary artery measurements using frequency-domain optical coherence tomography. *Int Heart J.* 2013;54:64-7.

16. Gonzalo N, Garcia-Garcia HM, Serruys PW, Commissaris KH, Bezerra H, Gobbens P, Costa M, Regar E. Reproducibility of quantitative optical coherence tomography for stent analysis. *EuroIntervention.* 2009;5:224-32.

17. Tanimoto S, Rodriguez-Granillo G, Barlis P, de Winter S, Bruining N, Hamers R, Knappen M, Verheye S, Serruys PW, Regar E. A novel approach for quantitative analysis of intracoronary optical coherence tomography: high inter-observer agreement with computer-assisted contour detection. *Catheter Cardiovasc Interv.* 2008;72:228-35.

18. Jamil Z, Tearney G, Bruining N, Sihan K, van Soest G, Ligthart J, van Domburg R, Bouma B, Regar E. Interstudy reproducibility of the second generation, Fourier domain optical coherence tomography in patients with coronary artery disease and comparison with intravascular ultrasound: a study applying automated contour detection. *Int J Cardiovasc Imaging.* 2013;29:39-51.

19. Grundeken MJ, Lu H, Mehran R, Cutlip DE, Leon MB, Yeung A, Koch KT, Montalescot G, van Geuns RJ, Spaargaren R, Buchbinder M. APPOSITION V: STENTYS coronary stent system clinical trial in subjects with ST-segment elevation myocardial infarction--rationale and design. *Am Heart J.* 2014;168:652-60.

20. Sianos G, Papafaklis MI, Daemen J, Vaina S, van Mieghem CA, van Domburg RT, Michalis LK, Serruys PW. Angiographic stent thrombosis after routine use of drug-eluting stents in ST-segment elevation myocardial infarction: the importance of thrombus burden. *J Am Coll Cardiol.* 2007;50:573-83.

Supplementary data

Online Appendix. Methods.

Online Table 1. Baseline clinical and procedural characteristics.

Online Table 2. Differences in OCT variables between resolved and persistent ISA in self-expanding and balloon-expandable stents.

Online Table 3. Baseline and follow-up quantitative coronary analysis.

Online Figure 1. Mechanisms of ISA changes.

Supplementary data

Online Appendix. Methods

ANGIOGRAPHIC ASSESSMENT

Quantitative coronary angiography (QCA) was performed using the CAAS 5 analysis system (Pie Medical BV, Maastricht, The Netherlands). In each patient, the following QCA parameters were measured in the stented segment and the peri-stent segments (defined by a length 5 mm proximal and distal to the stent edge): minimal lumen diameter (MLD), reference diameter obtained by an interpolated method, and percentage diameter stenosis (%DS). For the assessment of vasoconstriction/relaxation, the mean lumen diameter of the remote distal segment (5 to 20 mm distal to the stented segment) was measured using QCA[9]. Intracoronary thrombus was angiographically identified and scored in five grades as previously described. Thrombus grade was assessed after flow achievement with crossing of a guidewire[20].

QUANTITATIVE ANALYSIS ON OCT

The OCT measurements were performed with QCU-CMS software (Medis medical imaging systems bv, Leiden, The Netherlands) by analysts who were blinded to patient and procedural information. The cross-sectional areas of stent, lumen, prolapse and isolated intraluminal defect were measured at 1 mm intervals[7,10]. The prolapse area was defined as the convex-shaped area of tissue protrusion between adjacent stent struts towards the lumen, without disruption of the continuity of the luminal vessel surface. Isolated intraluminal defect refers to a fixed structure separated from the vessel wall seen in the analysed cross-section and probably attached to the vessel wall at a proximal or distal site in a different cross-section.

Frames were excluded from the analysis if there were overlapping struts, or if there was a non-uniform rotational distortion, and if the struts and vessel wall could not be visualised due to insufficient blood clearance or an inadequately flushed OCT catheter.

Online Table 1. Baseline clinical and procedural characteristics.

	Self-expanding (n=35)	Balloon-expandable (n=34)	*p*-value
Baseline clinical characteristics			
Age, years (mean±SD)	61.1±12.8	59.0±11.3	0.49
Male, n (%)	30 (85.7)	28 (82.4)	0.70
Diabetes mellitus, n (%)	7 (20.0)	4 (11.8)	0.35
Hypertension, n (%)	15 (42.9)	18 (52.9)	0.40
Hyperlipidaemia, n (%)	16 (45.7)	16 (47.1)	0.91
Current smoker, n (%)	19 (54.3)	25 (73.5)	0.10
Prior PCI, n (%)	0 (0.0)	0 (0.0)	
Prior CABG, n (%)	0 (0.0)	0 (0.0)	
Prior MI, n (%)	0 (0.0)	0 (0.0)	
Symptoms onset to PCI, hrs	2.0 [1.5-4.0]	3.0 [2.0-4.0]	0.29
Symptoms onset to PCI <3 hrs, n (%)	24 (68.6)	19 (55.9)	0.35
Symptoms onset to PCI >6 hrs, n (%)	3 (8.6)	5 (14.7)	0.40
Procedural characteristics			
RCA, n (%)	14 (40.0)	18 (52.9)	0.49
LAD, n (%)	16 (45.7)	11 (32.4)	
LCX, n (%)	5 (14.3)	5 (14.7)	
Initial TIMI flow grade 0/1, n (%)	22 (62.9)	18 (52.9)	0.40
Thrombus grade 4, n (%)	15 (42.9)	19 (55.9)	0.20
Thrombus aspiration, n (%)	25 (71.4)	29 (85.3)	0.16
Predilatation, n (%)	20 (57.1)	14 (41.2)	0.19
Post-dilatation, n (%)	22 (62.9)	8 (23.5)	0.001
Post TIMI flow grade 0/1, n (%)	0 (0.0)	0 (0.0)	0.40

Online Table 2. Differences in OCT variables between resolved and persistent ISA in self-expanding and balloon-expandable stents.

	Self-expanding		*p*-value	Balloon-expandable		*p*-value
	Resolved ISA	Persistent ISA		Resolved ISA	Persistent ISA	
No. of segments	15	13		12	39	
OCT qualitative analysis post procedure						
Located at stent edge, n (%)	4 (26.7)	6 (46.2)	0.29	3 (25.0)	11 (28.2)	0.83
Located at culprit lesions, n (%)	6 (40.0)	2 (15.4)	0.15	4 (33.3)	17 (43.6)	0.53
Intra-stent dissection, n (%)	4 (26.7)	5 (38.5)	0.51	4 (33.3)	20 (51.3)	0.28
OCT quantitative analysis post procedure						
Max ISA detachment distance, µm	178 [78-363]	105 [90-162]	0.06	105 [90-162]	237 [134-363]	0.01
Max ISA area, mm^2	0.24 [0.16-0.41]	0.45 [0.34-0.69]	0.08	0.19 [0.15-0.30]	0.53 [0.25-1.55]	0.10
ISA volume, mm^3	0.15 [0.08-0.39]	0.29 [0.17-0.53]	0.22	0.13 [0.09-0.20]	0.43 [0.16-2.36]	0.10
Mean stent area, mm^2	8.26±2.65	6.87±2.23	0.15	9.81±2.08	8.76±2.16	0.16
Mean lumen area, mm^2	8.88±2.53	7.79±2.41	0.25	9.72±1.93	9.13±2.38	0.43
Mean protrusion area, mm^2	0.02 [0.00-0.24]	0.04 [0.01-0.07]	0.99	0.18 [0.12-0.45]	0.19 [0.09-0.36]	0.96
Minimum stent area (MSA), mm^2	7.17±2.28	5.75±2.11	0.13	9.30±2.11	8.19±2.09	0.11
MSA <5.0 mm^2, n (%)	4 (26.7)	3 (23.1)	0.83	0 (0.0)	2 (5.1)	1.00
Eccentricity index at MSA	0.86 [0.86-0.92]	0.87 [0.84-0.92]	0.65	0.93 [0.92-0.95]	0.92 [0.86-0.95]	0.22
% Area stenosis (AS),%	13.3 [5.9-19.7]	26.3 [9.3-30.5]	0.07	4.6 [-1.0-6.0]	5.8 [-1.6-9.3]	0.67
% AS >20%, n (%)	4 (26.7)	8 (61.5)	0.07	0 (0.0)	2 (5.1)	1.00

Online Table 3. Baseline and follow-up quantitative coronary analysis.

	Self-expanding (n=35)	Balloon-expandable (n=34)	*p*-value
Pre procedure			
Lesion length, mm	18.5 [10.6-24.7]	17.7 [15.5-22.5]	0.85
RVD, mm	2.63±0.44	2.80±0.54	0.16
MLD, mm	0.84±0.28	0.95±0.30	0.05
DS,%	66.3±12.8	65.8±10.6	0.65
Dmax, mm	3.22±0.48	3.41±0.68	0.24
Post procedure			
Stent length, mm	19.2 [18.1-24.4]	20.3 [16.8-22.6]	0.89
RVD, mm	2.82±0.44	3.12±0.39	<0.01
MLD, mm	2.40±0.43	2.74±0.40	<0.01
DS,%	15.2±6.82	12.5±5.1	0.07
Acute gain, mm	1.56±0.42	1.79±0.47	0.02
Mean remote distal segment, mm	2.25±0.50	2.57±0.66	0.04
FOLLOW-UP AT 3 DAYS			
Stent length, mm	19.2 [18.1-24.1]	20.0 [16.5-22.1]	0.83
RVD, mm	2.93±0.43	3.05±0.36	0.27
MLD, mm	2.49±0.47	2.69±0.40	0.05
DS,%	14.9±7.96	12.0±7.1	0.06
Lumen loss, mm	–0.10±0.25	0.05±0.22	0.02
Mean remote distal segment, mm	2.33±0.46	2.58±0.61	0.03
Diff. remote distal segment, mm	0.06 [-0.02-0.14]	0.00 [-0.09-0.19]	0.20
FUP/post remote distal segment	1.02 [0.99-1.06]	1.00 [0.95-1.08]	0.20
Vasorelaxation (FUP/post remote distal segment >1.05), n (%)	11 (32.4)	11 (31.4)	1.00

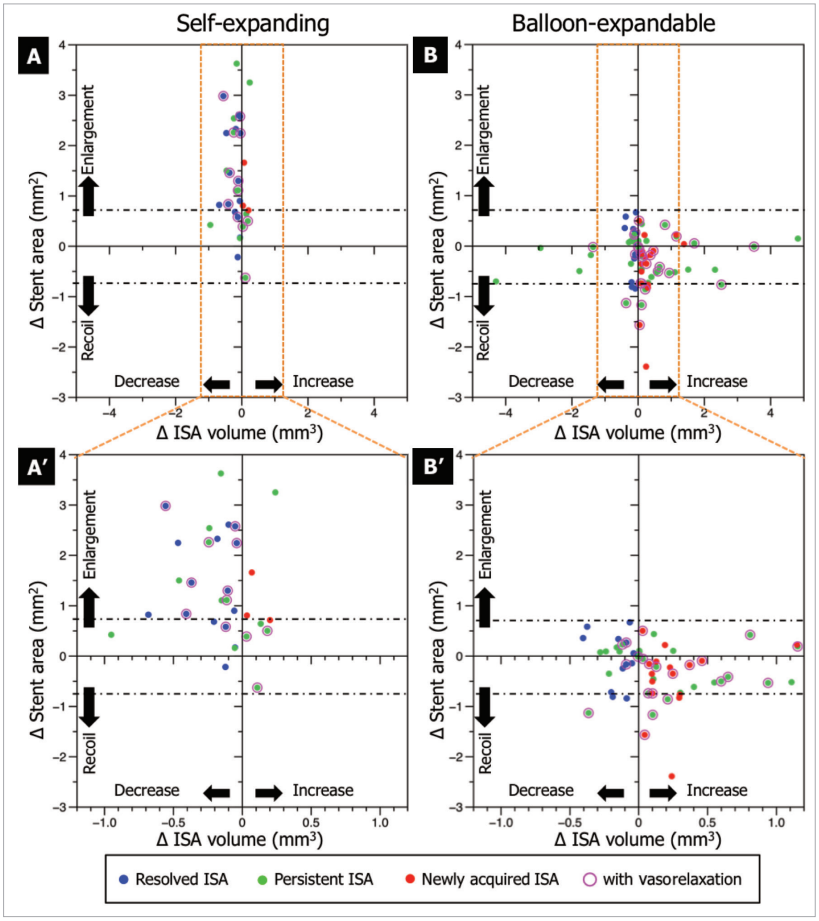

Online Figure 1. *Mechanisms of ISA changes. The differences in stent area and ISA volume are shown in the scatter plot (self-expanding: A, A'; balloon-expandable: B and B'). The blue dots depict the resolved ISA, the green dots indicate the persistent ISA, and the pink dots identify the spots with the newly acquired ISA. The purple circle shows the segments with vasorelaxation. The black dash-dot line shows the border of stent enlargement and "early" recoil. The dots above the black dash-dot line show the segments with stent enlargement, the dots under the black dash-dot line show the segments with "early" stent recoil. The resolved ISA and persistent ISA with decreasing ISA volume caused by stent enlargement were observed only in self-expanding stents. The newly acquired ISA and persistent ISA with increasing ISA volume caused by "early" recoil were observed only in balloon-expandable stents.*

5.2 Neointimal formation at mid-term follow-up in TROFI I study

Serial optical frequency domain imaging in STEMI patients: the follow-up report of TROFI study.

Eur Heart J Cardiovasc Imaging. 2014;15:987-95.
[Original research paper, Impact Factor : 4.11]

García-García HM, Muramatsu T, Nakatani S, Lee IS, Holm NR, Thuesen L, van Geuns RJ, van der Ent M, Borovicanin V, Paunovic D, Onuma Y, Serruys PW.

Serial optical frequency domain imaging in STEMI patients: the follow-up report of TROFI study

Hector M. García-García[1,2]*, Takashi Muramatsu[1], Shimpei Nakatani, Il Soo Lee[1], Niels Ramsing Holm[3], Leif Thuesen[3], Robert-Jan van Geuns[1], Martin van der Ent[4], Vladimir Borovicanin[5], Dragica Paunovic[5], Yoshinobu Onuma[1], and Patrick W. Serruys[1]

[1]Department of Interventional Cardiology, Thoraxcenter, Erasmus MC, 's-Gravendijkwal 230, 3015 CE Rotterdam, The Netherlands; [2]Cardialysis B.V., Rotterdam, The Netherlands; [3]Aarhus University Hospital, Skejby 8200, Denmark; [4]Maasstad ziekenhuis, Rotterdam 3079 DZ, The Netherland; and [5]Terumo Europe, Leuven, Belgium

Received 8 January 2014; accepted after revision 17 February 2014; online publish-ahead-of-print 23 March 2014

Aims To investigate the incidence of incomplete stent apposition and to explore the impact of the presence of thrombus and protruding plaque after stent implantation on neointima formation at follow-up in ST-segment elevation myocardial infarction (STEMI) patients with serial optical frequency domain imaging (OFDI) investigations.

Methods and results In a multi-centre study, 141 patients with ST elevation myocardial infarction <12 h from onset were randomized to either PPCI with thrombectomy (TB) using an Eliminate catheter (TB: $n = 71$) or without TB (non-TB: $n = 70$). OFDI after drug-eluting stenting was performed using TERUMO OFDI system. Per protocol, at follow-up 49 patients segments were reimaged. At post-procedure and follow-up, there were no differences in stent and lumen areas between the two groups. At follow-up, per strut-level analysis, percentage of incompletely apposed struts was 0.42 ± 0.94 vs. $0.38 \pm 0.77\%$ ($P = 0.76$), and percentage of covered struts was 92.7 ± 7.2 vs. $94.4 \pm 9.2\%$ ($P = 0.47$) in the TB and non-TB groups, respectively. There was a positive correlation between intra-stent structure (ISS) volume at post-procedure and the neointima volume at 6-month follow-up (Pearson's $r = 0.409$, $P = 0.04$). Up to 12 months, there have been two and four patients having target vessel failure in the TB and in the non-TB groups, respectively.

Conclusions In patients with STEMI, there were no significant differences in OFDI parameters between TB and non-TB groups at both post-procedure and 6-month follow-up. However, ISS volume at post-procedure was positively associated with neointimal volume at 6-month follow-up.

Keywords optical coherence tomography • coronary artery disease • acute myocardial infarction • coronary thrombosis • prolapse

Introduction

Primary percutaneous coronary intervention (PCI) has been recommended for the treatment of patients with ST-segment elevation myocardial infarction (STEMI).[1] In this highly thrombotic milieu, thrombus aspiration has been advocated.[2,3] Nevertheless, the remnant of thrombus and protruding plaque following stent implantation has been not sufficiently studied.[4] More importantly, little is known about the fate of residual thrombotic/protruding material existing around the struts.

Intravascular optical coherence tomography (OCT) is a light-based imaging modality that provides a high-resolution image of coronary arteries and enables quantification of the remaining intra-stent structures (ISS) such as tissue prolapse and thrombus after stenting.[5,6] At follow-up, evaluation of intra-stent neointima formation can be also achieved in a precise manner using OCT. The recently developed optical frequency domain imaging (OFDI) technique, an analogue of the Fourier-domain OCT, is the state of the art of this technology and commonly used in the current clinical setting.

The aim of this study is to investigate the incidence of incomplete stent apposition (ISA) and to explore the impact of the presence of thrombus and protruding plaque after stent implantation on neointima formation at follow-up in STEMI patients with serial OFDI investigations.

* Corresponding author. Tel: +31 10 206 28 28; fax: +31 10 206 28 44, Email: hect2701@gmail.com; hgarcia@cardialysis.nl; hect2701@yahoo.es

Methods

Study population

We investigated the patients enrolled in the TROFI trial. This is a prospective, randomized controlled, single blinded, multicenter clinical study enrolling 141 STEMI patients at five European sites.[7] Briefly, STEMI patients having an angiographically visible stenosis (>30%) or TIMI ≤ 2 in a single *de novo*, native, previously unstented vessel were considered for enrolment. Patients were randomized in a 1:1 ratio to receiving primary PCI either with TB ($n = 71$) or without TB ($n = 70$) prior to biolimus-A9 eluting metallic stent (Nobori®; Terumo Europe, Leuven, Belgium) implantation. The primary endpoint was defined as minimal flow area which was measured by OFDI after stenting during the baseline procedure. Per protocol, 49 patients underwent angiography and OFDI follow-up in three predefined enrolling centres.

This study protocol was approved by the Ethics Review Committee in each participating site, and written informed consent was obtained from each enrolled patient.

Treatment procedure

In the TB arm, multiple pullbacks with the TB catheter (Eliminate®, Terumo, Tokyo, Japan) were recommended until no further decrease of the intraluminal mass on angiography could be obtained. At least two thrombus aspirations had to be done and the TB procedure could be stopped only when there was no more thrombotic material in the aspirate for at least two consecutive aspirations. In case of angiographic luminal defect after stenting, an additional aspiration could be performed. Per protocol, the operator was blinded to the OFDI results during the procedure.

The Nobori DES was implanted either after pre-dilatation or in a direct stenting manner. If pre-dilatation was performed, the use of a commercially available balloon with a length not exceeding the length of the stent to be implanted was recommended. Full lesion coverage had to be ensured by implantation of one or multiple stents. Post-dilatation after stenting could be performed at the discretion of the investigator in either treatment arm.

Image acquisition

As long as patient's haemodynamics was stable, intracoronary administration of 0.2 mg nitroglycerin was given before the OFDI imaging procedure. This imaging procedure was performed with a TERUMO OFDI system (LUNAWAVE®, FastView®; Terumo Europe, Leuven, Belgium). The images were acquired using a non-occlusive technique at a rate of 160 frames/s during an automated pullback of the catheter at a speed of 20 mm/s. The pullback was performed during continuous intracoronary injection of contrast medium through the guiding catheter using an injection pump at a flow rate of 3–4 mL/s for a maximum of 4 s (300 psi). The imaging data once saved in the console were converted into AVI files and then transferred for the off-line analyses.

Off-line imaging analyses and definition

Off-line imaging analyses were performed at an independent imaging corelab (Cardialysis, Rotterdam, The Netherlands). A quantitative analysis software (QIVUS, MEDIS, Leiden University, Leiden, The Netherlands) was used for the OFDI analyses.

Region of interest (ROI) was selected as the stented segment, which was defined as the segment between the most distal and proximal frame where metallic stent struts were visible around the whole vessel circumference.[8] The stent and lumen areas were semi-automatically traced at every 1 mm. Neointima area was defined as the difference between stent and lumen areas (in absence of ISA). Definitions of ISA and coverage have been consistently described and reported in the literature.[9] In addition, we analyzed all individual masses within the stent area which were defined as ISS. ISS was categorized into ISS attached to vessel wall (i.e. thrombus or prolapse) and non-attached ISS.[6] These definitions were based on the following concepts: plaque prolapse has been defined as a convex-shaped protrusion of tissue between adjacent stent struts toward the lumen without disruption of the continuity of the luminal vessel surface.[10] At variance with this definition, plaque prolapse as seen in acute myocardial infarction may have a disrupted and irregular surface, and adjacent struts may be embedded or even buried in the prolapsing masses. Consequently, plaque prolapse is frequently indistinguishable from an intraluminal mass attached to the vessel wall, which is presumably thrombus. Therefore, in this study, plaque prolapse and thrombus attached to the vessel wall were categorized as a single variable, attached ISS.[7]

In order to achieve a more accurate estimation for ISS volume, the cross-sectional ISS analysis was performed in every frame along the whole stented region. When more than two attached or non-attached ISS were detected in an analyzed cross-section, the ISS area was calculated by cumulating all individual ISS areas. If there is no ISS in an analyzed cross-section, ISS area was regarded as zero. ISS volume was calculated by numerical integration based on the disk summation method, which formula is shown as follows:

$$\text{ISS volume } (\text{mm}^3) = \sum_{i=1}^{n} \{\text{ISSarea}(i)\} \times h$$

where n indicates the number of analyzed frames in ROI and h indicates the width of sampling distance (0.125 mm).

The OCT healing score is a weighted index that combines the following parameters:

(i) presence of ISS is assigned weight of '4';
(ii) presence of both malapposed and uncovered struts (%MU) is assigned a weight of '3';
(iii) presence of uncovered struts alone (%U) is assigned a weight of '2'; and finally,
(iv) presence of malapposition alone (%M) is assigned a weight of '1'.

Neointimal healing score = (%ISS × '4') + (%MU × '3') + (%U × '2') + (%M × '1')

Data monitoring

The monitoring for this study was conducted by sponsor or sponsor designee in all centres. One hundred percent source data verification were performed including device malfunctions and serious events. The independent clinical events committee (CEC), which comprised interventional and/or non-interventional cardiologists, adjudicated all clinical events and clinical endpoints based on protocol. The CEC members were not participants in the study and were blind to OFDI imaging results of the study.

Clinical outcomes

The main clinical endpoint was target vessel failure (TVF) defined as cardiac death, reinfarction in the territory of infarction-related vessel (Q wave and non-Q wave), or clinically driven target vessel revascularization. Stent thrombosis was adjudicated according to academic research consortium definition.[11]

Statistical analysis

Continuous variables are presented as mean ± standard deviation (SD), and categorical variables as percentages. Comparison was performed by unpaired *t*-test between the randomized groups and by paired *t*-test

between post-procedure and follow-up if continuous variable was normally distributed. In case of skewed distribution, the same approach was used after logarithmic transformation. Categorical variables were tested by Fisher's exact test. Correlations were tested by Pearson's correlation coefficient (r). All statistics were performed using PASW statistics18 software (SPSS Inc., Chicago, IL, USA). $P < 0.05$ was considered statistically significant.

Results

Between 24 November 2010 and 11 October 2011, 141 patients (71 patients in the TB arm and 70 patients in the non-TB arm) were enrolled at five European sites. In three predefined centres, the enrolled patients were followed up angiographically and with OFDI at 6 months (26 patients in the TB arm and 25 patients in the non-TB arm) (*Figure 1*). Paired (post-procedure and follow-up) OFDI recordings were available in 25 and 24 patients in the TB and the non-TB arms, respectively. Baseline characteristics of the patients were well matched between the two groups (*Table 1*). The TB device reached and crossed the lesion in all cases. The number of aspirations was 1.81 $\pm$ 0.40. The number of stent per lesion, total stent length, and diameter are comparable between the two groups.

In the pre- and post-procedural angiographic assessments and TIMI flow grade were comparable in both groups *Table 2*.

OFDI results

At post-procedure, there were no differences in stent and lumen areas between the two groups. ISA area was 0.12 $\pm$ 0.20 vs. 0.07 $\pm$ 0.11 mm^2 in the TB and non-TB groups, respectively (P = 0.75). Similarly, the OCT healing score did not differ between the two groups (202 $\pm$ 45 vs.196 $\pm$ 17, P = 0.49) *Table 3*.

At 6 months follow-up, there were also no differences in lumen, ISA or neointima areas between the two groups. Per strut-level analysis, percentage of ISA struts was 0.42 $\pm$ 0.94 vs. 0.38 $\pm$ 0.77% (P = 0.76), and percentage of covered struts was 92.7 $\pm$ 7.2 vs. 94.4 $\pm$ 9.2% (P = 0.47) in the TB and non-TB groups, respectively. The OCT healing score considerably decreased from baseline in both groups, but was not significantly different between the two groups (17 $\pm$ 16 in the TB and 13 $\pm$ 20 in non-TB group, P = 0.49) *Table 3*.

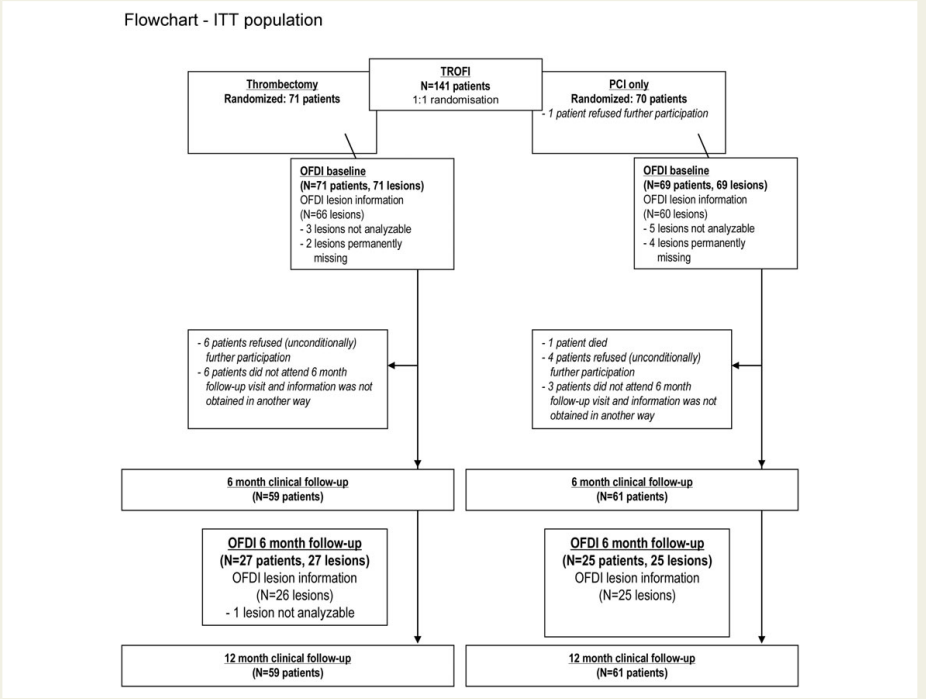

Figure 1: Flow chart showing patient disposition.

Table 1 Baseline and procedure characteristics

Demographics	Thrombectomy (*N* = 26)	Non-Thrombectomy (*N* = 25)	*P*
Age	59 ± 10	57 ± 13	0.42
Male (%)	77	76	0.94
Heart rate	73.77 ± 21.59	71.76 ± 14.68	0.7
Risk factors (%)			
Diabetes mellitus	7.7	8.0	0.97
Insulin	0.0	0.0	
Current smoking	58	52	0.49
Hypercholesterolemia	42	20	0.08
Hypertension	38	28	0.43
Family history of CAD	50	56	0.66
Procedural details			
Stents implanted per lesion	1.23 ± 0.6	1.36 ± 0.8	0.5
Mean total stent length/lesion (mm)	23.2 ± 10.5	25.4 ± 13.1	0.52
Mean stent diameter (mm, nominal)	3.1 ± 0.39	3.1 ± 0.37	0.64
Number of aspiration/lesion	1.81 ± 0.40		
Device successfully reached (%)	100		
Device successfully crossed (%)	100		
Thrombus successfully removed (%)	100		

Table 2 Quantitative coronary angiography pre- and post-PCI

	Thrombectomy (26 lesions)	Non-Thrombectomy (25 lesion)	*P*
Preprocedure			
TIMI flow (%)			0.38
0	36.0	29.2	
1	4.0	12.5	
2	32.0	16.7	
3	28.0	41.7	
Thrombus burden index before wiring (%)			0.81
0	4.0	4.2	
1	8.0	12.5	
2	4.0	8.3	
3	44.0	33.3	
4	4.0	12.5	
5	36.0	29.2	
Lesion length (mm)	15.3 ± 7.9	14.0 ± 4.9	0.64
RVD (mm)	2.8 ± 0.45	2.7 ± 0.52	0.27
Minimal lumen diameter (mm)	0.48 ± 0.45	0.56 ± 0.60	0.61
% Diameter stenosis (mm)	82.4 ± 15.8	79.4 ± 21.6	0.59
Post-procedure			
TIMI flow (%)			
3	100	100	1.0
Stent length (mm)	21.1 ± 10.5	20.2 ± 8.4	0.75
RVD post (mm)	2.9 ± 0.45	2.8 ± 0.50	0.61
Minimal lumen diameter post (mm)	2.5 ± 0.44	2.5 ± 0.52	0.88
% Diameter stenosis	12.9 ± 7.7	10.1 ± 7.3	0.20

Table 3 **OFDI results**

Post-procedure	Thrombectomy (*N* = 25)	Non-Thrombectomy (*N* = 24)	*P*-value
Stent length (mm)	24.8 ± 12.1	21.8 ± 7.9	0.44
Mean stent area (mm^2)	8.4 ± 2.5	8.2 ± 2.2	0.75
Minimum stent area (mm^2)	7.1 ± 2.2	6.9 ± 2.2	0.82
Mean flow area (mm^2)	8.0 ± 2.2	7.9 ± 2.1	0.84
Minimum flow area (mm^2)	6.5 ± 2.0	6.4 ± 2.1	0.82
Mean attached intra-stent structure (prolapse) (mm^2)	0.42 ± 0.29	0.31 ± 0.14	0.10
Mean Non-attached intra-stent structure (mm^2)	0.01 ± 0.01	0.01 ± 0.02	0.31
Mean lumen area (mm^2)	8.0 ± 2.2	7.9 ± 2.1	0.84
Minimum lumen area (mm^2)	6.5 ± 2.0	6.4 ± 2.1	0.82
Minimum lumen diameter (mm)	2.5 ± 0.46	2.5 ± 0.45	0.97
Mean Incomplete strut apposition area (mm^2)	0.12 ± 0.20	0.07 ± 0.11	0.75
ISA struts (%)	5.9 ± 9.1	3.1 ± 3.5	0.47
Healing score	202 ± 45	196 ± 17	0.49
Follow-up			
Mean stent area (mm^2)	8.2 ± 2.6	7.8 ± 2.1	0.52
Minimum stent area (mm^2)	6.9 ± 2.2	6.7 ± 2.2	0.70
Mean flow area (mm^2)	7.6 ± 2.5	7.1 ± 2.0	0.43
Minimum flow area (mm^2)	6.1 ± 2.2	5.6 ± 2.1	0.48
Mean lumen area (mm^2)	7.6 ± 2.5	7.1 ± 2.0	0.43
Minimum lumen area, mm^2	6.1 ± 2.2	5.6 ± 2.1	0.48
Minimum lumen diameter (mm)	2.5 ± 0.48	2.4 ± 0.48	0.41
Mean ISA area (mm^2)	0.03 ± 0.06	0.02 ± 0.05	0.72
Maxi ISA area (mm^2)	0.24 ± 0.48	0.37 ± 0.80	0.48
Mean number of struts	249 ± 139	225 ± 74	0.79
ISA struts (%)	0.42 ± 0.94	0.38 ± 0.77	0.76
Covered struts (%)	92.7 ± 7.2	94.4 ± 9.2	0.47
Healing score	17 ± 16	13 ± 20	0.49
Neointima area (mm^2)	0.69 ± 0.45	0.78 ± 0.46	0.37
Neointima volume (mm^3)	15.8 ± 16.9	13.7 ± 9.2	0.80

Mean intra-stent structure (protrusion + intraluminal mass).

The three components that determine the flow area (where the blood flows) are: (i) ISS area (attached and non-attached) and (ii) ISA; therefore, their isolated or combined presence was analyzed in 2400 (1189 at baseline and 1211 at follow-up) frames within ROI. In the Venn diagrams at post-procedure (*Figure 2*), it appears that the most common isolated observation was prolapse of the material into the lumen (54.3%). The non-attached ISS consistently co-existed with prolapse (5.97%), with malapposition (0.17%) or with both (1.51%), but not isolated. In the same cross-section, prolapse and malapposition (11.9%) could co-exist. Malapposition alone was a quite rare phenomenon (2.27%). At 6 months follow-up, most of frames showed only neointima (81.1%), or in combination with either non-attached ISS (1.24%) or with ISA (1.16%). Only 0.83% of the frames showed neointima, non-attached ISS, and ISA. More importantly, there were 15.7% of the frames without any neointima which showed the clustering of the uncovered struts.

There was a moderate, positive correlation between ISS volume at post-procedure and the neointima volume at 6 months follow-up (Pearson's $r = 0.409$, $P = 0.04$) (*Figure 3*).

Clinical outcomes

At up to 12 months, there have been two patients having TVF in the TB group (*Table 4*). One of them has had stent thrombosis within hospitalization and has been described in the primary endpoint report of this study.[7] In addition, there has been one patient with MI. In the non-TB group, there have been four patients with TVF. One of them had died between 1 and 6 months follow-up.

Discussion

The main findings of this report are: (i) there were no differences in all OFDI-derived qualitative and quantitative parameters between TB and non-TB groups neither at post-procedure nor at 6 months follow-up; (ii) amongst three determinants of the flow area (i.e. prolapse/neointima, non-attached ISS, and ISA), prolapse and neointima hyperplasia were most prevalent at post-procedure and follow-up, respectively; (iii) there is a moderate correlation between ISS at baseline and neointima at follow-up; (iv) non-attached ISS, as an isolated

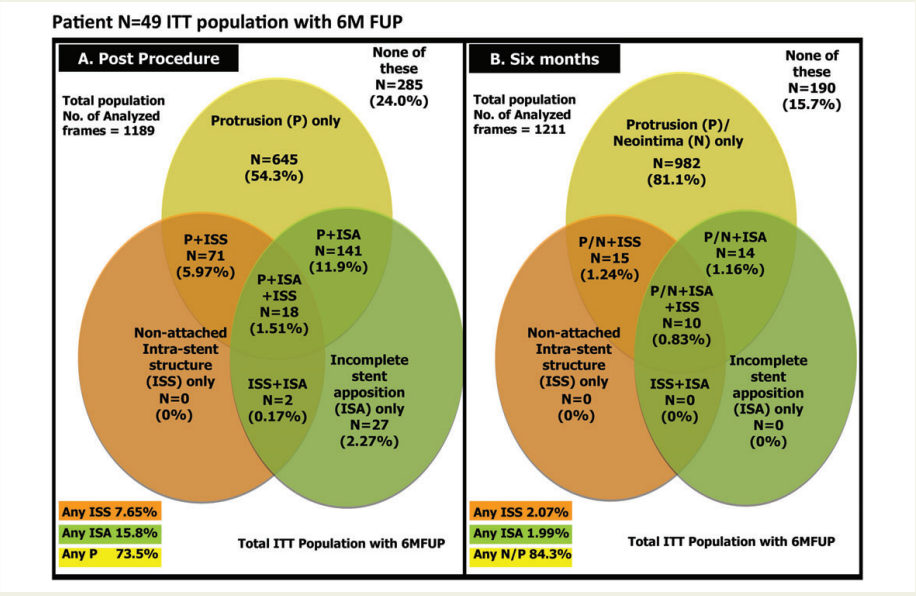

Figure 2: The Venn diagram shows the relationship of the three components that determine the flow area. This means the area where the blood flows, these are: intra-stent structure (ISS) either attached (i.e. prolapse at pos-PCT and neointima at follow-up) or non-attached (i.e. intraluminal mass); and incomplete stent apposition (ISA); in panel A, it appears that the most common isolated observation was prolapse of the material into the lumen (54.3%). The non-attached ISS consistently co-existed with prolapse (5.97%), with malapposition (0.17%), or with both (1.51%). In the same cross-section, prolapse and malapposition (11.9%) could co-exist. Malapposition alone was a quite rare phenomenon (2.27%). (B) At 6 months follow-up, most of frames showed only neointima (81.1%), or in combination with either with non-attached ISS (1.24%) or with ISA (1.16%). Only 0.83% of the frames showed neointima, non-attached ISS, and ISA. More importantly, there were 15.7% of the frames without any neointima which showed the clustering of the uncovered struts.

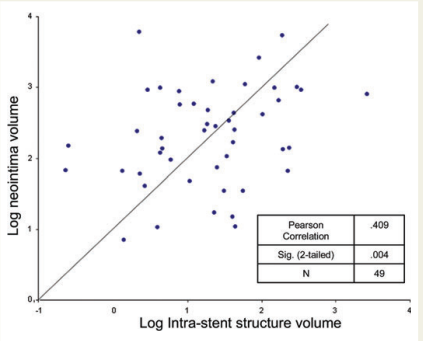

Figure 3: Correlation between ISS and neointima volumes.

finding, does not exist neither at baseline nor at follow-up; and (v) despite all patients had STEMI and were treated with DES, both factors associated with ISA, there was an important reduction in ISA from post-procedure to follow-up (15.8–1.99% of frames).

DES in a thrombotic lesion is associated with less strut coverage

Newer drug-eluting stents have demonstrated a reduction in incidence of adverse cardiac events when compared with bare-metal stents for the treatment of STEMI at 1 year.[12] Despite this, there are still concerns about a potentially higher risk of stent thrombosis (ST) after DES implantation during primary PCI at a later time follow-up. The two most common findings associated with ST are lack of endothelium coverage and presence of ISA. Morphometric analysis showed that ruptured plaque had significantly less neointimal thickness, greater fibrin deposition and inflammation, and higher prevalence of uncovered struts than stable plaque (49 [16, 96] vs. 9 [0, 39%], $P = 0.01$).[13] One plausible explanation is the fact that these necrotic core rich lesions, which are more avascular and less

Table 4 Non-hierarchical clinical outcomes up to 12 months follow-up

N (%)	TB (*N* = 71)				Non-TB (*N* = 70)			
	Discharge	<1 month	<6 months	Total 12 months	Disch	<1 month	<6 months	Total 12 months
TVF	1 (1.4)	1 (1.4)	1 (1.4)	2 (2.8)	1 (1.4)	1 (1.4)	3 (4.3)	4 (5.7)
All-cause mortality	0	0	0	0	0	0	1 (1.4)	1 (1.4)
Cardiac death	0	0	0	0	0	0	1 (1.4)	1 (1.4)
Non-cardiovascular death	0	0	0	0	0	0	0	0
Vascular death	0	0	0	0	0	0	0	0
Any myocardial (re) infarction	0	0	0	1 (1.4)	0	0	0	0
Target vessel revascularization	1 (1.4)	1 (1.4)	1 (1.4)	2 (2.8)	1 (1.4)	1 (1.4)	2 (2.8)	3 (4.3)
Stent thrombosis	1 (1.4)	1 (1.4)	1 (1.4)	1 (1.4)	0	0	0	0

Target vessel failure (TVF), defined as cardiac death, reinfarction in the territory of infarction-related vessel (Q wave and non-Q wave), or clinically driven target vessel revascularization.

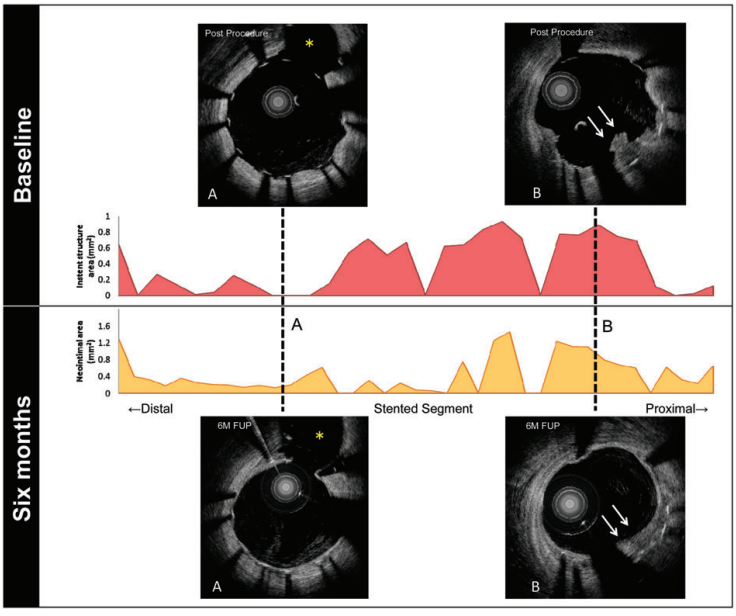

Figure 4: Case examples showing the relationship between ISS and neointima. In the upper panel (baseline), the area graph shows the trend of the ISS over the frames from distal to proximal. In the bottom panel, the area graph shows the distribution of neointima area. In general, it can be observed that the neointima formation occurs in regions where at post-PCI the ISS was present (red regions correspond to yellow regions). The corresponding cross-sections from baseline and follow-up (A and B) exemplified this further. (A) At baseline, there was no ISS and the corresponding cross-section at follow-up shows minimal neointima. In contrast, in (B) at baseline, ISS was present (white arrows) and the same angular sector shows neointima at follow-up.

cellular, are less prone to be covered by migrating cells.[14] In addition, the biolimus-A9 is highly lipophilic (10 times more lipophilic than sirolimus) and thereby has great affinity for necrotic core which may result in higher concentration of the drug locally. Further, the superimposed thrombus will increase the drug uptake.[14] Taken all together, it means that the tissue growth inhibition will be marked in these lesions. In the present study, however, the percentages of covered struts were observed in 92.7 $\pm$ 7.2% in TB group and 94.4 $\pm$ 9.2% in non-TB group at 6 months follow-up ($P = 0.47$), similarly to that reported for all-comer populations—93.9%—in a pooled data from the LEADERS and the RESOLUTE OCT substudies, including stable and STEMI patients.[15] This is a fair comparison, since all these data have been analyzed in the same imaging corelab, using exactly the same methodology and definitions.

We found a moderate positive relationship between the post-procedural ISS volume and neointima formation at 6 months follow-up. It has been described that the thrombus can nest and promote the growth of smooth muscle cells. This may be due to the presence of chemoattractans and growth factors in the thrombotic milieu.[16]

The exquisite analysis of prolapse and thrombus can only be achieved by OCT/OFDI. It has been reported that prolapse and thrombus can be detected in 100 and 54% of the cases by OFDI and only in 3 and 40% by IVUS.[8] This may explain why IVUS has failed to show any relationship between prolapse and restenosis.[17] Interestingly, an example case demonstrated that the location of ISS at post-procedure well matched that of neointima at follow-up (*Figure 4*).

Incomplete strut apposition

In both groups, the prevalence of ISA was very low at 6 months follow-up (0.42 vs. 0.38% for TB and non-TB groups, respectively). On the contrary to our assumption of the dissolution of thrombus existing between stent struts and vessel wall together with the profound neointima inhibition due to high concentration of the antiproliferative drug, the incidence of late ISA in STEMI patients was very low in the present study. Actually, the incidence (0.6%) is similar, if not smaller, to another report in which only one third of patients had STEMI.[18] Needless to say, the observed percentage of malapposed struts in this study at 6 months might increase over time. Even in more stable populations, the percentage of malapposed struts (at $>$5 years), is higher (1.2% for SES and 0.7% for PES) than the one reported here.[19] The reason for this cannot be only attributed to the longer term follow-up but also to the stent type. For example, it has been shown that the underlying mechanism(s) of ST is due to localized strut hypersensitivity in SES, whereas malapposition secondary to excessive fibrin deposition is mainly in PES at very long-term follow-up.[20]

Clinical implications

It has been observed that thrombus aspiration improves ST segment resolution and myocardial blush scores, and a reduction in cardiac mortality was observed in the TAPAS study.[21] In our study, adjunctive TB was not associated with any significant benefit in terms of flow area at post-procedure or ISA at 6 months follow-up.

Study limitations

First of all, the intraluminal mass outside the stent area was not taken into account in this study. In STEMI patients, the stent struts might be buried in thrombotic mass and potentially some amount of thrombus existed in the space between the struts and vessel wall. It was also challenging to depict the precise boundary between the vessel wall and thrombus behind the stent struts because of acoustic shadow and light-intensity attenuation by red thrombus. Secondly, as per protocol, only patients from selected centres have come back for follow-up imaging, which resulted in only 49 patients with repeated OFDI.

Conclusions

In patients with STEMI, there were no significant differences in OFDI parameters between TB and non-TB groups at both post-procedure and 6 months follow-up. However, ISS volume at post-procedure was positively associated with neointimal volume at 6 months follow-up. DES with biodegradable polymer showed to be safe with very low adverse events rate up to 1 year.

Conflict of interest: V.B. and D.P. are Terumo employees. The rest of authors have no conflict of interest to declare.

References

1. Wijns W, Kolh P, Danchin N, Di Mario C, Falk V, Folliguet T *et al.* Guidelines on myocardial revascularization: The Task Force on Myocardial Revascularization of the European Society of Cardiology (ESC) and the European Association for Cardio-Thoracic Surgery (EACTS). *Eur Heart J* 2010;**31**:2501–55.
2. Svilaas T, Vlaar PJ, van der Horst IC, Diercks GF, de Smet BJ, van den Heuvel AF *et al.* Thrombus aspiration during primary percutaneous coronary intervention. *N Engl J Med* 2008;**358**:557–67.
3. Frobert O, Lagerqvist B, Olivecrona GK, Omerovic E, Gudnason T, Maeng M *et al.* Thrombus aspiration during ST-segment elevation myocardial infarction. *N Engl J Med* 2013;**369**:1587–97.
4. Magro M, Regar E, Gutierrez-Chico JL, Garcia-Garcia H, Simsek C, Schultz C *et al.* Residual atherothrombotic material after stenting in acute myocardial infarction – an optical coherence tomographic evaluation. *Int J Cardiol* 2013;**167**:656–63.
5. Muramatsu T, Serruys PW, Onuma Y. Thrombotic arch in ST-segment elevation myocardial infarction: comparison between two-dimensional and three-dimensional optical frequency domain imaging. *Eur Heart J* 2012;**33**:1510.
6. Muramatsu T, Garcia-Garcia HM, Lee IS, Bruining N, Onuma Y, Serruys PW. Quantitative optical frequency domain imaging assessment of in-stent structures in patients with ST-segment elevation myocardial infarction. *Circ J* 2012;**76**:2822–31.
7. Onuma Y, Thuesen L, van Geuns RJ, van der Ent M, Desch S, Fajadet J *et al.* Randomized study to assess the effect of thrombus aspiration on flow area in patients with ST-elevation myocardial infarction: an optical frequency domain imaging study – TROFI trial. *Eur Heart J* 2013;**34**:1050–60.
8. Okamura T, Gonzalo N, Gutierrez-Chico JL, Serruys PW, Bruining N, de Winter S *et al.* Reproducibility of coronary Fourier domain optical coherence tomography: quantitative analysis of in vivo stented coronary arteries using three different software packages. *EuroIntervention* 2010;**6**:371–9.
9. Gonzalo N, Garcia-Garcia HM, Serruys PW, Commissaris KH, Bezerra H, Gobbens P *et al.* Reproducibility of quantitative optical coherence tomography for stent analysis. *EuroIntervention* 2009;**5**:224–32.
10. Gonzalo N, Serruys PW, Okamura T, Shen ZJ, Onuma Y, Garcia-Garcia HM *et al.* Optical coherence tomography assessment of the acute effects of stent implantation on the vessel wall: a systematic quantitative approach. *Heart* 2009;**95**:1913–9.
11. Cutlip DE, Windecker S, Mehran R, Boam A, Cohen DJ, van Es GA *et al.* Clinical end points in coronary stent trials: a case for standardized definitions. *Circulation* 2007;**115**:2344–51.
12. Raber L, Kelbaek H, Ostojic M, Baumbach A, Heg D, Tuller D *et al.* Effect of biolimus-eluting stents with biodegradable polymer vs bare-metal stents on cardiovascular events among patients with acute myocardial infarction: the COMFORTABLE AMI randomized trial. *Jama* 2012;**308**:777–87.
13. Nakazawa G, Finn AV, Joner M, Ladich E, Kutys R, Mont EK *et al.* Delayed arterial healing and increased late stent thrombosis at culprit sites after drug-eluting stent

placement for acute myocardial infarction patients: an autopsy study. *Circulation* 2008;**118**:1138–45.
14. Finn AV, Nakazawa G, Kolodgie F, Virmani R. Drug eluting or bare metal stent for acute myocardial infarction: an issue of safety? *Eur Heart J* 2009;**30**: 1828–30.
15. Gutierrez-Chico JL, Regar E, Nuesch E, Okamura T, Wykrzykowska J, di Mario C *et al.* Delayed coverage in malapposed and side-branch struts with respect to well-apposed struts in drug-eluting stents: in vivo assessment with optical coherence tomography. *Circulation* 2011;**124**:612–23.
16. MacLeod DC, Strauss BH, de Jong M, Escaned J, Umans VA, van Suylen RJ *et al.* Proliferation and extracellular matrix synthesis of smooth muscle cells cultured from human coronary atherosclerotic and restenotic lesions. *J Am Coll Cardiol* 1994;**23**: 59–65.
17. Hong MK, Park SW, Lee CW, Kang DH, Song JK, Kim JJ *et al.* Long-term outcomes of minor plaque prolapsed within stents documented with intravascular ultrasound. *Catheter Cardiovasc Interv.* 2000;**51**:22–6.
18. Gonzalo N, Barlis P, Serruys PW, Garcia-Garcia HM, Onuma Y, Ligthart J *et al.* Incomplete stent apposition and delayed tissue coverage are more frequent in drug-eluting stents implanted during primary percutaneous coronary intervention for ST-segment elevation myocardial infarction than in drug-eluting stents implanted for stable/unstable angina: insights from optical coherence tomography. *JACC Cardiovasc Interv* 2009;**2**:445–52.
19. Raber L, Baumgartner S, Garcia HM, Kalesan B, Justiz J, Pilgrim T *et al.* Long-term vascular healing in response to sirolimus- and paclitaxel-eluting stents: an optical coherence tomography study. *JACC Cardiovasc Interv* 2012;**5**:946–57.
20. Nakazawa G, Finn AV, Vorpahl M, Ladich ER, Kolodgie FD, Virmani R. Coronary responses and differential mechanisms of late stent thrombosis attributed to first-generation sirolimus- and paclitaxel-eluting stents. *J Am Coll Cardiol* 2011;**57**:390–8.
21. Vlaar PJ, Svilaas T, van der Horst IC, Diercks GF, Fokkema ML, de Smet BJ *et al.* Cardiac death and reinfarction after 1 year in the thrombus aspiration during percutaneous coronary intervention in acute myocardial infarction study (TAPAS): a 1-year follow-up study. *Lancet* 2008;**371**:1915–20.

Summary

Summary and Conclusions

The imaging methods such as IVUS, OCT or MSCT are being increasingly used in studies of permanent metallic and bioresorbable devices. This imaging modalities (or 'these images') enable us to perform specific analyses and evaluate the coronary devices precisely. In addition to the standard measurements, specific methods to evaluate plaque composition, device vessel interactions and temporal changes of the device itself were developed and validated in preclinical and clinical studies. I was involved prospectively in this process of development with a team of fellows.

More specifically, automatic detection algorithm on optical coherence tomography (OCT) of a bioresorbable scaffold strut was developed to enable fast and complete analysis of polymeric device (Chapter 1.1). The quantitative assessment method of light intensity of the struts was established for monitoring of bioresorption (Chapter 1.2). As a next step, the attenuation of the light signal was used to evaluate the calcified lesions, which is considered to be a drawback of bioresorbable technologies (Chapter 1.3). For both metallic and polymeric coronary devices, the 3D foldout views to summarize and present the entire data acquired during the OCT pullback were developed (Chapters 4.2 and 5.1). The methods on multi-slice computed tomography (MSCT) was established to discern metallic markers from coronary calcification (Chapter 1.4).

Some of the above mentioned methods were validated in pre-clinical models and clinical studies. The echogenicity of intravascular ultrasound (IVUS) as a surrogate of molecular weight loss was tested in a porcine model using the gel permeate chromatography (Chapter 3.2). OCT light intensity analysis was validated as an imaging method to quantify the integration process of bioresorbable scaffolds (Chapter 3.1). In addition, it was demonstrated that the surge of light intensity precedes the late lumen enlargement. The concept of high shear flow disturbance in malapposed struts and delayed neointimal coverage was hypothesized and tested in clinical OCT series (Chapter 3.3).

In advent of coronary bioresorbable scaffold technologies, several randomized controlled trials were conducted to compare such a device with a permanent metallic stent. In imaging analysis, the inherent difference between metal and polymer caused systematic bias when the conventional methods were applied. In the context of the TROFI II trial and ABSORB Japan trial, we have established the comparative methods to enable "apple and apple" comparison instead of "apple and orange" ("Apples and pears" in Dutch) comparison (Chapter 2.1).

These methods were applied to imaging analysis of the clinical trials such as APPOSITION II,

TROFI I, ABSORB Cohort B, and BVS STEMI FIRST study. In APPOSITION II trial, the 3D presentation of struts showed a significant reduction of a malapposition in the self-expanding stent arm 3 days after implantation. In the control arm, malapposition increased due to vasodilatation and resorption of thrombotic material 3 days after ST-segment elevation myocardial infarction (Chapter 5.1). In TROFI I, the full frame analysis of intra-stent structures demonstrated that the protrusion of tissue at the time of the primary percutaneous coronary intervention (PCI) correlated to neo-intimal tissue at follow-up (Chapter 5.2). In the ABSORB Cohort B, the causes of early, late, and very late angiographic scaffold restenosis were investigated using IVUS, IVUS-VH, and OCT. The hypothesis of late collapse of scaffold was not verified in this cohort (Chapter 4.3). The 3-year and 5-year OCT follow-up data were scrutinized to investigate the edge vascular response (Chapters 4.4 and 4.5). In the limited population with serial imaging follow-up, the edge effect was not confirmed. The foldout view method was applied to demonstrate a concept of shielding the underlying plaque after implantation bioresorbable scaffold (Chapter 4.6). MSCT and OCT were used to follow-up a patient with aneurysmal changes after implantation of the bioresorbable scaffold (Chapter 4.1). The early performance of a bioresorbable scaffold in a setting of ST-segment elevation myocardial infarction was demonstrated in the BVS STEMI FIRST study with a visualization of the protruding plaque and thrombus on 3 dimensional OCT (Chapter 4.7).

Conclusion

In this thesis, we established and validated novel methods for evaluation of metallic and polymeric devices. Furthermore, standardized methods for comparison of metallic stents and bioresorbable scaffolds were proposed. These methods were further applied in clinical trials to evaluate acute and long-term performance of coronary implants for the treatment of coronary artery disease.

Samenvatting

Samenvatting en conclusies

Beeldvormende technieken zoals IVUS, OCT en MSCT worden in toenemende mate gebruikt in studies naar metalen en biologisch oplosbare stents. De verkregen beelden van deze beeldvorming geven de mogelijkheid om specifieke analyses te verrichten naar coronaire stents. Als toevoeging op reeds bestaande meetmethoden, heb ik mij tijdens mijn promotietraject, in een team samen met andere arts-onderzoekers, bezig gehouden met de ontwikkeling van nieuwe specifieke meetmethoden om de compositie van coronaire plaques te evalueren, om stent-vaatwand interacties te onderzoeken en om de veranderingen over tijd van de stents zelf te vervolgen. Deze nieuwe meetmethoden hebben wij ontwikkeld en gevalideerd in zowel preklinische als klinische studies.

Meer specifiek hebben we ons bezig gehouden met een algoritme om op optical coherence tomography (OCT) beelden stentdelen van de biologisch oplosbare stent automatisch te kunnen detecteren. Dit nieuwe algoritme maakt het mogelijk om een snelle en complete analyse te kunnen verrichten waar dit voorheen geheel handmatig gedaan moest worden (hoofdstuk 1.1). We hebben ook een kwantitatieve methodologie ontwikkeld waarbij we gebruik maakten van de licht intensiteit van de biologisch oplosbare stentdelen om de mate van resorptie door de tijd heen te kunnen monitoren (hoofstuk 1.2). Als volgende stap hebben we ons gericht op de attenuatie van het door de OCT uitgezonden licht signaal om kalk te detecteren (hoofdstuk 1.3). De zogenaamde ‘3D foldout views’, waarbij we als het ware de stent in 3D reconstrueren om vervolgens ‘uit te vouwen’, hebben we ook toegepast om in één oogopslag de volledige data van de OCT pullback te kunnen presenteren (hoofdstukken 4.2 en 5.1). tevens ontwikkelden we een methodologie om op multi-slice computed tomography (MSCT) coronaire vaatwandverkalking te kunnen onderscheiden van de metalen ‘markers’ (die in de biologisch oplosbare stent zijn ingebouwd om de twee ‘uiteinden’ te kunnen zien tijdens angiografie) (hoofdstuk 1.4).

Sommige van de hierboven beschreven methodes zijn gevalideerd in preklinische modellen en anderen in klinische studies. ‘Echogenicity’ (de mate van terugkaatsing van de geluidsgolf in echotechnieken) van het intravascular ultrasound (IVUS) signaal werd gebruikt als surrogaat voor het verlies van moleculaire massa en hebben we getest in een diermodel met varkens (hoofdstuk 3.2). Tevens hebben we een methode gevalideerd waarbij we licht intensiteit van het OCT signaal gebruiken om de mate van het integratie van de stentdelen van de biologisch oplosbare stent te kunnen kwantificeren (hoofdstuk 3.1). Bovendien hebben we waargenomen

dat een snelle stijging (over tijd) van de licht intensiteit voorafgaat aan de verwijding van het lumen (de zogeheten 'late lumen enlargement'). De samenhang tussen de hoge stroomsnelheid en verstoring van de bloedstroom rond stentdelen die niet goed aanliggen tegen de vaatwand ('malapposed struts') enerzijds en vertraagde endotheliale bekleding van dezelfde stentdelen gedurende follow-up werd onderzocht middels OCT (hoofdstuk 3.3).

Met de komst van biologisch oplosbare stent technologieën, zijn verschillende gerandomiseerde studies uitgevoerd om deze oplosbare stents te vergelijken met onoplosbare metalen stents. Wanneer bevindingen van de beeldvormende technieken middels conventionele definities worden toegepast, zorgen de onvermijdelijke verschillen tussen metalen en oplosbare stents er voor dat er een systematische bias optreed. Wij hebben dan ook nieuwe definities geformuleerd zodat we voortaan 'appels met appels' vergelijken, i.p.v. 'appels met peren' (hoofdstuk 2.1).

Al deze hierboven beschreven methodes werden toegepast op verscheidene klinische studies zoals APPOSITION II, TROFI I, ABSORB Cohort B, and BVS STEMI FIRST studies. In APPOSITION II, de drie-dimensionele presentatie van de stentdelen van de zelf-ontplooiende Stentys stent liet zien dat het aantal niet goed aanliggende stentdelen ('malapposed struts') significant was afgenomen 3 dagen na stentplaatsing vergeleken met direct na stentplaatsing. In de controle groep, waarin conventionele metalen stents werden gebruikt, nam het aantal niet goed aanliggen stentdelen juist toe 3 dagen na stentpaatsing. Deze toename werd verklaard door vasodilatatie en resorptie van thrombus (hoofdstuk 5.1). In de TROFI I studie lieten we zien dat de mate van weefsel protrusie tussen de verschillende stentdelen net na stentplaatsing (in de setting van stenting bij acute myocardinfarcten) gerelateerd was aan de hoeveelheid weefsel op de stent bij follow-up (hoofdstuk 5.2). In de ABSORB Cohort B studie lieten we de oorzaken zien van restenose in de biologisch oplosbare stents, onderverdeeld naar het moment van de restenose. De hypothese dat oplosbare stents in elkaar zouden kunnen zakken gedurende de follow-up werd in deze studie niet bevestigd (hoofdstuk 4.3). Nauwkeurige analyses van de 3 en 5 jaars OCT follow-up data werden verricht op de reactie van de coronaire vaatwand op de randen van de geïmplanteerde stents (hoofdstukken 4.4 en 4.5). In de patiënten in wie de follow-up serieel beschikbaar was werd er geen effect gezien van de stentranden op de vaatwand. De 'fold-out view' werd gebruikt om te laten zien hoe de oplosbare stent een onderliggende plaque als een soort van schild kan bedekken (hoofdstuk 4.6). MSCT en OCT werden gebruikt om de follow-up van 1 patiënt met aneurysmatische veranderingen van de vaatwand na oplosbare stentplaatsing te vervolgen (hoofdstuk 4.1). De vroege werkzaamheid

van de oplosbare stent in de setting van behandeling van acuut myocardinfarct werd onderzocht in de BVS STEMI FIRST studie. In deze studie werd met 3D OCT de protrusie van zowel plaque als thrombus tussen de stentdelen gevisualiseerd (hoodstuk 4.7).

Conclusies

In dit proefschrift hebben we nieuwe methodes ontwikkeld en gevalideerd die gebruikt kunnen worden voor de evaluatie van zowel metalen als oplosbare stents. Tevens hebben wij gepoogd om de methodologie van de verschillende beeldvormende technieken te standaardiseren zodat verschillen tussen metalen en oplosbare stents zonder bias onderzocht kunnen worden. Al deze methodes zijn vervolgens toegepast in klinische studies om zowel acute als late effecten van de verschillende coronaire stents te onderzoeken.

Curriculum Vitae

CURRICULUM VITAE

Name:	SHIMPEI NAKATANI
Date of Birth:	10th May, 1979
Place of Birth:	Osaka, Japan
Nationality:	Japanese

Education

1995-1998	Osaka Seiko High School, Osaka, Japan
1999-2005	Osaka University School of Medicine, Osaka, Japan

Professional Training and Employment:

2005-2007	Resident in Internal Medicine, Osaka Rousai Hospital, Osaka, Japan
2007-2010	Fellow in Cardiology, Osaka Rousai Hospital, Osaka, Japan
2010-2013	Staff Doctor in Cardiology, Sakurabashi Watanabe Hospital, Osaka, Japan
2013-2015	Research fellow in interventional cardiology at Thorax center, Erasmus MC, Rotterdam
2015-2016	Staff Doctor in Cardiology, Sakurabashi Watanabe Hospital, Osaka, Japan
2016-	Assistant Head Physician in Cardiology, Osaka Police Hospital, Osaka, Japan

License and Certification

2005	Japanese Medical License (No.448841)
2012	Board Certified Member of the Japanese Society of Internal Medicine (No.48950)
2015	Board Certified Member of the Japanese Association of Cardiovascular Intervention and Therapeutics (No.10241)

List of publications

LIST OF PUBLICATIONS

1. **Bioresorption and Vessel Wall Integration of a Fully Bioresorbable Polymeric Everolimus-Eluting Scaffold: Optical Coherence Tomography, Intravascular Ultrasound, and Histological Study in a Porcine Model With 4-Year Follow-Up**

   Nakatani S, Ishibashi Y, Sotomi Y, Perkins L, Eggermont J, Grundeken MJ, Dijkstra J, Rapoza R, Virmani R, Serruys PW, Onuma Y.

   JACC Cardiovasc Interv. 2016:838-51

2. **Edge Vascular Response After Resorption of the Everolimus-Eluting Bioresorbable Vascular Scaffold - A 5-Year Serial Optical Coherence Tomography Study.**

   Tateishi H, Suwannasom P, Sotomi Y, **Nakatani S**, Ishibashi Y, Tenekecioglu E, Abdelgani M, Cavalcante R, Zeng Y, Grundeken MJ, Albuquerque FN, Veldhof S, Onuma Y, Serruys PW; investigators of the ABSORB Cohort B study.

   Circ J. 2016 Mar 3.

3. **Relation Between Bioresorbable Scaffold Sizing Using QCA-Dmax and Clinical Outcomes at 1 Year in 1,232 Patients From 3 Study Cohorts (ABSORB Cohort B, ABSORB EXTEND, and ABSORB II).**

   Ishibashi Y, **Nakatani S**, Sotomi Y, Suwannasom P, Grundeken MJ, Garcia-Garcia HM, Bartorelli AL, Whitbourn R, Chevalier B, Abizaid A, Ormiston JA, Rapoza RJ, Veldhof S, Onuma Y, Serruys PW.

   JACC Cardiovasc Interv. 2015:1715-26.

4. **Incidence and potential mechanism of resolved, persistent and newly acquired malapposition three days after implantation of self-expanding or balloon-expandable stents in a STEMI population: insights from optical coherence tomography in the APPOSITION II study.**

   Nakatani S, Onuma Y, Ishibashi Y, Karanasos A, Regar E, Garcia-Garcia HM, Tamburino C, Fajadet J, Vrolix M, Witzenbichler B, Eeckhout E, Spaulding C, Reczuch K, La Manna A, Spaargaren R, Capodanno D, Van Langenhove G, Verheye S, Serruys PW, van Geuns RJ.

   EuroIntervention. 2015:885-94.

5. **Comparative analysis method of permanent metallic stents (XIENCE) and bioresorbable poly-L-lactic (PLLA) scaffolds (Absorb) on optical coherence tomography at baseline and follow-up.**
   Nakatani S, Sotomi Y, Ishibashi Y, Grundeken MJ, Tateishi H, Tenekecioglu E, Zeng Y, Suwannasom P, Regar E, Radu MD, Räber L, Bezerra H, Costa MA, Fitzgerald P, Prati F, Costa RA, Dijkstra J, Kimura T, Kozuma K, Tanabe K, Akasaka T, Di Mario C, Serruys PW, Onuma Y.
   EuroIntervention. 2015 ;11(6). pii: 20150528-02.
6. **Impact of the orbital atherectomy system on a coronary calcified lesion: quantitative analysis by light attenuation in optical coherence tomography.**
   Sotomi Y, Shlofmitz RA, **Nakatani S**, Onuma Y, Serruys PW..
   EuroIntervention. 2015 ;11(5):e1.
7. **Fate of Bioresorbable Vascular Scaffold Metallic Radio-Opaque Markers at the Site of Implantation After Bioresorption.**
   Suwannasom P, Onuma Y, Campos CM, **Nakatani S**, Ishibashi Y, Tateishi H, Grundeken MJ, Stanetic B, Nieman K, Jonker H, Garcia-Garcia HM, Serruys PW; investigators of ABSORB Cohort A, B and EXTEND trials.
   JACC Cardiovasc Interv. 2015 ;8(8):1130-2.
8. **Incidence and Potential Mechanism(s) of Post-Procedural Rise of Cardiac Biomarker in Patients With Coronary Artery Narrowing After Implantation of an Everolimus-Eluting Bioresorbable Vascular Scaffold or Everolimus-Eluting Metallic Stent.**
   Ishibashi Y, Muramatsu T, **Nakatani S**, Sotomi Y, Suwannasom P, Grundeken MJ, Cho YK, Garcia-Garcia HM, van Boven AJ, Piek JJ, Sabaté M, Helqvist S, Baumbach A, McClean D, de Sousa Almeida M, Wasungu L, Miquel-Hebert K, Dudek D, Chevalier B, Onuma Y, Serruys PW.
   JACC Cardiovasc Interv. 2015 ;8(8):1053-63.
9. **Snowshoe Versus Ice Skate for Scaffolding of Disrupted Vessel Wall.**
   Serruys PW, Suwannasom P, **Nakatani S**, Onuma Y.
   JACC Cardiovasc Interv. 2015 ;8(7):910-3.
10. **Alternative stents in ST-segment elevation myocardial infarction: improving the efficacy of primary percutaneous coronary intervention.**
    Yetgin T, **Nakatani S**, Onuma Y, van Geuns RJ.
    Future Cardiol. 2015 ;11(3):347-57. doi: 10.2217/fca.15.26.

11. **Relation Between Bioresorbable Scaffold Sizing Using QCA-Dmax and Clinical Outcomes at 1 Year in 1,232 Patients From 3 Study Cohorts (ABSORB Cohort B, ABSORB EXTEND, and ABSORB II).**
Ishibashi Y, **Nakatani S**, Sotomi Y, Suwannasom P, Grundeken MJ, Garcia-Garcia HM, Bartorelli AL, Whitbourn R, Chevalier B, Abizaid A, Ormiston JA, Rapoza RJ, Veldhof S, Onuma Y, Serruys PW.
JACC Cardiovasc Interv. 2015 ;8(13):1715-26.

12. **Incidence and potential mechanism of resolved, persistent and newly acquired malapposition three days after implantation of self-expanding or balloon-expandable stents in a STEMI population: insights from optical coherence tomography in the APPOSITION II study.**
Nakatani S, Onuma Y, Ishibashi Y, Karanasos A, Regar E, Garcia-Garcia HM, Tamburino C, Fajadet J, Vrolix M, Witzenbichler B, Eeckhout E, Spaulding C, Reczuch K, La Manna A, Spaargaren R, Capodanno D, Van Langenhove L, Verheye S, Serruys PW, van Geuns RJ.
EuroIntervention. 2015 ;11(7). pii: 20150309-10.

13. **Comparison between two- and three-dimensional quantitative coronary angiography bifurcation analyses for the assessment of bifurcation lesions: A subanalysis of the TRYTON pivotal IDE coronary bifurcation trial.**
Muramatsu T, Grundeken MJ, Ishibashi Y, **Nakatani S**, Girasis C, Campos CM, Morel MA, Jonker H, de Winter RJ, Wykrzykowska JJ, García-García HM, Leon MB, Serruys PW, Onuma Y; TRYTON Pivotal IDE Coronary Bifurcation Trial Investigators..
Catheter Cardiovasc Interv. 2015 ;86(3):E140-9.

14. **Development and receding of a coronary artery aneurysm after implantation of a fully bioresorbable scaffold.**
Nakatani S, Ishibashi Y, Suwannasom P, Grundeken MJ, Høj Christiansen E, Onuma Y, Serruys PW; ABSORB Cohort B Investigators.
Circulation. 2015 ;131(8):764-7.

15. **Echogenicity as a surrogate for bioresorbable everolimus-eluting scaffold degradation: analysis at 1-, 3-, 6-, 12- 18, 24-, 30-, 36- and 42-month follow-up in a porcine model.**
Campos CM, Ishibashi Y, Eggermont J, **Nakatani S**, Cho YK, Dijkstra J, Reiber JH, Sheehy A, Lane J, Kamberi M, Rapoza R, Perkins L, Garcia-Garcia HM, Onuma Y, Serruys PW.
Int J Cardiovasc Imaging. 2015 ;31(3):471-82.

16. **Incidence and imaging outcomes of acute scaffold disruption and late structural discontinuity after implantation of the Absorb everolimus-eluting fully bioresorbable vascular scaffold: optical coherence tomography assessment in the ABSORB Cohort B trial.**
Onuma Y, Serruys PW, Muramatsu T, **Nakatani S**, van Geuns RJ, de Bruyne B, Dudek D, Christiansen E, Smits PC, Chevalier B, McClean D, Koolen J, Windecker S, Whitbourn R, Meredith I, Garcia-Garcia HM, Veldhof S, Rapoza R, Ormiston JA.
JACC Cardiovasc Intv. 2014;7:1400-11.

17. **Scaffold and edge vascular response following implantation of everolimus-eluting bioresorbable vascular scaffold: a 3-year serial optical coherence tomography study.**
Zhang YJ, Iqbal J, **Nakatani S**, Bourantas CV, Campos CM, Ishibashi Y, Cho YK, Veldhof S, Wang J, Onuma Y, Garcia-Garcia HM, Dudek D, van Geuns RJ, Serruys PW; ABSORB Cohort B Study Investigators..
JACC Cardiovasc Interv. 2014 ;7(12):1361-9.

18. **Bioresorbable vascular scaffold treatment induces the formation of neointimal cap that seals the underlying plaque without compromising the luminal dimensions: a concept based on serial optical coherence tomography data.**
Bourantas CV, Serruys PW, **Nakatani S**, Zhang YJ, Farooq V, Diletti R, Ligthart J, Sheehy A, van Geuns RJ, McClean D, Chevalier B, Windecker S, Koolen J, Ormiston J, Whitbourn R, Rapoza R, Veldhof S, Onuma Y, Garcia-Garcia HM.
EuroIntervention. 2015 ;11(8):746-56.

19. **Automatic detection of bioresorbable vascular scaffold struts in intravascular optical coherence tomography pullback runs.**
Wang A, **Nakatani S**, Eggermont J, Onuma Y, Garcia-Garcia HM, Serruys PW, Reiber JH1, Dijkstra J.M.
Biomed Opt Express. 2014 Sep 12;5(10):3589-602.

20. **Definite and probable bioresorbable scaffold thrombosis in stable and ACS patients.**
Ishibashi Y, **Nakatani S**, Onuma Y.
EuroIntervention. 2015 ;11(3):e1-2.

21. **In vitro validation and comparison of different software packages or algorithms for coronary bifurcation analysis using calibrated phantoms: implications for clinical practice and research of bifurcation stenting.**
Ishibashi Y, Grundeken MJ, **Nakatani S**, Iqbal J, Morel MA, Généreux P, Girasis C, Wentzel JJ, Garcia-Garcia HM, Onuma Y, Serruys PW.
Catheter Cardiovasc Interv. 2015 ;85(4):554-63.

22. **Temporal evolution of strut light intensity after implantation of bioresorbable polymeric intracoronary scaffolds in the ABSORB cohort B trial-an application of a new quantitative method based on optical coherence tomography.**
Nakatani S, Onuma Y, Ishibashi Y, Eggermont J, Zhang YJ, Campos CM, Cho YK, Liu S, Dijkstra J, Reiber JH, Perkins L, Sheehy A, Veldhof S, Rapoza R, van Es GA, Garcia-Garcia HM, van Geuns RJ, Serruys PW; ABSORB Cohort B investigators.
Circ J. 2014;78(8):1873-81.

23. **Anatomically correct three-dimensional coronary artery reconstruction using frequency domain optical coherence tomographic and angiographic data: head-to-head comparison with intravascular ultrasound for endothelial shear stress assessment in humans.**
Papafaklis MI, Bourantas CV, Yonetsu T, Vergallo R, Kotsia A, **Nakatani S**, Lakkas LS, Athanasiou LS, Naka KK, Fotiadis DI, Feldman CL, Stone PH, Serruys PW, Jang IK, Michalis LK.
EuroIntervention. 2015 ;11(4):407-15.

24. **Incomplete stent apposition causes high shear flow disturbances and delay in neointimal coverage as a function of strut to wall detachment distance: implications for the management of incomplete stent apposition.**
Foin N, Gutiérrez-Chico JL, **Nakatani S**, Torii R, Bourantas CV, Sen S, Nijjer S, Petraco R, Kousera C, Ghione M, Onuma Y, Garcia-Garcia HM, Francis DP, Wong P, Di Mario C, Davies JE, Serruys PW.
Circ Cardiovasc Interv. 2014 ;7(2):180-9.

25. **Assessing bioresorbable coronary devices. Methods and parameters.**
García-García HM, Serruys PW, Campos CM, Muramatsu T, **Nakatani S**, Zhang YJ, Onuma Y, Stone GW.
JACC Cardiovasc Imaging. 2014;7:1130-48.

26. **Early (before 6 months), late (6-12 months) and very late (after 12 months) angiographic scaffold restenosis in the ABSORB Cohort B trial.**
Nakatani S, OnumaY, Ishibashi Y, Muramatsu T, Iqbal J, Zhang YJ, van Geuns RJ, Ormiston JA, Serruys PW; on behalf of the ABSORB Cohort B investigators.
Eurointervention. 2015 ;10(11):1288-98

27. **Lessons learned from acute and late scaffold failures in the ABSORB EXTEND trial.**
Ishibashi Y, Onuma Y, Muramatsu T, **Nakatani S**, Iqbal J, Garcia-Garcia HM, Bartorelli AL, Whitbourn R, Abizaid A, Serruys PW.
Eurointervention. 2014;10:449-57.

28. **Everolimus-eluting bioresorbable vascular scaffolds for treatment of patients presenting with ST-segment elevation myocardial infarction: BVS STEMI first study.**
Diletti R, Karanasos A, Muramatsu T, **Nakatani S**, Van Mieghem NM, Onuma Y, Nauta ST, Ishibashi Y, Lenzen MJ, Ligthart J, Schultz C, Regar E, de Jaegere PP, Serruys PW, Zijlstra F, van Geuns RJ.
Eur Heart J. 2014;35:777-86.

29. **Complex bifurcation percutaneous coronary intervention with the Absorb bioresorbable vascular scaffold.**
Dzavík V, Muramatsu T, Crooks N, **Nakatani S,** Onuma Y.
Eurointervention. 2013;9:888.

30. **Implications of a bioresorbable vascular scaffold implantation on vessel wall strain of the treated and the adjacent segments.**
Bourantas CV, Garcia-Garcia HM, Campos CA, Zhang YJ, Muramatsu T, Morel MA, **Nakatani S**, Gao X, Cho YK, Isibashi Y, Gijsen FJ, Onuma Y, Serruys PW.
Int J Cardiovasc Imaging. 2014;30:477-84.

31. **Simultaneous occlusion of left anterior descending and left circumflex arteries by very late stent thrombosis: vascular response to drug-eluting stents assessed by intravascular ultrasound.**
Yamawaki M, Onuma Y, Nakano M, Muramatsu T, **Nakatani S**, Ishibashi Y, Ishimori H, Hirano K, Ito Y, Tsukahara R, Muramatsu T.
Heart and Vessels. 2015 ;30(6):824-9.

32. **Early and late optical coherence tomography findings following everolimus-eluting bioresorbable vascular scaffold implantation in myocardial infarction: a preliminary report.**
Karanasos A, Muramatsu T, Diletti R, Nauta S, Onuma Y, Lenzen M, **Nakatani S**, van Mieghem NM, Schultz C, de Jaegere PP, Serruys PW, Zijlstra F, Regar E, van Geuns RJ.
Hellenic J Cardiol. 2015;56:125-35.

33. **Fast virtual functional assessment of intermediate coronary lesions using routine angiographic data and blood flow simulation in humans: comparison with pressure wire - fractional flow reserve.**
Papafaklis MI, Muramatsu T, Ishibashi Y, Lakkas LS, **Nakatani S**, Bourantas CV, Ligthart J, Onuma Y, Echavarria-Pinto M, Tsirka G, Kotsia A, Nikas DN, Mogabgab O, van Geuns RJ, Naka KK, Fotiadis DI, Brilakis ES, Garcia-Garcia HM, Escaned J, Zijlstra F, Michalis LK, Serruys PW.
Eurointervention. 2014;10:574-83.

34. **Serial optical frequency domain imaging in STEMI patients: the follow-up report of TROFI study.**
García-García HM, Muramatsu T, **Nakatani S**, Lee IS, Holm NR, Thuesen L, van Geuns RJ, van der Ent M, Borovicanin V, Paunovic D, Onuma Y, Serruys PW.
Eur Heart J Cardiovasc Imaging. 2014;15:987-95.

35. **How clinically effective is intravascular ultrasound in interventional cardiology? Present and future perspectives.**
Nakatani S, Proniewska K, Pociask E, Paoletti G, de Winter S, Muramatsu T, Bruining N.
Expert Rev Med Devices. 2013;10:735-49.

Acknowledgement

ACKNOWLEDGEMENT

I would like to say thank you to everyone who have sustained me to achieve this thesis. First, I greatly appreciate my father for his huge support continuously. You never ask me the detailed thing, but care about me every time, which is the traditional Japanese style of father's affection. With your silent warmth, I successfully started to study abroad just 6 months after planning and encouraged me to continue working at the two big accidents with our family during the fellow-ship. You did not have enough money by the income of the university hospital to feed the four brothers including me, therefore You could not get the Ph.D. status. It is my great pleasure that I achieved the Ph.D. status instead of you by your full support.

Prof. Patrick W Serruys, you are one of the most famous cardiologists in the world, but for me, the most friendly professor in my life. I was very surprised that you sometimes asked my opinions. Compared to your intelligence, my opinion was no meaning and no intelligence. Of course, I know it was your style of education, however it would be the pride of a lifetime that I discussed something with Prof. Serruys on even ground. In addition, I appreciated that you accepted my character as a "Osaka boy", whose attitude was completely different from the previous polite Japanese fellows. I could enjoy working as your research fellow in Rotterdam with my natural style of "Osaka boy".

Yoshi-san, I honestly appreciate your support during the stay in Rotterdam and the process of achieving this thesis. At the first time we met in Kokura Live Japan for the interview, I decided to work with you by intuition since I felt that you have everything which I do not have. As I worked with you almost every day, I confirmed that your thinking and your reactions were completely different from mine, which inspired and thought me a lot of things. In private life, you care my family, Mako and my wife, kindly and supported us when we had a hard time due to the accidents. I will never forget your mercy to us.

Dear the members of doctoral committee: Prof. R.J. van Geuns, Dr. E.S. Regar, Prof. J.H.C. Raiber, Prof. Y. Ozaki, Dr. J. Wykrzykowska, Dr. J. Dijkstra. Sincerely I would like to thank all of you for critical evaluation of my thesis.

Yuki-sensei, we shared everything during the stay in Rotterdam. The period of stay was almost same, the family members were almost similar, but the characters were completely different. I guess that we can live together with the good relationship separately. It was very appreciated that you helped my research and recovered a lot of things, especially when the "Christmas shock". Let's enjoy our thesis!

Dear Maik, it was my great pleasure that we met and become a friends in the Netherlands. When I came back to the Netherlands after 1 months stay in Japan, you sit the space which I worked comfortably. At that time, you kindly make my space, of course, with your space. I thought that you are the master of making the relationship with so-called "win win". Your attitude was very polite and honest compared to my "Osaka boy". It was a very good memory that we traveled Kobe Japan for CCT 2014 together. Please keep in touch for a long time.

It was a special experience to work with so many international fellows from Thorax Center: Takashi Muramatsu, Chris Bourantas, Yao-Jun Zhang, Javaid Iqbl, Roberto Diletti, Carlos Campos, Yun-Kyong Cho, Pannipa Suwannasom, Hiroki Tateishi, Erhan Tenekecioglu, Yaping Zeng and Yohei Sotomi. I would like to say thank you for sharing the time in the Netherlands.

It was very exciting to collaborate with the Laiden University: Jouke Dijkstra, Jeroen Eggermont, Shengnan Liu (Nancy), Ancong Wang and Medis team. This thesis would not exist without the team collaboration with you.

Maria-angele Morel, thank you for your kindness to fellows and invited us to the traditional Dutch ceremony many times. We could enjoy them and understood the Dutch style very well. I must thank many staffs working in the CARDIALYSIS for their kind friendship and technical assistance.

My deep appreciation goes to the staff of EuroIntervention: Paul Cummins and Sylvie.

Dear Hanny-san, you are the big sister of Japanese fellows. When we were very afraid of the new life in Netherlands, your kind support with tender care encouraged us to survive. And your Japanese words such as “Arigato Gozaimasu” or “Ohayo Gozaimasu” made us relived in Cardyalisis.

Finally, I would like to say thank you to the doctor who I respect the best, Eriko Nakatani. You supported me as my wife, managed our family as Mako’s mother and encourage my challenge of achieving this thesis as my partner.

May 2016,
With my best regards,
Shimpei